Developing Image-Guided, Bedside 3D Printing Practice in Plastic & Reconstructive Surgery

Michael P Chae

MBBS, BMedSc

Supervisors:

Professor Julian A Smith

A/Professor David J Hunter-Smith

Professor Warren M Rozen

A thesis submitted for the degree of Doctor of Philosophy at

Monash University in 2019

Department of Surgery (Monash Medical Centre)

School of Clinical Sciences at Monash Health

Faculty of Medicine, Nursing and Health Sciences

2 Copyright Notice

I certify that I have made all reasonable efforts to secure copyright permissions for third-party content included in this thesis and have not knowingly added copyright content to my work without the owner's permission.

3 Abstract

Modern imaging technologies are essential for preoperative planning in plastic and reconstructive surgery (1-3). Evidences demonstrate that enhanced visualization of microvascular anatomy and tissue perfusion lead to significant improvement in clinical outcomes (4-6). In breast reconstructive surgery, computed tomographic angiography (CTA) is considered the gold standard perforator imaging technology due to its high accuracy and reliability (5, 7-14). However, currently all imaging modalities are limited by being displayed on a 2D surface, such as a computer screen. In contrast, a patient-specific, 3D-printed biomodel can provide tactile feedback enhancing spatio-temporal understanding of the anatomy (15).

As key patents began to expire in early 2000s, 3D printing, also known as additive manufacturing or rapid prototyping, has become relatively affordable and accessible for clinicians (16-20) (Figure 3.1).

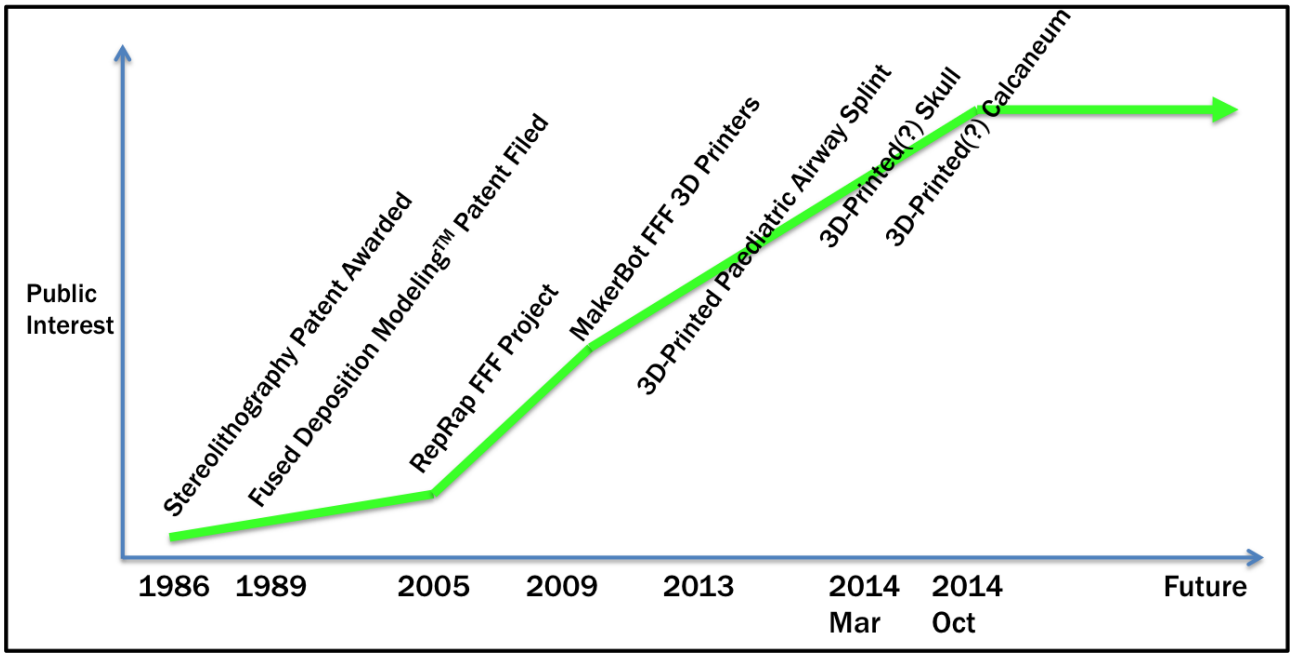

Figure 3.1. Increasing public interest and adoption of 3D printing technology in medical application.

In summary, it appears most useful for aiding preoperative planning (21), developing intraoperative guidance devices (22), educating patients and junior surgical trainees (23), and designing patient-specific custom prosthesis (16-18, 24).

Despite its potential, widespread adoption of 3D printing in clinical setting has been limited due to its perceived high cost and technical difficulty (25, 26). As a result, clinicians have resorted to outsourcing it, which adds cost and lead time that may be appropriate in certain clinical indications (26). Hence, the current research project has been undertaken to develop an in-house 3D printing service for application in plastic and reconstructive surgery that is affordable, easy-to-use and reproducible, thereby “bringing it to the bedside”.

Firstly, accuracy and validity of the bespoke Peninsula 3D printing workflow is investigated. This is followed by studies demonstrating its utility in various clinical indications in plastic and reconstructive surgery. Finally, this technology has been translated to use in post-mastectomy autologous breast reconstruction setting.

4 Declaration

This thesis contains no material which has been accepted for the award of any other degree or diploma at any university or equivalent institution and that, to the best of my knowledge and belief, this thesis contains no material previously published or written by another person, except where due reference is made in the text of the thesis.

Michael P Chae

Date: 12/03/2019

5 Publications during enrolment

Thesis including published works declaration

I hereby declare that this thesis contains no material which has been accepted for the award of any other degree or diploma at any university or equivalent institution and that, to the best of my knowledge and belief, this thesis contains no material previously published or written by another person, except where due reference is made in the text of the thesis.

This thesis includes 13 original papers published in peer-reviewed journals, 2 peer-reviewed book chapters, 4 submitted publications and 1 poster presentations. The core theme of the thesis is advancement of 3D imaging and printing techniques in plastic and reconstructive surgery. The ideas, development and writing up of all the papers in the thesis were the principal responsibility of myself, the student, working within the Department of Surgery (Monash Medical Centre), School of Clinical Sciences at Monash Health, Faculty of Medicine, Nursing and Health Sciences under the supervision of Prof Julian Smith, A/Prof David Hunter-Smith, and A/Prof Warren Rozen.

The inclusion of co-authors reflects the fact that the work came from active collaboration between researchers and acknowledges input into team-based research.

In the case of 4 chapters, my contribution to the work involved the following:

Thesis Chapter	**Publication Title**	**Status** *(published, in press, accepted or returned for revision, submitted)*	**Nature and % of student contribution**	**Co-author name(s) Nature and % of Co-author's contribution***	**Co-author(s), Monash student Y/N***
Chapter 10.1	Comparative analysis of fluorescent angiography, computed tomographic angiography and magnetic resonance	Published	80%. Concept, data collection, data analysis, writing	1) David Hunter-Smith, concept, data analysis, edit 10%	N
				2) Warren Rozen, concept, data analysis, edit 10%	N

	angiography for planning autologous breast reconstruction				
Chapter 10.2	Emerging applications of bedside 3D printing in plastic surgery	Published	65%. Concept, data collection, data analysis, writing	1) Warren Rozen, concept, data analysis, edit 10%	N
				2) Paul McMenamin, edit 5%	N
				3) Michael Findlay, edit 5%	N
				4) Robert Spychal, edit 5%	N
				5) David Hunter-Smith, concept, data analysis, edit 10%	N
Chapter 12.1.2	Comparative study of software techniques for 3D mapping of perforators in DIEP flap planning	Published	55%. Data collection, data analysis, writing	1) Warren Rozen, concept, data collection, data analysis, edit 40%	No
				2) David Hunter-Smith, concept, data analysis, edit 5%	No
Chapter 12.1.3.1	The accuracy of clinical 3D printing in plastic surgery: literature review and in vivo validation study	Submitted	70%. Concept, data collection, data analysis, writing	1) Ru Dee Chung, data analysis 5%	Y
				2) Julian Smith, edit 5%	N
				3) Warren Rozen, concept, data analysis, edit 10%	N
				4) David Hunter-Smith, concept, data analysis, edit 10%	N
Chapter	Use of three-	Published	55%. Concept,	1) Miguel Cabalag,	N

12.2.1.1	dimensional printed “haptic” models for preoperative planning in an Australian plastic surgery unit		data collection, data analysis, writing, edit	data analysis, writing 20%	
				2) George Miller, data analysis, edit 10%	N
				3) Warren Rozen, concept, data analysis, edit 5%	N
				4) David Hunter-Smith, concept, data analysis, edit 10%	N
Chapter 12.2.2.2	3D-printed haptic “reverse” models for preoperative planning in soft tissue reconstruction	Published	60%. Concept, data collection, data analysis, writing	1) Frank Lin, data collection 5%	N
				2) Robert Spychal, edit 5%	N
				3) David Hunter-Smith, concept, data analysis, edit 15%	N
				4) Warren Rozen, concept, data analysis, edit 15%	N
Chapter 12.2.2.3	3D volumetric modeling and microvascular reconstruction of irradiated lumbosacral defects after oncologic resection	Published	55%. Data collection, data analysis, writing	1) Emilio Garcia-Tutor, concept, data collection, writing, edit 15%	No
				2) Marco Romeo, concept, data collection, edit 10%	No
				3) David Hunter-Smith, concept, data analysis 10%	No
				4) Warren Rozen, concept, data analysis 10%	No
Chapter	4D printing: a new	Published	55%. Concept,	1) David Hunter-	N

12.2.4.1	evolution in CT-guided stereolithographic modeling. Principles and applications		data collection, data analysis, writing	Smith, concept, data analysis 10%	
				2) Inoka De Silva, data collection 5%	N
				3) Stephen Tham, concept, data collection 10%	N
				4) Robert Spychal, data analysis 5%	N
				5) Warren Rozen, concept, data analysis 15%	N
Chapter 12.2.4.3	Direct augmented reality computed tomographic angiography technique (ARC): an innovation in preoperative imaging	Published	65%. Concept, data collection, data analysis, writing	1) Dasun Ganhewa, data collection 5%	Y
				2) David Hunter-Smith, concept, data analysis, edit 10%	N
				3) Warren Rozen, concept, data collection, data analysis, edit 20%	N
Chapter 12.3.1.1	The extended DIEP flap	Published	55%. Data collection, data analysis, writing	1) Venkat Ramakrishnan, concept, data collection, data analysis 20%	N
				2) David Hunter-Smith, concept, data collection, data analysis 10%	N
				3) Warren Rozen, concept, data collection, data analysis 15%	N

Chapter 12.3.1.2	Breast volumetric analysis for aesthetic planning in breast reconstruction: a literature review of techniques	Published	75%. Concept, data collection, data analysis, writing	1) Warren Rozen, concept, edit 10%	N
				2) Robert Spychal, edit 5%	N
				3) David Hunter-Smith, concept, edit 10%	N
Chapter 12.3.2.1	3D volumetric analysis for planning breast reconstructive surgery	Published	75%. Concept, data collection, data analysis, writing	1) David Hunter-Smith, concept, edit 10%	N
				2) Robert Spychal, edit 5%	N
				3) Warren Rozen, concept, edit 10%	N
Chapter 12.3.2.2	3D-printed, patient-specific DIEP flap templates for preoperative planning in breast reconstruction: A prospective case series	Submitted	60%. Concept, data collection, data analysis, writing	1) David Hunter-Smith, concept, data collection, data analysis, edit 15%	N
				2) Ru Dee Chung, data analysis 5%	Y
				3) Julian Smith, edit 5%	N
				4) Warren Rozen, concept, data collection, data analysis edit 15%	N
Chapter 12.3.2.3	Enhanced preoperative deep inferior epigastric artery perforator flap planning with a 3D-printed perforasome template: Technique and case report	Published	60%. Concept, data collection, data analysis, writing	1) David Hunter-Smith, concept, data collection, data analysis, edit 15%	N
				2) Marie Rostek, edit 5%	N
				3) Julian Smith, edit 5%	N

				4) Warren Rozen, concept, data collection, data analysis edit 15%	N
Chapter 12.3.2.4	Enhancing breast projection in autologous reconstruction using the St Andrew's Coning Technique and 3D volumetric analysis	Published	55%. Concept, data collection, data analysis, writing	1) Warren Rozen, concept, edit 10%	N
				2) Nakul Patel, concept, data collection, data analysis 15%	N
				3) David Hunter-Smith, edit 5%	N
				4) Venkat Ramakrishnan, concept, data analysis, edit 15%	N
Chapter 12.3.3.1	3D bioprinting in nipple areolar reconstruction: Principles and clinical techniques	Published	60%. Concept, data collection, data analysis, writing	1) David Hunter-Smith, concept, edit 10%	No
				2) Warren Rozen, concept, edit 10%	No
				3) Sean Murphy, edit 10%	No
				4) Anthony Atala, edit 10%	No
Chapter 12.3.3.2	3D bioprinting adipose tissue for breast reconstruction	Published	60%. Concept, data collection, data analysis, writing	1) David Hunter-Smith, concept, edit 10%	No
				2) Sean Murphy, edit 10%	No
				3) Michael Findlay, concept, data analysis 20%	No
Chapter 13.1	3D imaging and printing techniques in plastic and	Submitted	60%. Concept, data collection, data analysis,	1) David Hunter-Smith, concept, edit 20%	No

	reconstructive surgery: established techniques		writing	2) Warren Rozen, concept, edit 20%	No
Chapter 13.2	3D imaging and printing techniques in plastic and reconstructive surgery: emerging techniques	Submitted	60%. Concept, data collection, data analysis, writing	1) David Hunter-Smith, concept, edit 20%	No
				2) Warren Rozen, concept, edit 20%	No

**If no co-authors, leave fields blank*

I have renumbered sections of submitted or published papers in order to generate a consistent presentation within the thesis.

Student signature: [redacted] **Date:** 14/12/2018

The undersigned hereby certify that the above declaration correctly reflects the nature and extent of the student's and co-authors' contributions to this work. In instances where I am not the responsible author I have consulted with the responsible author to agree on the respective contributions of the authors.

Main Supervisor signature: [redacted] **Date:** 14/12/2018

6 Acknowledgements

My Supervisors:

This work would have been impossible without abundant support and astute guidance from my supervisors. More often than not, I would question our original research hypothesis and become despondent at my own progress. At these difficult times, they were always present to provide constructive feedbacks and encourage me emotionally to push through the barriers in the path towards “truth-seeking” and completion of this thesis.

Prof Julian Smith

A/Prof David Hunter-Smith

Prof Warren Rozen

Collaborators:

Current list does not do the justice of including all the people who have helped and contributed towards the completion of this body of work. However, the following group of institutions and professional people are especially worth mentioning, for their support without much in the way of retribution, I am forever in debt.

Department of Surgery, Peninsula Health:
As my “home base” institution where I first began my work as a junior medical officer, the support I received from Peninsula Health, both intellectually and financially, has been incredible. Luckily, they had faith in our endeavour, which we had taken “advantage” of in order to purchase five 3D printers, newest computer suites and a dedicated space to establish our bespoke 3D PRINT laboratory.

A/Prof Robert Spychal

Ms Marie Rostek

Mr Mathew Lee

Mr George Pratt

Dr Rhys Van Der Rijt

Dr Robert Capstick

Dr Felicity Connon

Dr Jessie Xu

Dr Dasun Ganhewa

Dr Bethany Reynolds

Dr Vicky Tobin

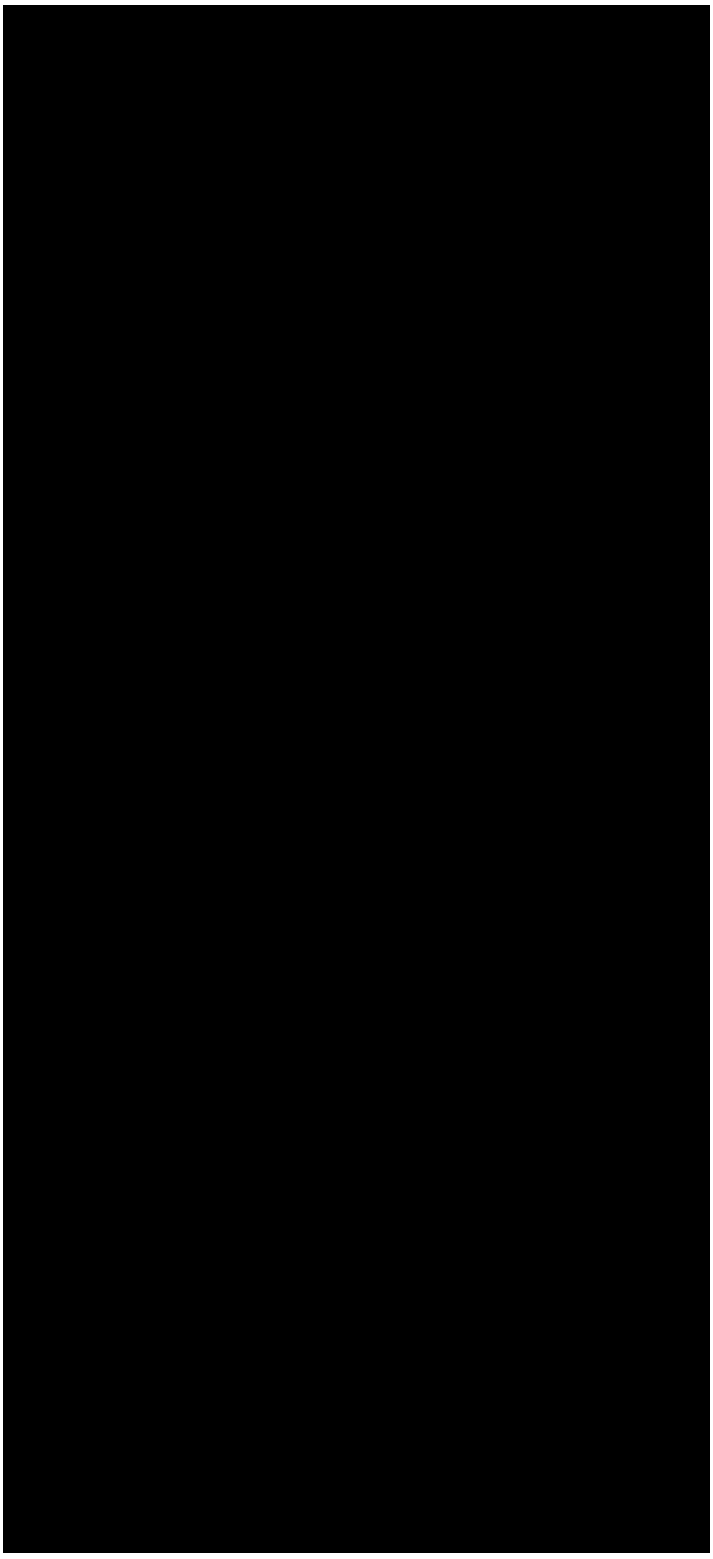

Department of Plastic Surgery, Eastern Health:

When I needed more patients, Eastern Health has been generous in not only providing these cases but also the following list of incredible medical professionals whose intellectual support and company, I had the pleasure of encountering. I owe this thesis to them.

Mr Dean White

Mr Frank Lin

Mr Alex Yuen

Ms Beryl Tan

Mr Snazz Shah

Dr Justin Easton

Dr Kim Hughes

Dr Saj Shukula

Ramsay Health:

Similarly, Ramsay Health has been generous in providing access to their patients and extending my recruitment.

Dr Carola Whitton

Department of Radiology, Peninsula Health:

Without their trust in our research project and generous access to the imaging facilities, it would haven't been impossible to scan so many objects and patients, for which I owe immense gratitude.

Mr Andrew Bickell

7 Figures and Tables

Chapter 3

Figure 3.1: Increasing public interest and adoption of 3D printing technology in medical application.

Chapter 10.1

Table 10.1.1: Comparison of basic characteristics of the perforator imaging technologies. Abbreviation: ICGA: indocyanine green angiography; CTA: computed tomographic angiography; MRA: magnetic resonance angiography; NA: not applicable; 3D: three-dimensional.

Table 10.1.2: Comparison of accuracy of the perforator imaging technologies. Abbreviations: FA: fluorescent angiography; CTA: computed tomographic angiography; MRA: magnetic resonance angiography; P: prospective study; R: retrospective study; ICGD: indocyanine green dye; FD: fluorescein dye; N/A: not available; EP: equilibrium phase.

Table 10.1.3: Comparison of clinical outcomes from the perforator imaging technologies. Abbreviations: FA: fluorescent angiography; CTA: computed tomographic angiography; MRA: magnetic resonance angiography; P: prospective study; R: retrospective study; vs: versus; NA: not available.

Figure 10.1.1: Computed tomographic angiogram (CTA) with volume rendered technique (VRT) reformat, demonstrating a large 1.5mm perforator (blue arrow) and multiple smaller perforators (yellow arrows) at the point at which they pierce the anterior rectus sheath. A numbered grid is centered at the umbilicus for localization. The superficial inferior epigastric artery (SIEA) and vein (SIEV) on each side is demonstrated.

Figure 10.1.2: Computed tomographic angiogram (CTA) with volume rendered technique (VRT) reformat, demonstrating the branching pattern of the deep inferior epigastric arteries (DIEAs). The left side is a type 2 (bifurcating) pattern and the right is a type 3 (trifurcating) pattern. U = Umbilicus.

Figure 10.1.3: Computed tomographic angiogram (CTA) with axial maximum intensity projection (MIP) reformat, demonstrating the subcutaneous course of perforators. Based on the subcutaneous distribution and branching pattern of the perforator selected (arrow), a preoperative estimate of well-vascularized flap volume can be achieved.

Figure 10.1.4: Volume-rendered, three dimensional reconstructions of the cutaneous perforators of the deep inferior epigastric artery (DIEA) using computed tomography angiography (CTA) on the left, and magnetic resonance angiography (MRA) on the right. Three large (>1mm) perforators were demonstrated with both modalities (light blue arrows), while one large perforator was demonstrated on CTA alone (dark blue arrow).

Chapter 10.2

Figure 10.2.1: Steps involved from imaging to 3D-printed models. Abbreviations: DICOM: digital imaging and communications in medicine; CT: computed tomography; MRI: magnetic resonance imaging

Table 10.2.1: A summary of the most commonly used 3D printing techniques in medical application. Abbreviations: SLA: stereolithography; MJM: multijet modeling; SLS: selective laser sintering; BJT: binder jet technique; FDM: fused deposition modeling.

Figure 10.2.2: 3D printed haptic model of a heart and the great vessels fabricated using Projet x60 series 3D printers.

Table 10.2.2: A summary of 3D modeling softwares that can convert a DICOM data from a standard CT/MRI scans into a CAD file. Abbreviations: STL: standard tessellation language; OS: operating system; Y: yes; N: no; W; Windows OS; M: Mac OS.

Table 10.2.3: A summary of commercially available 3D printers from ten leading 3D printing companies in the world. Where a 3D printer series is characterized, the lowest cost, largest print area, lowest print resolution, largest printer size and greater printer weight are selected for comparison. Abbreviations: SLA: stereolithography; MJM: multijet modeling; SLS: selective laser sintering; BJT: binder jet technique; FDM: fused deposition modeling; cm: centimeter; kg: kilograms; nm: nanometers; N/A: not available.

Table 10.2.4: A summary of average raw material cost of each 3D printing technique. Abbreviations: SLA: stereolithography; MJM: multijet modeling; SLS: selective laser sintering; BJT: binder jet technique; FDM: fused deposition modeling; L: liter.

Table 10.2.5: A summary of published application of 3D printing in Plastic and Reconstructive Surgery. Abbreviations: DIEA: deep inferior epigastric artery; 4D: four dimensional; N/A: not available.

Figure 10.2.3: Photograph of the soft tissue ankle defect showing the exposed metal hardware from a previous ankle reconstruction.

Figure 10.2.4: 3D image of the right (pathological) ankle is juxtaposed to the left (normal) ankle (A). The left ankle is reflected (B) and superimposed on to the right ankle (C). These

images are subtracted from each other to produce a “reverse” model of the soft tissue defect (D-F).

Figure 10.2.5: 3D printed haptic model of the soft tissue ankle defect.

Figure 10.2.6: 3D printed haptic model of the “reverse” image representing the wound defect.

Figure 10.2.7: 3D reconstructed CT images of a patient with breast asymmetry post-mastectomy (A) and the 3D printed breast model of the same patient (B).

Figure 10.2.8: 4D printed haptic models of carpal and metacarpal bones demonstrating thumb abduction (from left to right).

Chapter 11.1

Table 11.1.1: Parameters used for standard CTA.

Chapter 12.1.1

Figure 12.1.1.1: (A) Our original set-up consisted of simply a laptop computer and a desktop 3D printer. (B) As our funding and productivity grew, we set up in a designated office space within the Peninsula Health Department of Surgery with larger and faster desktop personal computer and a wide array of 3D printers. Appropriately, we have named it 3D PRINT (Peninsula health Reconstructive Imaging and Nascent Technology) laboratory.

Figure 12.1.1.2: Summary of 3D printing process. Initially, the patient data from an imaging source, such as CT, MRI and 3D photography, are exported in DICOM file format. Using image rendering software, DICOM files are 3D rendered into STL file format, isolating the region of interest. Using image processing software, further modifications can be applied, such as surface smoothing. Using image slicing software, the files are converted into G-code file format, which is compatible with 3D printers.

Figure 12.1.1.3: 3D printers owned by 3D PRINT laboratory. (A) Ultimaker 3E, (B) Moment 1, (C) Replicator Z18, (D) Cube 2, (E) M-One.

Table 12.1.1.1: Summary of 3D printers owned by 3D PRINT laboratory. Abbreviations: FFF: fused filament fabrication; SLA: stereolithography.

Table 12.1.1.2: Pre-print checklist for 3D printing.

Chapter 12.1.2

Table 12.1.2.1: Computed tomographic scan parameters. Abbreviations: CT: computed tomographic; HU: Hounsfield units.

Figure 12.1.2.1: Colour look-up table (CLUT) and ray cast lighting properties in Siemens Syngo InSpace 4D (Siemens, Erlangen, Germany).

Figure 12.1.2.2: Colour look-up table (CLUT) in Osirix (Pixmeo, Geneva, Switzerland), designed for perforator imaging.

Table 12.1.2.2: Mean transverse distance of DIEA perforators from the midline as identified using the 3D imaging softwares: Siemens Syngo InSpace 4D (Siemens, Erlangen, Germany) and Osirix (Pixmeo, Geneva, Switzerland).

Figure 12.1.2.3: Preoperative computed tomographic angiography (CTA), volume-rendered reconstruction of the abdominal wall vasculature with (A) Osirix (Pixmeo); and (B) Siemens Syngo InSpace 4D (Siemens). Both techniques clearly demonstrate several large periumbilical perforators (Blue arrows), and highlight features of the abdominal wall soft tissues.

Table 12.1.2.3: Comparing the mean transverse distance of DIEA perforators from the midline calculated using Siemens Syngo InSpace 4D (Siemens, Erlangen, Germany) to the intraoperative measurements.

Table 12.1.2.4: Comparing the mean transverse distance of DIEA perforators from the midline calculated using Osirix (Pixmeo, Geneva, Switzerland) to the intraoperative measurements.

Table 12.1.2.5: Analysis of discrepancy found in the perforator localization between imaging and operative findings and their distribution between medial and lateral rows.

Chapter 12.1.3.1

Figure 12.1.3.1.1: Steps involved in creating a CT-based 3D-printed anatomical biomodel. Error can be introduced at each step. Abbreviations: CT: computed tomography; DICOM: digital imaging and communications in medicine; STL: standard tessellation language.

Figure 12.1.3.1.2: Design of our validation study using radius of chicken (*Gallus gallus domesticus*). A: butchered chicken wing; B: digital Vernier caliper (Kincrome; Scoresby, VIC, Australia); C: dissected chicken radius with its articular cartilages removed; D: measuring the bone length directly from CT scan using software ruler within OsiriX program (Pixmeo, Geneva, Switzerland); E: measuring the bone length from its 3D-reconstructured STL file using software ruler within Autodesk MeshMixer program

(Autodesk Inc., San Rafael, CA, USA); F: measuring the bone length from its 3D-printed model using the caliper. Abbreviations: CT: computed tomography; STL: standard tessellation language.

Table 12.1.3.1.1: Summary of studies that assess the accuracy of medical 3D printing using linear measurements on cadaveric specimens Abbreviations: CT: computed tomography; MDCT: multidetector CT; CBCT: cone beam CT; mm: millimetre; Y: yes; N: no; SLA: stereolithography; BJT: binder jet technique; SLS: selective laser sintering; FFF: fused filament fabrication; PJT: PolyJet technology; N/A: not available; CMM: coordinate measuring machine.

Table 12.1.3.1.2: Summary of difference of the maximum length of chicken radius bone (gold standard) against CT DICOM images (CT), image segmentation (SEG), and 3D-printed models (3DP). Abbreviations: CT: computed tomography; SEG: image segmentation; 3DP: 3D printing; CI: confidence interval; mm: millimetre.

Chapter 12.1.3.2

Figure 12.1.3.2.1: Photograph of the 50 rocks used for volumetric analysis by water displacement (left) and Screenshot of 3D reconstructed virtual models of the rocks by 3D slicer (right).

Figure 12.1.3.2.2: Screenshot of segmented trapezium (Pink, left) and Pisiform (Purple, centre) and 3D virtual surface model of trapezium and pisiform (right).

Table 12.1.3.2.1: Volumetric analysis of the rocks by water displacement and 3D slicer.

Table 12.1.3.2.2: The volumes of the trapezium and pisiform surface models (average ± standard deviation) measured using 3D slicer for the inter-user variability studies.

Table 12.1.3.2.3: Shows the volumes of the trapezium and pisiform surface models (average volume ± standard deviation) measured using the 3D slicer for the intra-user variability studies.

Chapter 12.2.1.1

Figure 12.2.1.1.1: (clockwise from left to right) preoperative clinical photograph, three-dimensional computed tomography showing erosion of right hemi-mandible, three-dimensional reconstruction with associated soft tissue tumour.

Figure 12.2.1.1.2: (from left to right) three-dimensional model of right hemi-mandible without tumour, three-dimensional model with soft tissue tumour and intraoperative specimen.

Figure 12.2.1.1.3: Seven-month post-operative three-dimensional computed tomography and clinical photograph.

Chapter 12.2.1.2

Figure 12.2.1.2.1: Bone scan showed multilevel facet arthropathy and an extensive scoliosis concave to the left.

Figure 12.2.1.2.2: CT scan showed severe multilevel degenerative disc disease, marked curvature of the spine at the thoracolumbar junction and compensatory lumbar curvature. Extensive facet arthropathy and calcific arachnoiditis.

Figure 12.2.1.2.3: The 3D reconstructions were hard to use, only allowed short and long axis rotation and as presented were not optimised for caudad-cephalad viewing.

Figure 12.2.1.2.4: The 3D model was slow to print but gave great detail and allowed unlimited long, short axis rotation and everything in between.

Figure 12.2.1.2.5: AP and lateral spine X-rays showing implanted stimulator leads.

Chapter 12.2.2.2

Figure 12.2.2.2.1: Soft tissue defect overlay the right ankle, with ankle prosthesis exposed.

Figure 12.2.2.2.2: 3D reconstructed volume-rendered computed tomography (CT) image of the recipient site demonstrated the soft tissue defect, performed with Osirix software (Pixmeo, Geneva, Switzerland).

Figure 12.2.2.2.3: (A) Cropped 3D images of the right and left ankle were loaded into Magics software (Materialise) and placed side-by-side in anatomical position. (B) Left ankle was reflected on Y–Z plane so that it was aligned and pointed in the same direction as the right ankle. (C) Mirror image of the left ankle was superimposed on the right ankle. (D–F) Right ankle and the intersected parts were “subtracted” from the mirrored image of left ankle using Boolean function available in the Magics software.

Figure 12.2.2.2.4: 3D printed model of the right ankle was created using the Cubify software and printed by the Cube 2 printer.

Figure 12.2.2.2.5: 3D printed model of the “reverse image” was created using the Cubify software and printed by the Cube 2 printer.

Figure 12.2.2.2.6: (A) Cropped 3D images of the forearm donor site were loaded into Magics software (Materialise), with the previously developed “defect analysis” image loaded side-by-side in anatomical positions. (B-C) The donor site and the “reverse image” were superimposed. (D-E) The “reverse image” was “subtracted” from the forearm to evaluate the reconstructive needs during harvest.

Figure 12.2.2.2.7: Defect was reconstructed with free radial forearm flap, and demonstrated appropriate filling of the soft tissue defect.

Chapter 12.2.2.3

Table 12.2.2.3.1: Patient demographics and operative details. Abbreviations: M: male; F: female; SCC: squamous cell carcinoma; RIS: radiation-induced sarcoma; ES: Ewing’s sarcoma; P: primary; R: recurrence; SGA: superior gluteal artery; SA: subcostal artery; I: immediate; D: delayed’ Y: yes; N: no.

Figure 12.2.2.3.1: Preoperative computed tomography scan, showing the three-dimensional nature of a sacral defect.

Figure 12.2.2.3.2: Surface-rendered reconstruction images derived from a preoperative computed tomography scan, showing the three-dimensional nature of a sacral defect (A-C: three dimensional rotating views).

Figure 12.2.2.3.3: Three-dimensional (3D) printed model of the sacral defect shown in Figure X2, produced using a 3D printer (Cube 2 printer; 3D Systems, Rock Hill, SC, USA) (A-C: three dimensional rotating views).

Figure 12.2.2.3.4: A 25 cm x 10 cm surface area sacral defect requiring reconstruction.

Figure 12.2.2.3.5: A free latissimus dorsi myocutaneous flap was selected for reconstruction of the defect, with donor site marked.

Figure 12.2.2.3.6: Free latissimus dorsi myocutaneous flap harvested, with templated skin paddle and muscle for volumetric filling.

Figure 12.2.2.3.7: Flap inset into sacral defect, with adjacent remnants of previous locoregional reconstructive flaps.

Figure 12.2.2.3.8: A 18 cm x 20 cm surface area sacral defect requiring reconstruction.

Figure 12.2.2.3.9: Free latissimus dorsi muscle only flap inset into the defect.

Chapter 12.2.3.1

Figure 12.2.3.1.1: CT data of the hand during key pinch is 3D reconstructed using (A) surface rendering and (B) volume rendering function in Osirix (Pixmeo, Geneva, Switzerland). (C) The 3D image is exported on to Cubify (3D Systems, Rock Hill, SC) to be rendered suitable for 3D printing.

Figure 12.2.3.1.2: 3D-printed haptic models representing carpal and metacarpal bones during various hand movements: abduction (left), opposition (center), and key pinch (right).

Figure 12.2.3.1.3: 4D-printing demonstrating the transition of carpal and metacarpal bones during opposition (from left to right).

Figure 12.2.3.1.4: Summary of graphs demonstrating the “abduction” angle (first row) and the “flexion” angle (second row) measured using a goniometer or directly from the 4D CT data.

Table 12.2.3.1.1: Print duration of each stage of 4D-printed thumb movements.

Table 12.2.3.1.2: Summary of angles calculated between the first and the second metacarpal bones during various thumb movement.

Chapter 12.2.3.2

Figure 12.2.3.2.1: Direct augmented reality computed tomographic angiography technique (ARC) setup: comprising the MacBook Pro portable computer (Apple Inc., Cupertino, CA, USA), Philips PicoPix Pocket Projector (Philips, Amsterdam, The Netherlands), a 15-cm ruler and OsiriX computer software (Pixmeo, Geneva, Switzerland).

Figure 12.2.3.2.2: Direct augmented reality computed tomographic angiography technique (ARC) for thigh flap perforator mapping (in a case of an anterolateral thigh flap). (A) Maintaining the same distance of the projector away from the patient at calibration, the 3D-reconstructed image of ALT perforators is loaded on OsiriX software and projected onto the patient’s thigh, marking the cutaneous perforator location (blue arrow). (B) A maximum intensity projection (MIP) reconstruction view of the perforator is projected onto the patient’s thigh to show the intramuscular course of the perforator selected. (C) The same MIP reconstruction view of the perforator is used to show the source vascular pedicle.

Figure 12.2.3.2.3: Direct augmented reality computed tomographic angiography technique (ARC) for deep inferior epigastric artery (DIEA) perforator (DIEP) flap planning. (A) Maintaining the same distance of the projector away from the patient at calibration, the 3D-reconstructed image of DIEA perforators is loaded on OsiriX software and projected onto the patient’s abdomen, marking the cutaneous perforator location (blue arrow). Yellow arrows demonstrates smaller perforators. (B) A maximum intensity projection (MIP)

reconstruction view of the perforator is projected onto the patient's abdomen to show the subcutaneous course of the perforator selected. (C) The same MIP reconstruction view of the perforator is used to show the intramuscular course of the perforator selected. (D) The same MIP reconstruction view of the perforator is used to show the source vascular pedicle.

Chapter 12.3.1.1

Figure 12.3.1.1.1: Vasculature of the deep tissues of the anterior abdominal wall demonstrated on fresh cadaveric injection (27). Red arrow: deep inferior epigastric artery. Black arrow: deep circumflex iliac artery. Green arrow: intercostal arteries. Purple arrow: deep superior epigastric artery (Reproduced with permission)

Figure 12.3.1.1.2: The three branching patterns of the deep inferior epigastric artery (DIEA). The DIEA is shown as a single, bifurcating or trifurcating trunk below the umbilicus. The arcuate line is dotted. This presents the findings of the original study by Moon and Taylor (28).

Figure 12.3.1.1.3: X-ray of the abdominal wall, demonstrating the course of the deep inferior epigastric artery (DIEA) and the location of its perforators (metallic beads) (29) (Reproduced with permission)

Figure 12.3.1.1.4: Deep inferior epigastric artery (DIEA) perforator flap with 3 perforators highlighted (green) emerging from rectus abdominis to supply the lower abdominal flap (8). (Reproduced with permission)

Figure 12.3.1.1.5: X-ray of two transverse periumbilical sections of the anterior abdominal wall, with the perforators highlighted (red) to demonstrate the significant transverse course through the rectus abdominis muscle, from their origins on the deep inferior epigastric artery (DIEA) to their points of exit from the muscle (30). (Reproduced with permission)

Figure 12.3.1.1.6: Perfusion zones of the lower abdominal flap supplied by the deep inferior epigastric artery (DIEA) (red arrow). Left: conventional classification (31). Right: contemporary classification (32). (Reproduced with permission)

Table 12.3.1.1.1: Classification of stacked DIEP flaps. Adapted from Hamdi *et al* (33). Abbreviations: SIEA: superficial inferior epigastric artery; DIEP: deep inferior epigastric artery perforator.

Figure 12.3.1.1.7: Harvest of the cranial extension of the DIEP flap with subscarpal fat extension. (34) (Reproduced with permission)

Figure 12.3.1.1.8: Demonstration of the thickness of the cranial extension of the DIEP flap with subscarpal fat extension (A) and subscarpal fat extension lifted with forceps (B). (Reproduced with permission)

Chapter 12.3.1.2

Table 12.3.1.2.1: Summary of all reported breast volumetric analysis techniques, except 3D surface imaging. Abbreviations: N/A: not available; CT: computed tomography; MRI: magnetic resonance imaging; MD: mean deviation; CC: correlation coefficient.

Table 12.3.1.2.2: Summary of all 3D surface imaging techniques. Abbreviations: N/A: not available; MD: mean deviation; CC: correlation coefficient; ICC: interclass coefficient; EE: estimate of error; CR: coefficient of reproducibility; ME: mean error; yr: year; fps: frames per second; s: second; ms: millisecond.

Figure 12.3.1.2.1: Volume-rendered 3D reconstructed images of breasts segmented from a computer tomographic (CT) scan using Osirix software (Pixmeo, Geneva, Switzerland), from which volume differential can be calculated. A: anterior view of the right breast; B: anterior view of the left breast; C: lateral view of the right breast; D: lateral view of the left breast. Reproduced with permission from Chae *et al* (35).

Figure 12.3.1.2.2: 3D printed haptic model of the breasts in Figure 12.3.1.2.1 using Cube 2 printer (3D Systems, Rock Hill, SC) and polylactic acid (PLA) filaments. Reproduced with permission from Chae *et al* (35).

Chapter 12.3.1.3

Figure 12.3.1.3.1: PRISMA attrition flow diagram (36)

Table 12.3.1.3.1: Demographics of included studies. *: based on the American Society of Plastic Surgeons Rating Levels of Evidence and Grading Recommendations. Abbreviations: CDU: colour Doppler ultrasound; CTA: computed tomographic angiography; MRA: magnetic resonance angiography; DIRT: dynamic infrared thermography; ICG: indocyanine-green.

Figure 12.3.1.3.2: A 3D volume-rendered reconstruction from an axial slice CTA of the abdomen, showing DIEA perforators and a true anastomosis linking a medial and lateral row perforator.

Figure 12.3.1.3.3: Axial slice CTA image of the abdomen with maximum intensity projection, illustrating a left hemi-abdomen medial row perforator vessel and its branches.

The green arrow shows the perforator's exit point from rectus sheath; the blue arrow shows the primary branching point.

Chapter 12.3.2.1

Figure 12.3.2.1.1: Preoperative clinical photograph, demonstrating breast asymmetry in the setting of previous left post-mastectomy breast reconstruction.

Figure 12.3.2.1.2: Surface-rendered three-dimensional (3D) reconstruction of a computed tomographic (CT) scan of the breasts, performed with Osirix (Pixmeo, Geneva, Switzerland) software.

Figure 12.3.2.1.3: Three-dimensional analysis of breast parenchymal volume, after selective cropping of the skin and chest wall from scan data, using volume-rendered three-dimensional (3D) reconstruction of a computed tomographic (CT) scan of the breasts with Osirix (Pixmeo) software: (A) right breast anterior view; (B) left breast anterior view; (C) right breast lateral view; (D) left breast lateral view.

Figure 12.3.2.1.4: Production of a three-dimensional "subtracted" volume difference between breasts, using volume-rendered CT data in Magics software (Materialize, Leuven, Belgium). Volume-rendered computed tomography (CT) images are aligned. (A) a mirror image of one breast is created to align both breasts unidirectionally; (B) the two volumes superimposed; (C) and the volumes are "subtracted" from one another to produce the volume difference (D).

Figure 12.3.2.1.5: A three-dimensional (3D)-printed haptic, tactile biomodel of the breasts, produced from computed tomography (CT) data. Printing performed with the Cube 2 printer (3D Systems, Rock Hill, SC, USA) using Cubify software (3D Systems), and using white polylactic acid (PLA) filament ink.

Chapter 12.3.2.2

Table 12.3.2.2.1: Computed tomographic angiography scan parameters.

Figure 12.3.2.2.1: 3D printing software. (A) Using 3D Slicer software (Surgical Planning Laboratory, Boston, MA USA), CTA scan data is converted into a 3D image of the abdominal wall and holes and lines are placed appropriately to indicate the location of DIEA perforators, their intramuscular course and the DIEA pedicle. (B) Using Autodesk MeshMixer software (Autodesk, Inc., San Rafael, CA USA), the 3D image is cropped into appropriate size and the holes/lines are enlarged to fit marking pens. (C) Using Cura

software (Ultimaker, Geldermalsen, Netherlands), the final file is converted to a 3D printer-friendly file. Abbreviations: CTA: computed tomographic angiography; DIEA: deep inferior epigastric artery.

Figure 12.3.2.2.2: 3D printers. (A) Ultimaker 3E printer (Ultimaker, Geldermalsen, Netherlands). (B) Moment 3D printer (Moment, Seoul, South Korea).

Figure 12.3.2.2.3: Clinical application of the 3D-printed DIEP template in use. The template was orientated on the abdomen by the umbilicus, notch at the pubic symphysis and the abdominal skin crease (A). Markings from the template were used for flap design and the skin island (B). Abbreviation: DIEP: deep inferior epigastric artery perforator.

Table 12.3.2.2.2: Comparison of patient demographics between the group using the 3D-printed DIEP template and the historical control. Abbreviations: BMI: body mass index; DIEP: deep inferior epigastric artery perforator flap; MS-TRAM: muscle-sparing transverse rectus abdominis muscle flap.

Table 12.3.2.2.3: Comparison of perforator distance measurements between 3D-printed DIEP template, intraoperative measurement, handheld Doppler probe, and CTA. Abbreviation: DIEP: deep inferior epigastric artery perforator; CTA: computed tomographic angiography.

Table 12.3.2.2.4: Impact on operating time using the DIEP template. Abbreviation: DIEP: deep inferior epigastric artery perforator.

Table 12.3.2.2.5: Summary of responses from the surgeon perception survey and comparison of responses between flap-raising surgeons against the second surgeons and surgeons against surgical trainees.

Chapter 12.3.2.3

Figure 12.3.2.3.1: 3D-printed perforasome template placed on top of 3D-printed DIEP template of the same patient demonstrating their accurate alignment.

Figure 12.3.2.3.2: 3D-printed DIEP template used to mark the location of DIEA perforators, their intramuscular course, and the DIEA pedicle.

Figure 12.3.2.3.3: 3D-printed perforasome template used to mark the subcutaneous branches of DIEA perforators and their linking vessels.

Figure 12.3.2.3.4: The markings are used to estimate the size and shape of each perforasome to aide with flap design.

Chapter 12.3.2.4

Figure 12.3.2.4.1: Standard preoperative photograph of a patient planned for breast reconstruction, with 2D images achieved using a commercial 3D scanner, VECTRA XR scanner (Canfield Scientific, Fairfield, NJ, USA).

Figure 12.3.2.4.2: Pixelated photograph of the same patient as Figure 1, with contoured images achieved using a commercial 3D scanner, VECTRA XR scanner (Canfield Scientific, Fairfield, NJ, USA).

Figure 12.3.2.4.3: 3D photograph of the same patient as Figure 1, with contoured images achieved using a commercial 3D scanner, VECTRA XR scanner (Canfield Scientific, Fairfield, NJ, USA).

Figure 12.3.2.4.4: 3D-print using the MakerBot Z18 3D printer (MakerBot Industries), of the same patient as Figure 12.3.2.4.1.

Figure 12.3.2.4.5: The surgical coning technique (same patient as other Figures): The breast base is transcribed onto the skin surface of the flap (A), in order to plan the central focus of coning for maximum projection. The non-projected flap is highlighted (B). The flap undersurface is used for placement of the coning sutures, placed through the sub-scarpa's fat, and a continuous loose purse-string technique is used in this fashion to encircle the planned breast base, before tying the suture loosely (C). The sutures are placed superficially in order to avoid deep penetration which may occlude intra-flap vasculature. Two to three further such purse-string rings are created as needed, in increasing diameters from the initial purse-string, in order to create the desired amount of projection (D).

Chapter 12.3.3.1

Table 12.3.3.1.1: Summary of 3D bioprinting techniques. Abbreviations: LIFT: laser-induced forward transfer; ITOP: integrated tissue organ printer.

Table 12.3.3.1.2: Summary of 3D scaffold materials used in adipose tissue regeneration. Abbreviations: ECM: extracellular matrix; ADSC: adipose-derived stem cells; N/A: not applicable; HA: hyaluronic acid; DAT: decellularized adipose tissue; EHS: Engelbreth-Holm-Swarm; polycaprolactone: PCL; polylactic acid: PLA; poly(lactic-*co*-glycolic acid): PLGA; polyethylene glycol: PEG; poly(amidoamine) oligomer: OPAA; PAA: poly(amidoamine); PGS: poly(glycerol sebacate); PLLA: poly(L-lactic acid); PDM: placental decellular matrix; XLHA: cross-linked hyaluronic acid.

Table 12.3.3.1.3: List of adipogenic and angiogenic growth factors used to support 3D bioprinting adipose tissue. Abbreviations: FGF-2: fibroblast growth factor-2; TGF-β1: transforming growth factor-beta 1; PDGF-BB: platelet-derived growth factor receptor B; vascular endothelial growth factor; bFGF: basic fibroblast growth factor: EGF: epidermal growth factor; IGF-1: insulin-like growth factor.

Chapter 12.3.3.2

Figure 12.3.3.2.1: A 3D-printed biomodel of breasts, produced from routine CT data. Printing performed using Cube 2 printer (3D Systems, Rock Hill, SC, USA), 3D Slicer software (Surgical Planning Laboratory, Boston, MA, USA), and white polylactic acid (PLA) filaments.

Figure 12.3.3.2.2: A 3D-printed biomodel of nipple using (A) CT and (B) MRI scans. Printing performed using Moment 3D printer (Moment, Seoul, South Korea) and 3D Slicer.

Table 12.3.3.2.1: Summary of 3D bioprinting techniques. Abbreviations: LIFT: laser-induced forward transfer; ITOP: integrated tissue organ printer.

Table 12.3.3.2.2: Summary of 3D-bioprinted or tissue-engineered NAC reconstructions. Abbreviations: N/A: not applicable.

Chapter 13.1

Table 13.1.1: Summary of 3D image rendering software.

Figure 13.1.1: CTA-based 3D perforator mapping in DIEP flap planning performed using OsiriX software. (A) MIP reconstruction demonstrating the intramuscular and subcutaneous course of each perforator, (B) VRT reconstruction demonstrating the location of the perforators (blue arrows) as they emerge from the rectus sheath in reference to the umbilicus (marked). CTA: computed tomographic angiography; 3D: three-dimensional; DIEP: deep inferior epigastric artery perforator; MIP: maximum intensity projection; VRT: volume-rendered technique; DIEA: deep inferior epigastric artery.

Figure 13.1.2: MRI-based 3D volumetric analysis in planning breast reconstructive surgery demonstrating 611 mL on the right breast and 635 mL on the left breast, performed using OsiriX software (Pixmeo).

Table 13.1.2: Summary of software platforms capable of performing 3D volumetric analysis from CT and MRI. Abbreviations: CT: computed tomography; MRI: magnetic resonance imaging; DIEP: deep inferior epigastric artery perforator.

Table 13.1.3: Use of CT/MRI-based 3D-printed haptic models for preoperative planning in plastic and reconstructive surgery. Abbreviations: CT: computed tomography; CTA: computed tomographic angiography; MRI: magnetic resonance imaging; DIEP: deep inferior epigastric artery perforator; SCC: squamous cell carcinoma; FFF: fused filament fabrication; IMA: internal mammary artery.

Figure 13.1.3: 3D-printed biomodel of breasts in planning reconstruction using Cube 2 printer (3D Systems, Rock Hill, SC, USA). Reproduced with permission from (35).

Table 13.1.4: Summary of all studies investigating the use of image-guided 3D-printed surgical guide in mandibular reconstruction with free fibular flap. Abbreviations: CT: computed tomography; CTA: computed tomographic angiography; SLM: selective laser melting; SLA: stereolithography; SLS: selective laser sintering; FFF: fused filament fabrication.

Chapter 13.2

Table 13.2.1: Summary of image-guided navigation systems used in reconstructive plastic surgery. Abbreviations: DIEP: deep inferior epigastric artery perforator; ALT: anterolateral thigh; DCIA: deep circumflex iliac artery.

Table 13.2.2: Summary of augmented reality devices used in reconstructive plastic surgery. Affordability of each device and software is determined by whether it costs less than AUD $500 outright or per year in subscription or is free. DIEP: deep inferior epigastric artery perforator; N/A: not available.

Figure 13.2.1: Projection of ALT perforators preoperatively using CTA-based direct augmented reality technique performed using OsiriX software (Pixmeo) and Philips PicoPix pocket projector (Koninklijke Philips NV, Amsterdam, The Netherlands). Purple line indicates marking of a line between traditional anatomical landmarks. The mark on the line correlated exactly with the location of the ALT perforator. Abbreviations: ALT: anterolateral thigh perforator; CTA: computed tomographic angiography.

Figure 13.2.2: Evolution of 3D imaging and printing technique from 3D-reconstructed images and a basic 3D-printed model (A1-4) to clinically useful 3D printing application in perforator-based breast reconstructive surgery (B1-6) to advanced image analysis technology, such as augmented reality and CAVE2 facility (C1-6). (A1) 2D-reconstructed CTA image of the abdominal wall vasculature. (A2) 3D-reconstructed CTA image of the same patient in A1. (A3) Segmented image of the DIEA of the same patient in A1. (A4) 3D-printed model of the DIEA in A3. (B1) Segmented image of the abdominal wall and

DIEA that spurned the idea of creating a template for preoperative planning. (B2) Patient-specific, bespoke “DIEP template” is 3D-printed and placed on the patient’s abdominal wall to help locate DIEA perforators and its pedicle. (B3) This information is used for flap designing. As 3D printing technique advanced, we are able to create both a standard DIEP template (B4) and a “perforasome template” (B5), which can additionally identify each perforasome (B6). (C1-6) Augmented reality can significantly reduce the time and labour cost involved in 3D printing by enabling direct viewing and real-time interaction with the image data. (C1) Our published direct ARC (augmented reality CTA) technique set-up using a handheld projector demonstrating 2D-reconstructed (C2) and 3D-reconstructed (C3) images on the patient’s abdomen. As technology advances, we envision that greater software processing power will enable display of greater anatomical information, such as intramuscular course of a DIEP (C4), and translation into a user-friendly, interactive platform for clinicians (C5). (C6) The latest CAVE2 facility at Monash University (Melbourne, Victoria, Australia) housing 84 million pixel stereoscopic display with powerful real-time motion tracking capability will enable interactive, seamless visualisation of relevant anatomy for preoperative planning and collaborative discussion. Reprinted with permission from Chae *et al* (37), Chae *et al* (38) and Chae *et al* (39). Abbreviations: CTA: computed tomographic angiography; DIEA: deep inferior epigastric artery; DIEP: deep inferior epigastric artery perforator.

Chapter 14

Figure 14.1: Evolution of 3D imaging and printing technique from 3D-reconstructed images and a basic 3D-printed model (A1-4) to clinically useful 3D printing application in perforator-based breast reconstructive surgery (B1-6) to advanced image analysis technology, such as augmented reality and CAVE2 facility (C1-6). (A1) 2D-reconstructed CTA image of the abdominal wall vasculature. (A2) 3D-reconstructed CTA image of the same patient in A1. (A3) Segmented image of the DIEA of the same patient in A1. (A4) 3D-printed model of the DIEA in A3. (B1) Segmented image of the abdominal wall and DIEA that spurned the idea of creating a template for preoperative planning. (B2) Patient-specific, bespoke “DIEP template” is 3D-printed and placed on the patient’s abdominal wall to help locate DIEA perforators and its pedicle. (B3) This information is used for flap designing. As 3D printing technique advanced, we are able to create both a standard DIEP template (B4) and a “perforasome template” (B5), which can additionally identify each perforasome (B6). (C1-6) Augmented reality can significantly reduce the time and labour cost involved in 3D printing by enabling direct viewing and real-time interaction with the

image data. (C1) Our published direct ARC (augmented reality CTA) technique set-up using a handheld projector demonstrating 2D-reconstructed (C2) and 3D-reconstructed (C3) images on the patient's abdomen. As technology advances, we envision that greater software processing power will enable display of greater anatomical information, such as intramuscular course of a DIEP (C4), and translation into a user-friendly, interactive platform for clinicians (C5). (C6) The latest CAVE2 facility at Monash University (Melbourne, Victoria, Australia) housing 84 million pixel stereoscopic display with powerful real-time motion tracking capability will enable interactive, seamless visualisation of relevant anatomy for preoperative planning and collaborative discussion. Abbreviations: CTA: computed tomographic angiography; DIEA: deep inferior epigastric artery; DIEP: deep inferior epigastric artery perforator.

Chapter 16.2.1

Figure 16.2.1.1: PRISMA flow diagram for study selection.

Figure 16.2.1.2: Posterior (a) and anterior (b) view of the printed 3D model. Metastases in different segments are labeled as metastasis (mets) 4a/4b, 6 and 7. Inferior vena cava labeled as IVC. Magnified view of metastasis in segment 6 (c).

Figure 16.2.1.3: CT scan in coronal view (a). Points of measurements in axial view, taken transverse and longitudinal (b, c and d) are colour-coded accordingly. Measurements plotted comparing measurements in CT versus 3D printed model.

8 Table of Contents

9 Aims and Hypotheses

Aims

To develop an image-guided bedside 3D printing technique that is convenient and affordable for clinicians and validate its accuracy using phantom models and animal bones

To develop and explore the utility of our 3D printing technique in plastic and reconstructive surgery, including other surgical disciplines, and demonstrate its effect in preoperative planning, intraoperative surgical guidance and patient education

To develop a surgical planning tool for perforator-based breast reconstructive surgery using our novel 3D printing technique, validate it and demonstrate potential clinical benefits

Hypotheses

That our novel bedside 3D printing technique can reliably produce accurate anatomical models within clinical significance.

That our bedside 3D printing technique can be utilised in plastic and reconstructive surgery to produce anatomical models from conventional imaging resources with high accuracy and reliability for preoperative planning, intraoperative surgical guidance and patient education

That our innovative 3D-printed surgical planning tools for perforator-based breast reconstructive surgery, named “DIEP templates” and “perforasome templates”, can accurately and reliably identify relevant perforators and perforasomes leading to improved flap design, surgeon confidence and surgical outcomes

10 Introduction

10.1 Summary of Imaging Modalities Used in Plastic and Reconstructive Surgery

PUBLISHED (Publication): ***Chae MP***, Hunter-Smith DJ, Rozen WM. Comparative analysis of fluorescent angiography, computed tomographic angiography and magnetic resonance angiography for planning autologous breast reconstruction. *Gland Surgery*. 2015; 4(2):164-178.

Chapter Summary

Introduction: The high incidence of breast cancer and growing number of breast cancer patients undergoing mastectomy has led to breast reconstruction becoming an important part of holistic treatment for these patients. In planning autologous reconstructions, preoperative assessment of donor site microvascular anatomy with advanced imaging modalities has assisted in the appropriate selection of flap donor site, individual perforators, and lead to an overall improvement in flap outcomes. In this review, we compare the accuracy of fluorescent angiography, computed tomographic angiography (CTA), and magnetic resonance angiography (MRA) and their impact on clinical outcomes.

Method: A review of the published English literature dating from 1950 to 2015 using databases, such as PubMed, Medline, Web of Science, and EMBASE was undertaken.

Results: Fluorescent angiography is technically limited by its inability to evaluate deep-lying perforators and hence, it has a minimal role in the preoperative setting. However, it may be useful intraoperatively in evaluating microvascular anastomotic patency and the mastectomy skin perfusion. CTA is currently widely considered the standard, due to its high accuracy and reliability. Multiple studies have demonstrated its ability to improve clinical outcomes, such as operative length and flap complications. However, concerns surrounding exposure to radiation and nephrotoxic contrast agents exist. MRA has been explored, however despite recent advances, the image quality of MRA is considered inferior to CTA.

Conclusion: Preoperative imaging is an essential component in planning autologous breast reconstruction. Fluorescent angiography presents minimal role as a preoperative imaging modality, but may be a useful intraoperative adjunct to assess the anastomosis and the mastectomy skin perfusion. Currently, CTA is the gold standard preoperatively. MRA has a role, particularly for women of younger age, iodine allergy, and renal impairment.

Introduction

Given the high prevalence and incidence of breast cancer in society (40, 41) and a growing number of women with breast cancer opting for mastectomy over breast-conserving operations (42), breast reconstruction has become an important part of breast cancer management. It can improve patients' psychosexual well-being and their overall psyche in response to breast cancer management (43-47). Autologous breast reconstruction (and in particular those with perforator-based free flaps) has demonstrated a natural-appearing, aesthetically-pleasing, long-lasting restorative option, with acceptable level of donor site morbidity, such as abdominal bulge or hernia (48, 49). Recent advancements in operative techniques and imaging modalities have facilitated complex microvascular breast reconstructions to become safer, more reliable procedures (33, 50, 51).

Various autologous tissues have been utilized for breast reconstruction, such as omentum (52), latissimus dorsi (53-56), deep circumflex iliac artery (groin) flap (57, 58), lateral thigh (tensor fascia latae) flap (59), gluteal musculocutaneous flap (60-63), gracilis flap (64), and triceps flap (65). In recent times, the anterior abdominal wall has become the most frequently used donor site due to the added aesthetic benefit at the donor site, akin to a concomitant abdominoplasty. Initially, transverse rectus abdominis muscle (TRAM) flaps were successful in providing adequate volume replacement for breast reconstructions (31, 66). However, a high rate of donor site morbidity, such as rectus abdominis muscle weakness and ventral hernia, resulted in the development of muscle-sparing techniques, mainly the deep inferior epigastric artery perforator (DIEP) flaps (49, 67). DIEP flaps are fasciocutaneous flaps based on musculocutaneous perforators derived from the deep inferior epigastric artery (DIEA) (68, 69). They were able to provide sufficient tissue volume and a superior functional and aesthetic outcome at the donor site than the TRAM flaps (50, 70). However, early studies reported a steep learning curve of the microsurgical technique leading to a longer dissection time, and increased flap complications, such as fat necrosis and flap loss (71). To this effect, the use of preoperative imaging has been instrumental.

Preoperative assessment of the donor site microvasculature anatomy with advanced imaging modalities has assisted surgeons in the appropriate selection of the donor site, perforator, and flap leading to an overall improvement in the flap outcomes (4, 5). According to the consensus reached at the Navarra meeting, a perforator should be

selected on the basis of its caliber, central location within the flap, direct venous connection with the main superficial venous system, and it preferably demonstrates a broach subcutaneous branching pattern and has a shorter intramuscular (IM) course for ease of dissection (72). Hence, an ideal preoperative imaging technique should accurately demonstrate the individual variations in the location and caliber of the perforators, their IM course, and the branching pattern of the DIEA (73). Early investigators have relied on handheld Doppler probes and color duplex ultrasonography to detect perforators, characterize them in flow velocity and resistivity, and create a perforator map on the abdominal wall (50, 74, 75). Both ultrasound techniques are inexpensive, do not expose patients to radiation or potentially nephrotoxic intravenous contrast agents, can detect perforators with diameter greater than 0.5 mm, identify any underlying vessel damage secondary to arthrosclerosis or previous surgery (76-79). However, they are subject to significant inter-observer variability, and are associated with poor consistency with intraoperative findings, high false positive and negative rates (6, 74, 80, 81). Hence, they are now superseded by modern imaging technologies with objective findings, such as fluorescent angiography, computed tomographic angiography (CTA), and magnetic resonance angiography (MRA).

In this review, we evaluate the accuracy of fluorescent angiography, CTA, and MRA, and compare their impact on the clinical outcomes of patients undergoing autologous breast reconstruction, mainly TRAM and DIEP flaps, since they have attracted the most number of clinical studies and have provided the highest level of evidence (3).

Methods

We reviewed the published English literature from 1950 to 2015 from well-known databases, such as PubMed, Medline, Web of Science, and EMBASE, using search terms, such as “autologous breast reconstruction”, “DIEP flap”, “fluorescent angiography”, “computed tomographic angiography”, and “magnetic resonance angiography”.

Results

Fluorescent angiography

Fluorescence angiography utilizes intravenous dyes that fluoresce and emit infrared energy upon excitation by a light source, which produces real-time videos that facilitate evaluation of the anastomotic patency and the extent of soft tissue perfusion (82, 83). Originally, the investigators employed fluorescein dye, which accumulates extracellularly in the soft tissue, fluoresces upon excitation by the ultraviolet (UV) light, and is renally excreted (84, 85). However, the long time it takes to reach the maximum intensity (15 minutes), relatively frequent adverse effects, reports of allergic reaction, and the steep learning curve associated with using a Woods lamp for interpretation have resulted in the fluorescein dye being replaced by the indocyanine green (ICG) dye. ICG is an FDA-approved, biliary excreted, water-soluble dye that enables image capture within 2-3 minutes of intravenous administration (86). ICG is excited by laser and transmits infrared energy that is recorded by devices equipped with inbuilt software algorithms that generate quantitative data, such as LifeCell SPY system (LifeCell Corp, Branchburg, New Jersey), IC-View (Pulsion Medical Systems AG, Munich, Germany), and FLARE imaging system (Beth Israel Deaconess Medical Center, Boston, MA) (87-89). Furthermore, ICG has a short half-life (3-4 minutes) (90), which enables multiple consecutive measurements, in contrast to fluorescein, which is retained in the tissues (91). It strongly binds to the plasma proteins leading to rapid washout from the circulation and has a superior side effect profile with a low rate of anaphylaxis (1 in 42,000) (Table 10.1.1) (92, 93).

	ICGA	CTA	MRA
Availability	+	+++	+
Cost (USD)	795 (94)	400 (95)	600 (96, 97)
Image acquisition	2-3 min (86)	<10 sec	20 min
Breath holding during scanning	NA	5 sec (98)	20 sec (99)
Reproducibility	+	+++	++
Operator dependence	Yes	No	No
Patient size dependence	Yes	No	No

Panoramic view	Yes	Yes	Yes
3D view	No	Yes	Yes

Table 10.1.1. Comparison of basic characteristics of the perforator imaging technologies. Abbreviation: ICGA: indocyanine green angiography; CTA: computed tomographic angiography; MRA: magnetic resonance angiography; NA: not applicable; 3D: three-dimensional.

Laser-assisted ICG fluorescence angiography (LA-ICGFA) has demonstrated utility by characterizing vascular flow dynamics and tissue perfusion in various disciplines (100-108). In reconstructive surgery, investigators have utilized LA-ICGFA intraoperatively to assess the patency of microvascular anastomosis in free flaps (109, 110) and calculate the intrinsic transit time through the anastomosis (111) that correlate with postoperative flap compromise and accurately predict early re-exploration. One of the significant limitations of LA-ICGFA is that it can only provide information a few millimeters deep from the skin (88). This is adequate for evaluating thin areas, such as the extremities, head and neck, and the trunk (112). However, since majority of autologous breast reconstructions are based on the abdomen and a thick pannus is preferred for a DIEP flap, LA-ICGFA has a minimal role in the preoperative planning (88). In breast reconstruction, LA-ICGFA may be useful intraoperatively during flap harvest to assess the flap perfusion, confirm blood flow within the microvascular anastomosis, and detect acute changes in the flap circulation, such as arterial occlusion, venous thrombosis, and pedicle torsion (113). Moreover, it can be used to evaluate the perfusion of mastectomy skin flaps and facilitate the reconstructive surgeon to debride areas that are likely to develop necrosis (94).

A number of studies in the literature have examined the accuracy of LA-ICGFA in estimating postoperative complications, such as mastectomy skin flap necrosis (114-116), partial flap necrosis (86) and microvascular thrombosis (Table 10.1.2) (111). Using fluorescein dye, Losken *et al* reported a sensitivity and specificity of 75% and 71% respectively to detect mastectomy skin flap necrosis (114). Using ICG dye, Newman *et al* retrospectively reviewed and derived that LA-ICGFA can detect postoperative skin necrosis with a sensitivity and specificity of 100% and 91% respectively (115). In a prospective study of 51 implant breast reconstructions in 32 patients, Phillips *et al* compared the efficacy of fluorescein to the ICG dye and reported that both dyes have the same sensitivity of 90% in detecting skin necrosis but ICG had a slightly superior

specificity (116). In a retrospective study of 10 patients undergoing TRAM flaps, Yamaguchi *et al* report that intraoperative LA-ICGFA can detect partial flap necrosis with a sensitivity of 75% (86). Moreover, Holm *et al* have demonstrated that LA-ICGFA accurately detects microvascular thrombosis as the cause of free flap re-exploration with a sensitivity of 100% and specificity of 86% (111).

FA	***Author***	***Year***	***P/R***	***Patients***	***Dye***	***Sensitivity***	***Specificity***
	Yamaguchi (86)	2004	R	10	ICGD	75%	N/A
	Losken (114)	2008	P	42	FD	75%	71%
	Newman (115)	2010	R	12	ICGD	100%	91%
	Holm (111)	2010	P	20	ICGD	100%	86%
	Phillips (116)	2012	P	32	FD	90%	30%
	Phillips (116)	2012	P	32	ICGD	90%	50%
CTA	***Author***	***Year***	***P/R***	***Patients***	***CTA Rows***	***Sensitivity***	***Specificity***
	Alonso-Burgos (117)	2006	P	6	4	100%	N/A
	Rosson (12)	2007	P	17	64	100%	N/A
	(8)	2008	P	8	64	100%	N/A
	Rozen (96)	2009	P	6	64	100%	N/A
	Gacto-Sanchez (118)	2010	P	12	16	100%	N/A
	Scott (80)	2010	P	22	64	94.30%	N/A
	Masia (119)	2010	P	36	64	100%	N/A
	Pauchot (98)	2012	P	10	64	84.30%	100%
	Tong (120)	2012	R	69	128	79%	92%
	Cina (97)	2013	P	23	64	95.60%	N/A
	Pellegrin (121)	2013	R	41	64	97.60%	N/A
MRA	***Author***	***Year***	***P/R***	***Patients***	***MRA Tesla***	***Sensitivity***	***Specificity***
	Rozen (96)	2009	P	6	1.5 & 3.0	50%	100%
	Chernyak (122)	2009	P	19	3	97%	N/A
	Greenspun (123)	2010	P	31	3	96%	N/A
	Newman (124)	2010	P	25	1.5	99%	N/A
	Alonso-Burgos	2010	P	8	3	100%	N/A

	(125)						
	Masia (126)	2010	P	56	1.5	100%	N/A
	Pauchot (98)	2012	P	10	64	95.70%	100%
	Cina (97)	2103	P	23	64	91.30%	N/A
	Versluis (127)	2013	P	23	1.5 EP	100%	N/A

Table 10.1.2. Comparison of accuracy of the perforator imaging technologies. Abbreviations: FA: fluorescent angiography; CTA: computed tomographic angiography; MRA: magnetic resonance angiography; P: prospective study; R: retrospective study; ICGD: indocyanine green dye; FD: fluorescein dye; N/A: not available; EP: equilibrium phase.

In the literature, there are only two studies where using LA-ICGFA is correlated with clinical outcomes (Table 10.3) (94, 128). Komorowska *et al* applied LA-ICGFA intraoperatively in 24 consecutive patients undergoing breast reconstruction and the areas of inadequate dye penetration suggesting poor tissue perfusion were resected (128). The authors reported that a resultant total complication rate of 4%, which was lower than 15.1% recorded from their previous 148 patients and 206 breast reconstructions ($p < 0.01$) (128). Duggal *et al* retrospectively reviewed the clinical outcomes in 184 patients undergoing breast reconstructions receiving intraoperative LA-ICGFA (94). The authors report that LA-ICGFA was associated with a significant reduction in mastectomy skin flap necrosis ($p = 0.01$) and re-operation rate ($p = 0.009$). There was also a trend demonstrated in the reduction of partial and complete flap loss rate ($p = 0.237$ and $p = 1.00$, respectively).

	Author	*Year*	*Patients*	*Control*	*Reduction in operative time (min)*		*Mastectomy skin necrosis*	*Flap complications*				*Donor site morbidity*	*Incidental findings*
					Flap harvest	*Total*		*Total*	*Fat necrosis*	*Partial flap loss*	*Complete flap loss*	*Abdominal bulge/herniation*	
ICGA	Komorowska-Timek (128)	2010	20	148				4% vs 15.1% **(*p* < 0.01)**					
	Duggal (94)	2014	71	59			13% vs 23.4% **(*p* = 0.01)**			14% vs 22% (*p* =0.237)	1.4% vs 3.4% (*p* =1)		
CTA	Masia (129)	2006	30	30		100							
	Rozen (8)	2008	8	NA					0%	0%	0%		
	Rozen (5)	2008	40	48		9.8 (unilateral) (*p* = 0.57) 76.5 (bilateral) (*p* = 0.079)			7.5% vs 16.7% (*p* = 0.19)	0% vs 10.4% **(*p* = 0.024)**	0% vs 0%	0% vs 14.6% **(*p* = 0.006)**	
	Uppal (130)	2009	26	NA		76 **(*p* < 0.005)**							
	Casey (131)	2009	68	145		89 (unilateral) **(*p* < 0.01)** 142 (bilateral)			10.9% vs 13.4% (*p* > 0.05)		2% vs 3.8% (*p* > 0.05)	1% vs 9.1% **(*p* < 0.05)**	

						(*p* < 0.01)							
	Smit (13)	2009	70	68		90 **(*p* 0.001)**				0% vs 4%	0% vs 1%		
	Ghattaura (132)	2010	50	50		77 (unilateral) **(*p* < 0.001)** 27 (bilateral) (*p* > 0.05)				4% vs 0%		0% vs 6%	
	(119)	2010	357	100	100 **(*p* < 0.05)**					2% vs 12%	1% vs 4%		
	(133)	2010	22	22	96 **(*p* < 0.05)**					5% vs 9%	0% vs 5%		
	Gacto-Sanchez (118)	2010	35	35	98 **(*p* < 0.001)**	127 **(*p* < 0.001)**			Total complications: 0 vs 14 **(*p* < 0.001)**			2 vs 15 **(*p* = 0.001)**	
	Fansa (134)	2011	20	20	26 **(*p* < 0.028)**								
	Tong (120)	2012	51	18		140 (unilateral) **(*p* = 0.017)** 117 (bilateral) **(*p* = 0.05)**				5% vs 4% (*p* = 1)	1% vs 0% (*p* = 1)		36%
	Malhotra (135)	2013	100	100		85 **(*p* < 0.05)**			No difference				
	Pellegrin (121)	2013	41	NA									29.30%
MRA	Rozen (96)	2009	6	NA					No difference between MRA and CTA				

	Schaverien (136)	2011	126	NA	25 (unilateral) ($p > 0.05$) 40 (bilateral) ($p > 0.05$)					Reduction ($p < 0.05$)			

Table 10.1.3. Comparison of clinical outcomes from the perforator imaging technologies. Abbreviations: FA: fluorescent angiography; CTA: computed tomographic angiography; MRA: magnetic resonance angiography; P: prospective study; R: retrospective study; vs: versus; NA: not available.

Computed tomographic angiography (CTA)

First reported by Masia *et al* in 2006 (129), CTA is widely used for preoperative imaging and planning free tissue transfers by numerous institutions around the world and is currently considered the best of the three options due to its high accuracy and reliability (Table 1) (5, 6, 9-14, 137). Ongoing advances in CTA, such as an increasing number of detector rows, ensure that the modality remains fast and produces high detail (3). For interpretation, the scan data can be three-dimensionally (3D) reconstructed digitally on either a free software, such as Osirix (Pixmeo, Geneva, Switzerland), or a commercially available software, such as *Siemens Inspace* (Siemens, Berlin, Germany). Using 3D volume rendering technique in the software facilitates the creation of a perforator location map and illustrates the subcutaneous course of the perforators (Figure 10.1.1); and secondly, the maximum intensity projection technique can help visualize the vascular pedicle in the coronal plane (Figure 10.1.2) and in the axial plane, which can further depict its IM course (Figure 10.1.3) (118, 138).

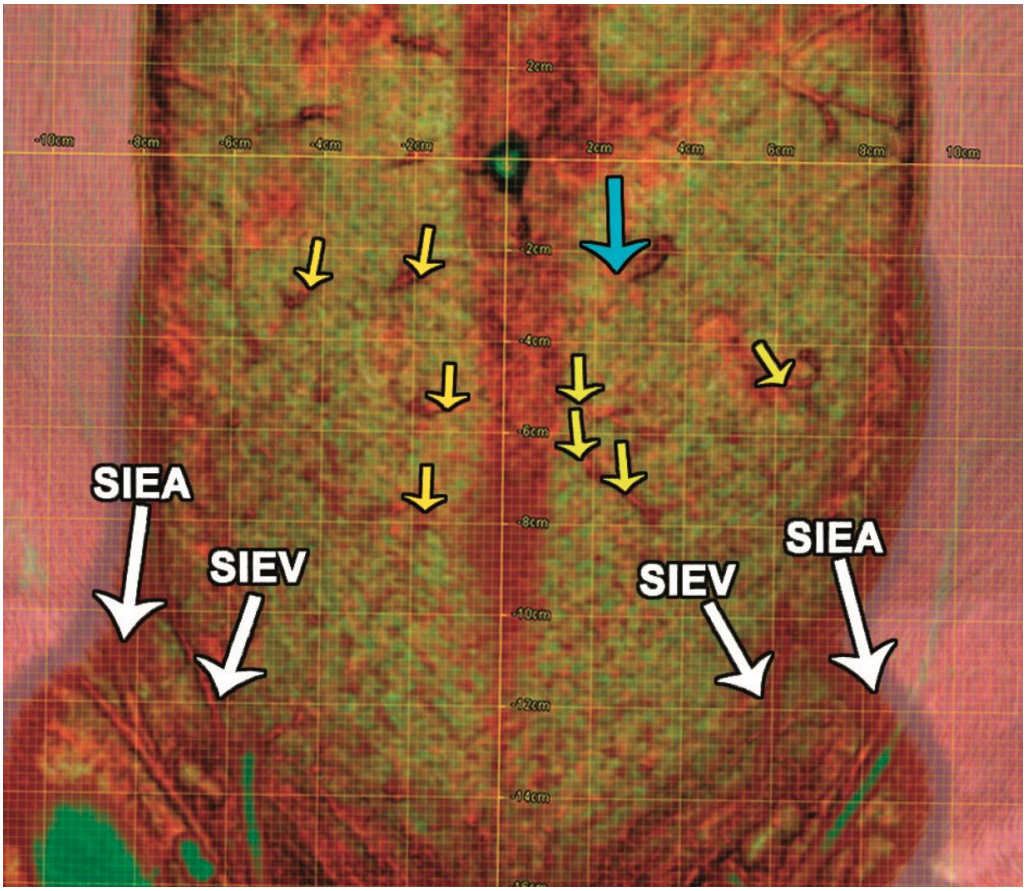

Figure 10.1.1: Computed tomographic angiogram (CTA) with volume rendered technique (VRT) reformat, demonstrating a large 1.5mm perforator (blue arrow) and multiple smaller

perforators (yellow arrows) at the point at which they pierce the anterior rectus sheath. A numbered grid is centered at the umbilicus for localization. The superficial inferior epigastric artery (SIEA) and vein (SIEV) on each side is demonstrated.

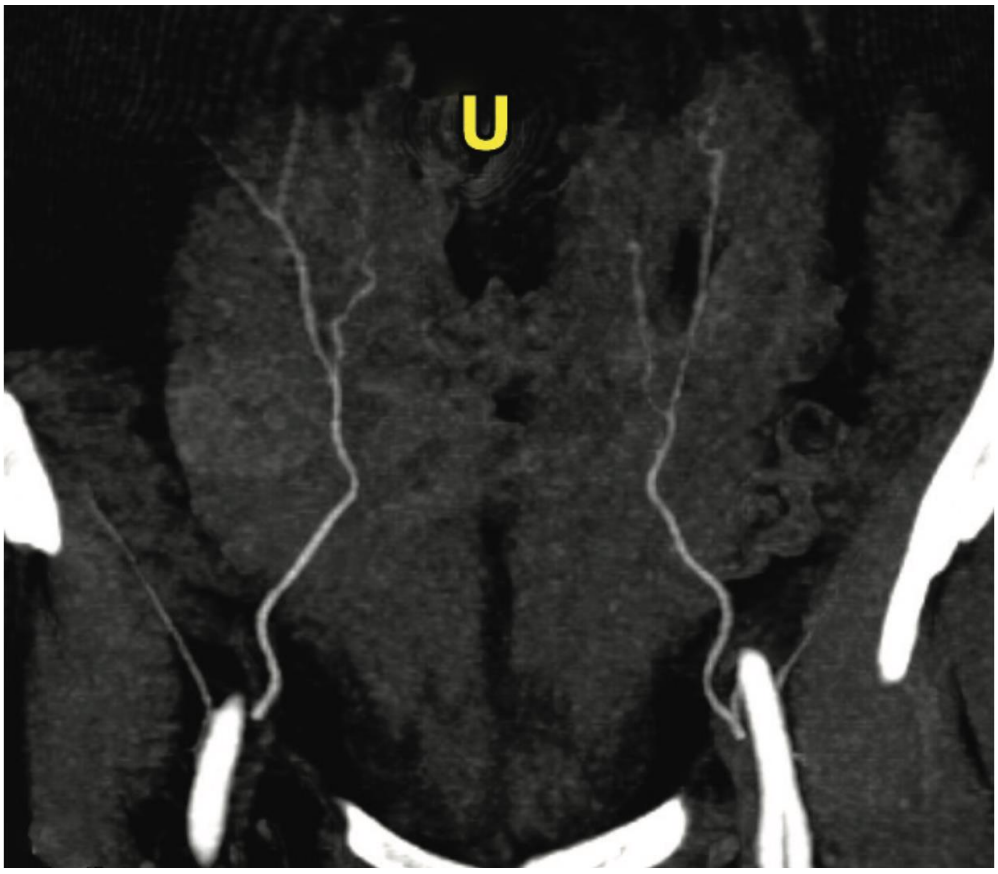

Figure 10.1.2: Computed tomographic angiogram (CTA) with volume rendered technique (VRT) reformat, demonstrating the branching pattern of the deep inferior epigastric arteries (DIEAs). The left side is a type 2 (bifurcating) pattern and the right is a type 3 (trifurcating) pattern. U = Umbilicus. Reproduced with permission from: Rozen and Ashton (139)

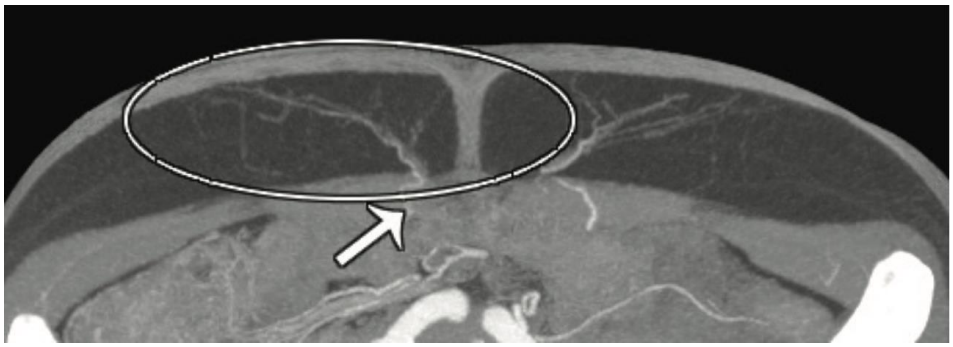

Figure 10.1.3: Computed tomographic angiogram (CTA) with axial maximum intensity projection (MIP) reformat, demonstrating the subcutaneous course of perforators. Based on the subcutaneous distribution and branching pattern of the perforator selected (arrow), a preoperative estimate of well-vascularized flap volume can be achieved. Reproduced with permission from: Rozen and Ashton (139)

The major advantages of CTA are its wide availability, affordability, non-invasive nature, high reproducibility and operator-independence. Furthermore, it has a fast scanning time of less than 5 minutes (4) and produces images in high spatial resolution and in multiplanar or 3D panoramic views that facilitates ease of interpretation. As a result, the location, caliber, and course of musculocutaneous perforators as small as 0.3 mm in diameter can be readily displayed (6). In contrast to ultrasonography, the image quality is less affected by the body habitus (6) and it can clearly demonstrate both DIEA and superficial inferior epigastric artery (SIEA), and their branching patterns. In addition, the CTA can be used to screen for comorbidities, such as metastatic diseases, and detect any underlying abdominal wall defects (3) or other incidentally discovered lesions, such as angiomyolipoma and adrenal mass, that may alter the surgical management (120, 121).

A plethora of studies have been reported in the literature demonstrating high accuracy of CTA in detecting perforators suitable for perforator-based free flap reconstructions (Table 2). Most investigators report sensitivity and specificity close to 100% (6, 7, 12, 80, 97, 98, 117-121). Furthermore, CTA can also characterize the DIEA branches, intramuscular course, and both superficial and deep venous systems supporting a flap with high sensitivity (100%, 97.1%, 91.3%, 94.4%, respectively) (97). In comparison to Doppler ultrasound, Rozen *et al* demonstrated that CTA produces superior visualization of the DIEA, its branching pattern, its perforators (p = 0.0078), and additionally, the SIEA (6). Similarly, Scott *et al* exhibit that CTA is significantly more sensitive than color Duplex ultrasound in detecting the top two perforators (94.3% vs 66.3%, respectively) (80). Compared to the MRA, CTA has a superior fat-to-vessel contrast (p = 0.007), but a poorer muscle-to-vessel contrast (p = 0.001) (98). The former indicates that CTA is able to produce higher quality images of the subcutaneous course of a perforator; however, the latter signifies that MRA is technically superior at delineating the intramuscular course of a perforator.

Enhanced understanding of the microvascular anatomy facilitated by CTA has assisted reconstructive surgeons in selecting an appropriate donor site, perforator, and flap, and numerous studies demonstrate that this has directly translated into an improvement in the clinical outcomes (Table 3). The studies have reported a significant reduction in the flap harvest time and the total operative time (5, 13, 118-120, 129-136). This leads to reduced exposure to general anesthesia, reduced risk of infection, and reduced intraoperative bleeding (6). Furthermore, the use of CTA for preoperative planning is associated with a reduction in postoperative flap complications, such as fat necrosis, partial, and total flap loss, and donor site morbidity, such as abdominal bulge and herniation (6, 9, 13, 118-120, 131-133). Interestingly, one study by Malhotra *et al* demonstrated no improvement in flap complications from preoperative CTA, even though there was a significant reduction in the operative time ($p < 0.05$), intraoperative blood loss ($p < 0.05$), and inpatient hospital stay ($p < 0.05$) (135).

The main limitations associated with CTA stem from potential sensitivity to the iodinated intravenous contrast, contrast-induced nephrotoxicity in patients with renal impairment, and exposure to ionizing radiation. The latest CTA scanning protocols that assess a targeted area for identifying abdominal wall perforators (140) and the development of radiation dose reduction software and algorithms in the latest scanners (96, 141) have decreased the average radiation exposure to 5 mSv per scan (97, 129, 142). This dose is equivalent of two abdominal X-rays, is significantly lower than a routine abdominal CT scan (98), and is theoretically associated with a 1-in-4,270 risk of fatal radiation-induced cancer (143). Moreover, perforators at the recipient site are not simultaneously imaged in order to minimize radiation. Most often, the patients have had a contrast-CT scan of the chest wall for their original breast cancer staging. Nonetheless, the recipient vessels, most commonly the internal mammary perforators, can be adequately visualized using a handheld Doppler probe (140). Furthermore, thoracic imaging poses risk to the radiation-sensitive contralateral breast and thyroid.

Magnetic resonance angiography (MRA)

Recently, MRA with Gadolinium-based contrast has become popular in order to bypass the risk of radiation associated with CTA (Table 1) (96). Recent advances in the image acquisition technique, introduction of novel contrast agents, and increasing availability of MRI scanners with stronger field strength have significantly improved the accuracy and the

quality of MRA images (144). Delayed equilibrium phase (EP) technique acquires images when both the artery and the vein are enhancing, compared to the conventional first-pass, or arterial-phase, technique (127). As a result, EP facilitates a longer image acquisition time leading to higher spatial and contrast resolution, produces diagnostic quality data despite minor motion artifacts, and has 100% sensitivity in detecting abdominal perforators (127). In addition, investigators have reported prone position to minimize respiratory-related motion artifacts (123, 145, 146). However, this method remains controversial since it alters the natural curved anatomy of the abdomen compromising the image quality of the perforators and since patients are indeed operated in supine position (97).

In contrast to the conventional gadolinium contrast agents, extracellular contrast agents, such as gadobenate dimeglumine, offer slightly higher relaxivity (147). However, it only has a short half-life of 100 seconds (147). Newer blood pool contrast agents, mainly gadofosveset trisodium (148), has demonstrated superior quality images secondary to a longer imaging window and a relatively large R1 (149). Gadofosveset trisodium has a long half-life of 28 minutes and reversibly binds to serum albumin with high fraction (90%) (150) leading to stronger contrast enhancement of the vessels (151, 152). Stronger field strength 3.0T scanners are increasingly becoming commonplace. They demonstrate superior spatial resolution and augment gadolinium-based contrast enhancements with reduced acquisition time and a decreased susceptibility to motion artifacts (153-156).

One of the significant benefits of MRA is that it eliminates exposure to ionizing radiation. Furthermore, gadolinium-based contrast agents have a safer risk profile, such as the rate of acute allergic reaction (0.07% vs 3%), in comparison to radioactive contrasts (157, 158). Thus, MRA may be advantageous in patients with younger age, iodine allergy, and impaired renal function. Moreover, muscle-to-vessel contrast ratio is superior in MRA, compared to CTA, leading to a clearer depiction of the perforator IM course (98). In autologous breast reconstructions, there is a growing number of reports demonstrating its accuracy in delineating perforators and its potential role in improving clinical outcomes.

Despite high specificity (100%), Rozen *et al* reported in an earlier study that MRA has low sensitivity (50%) in detecting abdominal wall perforators for breast reconstruction, suggesting it as an inferior option to CTA for perforator mapping purposes (Figure 10.1.4) (96). Advances in the imaging technique, contrast agents, and the application of higher field strength scanners have improved its accuracy in the last decade (Table 10.1.3) (4).

As a result, more recent studies report a high sensitivity (91.3% to 100%) with MRA (97, 98, 122, 123, 125-127). Of note, the accuracy of IM course depiction is high with MRA (97, 124-126). In contrast to CTA, there is a relative paucity in the literature describing MRA for a large clinical series describing its impact on clinical outcomes. Schaverin *et al* report that in 126 patients, MRA reduced the rate of partial flap loss ($p < 0.05$) and the total operative time in both unilateral and bilateral cases by 25 minutes and 40 minutes, respectively (136). However, the latter did not reach statistical significance. In an early study, Rozen *et al* demonstrated that using MRA reduced the incidence of flap complications to 0% in 6 patients (139).

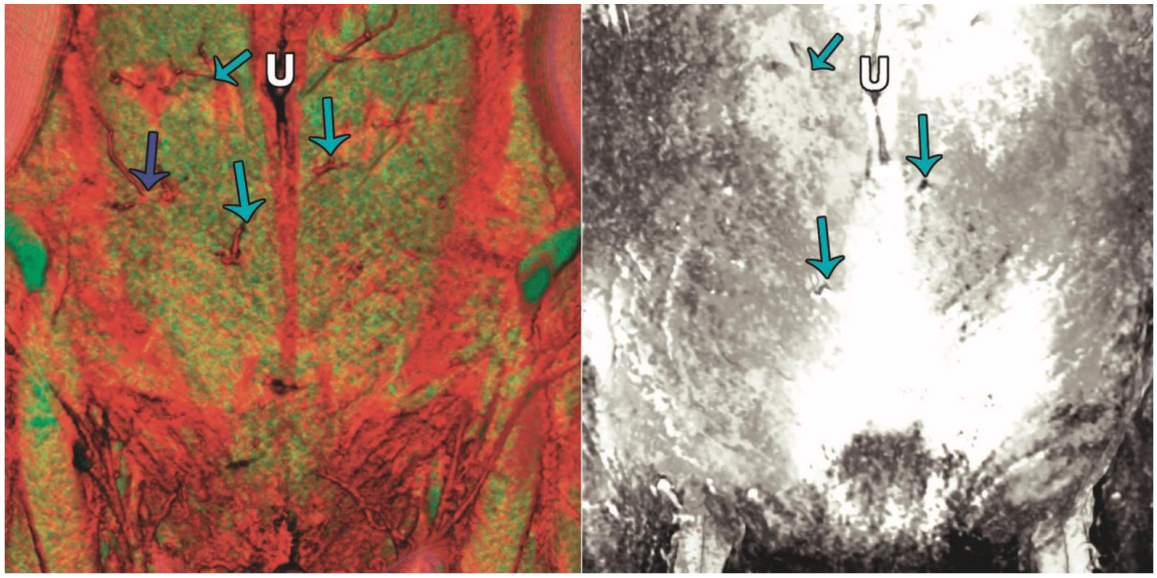

Figure 10.1.4: Volume-rendered, three dimensional reconstructions of the cutaneous perforators of the deep inferior epigastric artery (DIEA) using computed tomography angiography (CTA) on the left, and magnetic resonance angiography (MRA) on the right. Three large (>1mm) perforators were demonstrated with both modalities (light blue arrows), while one large perforator was demonstrated on CTA alone (dark blue arrow). Reproduced with permission from: Rozen *et al* (96)

One of the major drawbacks of MRA is related to its relatively high cost and low availability since an average MRA scan costs USD 600, compared to USD 400 for a CTA (139). Furthermore, due to its poor spatial resolution, MRA is limited at detecting perforators smaller than 0.8 mm in diameter (139). However, the recent introduction of novel contrast agents (159) and higher field strength scanners (160) are expected to improve on this limitation. Moreover, due to an expanded examination window, MRA is more susceptible to

motion artifacts and requires the patients to breath-hold for a long period of time. Despite its safer profile compared to ionizing contrast agents, gadolinium-based agents still presents with adverse effects, such as nephrogenic systemic fibrosis (161-164). Only 200 cases have been reported worldwide and this appears to be predisposed in patients with underlying impaired renal function. In addition, MRA is absolutely contraindicated in patients with severe obesity, implanted defibrillator or a pacemaker, implanted ferromagnetic device, and a cochlear implant. It is relatively contraindicated in patients with artificial heart valves and other types of implants. It is difficult to perform in patients with claustrophobia, severe anxiety, and confusion who are unable to lie still.

Discussion

Breast cancer is the most common cancer worldwide and is associated with the most common cancer-related deaths in women worldwide (41, 165). Since an increasingly number of women opt for mastectomy (42), postmastectomy breast reconstruction has become an essential component of the holistic treatment in patients with breast cancer to ensure their psychosexual wellbeing. To this end, breast reconstruction with autologous tissue has been demonstrated to provide the most functional and aesthetically pleasing outcome. Abdominal wall-based, rectus muscle-sparing DIEP flaps are considered the gold standard since they provide ample volume without causing significant donor site morbidity (49, 67). However, DIEP flaps are associated with longer microsurgical dissection leading to longer operative times and an increase in the postoperative microvascular complications.

To this effect, preoperative planning with modern imaging technology has become a crucial component of fashioning a DIEP flap for breast reconstruction. Handheld Doppler probes and color Duplex ultrasound are the first modality to be adapted for use in the preoperative setting (166). Although widely available and affordable, Doppler ultrasound is not sensitive or specific enough to be reliable and used routinely (6). Furthermore, it is susceptible to inter-observer variability and is unable to illustrate SIEA anatomy (80). Fluorescent angiography has been studied to preoperatively delineate the caliber and the location of the perforators (167). However, since this technology is only able to provide information up to a few millimeters deep from the skin and thick abdominal pannus is preferred in DIEP flaps, it has become less frequently used preoperatively (88). Instead, investigators are now using LA-ICGFA to assess microvascular anastomotic patency intraoperatively and evaluate perfusion in mastectomy skin flap (88, 110).

Since CTA was first reported for breast reconstruction by Masia *et al* (129), it has become the preferred preoperative imaging modality due to its high accuracy and reliability (7, 73, 119). With a free software, 3D images of the perforator anatomy can be created, from which its caliber, location, subcutaneous branching pattern, the DIEA and the SIEA anatomy can be easily visualized (138, 168). However due to concerns surrounding radiation exposure, high-risk contrast agents, and contrast-related nephrotoxicity, MRA has been investigated recently as an alternative (96, 119). Despite early findings suggesting low sensitivity in detecting perforators (96), recent advances in the image

acquisition technique, the introduction of higher quality contrast agents, and availability of stronger 3.0T scanners have enhanced the quality of perforator imaging from MRA (4, 123, 159). However, the image quality of CTA remains superior to the latest MRA technology. As a result, the latter has currently only preferred for a subset of patients in the younger age group, with iodine allergy and impaired renal function.

Conclusion

Preoperative imaging is an essential component of planning postmastectomy autologous breast reconstructions with DIEP flaps. Fluorescent angiography technology has been investigated as a preoperative imaging tool in the past. However, the investigators have demonstrated that it may instead be a useful intraoperative adjunct to evaluate the patency of microvascular anastomosis and the mastectomy skin perfusion. Currently, CTA is and remains the gold standard preoperative imaging modality due to its high accuracy, sensitivity, and specificity. In order to eliminate the radiation risk from CTA and the toxicity from radiosensitive contrast agents, MRA has been investigated in its role. Despite recent advancements, the image quality of MRA is still inferior to CTA and its widespread use is limited by high cost and lack of availability. Hence, MRA is best reserved for a subset of patients who are at a high risk from CTA, such as women with younger age, iodine allergy, and renal impairment.

10.2 Introduction of 3D Printing in Plastic and Reconstructive Surgery

PUBLISHED (Publication): ***Chae MP***, Rozen WM, McMenamin PG, Findlay MW, Spychal RT, Hunter-Smith DJ. Emerging applications of bedside 3D printing in plastic surgery. Front Surg. 2:25. doi: 10.3389/fsurg.2015.00025

Chapter Summary

Introduction: Modern imaging techniques are an essential component of preoperative planning in plastic and reconstructive surgery. However, conventional modalities, including three-dimensional (3D) reconstructions, are limited by their representation on 2D workstations. 3D printing, also known as rapid prototyping or additive manufacturing, was once the province of industry to fabricate models from a computer-aided design (CAD) in a layer-by-layer manner. The early adopters in clinical practice have embraced the medical imaging-guided 3D printed biomodels for their ability to provide tactile feedback and a superior appreciation of visuospatial relationship between anatomical structures. With increasing accessibility, investigators are able to convert standard imaging data into a CAD file using various 3D reconstruction softwares and ultimately fabricate 3D models using 3D printing techniques, such as stereolithography (SLA), multijet modeling (MJM), selective laser sintering (SLS), binder jet technique (BJT), and fused deposition modeling (FDM). However, many clinicians have questioned whether the cost-to-benefit ratio justifies its ongoing use.

Method: A review of the published English literature dating from 1950 to 2015 using databases, such as PubMed, Medline, Web of Science, and EMBASE was undertaken.

Results: The cost and size of 3D printers have rapidly decreased over the past decade in parallel with the expiration of key 3D printing patents. Significant improvements in clinical imaging and user-friendly 3D software have permitted computer-aided 3D modelling of anatomical structures and implants without out-sourcing in many cases. These developments offer immense potential for the application of 3D printing at the bedside for a variety of clinical applications.

Conclusion: In this review existing uses of 3D printing in plastic surgery practice spanning the spectrum from templates for facial transplantation surgery through to the formation of

bespoke craniofacial implants to optimize post-operative aesthetics are described. Furthermore, we discuss the potential of 3D printing to become an essential office-based tool in plastic surgery to assist in preoperative planning, developing intraoperative guidance tools, teaching patients and surgical trainees, and producing patient-specific prosthetics in everyday surgical practice.

Introduction

Advanced medical imaging has become an essential component of preoperative planning in plastic surgery. In breast reconstructive surgery, the introduction of computed tomographic angiography (CTA) has enabled surgeons to improve clinical outcomes (5) through accurate and reliable prospective selection of the donor site, flap, perforators, and the optimal mode of dissection (6, 7). Recent development of three-dimensional (3D) and 4D CTA techniques have enhanced spatial appreciation of the perforator vessels, their vascular territory and dynamic flow characteristics preoperatively (169, 170). However, current imaging modalities are limited by being displayed on a 2D surface, such as a computer screen. In contrast, a 3D printed haptic biomodel allows both the surgeon and the patient to develop a superior understanding of the anatomy and the procedure with the goal of improved operative planning through the ability to interact directly with a model of the patient-specific anatomy. Historically, the technically challenging nature of 3D software and the high prices of early 3D printers usually meant that clinicians keen to exploit these advantages had to outsource 3D printing and the cost of outsourcing often precluded it from being implemented widely. In this review, we analyze how recent advancements have enabled 3D printing to transition from the research and development laboratory to the clinical ‘bedside’ potentially making it a ubiquitous application in plastic surgery.

Methods

We reviewed the published English literature from 1950 to 2015 from well-known databases, such as PubMed, Medline, Web of Science, and EMBASE, using search terms, such as “autologous breast reconstruction”, “DIEP flap”, “fluorescent angiography”, “computed tomographic angiography”, and “magnetic resonance angiography”.

Results

3D Printing

3D printing, also known as rapid prototyping or additive manufacturing, describes a process by which a product derived from a computer-aided design (CAD) is built in a layer-by-layer fashion (Figure 10.2.1) (17-19). In contrast to the conventional manufacturing processes like injection molding, 3D printing has introduced an era of design freedom and enabled rapid production of customized objects with complex geometries (171-173). One of the major advantages of 3D printing is the capacity to directly translate a concept into an end product in a convenient, cost-efficient manner especially when translated into large-scale. It eliminates the typical intermediary stages involved in a product development, such as development, production, assembly lines, delivery, and warehousing of parts (174), and the subsequent savings made from using fewer materials and labor lead to an overall reduction in the cost of production (175).

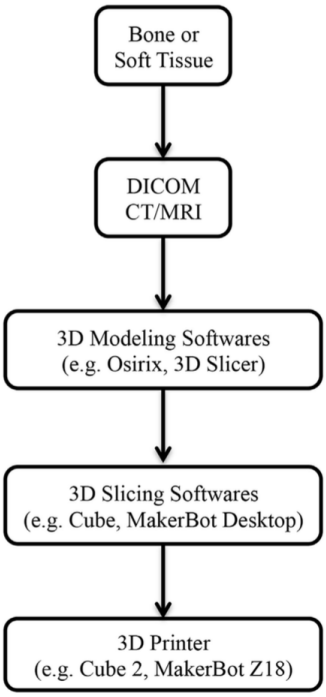

Figure 10.2.1. Steps involved from imaging to 3D-printed models. Abbreviations: DICOM: digital imaging and communications in medicine; CT: computed tomography; MRI: magnetic resonance imaging

3D printing has been utilized in industrial design since the 1980s; however, it has only become adapted for medical application in the last decade (20). Imaging data from routine computed tomography (CT) or magnetic resonance imaging (MRI) can be converted into a CAD file using a variety of 3D software programs, such as Osirix (Pixmeo, Geneva, Switzerland) or 3D Slicer (Surgical Planning Laboratory, Boston, MA) (Figure 1). These files are processed into data slices suitable for printing by proprietary softwares from the 3D printer manufacturers. While a range of 3D printing techniques have been developed for industrial use; stereolithography, multi-jet modeling (MJM), selective laser sintering (SLS), binder jetting, and fused deposition modeling (FDM) are the main approaches have been explored in the clinical setting (Table 10.2.1). We will explore each of these to evaluate their current and potential applications in clinical practice for both bony and soft tissue reconstruction.

3D Printing Techniques	Pros	Cons
SLA	• Current gold standard • High resolution • Increased efficiency with increase in print size • Detailed fabrication of internal structures	• >1 day of printing time required • Require extensive post-production manual handling • High cost related to the materials, the printer, and the maintenance
MJM	• High resolution • Minimal post-production manual handling • Multiple materials	• High cost related to the material and printer • Poorer surface finishing than SLA
SLS	• Not require support structures • Smooth surface finishing • Print delicate structures • Print in metal	• Require post-production manual handling • High cost related to the materials, the printer, and the maintenance • Require expert handling of the printer
BJT	• Not require support structures • Multiple colors	• Brittle • Require extensive post-

	• Multiple materials	production manual handling • Poor surface finish
FDM	• Low cost • Minimal maintenance • High availability of printers	• Require post-production manual removal of support structures • Poor surface finish • Mono-color and mono-material with the current technology

Table 10.2.1. A summary of the most commonly used 3D printing techniques in medical application. Abbreviations: SLA: stereolithography; MJM: multijet modeling; SLS: selective laser sintering; BJT: binder jet technique; FDM: fused deposition modeling.

Types of 3D Printing

Stereolithography

Stereolithography is the earliest 3D printing technology described for fabricating biomodels, where a layer of liquid photopolymer or epoxy resin in a vat is cured by a low-power ultraviolet (UV) laser (176). Excess raw materials and the supporting structures must be manually removed from the final product and cured in a UV chamber (177-179). Currently, stereolithography is considered the gold standard in 3D biomodel production and can yield resolutions of up to 0.025 mm. Moreover, its efficiency increases when constructing larger objects and is able to faithfully reproduce internal structural details (180). However, the need for manual post-build handling makes it labor-intensive and it still takes more than a day to produce a large model. Furthermore, in comparison to other 3D printing techniques, it is considered more expensive due to the high cost of the raw materials and for the printer upkeep (181, 182). Recently, an interesting development has introduced a technique, called continuous liquid interface production (CLIP), which simplifies the traditional stereolithography and increases the production speed by harnessing oxygen inhibition of UV-curable resin photopolymerization (183). This emerging modality has yet to be evaluated in plastic and reconstructive surgery.

MultiJet Modeling (MJM)

MJM printing, also known as MultiJet Printing (3D Systems, Rock Hill, SC) or Poly Jet Technology (Stratasys, Edina, MN), is akin to stereolithography, but the liquid photopolymer is immediately cured by the UV light preventing the time-consuming post-processing in the UV chamber and the prototypes are built with gel-like support materials that are readily dissolvable in water (184). MJM can manufacture models with high resolution (16 micron) that is comparable to or better than stereolithography, with an added benefit of the capacity to print in multiple materials for the desired degree of tensile strength and durability. Furthermore, a MJM printer is easier to maintain than a stereolithography set-up. However, the high price of these printers makes MJM more suitable for large-scale productions than for office-based/bedside desktop application.

Selective laser sintering (SLS)

SLS describes a process where powdered forms of thermoplastic, metal, glass or ceramic material are sintered by high-power laser beams in a layer-by-layer fashion (185, 186). Similar to stereolithography, the unsintered powders must be brushed away from the final product; however, they provide support and eliminate the need for support structures. As a result, SLS yields models with smoother surface finish and facilitates the production of delicate structures with high accuracy. Furthermore, the unsintered powders can be reused leading to a reduction in cost compared to stereolithography (181, 187). However, SLS remains significantly more expensive than Binder Jet Technique (below) and FDM, due mainly to the cost of the printer. In addition, SLS printers can be potentially hazardous due to the presence of lasers, pistons and gas chambers that can reach extremely high temperatures and hence, requires expert handling. These features have discouraged it from being widely implemented in non-industrial settings.

Binder Jet Technique (BJT)

BJT, or powder bed technique, is the first 3D printing approach that reduced the cost of 3D printers, thereby enabling a widespread consumerization of 3D printing (188). Similar to the SLS process, printer heads eject a binder material along with colored dye onto a layer of powder, fusing them layer-by-layer into a plaster model (189). Unfused powders provide adequate support for the “overhanging” designs and hence, simultaneous deposition of support structures is rarely required. Moreover, binder jet 3D printers can print in multiple colors and materials, and have multiple printer heads for faster printing. One of the major

drawbacks of binder jetting is that the final product usually lacks strength and has a poorer surface finish than stereolithography or SLS. Hence, all models require post-production strengthening with materials, such as melted wax, cyanoacrylate glue or epoxy.

Fused Deposition Modeling (FDM)

FDM is the most commonly used consumer 3D printing technology available currently and is also the most affordable (182, 190, 191). A melted filament of thermoplastic material is extruded from a nozzle moving in the x-y plane and solidifies upon deposition on a build plate (192). After each layer, the build plate is lowered 0.1 mm and the process is repeated until the final product is produced. Acrylonitrile-butadiene-styrene (ABS) and polylactic acid (PLA) are the most frequently used raw materials in FDM printers. A notable shortcoming for the use of FDM in medical applications is that most anatomical structures have complex shapes and hence, would require support structures. Although they are easy to remove manually, the aftermath generally leaves superficial damage to the model compromising its surface finish and esthetics. Hollow internal structures or blind-ended openings are particularly difficult to clean build material from. Furthermore, most household FDM printers are currently limited to fabricating in mono-color and mono-material. However, this can be overcome by recently developed dual-extruder technology, where two filaments of different color or material can be extruded from a common printer head. It is currently found in printers, such as MakerBot Replicator 2X Experimental (MakerBot Industries, New York, New York), Cube 3 (3D Systems, Rock Hill, SC), and Creatr x1 (Leapfrog, Emeryville, CA). Moreover, the second extruder can be configured to build support structures using MakerBot Dissolvable Filament (MakerBot Industries), made up of High Impact Polystyrene (HIPS) (193). When the final product is immersed in water with limonene, a widely available citrus-scented solvent, the support structures selectively dissolve away within 8 to 24 hours but these dual extruder printers have not yet become established in the mainstream.

3D Printing in Medicine

In the last decade or so, researchers have demonstrated a wide range of uses for 3D printing across numerous surgical disciplines. Clinically, 3D printed haptic biomodels provide a tactile feedback and enables users to simulate complex anatomical movements, such as articulation at the temporomandibular joint, that are difficult to reproduce in a

computer software (194). As a result, they facilitate an enhanced appreciation of the visuospatial relationship between anatomical structures for the surgeons (15). This can translate into shorter operative time, reduced exposure to general anesthesia, shorter wound exposure time and reduced intraoperative blood loss (179, 195, 196).

Preoperative Planning

In preoperative planning, 3D printed biomodels have been beneficial in orbital and mandibular reconstruction in maxillofacial surgery (182, 197-201); craniofacial, skull base, and cervical spine reconstruction in neurosurgery (195); prefabrication of bony fixation plates and planning excision of bony lesions in orthopedic surgery (202, 203); mapping complex congenital heart defects and tracheobronchial variation in cardiothoracic surgery and cardiac transplantation (187, 204-212) (Figure 10.2.2); endovascular repair of abdominal aortic aneurysm and aortic dissection in vascular surgery (213-215); partial nephrectomy for renal tumors in urology (216); osteoplastic flap reconstruction of frontal sinus defects in ear, nose, and throat surgery (217, 218); and hepatectomy and liver transplantation in general surgery (219-221).

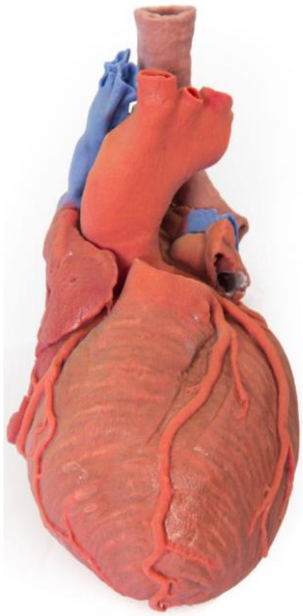

Figure 10.2.2. 3D printed haptic model of a heart and the great vessels fabricated using Projet x60 series 3D printers. Reproduced with permission from Centre for Human Anatomy and Education

Intraoperative Guidance

Furthermore, 3D softwares have been used to fabricate patient-specific surgical templates and intraoperative guidance devices to aid surgeons in maxillofacial surgery (222-227), neurosurgery (228), orthopedic surgery (229), hand surgery (230), and general surgery (231).

Education

3D printed haptic biomodels can be useful for educating patients during medical consultations and training surgical trainees (190, 205, 232-241).

Customized Prosthesis

Moreover, 3D printing has enabled rapid and convenient production of customized implants. Investigators have manufactured patient-specific mandibular implants in maxillofacial surgery (242-244), cranial vault implants for cranioplasty in neurosurgery (245, 246), hip implants in orthopedic surgery (247, 248), and a bioresorbable airway splint for complex tracheobronchomalacia in pediatric cardiothoracic surgery (249).

Allied Health

In other areas of medicine, 3D printing has revolutionized the manufacturing of hearing aids and currently 99% of all hearing aids in the world are 3D printed (250). Additionally, 3D printing has helped make complex diagnoses in forensic medicine (251); reformed anatomy education (252); helped in planning repairs of Charcot's foot in podiatry (253); permitted the fabrication of custom-made dental implants in dentistry (254-256); produced patient-specific 3D printed medication in pharmaceutical industry (257, 258); and assembled custom-design tissue scaffolds in regenerative medicine (259, 260).

3D Printing at the Bedside

Despite a vast potential scope of 3D printing in clinical practice and significant media interest with frequent reports of the latest innovative advancements made using this technology (25). the incorporation of 3D printing as a clinical bedside application has not

been widespread (26). One potential barrier is the perception amongst clinicians that 3D printing is technically sophisticated and is reserved for planning intricate operations and devising highly specialized implants (26). As a result, 3D printing is often outsourced to an external company, which compounds the cost and time. This demonstrates a lack of awareness of the increasing accessibility of the 3D softwares and the declining cost of the 3D printers (26).

3D Reconstruction Software

In order to fabricate a 3D biomodel, two types of software are required; firstly, a "3D modeling" software that translates the DICOM (digital imaging and communications in medicine) files from CT/MRI scans into a CAD file, and secondly, a "3D slicing" software that divides the CAD file into thin data slices suitable for 3D printing (261).

3D Modeling Software

A range of 3D modeling softwares is available (Table 2); however, early ones, such as Mimics (Materialise NV, Leuven, Belgium), would incur a high cost for the initial purchase and for the ongoing software updates. Driven by the consumerization of 3D printing and an increasing number of both professional and community software developers, free open-source softwares, such as Osirix (262) and 3D Slicer (263-265), have become widely utilized. Our group prefers using them due to the latter's expansive developer community base, called the Slicer Community, a plethora of plug-in functions, and a user interface that is intuitive to an individual with no engineering background (18, 35). An ideal 3D modeling software should be free; capable of highlighting the region of interest and eliminate undesired areas using the threshold and the segmentation function respectively; export the 3D model as a CAD file in a universally-accepted 3D file format, such as STL (standard tessellation language); and possess an easy-to-use interface. Encouragingly, there are numerous 3D modeling softwares available in the market currently that fit all of the criteria (Table 10.2.2).

Name	**Company**	**Free**	**Threshold/ Segmentation**	**Export STL**	**Easy User Interface**	**OS Platform**
3D Slicer	Surgical Planning Laboratory	Y	Y	Y	Y	W, M

MITK	German Cancer Research Centre	Y	Y	Y	Y	W, M
Osirix	Pixmeo	Y	Y	Y	Y	M
MIPAV	NIH CIT	Y	Y	Y	N	W, M
MeVisLab	MeVis Medical Solutions AG	Y	Y	Y	N	W, M
InVesalius	CTI	Y	Y	Y	N	W, M
Mimics	Materialise NV	N	Y	Y	Y	W, M
Avizo / Amira	FEI Visualization Science Group	N	Y	Y	Y	W, M
3D Doctor	Able Software	N	Y	Y	Y	W
Dolphin Imaging 3D	Dolphin Imaging & Management	N	Y	Y	Y	W
Analyze	AnalyzeDirect	N	Y	Y	N	W, M
GuideMia	GuideMia	N	Y	Y	N	W, M
OnDemand3D	CyberMed	N	N	Y	N	W, M
VoXim	IVS Technology	N	Y	Y	N	W
ScanIP	Simpleware	N	Y	Y	N	W

Table 10.2.2. A summary of 3D modeling softwares that can convert a DICOM data from a standard CT/MRI scans into a CAD file. Abbreviations: STL: standard tessellation language; OS: operating system; Y: yes; N: no; W; Windows OS; M: Mac OS.

3D Slicing Software

3D slicing softwares digitally “slice” a CAD file into layers suitable for 3D printing. However, they are also useful for altering the orientation of the CAD file relative to the printer build plate to give an optimal direction, which minimizes the requirement for the support structures and, in turn, reduces the amount of material used and therefore also reduces the printing time. This process can be readily performed using proprietary softwares that accompany the 3D printers at no extra cost and usually possess a simple graphic user interface, such as Cube software (3D Systems) and MakerBot Desktop (MakerBot Industries).

3D Printers

The cost of early 3D printers, consisting of mostly the stereolithography type described above, precluded widespread adoption of 3D printing in the initial years; however, the expiration of key patents surrounding stereolithography and FDM in the last decade has

fueled a surge in the number of commercial developers leading to an increase in the availability and a significant reduction of the cost (Table 10.2.3). Several affordable stereolithography 3D printers have entered the market since then, such as Form 1+ (Formlabs, Somerville, MA) and ProJet 1200 (3D Systems). However, they are capable of building only small designs (i.e. 12.5 x 12.5 x 16.5 cm) and hence, remain unsuitable for many applications. Similarly, current MJM and SLS 3D printers are generally bulky, expensive, and require specialized skills for safe handling of the hardware and its maintenance. Binder jet 3D printers are gradually being avoided due to the brittle quality of the end-products and the large size of the printer. Currently, FDM 3D printers are the preferred option as a desktop application in medicine for their affordability and practicality. The accuracy and the quality of FDM products are comparable to stereolithography, SLS, and binder jet (266-268). Furthermore, FDM incurs the least cost in maintenance from ongoing print materials (Table 10.2.4).

Type	Name	Company	Cost (USD)	Print Area (cm)	Print Resolution (nm)	Printer Size (cm)	Printer Weight (kg)
SLA	Form 1+	Formlabs	3,999	12.5x12.5x16.5	25	30.0x28.0x45.0	8
SLA	ProJet 1200	3D Systems	4,900	4.3x2.7x15.0	30.5	22.9x22.9x35.6	9
SLA	ProJet 6000	3D Systems	200,000	25.0x25.0x25.0	50	78.7x73.7x183.0	181
SLA	ProJet 7000	3D Systems	300,000	38.0x38.0x25.0	50	98.4x85.4x183.0	272
SLA	ProX 950	3D Systems	950,000	150.0x75.0x55.0	50	220.0x160.0x226.0	1951
MJM	Objet 24 series	Stratasys	19,900	23.4x19.2x14.9	28	82.5x62.0x59.0	93
MJM	Objet 30 series	Stratasys	40,900	29.4x19.2x14.9	28	82.5x62.0x59.0	93
MJM	ProJet 3510 series	3D Systems	69,500	29.8x18.5x20.3	16	29.5x47.0x59.5	43.4
MJM	Objet Eden	Stratasys	123,000	49.0x39.0x20.0	16	132.0x99.0x120.0	410
MJM	ProJet 5000	3D Systems	155,000	53.3x38.1x30.0	32	60.3x35.7x57.1	53.8
MJM	ProJet 5500X	3D Systems	155,000	53.3x38.1x30.0	29	80.0x48.0x78.0	115.7
MJM	Connex series	Stratasys	164,000	49.0x39.0x20.0	16	140.0x126.0x110.0	430
MJM	Objet	Stratasys	164,000	49.0x39.0x20.0	16	142.0x112.0x113.0	500

	Connex series						
MJM	Objet 1000	Stratasys	614,000	100.0x80.0x50.0	16	280.0x180.0x180.0	1950
SLS	sPro series	3D Systems	300,000	55.0x55.0x46.0	80	203.0x160.0x216.0	2700
SLS	ProX series	3D Systems	500,000	38.1x33.0x45.7	100	174.4x122.6x229.5	1360
BJT	ProJet 160	3D Systems	40,000	23.6x18.5x12.7	100	74.0x79.0x140.0	165
BJT	ProJet 260C	3D Systems	40,000	23.6x18.5x12.7	100	74.0x79.0x140.0	165
BJT	ProJet 360	3D Systems	40,000	20.3x25.4x20.3	100	122.0x79.0x140.0	179
BJT	ProJet 460 Plus	3D Systems	40,000	20.3x25.4x20.3	100	122.0x79.0x140.0	193
BJT	ProJet 4500	3D Systems	40,000	20.3x25.4x20.3	100	162.0x80.0x152.0	272
BJT	ProJet 660 Pro	3D Systems	40,000	25.4x38.1x20.3	100	188.0x74.0x145.0	340
BJT	ProJet 860 Plus	3D Systems	40,000	50.8x38.1x22.9	100	119.0x116.0x162.0	363
FDM	Huxley Duo	RepRapPro	453	13.8x14.0x9.5	12.5	26.0x28.0x28.0	4.5
FDM	Mendel	RepRapPro	586	21.0x19.0x14.0	12.5	50.0x46.0x41.0	8
FDM	Ormerod 2	RepRapPro	702	20.0x20.0x20.0	12.5	50.0x46.0x41.0	6
FDM	Tricolour Mendel	RepRapPro	863	21.0x19.0x14.0	12.5	50.0x46.0x41.0	8
FDM	Cube 3	3D Systems	999	15.3x15.3x15.3	70	33.5x34.3x24.1	7.7
FDM	Buccaneer	Pirate 3D	999	14.5x12.5x15.5	85	25.8x25.8x44.0	8
FDM	Original+	Ultimaker	1,238	21.0x21.0x20.5	20	35.7x34.2x38.8	N/A
FDM	Replicator mini	MakerBot	1,375	10.0x10.0x12.5	200	29.5x31.0x38.1	8
FDM	Creatr	Leapfrog	1,706	20.0x27.0x20.0	50	60.0x50.0x50.0	32
FDM	Replicator 2	MakerBot	1,999	28.5x15.3x15.5	100	49.0x42.0x38.0	11.5
FDM	LulzBot TAZ 4	Aleph Objects	2,195	29.8x27.5x25.0	75	668.0x52.0x51.5	11
FDM	AW3D HDL	Airwolf 3D	2,295	30.0x20.0x28.0	100	61.0x44.5x46.0	17
FDM	Creatr HS	Leapfrog	2,373	29.0x24.0x18.0	50	60.0x60.0x50.0	40
FDM	Replicator 2x	MakerBot	2,499	24.6x15.2x15.5	100	49.0x42.0x53.1	12.6
FDM	Ultimaker 2	Ultimaker	2,500	23.0x22.5x20.5	20	35.7x34.2x38.8	N/A
FDM	Replicator 5th gen	MakerBot	2,899	25.2.19.9x15.0	100	52.8x44.1x41.0	16
FDM	AW3D HD	Airwolf 3D	2,995	30.0x20.0x30.0	60	61.0x44.5x46.0	17
FDM	Cube Pro	3D Systems	3,129	20.0x23x27.0	100	57.8x59.1x57.8	44
FDM	AW3D	Airwolf 3D	3,495	30.0x20.0x30.0	60	61.0x44.5x46.0	17

	HDX						
FDM	AW3D HD2X	Airwolf 3D	3,995	27.9x20.3x30.5	60	61.0x45.7x45.7	18
FDM	Creatr xl	Leapfrog	4,988	20.0x27.0x60.0	50	75.0x65.0x126.0	37
FDM	Replicator Z18	MakerBot	6,499	30.5x30.5x45.7	100	49.3x56.5x85.4	41
FDM	Xeed	Leapfrog	8,705	35.0x27.0x60.0	50	101.0x66.0x100.0	115
FDM	Mojo	Stratasys	9,900	12.7x12.7x12.7	178	63.0x45.0x53.0	27
FDM	uPrint	Stratasys	13,900	20.3x15.2x15.2	254	63.5x66.0x94.0	94
FDM	Objet Dimension series	Stratasys	40,900	25.4x25.4x30.5	178	83.8x73.7x114.3	148
FDM	Fortus series	Stratasys	184,000	91.4x61.0x91.4	127	277.2x168.3x202.7	2869

Table 10.2.3. A summary of commercially available 3D printers from ten leading 3D printing companies in the world. Where a 3D printer series is characterized, the lowest cost, largest print area, lowest print resolution, largest printer size and greater printer weight are selected for comparison. Abbreviations: SLA: stereolithography; MJM: multijet modeling; SLS: selective laser sintering; BJT: binder jet technique; FDM: fused deposition modeling; cm: centimeter; kg: kilograms; nm: nanometers; N/A: not available

Type of 3D Printing	**Average Cost of Print Material (USD)**
SLA	200 per L
MJM	300 per kg
SLS	500 per kg
BJT	100 per kg
FDM	50 per kg

Table 10.2.4. A summary of average raw material cost of each 3D printing technique. Abbreviations: SLA: stereolithography; MJM: multijet modeling; SLS: selective laser sintering; BJT: binder jet technique; FDM: fused deposition modeling; L: liter

3D Printing in Plastic & Reconstructive Surgery

In plastic and reconstructive surgery, 3D printed haptic biomodels can potentially play a significant role in preoperative planning, intraoperative guidance, training and teaching, and fashioning patient-specific prosthesis (Table 10.2.5).

Application		**Example**	**Reference**
Preoperative Planning	Soft Tissue Mapping	Breast Reconstruction	(35)
		Ear Reconstruction	(269, 270)
		Nasal Reconstruction	(271)
		Mandibular Soft Tissue Tumor Resection	(272)
		"Reverse" Model of Ankle Defect	(273)
		Sacral Defect	(274)
	Vascular Mapping	Internal Mammary Artery Perforators	(275)
		DIEA Perforators	(18)
	Bony Mapping	Basal Thumb Osteoarthritis	(18)
	4D Printing	Thumb Movement	(276)
Intraoperative Guidance		Bone Reduction Clamp	(230)
Surgical Training		N/A	
Patient Education		N/A	
Patient-Specific Prosthesis		Craniofacial Implant	(277)
		"Ear and Nose Library"	(278, 279)

Table 10.2.5. A summary of published application of 3D printing in Plastic and Reconstructive Surgery. Abbreviations: DIEA: deep inferior epigastric artery; 4D: four dimensional; N/A: not available

Preoperative Planning: Soft Tissue Mapping

Perforator flap surgery is routinely performed in the reconstruction of large soft tissue defects after trauma or an oncologic resection. Preoperative planning with computed tomographic angiography (CTA) has revolutionized the field by enabling the reconstructive surgeon to identify an ideal donor site, flap, and perforator for a free flap transfer (5, 73), facilitating a greater flap success rate and an overall improvement in the clinical outcomes

(6, 7, 72). In addition to CTA, 3D biomodels can provide an additional layer of clinical information through visual and tactile examination.

In a recent report, our research group described a technique of fashioning a “reverse” model representing a soft tissue ankle defect that was utilized for planning a perforator flap-based reconstruction (Figure 10.2.3) (273).

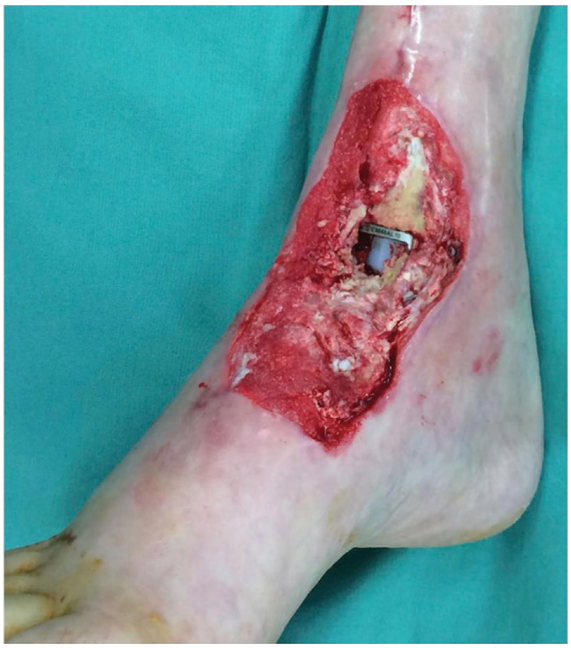

Figure 10.2.3. Photograph of the soft tissue ankle defect showing the exposed metal hardware from a previous ankle reconstruction. Reproduced with permission from Chae *et al* (273)

Routine CTA of the lower limbs (i.e. recipient site) and the forearms (i.e. donor site) were conducted and the DICOM data was converted into a CAD file using Osirix. The 3D image of the normal contralateral ankle was mirrored, superimposed over the image of the pathological side, and after digital subtraction using Magics software (Materialise NV, Leuven, Belgium), a “reverse” model representing the wound defect is created (Figure 10.2.4).

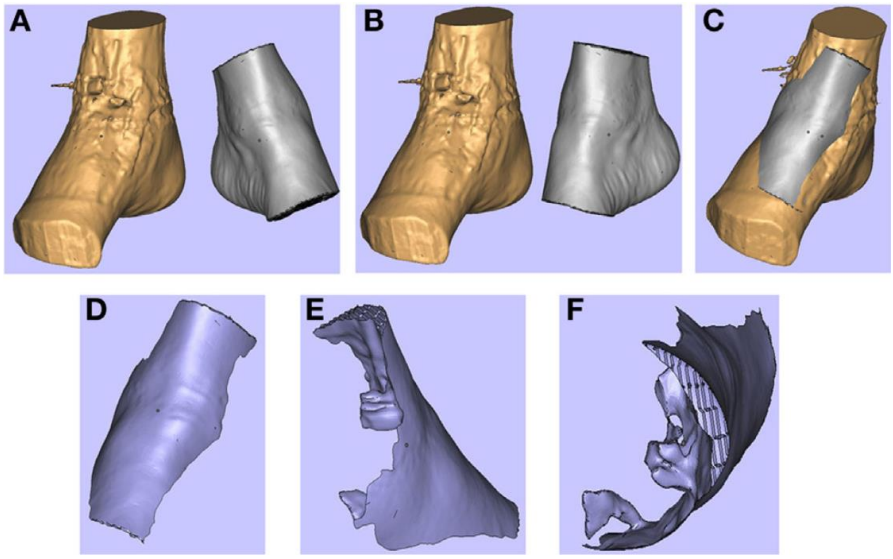

Figure 10.2.4. 3D image of the right (pathological) ankle is juxtaposed to the left (normal) ankle (A). The left ankle is reflected (B) and superimposed on to the right ankle (C). These images are subtracted from each other to produce a "reverse" model of the soft tissue defect (D-F). Reproduced with permission from Chae *et al* (273)

This mirroring function can also be performed in free open-source softwares, such as Osirix and 3D Slicer. This helped the surgeon preoperatively appreciate the length, width, and depth of the free flap that needed to be harvested in order to adequately cover the defect. Both the pathological ankle and the "reverse" model were fabricated in PLA filaments using a Cube 2 printer (3D Systems) (Figures 10.2.5 & 10.2.6).

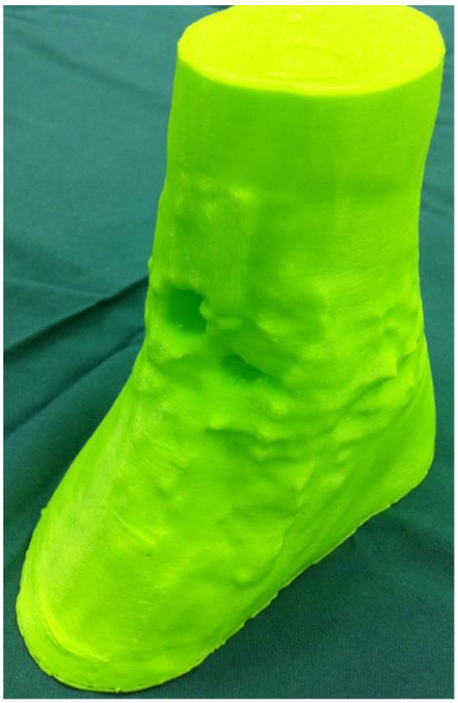

Figure 10.2.5. 3D printed haptic model of the soft tissue ankle defect. Reproduced with permission from Chae *et al* (273)

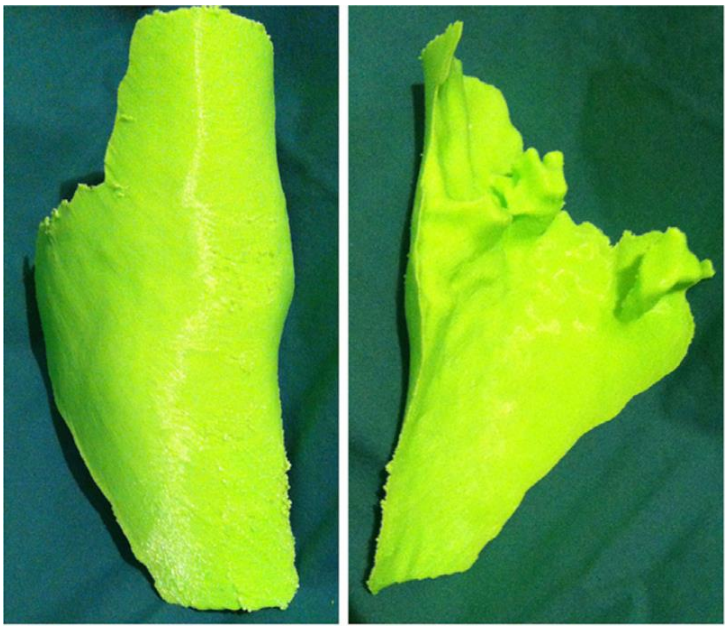

Figure 10.2.6. 3D printed haptic model of the "reverse" image representing the wound defect. Reproduced with permission from Chae *et al* (273)

We also recently demonstrated the utility of a 3D printed biomodel for planning perforator flap reconstruction of a sacral wound defect post-oncologic resection (274). Likewise, we used Osirix to translate the preoperative sacral CTA data into a CAD file. Due to the maximal build dimensions of the Cube 2 printer (i.e. 16 x 16 x 16 cm) the 3D image of the sacral defect was scaled down using the Cube software. The haptic model still accurately represented the shape and depth of the defect and its relationship with the surrounding anatomical structures.

3D printing can potentially be a valuable tool in the assessment of soft tissue volume. Volumetric analysis is an essential component of breast reconstructive surgery and currently surgeons rely on 2D photography or 3D scanning technology, such as VECTRA (Canfield Imaging Systems, Fairfield, NJ) (280), and subjective visual assessment. One of the main limitations of 3D photography like VECTRA is the inability to account for an underlying chest wall asymmetry that may incorrectly lead to an asymmetrical appearance despite equal breast parenchymal volumes. Moreover, the accuracy of each scan is reliant

on the patients standing with their back flat against a wall, which may not be feasible in certain conditions, such as kyphosis or scoliosis. Recently, we reported the use of a 3D printed model of a patient with post-mastectomy breast asymmetry for preoperative planning (Figure 10.2.7) (233). Despite being scaled down to fit the build size of the printer, having an accurate physical replica helped surgeons appreciate the difference in the breast shape and volume. Furthermore, using the segmentation function in Osirix we were able to quantify the breast parenchymal volume difference.

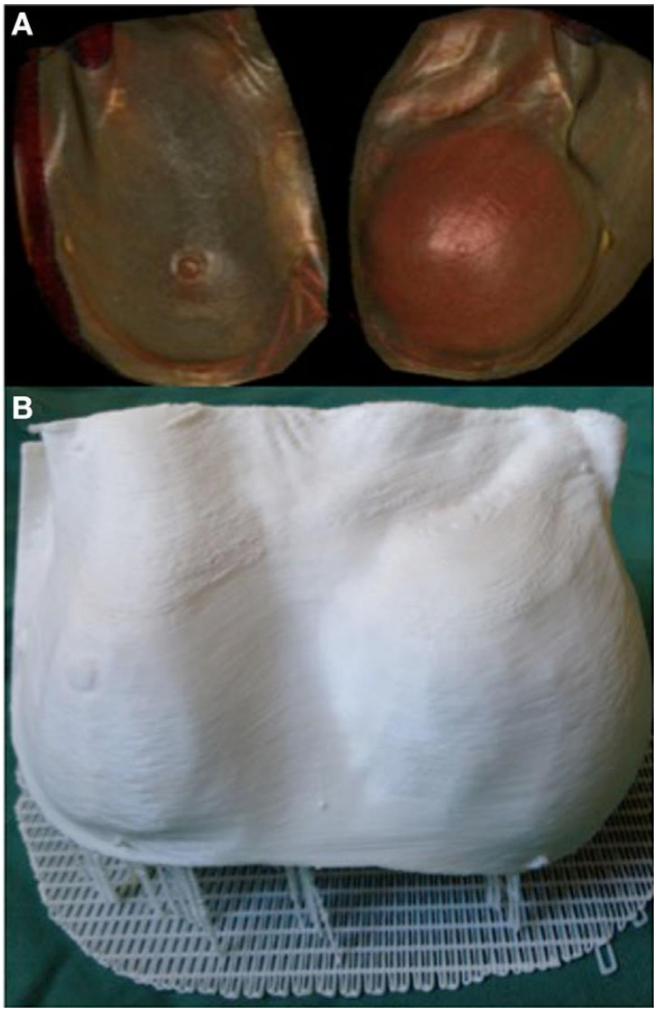

Figure 10.2.7. 3D reconstructed CT images of a patient with breast asymmetry post-mastectomy (A) and the 3D printed breast model of the same patient (B). Reproduced with permission from Chae *et al* (35)

Preoperative Planning: Vascular Mapping

Understanding the vascular anatomy of perforators and their relationship with the regional anatomical structures is critical in perforator flap surgery and to this effect, CTA is currently the gold standard preoperative investigation (5, 6, 73, 139). Recently, Gillis and Morris reported a cadaveric study where a model of internal mammary artery perforators and the neighboring ribs was fabricated using a binder jet 3D printer (ProJet x60 series, 3D Systems) (275). The authors demonstrated the benefits of physically interacting with the model and the ability to visualize it in multiple planes to aid dissection and identification of the dominant perforator. However, they also noted a significant cost associated with outsourcing the 3D printing (USD 400-1,200) and the print material was too delicate for small-size blood vessels that required post-production strengthening with wax coating.

Likewise, our group 3D printed the perforator anatomy for planning a deep inferior epigastric artery perforator (DIEP) flap breast reconstruction. From the preoperative CTA, we created a CAD file of the deep inferior epigastric artery (DIEA) with the surrounding bony landmarks using 3D Slicer and the Cube 2 printer. Despite having to scale down the model to fit the printer dimensions, surgeons could intuitively discern the arterial anatomy from the replica. Interestingly, the current technique impeded the perforators of DIEA to be 3D printed. Considering that the DICOM data of the CTA and the Cube 2 printer have a resolution of 0.625 mm and 0.200 mm respectively, and the mean diameter of a DIEA perforator ranges between 1 and 1.4 mm (72), this may be most likely explained as a limitation of the 3D modeling software, 3D Slicer. This may be prevented in the future by installing free add-on software functions, such as Vascular Modeling Toolkit (VMTK, Orobix, Bergamo, Italy), in 3D Slicer, that are designed to specifically segment vascular structures. Currently, these are still early in the development phase and are difficult to manipulate without significant computer engineering proficiencies. As the field advances, we would naturally expect the user interface of these softwares to become easier to use.

Preoperative Planning: Bony Mapping

3D printing bony pathology in the forearm, wrist, and hand is another suitable utility of this technology in plastic and reconstructive surgery. CT scans have been the most commonly used imaging modality for medical 3D printing. Since they readily differentiate bones, 3D printing bony structures has become well established in various surgical disciplines, such as maxillofacial surgery (181, 182, 194, 281-283), neurosurgery (195, 228, 246), and orthopedic surgery (284-288). Using Osirix and Cube 2 printer, our research group 3D

printed a model of a subluxed first carpometacarpal joint. Being able to visualize the model from various angles and the tactile feedback facilitated an intuitive understanding of the anatomical relationship between the first metacarpal and the trapezium. The information was useful for planning the optimal method of reduction.

A New Evolution: 4D Printing

Recently, we described for the first time the concept of applying 3D printing to 4D CT scans, or 4D printing, where time is added as the fourth dimension to the standard 3D printing (276). 4D CT is a novel imaging modality developed to remove motion artifacts from organs, such as lungs, in order to enhance the image quality and facilitate precise delivery of radiotherapy (289, 290). In plastic surgery, investigators have utilized 4D CTA to assess the vascular territories and the dynamic flow characteristics of an individual perforator (169, 170). Using Osirix and Cube 2 printer, our group 3D printed the carpal and metacarpal bones of a patient in life-size at various stages of the thumb movement, such as thumb abduction (Figure 10.2.8). In contrast to the 3D reconstructions on a 2D computer screen and 3D models, 4D printed haptic models accurately depicted the position of the carpal bones during each movement and enabled an instinctive appreciation of the spatiotemporal relationship between them. One of the major disadvantages was the reliance on the clinician reviewing the 4D CT data to select the scans most representative of the carpal bone transition during each movement for 3D printing. This can be overcome as 3D printers become faster thus allowing more models to be fabricated.

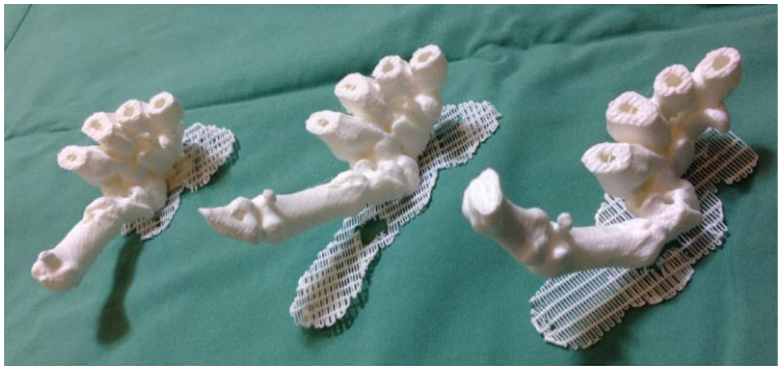

Figure 10.2.8. 4D printed haptic models of carpal and metacarpal bones demonstrating thumb abduction (from left to right). Reproduced with permission from Chae *et al* (276)

Intraoperative Guidance

The convenience of 3D printing has propelled an innovation in custom designs of surgical templates and equipments that helps guide the surgeon intraoperatively. In the literature, investigators have demonstrated the utility of 3D printing a modified army/navy surgical retractor (231); patient-specific orthognathic templates to guide osteotomy (226) and mandibular fracture reduction device (291) in maxillofacial surgery; screw fixation guide system in spinal neurosurgery (292); and drill templates to aid surgical correction of multilevel cervical spine instability in orthopedic surgery (229). In plastic and reconstructive surgery, Fuller *et al* illustrated how 3D printing can expedite the development of a custom-made bone reduction clamp design for hand fractures, in comparison to the conventional processes that can become protracted and actually be discouraging to innovation (230). The authors collaborated with an engineer to produce 3D prototype designs and converted them into CAD files using free 3D softwares, such as SketchUp (Trimble Navigation, Sunnyvale, CA) and MeshLab (ISTI-CNR, Pisa, Italy) respectively. 3D printing of the FDM prototypes was outsourced, costing USD 75 and 1-3 days for the delivery to arrive. The final design was manufactured in metal using an additive manufacturing technique, called direct metal laser sintering, and was again outsourced, costing USD 1200 and 2 days for the delivery. The authors acknowledged that the 3D softwares for designing prototypes are currently not intuitive for clinicians with only basic computer proficiency. Furthermore, the final cost exceeded the cost of purchasing a standard equipment. However, as 3D printing technology advances and the 3D printing is performed “in-house”, the difference may become minimal in the future.

Surgical Training

Detailed knowledge of anatomical structures and their spatial relationships are essential assets of a plastic surgeon and objectives of a surgical training program. Through the standard medical training, a surgical aspirant can gain procedural experiences from performing dissections on human cadavers as a medical student and assisting senior surgeons in the operating theater as a resident, leading towards a gradual acquisition of competence. However, human cadavers are becoming relatively scarce from the anatomical education curricula due to high maintenance costs, cultural and social controversies, and safety issues associated with the formalin-containing embalming fluids (252, 293). Furthermore, the operative experience gained as an assistant to a senior surgeon is secondary to a primary operator experience. To this end, 3D printed anatomical

models can serve as an accurate, tactile visualization tool and a surgical simulation device. Moreover, 3D printed haptic biomodels can be utilized to reproduce complex, patient-unique pathologies that facilitate the surgical trainees to preoperatively predict potential intraoperative challenges and postoperative outcomes and aid in their learning. Subsequent improvement in the surgeon's competence may lead to enhanced clinical outcomes and a reduced risk of complications. Investigators from various surgical disciplines have demonstrated the utility of 3D printing in training, such as neurosurgery (232-237, 294, 295), cardiothoracic surgery (214, 238-240, 296-298), urology (241, 299), and general surgery (190) However, one of the major limitations currently is the ability to print in materials that closely mimic the biomechanical properties and modulus of real human tissue as well as possessing realistic colors. As more materials enter the scope of 3D printing, future 3D printed biomodels will be able to more closely reproduce true anatomy (210, 232, 234, 239).

Patient Education

3D printed replicas can be useful to facilitate the physician-patient interaction during a consultation with the aim of improved understanding of the intended procedure, its potential outcomes and complications and thus can form an important aspect of informed consent. Traditional CT/MRI scans are often difficult to comprehend for patients from a non-medical background. In recent times, plastic surgeons have utilized 3D scanning technology, such as VECTRA (Canfield Imaging Systems, Fairfield, NJ), to accurately simulate potential outcomes from a cosmetic procedure on a computer screen (280). However, studies have consistently demonstrated that visual and tactile feedback from a 3D haptic model provides a superior understanding of anatomical details compared to 2D or 3D imaging techniques (15, 218, 300).

Patient-Specific Prosthesis

As modern medicine ultimately progresses towards individualized treatment approaches, customizability of 3D printing can transform the manufacturing of patient-specific prostheses to being widely accessible and affordable. In comparison to a standard implant, a custom-made one is more likely to yield superior functional and esthetic outcomes (301, 302). Typical 3D printing materials can be sterilized using chemicals, such as Food and Drug Administration approved glutaraldehyde protocols (231), steam (181), and gas (303)

for intraoperative handling. In the last decade, investigators have reported 3D printed prostheses of nose (278, 304), ears (279, 305-308), eyes (309, 310), face (311, 312), and hand (17, 313). Furthermore, an Italian research group led by De Crescenzio and Ciocca has established an “Ear and Nose Library” where CAD files of 3D scanned ears and noses of normal university students are stocked (278, 279). When patients have pathology affecting both ears or the entire nose that impedes mirroring of the normal contralateral side to reconstruct the defect, the clinicians can select the most suitable CAD file from this database to fashion a prosthesis. In plastic surgery, standard breast implants are available in different volumes, but in a limited number of shapes. To this effect, 3D printed breast implants customized to conform to the individual variations in the chest wall anatomy and the patient’s desired breast shape and size may lead to a more esthetic and satisfactory outcome.

Most reports have indicated that 3D printed custom prostheses provide superior esthetics in comparison to the traditional wax-based handcrafted prosthetics (305, 307, 308). Furthermore, customized implants eschew the need to intraoperatively modify and adjust associated with the standard implants, which can directly lead to improved clinical outcomes, such as a reduction in the length of surgery, reduced exposure to anesthetics, and a decreased risk of complications like infection (314, 315). Currently, one of the major drawbacks is that most custom implants are manufactured using expensive 3D printing techniques, such as MJM (310) and SLS (304, 313). In contrast, the affordable FDM 3D printers are used to fabricate negative molds for silicone or wax-based casts, which ironically increases the overall production time and cost (278, 279, 305-307, 309, 311). This is mainly because at present, only ABS and PLA filaments are available for FDM and their hard material characteristic makes them unsuitable for producing soft tissue prosthetics. However, as research and development in 3D printing continues to grow exponentially and more materials become available for FDM, we expect to be able to directly create a custom-made prosthesis affordably in the near future.

Conclusion

In the last decade, image-guided 3D printed haptic biomodels have proven to represent a valuable adjunct to the conventional 2D imaging modalities in plastic surgery for preoperative planning, producing intraoperative guidance tools, educating surgical trainees and patients, and fashioning patient-specific implants. In the early years, the technical complexity of 3D softwares and the prohibitive cost of 3D printers restricted accessibility of 3D printing in medicine. The expiration of key 3D printing patents has fueled an exponential development in the field and a significant reduction in the cost. Ultimately, we envision that 3D printing has the potential to become ubiquitous and function as an essential clinical bedside tool for a plastic surgeon.

11 Summary of All Materials and Methods

Chapter Summary

The current research project has required an array of medical imaging modalities, 3D printing software and hardware, performed under ethics approval. This chapter summarises all of the materials and methods utilised. Each chapter included in the thesis contains further detailed description of materials and methods used specifically in each experiment.

11.1 Imaging Sources

In order to produce 3D-printed biomodels, firstly the anatomical structures must be imaged and so we have utilized routine medical imaging modalities, such as computed tomographic angiography (CTA) and magnetic resonance imaging (MRI) and novel technologies, such as a 3D scanner. CTA and MRI are all conducted at radiology departments of Monash University-affiliated hospital, such as Peninsula Health and Eastern Health, and at an outpatient radiology centre, such as Future Medical Imaging Group (FMIG; Hawthorn, VIC). 3D scanner is performed in outpatient setting by single operator (MPC).

CTA

CTA was performed using standardized “single-volume” acquisition technique that ensures maximal image quality of perforators and minimal radiation exposure, as previously described by Phillips et al (14). Siemens SOMATOM Sensation 64 multi-detector row computed tomography scanner (Siemens Medical Solutions, Erlangen, Germany) is used and the scan parameters are summarized in Table 11.1.1.

Parameters	
Scanner	Siemens SOMATOM Sensation 64
Scan type	Helical multi-detector row CT angiography
Slice thickness	64 detector row x 0.6 mm collimator width
Helical detector pitch	0.9
Gantry rotation speed	0.37 sec
Tube potential	120 kV
Tube current	180 mA
Contrast	Omnipaque 350 100 ml IV injection 4 ml per second
Scanning range	Pubic symphysis to 4 cm above umbilicus
Scanning direction	Caudo-cranial
Bolus tracking	+100 HU from common femoral artery with minimal delay

Automatic dose modulation (Siemens Care Dose 4D)	Disabled
Imaging reconstruction	1 mm/0.75 mm overlapping axial images

Table 11.1.1. Parameters used for standard CTA.

MRI

Non-contrast MRI was performed using a 3.0 Tesla Siemens Magnetom Trio scanner (Siemens Medical Solutions, Erlangen, Germany) with standard soft tissue protocols.

3D Scanner

3D scanning was performed using a portable device that attaches to a standard smartphone (iPhone 6 Plus; Apple Inc, Cupertino, CA, USA), called iSense™ (3D Systems, Rock Hill, SC, USA), that has a scan volume of 3 x 3 x 3 metres and operating range of 0.4 - 3.5 metres.

11.2 3D Printing

In order to prepare scan data from the imaging sources into a 3D print, it needs to be processed by three types of 3D software suites: modelling, processing and slicing software.

3D Modelling Software

Using these software, Digital Imaging and COmmunications in Medicine (DICOM) files of CTA and MRI are processed to isolate anatomical areas of interest and manipulated to create surgical guidance devices. For this project, we have used: OsiriX (Pixmeo, Geneva, Switzerland), 3D Slicer (Surgical Planning Laboratory, Boston, MA, USA) and Autodesk MeshMixer (Autodesk Inc, San Rafael, CA, USA).

OsiriX Software

Some DICOM files contain metadata (i.e. patient demographics and indication for the scan) that may render them unrecognisable by 3D Slicer. Hence, they are first imported into OsiriX, where only the series of images without its metadata can be selected and then exported as DICOM files. OsiriX is freely available from the company's website (www.osirix-viewer.com).

3D Slicer Software

Available for free on its website (www.slicer.org), bulk of processing to produce a 3D print occurs in 3D Slicer. Once the DICOM files are uploaded, images are rendered most commonly using the following tools: thresholding, manual segmentation and volumetric analysis. Final file is exported in Standard Tessellation Language (STL) file format.

3D Processing Software

Autodesk MeshMixer

Similarly, MeshMixer is available for free on its website (www.meshmixer.com). This is most commonly used to enhance the final 3D image for ready to 3D print. Final file is, again, exported in STL format.

3D Slicing Software

STL file of a 3D image must be transformed into a G-code file format, for it to be 3D printed. A G-code is a step-by-step instruction for the printer to produce the final model. Most often, 3D slicing software arrive accompanying their 3D printers. For our Moment 3D printer (Moment, Seoul, South Korea), we have used Simplify3D® software (Simplify3D, Cincinnati, OH, USA) and, for Ultimaker 3E printer (Ultimaker, Geldermalsen, Netherlands).

3D Printers

For this project, we have used two fused filament fabrication (FFF) 3D printers: Moment (AUD 3,300; print dimension: 14.5 x 14.5 x 14.5 cm) and Ultimaker 3E (AUD 6,000; print dimension: 21 x 21 x 30.5 cm)

11.3 Ethics Approval

Ethical approval was prospectively sought for all study components. The following are the ethical committee approvals for each component.

Ethics approval for the access to and use of patient-based medical imaging (CTA, MRI, 3D scanning) for 3D printing in plastic and reconstructive surgery is sought at the following institutions in order to conduct this study.

- Peninsula Health (Human Research Ethics Committee Approval Project Number LRR/14/PH/33)
    - Objective of this ethics approval is to validate Peninsula 3D printing technique, using both quantitative and qualitative methods, in patients who will undergo a planned reconstructive surgical procedure at Peninsula Health without causing any additional intervention or change in the management of the patients as a result of this technique.
    - This approval has enabled prospective access up to 300 consecutive adult patients treated at Peninsula Health for the duration of current study.
- Eastern Health (Human Research Ethics Committee Approval Project Number LR63/2016)
    - Objective of this ethics approval is to validate Peninsula 3D printing technique, using both quantitative and qualitative methods, in patients who will undergo a planned reconstructive surgical procedure at Eastern Health without causing any additional intervention or change in the management of the patients as a result of this technique.
    - This approval has enabled prospective access up to 300 consecutive adult patients treated at Eastern Health for the duration of current study.
- Ramsay Health: Ethics Approval
    - Objective of this ethics approval is to validate Peninsula 3D printing technique, using both quantitative and qualitative methods, in patients who will undergo a planned reconstructive surgical procedure at Ramsay Health without causing any additional intervention or change in the management of the patients as a result of this technique.
    - This approval has enabled prospective access up to 300 consecutive adult patients treated at Ramsay Health for the duration of current study.

Ethics approval is sought in order to evaluate the utility of 3D printed models as patient educational tools.

- Peninsula Health (Human Research Ethics Committee Approval Project Number LRR/16/PH/10)
    - Objective of this techniques approval is assess the patients' ability to retain complex anatomical information, such as basal thumb osteoarthritis and carpal bone fracture, after viewing a short educational video clip with or without a 3D-printed model.
    - This approval has enable prospective collection of data in 100 consecutive adult patients being treated at Peninsula Health for a different surgical indication.

12. Results

12.1 Establishing Bedside 3D Printing Technique

12.1.1 Describing the Peninsula 3D Printing Workflow

Setting up a bedside 3D printing laboratory requires the following:

- Dedicated office space with:
    - Personal computer (PC)
    - Internet connection (optional)
    - Post-print processing tools such as pliers, sharp scissors and acetone
    - Well-ventilated but not exposed to strong drafts of air
- 3D printing software suites:
    - Image rendering software
    - Image processing software
    - Image slicing software
- 3D printer:
    - Printer head
    - Filament
    - Build plate

Dedicated Office Space

With the help of funding from Peninsula Health Department of Surgery Research and Innovation grant (AUD 20,000) and Monash Medical Centre Department of Surgery Research grant (AUD 20,000), I was able to help set up 3D Peninsula health Reconstructive Imaging and Nascent Technology (3D PRINT) laboratory based at Frankston Hospital, Victoria Australia. The bespoke “laboratory” has evolved from a laptop computer connected to a 3D printer to a designated office with 28 inch-wide touchscreen-enabled computer with five 3D printers and a selection of post-printing processing tools (Figure 12.1.1.1).

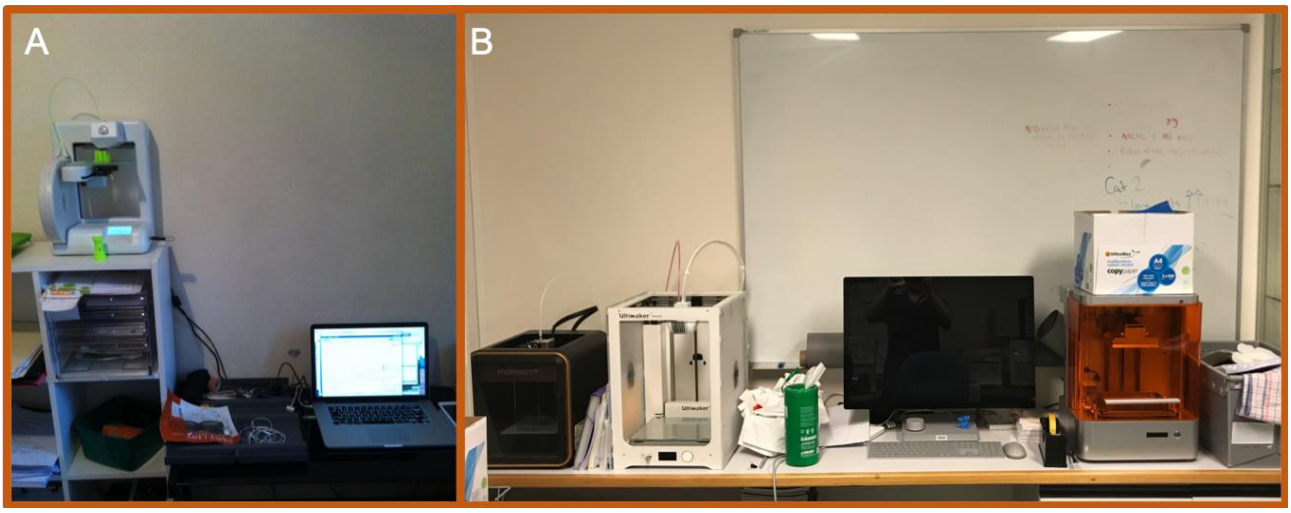

Figure 12.1.1.1. (A) Our original set-up consisted of simply a laptop computer and a desktop 3D printer. (B) As our funding and productivity grew, we set up in a designated office space within the Peninsula Health Department of Surgery with larger and faster desktop personal computer and a wide array of 3D printers. Appropriately, we have named it 3D PRINT (Peninsula health Reconstructive Imaging and Nascent Technology) laboratory

Given the amount of heat produced during 3D printing, the room needs to be well ventilated. However, the 3D printers still need to be protected from strong drafts of air from corridor or direct current from air conditioning. Irregular room temperature can affect melted extrusion and deposition of thermoplastic filaments leading to warped, inconsistent final result.

3D Printing Software Suites

In order to create a 3D-reconstructed image suitable for 3D printing, firstly the patient data from an imaging source need to be exported in DICOM (digital imaging and communications in medicine) file format, a universally-accepted basic medical image file. For superior final resolution, finer slice thickness (ideally less than 1 mm) are preferred. When a scan is initially performed, the data is stored in fine slices. However, a 3D printing researcher needs to be aware that most radiology centres discard these fine slices after a certain period (usually a week) and keep thick slices (i.e. 3-5 mm) in order to reduce storage burden. Despite being basic, DICOM files from different radiology centres may present slightest difference in software language that may deem incompatible with some 3D image rendering software. In order to tackle this problem, I have incorporated the use

of OsiriX software where I import them onto it first where they are homogenised and exported as consistently compatible DICOM files.

For 3D rendering, three types of 3D printing software suites are required (Figure 12.1.1.2).

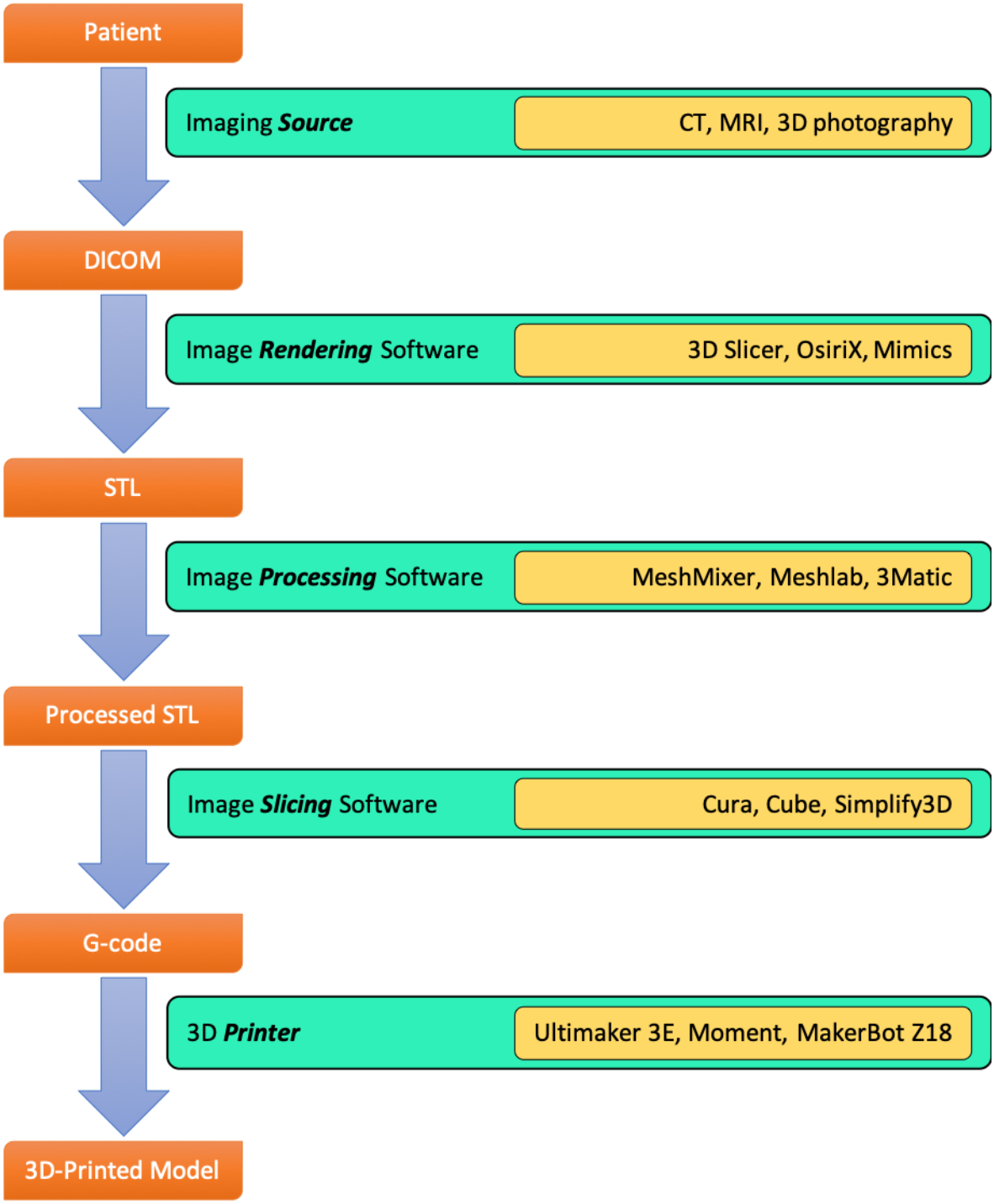

Figure 12.1.1.2. Summary of 3D printing process. Initially, the patient data from an imaging source, such as CT, MRI and 3D photography, are exported in DICOM file format. Using image rendering software, DICOM files are 3D rendered into STL file format, isolating the region of interest. Using image processing software, further modifications can be applied,

such as surface smoothing. Using image slicing software, the files are converted into G-code file format, which is compatible with 3D printers.

Image rendering software, such as 3D Slicer, OsiriX and Mimics, are used to highlight the region of interest using the process known as segmentation. Detailed explanation of how to perform segmentation in each software suite is beyond the scope of the current thesis. Suffice to say, all suites come with basic manual available on companies' websites. Briefly, segmentation usually begins with semi-automated thresholding function where user can select all region of interest within a range of Hounsfield units. Then, the operator needs to manually segment using various "paint" and "erase" tools.

Image processing software, such as MeshMixer, Meshlab and 3Matic, are useful to modify or add extra dimension to the 3D-reconstructed image. Functions, such as surface smoothing, cropping, resizing, labelling and creating surface moulds, can be performed on these software suites.

Image slicing software, such as Cura, Cube and Simplify3D, are usually provided with the purchase of a 3D printer. Unlike the image rendering and processing software, they need to convert 3D-reconstructed STL files into 3D printer-friendly file, called G-code. As a result, they are specific to each printer. A G-code is a set of step-by-step software instructions for the 3D printer to produce the final model.

3D Printer

I have set up 3D PRINT laboratory using affordable 3D printers (Figure 12.1.1.3 and Table 12.1.1.1):

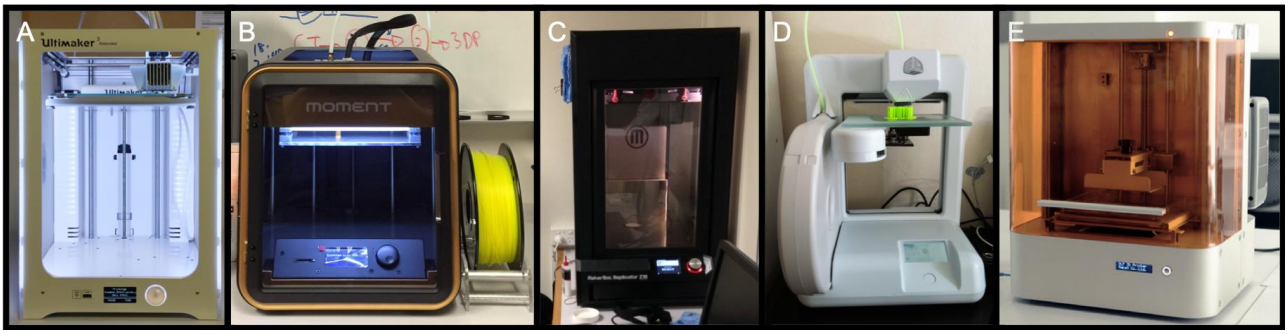

Figure 12.1.1.3. 3D printers owned by 3D PRINT laboratory. (A) Ultimaker 3E, (B) Moment 1, (C) Replicator Z18, (D) Cube 2, (E) M-One

Type	3D Printer	Company	Maximum Build Dimension (cm)	Cost (AUD)
FFF	Ultimaker 3E	Ultimaker (Geldermalsen, The Netherlands)	21.5 *x* 21.5 *x* 30	6,000
FFF	Moment 1	Moment (Seoul, South Korea)	14.5 *x* 14.5 *x* 14.5	3,300
FFF	Replicator Z18	MakerBot Inc (New York, NY, USA)	30.5 *x* 30.5 *x* 45.7	8,800
FFF	Cube 2	3D Systems (Rock Hill, SC, USA)	14 *x* 14 *x* 14	1,499
SLA	M-One	Makex (Zhejiang, China)	14.5 *x* 11 *x* 17	6,000

Table 12.1.1.1. Summary of 3D printers owned by 3D PRINT laboratory. Abbreviations: FFF: fused filament fabrication; SLA: stereolithography.

Using instruction manual from the company, 3D printers can be relatively easily installed in any office. In comparison, running each print can pose a steep learning curve. In general, a researcher can achieve a consistent outcome by following a checklist of tasks before each print (Table 12.1.1.2).

Printer Head		
	Z-resolution	
	Speed	
	Support Structure	
Filament		
	Type	
	Diameter	
	Loading	
	Feeder	
Build Plate		
	Technique	
	Temperature	

	Environment	

Table 12.1.1.2. Pre-print checklist for 3D printing.

Printer Head

Printer heads move in Cartesian coordinates (i.e. x-y-z). Accuracy of their movement in X-Y plane (i.e. XY-resolution) depends on the gearing and is, hence, fixed. However, the thickness of each layer of print deposited (i.e. Z-resolution) is adjustable in image slicing software prior to print. Given that diameter of a standard printer head nozzle is 0.4 mm, an ideal Z-resolution is between 0.1-0.2 mm. Smaller layer thickness increases the number of layers that needs to be deposited, which increases the likelihood of print error, such as warping. Speed of print head can be adjusted so that it slows down where details need to be preserved and quickens in less important steps. Where there are overhanging parts in a build, image slicing software adds support structures to accommodate. However, they leave unsightly surface finish when removed post-print. Hence, a researcher can alter the build orientation to minimise support structure requirement.

Filament

A wide variety of filaments are compatible with FFF 3D printers, such as polylactic acid (PLA), acrylonitrile butadiene styrene (ABS), polyamides (nylon) and thermoplastic polyurethane (TPU-95A). PLA is the most commonly used filament due to its compatibility from low melting point (200 degrees Celsius) and ease of use. In comparison, ABS produces smoother surface finish and is less likely to clog printer head nozzle. However, it is associated with higher melting point (230 degrees Celsius) and at high temperatures, can degrade into its carcinogenic constituents (i.e. butadiene and acrylonitrile). Nylon is stronger than PLA and ABS, and is a ubiquitous material used in medical application. However, it has a poorer adhesive properties to the build plate and readily warp, reducing the surface finish. TPU-95A is a semi-flexible material that is also found commonly in medical application, such as breast implants. However, similar to nylon, it is a relatively new material to be introduced in 3D printing and more experience is required.

Diameter of the most commonly used filament is 1.75 mm. Interestingly, the latest 3D printers, like Ultimaker 3E, have adopted wider filaments (i.e. 2.85 mm), which appears to

increase their storage lifespan from degradation. However, this remains to be proven scientifically. At the start of each print, it is a good practice to unload and reload the filament into the printer head. Often, the remaining filament material has changed its material properties from cooling and reheating, which can lead to blockage and inconsistent outcome. In addition, it is important to ensure that the filament feeder wheel is free from tangling and obstruction.

Build Plate

One of the most common reason for aborting a 3D print is due to unsuccessful adhesion of the first layer to the build plate. To this effect, there are strategies that can be deployed in the image slicing software, such as creating a ramp that is deposited first and then discarded post-print or a wide brim of print around the first layer that provides protection from temperature changes. In addition, build plate can be wrapped with blue adhesion tape or glue. Recently, the latest 3D printers are adopting heated build plate as standard, which provides a consistent temperature for optimal filament adhesion. Depending on the filament material being used, the build plate temperature can be modified in the image slicing software. Lastly, it is important to ensure that the build plate is away from cold drafts of air from the corridor or air conditioning to prevent temperature changes.

12.1.2 Accuracy of 3D Printing Software

PUBLISHED (Publication): ***Chae MP***, Hunter-Smith DJ, Rozen WM. (2016) Comparative study of software techniques for 3D mapping of perforators in DIEP flap planning. Gland Surg. 5(2): 99-106. PMID: 27047778

Chapter Summary

Introduction: Computed tomographic angiography (CTA) is currently considered the gold standard imaging modality for preoperative planning autologous breast reconstruction with deep inferior epigastric artery perforator (DIEP) flap. Improved anatomical understanding from CTA has translated to enhanced clinical outcomes. To achieve this, the use of appropriate computed tomography hardware and software is vital. Various CT scanners and contrast materials have been demonstrated to consistently produce adequate scan data. However, the availability of affordable and easily accessible imaging software capable of generating 3D volume-rendered perforator images to clinically useful quality has been lacking. Osirix (Pixmeo, Geneva, Switzerland) is a free, readily available medical image processing software that shows promise. We have previously demonstrated in a case report the usefulness of Osirix in localizing perforators and their course.

Methods: In the current case series of 50 consecutive CTA scans, we compare the accuracy of Osirix to a commonly used proprietary 3D imaging software, Siemens Syngo InSpace 4D (Siemens, Erlangen, Germany), in identifying perforator number and location. Moreover, we compared both programs to intraoperative findings.

Results: We report a high rate of concordance with Osirix and Siemens Syngo InSpace 4D (99.6%). Both programs correlated closely with operative findings (92.2%). Most of discrepancies were found in the lateral row perforators (90%).

Conclusion: In the current study, we report the accuracy of Osirix that is comparable to Siemens Syngo InSpace 4D, a proprietary software, in mapping perforators. However, it provides an added advantage of being free, easy-to-use, portable, and potentially a superior quality of 3D reconstructed image.

Introduction

Currently, computed tomographic angiography (CTA) is considered the gold standard perforator imaging technique for preoperative planning an autologous breast reconstruction with deep inferior epigastric artery (DIEA) perforator (DIEP) flap (73, 316). The scan data can be 3D reconstructed to produce a "perforator map" that assists surgeons in selecting an appropriate perforator, donor site, and the flap. A plethora of studies have demonstrated high accuracy of CTA in detecting perforators, reporting sensitivity and specificity close to 100% (5, 12, 80, 97, 98, 117, 119-121, 129). In comparison to other perforator imaging modalities, such as Doppler ultrasound and magnetic resonance angiography, CTA has demonstrated superior visualization of the perforators and their subcutaneous course, respectively (6, 98). These benefits have translated into improved clinical outcomes, such as increased flap survival, reduced donor site morbidity, and reduced operating time (5-7, 13, 118-120, 129-136). To this end, appropriate use of hardware and software is essential to obtain optimal perforator data from CTA.

Through various scanner hardware brands (i.e. Siemens, Toshiba, and Philips), varying number of multi-detector rows (i.e. 4-slice to 320-slice scanners) and differing contrast media and volumes, all scanners and techniques are able to achieve high quality and clinically useful images (73, 316). In addition, we have published optimized CTA scanning techniques that enhance perforator visualizations, such as initiating contrast bolus trigger at the common femoral artery, moving the computed tomography table caudo-cranially, and disabling the Siemens CareDose4D feature (5).

High cost and limited accessibility of 3D imaging softwares that generate 3D reconstructions suitable for clinical use have been challenging for hospitals with relatively limited resources. Most of the currently available proprietary softwares, such as Siemens Syngo InSpace 4D (Siemens, Erlangen, Germany) (7) and VoNaviX (IVS Technology, Chemnitz, Germany) (138) and are expensive. Some are not readily accessible outside the institution where it was originally developed, such as virSSPA (University Hospitals Virgen del Rocio, Sevilla, Spain) (317). Furthermore, many programs available cannot provide adequate images, with some not able to visualize perforators to a clinically useful degree. One particular program that we have found that can achieve optimal images is Siemens Syngo InSpace 4D (5). The program enables users to assign color to various

contrast values using color look-up table (CLUT) function, providing superior contrast resolution to the 3D reconstructions. Again however, the cost and availability are significant limitations. Previously, we have demonstrated the application of a free 3D imaging program, Osirix (Pixmeo, Geneva, Switzerland).

Osirix is a free imaging processing software, specifically designed for medical imaging by a radiologist, and is readily downloaded online for use unreservedly (262). It is able to produce the same or better images than the currently available programs on a user-friendly interface. Furthermore, Osirix can be readily operated on a laptop computer, which enables viewing in the operating theatre or at home. Similar to Siemens Syngo InSpace, Osirix enables the user to create 3D volume-rendered reconstructions and assign colors using an appropriate CLUT function to optimize visualization of perforators and their course, as demonstrated in our previous case report (73).

In the current study, we investigate the accuracy of the freely available 3D imaging software, Osirix, by comparing it to the proprietary program, Siemens Syngo InSpace 4D, and also comparing both softwares to the intraoperative findings.

Methods

The study design was a prospective case series. 50 consecutive patients (i.e. 100 hemi-abdominal walls) underwent CTA prior to a DIEP flap breast reconstruction. All patients were aged between 30 and 60 years and spanned a wide range of body habitus. All imaging findings were recorded by a single operator and all intraoperative findings were recorded by the operating surgeon.

Computed Tomographic Angiography Technique

All scans were performed at a single institution (Future Medical Imaging Group, Melbourne, Australia) using a standardized protocol that has been modified and improved from the conventional CTA methodology in order to maximize the image quality and minimize radiation exposure (5, 6). The computed tomography scanner used was a Siemens SOMATOM Sensation 64 multi-detector row computed tomography scanner (Siemens Medical Solutions, Erlangen, Germany) and the scan parameters are summarized in Table 12.1.2.1.

Parameters	
Scanner	Siemens SOMATOM Sensation 64
Scan Type	Helical Multi Detector Row CT Angiography
Slice Thickness	64 Detector Row x 0.6 mm collimator width
Helical Detector Pitch	0.9
Gantry Rotation Speed	0.37 s
Tube Potential	120 kV
Tube Current	180 mA
Contrast	Omnipaque 350 100 ml IV injection 4 ml per second
Scanning Range	Pubic Symphysis to 4 cm above Umbilicus
Scanning Direction	Caudo-Cranial
Bolus Tracking	+100 HU from Common Femoral Artery with minimal delay
Automatic Dose Modulation (Siemens CareDose 4D)	Disabled

Imaging Reconstruction	1 mm/0.7 mm overlapping axial images

Table 12.1.2.1. Computed tomographic scan parameters. Abbreviations: CT: computed tomographic; HU: Hounsfield units

Patients were scanned in a position matching operative positioning: supine, with no clothing or straps to deform the abdominal contour. The scan range was limited to the tissue used intraoperatively and thus spanned from the pubic symphysis to 4 cm above the level of umbilicus. A bolus of 100 ml of intravenous Omnipaque 350 was used for contrast, without oral contrast. We have previously described three major modifications introduced to the standard CTA protocol in order to enhance the arterial phase filling and the resolution of cutaneous vasculature (141). Briefly, the contrast bolus trigger to begin scanning was taken at the common femoral artery; the computed tomography table movement was reversed to scan caudo-cranially from the pubic symphysis to match the filling of DIEA; and the Siemens CareDose4D feature was disabled, which maximized the abdominal wall signal-to-noise ratio.

Scan Analysis

CTA scans were analyzed using both imaging softwares: Siemens Syngo InSpace 4D (Version 2006A; Siemens, Erlangen, Germany) and Osirix (Pixmeo, Geneva, Switzerland). The thin-slice (i.e. 1 mm or less) axial raw data were reformatted into 3D volume-rendered reconstructions and maximum intensity projections to identify the number and location of perforators, and the branching pattern of DIEA (28).

Perforator Mapping

3D-reconstructed images of the abdominal wall perforators are generated using volume-rendering technique (VRT) and maximum intensity projection (MIP) techniques. VRT reconstructions required the use of the CLUT function found in both of the image processing softwares. Additionally in Osirix (Pixmeo, Geneva, Switzerland), we applied Gaussian blur to the final 3D reconstruction facilitating the removal of interference within the data (Figure 12.1.2.1 and 12.1.2.2). All infraumbilical perforators with diameter greater than 0.5 mm were identified and mapped on VRT reconstructions. Arrowheads were placed at the point of emergence of each perforator from the anterior rectus sheath. They

were overlaid on to a 2D representation of each patient's abdominal wall with a grid of 4 mm squares applied to the image centered on the umbilicus as reference point. The transverse distances of each perforator from the midline were recorded to the closest 0.5 cm. The perforators were recorded as found in medial or lateral row. MIP reconstructions were used to illustrate intramuscular course of the perforators.

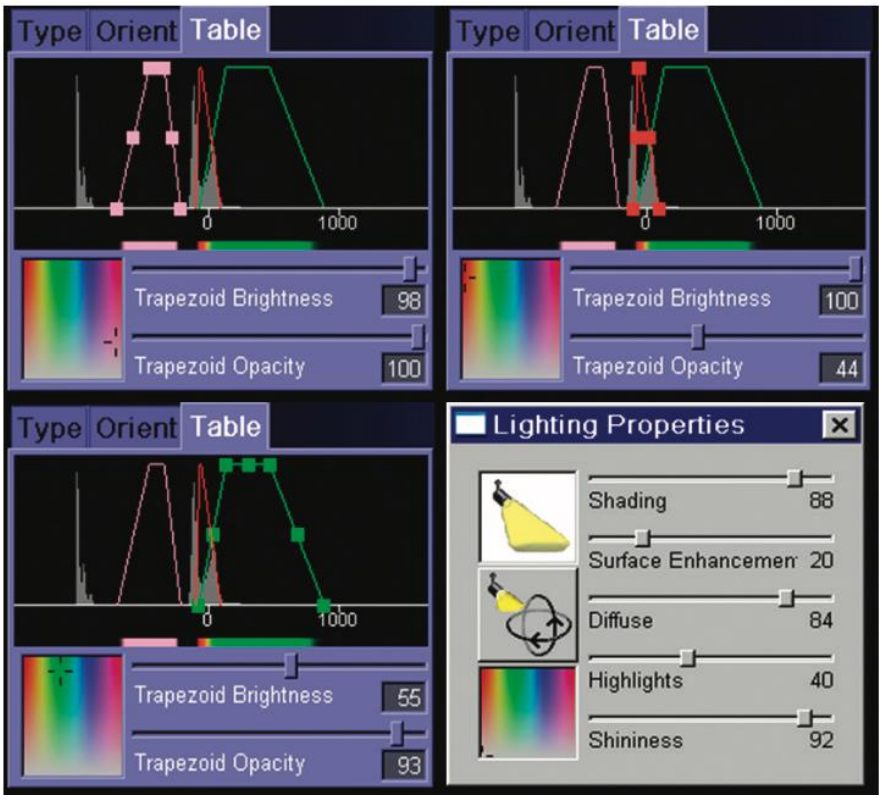

Figure 12.1.2.1. Colour look-up table (CLUT) and ray cast lighting properties in Siemens Syngo InSpace 4D (Siemens, Erlangen, Germany).

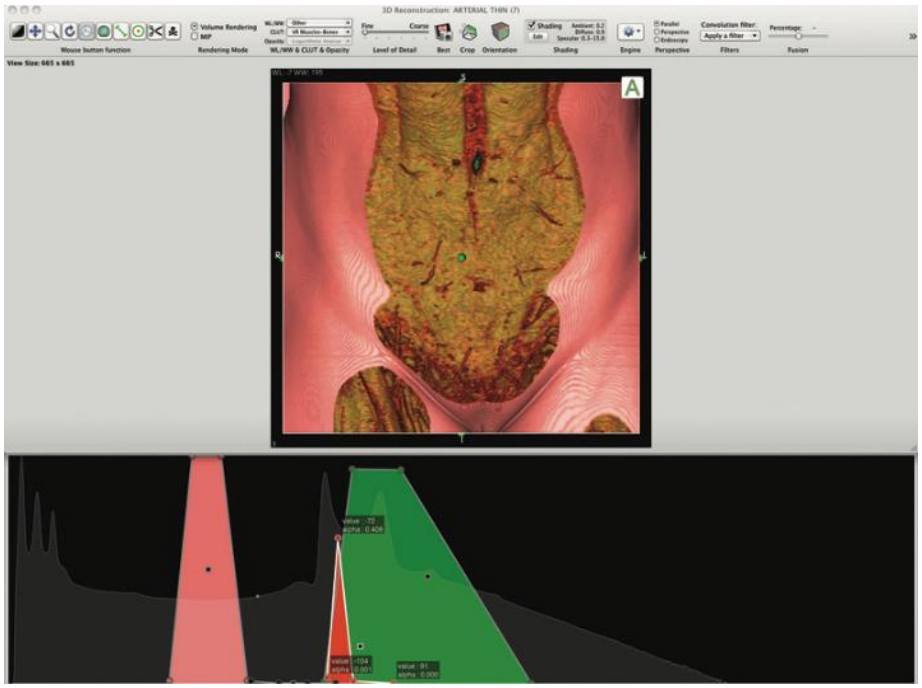

Figure 12.1.2.2. Colour look-up table (CLUT) in Osirix (Pixmeo, Geneva, Switzerland), designed for perforator imaging.

Intraoperative Measurements

The perforator locations were compared with operative findings, where they were located on equivalent grids. Intraoperative grids were placed over the lower abdominal wall, with the umbilicus and midline as references, and the location of perforators was documented on it with sterile pens. A 0.5-cm margin of error was given for the location of each perforator. This was a conservative figure given as an estimate of the combined error associated with the calculation of concordance, and included the following factors: CTA error (e.g. patient movement, venous contamination), CTA reporting error (e.g. multiplanar reformatting error, reading error), intraoperative measurement error (e.g. limitation of measurement tool, reading error), and patient error (e.g. umbilical shift, abdominal pannus mobility). For the purpose of comparison, the operative findings were considered the standard.

All perforators were explored bilaterally, including the perforators not included in the flap. All perforators greater than 0.5 mm in diameter were included in the study and recorded in the manner described. As achieved during the CTA scan interpretation, the perforators identified intraoperatively comprised arterial perforators and not adjacent veins.

Statistical Analysis

The perforator locations were recorded as exact values and the findings were compared between the two software programs. In addition, the data from each program was compared to the operative findings. The comparative analysis was conducted using SPSS Statistics software package (IBM, Armonk, New York) and the outcomes were analyzed using paired Student's *t*-test. A *P*-value of <0.05 was accepted as statistically significant.

Results

A total of 50 CTA scans were performed in 50 consecutive cases (i.e. 100 hemi-abdominal walls) that identified 512 perforators of DIEA at an average of 5.12 perforators per hemi-abdomen. Concordance between Siemens Syngo InSpace 4D (version 2006A; Siemens, Erlangen, Germany) and Osirix (Pixmeo, Geneva, Switzerland) in accurately identifying perforator locations, and comparison between each of the software programs to intraoperative findings were evaluated.

Between Siemens Syngo InSpace 4D and Osirix, 510 out of 512 perforators (99.6%) had concordance. The two discordant perforators between the imaging programs were located in the lateral row and had only 0.5 cm of difference. Mean transverse distance from the midline using both software programs was 3.36 cm, with no statistical difference between them for measuring perforator location (Table 12.1.2.2 and Figure 12.1.2.3).

	Siemens Syngo InSpace 4D	Osirix	Difference	*P* value
Perforator Location Lateral-to-Midline (mean)	3.36 cm	3.36 cm	0 cm	1

Table 12.1.2.2. Mean transverse distance of DIEA perforators from the midline as identified using the 3D imaging softwares: Siemens Syngo InSpace 4D (Siemens, Erlangen, Germany) and Osirix (Pixmeo, Geneva, Switzerland).

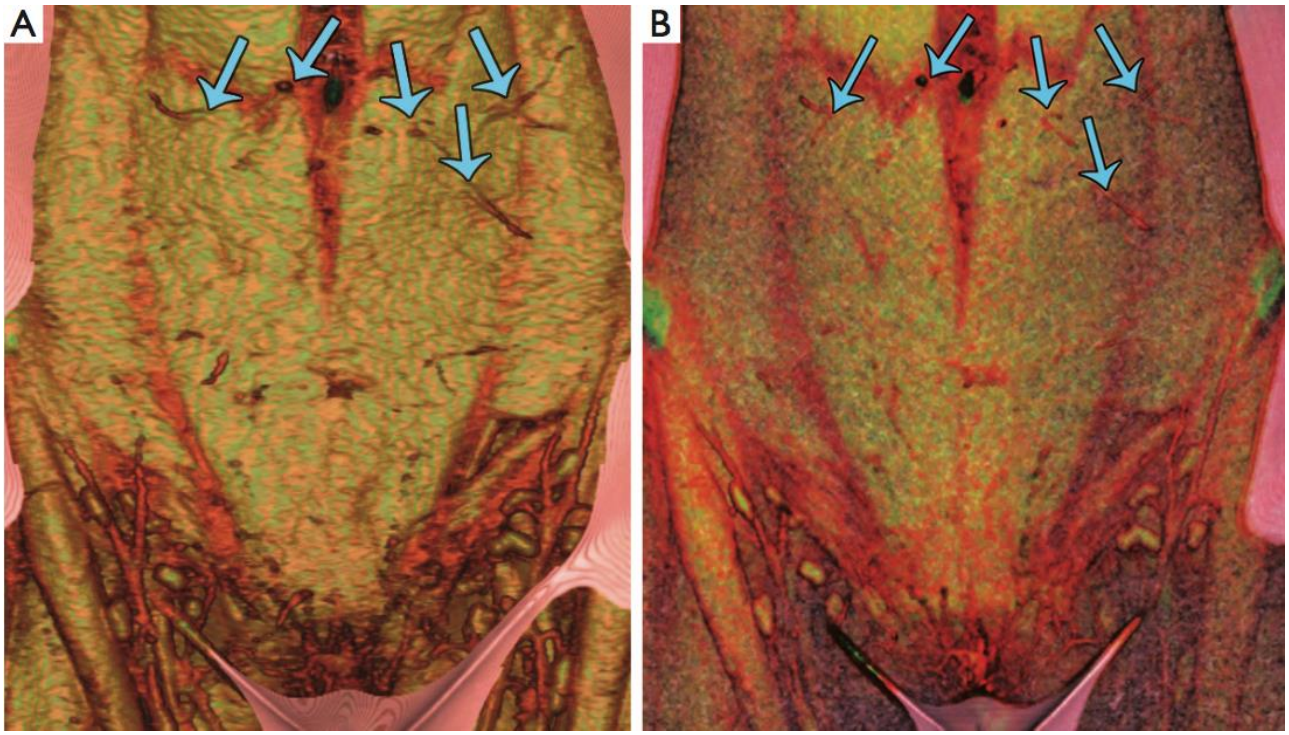

Figure 12.1.2.3. Preoperative computed tomographic angiography (CTA), volume-rendered reconstruction of the abdominal wall vasculature with (A) Osirix (Pixmeo); and (B) Siemens Syngo InSpace 4D (Siemens). Both techniques clearly demonstrate several large periumbilical perforators (Blue arrows), and highlight features of the abdominal wall soft tissues.

Between each of the softwares and the operative findings, there was a mean difference of 0.7 mm per perforator using both programs (Table 12.1.2.3 and 12.1.2.4). Although this difference was statistically significant ($P < 0.01$), this was not a clinically significant difference (i.e. less than 1 mm).

	Siemens Syngo InSpace 4D	Operative Findings	Difference	*P* value
Perforator Location Lateral-to-Midline (mean)	3.36 cm	3.43 cm	0.07 cm	<0.01

Table 12.1.2.3. Comparing the mean transverse distance of DIEA perforators from the midline calculated using Siemens Syngo InSpace 4D (Siemens, Erlangen, Germany) to the intraoperative measurements.

	Osirix	Operative Findings	Difference	*P* value
Perforator Location Lateral-to-Midline (mean)	3.36 cm	3.43 cm	0.07 cm	<0.01

Table 12.1.2.4. Comparing the mean transverse distance of DIEA perforators from the midline calculated using Osirix (Pixmeo, Geneva, Switzerland) to the intraoperative measurements.

An analysis of perforators that had a difference between imaging and intraoperative findings was undertaken, with 40 perforators (7.8%) discordant between imaging and operative findings (Table 12.1.2.5). Of 18 perforators that had 0.5 cm difference with operative finings, 7 were located in medial row and 11 in lateral row. Of 12 perforators that had 1 cm difference, 5 were located in medial row and 7 in lateral row. Of 8 perforators that had 1.5 cm difference, 1 was located in medial row and 7 in lateral row. Of 2 perforators that had 2 cm difference, none were located in medial row and 2 in lateral row. Medial row perforators accounted for 13 out of 40 discordant results (32.5%) and lateral row 27 out of 40 (67.5%). Hence, imaging was more accurate when assess medial row perforators (32.5% vs 67.5%). Furthermore, when specifically assessing the larger discrepancies (>1 cm), medial row accounted for only 1 out of 10 (10%) and lateral row 9 out of 10 (90%).

	Medial Row	Lateral Row	Total
Imaging : Operative discrepancy 0.5 cm (number of perforators)	7	11	18
Imaging : Operative discrepancy 1.0 cm (number of perforators)	5	7	12
Imaging : Operative discrepancy 1.5 cm (number of perforators)	1	7	8

Imaging : Operative discrepancy 2.0 cm (number of perforators)	0	2	2
Total	13	27	40

Table 12.1.2.5. Analysis of discrepancy found in the perforator localization between imaging and operative findings and their distribution between medial and lateral rows.

Discussion

Improved understanding of DIEA and its perforators from CTA has assisted reconstructive surgeons in the selection of appropriate donor site, perforator, and flap, which translated to significant improvement in clinical outcomes (5, 6, 8, 9, 13, 119, 120, 129-136, 317). To achieve this, the use of appropriate hardware and software is vital. For CTA hardware, computed tomographic scanners from various brands using different multi-detector rows with varying IV contrast materials and volumes have demonstrated in the literature to deliver consistently sufficient scan data (6, 117, 118, 120, 129, 316). In contrast, the high cost and limited accessibility of image processing software that can produce clinically useful 3D volume-rendered reconstructions have limited a wide application of CTA. To this effect, Osirix, a medical imaging program available for free online, have been useful. It is capable of producing the same or superior quality 3D reconstructions than the proprietary softwares and has added advantages of user-friendly interface and portability.

We have previously described the potential utility of Osirix for preoperatively planning a DIEP flap breast reconstruction in a case report (73). In the current case series, we demonstrate that Osirix is as accurate as the commonly used proprietary software, Siemens Syngo InSpace 4D, in identifying perforator number and location (99.6%). Furthermore, the measurements from both programs closely correlated to the operative findings (92.2%). The discordance between imaging and operative findings was most pronounced in assessing lateral row perforators (90% vs 10%). For the purpose of the current study, we forewent comparing perforator diameters since these measurements can be made on standard axial slices of a CTA, regardless of the software program.

In addition to its accuracy in perforator localization, Osirix has the potential to yield superior quality 3D images than Siemens Syngo InSpace 4D due to its 16-bit CLUT function and the capacity to apply Gaussian blur after the 3D reconstruction to reduce interference. Furthermore, Osirix exhibits an easy-to-navigate user interface that is readily accessible to clinicians without technological background and it is compatible on Mac operating system. As a result, surgeons can access the 3D reconstructed images on their portable computer in the operating theatre or at home.

One of the limitations of the current study is our relatively small sample size. A larger randomized study with greater sample size will be required to further validate our findings.

Moreover, a future study may consider comparing Osirix to a host of other proprietary softwares, such as VoNaviX, and their impact on clinical outcomes. For the purpose of this study, the comparative analysis was performed in cases of autologous breast reconstruction with DIEP flap. However, validating Osirix in assessing other free flap options for autologous breast reconstruction may be of value.

Conclusion

This comparative analysis demonstrates that the accuracy of Osirix, a freely available medical image processing software, is concordant with Siemens Syngo InSpace 4D, a commonly utilized proprietary software, in localizing perforators for autologous breast reconstruction with DIEP flaps. Measurements from both programs correlated equally to the intraoperative findings. Most of the discrepancies arose in the lateral row perforators.

12.1.3 Accuracy of 3D Printing Hardware

12.1.3.1 Validation Study Using Linear Measurement

Submitted (Publication): ***Chae MP***, Chung RD, Smith JA, Rozen WM, Hunter-Smith DJ. (2018) The accuracy of clinical 3D printing in plastic surgery: literature review and in vivo validation study. Gland Surg.

Chapter Summary

Introduction: A growing number of studies demonstrate the benefits of 3D printing in improving surgical efficiency and subsequently clinical outcomes. However, the number of studies evaluating the accuracy of 3D printing techniques remains scarce.

Method: All publications appraising the accuracy of 3D printing between 1950 and 2018 were reviewed using well-established databases, including PubMed, Medline, Web of Science and Embase. An *in vivo* validation study of our 3D printing technique was undertaken using unprocessed chicken radius bones (*Gallus gallus domesticus*). Calculating its maximum length, we compared the measurements from computed tomography (CT) scans (CT group), image segmentation (SEG group) and 3D-printed (3DP) models (3DP group).

Result: 28 comparison studies in 19 papers have been identified. Published mean error of CT-based 3D printing techniques were 0.46 mm (1.06%) in stereolithography, 1.05 mm (1.78%) in binder jet technology, 0.72 mm (0.82%) in PolyJet technique, 0.20 mm (0.95%) in fused filament fabrication and 0.72 mm (1.25%) in selective laser sintering. In the current in vivo validation study, mean errors were 0.34 mm (0.86%) in CT group, 1.02 mm (2.51%) in SEG group and 1.16 mm (2.84%) in 3DP group.

Conclusion: Our Peninsula 3D printing technique using a fused filament fabrication 3D printer produced accuracy similar to the published studies (1.16 mm, 2.84%). There was a statistically significant difference ($p < 10^{-4}$) between the CT group and the latter SEG and 3DP groups indicating that most of the error is introduced during image segmentation stage.

Introduction

A growing number of studies demonstrate the utility of 3D printing for preoperative planning, creating intraoperative guidance devices, improving patient education and medical training, and designing patient-specific implants (16, 17, 318). Moreover, 3D printing may improve surgical efficiency and accuracy (319), leading to reduced operating time and subsequent health economic benefits (320). However, 3D printing has not yet been incorporated as part of routine clinical practice due to several significant shortcomings (321).

The main limitations of 3D printing are high cost, lengthy production time and perceived inaccuracy of the models (321). Recently, the cost and production time of 3D printing have reduced significantly by the introduction of affordable 3D printers and free software suites (318, 322, 323). Encouraged by this, Chae *et al* have published the Peninsula 3D printing technique using a desktop 3D printer and an open-source 3D software (318). However, there is a relative paucity of studies investigating the accuracy of 3D printing in the literature (324).

Error can be introduced at any stage of 3D printing, but mainly during image acquisition and segmentation (Figure 12.1.3.1.1) (321, 325-327). Most studies have examined the accuracy of 3D printing techniques by comparing linear measurements of the original object to the final 3D-printed model (180, 191, 252, 266, 267, 328-341).

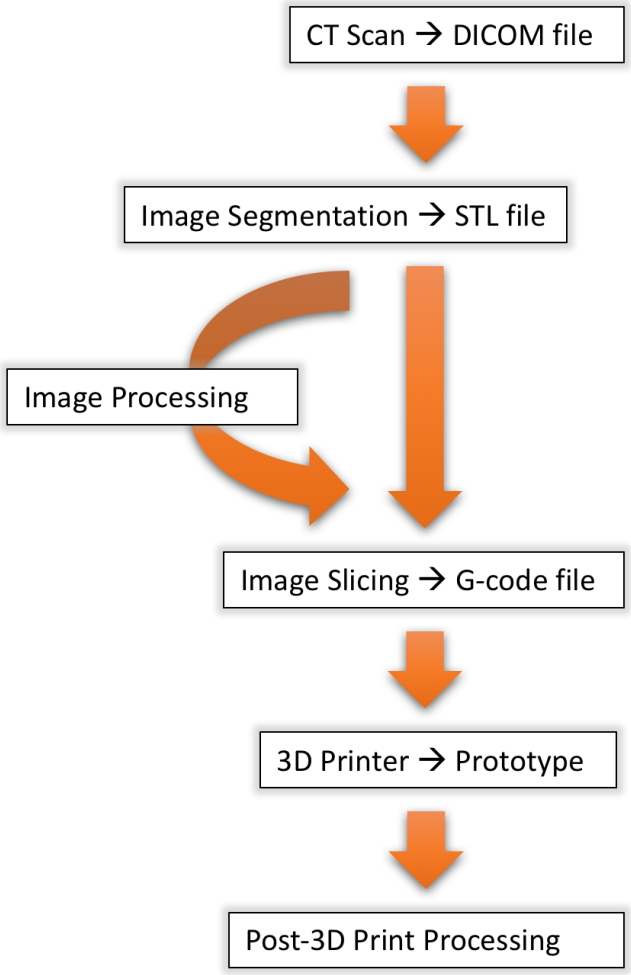

Figure 12.1.3.1.1. Steps involved in creating a CT-based 3D-printed anatomical biomodel. Error can be introduced at each step. Abbreviations: CT: computed tomography; DICOM: digital imaging and communications in medicine; STL: standard tessellation language.

The current study reviews of all published studies where accuracy of image-guided 3D printing of cadaveric specimens are evaluated. Subsequently, an *in vivo* validation study of the published Peninsula 3D printing technique (318) using the chicken radius bone (*Gallus gallus domesticus*) is conducted.

Methods

Literature Review

A review was undertaken reviewing the published English literature from 1950 to 2018 from well-established databases, such as PubMed, Medline, Web of Science and Embase using search terms, such as “3D printing”, “additive manufacturing”, “rapid prototyping”, “stereolithography”, “CT”, “MRI”, “accuracy”, “precision”, “validation”, “evaluation” and “comparison”. Secondary references found through bibliographic linkage were also retrieved.

Inclusion Criteria

Only studies using cadaveric specimens where their direct measurements could be obtained as gold standard were included. Anatomical structures were chosen over generically-shaped phantoms since they pose greater challenge in dimensional assessment and the findings will be more relevant to clinical application. Only studies using CT as imaging source were included since an overwhelming majority of medical 3D printing has been conducted using it
(324).

Exclusion Criteria

Studies were excluded if authors indirectly deduce the accuracy of 3D printing by analysing the clinical placement of implants or screws using 3D-printed surgical guides since this introduces potentially confounding clinical variables (342-348). Studies using qualitative (349) or volumetric assessment (350), instead of linear measurements, to report 3D printing accuracy were excluded (351-353).

Validation Study

The chicken radius bone was chosen for this study, instead of other bones such as the humerus, femur, tibia or fibula, since its length and shape closely resembles the human proximal phalanx (range of 37-44 mm vs 32-45 mm, respectively) (Figure 12.1.3.1.2) (354). Furthermore, it is readily available from the butchers intact in large numbers,

compared to other parts of the chicken that are normally discarded or damaged during preparation. This validation study was approved by the Human Research Ethics Committee at Peninsula Health.

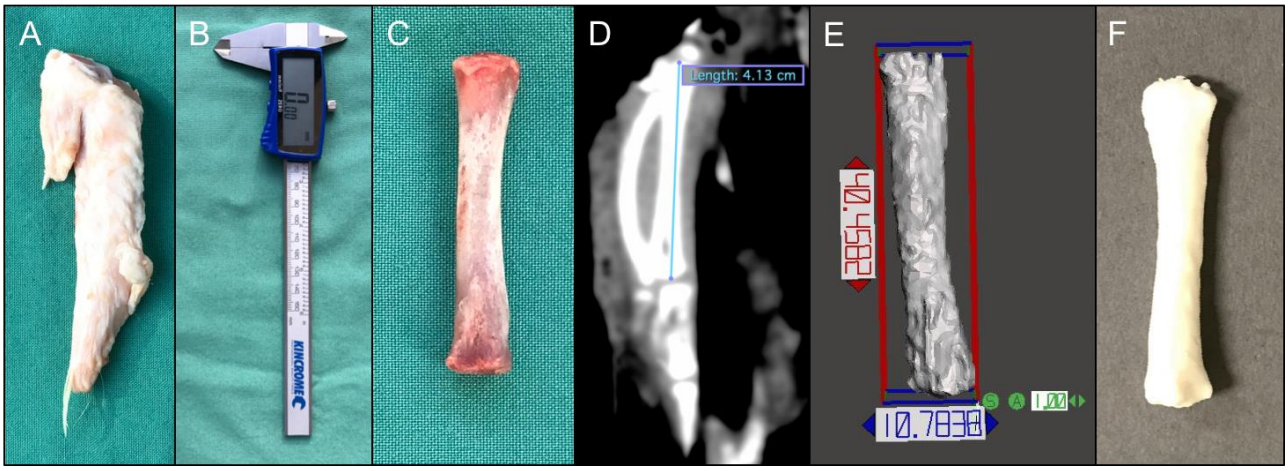

Figure 12.1.3.1.2. Design of our validation study using radius of chicken (*Gallus gallus domesticus*). A: butchered chicken wing; B: digital Vernier caliper (Kincrome; Scoresby, VIC, Australia); C: dissected chicken radius with its articular cartilages removed; D: measuring the bone length directly from CT scan using software ruler within OsiriX program (Pixmeo, Geneva, Switzerland); E: measuring the bone length from its 3D-reconstructured STL file using software ruler within Autodesk MeshMixer program (Autodesk Inc., San Rafael, CA, USA); F: measuring the bone length from its 3D-printed model using the caliper. Abbreviations: CT: computed tomography; STL: standard tessellation language.

In Vitro Measurement

The entire defeathered chicken wing was wrapped in cling wrap, placed inside a radiolucent polypropylene-based standard household container, and CT scanned. Then, the radius was dissected out and its articular cartilages removed. Maximum length of the bone was measured using a digital Vernier caliper (Kincrome, Scoresby, VIC, Australia). Out of 50 chicken wings scanned, eleven were removed from the study due to detection of their unrecognised midshaft fractures from the CT scan, which can compromise reliability of the caliper measurements.

CT Image Acquisition

CT scanning was performed using Siemens SOMATOM Definition AS scanner (Siemens AG, Erlangen, Germany) and hand/wrist scanning protocol. The scan parameters were as follows: tube voltage of 120 kV, tube current exposure time product of 35 mA, single collimation width of 0.6 mm and slice thickness of 0.6 mm. The images were then reconstructed using the bone window and exported in Digital Imaging and COmmunication in Medicine (DICOM) format (1,054 images). The length of each chicken radius was measured from the CT scan using OsiriX software (Pixmeo, Geneva, Switzerland) and recorded to two decimal places (Figure 12.1.3.1.2).

Image Segmentation

The DICOM files were reconstructed into 3D images using free, open-source 3D Slicer software (Surgical Planning Laboratory, Boston, MA, USA) as previously reported and exported in standard tessellation language (STL) format (37, 318, 355). Briefly, using “ThresholdEffect” function, a range was set from the Hounsfield unit-derived values in order to automatically segment chicken radius from the surrounding soft tissue. Using “PaintEffect” tool, minor surface artefacts were manually removed. Each radius was labelled and exported separately. The length of each bone was measured from its 3D-reconstructed image, or STL file, using Autodesk MeshMixer software (Autodesk Inc., San Rafael, CA, USA).

3D Printing

Each STL file was converted into a 3D printer-friendly G-code file using Cura software (Ultimaker, Geldermalsen, The Netherlands). The bones were 3D-printed in thermoplastic polylactic acid (PLA) filament using a desktop, fused filament fabrication (FFF) Ultimaker 3 Extended 3D printer (Ultimaker, Geldermalsen, The Netherlands).

Statistical Analysis

All measurements were repeated three times and the average was recorded in millimetres to two decimal places. Comparative analysis was performed using Stata statistical software package (StataCorp, College Station, TX, USA). The mean lengths were analysed using one-way ANOVA technique. Using direct caliper measurements as the

gold standard, the difference was measured and analysed using unpaired two-sample *t*-test with unequal variances, with Welch approximation. P value of less than 0.05 was accepted as statistically significant.

Results

Literature Review

Characteristics of the Published 3D Printing Validation Studies

There were 28 comparison studies within 19 papers which examined the accuracy of medical 3D printing between 1994 and 2016 (Table 2). Majority of investigators use multidetector CT (MDCT) over cone-beam CT (CBCT) as imaging modality (24 vs 4 studies). Cadaveric skull and mandible are most commonly used as specimens (16 and 10 studies, respectively). This is most likely due to the fact that 3D printing has been most extensively studied for application in cranio-maxillofacial surgery. Relatively consistent quality of CT images has been acquired as evidenced by a narrow range of CT layer thickness used (0.5-2.5 mm). Majority of papers have reported 3D printing in-house, rather than outsourcing to an external company (14 vs 5 papers). Encouragingly, this appears to be a growing trend (median year of publication: 2011.5 vs 2009 respectively). Linear measurements were made more commonly using a caliper than automated CMM (22 vs 6 studies).

Published Accuracy of 3D Printing

Stereolithography and binder jet technique were most commonly investigated (10 and 7 studies, respectively), followed by newer selective laser sintering (4 studies), fused filament fabrication (4 studies) and PolyJet technology (3 studies) (Table 12.1.3.1.1).

	Author	Year	Specimen	Outsource (Y/N)	CT		3D Printer			3D Printing Software		Mode of Measurement	Mean Difference		Reference
					Type	Slice Thickness (mm)	Name	Company	*Z*-resolution (mm)	Name	Company		mm	%	
SLA	Primo *et al*	2012	Skull	Y	MDCT	N/A	ZPrinter 310	3D Systems	0.0762	Magics	Materialise NV	Caliper	N/A	0.62	(328)
	Taft *et al*	2011	Skull	N	MDCT	0.625	Viper 2si	3D Systems	0.0025	Mimics	Materialise NV	CMM	0.61	N/A	(329)
	Nizam *et al*	2006	Skull	N	MDCT	1.25	Viper 2si	3D Systems	0.0025	Mimics	Materialise NV	Caliper	0.23	0.08	(330)
	Choi *et al*	2002	Skull	N	MDCT	1.0	SLA 5000	3D Systems	0.00177	V-Works	CyberMed	Caliper	0.62	0.56	(331)
	Asaumi *et al*	2001	Skull	N	MDCT	1.0	N/A	D-MEC	N/A	N/A	N/A	Caliper	N/A	0.63	(332)
	Bouyssie *et al*	1997	Mandible	N	MDCT	1.0	SLA 250	3D Systems	0.0025	Mimics	Materialise NV	Caliper	0.12	2.10	(333)
	Ono *et al*	1994	Skull	N	MDCT	0.5	SCS-1000 HD	D-MEC	0.02	N/A	N/A	Caliper	0.33	0.68	(180)
	Barker *et al*	1994	Skull	Y	MDCT	1.5	SLA 250	3D Systems	0.0025	Analyze	AnalyzeDirect	Caliper	0.85	2.74	(334)
	Primo *et al*	2012	Skull	Y	CBCT	N/A	ZPrinter 310	3D Systems	0.0762	Magics	Materialise NV	Caliper	N/A	0.74-0.82	(328)
	Santana *et al*	2012	Mandible	Y	CBCT	N/A	N/A	N/A	N/A	N/A	N/A	Caliper	0.35-0.39	N/A	(335)
BJT	McMenamin *et al*	2014	Upper Limb	N	MDCT	1.0	ZPrinter 650	3D Systems	0.089	Rhinoceros 3D	Robert McNeel & Associates	Caliper	0.32	1.29	(252)
	Salmi *et al*	2013	Skull	N	MDCT	N/A	ZPrinter 450	3D Systems	0.089	Zeiss Calypso	Carl Zeiss	CMM	0.44-0.80	0.38-0.69	(336)
	Murugesan *et al*	2012	Mandible	N	MDCT	0.6	N/A	N/A	N/A	Mimics	Materialise NV	Caliper	N/A	1.67	(337)
	Ibrahim *et al*	2009	Mandible	Y	MDCT	N/A	ZPrinter 310	3D Systems	0.0762	N/A	N/A	Caliper	1.44	3.14	(266)
	Silva *et al*	2008	Skull	Y	MDCT	0.5	ZPrinter 310	3D Systems	0.0762	InVesalius	CTI	Caliper	1.07	2.10	(267)
	Change *et al*	2003	Skull	N	MDCT	1.5	ZPrinter 420	3D Systems	0.0762	Mimics	Materialise NV	Caliper	<2.00	2.10-4.70	(338)

	Olszewski *et al*	2014	Mandible	N	CBCT	0.5	Matrix 300+	Mcor Technologies	0.1	Maxilim	Medicim	CMM	0.36	1.87	(191)
SLS	Petropolis *et al*	2015	Skull	N	MDCT	1.0	EOSINT P 395	EOS GmbH	0.06	OsiriX	Pixmeo	Caliper	0.16	0.30	(339)
	Salmi *et al*	2013	Skull	N	MDCT	N/A	EOSINT P 800	EOS GmbH	0.12	Zeiss Calypso	Carl Zeiss	CMM	0.93	0.79	(336)
	Ibrahim *et al*	2009	Mandible	Y	MDCT	N/A	DTM Sinterstation 2000	3D Systems	0.254	N/A	N/A	Caliper	0.90	1.79	(266)
	Silva *et al*	2008	Skull	Y	MDCT	0.5	DTM Sinterstation 2000	3D Systems	0.254	InVesalius	CTI	Caliper	0.89	2.10	(267)
FFF	Ogden *et al*	2015	Vertebra	N	MDCT	0.625	Replicator 2	MakerBot	0.1	Analyze	AnalyzeDirect	Caliper	0.18	0.69	(340)
	Petropolis *et al*	2015	Skull	N	MDCT	1.0	CubeX	3D Systems	0.1	OsiriX	Pixmeo	Caliper	0.21	0.44	(339)
	Murugesan *et al*	2012	Mandible	N	MDCT	0.6	N/A	N/A	N/A	Mimics	Materialise NV	Caliper	N/A	1.73	(337)
	Maschio *et al*	2016	Mandible	N	CBCT	0.5	Up Plus 2	Beijing TierTime Technology	0.15	Maxilim	Medicim	CMM	0.37	3.76	(341)
PJT	Salmi *et al*	2013	Skull	N	MDCT	N/A	Objet Eden 350V	Stratasys	0.016	Zeiss Calypso	Carl Zeiss	CMM	0.20	0.18	(336)
	Murugesan *et al*	2012	Mandible	N	MDCT	0.6	N/A	N/A	N/A	Mimics	Materialise NV	Caliper	N/A	0.13	(337)
	Ibrahim *et al*	2009	Mandible	Y	MDCT	N/A	Objet Eden 330	Stratasys	0.016	N/A	N/A	Caliper	1.23	2.14	(266)

Table 12.1.3.1.1. Summary of studies that assess the accuracy of medical 3D printing using linear measurements on cadaveric specimens Abbreviations: CT: computed tomography; MDCT: multidetector CT; CBCT: cone beam CT; mm: millimetre; Y: yes; N: no; SLA: stereolithography; BJT: binder jet technique; SLS: selective laser sintering; FFF: fused filament fabrication; PJT: PolyJet technology; N/A: not available; CMM: coordinate measuring machine.

Stereolithography

Stereolithography (SLA) is the earliest 3D printing technology described and is considered the gold standard in 3D biomodel production (176). However, it is slow, relatively expensive and requires significant post-production manual processing (318). Most studies used MDCT over CBCT (8 vs 2 studies) at slice thickness of 0.5-1.5 mm, and cadaveric skull and mandible as specimens (8 and 2 studies, respectively) (180, 328-335). Highest *z*-resolution of SLA 3D printers ranged between 0.00177 mm and 0.0762 mm. Using MDCT, the mean absolute difference between the original specimen and its 3D-printed model was 0.46 mm (range: 0.12-0.85 mm) and relative difference 1.06% (0.08-2.74%). Using CBCT, the mean difference was 0.35-0.39 mm and 0.74-0.82%.

Binder Jet Technique

Binder jet technique (BJT), also known as powder bed technique, describes a process where a printer head ejects binder material and coloured dye simultaneously onto a bed of powder and fuses them layer-by-layer into a plaster model (189). Major benefits of BJT are that it forgoes support structures and can produce models in multiple colours and materials. However, the final product is brittle and requires extensive post-production manual processing (318). Similar to SLA, most studies used MDCT over CBCT (6 vs 1 studies) at slice thickness of 0.5-1.5 mm, and cadaveric skull, mandible and upper limb bones as specimens (3, 3, and 1 studies, respectively) (191, 252, 266, 267, 336-338). Highest *z*-resolution of BJT 3D printers ranged between 0.0762 mm and 0.12 mm. Using MDCT, the mean difference was 1.05 mm (0.32-2.00 mm) and 1.78% (0.38-3.14%). Using CBCT, the mean difference was 0.63 mm and 1.87%.

PolyJet Technology

PolyJet technology (PJT), also known as multijet modelling, is similar to SLA but the liquid photopolymer is immediately cured by the ultraviolet (UV) light preventing time-consuming post-production processing (184). A major benefit of PJT is its high resolution; however, its surface finish is still inferior to SLA and the printers remain expensive (318). All studies of PJT used MDCT at slice thickness of 0.6 mm, and cadaveric mandible and skull as specimens (2 and 1 studies, respectively) (266, 336, 337). Highest *z*-resolution of PJT 3D

printers was 0.016 mm. Using MDCT, the mean difference was 0.72 mm (0.20-1.23 mm) and 0.82% (0.13-2.14%).

Fused Filament Fabrication

Fused filament fabrication (FFF) is the most affordable consumer-grade 3D printing technology where a melted filament of thermoplastic material is extruded in a layer-by-layer fashion (182, 190). Major advantages of FFF is its cost and convenience; however, it almost inevitably requires simultaneous production of support structures and hence, yields the lowest quality of surface finish (318). Most studies used MDCT over CBCT (3 vs 1 studies) at slice thickness of 0.5-1.0 mm, and cadaveric mandible, skull, and vertebra as specimens (2, 1, and 1 studies, respectively) (337, 339-341). Highest *z*-resolution of FFF 3D printers ranged between 0.1 mm and 0.15 mm. Using MDCT, the mean difference was 0.20 mm (0.18-0.21 mm) and 0.95% (0.44-1.73%). Using CBCT, the mean difference was 0.37 mm and 3.76%.

Selective Laser Sintering

Selective laser sintering (SLS) is a technique where powdered forms of thermoplastic, metal, glass or ceramic material are sintered by high-power laser beams in a layer-by-layer manner (185). Similar to BJT, SLS foregoes support structures and is capable of producing delicate structures with smooth surface finishes. However, high-powered laser of SLS 3D printers requires expert handling for safety and hence, they are related to high cost (318). In contrast to SLA and BJT, all studies of SLS used MDCT at slice thickness of 0.5-1.0 mm, and cadaveric skull and mandible and upper limb bones as specimens (3 and 1 studies, respectively) (266, 267, 336, 339). Highest *z*-resolution of SLS 3D printers ranged between 0.06 mm and 0.254 mm. Using MDCT, the mean difference was 0.72 mm (0.16-0.93 mm) and 1.25% (0.30-2.10%).

Validation Study

Image segmentation took an average of 7.5 minutes per bone (4.2-13.4 minutes). 3D printing took an average of 28.8 minutes per model (25-37 minutes). Mean length of chicken radius bones from direct caliper measurements (i.e. the gold standard) was 39.54 mm (36.64-43.75 mm). Mean length from CT scans was 39.32 mm (36.10-43.30 mm),

producing a difference of 0.22 mm from the gold standard (p = 1.00). Mean length from image segmentation was 40.56 mm (37.18-44.96 mm), producing a difference of 1.02 mm from the gold standard (p = 0.22). Mean length from 3D-printed models was 40.70 mm (37.17-45.00 mm), producing a difference of 1.16 mm from the gold standard (p = 0.10).

In order to calculate mean absolute and relative difference, measurements from the DICOM images of CT scans (CT group), image segmentation (SEG group) and 3D-printed models (3DP group) are subtracted from the gold standard for each bone (Table 12.1.3.1.2). Mean absolute difference from the CT group was 0.34 mm (standard deviation: 0.26-0.42 mm); SEG group: 1.02 mm (SD: 0.88-1.15 mm); and 3DP group: 1.16 mm (SD: 1.03-1.29 mm). Mean absolute difference from the CT group was significantly smaller than both SEG ($p < 10^{-4}$) and 3DP groups ($p < 10^{-4}$). However, there was no statistical significance between the SEG and 3DP groups (p = 0.13). Mean relative difference from CT group was 0.86% (SD: 0.66-1.06%); SEG group 2.51% (SD: 2.17-2.85%) and 3DP group 2.84% (2.54-3.15%). Similarly, mean relative difference of the CT group was significantly smaller than both SEG ($p < 10^{-4}$) and 3DP groups ($p < 10^{-4}$), but there was no statistical significance between latter two groups (p = 0.15).

Difference		CT	SEG	3DP
Absolute (mm)	Mean	0.34	1.02	1.16
	95% CI	0.26-0.42	0.88-1.15	1.03-1.29
	$p < 10^{-4}$ * p = 0.13 $p < 10^{-4}$ *			
Relative (%)	Mean	0.86	2.51	2.84
	95% CI	0.66-1.06	2.17-2.85	2.54-3.15
	$p < 10^{-4}$ * p = 0.15			

	$p < 10^{-4}$ *

Table 12.1.3.1.2. Summary of difference of the maximum length of chicken radius bone (gold standard) against CT DICOM images (CT), image segmentation (SEG), and 3D-printed models (3DP).

Abbreviations: CT: computed tomography; SEG: image segmentation; 3DP: 3D printing; CI: confidence interval; mm: millimetre.

Discussion

Despite a plethora of studies demonstrating numerous utility of 3D printing in surgery (16, 17, 318), there is a relative paucity of studies assessing its accuracy in a systematic manner. Current review of 28 comparison studies in 19 papers demonstrates that all 3D printing techniques using conventional MDCT have acceptable accuracy for clinical application with mean difference of less than 1-2 mm (1-2%): SLA: 0.46 mm (1.06%), BJT: 1.05 mm (1.78%), PJT: 0.72 mm (0.82%), FFF: 0.20 mm (0.95%) and SLS 0.72 mm (1.25%). However, it is worth noting that studies have used varying approaches, making them difficult to compare directly.

Some investigators have used CBCT as imaging source, which has lower cost, lower radiation and higher spatial resolution for bony micro-architecture than MDCT, but it is prone to motion artefact and is limited by small field of view (average of 6 x 6 cm) making it ideal for dental imaging (356). A wide variety of software programs has been used for image segmentation that differ in basic algorithm for creating 3D-reconstructed images. Some software suites are difficult to obtain for widespread application due to their high cost, such as Mimics (Materialise NV, Leuven, Belgium), or are limited to their local institution, such as V-Works (CyberMed, Seoul, South Korea). Similarly, 3D printers of the same technique can differ in accuracy amongst different brands and different models within the same brand.

Errors can be introduced at all stages of medical 3D printing (Figure 1), but occurs most frequently and most significantly during image acquisition and segmentation (321, 327, 357). In comparison to MRI, CT is associated with less geometric distortion (358) and, therefore, greater accuracy (334), especially when 3D printing bones (359). The greatest discrepancy can occur from incorrect selection of CT slice thickness when exporting DICOM images (331). CT images are routinely acquired in slice thickness of 0.6-2.0 mm, ideal for 3D printing; however, these are only stored temporarily and discarded after being converted to thicker 5.0 mm images to reduce storage cost (360). As scanners continue to evolve, errors from other aspects of CT, such as image noise, beam hardening, motion artefact, metal artefact and gantry tilt distortion, have significantly improved (361).

When evaluating the accuracy of 3D printing, it is important to differentiate it from describing the *z*-resolution, which indicates the thinnest layer of 3D print that can be

deposited per layer. However, this does not correlate with the overall accuracy of the final model, since increasing the number of layers that needs to be 3D-printed increases the potential for error and artefact (362).

Image segmentation involves partitioning DICOM images into multiple regions that correspond to an anatomical structure of interest and produces its digital 3D reconstruction (361). Due to its reliance on operator expertise for selecting appropriate threshold values and manual processing, image segmentation is highly susceptible to inter-operator variability and is potentially the most significant source of inaccuracy (326, 327, 363). In place of time-consuming traditional manual segmentation methods (364), semi-automated segmentation techniques have been developed, such as global thresholding (365), edge detection (366) and region growing (367). For 3D printing bones, global thresholding is the most commonly used technique (368, 369) and is also employed in our validation study. Despite its benefits, it still requires additional manual editing (327, 370). Recent improvements in artificial intelligence and machine learning capabilities pose interesting potential in this field (371). Furthermore, the size of each triangular mesh produced during 3D reconstruction, called triangulation algorithm, can impact accuracy of the final model (263).

Inaccuracy can still be introduced during post-segmentation image processing to further smooth or trim 3D images. However, this has improved significantly in recent times with software advancements and segmentation techniques (372). Slicing software and 3D printers are often packaged together and are generally considered precise by industry standards (373). The surface of 3D-printed models can be damaged during post-print processing to remove support structures, especially with FFF 3D printers. However, these superficial blemishes rarely significantly compromise the overall accuracy (361). Nonetheless, in our study, the models were 3D-printed in an upright position to minimise the amount of support structures that would need to be removed. Altogether, the errors encountered at all the steps combine and influence each other, making the sum of all errors not additive, but multiplicative (266, 324). As a result, when assessing 3D printing, the whole process from imaging to fabrication must be validated together.

The results from current validation study using chicken radius is comparable to the published reports. Interestingly, amongst the studies using FFF 3D printers, our mean absolute and relative differences compare higher than the published values (1.16 mm vs

0.20 mm and 2.84 vs 0.95%, respectively). One of the reasons for this discrepancy may be from soft tissue artefact. In our study, the bones are scanned as chicken wings and then dissected out afterwards. In other studies, the cadaveric specimens are scanned after being dissected, which would yield superior contrast and spatial resolution at bone-to-air interface. Moreover, unlike other expensive, proprietary image segmentation programs, such as Mimics (Materialise NV, Leuven, Belgium), Vitrea (Vital Images, Minnetonka, MN, USA) and OsiriX MD (Pixmeo, Geneva, Switzerland), we have used 3D Slicer used, which has not yet been approved by the US Food and Drugs Administration (FDA) for routine clinical application, albeit only for research purposes (374).

Nevertheless, one of the major limitations of this validation study is that the findings cannot be directly translated to 3D printing anatomical structures that are different in size to chicken radius, such as human femur or humerus. The mean absolute difference found in our study may be altered with other bones in the body with different soft tissue artefacts and their unique anatomical characteristics affecting image segmentation. The mean relative difference may not be translatable since the degree of inaccuracy between different human bones may not linearly correlate with their size.

Conclusion

There have been 28 comparison studies in 19 papers which demonstrate that all 3D printing techniques using conventional MDCT have acceptable accuracy for clinical application, with a mean difference from original anatomical specimens of less than 1-2 mm (1-2%): SLA: 0.46 mm (1.06%), BJT: 1.05 mm (1.78%), PJT: 0.72 mm (0.82%), FFF: 0.20 mm (0.95%), and SLS 0.72 mm (1.25%). The current validation study of the Peninsula 3D printing technique produced accuracy similar to the published studies (1.16 mm, 2.84%). There was a statistically significant difference ($p < 10^{-4}$) between the CT group and the latter SEG and 3DP groups indicating that most of the error is introduced during image segmentation stage.

12.1.3.2 Validation Study Using Volumetric Measurement

Chapter Summary

Introduction: 3D printing, a stepwise process, has multiple applications in surgery. Prior to printing, 3D virtual surface models (SM) are created on an image processing platform such as *3D slicer* to instruct a 3D printer what to print. SM are made through a process of thresholding and manual segmentation of medical images (CT scans). Their accuracy is crucial to the accuracy of the resultant 3D print. The objective of the current study was to validate the accuracy and user variability of SM created with *3D slicer* program.

Method: Accuracy of SM was determined by volumetric analysis of 50 rocks by water displacement and *3D slicer*. Intra and inter-user variability was assessed by volume analysis of multiple SM of the trapezium and pisiform bones using 50 CT wrist scans. The Interclass Correlation Coefficient (ICC) was determined for each study to determine the reliability of agreement between results.

Results: Volumetric analysis of rocks by *3D slicer* and water displacement showed an ICC of 0.996 (CI 0.993-0.997) corresponding to excellent reliability of agreement between the two methods. The ICC for intra and inter-user variability was 0.86 (CI 0.75-0.92) and 0.95 (CI 0.91-0.97) respectively, corresponding to good to excellent reliability of agreement between measurements made by a single or multiple individuals.

Conclusion: The current studies validate the accuracy and user variability of surface models generated by 3D slicer. Further studies will be useful for more rigorous validation of the different steps and software programs involved in 3D printing.

Introduction

Since its inception, 3D printing technology has found multiple applications in a range of surgical specialities. To date, the most widely utilised application of 3D printed objects in surgery are anatomical models for surgical planning and intraoperative facilitation of surgery (318, 375-377). The value of a 3D printed anatomical model intuitively lies in the accuracy with which it resembles the original anatomy.

The pathway involved in replicating anatomy as a 3D print is stepwise. It involves medical imaging, the use of a 3D modelling computer assisted design (CAD) software program and finally the use of a 3D printer. Each step in the pathway is integral to an accurate replication of anatomy (324). However, the greatest degree of variability in producing a 3D printed model is introduced by the use of the 3D modelling software. The purpose of the CAD program is to create a 3D virtual model or surface model (SM) from the medical imaging through a process of segmentation.

3D slicer (263) is such a program developed for image analysis with capabilities of processing medical imaging to create SM in a format which is recognised by 3D printer driver software, namely stereolithography (STL) file format. The SM created using 3D slicer are therefore only as accurate as the segmentation undertaken of the object of interest. This is a process which ranges from automated segmentation to manual segmentation which relies on the ability and judgement of the user. The current studies are aimed at validating the SM generated by 3D slicer and investigating intra and inter user variability and reproducibility of accurate SM.

Methods

An experimental comparative study was undertaken with the aim of validating user variability and accuracy of surface models created on 3D slicer by utilising both clinical imaging data of CT wrist scans, as well as CT imaging data from specifically selected rocks. Ethics approval for the use of anonymised CT wrist scans was granted through Peninsula Health Low Risk Ethics Committee. The studies were performed at a single institution, Frankston Public Hospital, with data collected by authors DG, RW and MC.

Study methods

The method used for creating a 3D surface model using 3D slicer program 4.6.2 is described herein.

CT scan images were uploaded to the *3D slicer program*. Once uploaded the contrast was adjusted to adequately view the images. Using the “Editor” module, a “thresholding effect” was applied to create a single label map. The “threshold effect” (which uses Hounsfield units to highlight structures of a certain density) was adjusted to maximally include the object of interest and exclude undesired background structures. Once the desired threshold was applied, any additional label visually connected to the desired object is deleted. This process was continued slice by slice in all planes: coronal, sagittal and transverse until the object of interest was completely islanded, on all planes and on all slices. One of two things can be done at this stage: “Change island effect” to label the object of interest with a different colour label to the background or “save island effect” to delete any back-ground label therefore only the object of interest remains labelled. The object of interest was then solidly filled with the same colour label, on all slices in all planes, using “paint effect”. A 3D SM was now created using “make model effect”. Details of the 3D SM, such as volume can be found in the “Models” module.

Three studies were carried out to validate the surface models produced by 3D slicer.

<u>Study 1: Accuracy of surface models produced by 3D slicer</u>

Volumes of objects derived by 3D slicer generated SM were compared with volumes derived by water displacement. Volumetric analysis by 3D slicer version 4.6.2: Garden

rocks, labelled 1-50, were placed through the Frankston hospital Emergency Department CT scanner. The CT images of the rocks were uploaded on to 3D slicer program version 4.6.2. The volume of each rock was derived by creating a SM of each rock as described previously. The process of segmentation was largely automated using 'threshold effect'. Volumetric analysis by water displacement: The volume of each of the 50 garden rocks were derived by water displacement: A 50ml syringe with its nose blocked was partially filled with an arbitrary amount of water. Each garden rock was consecutively placed inside the partially water filled syringe. The number of millilitres by which the water was displaced was recorded for each rock, to the accuracy of 1ml.

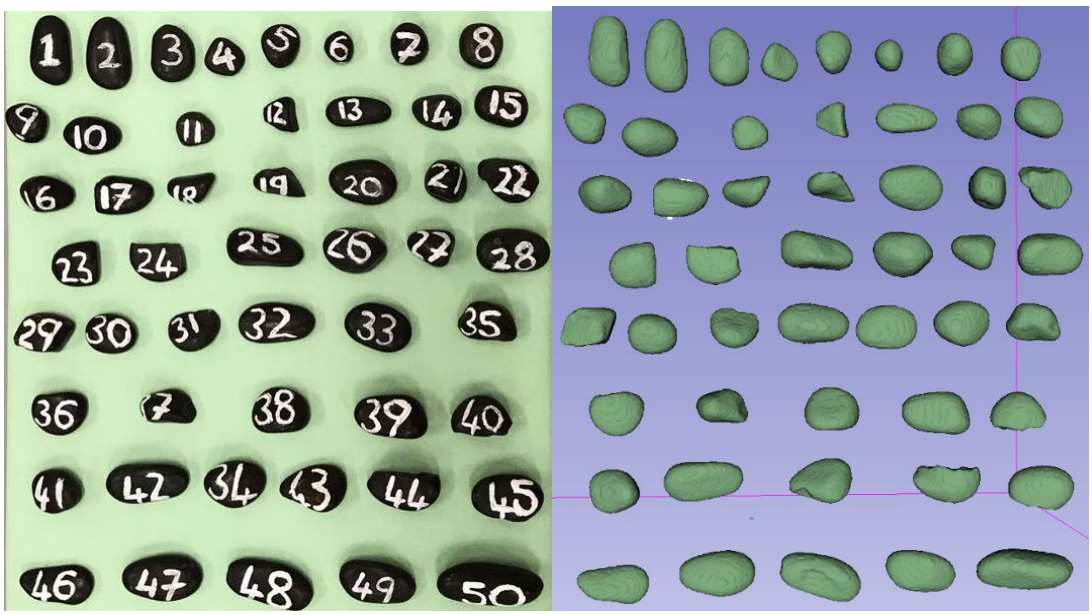

Figure 12.1.3.2.1. Photograph of the 50 rocks used for volumetric analysis by water displacement (left) and Screenshot of 3D reconstructed virtual models of the rocks by 3D slicer (right).

Study 2 and 3: Inter and intra-user variability in creating surface models with 3D slicer

The Computed tomography (CT) scans of 50 patients undergoing hand and wrist CTs at Frankston Hospital were identified and anonymised. Each CT scan was uploaded and the volumes of the trapezium and pisiform bones were derived by creating a SM of the carpal bone of interest using *3D slicer*. To compare intra-user variability, SM of the trapezium and pisiform bones from each scan were created by a single individual (DG), this was repeated after the scans were renamed to blind the researcher, so they were not influenced by the

first set of volume measurements made from the SM by the software. To compare inter-individual variability, SMs of the trapezium and pisiform bones from each CT scan were created by two individuals (DG and RW) independently and the volumes measured of each scan by each individual compared.

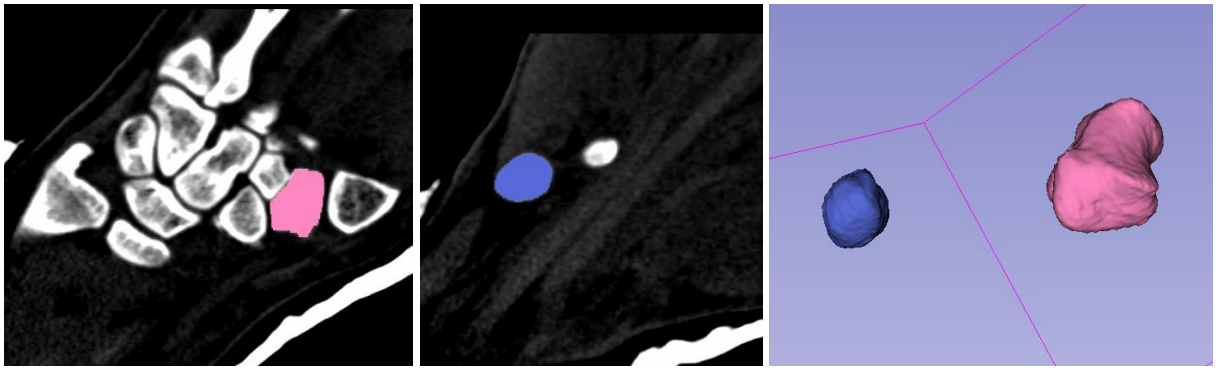

Figure 12.1.3.2.2. Screenshot of segmented trapezium (Pink, left) and Pisiform (Purple, centre) and 3D virtual surface model of trapezium and pisiform (right).

Statistical analysis

The distribution of data populations were assessed using the Shapiro Wilk test. Data which did not pass used non-parametric tests - either the Wilcoxon Signed Rank test or a One Way Repeated Measures analysis of Variance on Ranks to examine the statistical significance of the difference between repeated measurements made by one or between two individuals respectively. These tests investigated difference and did not investigate consistency or reliability.

The Interclass Correlation Coefficient (ICC) is a measure of consistency of measurements of the same items which are made by multiple researchers and was used to determine the reliability and agreement between results. ICC estimates and their 95% confidence intervals were calculated by both absolute agreement and consistency of agreement using two-way random-effects models. Interpretation of the of the ICC estimate may be made as follows: “values less than 0.5, between 0.5 and 0.75, between 0.75 and 0.9, and greater than 0.90 are indicative of poor, moderate, good, and excellent reliability, respectively”.

All tests were conducted using STATA (v14).

Theory

Surface model accuracy and user variability is not only important for validating accuracy of resultant 3D prints, but also carry important implications for clinical research. The 3D slicer program has capabilities which can be used for prototyping as well for clinical research. Accurate volumetric analysis in particular is important in clinical practice and research. One of the major applications of 3D slicer in clinical research has been for investigation of imaging as a biomarker of cancer treatment using volume rendering in 3D slicer. The current validation studies were performed complimentary to a larger project investigating morphological changes in the trapezium in base of thumb arthritis, hence the reason carpal bones and garden rocks of similar volumes to carpal bones were used for validation of methods. Furthermore, 3D slicer is an open access freely available program with multiple tools for image analysis with potential for broad application in 3D printing as well as clinical research (263).

Results

N=50	**Water Displacement (mm^3)**	**3D Slicer (mm^3)**	**Difference (mm^3)**
Median ± (95%) CI	5300 ± 632	5313 ± 621	32 ± 123
Mean ± standard deviation	5608 ± 2282	5597 ± 2243	11 ± 445

Table 12.1.3.2.1. Volumetric analysis of the rocks by water displacement and 3D slicer.

The two data populations (volume measurements of the rocks by water displacement and 3D Slicer) were assessed for normality using the Shapiro-Wilk test and failed ($P<0.05$), so their differences were assessed using a Wilcoxon Signed Rank test. This found there was not a statistically significant difference between the rock volume measurements made by volume displacement and 3D Slicer ($Z=0.893$, $P=0.374$).

As the normality test (Shapiro-Wilk) also failed for the intra- and inter-variability studies, non-parametric tests were also used to investigate whether there were significant differences between repeated measurements made by one individual or by two. There was no statistically significant difference between the repeated measurements made by one individual who was blinded to the objects' identities (first versus second measurement, $p=0.76$ by Wilcoxon Signed Rank Test) nor was there any statistically significant difference between measurements made by 2 individuals (measurements from DG vs RW, $p=1.00$, by One Way Repeated Measures analysis of Variance on Ranks). As above, these tests report any statistically significant differences but do not give an indication of variability and/or reliability of measurements; for this the ICC were calculated for the intra- and inter-variability studies.

	N	**Mean (mm^3)**
Trapezium Volume DG	48	2256 ± 619
Trapezium Volume RW	48	2345 ± 541
Difference	48	89 ± 895
Pisiform Volume DG	47	857 ± 317
Pisiform Volume RW	47	870 ± 286

Difference	47	13 ± 465

Table 12.1.3.2.2. The volumes of the trapezium and pisiform surface models (average ± standard deviation) measured using 3D slicer for the inter-user variability studies.

	N	**Mean (mm^3 ± standard deviation)**
Trapezium Volume 1	48	2266±628
Trapezium Volume 2	48	2326±585
Difference	48	53 ± 879
Pisiform Volume 1	47	839±308
Pisiform Volume 2	47	888±307
Difference	47	14 ± 415

Table 12.1.3.2.3. Shows the volumes of the trapezium and pisiform surface models (average volume ± standard deviation) measured using the 3D slicer for the intra-user variability studies.

Volumetric analysis of rocks by 3D slicer and water displacement had an ICC of 0.996 (CI 0.993-0.997) corresponding to excellent reliability of agreement between the two methods. The ICC for intra and inter-user variability was 0.86 (CI 0.75-0.92) and 0.95 (CI 0.91-0.97) respectively, corresponding to good to excellent reliability of agreement between measurements made by a single or multiple individuals.

Discussion

3D printing has the potential to individualise patient care in surgery. Currently, the main clinical application of 3D printed objects are anatomical models used for surgical planning and intraoperative use to facilitate surgery(38, 378). Furthermore, 3D printed prosthetic devices are currently in use by some centres. The speciality which most commonly implements 3D printing is craniomaxillofacial surgery (321, 375, 379). Other areas in plastic reconstructive surgery which have implemented 3D printing is hand surgery with 3D printed prosthetic phalanges, and breast surgery for preoperative planning and volume assessment. (377, 379, 380) Xi *et. al*. found the combination of MRI and 3D modelling was the most reliable tool in breast volume assessment (377, 380).

The systematic review by Martelli *et al* assessing the advantages and disadvantages of 3D printing in surgery found the main advantages to be gained were in preoperative planning and reducing operative times. The main reported limitation, along with additional cost and time required to prepare the 3D printed object, was the accuracy of the 3D print (321). The current series of studies were aimed at validating SM used in the process of creating 3D printed objects. It is a first series of studies to validate accuracy of SM generated by 3D slicer and assess user variability.

Validation of the SM created using 3D slicer was necessary, as the potential for user variability is introduced during the segmentation process. This is due to the combination of automated as well as manual segmentation used. Automated segmentation uses thresholding to highlight structures of a certain density or Hounsfield unit. Manual segmentation is done visually to include or exclude structures deemed necessary or unnecessary. The choice of the thresholding value as well as the manual segmentation relies on user judgment and experience, in the domain of anatomy concerned, as well as familiarity with the software in use. Hence the requirement to validate the process and accuracy of SM to ensure the resultant 3D printed objects can be accurately and reliably produced.

Volumetric analysis of rocks by Archimedes principles of water displacement and use of 3D slicer generated SM showed excellent reliability of agreement between the two methods, therefore validating the accuracy of SM produced and volumetric analysis by 3D slicer. In this instance, majority of the segmentation of the CT images of the rocks were

done using automated segmentation as each rock appears isolated from one another and is of uniform density. The current results however may not be applicable to scenarios which require both automated and manual segmentation e.g. anatomical structures of varying density, such as bone and soft tissue. The study done to validate inter and intra-user variability also showed good to excellent reliability of agreement between a single and multiple users. The inter-user ICC was higher suggesting greater reliability between users compared to a single user. A reason for the lower intra-user reliability may be due to a learning curve associated with using 3D slicer and the segmentation process. Furthermore, the absolute error difference for larger volume objects such as the trapezium was greater than for smaller volume objects such as the pisiform.

A review of the literature revealed a small number of other studies which validate the process and accuracy of 3D printing. The study by Smith et al used segmented CT images of the shoulder and hip joints to produce 3D printed reconstructions, which were then compared to the original cadaver specimens as well as the virtual surface model through 3-way shape analysis using laser scanning. The overall reproducibility from cadaver to 3D printed model had a root mean square error (RMSE) of 0.3 +/- 0.4mm. The RMSE from cadaver to surface model was 0.3+/-0.4mm and virtual model to 3D print was 0.1+/0.1mm, which suggests that the greatest error occurred in the segmentation process and accuracy of segmentation was the critical factor in determining accuracy of the 3D print. The study by McMenamin et al assessed the accuracy of 3D printing by comparing 3D printed upper limb prosections to the original. The image processing software Aviso was used in this study to segment the structures of interest using a combination of tools including thresholding. Quantitative analysis using callipers of structures 10mm or more showed a mean absolute error of 0.32mm. Repeatability and intra-observer variability was assessed by repeated measurements of maxillary dentition of the original specimen and a 3D reconstruction. The ICC for the repeated measurements (0.998, $p<0.001$) of the original specimen was similar to that of the 3D printed model (0.998, $p<0.001$). The authors conclude by advocating the use of 3D printed replicas as teaching aides due to high accuracy and reproducibility (252). The validation study by cone et al, again compare 3D printed replicas of animal long bones to the original specimens found the overall discrepancy in dimensions of 1%. The 3D printed models over represented the dimensions. The authors conclude that the 3D printed models have high repeatability, with prints being slightly larger than the original bones (381). The study by Khalil et al validated 3D printed models of premolars by volumetric analysis by water displacement of

the models and originals showed the mean volume difference ranged from 0.7 % to 1.9%. The authors conclude a high degree of accuracy of printed teeth compared to natural teeth (350). Similarly, the validation study by Maschio et al compared 3D printed mandibles to their respective dry specimens and found the mean absolute difference of 8 distances between the 4 mandibles was 0.37mm. This study also found that the error difference decreased for distances greater than 12mm from 3.76% to 0.93%. The authors conclude that the low-cost 3D printers used in this study produced models of similar dimensional accuracy to that of other well-established 3D printers (341).

Conclusion

The value of 3D printed anatomical models used for surgical planning and research relies on the accuracy of the model resembling the original anatomy. *3D slicer* can be used to generate accurate surface models resulting in accurate 3D printed objects, independent of user variability, in this setting.

12.2 3D Printing Application in Plastic and Reconstructive Surgery

12.2.1 Bony Mapping

12.2.1.1 Mandibular Reconstruction

PUBLISHED (Publication): Cabalag MS, ***Chae MP***, Miller GS, Rozen WM, Hunter-Smith DJ. (2015) Use of three-dimensional printed "haptic" models for preoperative planning in an Australian plastic surgery unit. ANZ J Surg. doi:10.1111/ans.13168

Chapter Summary

Introduction: 3D printing describes a process in which a solid model is fabricated from 3D computer data. We describe a case in which a 3D-printed model was used to aid in the preoperative planning of both tumour resection and subsequent free flap reconstruction.

Methods: A 68-year-old woman presented with a local recurrence of squamous cell carcinoma (SCC) invading into the angle of the right mandible. A three-dimensional (3D) printed model of the right hemi-mandible, with and without the associated soft tissue tumour, constructed using an in-house, low-cost 3D printer (MakerBot Replicator Z18, New York, NY, USA) was used in preoperative planning.

Results: 3D-printed biomodels helped to preoperatively plan the extent of surgical resection as well as the method of reconstruction required by allowing the surgeon to better understand the spatial relationships of surrounding structures

Conclusion: Use of 3D printing for preoperative planning complex reconstructive surgery and its potential appear promising.

Case Report

A 68-year-old woman presented with a local recurrence of squamous cell carcinoma (SCC) invading into the angle of the right mandible. The patient reported a fixed, soft tissue mass growing over 6 months and her past history was significant for a previous SCC of the right upper lip, surgically excised 4 years prior (Figure 12.2.1.1.1).

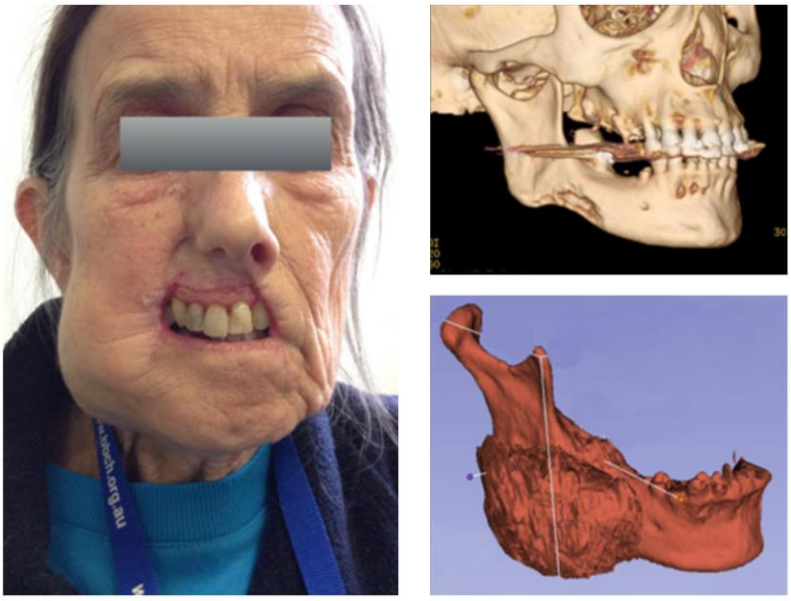

Figure 12.2.1.1.1. (clockwise from left to right) preoperative clinical photograph, three-dimensional computed tomography showing erosion of right hemi-mandible, three-dimensional reconstruction with associated soft tissue tumour.

There was no clinically detectable cervical or supraclavicular lymphadenopathy. Computed tomography (CT) and positron emission tomography (PET) scan revealed a 54 x 42 x 55 mm mass eroding into the angle of the right mandible and a second focus of fluorodeoxyglucose (FDG) uptake in the right mandibular ramus, but no neck or distant metastases. Fine-needle aspirate of the mass showed atypical squamous cells consistent with metastatic SCC.

In addition to the standard imaging modalities, preoperative planning was aided by the use of a three-dimensional (3D) printed model of the right hemi-mandible, with and without the associated soft tissue tumour, constructed using an in-house, low-cost 3D printer (MakerBot Replicator Z18, New York, NY, USA) (Figure 12.2.1.1.2).

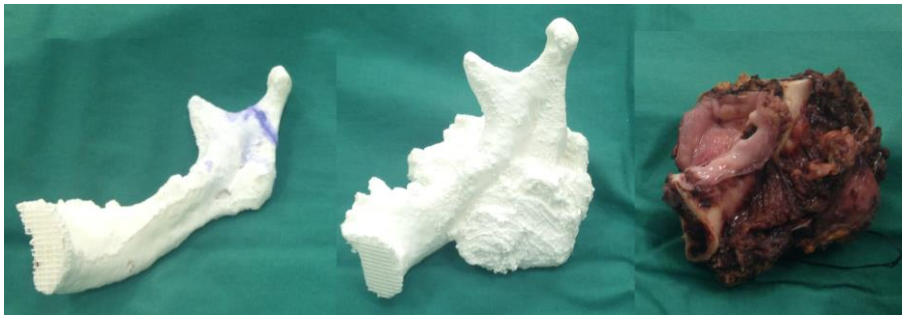

Figure 12.2.1.1.2. (from left to right) three-dimensional model of right hemi-mandible without tumour, three-dimensional model with soft tissue tumour and intraoperative specimen.

The patient underwent a right-sided modified radical neck dissection (levels 1-5), right mandibular resection (from distal-to-coronoid process to mid-symphysis) and reconstruction with a composite fibula free flap (Figure 12.2.1.1.3).

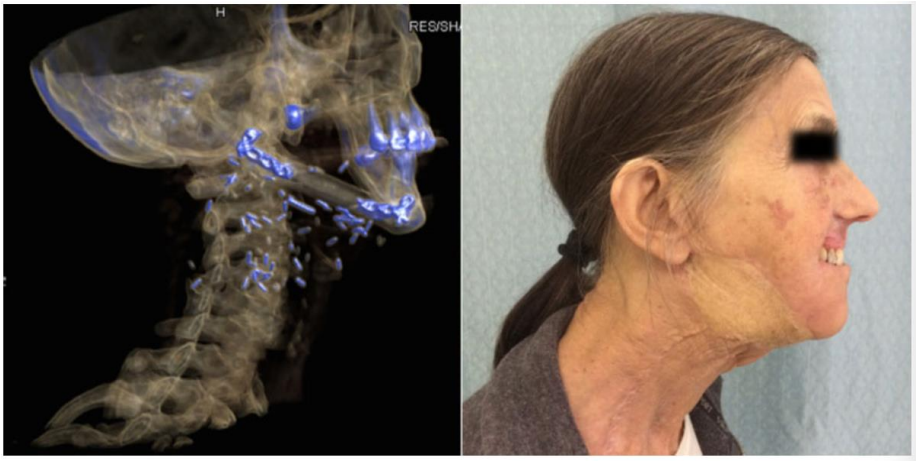

Figure 12.2.1.1.3. Seven-month post-operative three-dimensional computed tomography and clinical photograph.

3D printing describes a process in which a solid model is fabricated from 3D computer data. Fused deposition modelling (FDM), a 3D printing technique, is currently the most cost-effective, accessible and commonly used method and involves an additive process whereby melted thermoplastic filament is deposited onto a build plate in layers (186, 275). Using a 3D modelling program (Cubify, 3D Systems, Rock Hill, SC, USA), the process begins with the conversion of 2D CT data into a 3D virtual image, known as a computer-assisted design (CAD) file. The CAD file is then interpreted by the 3D printer to produce a

3D model. Although 3D printing has been utilized in industrial design for decades, it has only become adapted for medical applications within the last decade. Its increasing relevance in plastic surgery has become apparent, including in surgical planning and education, production of customized prostheses and volumetric analyses for breast reconstruction (17, 35, 382).

We describe a case in which a 3D-printed model was used to aid in the preoperative planning of both tumour resection and subsequent free flap reconstruction. We have recently utilized an in-house 3D printer to produce accurate models of bony and soft tissue pathologies derived from routine CT scans. Our current models of the mandible cost approximately AUD 25 each in thermoplastic filaments. The accuracy of FDM 3D printers is continually improving, with our current printer having an accuracy of 0.0025 mm and a resolution of 0.1 mm. hence, they are suitable for creating small complex anatomical models (275). Furthermore, the production time is fast, with the current model of a hemi-mandible taking approximately 3 hours to construct. Of note, this technology is potentially available to any hospital with access to a CT scanner.

3D printing a bony model is relatively simple and well established. In contrast, 3D printing of soft tissue poses a greater challenge, which we have overcome using the latest improved software and image processing techniques. To the best of our knowledge, we are one of the first centres globally to successfully use an in-house, consumer-level 3D printer to produce models of soft tissue tumours, with a level of accuracy that is clinically useful. Having two models to compare (i.e. one with bone only and another with bone and tumour attached) facilitated in planning the extent of surgical resection as well as the method of reconstruction required. The models allow the surgeon to better understand the spatial relationships of surrounding structures, clearly appreciate tumour morphology and provide a solid “haptic” object they can manipulate and view from multiple planes, thus providing a better understanding of the relevant anatomy. In this case, the patient’s mandible was readily viewed and the size and shape of the defect could be estimated, allowing accurate planning of reconstruction with a composite fibula free flap (Figure 2). Additionally, use of 3D print models may lead to improved surgical efficiency as well as help in the prediction of possible intraoperative complications, thus potentially reducing operative time (178, 182, 275).

Furthermore, the models are useful in facilitating discussion among surgeons and are excellent educational tools for both trainees and patients. In addition to maxillofacial cases, we have used similar models to help plan reconstruction for complex lower extremity defects (273). Importantly, 3D printing also has pertinent roles in other surgical specialties (211, 383).

12.2.1.2 Spine

PUBLISHED (Poster Presentation): ***Chae M***, Bronsema D, Monagle JP, Taverner MG. (2017) Three-dimensional printing: an aid to neuromodulation. Celebrating Research at Peninsula Health 2016

Chapter Summary

Introduction: 3D printing, also known as additive manufacturing or rapid prototyping, describes a technology where a computer-aided design (CAD) is fabricated in a layer-by-layer fashion. Being able to interact hands-on with a 3D-printed haptic biomodel enables superior visuospatial appreciation of the patient's unique anatomy and aids in individualised preoperative planning and is being integrated into the preoperative clinical workflow in many medical disciplines.

Aim: To explore the application of 3D printing in the preoperative planning of for the trial and implantation of a spinal cord stimulator in a patient with challenging spinal anatomy and to assess the feasibility of a successful epidural needle placement and lead insertion

Methods: Thin-slices (0.625 mm) of a high resolution CT scan of the patient's thoracolumbar spine and iliac crests was used to create a computer-aided design (CAD) model on 3D Slicer software (Surgical Planning Laboratory, Boston, MA). The CAD file was exported and converted into a 3D printer-friendly file using MakerBot Desktop software (MakerBot, New York, NY). The model was printed using a desktop 3D printer MakerBot Z18 (MakerBot, New York, NY).

Case: DW 73F, with severe kyphoscoliosis, osteoporosis and a long history of severe back pain that occasionally radiated to her right leg. Her relevant history includes unhelpful blocks, peripheral field nerve stimulator and failed percutaneous spinal catheter insertion. Pain related medications included meloxicam, duloxetine 60 mg mane, docusate sodium/senna 50/8 mg 2-4 daily, nitrazepam 5 mg nocte, Oxycodone 5 mg IR TDS PRN, oxycodone/naloxone 30/15 mg BD, paracetamol SR 1330 mg TDS, pregabalin 150 mg BD and prednisolone. Norspan, venlafaxine, TENS, baclofen, tapentadol, burst IV and regular oral ketamine, clonazepam, uncomfortable back brace, ultrasound guided right trochanteric bursa injection had been tried without success. Activity was severely restricted

by pain and she was less active and was resting in bed much of the time. She said her pain averaged 8/10, had been 5-8/10 in the preceding 24 hours. She said her current treatment relieved none of her pain. Pain related interference with activities of daily living was scored 45/70 on the Brief Pain Inventory indicating moderate-severe pain and moderate interference with daily activity. A MRI was contraindicated by her pacemaker.

Results: The model took 72 hours to print and another 2-3 hours of technician time to prepare the model. A good space was identified at T12/L1 and the model showed a right sided approach would give better access and thoracic spine lead placement. Two temporary Nevro octrode leads were inserted from the right at T12/L1 with the tips positioned offset at right T9 and left T8. 2 weeks later after a successful trial a permanent system was implanted. The system remains in site and continues to provide acceptable pain relief.

Discussion: Standard practice involves using preoperative imaging alone to plan surgery. This approach allows for discussion and “mental imagery” – but technical difficulties can arise during the procedure that have not been anticipated. 3D CT reconstructions enhance this process, but do not allow the hands-on experience. The 3D model allowed a “hands-on” planning of the approach. It allowed a number of approaches to be “walked through” – and the best of the available options chosen for the actual procedure. Patient positioning and needle access approaches being pre-planned aided in a successful outcome (which had not been achieved before).

Conclusion: The 3D model took additional time to prepare however it proved to be more useful than the CT-scan 3D reconstruction and made a useful contribution to the successful implantation of the spinal cord stimulator. This technology has potential application in planning difficult cases, making needle jigs and training.

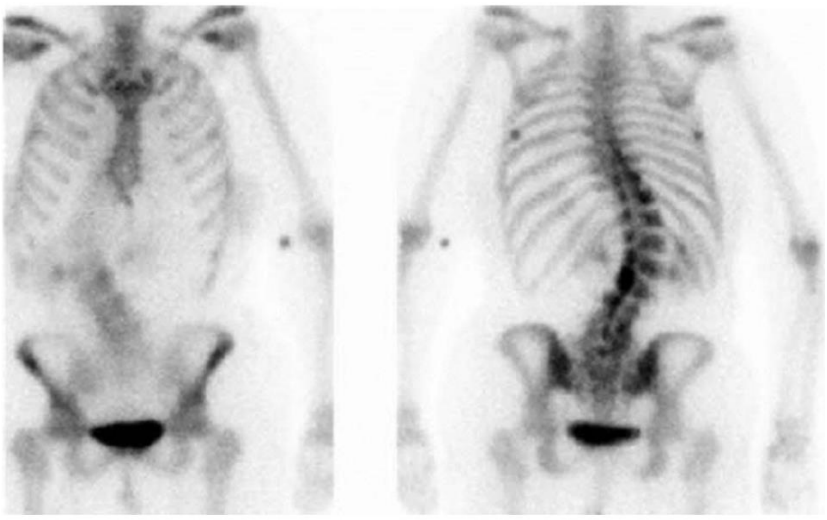

Figure 12.2.1.2.1. Bone scan showed multilevel facet arthropathy and an extensive scoliosis concave to the left.

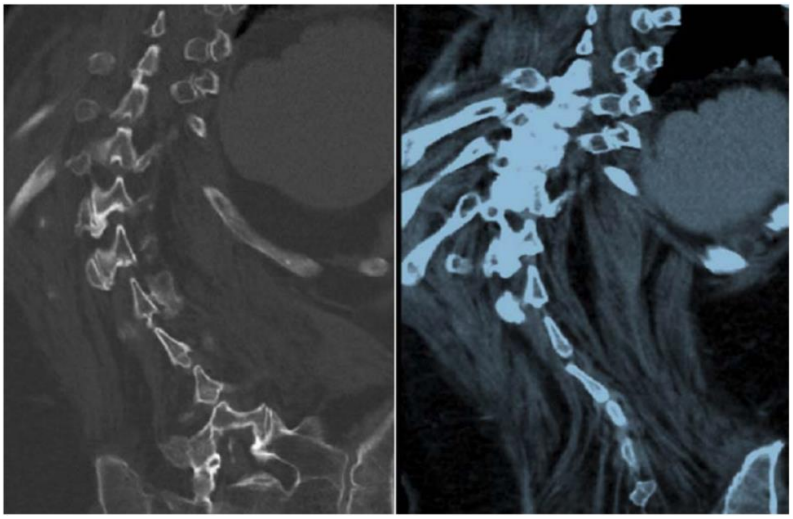

Figure 12.2.1.2.2. CT scan showed severe multilevel degenerative disc disease, marked curvature of the spine at the thoracolumbar junction and compensatory lumbar curvature. Extensive facet arthropathy and calcific arachnoiditis.

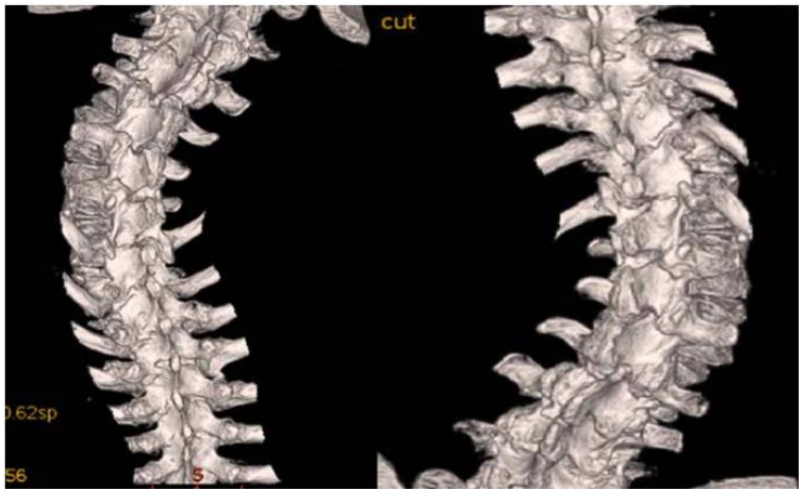

Figure 12.2.1.2.3. The 3D reconstructions were hard to use, only allowed short and long axis rotation and as presented were not optimised for caudad-cephalad viewing.

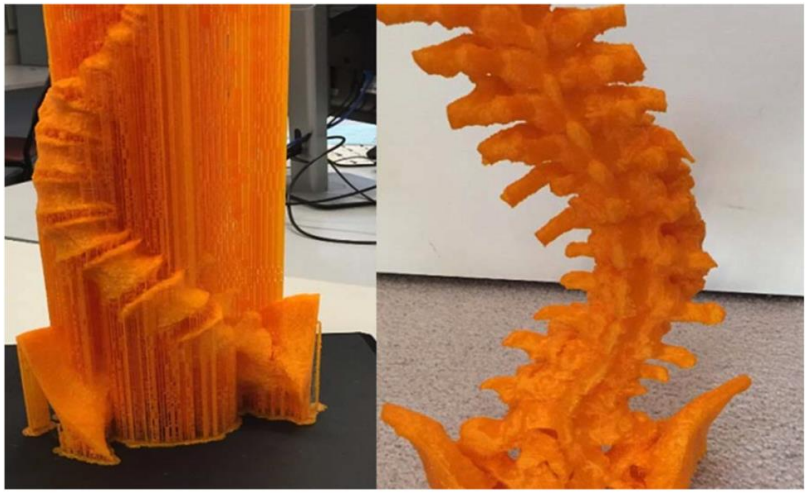

Figure 12.2.1.2.4. The 3D model was slow to print but gave great detail and allowed unlimited long, short axis rotation and everything in between.

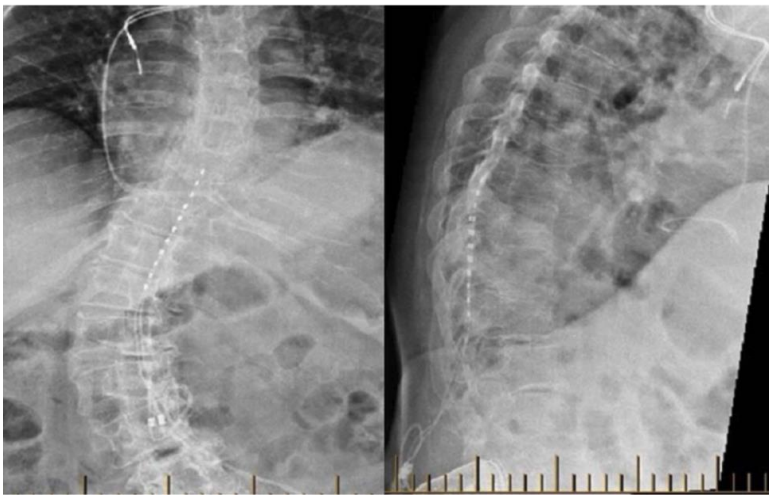

Figure 12.2.1.2.5. AP and lateral spine X-rays showing implanted stimulator leads.

12.2.2 Soft Tissue Mapping

12.2.2.1 Ankle Defect

PUBLISHED (Publication): ***Chae MP***, Lin F, Spychal RT, Hunter-Smith DJ, Rozen WM. (2015) 3D-printed haptic “reverse” models for preoperative planning in soft tissue reconstruction. Microsurg. 35(2):148-53. PMID: 25046728

Chapter Summary

Introduction: In reconstructive surgery, preoperative planning is essential for optimal functional and aesthetic outcome. Creating a three-dimensional (3D) model from two-dimensional (2D) imaging data by rapid prototyping has been used in industrial design for decades but has only recently been introduced for medical application. 3D printing is one such technique that is fast, convenient, and relatively affordable. In this report, we present a case in which a reproducible method for producing a 3D-printed "reverse model" representing a skin wound defect was used for flap design and harvesting. The experiments used in Chapter 10.2 will be used to demonstrate utility of the “reverse” image in comparison with standard imaging.

Methods: This comprised a 82-year-old man with an exposed ankle prosthesis after serial soft tissue debridements for wound infection. Soft tissue coverage and dead-space filling were planned with a composite radial forearm free flap (RFFF). Computed tomographic angiography (CTA) of the donor site (left forearm), recipient site (right ankle), and the left ankle was performed. 2D data from the CTA was 3D-reconstructed using computer software, with a 3D image of the left ankle used as a "control." A 3D model was created by superimposing the left and right ankle images, to create a "reverse image" of the defect, and printed using a 3D printer.

Results: The RFFF was thus planned and executed effectively, without complication.

Conclusion: To our knowledge, this is the first report of a mechanism of calculating a soft tissue wound defect and producing a 3D model that may be useful for surgical planning.

3D printing and particularly "reverse" modeling may be versatile options in reconstructive planning, and have the potential for broad application.

Introduction

For optimal restoration of function and appearance in re- constructive surgery, an accurate anatomical understand- ing of the defect is required. To this effect, preoperative planning with appropriate imaging techniques benefits both the excisional and reconstructive surgeon (73, 142, 384-386). Computed tomographic angiography (CTA) is one technique that has previously shown to improve operative outcomes while minimizing donor site morbidity (5, 6). It can aid in selecting the donor site, flap and vessel of choice for reconstruction (73). Furthermore, CTA is a relatively straight- forward procedure (137). A number of investigators have proven its efficacy in reducing operative time and reconstructive outcomes (5, 6, 95, 142, 387, 388).

In contrast to CTA, which produces three- dimensional (3D) visualization on a two-dimensional (2D) surface, rapid prototyping (RP) is a process of producing a 3D model layer-by-layer based on computer- aided design (CAD) data or imaging that precisely represents the anatomical details of a defect. Having been used for decades in industrial design, it has recently shown potential in medical applications, especially for implant design and preoperative planning (182). 3D models provide surgeons with a physical object that they can interact with hands-on for easier understanding of the morphology. This “haptic-modeling” has been shown in some settings to reduce operative time and facilitate superior operative outcomes (6, 142, 178, 388). Amongst numerous RP techniques, stereolithography is considered the gold standard in medical RP, but is labor-intensive, relatively expensive, slow, and recent publications bring into question issues regarding its environmental safety (180, 182, 389).

3D printing (3DP) is the latest RP technique where photopolymer materials are “jetted” in ultrathin layers and then “cured” by UV light for immediate handling and use. In comparison to stereolithography, it is faster, more convenient, less expensive, and more appropriate for producing small complex structures. In reconstructive surgery, 3DP has been used to model vascular perforator anatomy (275) and guide correction of pectus excavatum (390), mandibular deformities (182, 194, 391), facial deformities (181, 282, 303, 392), nasal defects (278), and skull deformities (393).

Although 3D printing itself has been widely described and increasingly used, a reproducible method for producing a 3D-printed “reverse model” has not yet been

described. In this report, we present a case in which a reproducible method for producing a 3D-printed “reverse model” representing a skin wound defect was used for flap design and harvesting.

Case Report

An 82-year-old man has undergone elective ankle replacement surgery, which was complicated by wound infection, dehiscence, and an exposed ankle prosthesis (Figure 12.2.2.1.1). Serial soft tissue debridements were per- formed by an orthopedic surgeon, and the patient was ultimately referred for soft tissue coverage and dead- space filling, with attempted salvage of the prosthesis. Reconstruction was planned with a composite radial forearm free flap, comprising a fasciocutaneous flap. Preoperative imaging was performed as routine, with multi-slice CTA of both the flap donor site and the recipient site. All imaging was performed with institutional ethics committee approval.

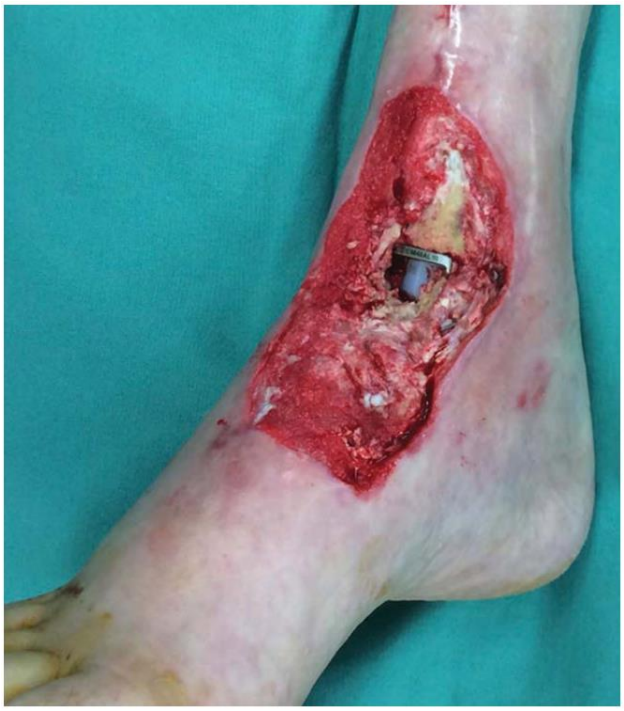

Figure 12.2.2.1.1. Soft tissue defect overlay the right ankle, with ankle prosthesis exposed.

Scan acquisition comprised arterial phase scanning, which eliminated venous contamination, avoided confusion between different structures, and maximized arterial filling. We used a protocol that triggered the scan from the origin of the pedicle, and scanned in the direction of blood flow through the perforating vessels of the flap.

Initial 2D software reconstruction used raw scan data recorded thin axial slices (0.7-mm-thick slices). Visual appreciation of the vascular anatomy was best achieved with the use

of software-generated 3D reconstructions. The freeware program “Osirix,” a third-party software program (Osirix, Version 4.1, Pixmeo, Geneva, Switzer- land) was used.

First, the recipient site was 3D-reconstructed via volume rendering using the Osirix 3D preset of soft tissue CT (i.e., soft tissue 1 skin) available within the provided software, and this was used to apply the skin layer on top of the 3D image. Crop function and scissor mouse functions were used judiciously to narrow down to defect (Figure 12.2.2.1.2). The 2D images were 3D reconstructed using the surface rendering function. The 3D reconstructed image was exported in standard tessellation language (STL) format. To evaluate the volume and shape of the defect, we created a 3D surface-rendered image of the normal left ankle in STL format for use as “control.” The above steps for producing the right ankle 3D image were repeated using the Osirix software for surface rendering, or can be achieved using 3D printer software (Cubify, 3D systems, Rock Hill, SC).

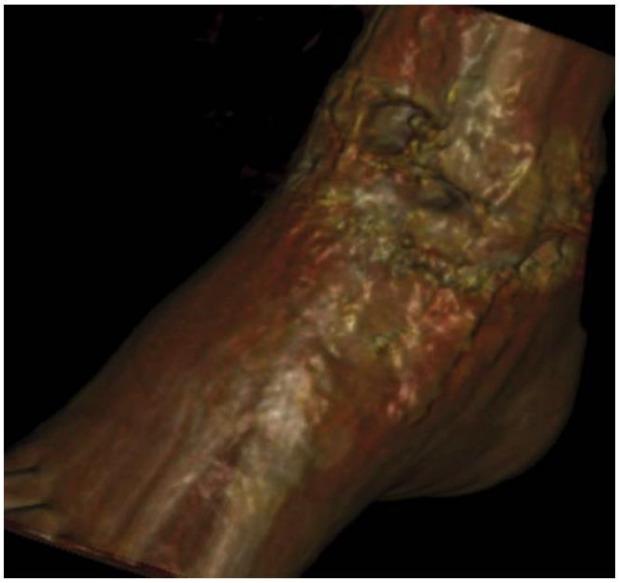

Figure 12.2.2.1.2. 3D reconstructed volume-rendered computed tomography (CT) image of the recipient site demonstrated the soft tissue defect, performed with Osirix software (Pixmeo, Geneva, Switzerland).

Volumetric and defect analysis were undertaken using Magics software (Materialise, Leuven, Belgium). STL files of both the right and left ankle were loaded on to the soft-ware and placed adjacent to each other in anatomical position (Figure 12.2.2.1.3A). Care was taken to align both objects on all X-, Y-, and Z-axis, using “interactive translate” function. In this illustrative case, a mirror image of the left ankle was produced by reflecting

it on the Y–Z plane, so that it aligned with the right ankle pointing in the same direction (Figure 12.2.2.1.3B). Using the “interactive translate” function, the mirrored left ankle was superimposed on to the right ankle so that the defect was “covered” (Figure 12.2.2.1.3C). This was achieved by superimposing the significant anatomical landmarks (such as the heel and the malleoli) common to both ankles first. Correct superimposition was confirmed by rotating the image 360 and viewing it in all angles. Then, the image of the right ankle and the intersected area was “subtracted” from the mirrored left ankle using “Boolean” function (Figure 12.2.2.1.3D-F).

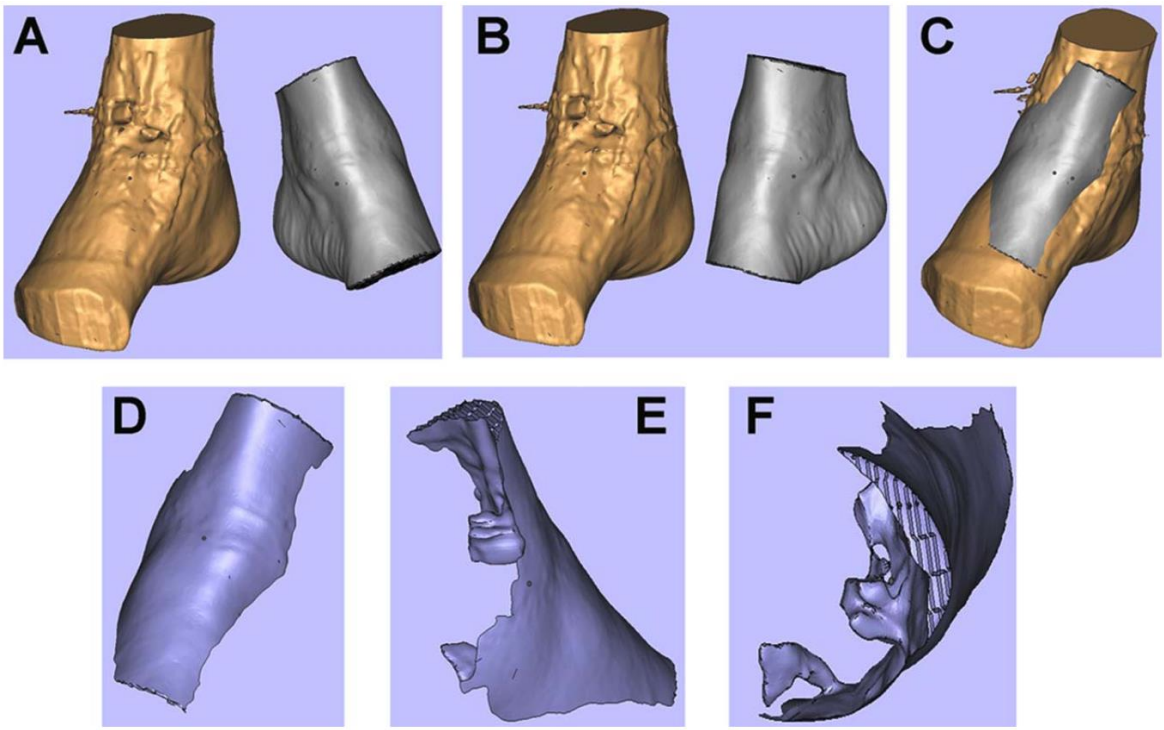

Figure 12.2.2.1.3. (A) Cropped 3D images of the right and left ankle were loaded into Magics software (Materialise) and placed side-by-side in anatomical position. (B) Left ankle was reflected on Y–Z plane so that it was aligned and pointed in the same direction as the right ankle. (C) Mirror image of the left ankle was superimposed on the right ankle. (D–F) Right ankle and the intersected parts were “subtracted” from the mirrored image of left ankle using Boolean function available in the Magics software.

The “reverse image” representing the skin defect was saved in STL format, essential since the 3D printer software can only recognize STL files. These images were directly loaded in to the Cubify software in lieu of the CT raw data to enable production of both anatomic

models (Figure 12.2.2.1.4) and pre-designed models based on the above defect analysis (Figure 12.2.2.1.5).

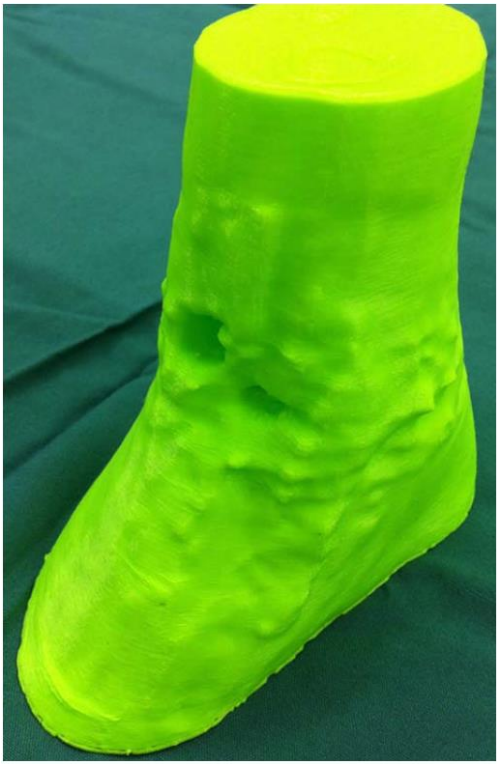

Figure 12.2.2.1.4. 3D printed model of the right ankle was created using the Cubify software and printed by the Cube 2 printer.

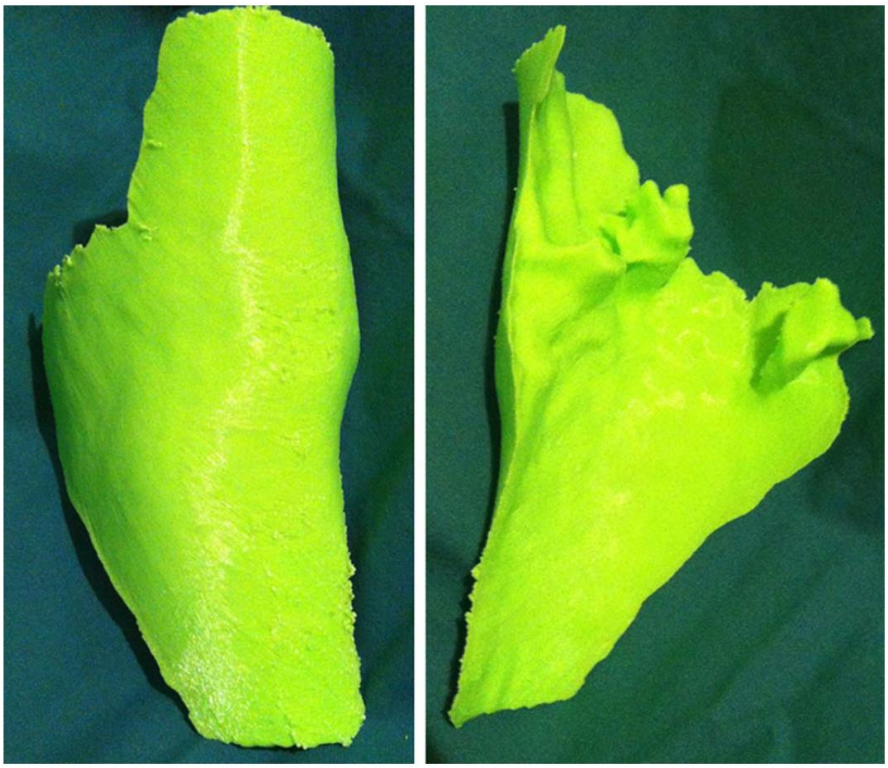

Figure 12.2.2.1.5. 3D printed model of the “reverse image” was created using the Cubify software and printed by the Cube 2 printer.

Volumetric flap planning was achieved using a 3D image of the donor site (i.e., left forearm). The same steps as described above for the production of the surface-rendered 3D image of the right ankle using Osirix were used (Figure 12.2.2.1.6). Using the Magics software, both forearm and the “reverse image” were placed adjacent to each other and aligned in the same direction (Figure 12.2.2.1.6A), and then superimposed over each other (Figure 12.2.2.1.6B-C). Using the “Boolean” function, the volume of the reverse image was “subtracted” away from the forearm (Figure 12.2.2.1.6D-E). This was used to preoperatively predict and intraoperatively guide flap harvest, to match the reconstructive needs of the recipient site.

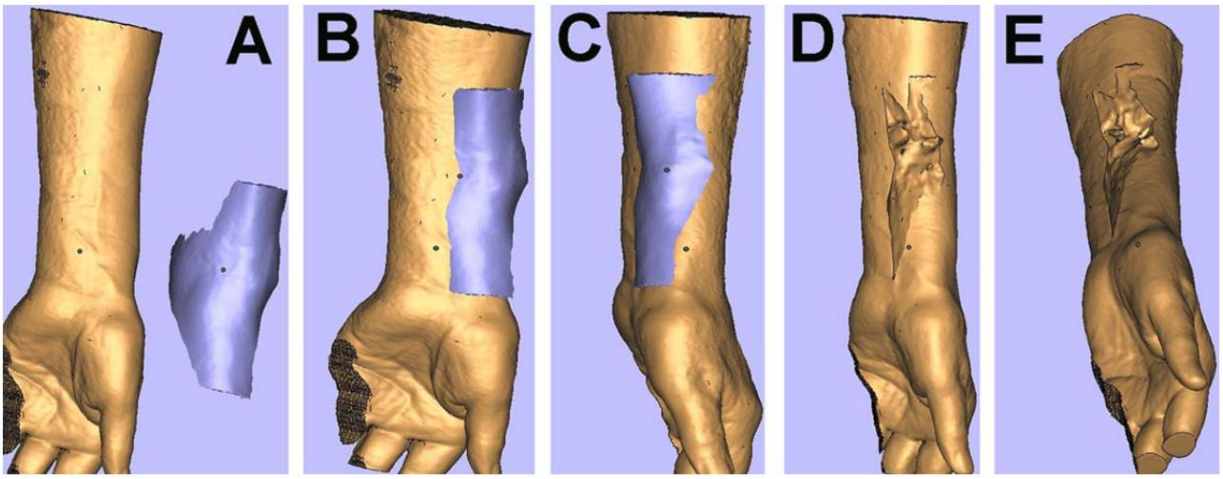

Figure 12.2.2.1.6. (A) Cropped 3D images of the forearm donor site were loaded into Magics software (Materialise), with the previously developed “defect analysis” image loaded side-by-side in anatomical positions. (B-C) The donor site and the “reverse image” were superimposed. (D-E) The “reverse image” was “subtracted” from the forearm to evaluate the reconstructive needs during harvest.

3D printing of defect and flap models, after analysis by Cubify software (3D Systems), was achieved by a single jet Cube 2 printer (3D Systems). The 3D software modeling was exported from the Cubify software and transferred to the Cube 2 printer. Printing of the right ankle required approximately 12.5 hours and the reverse image 8.5 hours.

Preoperatively, the 3D model of the right ankle was used to appreciate the size and the depth of the defect. The “reverse model” was placed immediately adjacent to the donor site to estimate the size of the flap for harvesting. The flap was thus designed to appropriately fill the soft tissue defect (Figure 12.2.2.1.7), with a small skin graft needed for extension of the pedicle (given that this was not part of the initial defect for volumetric planning). The flap and graft both healed well, with no donor or recipient-site complications.

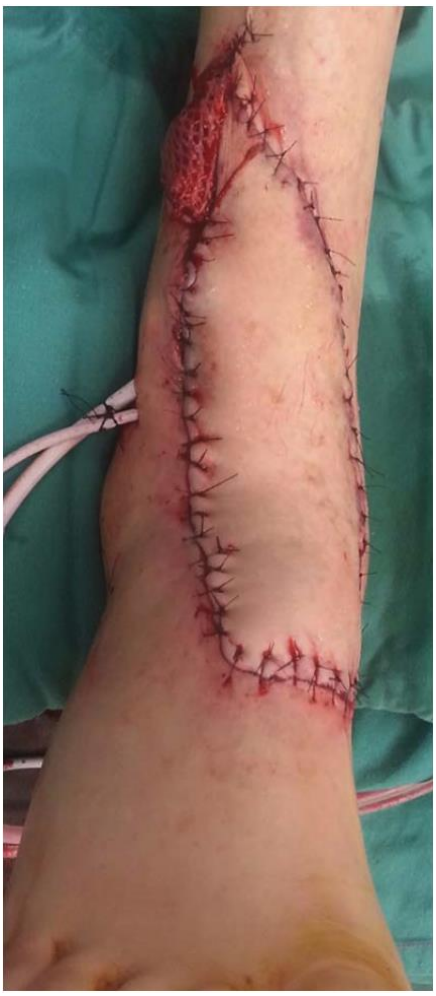

Figure 12.2.2.1.7. Defect was reconstructed with free radial forearm flap, and demonstrated appropriate filling of the soft tissue defect.

Discussion

An accurate understanding of the anatomy that has been distorted by trauma, cancer, or disease is useful in reconstructive surgery, such as a free flap repair. The current standard of practice involves imaging complex defects with CTA of both donor site and the recipient site for 3D visualization of the anatomical structures (142). Multiple software programs can effectively model the 3D data in 2D images, which our previous research has demonstrated are easy to interpret by surgeons and better demonstrate anatomical relationships of each vessel in a single image (8, 142). The raw data from CTA can be further processed to produce a 3D model by RP. The benefit of being able to physically interact with 3D models is that the models enhance the surgeon's understanding of the morphology, which may be significantly altered by the underlying pathology, and enable hands-on preoperative planning. Subsequent benefits may include decreased length of operation, wound exposure time, exposure to general anesthesia, and intraoperative blood loss (182).

Until recently, stereolithography has been considered the gold standard for medical RP. It is accurate to 0.1 mm and can produce large anatomical parts (334). However, it is relatively more labor-intensive and expensive because of the high cost of machine maintenance and the hardening materials used. Furthermore, a large model takes more than a day to manufacture, which is associated with increased production cost (180). Additionally, it may not be environmentally safe (389). In contrast, 3D printing provides an attractive alternative RP technique that can be accurate to 0.016 mm. It is faster, more convenient to use, and is associated with approximately one-third of the cost (182), and thus may be preferred for building smaller, more complex anatomical structures (275).

Constructing a 3D model of an external surface is relatively straightforward, however a "reverse image" that represents the wound defect may be helpful for the surgeons in the selection of an appropriate flap shape and size. We are one of the first in the literature to report a method of producing such "reverse image" using 3D printing. We achieved this using the non-pathological left ankle as a control to the pathological right side. After the models are superimposed on the Magics software (Materialise), they are "subtracted" from each other leaving behind a "reverse image" that depicts the skin defect. This was used to assess the flap shape and size on the donor site.

The advantage of our method lies in that it is flexible and can be applied to preoperative planning for a wide variety of free flap repair surgeries. Moreover, using appropriate printing materials, the 3D-printed models can be sterilized for intraoperative use. One limitation may be the relative cost despite being more affordable than stereolithography and the length of time required for production. We believe that as this technique becomes more widely accepted and used, the cost-benefit ratio will subsequently decrease.

Conclusion

Operative outcomes in reconstructive surgery can be improved by preoperative planning. In contrast to the current 2D imaging modalities such as CTA, 3D-printed models can provide tactile feedback that may enable the surgeon to use a hands-on approach to operative planning. We describe here a technique where the “reverse image” of a skin wound defect was created and used for flap design. Although a small skin graft was needed to cover the pedicle that was outside of the volumetrically modeled plan, the defect was otherwise appropriately reconstructed with the technique described. 3D printing, and in particular “reverse” planning also has the potential for use in other surgical disciplines. Outcome studies with such models would be a useful means to assessing their efficacy in the future.

12.2.2.2 Sacral Defect

PUBLISHED (Publication): Garcia-Tutor E, Romeo M, ***Chae MP***, Hunter-Smith DJ, Rozen WM. (2016) 3D volumetric modelling and microvascular reconstruction of irradiated lumbosacral defects after oncologic resection. Front Surg. 3:66. Doi:10.3389/fsurg.2016.00066 PMID: 28018904

Chapter Summary

Introduction: Locoregional flaps are sufficient in most sacral reconstructions. However, large sacral defects due to malignancy necessitate a different reconstructive approach, with local flaps compromised by radiation and regional flaps inadequate for broad surface areas or substantial volume obliteration. In this report, we present our experience using free muscle transfer for volumetric reconstruction, in such cases, and demonstrate three-dimensional (3D) haptic models of the sacral defect to aid preoperative planning.

Methods: Five consecutive patients with irradiated sacral defects secondary to oncologic resections were included, surface area ranging from 143-600 cm^2. Latissimus dorsi (LD)-based free flap sacral reconstruction was performed in each case, between 2005 and 2011. Where the superior gluteal artery was compromised, the subcostal artery (SA) was used as a recipient vessel. Microvascular technique, complications, and outcomes are reported. The use of volumetric analysis and 3D printing is also demonstrated, with imaging data converted to 3D images suitable for 3D printing with Osirix software (Pixmeo, Geneva, Switzerland). An office-based, desktop 3D printer was used to print 3D models of sacral defects, used to demonstrate surface area and contour and produce a volumetric print of the dead space needed for flap obliteration.

Results: The clinical series of LD free flap reconstructions is presented, with successful transfer in all cases, and adequate soft-tissue cover and volume obliteration achieved. The original use of the SA as a recipient vessel was successfully achieved. All wounds healed uneventfully. 3D printing is also demonstrated as a useful tool for 3D evaluation of volume and dead space.

Conclusion: Free flaps offer unique benefits in sacral reconstruction where local tissue is compromised by irradiation and tumor recurrence, and dead space requires accurate

volumetric reconstruction. We describe for the first time the use of the SA as a recipient in free flap sacral reconstruction. 3D printing of haptic bio-models is a rapidly evolving field with a substantial role in preoperative planning.

Introduction

A vast majority of sacral wounds derived from pressure sores can be treated with either a local or regional flap, as conventionally taught (394). However, where wounds span a large area from oncological resection, have substantial volume deficits or involve areas compromised by radiotherapy, locoregional flaps are relatively contraindicated. Radiation induces hypocellularity and hypovascularity in the normal tissue surrounding the tumor compromising its vascularity and, hence, its viability as a flap option (395, 396). Furthermore, reconstruction of the irradiated lumbosacral defects is curtailed by the reduced number and caliber of the vessels at the recipient site. Moreover, the need to restore a composite defect and the proximity of the anal region potentially increases the infection risk and present significant challenges for reconstructive surgeons.

In recent times, reconstructive surgeons have benefited from the availability of three-dimensional (3D) haptic bio-models for preoperative planning and flap designing (35). These models are produced by rapid prototyping (RP) techniques that use scan data from the conventional imaging modalities, such as the computed tomography (CT) and the magnetic resonance imaging (MRI). RP has been utilized in industrial design for decades; however, it has been adopted for medical application only in the last two decades. RP has introduced a convenient method of fabricating physical 3D models that accurately represent the anatomical structures and provide a tactile, or haptic, feedback to the clinician facilitating a superior understanding of the spatial relationship between structures (15). In medicine, stereolithography and 3D printing are the most extensively studied RP techniques. In contrast to stereolithography, 3D printing is a newer technology that is more affordable, quicker, and more convenient (182). 3D-printed haptic models have demonstrated utility in numerous surgical disciplines, such as maxillofacial (182) and orthopedic surgery (397). In plastic and reconstructive surgery, they have been useful in flap designing for soft tissue defects (273) and preoperative volumetric assessment of breast asymmetry (35).

The current paper reports our experience using a large voluminous free flap for a single-stage reconstruction of irradiated lumbosacral oncologic defects. The technique and surgical outcomes are assessed. The use of 3D haptic models of the sacral defect to aid preoperative planning and volumetric analysis is presented.

Patients and Methods

A case series of five consecutive patients were included, each of which were planned for microvascular reconstruction of an irradiated sacral defect, between 2005 and 2011. The series comprised one female and four males, with a mean age of 41.5 (range: 32-69). Each patient presented with a malignancy in the sacral region that was reconstructed by the senior author (EGT) following an oncologic resection and irradiation. The resection was either of a primary or a recurrent tumor and all patients received radiotherapy (Table 12.2.2.2.1). For each case, consideration of a muscle only, myocutaneous or fasciocutaneous flap was considered, with selection based on donor-site availability, volume filling and contour requirements. The specific flap selected in each case is described below.

Case	Age	Sex	Pathology	P/R	Recipient Vessels	I/D	Flap Surface Dimensions and Area	Colostomy	Complications	Follow-up (years)	Survival Outcomes
1	69	M	SCC	R	SGA	I	25 x 10 cm = 250 cm^2	Y	Nil	3	Long-term
2	38	M	SCC	P	SA	I	18 x 20 cm = 360 cm^2	Y	Nil	3	Long-term
3	35	F	RIS	R	SGA	I	11 x 13 cm = 143 cm^2	N	Nil	9	Mortality
4	32	M	ES	R	SGA	I	20 x 10 cm = 200 cm^2	N	Nil	7	Long-term
5	54	M	SCC	P	SA	D	20 x 30 cm = 600 cm^2	Y	Wound dehiscence requiring local flap	5	Mortality

Table 12.2.2.2.1. Patient demographics and operative details.

Abbreviations: M: male; F: female; SCC: squamous cell carcinoma; RIS: radiation-induced sarcoma; ES: Ewing's sarcoma; P: primary; R: recurrence; SGA: superior gluteal artery; SA: subcostal artery; I: immediate; D: delayed' Y: yes; N: no.

Surgical Technique

In delayed reconstructions, the volume and soft-tissue deficit was mapped preoperatively, while in immediate cases, this was able to be estimated based on resection planning. The 2D images from CT and MRI were used for initial evaluation of the planned reconstruction. Preoperative planning also involved the oncologic surgeon in surgical and reconstructive planning, in planning for estimated resection volumes. Flap choice was thus achieved, and where a skin paddle was sought, surface area able to be rapidly and accurately achieved.

The average wound surface was 359 cm^2 (range: 200–600 cm^2). In two cases, the skin surface defect was small enough for the skin island of the flap to adequately fill the surface defect. In two cases, the surface defects were larger and skin grafting was necessary. In one patient, the defect surface width was too broad and required closure with a tensor fascia lata flap. Regarding wound depth and volume, the LD flaps provided adequate tissue to fill and obliterate the cavity in all cases.

Consideration of a muscle only, myocutaneous or fasciocutaneous flap was considered, with selection based on donor-site availability, volume filling, and contour requirements as evaluated from imaging and bio-models. Ultimately, muscle only or myocutaneous latissimus dorsi (LD) flaps were selected in each case. In all cases, there was a volume requirement that exceeded the filling achievable with a fasciocutaneous flap, and the added benefits the longest pedicle possible was considered. Originally, deep inferior epigastric artery perforator flaps were also considered but were not used ultimately utilized as options.

Whenever they were available (three cases), superior gluteal artery (SGA) was the first-choice recipient vessel. In other cases where the gluteal arteries were damaged during the tumor resection or discarded due to their proximity to the tumor (two cases), subcostal artery (SA) of the eleventh rib was selected. All flap arteries and veins were anastomosed to recipient vessels in an end-to-end fashion. The location of a diverting stoma was planned based on imaging preoperatively and undertaken for wound care and patient positioning considerations.

Creation of a 3D-Printed Haptic Bio-Model

Imaging with either CT and/or MRI of the sacral region was used for volumetric analysis (Figure 12.2.2.2.1).

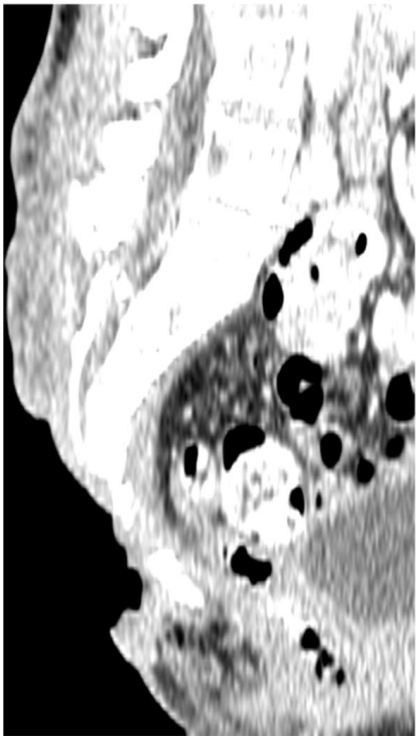

Figure 12.2.2.2.1. Preoperative computed tomography scan, showing the three-dimensional nature of a sacral defect.

Haptic models of sacral defects were fabricated using a 3D printer similar to a technique described previously (35). The 2D scan data from CT or MRI was uploaded on to a computer using a free, third-party software called Osirix (Pixmeo, Geneva, Switzerland). The data were 3D-reconstructed using the “surface rendering” function (Figure 12.2.2.2.2) and exported into a universal 3D file format called standard tessellation language (STL).

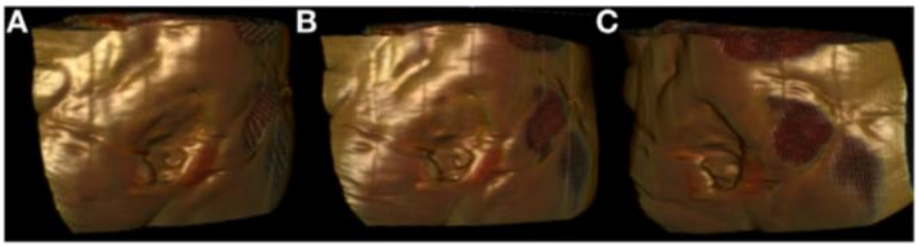

Figure 12.2.2.2.2. Surface-rendered reconstruction images derived from a preoperative computed tomography scan, showing the three-dimensional nature of a sacral defect (A-C: three dimensional rotating views).

The STL file was configured suitable for 3D printing using computer software, Cubify (3D Systems, Rock Hill, SC, USA), which accompanies the 3D printer (Cube 2 printer, 3D Systems). In Cubify (3D Systems), the model was reduced in size to fit within the maximum dimension of the printer (16 x 16 x 16 cm) and also orientated prone so that the defect was “pointing up” (Figure 12.2.2.2.3).

Figure 12.2.2.2.3. Three-dimensional (3D) printed model of the sacral defect shown in Figure X2, produced using a 3D printer (Cube 2 printer; 3D Systems, Rock Hill, SC, USA) (A-C: three dimensional rotating views).

Due to the mechanism of 3D printing where the thermoplastic filament was deposited in a layer-by-layer fashion, where the defect was “pointing sideways,” the printer deposited a support structure to fill the “gap in height” (273). Although the support structures were easily removable, they left a rough surface that compromised the aesthetics of the model. The model was comparable to scan data for volumetric analysis, and the benefits of a 3D model with haptic feedback were assessed.

Results

The LD free flap was successfully transferred in all cases (100% survival), with adequate soft-tissue cover and volume obliteration achieved. Each microvascular reconstruction with a free flap was performed in either the immediate post-resection setting or delayed if further irradiation or chemotherapy was planned. In the delayed cases, the open resected area was managed with local dressings and VAC therapy (KCI, San Antonio, TX, USA). In three cases, colostomy was necessary and presented an added advantage of preventing fecal contamination. Operative features of the patients are summarized in Table 12.2.2.2.1.

All wounds healed completely except one case, in which a minimal wound dehiscence occurred in the upper aspect of the sacrum defect, which required a lumbar artery perforator rotation flap to close. In three patients who had a colostomy, the wounds healed faster, especially in the caudal aspect of the flap near the perianal region, and required less postoperative care. There were no wound infections and obliteration of the dead space and volumetric defect in all cases.

The anastomoses to the SGA and SA were performed without any major complications that necessitated an intraoperative or a postoperative revision of the flap. Of note, the anastomoses to the SGA differed to those to the SA due to their shorter and ramified pedicle, which arose vertically between the muscle fibers. At three-year follow-up, three patients had survived. Two patients died within a year after the reconstruction secondary to tumor recurrence. All wounds had healed, with no donor-site complications and no need for secondary surgery.

Three-dimensional printing of sacral wound defects was achievable with either CT and/or MRI for all prints undertaken. The mean printing time for the scans was 12.5 hours, and approximately 40% of the printer cartridge was required for each case (Figure XA). The print was able to establish the cavity itself for haptic analysis, or able to be printed in a reverse manner, to demonstrate the volumetric defect itself.

Case Examples

Case 1

A 69-year-old man presented with a Marjolin's ulcer secondary to a 20-year history of pilonidal cyst. Originally, the lesion was resected from another institution and reconstructed with a bilateral V-Y advancement flap. The patient re-presented a year later to our institution with a local recurrence. Preoperative imaging was performed with both CT and MRI. 3D volumetric analysis was undertaken with this image, and planned resection margins were recorded, able to preoperatively map the need for a 25 cm by 10 cm surface area defect and modeling highlighting a depth ranging from 10 to 13 cm. Resection planning thus highlighted the need for sacrectomy, colectomy, and a definitive colostomy with bladder exposure within the bottom of the wound (Figure 12.2.2.2.4).

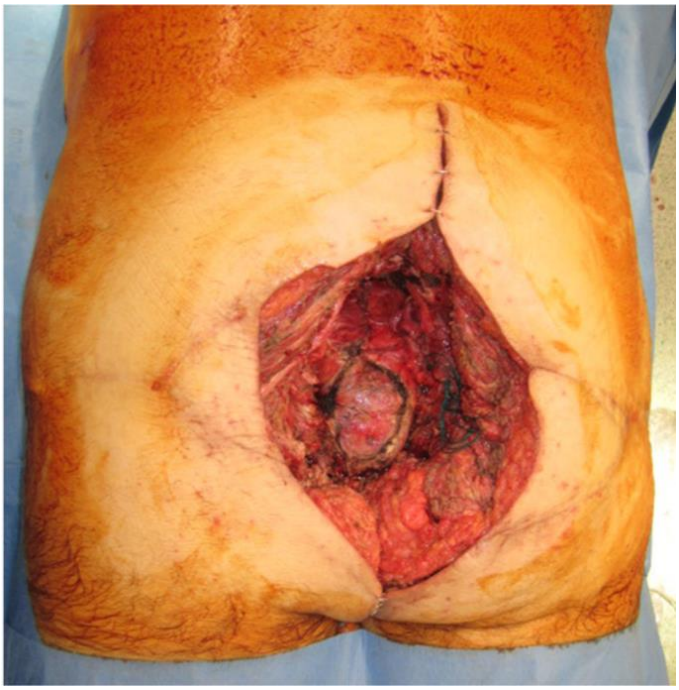

Figure 12.2.2.2.4. A 25 cm x 10 cm surface area sacral defect requiring reconstruction.

A free LD flap with a 25 x 10 cm skin paddle was chosen for reconstruction (Figure 12.2.2.2.5).

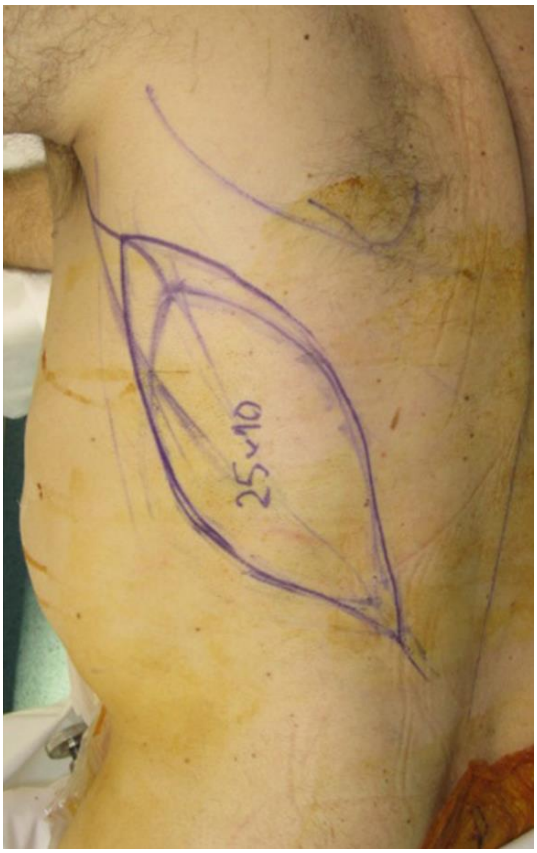

Figure 12.2.2.2.5. A free latissimus dorsi myocutaneous flap was selected for reconstruction of the defect, with donor site marked.

The flap was harvested with the entirety of the muscle and skin paddle (Figure 12.2.2.2.6), with arterial anastomosis performed to the SGA using an end-to-end technique and vein anastomosis performed using a Synovis microvascular coupler (Synovis Life Technologies, Birmingham, AL, USA).

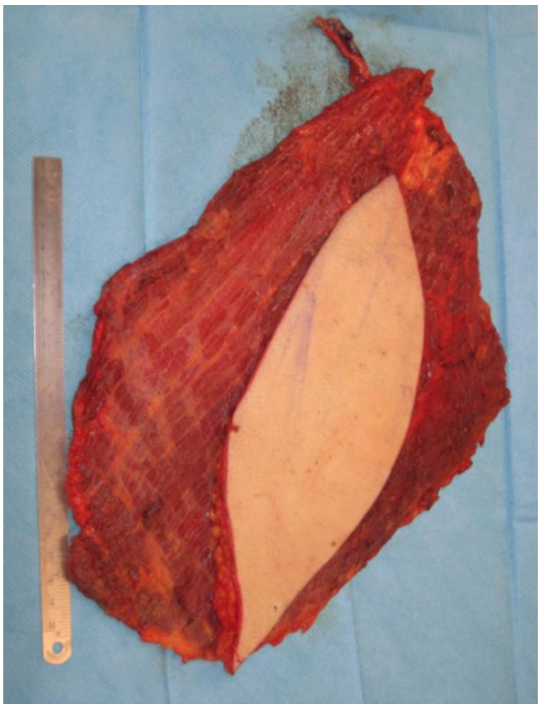

Figure 12.2.2.2.6. Free latissimus dorsi myocutaneous flap harvested, with templated skin paddle and muscle for volumetric filling.

The flap was thus able to fill the 3D volumetric dead-space and cover the defect (Figure 12.2.2.2.7).

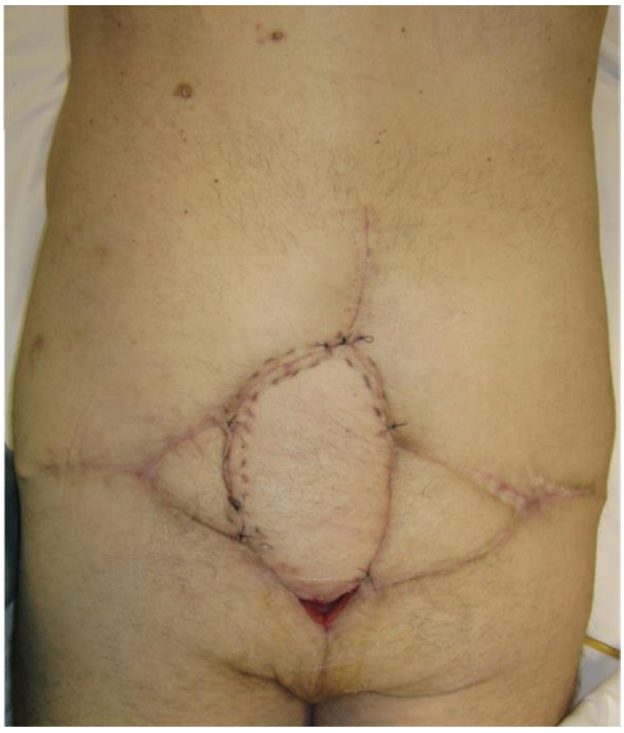

Figure 12.2.2.2.7. Flap inset into sacral defect, with adjacent remnants of previous locoregional reconstructive flaps.

There were no complications and good donor and recipient outcomes.

Case 2

A 38-year-old man presented with a Marjolin's ulcer following a long-standing pilonidal cyst for 15 years. The lesion had been previously resected, including the cortical portion of the sacrum, and irradiated. The general surgeons planned for an immediate reconstruction, with resection and colostomy planned.

Preoperative imaging was performed with both CT and MRI. 3D volumetric analysis was undertaken with this imaging, and planned resection margins were recorded, with an 18 cm by 20 cm surface area defect planned and modeling highlighting a depth ranging from 5 to 11 cm. This closely mirrored the ultimate resection, where the defect comprised an 18 cm × 20 cm surface area defect, with substantial dead space volume (Figure 12.2.2.2.8).

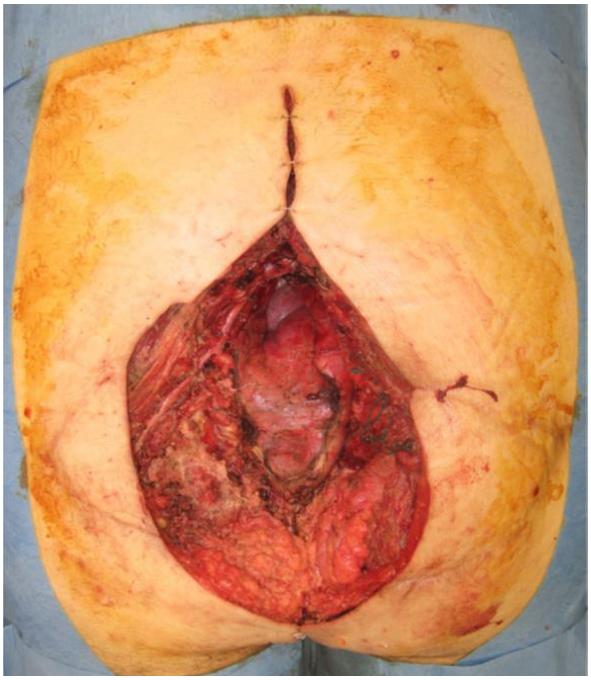

Figure 12.2.2.2.8. A 18 cm x 20 cm surface area sacral defect requiring reconstruction.

An LD muscle flap was chosen for reconstruction, and for the recipient vessel, the SA was chosen, since the SGA was too close to the resection area posing a risk of local recurrence and endangering the pedicle. The SA was exposed 15 cm cranial to the upper edge of the sacral defect, preventing the need for further operative morbidity. The vessels were anastomosed end-to-end, and despite some notable discrepancy in the caliber of donor and recipient veins, no complications eventuated. The flap suitably filled the defect (Figure 12.2.2.2.9), was skin-grafted and healed uneventfully.

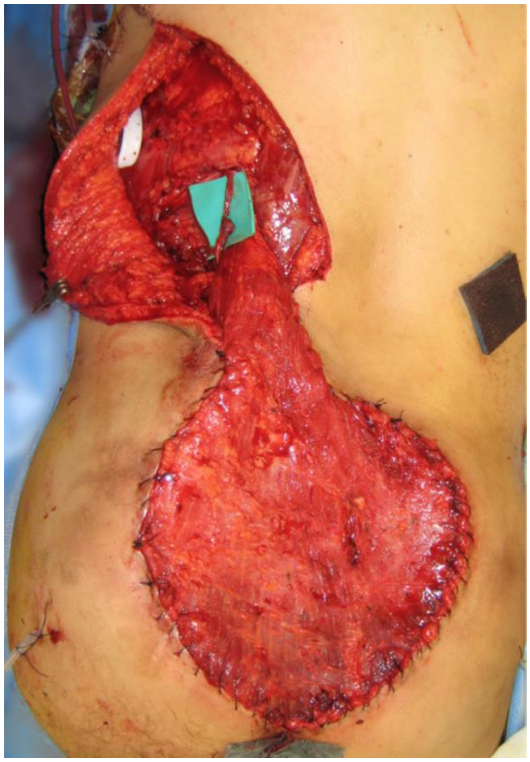

Figure 12.2.2.2.9. Free latissimus dorsi muscle only flap inset into the defect.

Discussion

According to the traditional reconstructive ladder, microsurgical free flap repairs exist at the top. Recent advancements in preoperative imaging and operative techniques demand a re-ordering of the reconstructive ladder (398, 399). With 3D templating for soft-tissue reconstruction, a decision as to where to step on the ladder is made clearer. 3D analysis and volumetric planning have been used extensively and published broadly in a range of fields: breast reconstruction, cutaneous defects, and dead space filling (182, 273, 397). The ability to interact hands-on with the haptic bio-models that accurately represent the anatomical structures has revolutionized the way reconstructive surgeons would plan preoperatively and design free flaps (35, 273). In this field of sacral reconstruction, the specific dead space and volumetric needs of a reconstructive choice makes the technology of 3D analysis and 3D printing well-suited. The optimal choice of flap, approach to harvest and technique of inset to adequately replace volume and surface tissues can be achieved successfully.

One current limitation of this technology arises from having to outsource the fabrication of the bio-models to external companies that incur significant costs and a long production time. As the 3D printers become mainstream and more affordable, clinicians are able to quickly produce anatomical models at their own desktop (17, 18, 35, 273). The model used in this study was small-size replica of a sacral defect due to the maximal dimensions afforded by a desk-top, office-based 3D printer (16 x 16 x 16 cm). Although the product was sufficiently detailed for the clinicians to appreciate the shape and depth of the defect, we expect to be able to print these lesions in life-size as the prices of larger 3D printers decrease. There are a range of office-based 3D printers available, the cheapest and the smallest of which make small models (16 x 16 x 16 cm), while there are other printers, such as MakerBot Z18 (MakerBot Industries, Brooklyn, New York, USA), that can print larger models (30 x 30 x 45 cm) exceeding the size of the defects described in this paper. We currently use both of these printers in our practice, and it is up to the individual surgeon to decide which is more preferred in terms of size, cost, and level of complexity. The smaller printer options are still useful in terms of comparative scale.

The current series comprises large defects, with substantial needs in volume and surface replacement. While locoregional flaps are the standard of care in most sacral wound defects, they are not plausible in many scenarios. Numerous local flap options have been

reported, including gluteal artery perforator flaps (400-402), gluteus maximus sliding flaps (403), paraspinal flaps (404), V-Y advancement flaps (405, 406), and regional anterolateral thigh flaps (407). However, they are relatively contraindicated in oncological sacral defects. Local flaps are compromised by the collateral damage to the normal surrounding tissues from radiotherapy and margins may not be completely clear of tumor spread. Regional flaps are disfiguring and may require more than one flap where a large defect needs to be covered, increasing donor site morbidity. As a result, where a wide, heavily irradiated tissue area needs to be covered, locoregional flaps frequently necessitate multiple procedures. In contrast, there is currently insufficient evidence regarding the use of a free-tissue transfer for reconstruction of large complex defects.

From our case series, we demonstrate that microsurgical free flaps provide an alternative that is safe and facilitates a single-stage reconstruction that, as overall, results in a reduction in operative exposure. Conventional wisdom dictates that free flaps naturally require longer operative time due to their technical complexity. However, from our experience working with two surgical teams operating simultaneously on the donor site and the recipient site, there was a minimal difference between the operative length of a local flap and a free flap. Where wound dehiscence occurred, most commonly in the transitional area between the irradiated and the non-irradiated tissues, locoregional flaps have been useful as an adjunct.

Less discussion of free flaps for sacral reconstruction exist, with interpolation flaps utilizing omentum (408), the vertical rectus abdominis myocutaneous (VRAM) flap (409-411), the LD flaps, the chimeric LD flaps combined with the serratus anterior, and the free fibula flap (412, 413). Consistent with previous authors' choice, the LD flap is reliable, easier, faster, and associated with less morbidities than many of the other options. Particularly, for volumetric filling, LD flaps provide increased volume and depth by the ability to fold on themselves. Recipient vessels are of particular importance in sacral reconstructions, with superior and inferior gluteal, deep femoral, inferior epigastric arteries all considered (412, 413), often requiring intra-abdominal access or an arteriovenous loop (413). We describe an alternate option, the SA, which has consistent anatomy, few side branches and a long pedicle (up to 10 cm) (414). The use of a free flap based on the eleventh intercostal artery was first described by Badran *et al* (415), and in 2006, Hamdi *et al* classified the intercostal perforator flaps into dorsal, lateral or anterior depending on the portion of the SA being used (416).

Conclusion

Free flaps may be a first-choice approach for sacral defects that are of substantial volume and have been irradiated. The relative lack of recipient vessels should not be a limitation, and we describe for the first time that the SA is a useful recipient in this setting. The volume of such defects can be assessed with traditional 2D imaging techniques, or with 3D-printed bio-models. Facilitated by modern preoperative planning technologies, 3D-printed haptic bio-models can map surface area and volume defects and may facilitate easier reconstruction planning.

12.2.3 Novel Techniques

12.2.3.1 3D/4D Printing

PUBLISHED (Publication): *Chae MP*, Hunter-Smith DJ, De Silva I, Tham S, Spychal RT, Rozen WM. (2015) 4D printing: a new evolution in CT-guided stereolithographic modelling. Principles and applications. J Reconstr Microsurg. 31(6):458-63. PMID: 25868154

Chapter Summary

Introduction: Over the last decade, image-guided production of three-dimensional (3D) haptic biomodels, or rapid prototyping (RP), has transformed the way surgeons conduct preoperative planning. In contrast to earlier RP techniques such as stereolithography, 3D printing has introduced fast, affordable office-based manufacturing. We introduce the concept of 3D/4D printing for the first time where 3D printing of 4D imaging is performed.

Methods: The bones of the thumb ray are 3D printed during various movements to demonstrate 3D/four-dimensional (4D) printing. Principles and validation studies are presented here.

Results: 4D computed tomography was performed using "single volume acquisition" technology to reduce the exposure to radiation. Three representative scans of each thumb movement (i.e., abduction, opposition, and key pinch) were selected and then models were fabricated using a 3D printer. For validation, the angle between the first and the second metacarpals from the 4D imaging data and the 3D/4D-printed model was recorded and compared.

Conclusions: We demonstrate how 3D/4D printing accurately depicts the transition in the position of metacarpals during thumb movement. With a fourth dimension of time, 4D printing delivers complex spatiotemporal anatomical details effortlessly and may substantially improve preoperative planning.

Introduction

Modern imaging techniques have enabled accurate preoperative planning in plastic and reconstructive surgery (139). Furthermore, reports demonstrate that this advancement can be translated to superior clinical outcomes and reduce operative length (417). In perforator flap surgery for breast reconstruction, preoperative computed tomographic angiography (CTA) reliably maps the vascular supply enabling the selection of donor site, flap, and the perforator (5, 418, 419). However, the interpretation of CTA scan data displayed on a two-dimensional (2D) computer screen and correlating it to intraoperative findings has been relatively difficult (178). To this effect, the introduction of 3D haptic biomodelling from rapid prototyping (RP) has been useful.

RP describes the process of fabricating a 3D physical model from a computer-aided design and stereolithography is the earliest RP technique adopted for medical application (18). A surgeon can interact with the haptic models in a “hands-on” fashion during preoperative planning and additionally use them for intraoperative guidance (273). Tactile feedback from the biomodels, in addition to their ability to accurately represent anatomical details, enables them to provide superior spatial information than a 3D visualisation on a computer screen (15).

Stereolithographic biomodels derived from computed tomography (CT) scans have been reported to accurately map the bony and vascular anatomy and is considered a “gold standard” in medical RP (178, 179). For example, fine arterial branches that can be missed on a 2D CT scan by a radiologist or a surgeon can be detected on a 3D-reconstructed image and then physically represented on a model (178). However, stereolithography is labour-intensive, relatively slow, and expensive (182). In contrast, the development of 3D printing has provided a more convenient, faster, and more affordable, alternative RP technology.

A 3D printer extrudes melted thermoplastic material and deposits it in a layer-by-layer fashion, creating an anatomically precise final product that can be handled immediately (18). This technology has shown both practical and clinical benefits in multiple surgical disciplines (182, 187, 397), including plastic surgery where 3D-printed haptic models have been utilised for volumetric analysis (35), flap design for soft tissue defect repair (273), surgical trainee education (17), and fabricating individualised prosthesis (278, 307, 309,

313). Interestingly, recent advancement in technology has allowed the incorporation of time, the fourth dimension, to medical imaging and haptic biomodelling.

Four-dimensional computed tomography (4D CT) is a recent imaging technology where an oversampled 3D CT scan data is 3D-reconstructed retrospectively according to the patient's respiratory motion (420). This technique reduces motion artefacts, enabling precise radiotherapy delivery to lung tumours (289, 290), breast cancers (421), and renal tumours (422). Its medical application has extended to include identifying parathyroid adenomas (423) and performing functional and morphological assessment of mechanical heart valves (424). In plastic surgery, 4D CT has been reported mostly for assessing perforator vascular dynamics (169, 170, 425).

In the current study, for the first time to our best knowledge, we describe 3D/4D printing, where time is represented by multiple haptic models depicting the movement of metacarpals during thumb movements. This revolutionary technique has the potential to alter the way surgeons assesses pathology.

Methods

In order to illustrate 4D printing, we performed 4D CT on the hand of a young female patient during thumb abduction, opposition, and key pinch. Haptic models of the bones were fabricated using a 3D printer and compared to their subsequent 4D CT images for accuracy. Institutional ethics approval was obtained and the patient gave verbal and written informed consent.

Results

Scan Acquisition

4D CT scanning was performed using a "single volume acquisition" technique previously described for perforator imaging (425). Briefly, we used a 320 multidetector row CT scanner (Aquilion One; Toshiba America Medical Systems, Tustin, California, USA). An axial scanning technique was used with slice collimation of 0.5 mm. 16 cm craniocaudal coverage meant that no concurrent table movement was required. Exposure parameters were 100-135 kVp and effective tube current of 400-580 mA depending on the patient's body mass index. The patient was instructed to perform three thumb movements and each movement was individually scanned.

3D Printing

3D printing was performed using a technique that we recently reported (35, 273). In short, the digital imaging and communications in medicine (DICOM) files of 4D CT were uploaded using Osirix software (Pixmeo, Geneva, Switzerland). Three scans that most accurately represented the transition in the metacarpals were selected for 3D printing. "Scissor" function was used to remove anatomical parts that obstructed view. Surface-rendered 3D visualisation images were created (Figure 12.2.4.1.1A), as well as volume-rendered images (Figure 12.2.4.1.1B), with both able to be manipulated with software during analysis. They were exported as standard tessellation language (STL) files and uploaded on to Cubify software (3D Systems, Rock Hill, SC, USA) for 3D printing on a Cube 2 printer (3D Systems, Rock Hill, SC, USA) (Figure 12.2.4.1.1C).

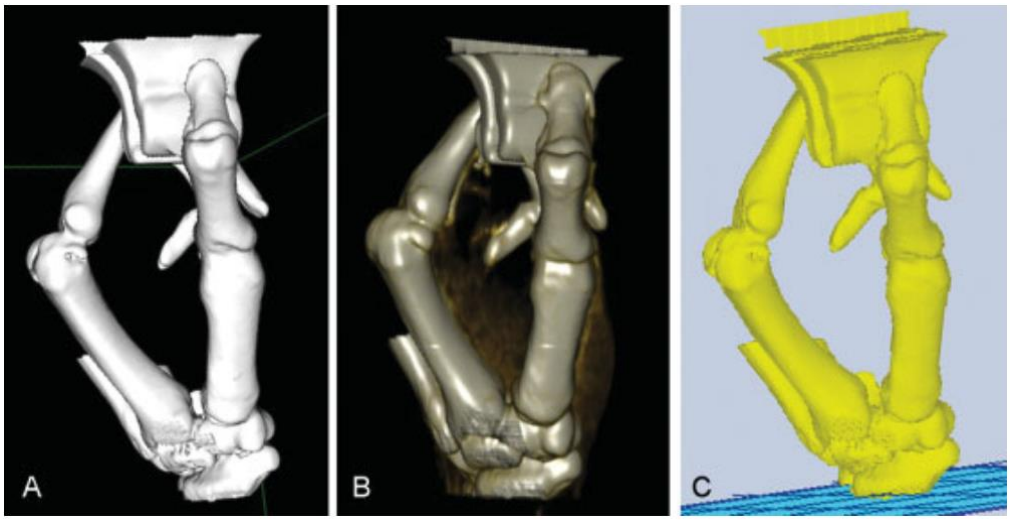

Figure 12.2.3.1.1. CT data of the hand during key pinch is 3D reconstructed using (A) surface rendering and (B) volume rendering function in Osirix (Pixmeo, Geneva, Switzerland). (C) The 3D image is exported on to Cubify (3D Systems, Rock Hill, SC) to be rendered suitable for 3D printing.

Support structures obscuring the view were removed manually using a surgical needle holder (Figure 12.2.4.1.2-3). Printing times for each thumb movement are summarised in Table 1. Of note, fabrication of a model in abduction and opposition were substantially shorter than key pinch (2 hours 7 minutes vs 6 hours 12 minutes). This is most likely due to the paper clip used to demonstrate key pinch being 3D-printed with the bones and its associated support structure materials.

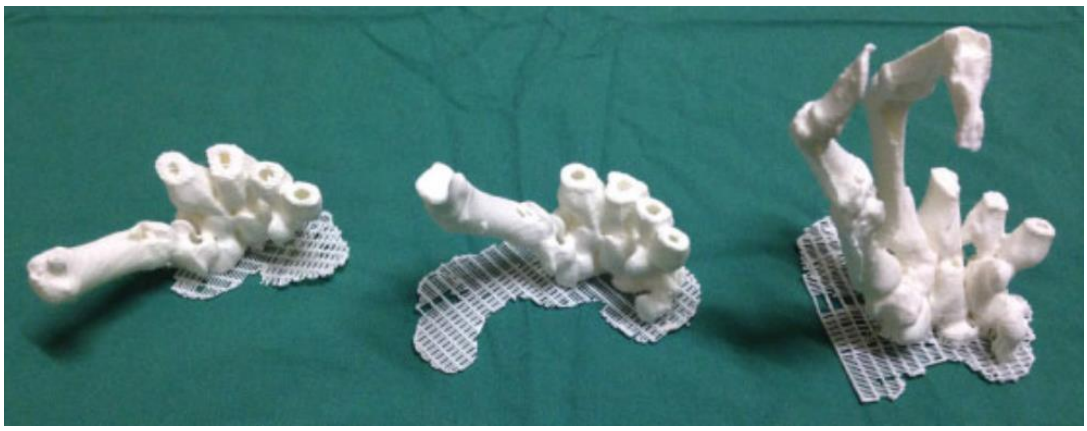

Figure 12.2.3.1.2. 3D-printed haptic models representing carpal and metacarpal bones during various hand movements: abduction (left), opposition (center), and key pinch (right).

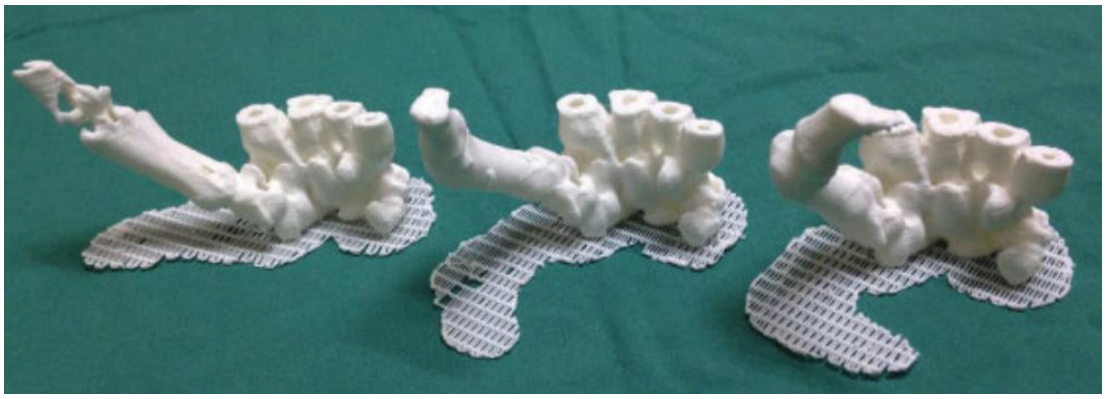

Figure 12.2.3.1.3. 4D-printing demonstrating the transition of carpal and metacarpal bones during opposition (from left to right).

Validation of 3D/4D Printing

The accuracy of 3D/4D printing technique was evaluated by calculating the change in the angle of the carpometacarpal joint. We used a method previously reported for measuring thumb opposition (426, 427). In short, the authors described two angles: “abduction” angle formed by the angle between the first and second metacarpals in the palmar plane, and “flexion” angle formed by the plane bounded by the palmar plane and the first metacarpal. The angles were either measured directly from the 4D CT data using the “angle” function in the Osirix software (Pixmeo, Geneva, Switzerland) or manually using a goniometer placed on the haptic models. For standardisation, the middle of the trapezium was used as a fulcrum and arms of the angle were extended up to the middle of the most distal aspect of the first or second metacarpal. In the 4D CT, the coronal view was used to identify the “abduction” angle and similarly, the sagittal view for the “flexion” angle. Where the first metacarpal “crosses” the second metacarpal during thumb opposition, the angle was indicated with a negative value.

In general, the goniometer tended to overestimate the “angles” (Figure 12.2.4.1.4). During thumb abduction, the “abduction” angle remained relatively static while the “flexion” angle gradually increased. This is explained by the fact that thumb abducts superiorly from the palmar plane and does not deviate in radial or ulnar direction. Similarly, during opposition, the thumb transitions superiorly as evidenced by increasing “flexion” angle, but additionally the “abduction” signal decreases as the thumb reaches across the palm. During key pinch, the thumb remains stationary in “flexion” angle, but the “abduction” angle decreases as the

first metacarpal presses the paper clip towards the second metacarpal and subsequently, increases.

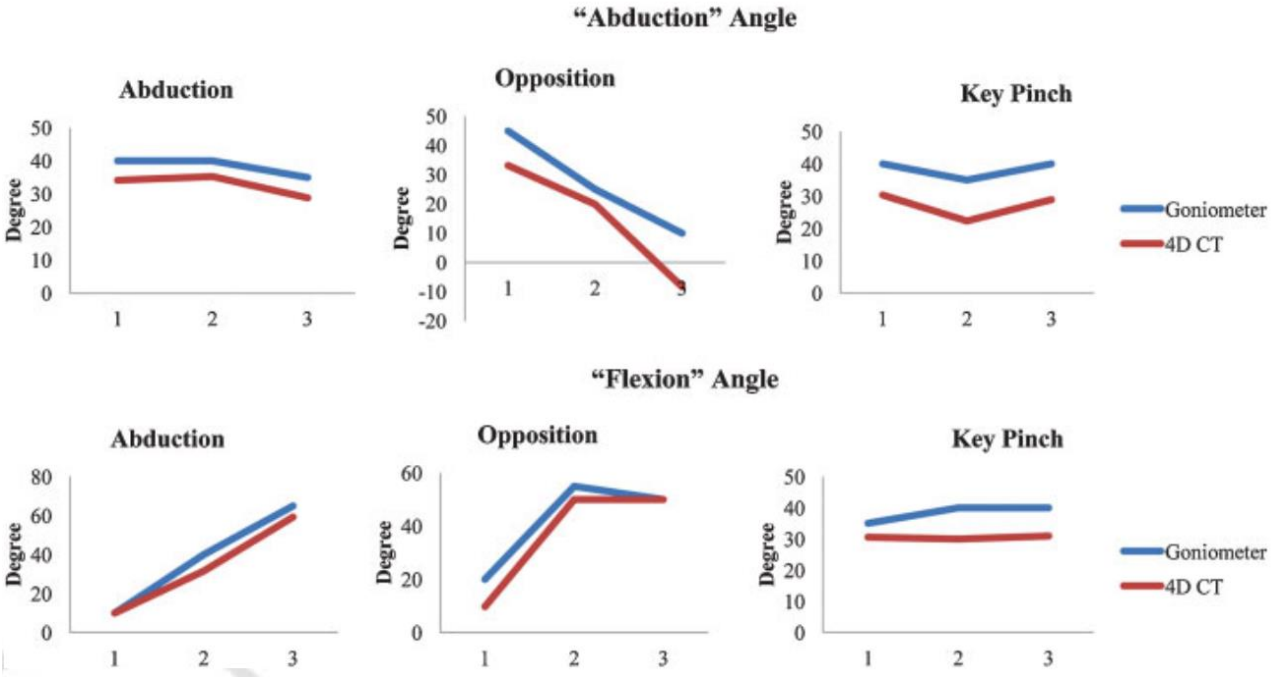

Figure 12.2.3.1.4. Summary of graphs demonstrating the "abduction" angle (first row) and the "flexion" angle (second row) measured using a goniometer or directly from the 4D CT data. X-axis indicates the stages of each thumb movement

Additionally, we investigated the relationship between the base of the first metacarpal and the trapezium further in thumb opposition. (Table 12.2.4.1.1 and 12.2.4.1.2) Firstly, the distal articular surface of the trapezium and the part of it articulating with the base of the first metacarpal were measured using a flexible ruler. We found that as the thumb opposes, the portion of the surface of trapezium articulating with the first metacarpal increased in ulnar direction (i.e. 53.85% to 84.62%). Furthermore, rotation of the first metacarpal on trapezium was detected using the angulation between the dorsal articular surface of the base of first metacarpal and the ridge of trapezium between the first and second metacarpals. Decrease in the angle (i.e. 50^{o} to 5^{o}) confirmed the rotation of the first metacarpal in ulnar-palmar direction during thumb opposition. Moreover, we calculated the distance between the tubercle of trapezium and pisiform in order to quantify the movement of trapezium. Pisiform was selected since previous reports showed that trapezium moves as a single entity with trapezoid, capitate, and hamate (428, 429). Although it was more obvious to the naked eye, there was only a small reduction in the

distance measured (28 to 27 mm). This may be due to using a ruler that is accurate to only 1 mm, and hence, any difference less than 1 mm may have been approximated up or down to the nearest millimetre.

Thumb Movement	**Figure**	**Stage**	**Print Duration**
Abduction	(Fig. 2 left)	1	2 hours 6 minutes
		2	1 hour 59 minutes
		3	2 hours 7 minutes
Opposition	(Fig. 2 centre; Fig. 3)	1	2 hours 9 minutes
		2	2 hours13 minutes
		3	2 hours 9 minutes
Key Pinch	(Fig. 2 right)	1	7 hours 24 minutes
		2	5 hours 29 minutes
		3	5 hours 43 minutes

Table 12.2.3.1.1. Print duration of each stage of 4D-printed thumb movements.

Thumb Movement	**Stage**	**4D CT**		**Goniometer**	
		"Abduction" Angle (^{o})	**"Flexion" Angle (^{o})**	**"Abduction" Angle (^{o})**	**"Flexion" Angle (^{o})**
Abduction	1	34.15	10.00	40	10
	2	35.29	31.56	40	40
	3	28.84	59.25	35	65
Opposition	1	33.18	9.82	45	20
	2	19.90	50.00	25	55
	3	-8.28	50.07	10	50
Key Pinch	1	30.31	30.60	40	35
	2	22.33	30.00	45	40
	3	28.88	30.95	40	40

Table 12.2.3.1.2. Summary of angles calculated between the first and the second metacarpal bones during various thumb movement.

Discussion

We report for the first time 3D/4D printing technique and it has the potential to revolutionise the way surgeons assess pathology for diagnostic and treatment planning purposes.

In most surgical disciplines, especially plastic and reconstructive surgery, 2D imaging, such as plain radiograph and CT, have become an integral component of preoperative work-up (5, 139). In perforator flap surgery, CTA has been a gold standard imaging modality in evaluation of the donor site and the recipient site for the selection of appropriate donor site, perforator and the flap (6, 73). It produces accurate anatomical details that has translated to enhanced clinical outcome, such as the reduced donor site morbidity, shortened operative length, and decreased other operative complications (7). However, the spatiotemporal information from 2D imaging is difficult to appreciate intuitively and comparing it to clinical findings intraoperatively has also been challenging (418). 3D haptic models eliminate these difficulties by providing spatial anatomical information in a tactile manner that is more instinctive.

RP has been utilised in industrial design for decades before it was adopted for medical application in the last decade. 3D prototypes built from 3D imaging, such as CT or magnetic resonance imaging (MRI), have enabled surgeons from various disciplines to preoperatively plan, simulate procedures, and predict outcome (182, 195, 430, 431). In plastic and reconstructive surgery, they have been useful for the mapping of soft tissue defects, breasts, and vasculature (18, 35, 273). In addition, they can be sterilised for intraoperative use (187, 303). Furthermore, the biomodels has facilitated the education of surgical trainees, potential improvement in clinician-patient communication, and manufacturing of customised prosthesis (218, 307, 432).

Stereolithography is the earliest RP technique used for medical application and is considered the current “gold standard”. Despite its ability to manufacture accurate templates in a large size, stereolithography requires considerable manual handling during production, is relatively slow, and remains relatively more expensive. In contrast, more novel 3D printing technology can similarly fashion anatomically accurate haptic prototypes in a faster and relatively more affordable manner (18, 35, 182). Moreover, as it is currently

garnering significant interest from the general public and the researchers, 3D printing has the potential to become far more capable, widespread, and less costly.

Recently, 4D CT technique has been introduced to improve the image quality of CT compromised by motion artefacts from organs, mainly lungs. 4D CT is performed by oversampling images at each position of interest and associating each image to its respective breathing signal during a respiratory cycle. The data is retrospectively analysed and yields a time-lapse geometrical dataset. In respiratory medicine, 4D CT has been investigated extensively to optimise targeted radiotherapy to lung tumours (289, 290). In plastic and reconstructive surgery, the technology has been primarily utilised for assessing the vascular territory and flow dynamics of perforators (170, 433). Initial concerns regarding high radiation exposure from 4D CT has been stymied by modifying scanning protocols. Rozen *et al* (141) has reported a "single volume acquisition" scanning method that significantly reduces the radiation dose to 1.78 mSv equivalent to 3 plain abdominal radiographs. However, relative contraindications to 4D CT still exist stemming from patient's poor renal function or allergies to iodinated contrast agents. Hence, some authors recommend a judicious use of the technology in certain age groups (434). In describing perforator vasculature, laser-assisted indocyanine green imaging is an alternative method. However, it is restricted to utility only intraoperatively (128).

We describe 3D/4D printing where the length, width, and height constitute the three dimensions and the time represented by the change in the position of the bones complete the fourth dimension. To this effect, we have 3D-printed 4D CT scans producing haptic biomodels that demonstrate the transition of metacarpal bones during thumb movements. Although our small sample size prohibits significant statistical derivation, the data demonstrate a strong correlation of the anatomical spatiotemporal information between the 3D/4D-printed biomodels and the 4D CT data.

4D printing has been previously coined in architectural design by Skylar Tibbits, a research scientist from The Self-Assembly Laboratory of Massachusetts Institute of Technology (MIT) (435, 436), he describes a 3D-printed object composed of multiple materials with differing chemical properties. Upon contact with water, certain component materials become "activated" and are able to contract, expand, fold, and adapt to their environment. Tibbits define the fourth dimension as the embedded capability of transformation from one shape to another (436). Although this model of "self-assembly" may eventually be adopted

for medical engineering and application, our proposition of using time as the fourth dimension is conceptually more intuitive and has a more direct implication for utility in surgical planning and altering clinical outcomes.

Conclusion

From stereolithographic biomodels to 3D-printed haptic models and now 3D/4D printing, image-guided biomodelling has evolved dramatically. In the near future, aided by increasing availability of the 4D CT scanners, 3D/4D printing has the potential to become widely accessible to provide superior spatiotemporal anatomical information for surgeons to improve clinical outcomes.

12.2.4.3 Augmented Reality Using 3D Technology

PUBLISHED (Publication): ***Chae MP***, Ganhewa D, Hunter-Smith DJ, Rozen WM. (2018) Direct augmented reality computed tomographic angiography technique (ARC): an innovation in preoperative imaging. Eur J Plast Surg. 41(4):415-20.

Chapter Summary

Introduction: Since the advent of free tissue transfer approximately 40 years ago, constant improvement particularly in the preoperative planning phase has led to flap success rate reaching 99% and improved patient outcomes. The use of imaging, such as computed tomographic angiography (CTA) or magnetic resonance angiography (MRA), for preoperative planning is now routine. However, current image modalities are restricted by being represented in two-dimension (2D) and have led to clinicians seeking novel methods of utilizing the scan data, such as augmented (AR) or virtual reality (VR) and holograms. These mixed reality devices facilitate natural mode of visual perception and have the capacity to introduce tactile feedback. However, most AR devices are currently expensive, bulky, complicated and require tedious image registration processes. We illustrate our projector-based direct AR technique using CTA, or ARC, for preoperative planning.

Methods: Our bespoke ARC method consists of compact, affordable hardware (MacBook, Philips pocket projector and a 15-cm ruler) and free, open-source software (OsiriX). We have utilized this technique in six cases of perforator flaps of the thigh and abdomen (anterolateral thigh (ALT), transverse gracilis (TUG) and deep inferior epigastric artery perforator (DIEP) free flaps).

Results: In all cases, 3D-reconstructed images of perforators from CTA were accurately projected on to the donor site. System calibration is rapid and convenient to use.

Conclusion: We describe a novel technique of projector-based AR CTA (or ARC) for preoperative planning in perforator flaps. The technique is affordable and readily reproducible.

Introduction:

Since the advent of free tissue transfer approximately 40 years ago (437), constant improvement particularly in the preoperative planning phase has led to improved patient outcomes (5). The use of relatively simple techniques, such as handheld Doppler ultrasound, to advanced imaging techniques, such as computed tomographic angiography (CTA) and magnetic resonance angiography (MRA), for purposes of preoperative planning is now routine. Pre-operative planning for perforator based free flaps, in particular, is important due to the high degree of anatomical variations. Therefore, patients with favourable, and more importantly unfavourable, anatomy can be identified, and the optimal perforator of choice can be utilised (72, 438).

However, current image modalities are restricted by being represented in two-dimensional (2D) platforms. As choices of preoperative imaging modalities consolidate, clinicians have sought novel methods of utilizing scan data from CTA or MRA to improve preoperative planning and surgical efficiency, such as augmented (AR) or virtual reality (VR) and holograms. These mixed reality devices facilitate natural mode of visual perception and have capacity to introduce tactile feedback that enhances situational awareness. However, most AR devices are currently expensive, bulky, have slow update rate and require tedious image registration process and complicated software suites (439, 440).

In the current case series, we illustrate our projector-based direct AR technique using CTA, or ARC, for preoperative planning perforator flaps, highlight a technique that is affordable, compact and readily reproducible.

Methods

In the current case series, we have utilized CTA-guided projector-based AR (or ARC) technique for preoperative planning of six cases – three anterolateral thigh (ALT), one transverse upper gracilis (TUG) and two deep inferior epigastric artery perforator (DIEP) free flaps – that is affordable and readily reproducible for future routine clinical application.

Scan Acquisition

CTA was performed using standardized “single-volume” acquisition technique that ensures maximal image quality and minimal radiation exposure, previously described by Rozen *et al* (141). A Siemens SOMATOM Sensation 64 multidetector row computed tomography scanner (Siemens Medical Solutions, Erlangen, Germany) was used, and the image was reconstructed in standard 0.75-mm thickness.

Technique

ARC set-up

In contrast to previously described papers utilising AR that required a large set of bulky equipment (439, 441, 442) and complicated software suites (440, 443, 444), our ARC set-up involves a compact, affordable array of compact hardware and free, open-source software (Figure 12.2.4.3.1): MacBook Pro (AUD 2,500; Apple Inc, Cupertino, CA, USA), Philips PicoPix pocket projector (AUD 450; Philips, Amsterdam, Netherlands), a 15-cm ruler (AUD 2) and OsiriX software (free; Pixmeo, Geneva, Switzerland).

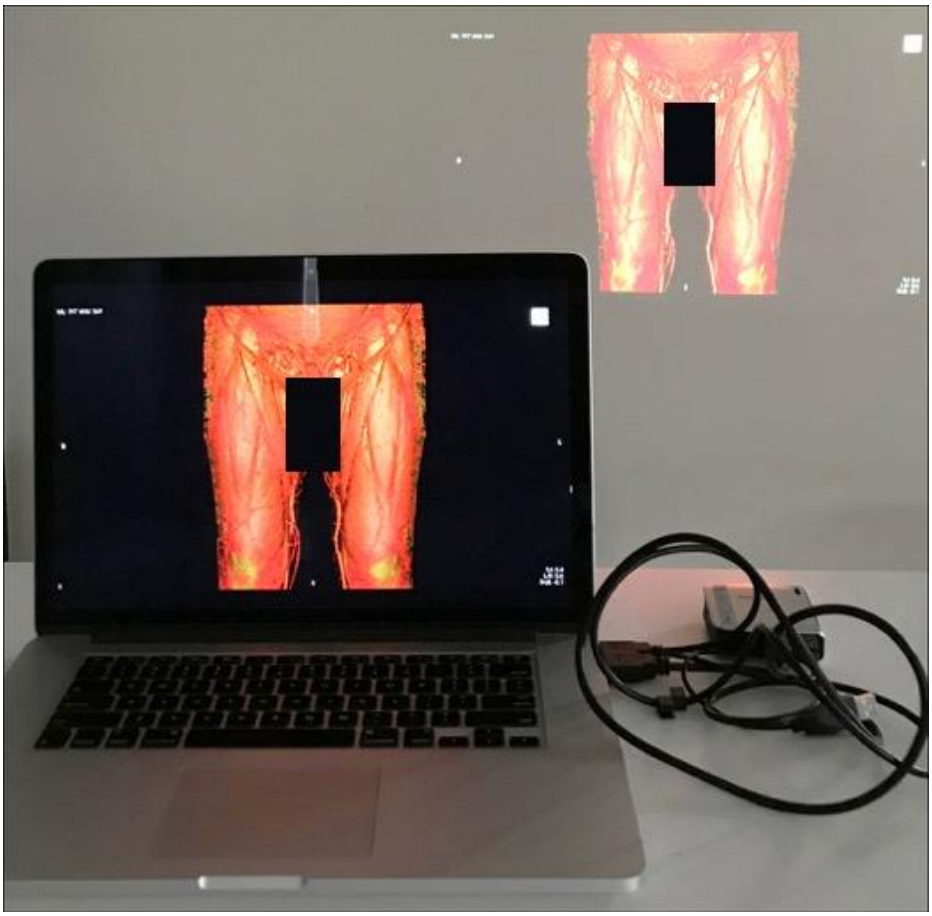

Figure 12.2.3.2.1. Direct augmented reality computed tomographic angiography technique (ARC) setup: comprising the MacBook Pro portable computer (Apple Inc., Cupertino, CA, USA), Philips PicoPix Pocket Projector (Philips, Amsterdam, The Netherlands), a 15-cm ruler and OsiriX computer software (Pixmeo, Geneva, Switzerland).

3D image generation

3D image of ALT perforators is reconstructed using our previously published technique (137). Briefly, Digital Imaging and COmmunications in Medicine (DICOM) files from preoperative CTA is imported into OsiriX software. Using volume-rendering technique (VRT) and colour look-up table (CLUT), the scan data is reconstructed in 3D where perforators are rendered red, subcutaneous tissue and skin transparent.

ARC calibration

Similar to standard AR systems, our ARC requires calibration by the user at the time of its application. A virtual line of any length can be created in OsiriX software using the “ruler” tool. Since our physical ruler was 15 cm-long, the line was kept within this length. Upon connecting the projector to the laptop via USB and HDMI cords, it is immediately ready for use. Once the patient is positioned supine on an operating table as they were during the CTA scan, the ruler is placed adjacent to the patient and the projector is held directly above. The “height” at which the projector is held is adjusted, up or down, until the virtual line and the physical ruler correspond exactly. This process is almost instantaneous and we have abandoned our original plan to time it for assessment.

ARC application

Maintaining the same distance of the projector away from the patient at calibration, the 3D-reconstructed image of ALT perforators is loaded on OsiriX software and projected on to the patient’s thigh (Figure 12.2.4.3.2) or abdomen (Figure 12.2.4.3.3). Bony landmarks on 3D reconstructed image, such as ASIS and patella, are useful to orientate the ARC correctly on the thigh. Perforator location exactly correlated with the Doppler marking.

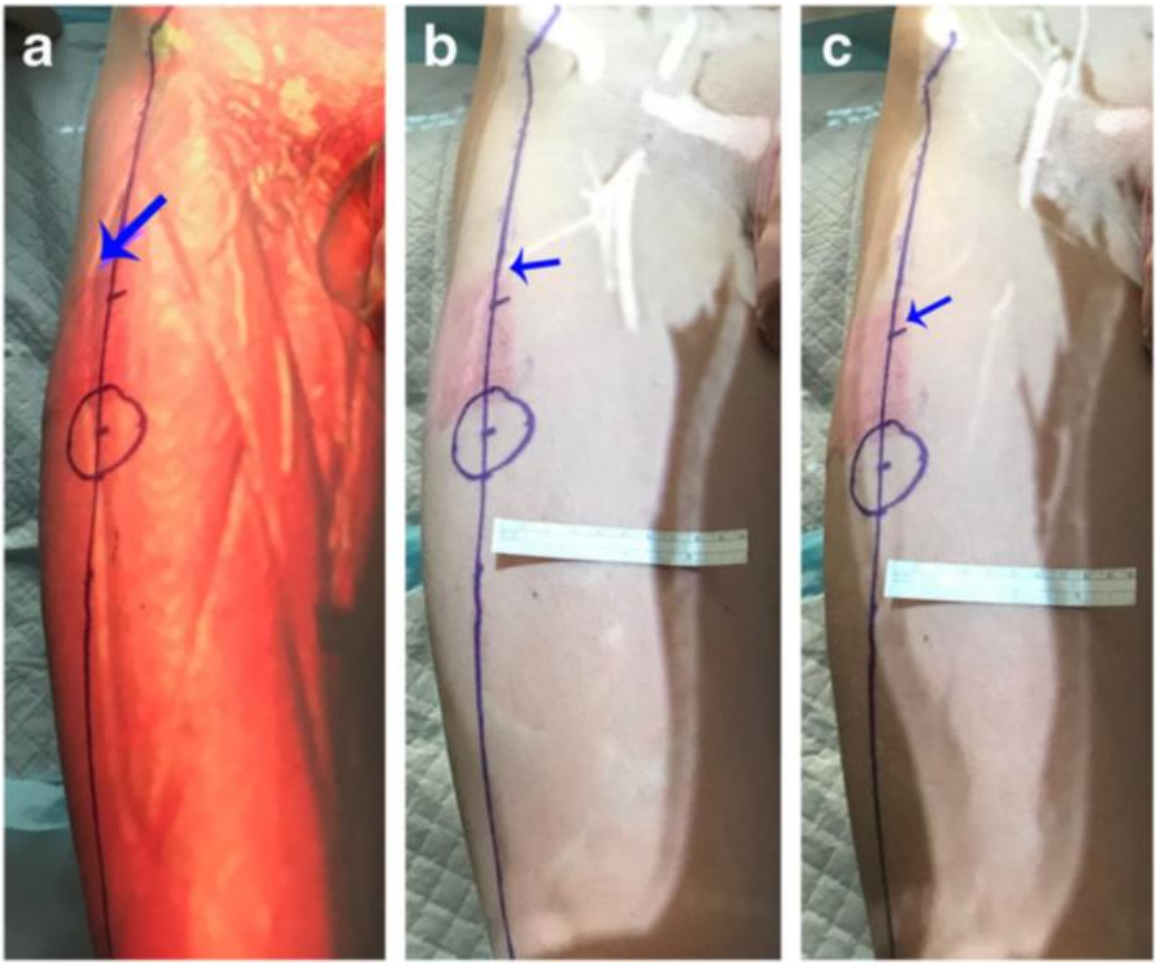

Figure 12.2.3.2.2. Direct augmented reality computed tomographic angiography technique (ARC) for thigh flap perforator mapping (in a case of an anterolateral thigh flap). (A) Maintaining the same distance of the projector away from the patient at calibration, the 3D-reconstructed image of ALT perforators is loaded on OsiriX software and projected onto the patient's thigh, marking the cutaneous perforator location (blue arrow). (B) A maximum intensity projection (MIP) reconstruction view of the perforator is projected onto the patient's thigh to show the intramuscular course of the perforator selected. (C) The same MIP reconstruction view of the perforator is used to show the source vascular pedicle.

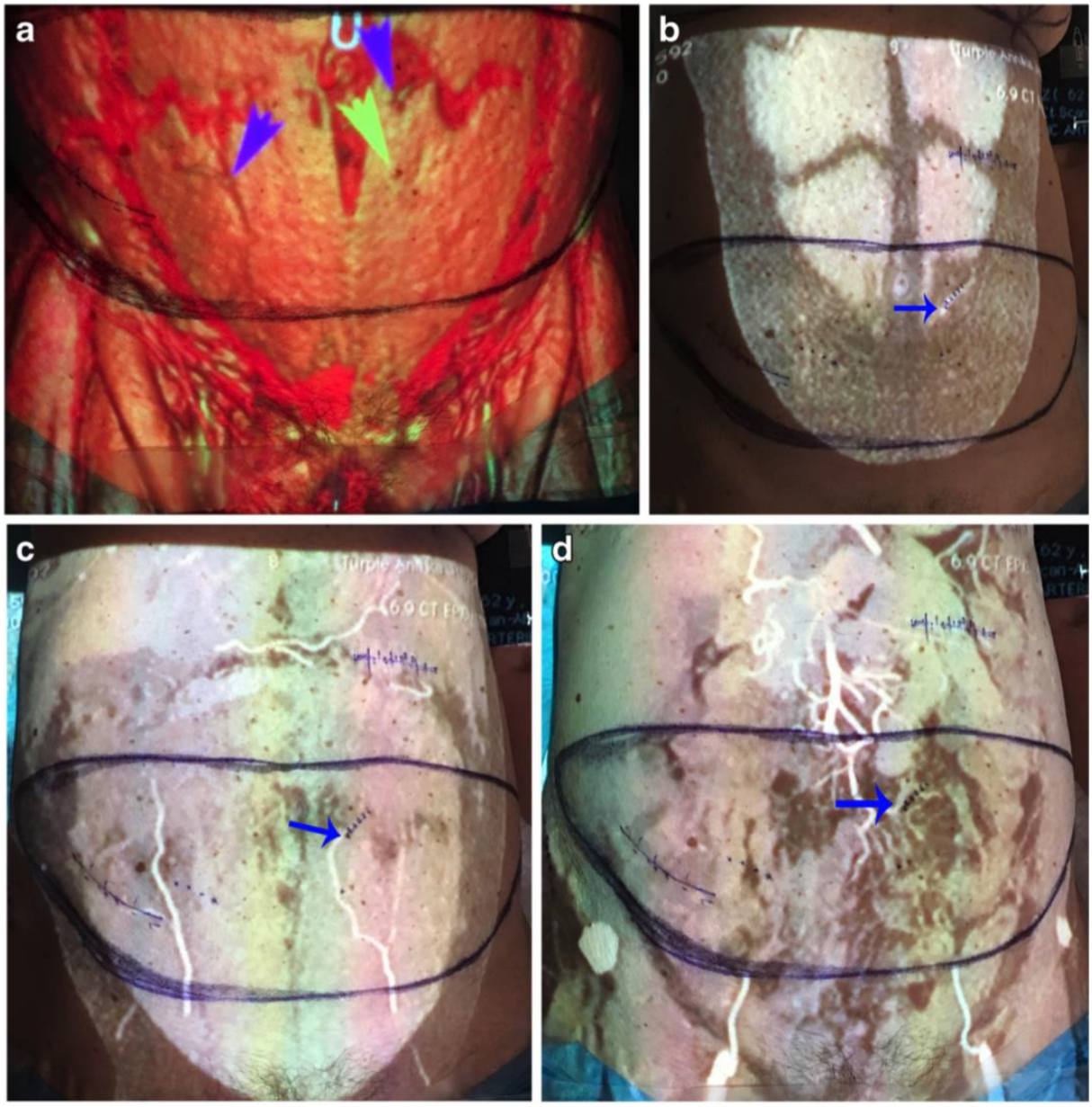

Figure 12.2.3.2.3. Direct augmented reality computed tomographic angiography technique (ARC) for deep inferior epigastric artery (DIEA) perforator (DIEP) flap planning. (A) Maintaining the same distance of the projector away from the patient at calibration, the 3D-reconstructed image of DIEA perforators is loaded on OsiriX software and projected onto the patient's abdomen, marking the cutaneous perforator location (blue arrow). Yellow arrows demonstrates smaller perforators. (B) A maximum intensity projection (MIP) reconstruction view of the perforator is projected onto the patient's abdomen to show the subcutaneous course of the perforator selected. (C) The same MIP reconstruction view of the perforator is used to show the intramuscular course of the perforator selected. (D) The same MIP reconstruction view of the perforator is used to show the source vascular pedicle.

Discussion

In the current case series, we illustrate our projector-based ARC technique for preoperative planning of six perforator-based free flaps that is affordable, compact and readily reproducible. It is a novel way of utilising CTA, and potentially MRA, images which may yet play a role in the continuum of evolution in preoperative planning in free flap surgery.

Since the advent of free tissue transfer approximately 40 years ago (437), constant improvement particularly in the preoperative planning phase has led to improved patient outcomes. The use of relatively simple techniques, such as handheld Doppler ultrasound, to advanced imaging techniques, such as CTA and MRA, for purposes of preoperative planning is now routine. Pre-operative planning for perforator based free flaps, in particular, is important due to the high degree of anatomical variations. Therefore, patients with favourable, and more importantly unfavourable, anatomy can be identified, and the optimal perforator of choice can be utilised (72, 438). These are important considerations in improving outcomes, decreasing morbidity, and reducing operative time and stress, perhaps to be achieved through constant improvement and evolution of pre-operative planning.

Imaging modalities

To date, numerous imaging modalities have been reported; however, due to various reasons, most clinicians only routinely use CTA or MRA with handheld Doppler probes as adjuncts in preoperative planning free flap reconstructions. Despite being non-invasive, portable, low-cost and easy to use, handheld Doppler probes and colour Doppler ultrasound are limited as stand-alone imaging due to their inherent limitations from low depth detection (20 mm) (445) and high operator-dependency, respectively (446). Despite radiation exposure, CTA is readily accessible, low-cost and has high sensitivity and specificity for perforator detection, including ALT flaps (438), leading to improved clinical outcomes and reduced operating times (130, 142). However, using appropriate contrast administration protocol, the radiation dose can be reduced to 6 mSV per scan which is equivalent to 2.5-3.3 years of background radiation (141). In contrast to CTA, MRA lacks radiation, however, it has lower spatial resolution that compromises visualisation of small-

calibre vessels and is limited by its high cost (96). Recent advances in MRA technology can yield high-quality images at higher speed but they are not yet widely available (447).

Imaging utilisation

As choice of preoperative imaging modalities have consolidated, clinicians have sought novel methods of utilizing the scan data from CTA and MRA to improve preoperative planning and surgical efficiency, such as AR or VR and holograms. In comparison to the current imaging technologies that are restricted to 2D viewing, these mixed reality platforms can enable natural 3D mode of visual perception and tactile feedbacks that enhances situational awareness and spatio-temporal understanding of involved anatomical structures.

AR/VR

First described by Boeing scientists Caudell and Mizell (448), AR is a technology that augments the user's visual field with superimposed real-time images that can be displayed either directly on the object in real-life, also known as projection method, or indirectly on a portable device, such as a head-mount display (HMD) or a smart phone (449). In contrast, simulation of real world based on computer graphics engulfs the user's entire visual perception in VR. Various surgical disciplines have reported the utility of AR: for calibrating stereotactic instruments in neurosurgery (450), fashioning craniofacial implants in maxillofacial surgery (451), enhancing visualisation in laparoscopic surgery (452) and identifying sentinel lymph nodes in breast cancer surgery (453). In plastic surgery, it appears broadly most useful for preoperative planning, intraoperative navigation and surgical training (454).

AR enables an extended "layer" and field of view that leads to intuitive real-time 3D visualization of anatomy both superficial and deep to the surface. However, most AR devices currently available in the market are expensive, bulky, complicated, have slow update rate and require tedious image registration processes. Using proprietary hardware and free software, Jiang *et al* have developed a CTA-based, direct AR technique that reduces cost, possesses system accuracy of 3.5 mm and is useful for raising thoracodorsal artery perforator flaps in dogs (439). Using a mini-projector, a compact near-infrared camera and compact set-up, Gan *et al* report a compact, direct AR technique that

detected skin perfusion after tail vein injection of ICG in mice (441). However, their set-up is so small and has poor resolution that it would be difficult to translate it to clinical application on an operating table.

In clinical application, Hummelink *et al* report their projection-based direct AR technique using handheld projector and proprietary software suites in three case series (440, 443, 444). In the first series (443), a 3D reconstruction of perforator locations produced from CTA scans is directly projected on to the abdomens of nine patients undergoing DIEP flap reconstruction and compared with handheld Doppler findings. The authors have found that using their novel technique a greater number of perforators are identified, compared to the Doppler ultrasound, and at a higher accuracy (84.3% vs 56.9%, $p = 0.03$). In addition, extra anatomical information, such as the location of inguinal lymph nodes, can be displayed (444). A major limitation is that the method is operator-dependent since the projector must be held steadily above the patient at a correct height without tremor in order to give accurate image of the anatomy. Interestingly, the authors have combined breast volumetric analysis from an expensive 3D scanner (3dMD Body; 3dMD LLC, Atlanta, GA, USA) in order to calculate the ideal flap volume and, subsequently, project the flap design that achieves the volume (440). Although novel and encouraging, current 3D surface imaging technology has a reported error rate of 13-16% (455) and, hence, its translation in larger patient cohort would be of interest. Similarly, Sotsuka *et al* have used a portable projector mounted on a fixed handstand for preoperative marking of perforators in a DIEP flap reconstruction (456). Interestingly, in this case report, 3D volume rendering of the CTA images is not performed prior to projection.

Hologram

A hologram displays reflective auto-stereoscopic (i.e. no wearable devices) 3D visuals that contain hogels (i.e. holographic elements) rather pixels or voxels where each hogel contains up to 1 million different perspective views. Hackett *et al* have studied the role of hologram in teaching cardiac anatomy to 19 volunteers (10 intervention vs 9 control) and found a superior overall performance in the test (89 vs 68, $p < 0.05$) (457). Furthermore, volunteers have demonstrated a trend in lower mental effort required in learning (4.9 vs 6.0, $p = 0.16$). By combining test performance to self-reported mental effort where higher performance and lower mental effort equates more efficient form of learning, hologram have shown high efficiency (0.61 vs -0.68). Recently, Makino *et al* have added tactile

feedback to holograms by using concentrated ultrasonic energy, however, this has yet to advance beyond prototypic stage (458).

Limitations

One of the major limitations of our bespoke ARC technique is interference from ambient lighting. The projector has a relatively low brightness of 100 lumens, which pales in comparison to a standard home theatre projector of 4,000 lumens. This meant that, for adequate utilisation, all lights in the operating theatre has to be turned off for the images to be visible, which can disrupt theatre flow and may compromise efficiency. From our experience, the project has to be held within an arm's length, less than one metre, above the patient. However, for added convenience the projector is light enough to be attached to an IV pole, for example, albeit the attached laptop would have to be supported on a surgical tray or anaesthetic machine.

Conclusion

We illustrate a novel technique of projector-based AR CTA (or ARC) for preoperative planning in perforator flaps. The technique is affordable and readily reproducible. It is a novel way of utilising CTA, and potentially MRA, images which may yet play a role in the continuum of evolution in preoperative planning and perhaps intraoperative use in free flap surgery.

12.3 3D Printing Application in Free Flap Breast Reconstruction

12.3.1 Current Surgical and Imaging Techniques

12.3.1.1 Anatomy and Evolution of Free Flap Breast Reconstructive Techniques

PUBLISHED (Publication): ***Chae MP***, Ramakrishnan V, Hunter-Smith DJ, Rozen WM. (2016) The extended DIEP Flap. In Shiffman MA (ed.), *Breast Reconstruction: Art, Science, and New Clinical Techniques* (pp. 793-805). Gewerbestrasse, Switzerland: Springer International Publishing Switzerland.

Chapter Summary

Introduction: In contrast to implant reconstruction, autologous reconstruction using abdominal wall perforator-based free deep inferior epigastric artery perforator (DIEP) flap produces more aesthetically-pleasing, natural-looking, and long-lasting outcome. In thin patients where there is an insufficient abdominal integument, DIEP flaps may be contraindicated.

Methods: A review of the published English literature dating from 1950 to 2015 using databases, such as PubMed, Medline, Web of Science, and EMBASE was undertaken.

Results: Arteries supplying the anterior abdominal wall integument can be divided into the deep and superficial system. Musculocutaneous perforators of the DIEA are anterior branches that traverse through the deeper tissues to supply the anterior abdominal wall integument. Recently, techniques have been described to “extend” the standard DIEP flap by augmenting its vasculature (i.e. stacked) or its tissue volume (shelved) during the flap harvest.

Conclusion: There are various options to extend the standard DIEP flap by its vasculature or tissue volume in order to achieve a greater flap volume for a superior aesthetic outcome.

Introduction

Given the high prevalence and incidence of breast cancer in our society - one in eight women in the United States will develop breast cancer in their lifetime (41) - and approximately 25 percent of the affected women will receive mastectomy (459), postmastectomy breast reconstruction has become a significant component in the holistic treatment of these patients. In contrast to synthetic implants that are associated with undesirable complications (460), breast reconstruction with autologous tissue has demonstrated a more aesthetically-pleasing, natural-looking, and a long-lasting restorative option (48). Aided by advancements in microsurgical techniques and radiological imaging modalities (7), complex microvascular breast reconstructions have evolved and become a safe, reliable, satisfactory procedure (33, 50, 51).

Since the days of Vincent Czerny, a German surgeon, who performed the first successful postmastectomy autologous breast reconstruction by autotransplanting a large lipoma from the lumbar region (461), a wide array of flap options have been discussed in the literature. Early donor sites included omentum (52) and latissimus dorsi (53-56). Despite being a workhorse flap choice for most reconstructions, the latissimus dorsi myocutaneous flaps are limited in breast reconstruction by their small volume, frequently requiring an implant being simultaneously inserted. Later, techniques to “extend” the latissimus dorsi flaps have been able to increase the flap volume (462-466). However, they were associated with significant donor site morbidity, such as large seromas.

After the first microvascular tissue transfer by Taylor and Daniel in 1975 (467), multiple donor sites for a myocutaneous flap have been studied for breast reconstruction, such as deep circumflex iliac artery (groin) flaps (57, 58), lateral thigh (tensor fascia latae) flaps (59), superior and inferior gluteal musculocutaneous flaps (60-63), gracilis flaps (64), and triceps flaps (65). Given the added aesthetic benefit akin to an abdominoplasty (or “tummy tuck”), abdominal integument quickly became a popular donor site.

The first musculocutaneous flap for autologous breast reconstruction based on rectus abdominis muscle was described by Robbins in 1979 (468). Then, Holmstrom *et al* (66) described a transverse technique, which was modified and popularized by Hartrampf *et al* (31) as a free transverse rectus abdominis muscle (TRAM) flap. For unilateral breast reconstruction, harvesting a contralateral unipedicled TRAM flap enabled the surgeons to

simultaneously harvest the flap and prepare the recipient site. Furthermore, a TRAM flap provided an ample volume for most breast reconstructions bypassing the need for an additional implant insertion. Moreover, the abdominal integument closely resembled the appearance and texture of the natural breasts providing a superior aesthetic outcome. However, TRAM flaps were frequently associated with partial flap necrosis due to venous congestion (7-31%), most commonly in the periphery of the flaps (Hartrampf zones III and IV), and abdominal wall morbidity from the rectus muscle weakness and subsequent ventral hernia (0.3-11%) (31, 469). As a result, muscle-sparing techniques evolved, such as deep inferior epigastric perforator (DIEP) flap (470, 471).

Based on the experimental studies by Taylor *et al* (472) demonstrating the feasibility of a flap based on paraumbilical perforators sacrificing a minimal amount of anterior rectus sheath and rectus muscle around the perforators, Onishi *et al* (69) described a DIEP flap on anatomical models for the first time. The DIEP flap is a fasciocutaneous flap based on the musculocutaneous perforators deriving from the deep inferior epigastric artery (DIEA). Subsequently, Koshima *et al* (68, 473) reported a case series using paraumbilical perforator-based fasciocutaneous flap for the reconstruction of contralateral groins and oral floors. Allen *et al* (49) is credited as the first to popularize the use of DIEP flap in breast reconstruction. The DIEP flaps provided the same benefits as the free TRAM flaps, such as adequate postmastectomy volume replacement, however, with a superior aesthetic and functional outcome at the abdominal donor site (50, 70). Moreover, they were associated with a lower rate of postoperative abdominal pain (474). Despite microsurgical techniques and meticulous vascular dissection necessitating an initial learning curve, reliable vasculature of the anterior abdominal integument that can be preoperatively imaged using modern techniques such as computed tomographic angiography (CTA) and the patient preference for the abdominal donor site means that the DIEP flap is now considered the “gold standard” postmastectomy autologous breast reconstructive option (5-7, 51, 73, 475, 476).

Anatomy of DIEP Flap

Arterial System of the Anterior Abdominal Wall

Arteries supplying the anterior abdominal wall integument can be divided into the deep and superficial system (Figure 12.3.1.1.1).

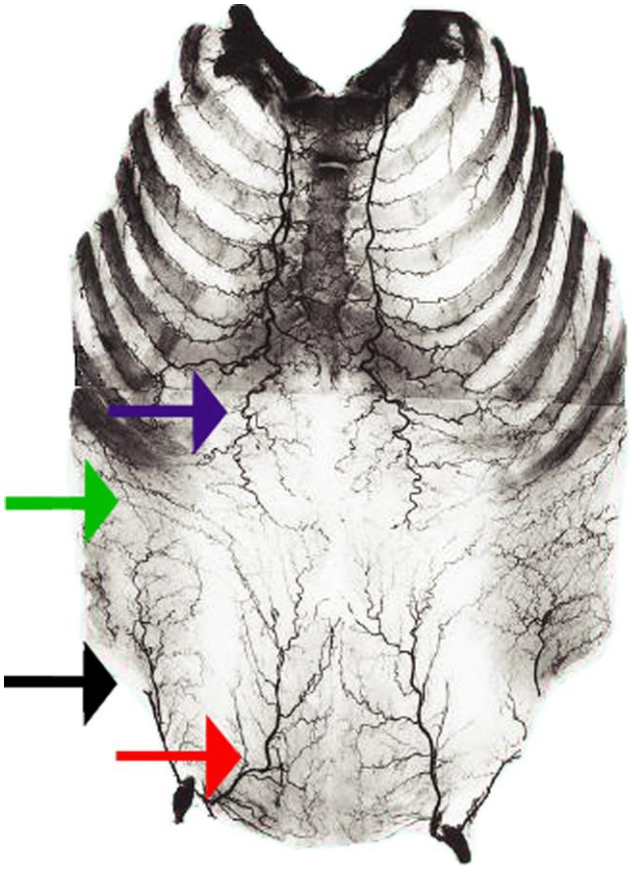

Figure 12.3.1.1.1. Vasculature of the deep tissues of the anterior abdominal wall demonstrated on fresh cadaveric injection (27). Red arrow: deep inferior epigastric artery. Black arrow: deep circumflex iliac artery. Green arrow: intercostal arteries. Purple arrow: deep superior epigastric artery (Reproduced with permission)

Deep System

The deep arterial system is composed of 2 major arteries - superiorly-based deep superior epigastric artery (DSEA) and inferiorly-based deep inferior epigastric artery (DIEA). DSEA and DIEA course caudally and cranially respectively and eventually anastomose with each other via multiple narrow “choke” vessels (472, 477, 478).

DSEA arises from the terminal branch of internal mammary artery at the level of the sixth costal cartilage, descends posterior to the lower costal cartilages, and leaves the thorax. It pierces the rectus sheath and lies on the posterior surface of the rectus abdominis muscle before dividing into three branches. The medial and lateral muscular branches become musculocutaneous perforators or course caudally, increasingly becoming small in diameter - called “choke” vessels - and anastomose with the branches from the DIEA. The lateral segmental branch tracks along the costal margin in the neurovascular plane and then, gives off branches that anastomose with intercostal arteries, deep branches that supply the posterior rectus sheath and peritoneum, or muscular branches. In general, the vessels of the DSEA are smaller in diameter compared to DIEA, the musculocutaneous perforators have shorter pedicle, and they supply a smaller vascular territory (29).

DIEA is the dominant vascular supply of the anterior abdominal wall (29, 467, 472). It arises from the medial aspect of the external iliac artery opposite the origin of deep circumflex iliac artery above the inguinal ligament. Close to its origin, it gives off a medial pubic branch that forms an abnormal obturator artery in 22%. It courses superomedially piercing the transversalis fascia and acquires two venae comitantes from the external iliac vein. Immediately before reaching the rectus abdominis muscle, it gives off a muscular branch directly into the lowermost part of the muscle. The main vessel pierces the rectus abdominis from its lateral border and divides most commonly into two primary branches below the level of the umbilicus.

Despite early anatomical accounts of cutaneous vasculature by Manchot and Salmon not accounting for any branching patterns of the DIEA (479-481), later reports have helped establish the current understanding of the three branching types of the DIEA (Figure 12.3.1.1.2): mono-, bi-, and trifurcating (28).

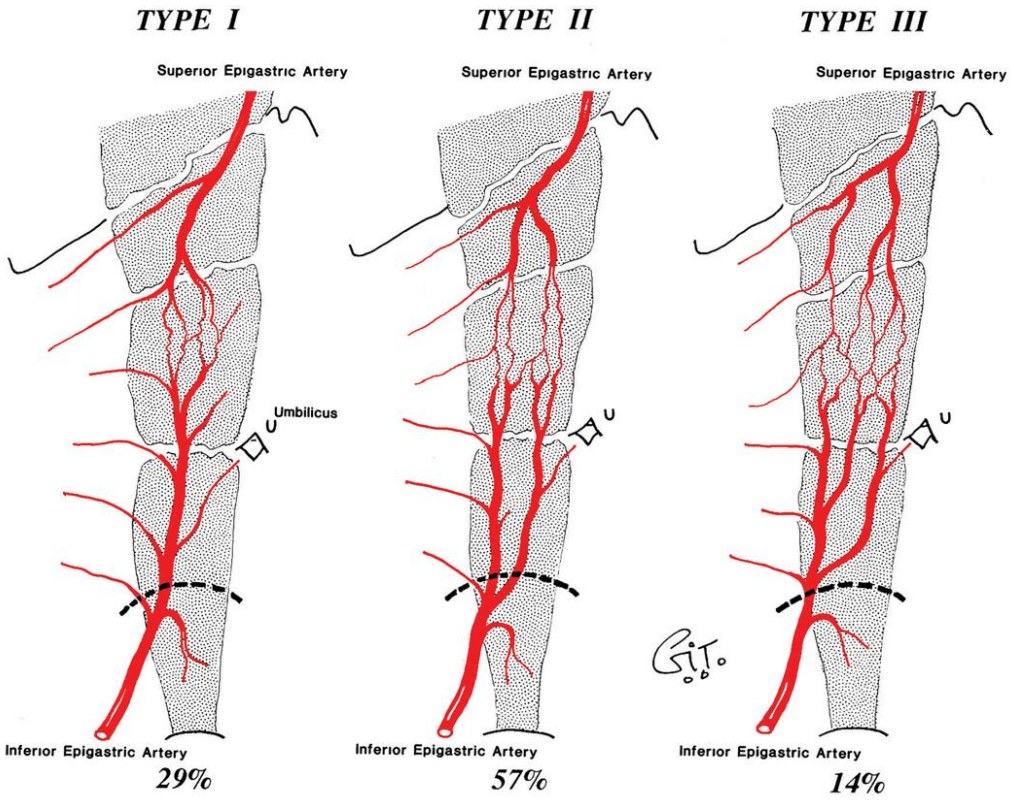

Figure 12.3.1.1.2. The three branching patterns of the deep inferior epigastric artery (DIEA). The DIEA is shown as a single, bifurcating or trifurcating trunk below the umbilicus. The arcuate line is dotted. This presents the findings of the original study by Moon and Taylor (28).

Milloy *et al* first described the pattern of dominance by medial or lateral branches of the bifurcating DIEA (482). Boyd *et al* first reported the existence of three major branches or trifurcating DIEA (29). The general consensus exists that the bifurcating pattern is most common (483-485) and trifurcating type is comparatively rare (486, 487). The understanding of the branch pattern is important clinically in intraoperative setting. The location of bifurcation or trifurcation can determine the extent of dissection and evidences demonstrate that the branching pattern directly correlates with the course of musculocutaneous perforators (5).

The primary branch of the DIEA ascends within the rectus abdominis muscle and gives off multiple branches. Laterally, it communicates with intercostal, subcostal, and lumbar arteries. Inferolaterally, it connects with the ascending branch of deep circumflex iliac artery (DCIA) and produces deep branches supplying the posterior rectus sheath and peritoneum, muscular branches supplying the rectus abdominis, and anterior branches

supplying the skin and subcutaneous tissues. Medially, a large umbilical artery arises immediately upon entry into the rectus abdominis and passes directly towards the umbilicus. Superiorly, multiple small caliber “choke” vessels arise that anastomose with the DSEA.

Superficial System

Superficial superior epigastric artery (SSEA) and superficial inferior epigastric artery (SIEA) constitute the superficial system. SSEA is a branch of DSEA that arises after it enters the thorax. SIEA is a branch of the common femoral artery. It courses superiorly in the subcutaneous plane supplying the anterolateral abdominal wall. It communicates superiorly with the SSEA, laterally with the perforators of external oblique derived from the intercostal arteries and SCIA, inferolaterally with superficial external pudendal artery (SEPA), and is connected to the DIEA via its deep surface.

DIEA Musculocutaneous Perforators

Musculocutaneous perforators of the DIEA are anterior branches that traverse through the deeper tissues to supply the anterior abdominal wall integument. They can be grouped into three vertical groups (28-30, 485-489). The medial group of fasciocutaneous perforators perforates through the linea alba while the middle group of musculocutaneous perforators emerges through the anterior rectus sheath, and the lateral group of fasciocutaneous perforators passes through the external oblique aponeurosis. The middle group, especially in the paraumbilical region, contains large-caliber perforators that traverse directly into the integument with minimal contribution to the muscle (490). Other perforators in the medial and lateral groups are of small diameter and hence, less significant clinically (Figure 12.3.1.1.3).

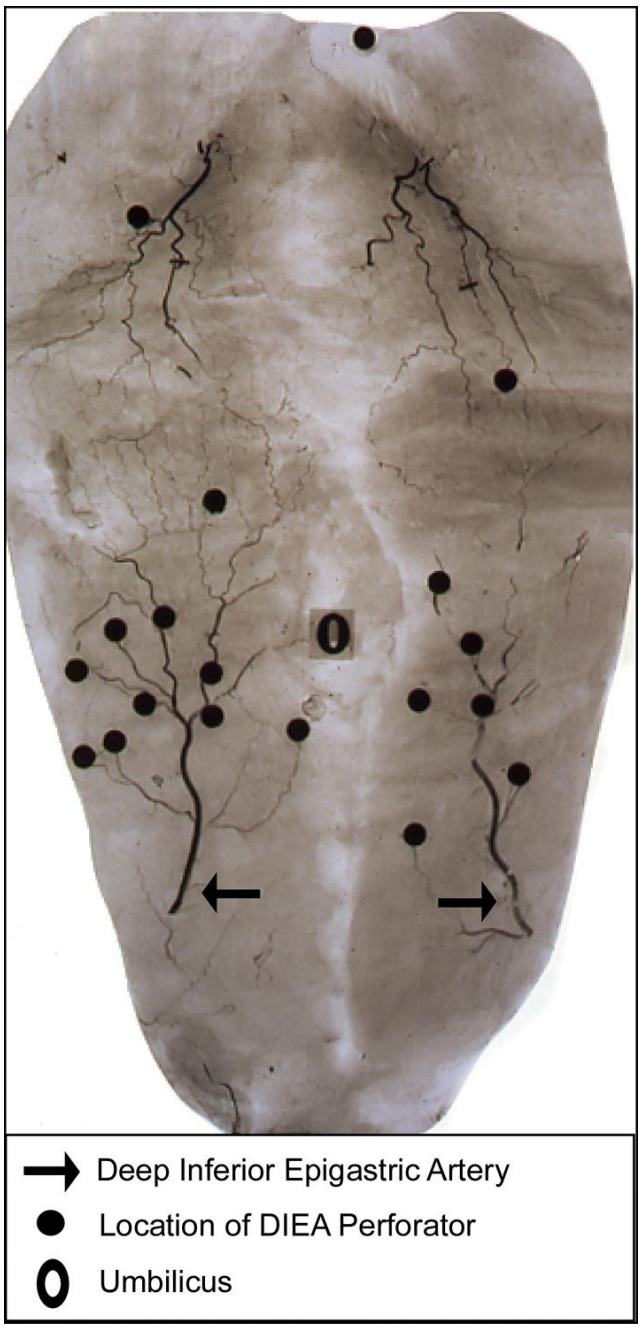

Figure 12.3.1.1.3. X-ray of the abdominal wall, demonstrating the course of the deep inferior epigastric artery (DIEA) and the location of its perforators (metallic beads) (29) (Reproduced with permission)

As DIEA perforators emerge from the rectus sheath, they flow in a direct, oblique manner through the adipose tissue layer and reach the Scarpa's fascia. Kikuchi *et al* (489) first described the subfascial and intramuscular components of the perforators and Rozen *et al* (30) quantitatively demonstrated that the intramuscular component courses both longitudinally and transversely. Interestingly, the latter group reported that the intramuscular course correlated with the branching patterns of the DIEA (30).

Aided by the introduction of CTA and its high-quality visualization of the subcutaneous vasculature, Rozen *et al* have demonstrated that the branching of the perforators occurs above the level of Scarpa's fascia in two planes: fascial plexus and subdermal plexus (425). Immediately superficial to the Scarpa's fascia in the fascial plexus, DIEA perforators branch out extensively, often into more than five vessels. They course obliquely and radially within the superficial layer of adipose tissue, known as Camper's fascia, and reach the subdermal layer. Majority of the anastomoses between adjacent perforators occur within the subdermal plexus across the so-called "choke" zones (491).

The caliber of perforators varies widely between patients and even within the same vascular territory in the same patient (425). However, their branching pattern would remain relatively consistent (425). Interestingly, the size of the DIEA perforators inversely correlates with the size of the ipsilateral SIEA and the effect was graded (492). The authors derived that the location of a vascular territory remains the same, but its size varies depending on the dominance between the adjacent vascular territories. Clinical studies of the DIEP flap have confirmed these findings (Figure 12.3.1.1.4).

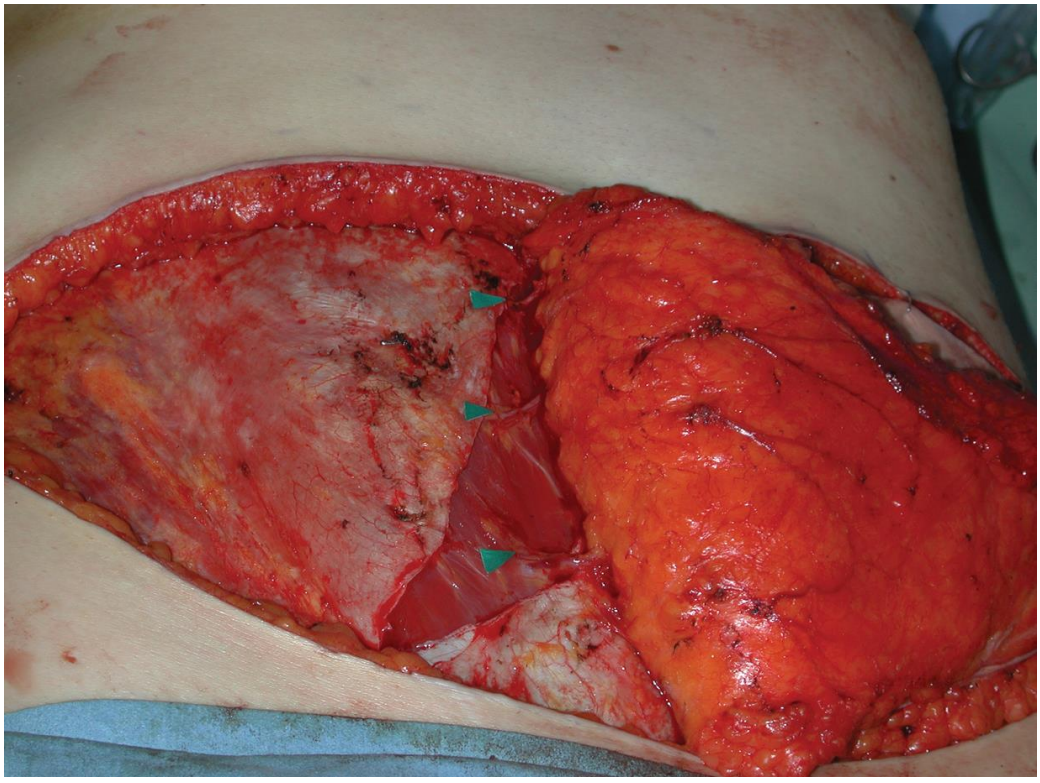

Figure 12.3.1.1.4. Deep inferior epigastric artery (DIEA) perforator flap with 3 perforators highlighted (green) emerging from rectus abdominis to supply the lower abdominal flap (8). (Reproduced with permission)

The authors were able to report a similar interplay between anterolateral thigh (ALT) and anteromedial thigh (AMT) flap.

Clinically, an optimal perforator has a short intra- and extramuscular course (Figure 12.3.1.1.5), which hastens the dissection time and avoids damage to the muscle (30, 472).

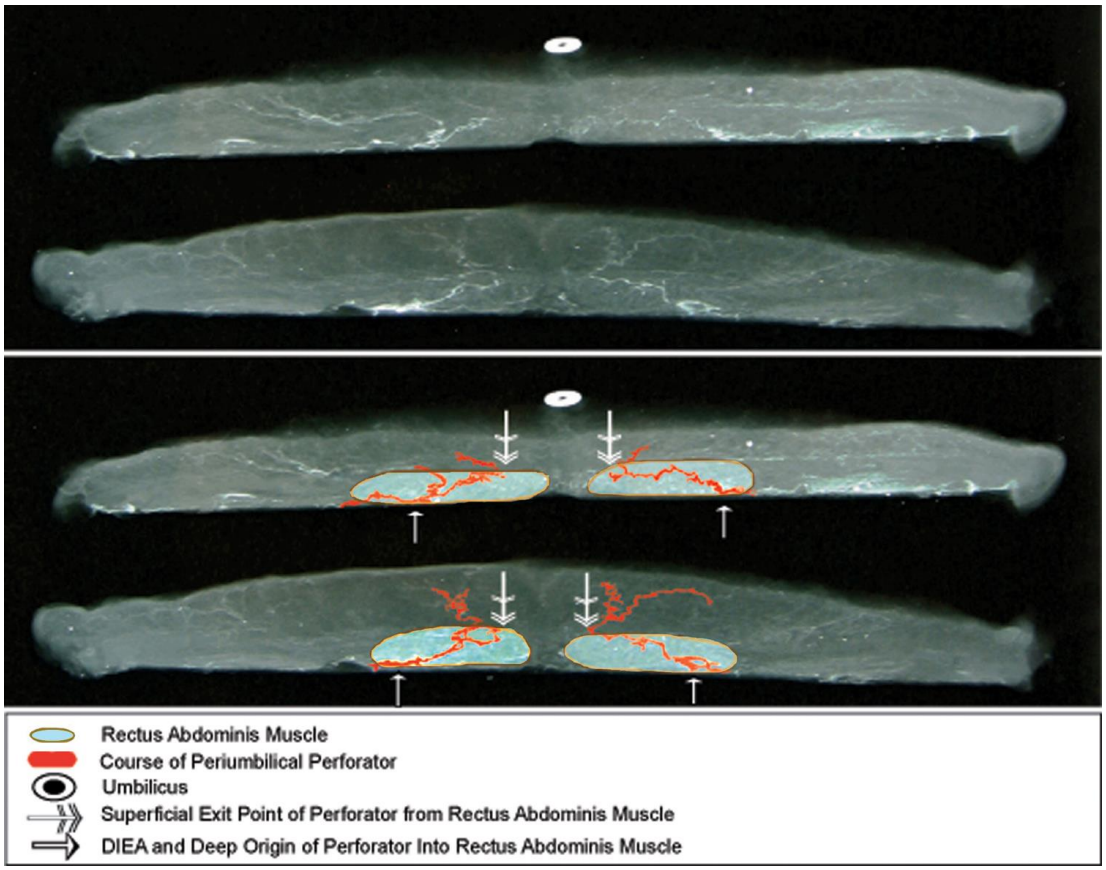

Figure 12.3.1.1.5. X-ray of two transverse periumbilical sections of the anterior abdominal wall, with the perforators highlighted (red) to demonstrate the significant transverse course through the rectus abdominis muscle, from their origins on the deep inferior epigastric artery (DIEA) to their points of exit from the muscle (30). (Reproduced with permission)

Furthermore, it has a relatively large vessel diameter for a superior blood flow. Throughout the literature, the exact measurement that would constitute a large perforator vessel has been inconsistently reported. However, the value has been steadily increasing and the most recent studies have used diameters greater than 1.5mm to define a large perforator (7, 493, 494). Additionally, a central location of the perforator in a flap and its wide

subcutaneous branching patterns are considered desirable qualities of a perforator in maximizing the flap perfusion (30, 472).

DIEA Perfusion Zones

Hartrampf Zones

Building on from the concept of angiosomes, vascular territories supplied by an artery (28, 477, 478), Hartrampf *et al* divided the anterior abdominal wall into four longitudinal zones in the order of their vascularity based empirically on the authors' clinical impression while performing TRAM flaps (31). Zones I and II are supplied by the ipsilateral and contralateral DIEA while zones III and IV are supplied by the ipsilateral and contralateral SIEA (Figure 12.3.1.1.6).

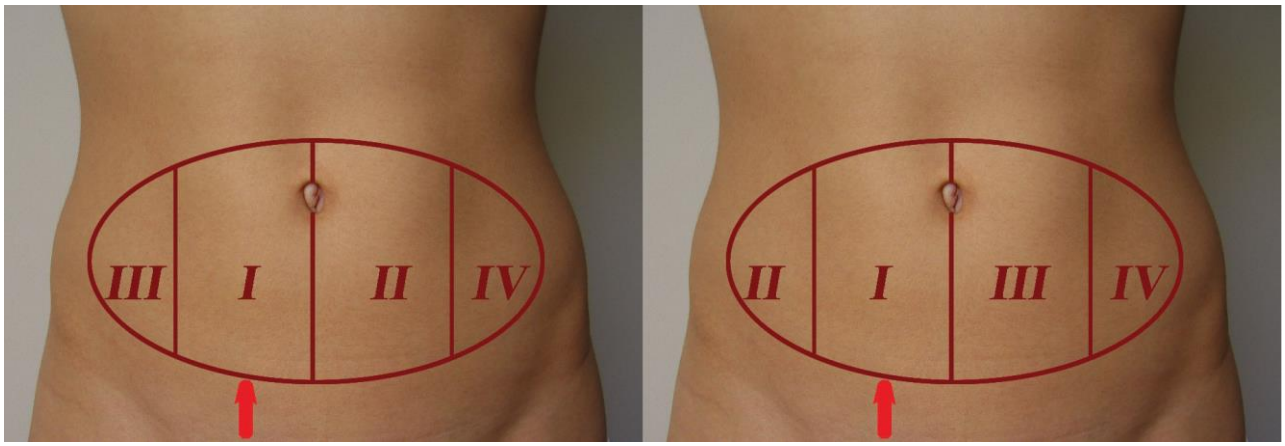

Figure 12.3.1.1.6. Perfusion zones of the lower abdominal flap supplied by the deep inferior epigastric artery (DIEA) (red arrow). Left: conventional classification (31). Right: contemporary classification (32). (Reproduced with permission)

Zone I is consistently reported in the literature as the most well perfused area due to being directly filled by the local perforators based on the DIEA. Similarly, zone IV has the poorest vascular filling simply due to their distance away from the DIEA and the blood having to flow through two "choke" zones (478, 495).

Holms Zones

As TRAM and DIEP flaps became popular choices of autologous breast reconstruction, clinical evidences arose that, indeed, the zone III has a greater viability than the zone II (496). This was first suggested by Dinner *et al* (497) and was confirmed using Doppler flow analysis by Hallock *et al* (498). While confirming strong vascularity in zone I and the opposite in zone IV, Holms *et al* and Yamaguchi *et al* have been able to demonstrate using indocyanine green dye injection and fluorescence videoangiography that perfusion in zone III occurs faster and in greater intensity compared to zone II (32, 86). Furthermore, Yamaguchi *et al* postulated that the poorly perfused areas correlated with areas of skin and fat necrosis (86). These findings were supported by studies measuring tissue oxygen requirements (499) and cadaveric studies showing a greater tendency for the perforators in zone I to be rotated towards the zone III (500). Further anatomic studies demonstrated that fewer vascular communications existed through the midline between zones I and II in comparison to ipsilateral zones I and III. As a result, the nomenclature of Hartrampf zones II and II has been changed to reflect the findings and the contemporary classification is popularly referred to as “Holms zones” in the literature.

Venous System of Anterior Abdominal Wall

Similar to the arterial system, deep and superficial systems exist for the venous drainage of the anterior abdominal wall (79, 478, 501). The valves in the deep system direct blood flow in deep inferior epigastric vein (DIEV) system caudally towards the DIEV and superior epigastric vein system cranially towards superior epigastric vein. Interestingly, the small veins connecting the adjacent venosomes are avalvular. The superficial system that communicates in the subdermal plexus and the axial veins that traverse the superficial tissues as venae comitantes of SIEA, SCIA and SEPA drain into the femoral vein. The superficial system also includes the venae comitantes of the arterial musculocutaneous perforators drain into the venae comitantes of DIEA. The deep and superficial venous systems communicate at the level above the umbilicus. They display large individual variance in dominance. However, in a venous congested flap, superficial system becomes the larger and dominant venous system (50, 502, 503).

Extended DIEP Flap

Indications for Extended DIEP Flap

Despite consistent success and superior aesthetic outcome, DIEP flaps are considered relatively contraindicated in patients with insufficient subcutaneous abdominal volume, who has had previous abdominal surgery such as a previous abdominoplasty and liposuction. In a thin patient, a unipedicled hemi-abdominal DIEP flap may not be provide adequate volume for reconstruction. Effort to achieve breast symmetry may be more difficult if the same patient has a large contralateral breast that she is not keen on receiving a breast reduction. In patients who have had an abdominal surgery such as a midline low abdominal scar from a caesarean delivery, there may exist an unreliable perfusion across the scars. Furthermore, the scarring may compromise the tissue flexibility during flap insetting and shaping leading to aesthetically poor outcome. In addition, previous abdominoplasty or liposuction poses a theoretical risk of causing damage to the perforator vessels leading to complications like fat necrosis, partial or even complete flap loss. Interestingly, some case reports have reported successful TRAM flaps despite patients having had liposuction previously, however, they are not commonly reported.

Alternative flap options have since been innovated and popularized for a brief period, however, most of them still remain a second-tier option to the DIEP flaps (51). Despite its poor reliability as a vascular pedicle and adequate caliber vessel is only present in 21% of patients (425, 504, 505), SIEA flap presents as an attractive choice if present. Due to minimal violation of the abdominal wall fascia or muscle, it is associated with minimal donor site morbidity (504). Furthermore, some authors have demonstrated the possibility of augmenting the SIEA flap in a two-stage procedure by clipping the ipsilateral DIEA (504, 506). However, this also introduces an additional procedure, a long transverse mid-abdominal scar, and perioperative risks associated with a delay abdominal procedure. Superior and inferior gluteal artery perforator (SGAP and IGAP) flaps are able to deliver ample tissue for breast reconstruction even in athletic patients (60, 507-509). However, the popularity of these flaps decreased due to difficulties faced during flap harvest from poor exposure, frequently short vascular pedicle and potential mismatch in the donor-recipient vessel size (510). Other flaps, such as the transverse upper gracilis (TUG) flap, extended latissimus dorsi flap, and profunda artery perforator (PAP) flap, have all been mooted but not yet replaced the gold standard DIEP (64, 464, 511).

Addition of artificial implants have been reported with TRAM flaps (512-514) and they have been reported with DIEP flaps also (515). Despite their simplicity, implants introduce their inherent morbidities (516, 517), such as the risk of capsular contracture and implant extrusion (518), risks associated with an additional surgery for the replacement of expanders with permanent implants (512).

More recently, techniques have been described to “extend” the standard DIEP flap by augmenting its vasculature or its tissue volume during the flap harvest.

Extended DIEP by Vasculature: Stacked Flap

In order to overcome the lack of volume from a unilateral hemi-abdominal DIEP flap, investigators have developed “stacked” DIEP flaps where the flap is harvested bilaterally and the DIEA from each side are anastomosed together before connecting to a single recipient vessel (519). Pennnington *et al* (520) first described the “stacking” using TRAM flaps and demonstrated their benefit in gaining sufficient tissue volume while adequately perfusing both Holms zone II and IV. In 1994, Blondeel and Boeckx (67) reported a case where the authors harvested the entire abdominal pannus with a midline laparotomy scar. The DIEA from each side were anastomosed to each other after connecting to the recipient vessel in a parallel fashion. The venous anastomosis was achieved in a Y connection of the flap comitantes to the transposed cephalic vein due to concerns in the size discrepancy with the internal mammary artery venae comitantes. In 2002, Ali *et al* (521) described a technique where two hemi-DIEP flaps were connected in series. One flap was completely de-epithelialized and then buried. The lateral branch of DIEA and venae comitantes from the exposed flap were anastomosed to the buried flap. The skin paddle of the exposed flap was used to represent the vascularity of both flaps.

In 2007, Figus *et al* (519) described a technique where a SIEA flap and the contralateral DIEA flap were anastomosed in series using a medial branch of the DIEA to the SIEA. The resultant stacked composite flap was able to benefit from a longer DIEP pedicle and the operative length was relatively short (less than five hours) secondary to easier harvesting of an additional SIEA flap. Furthermore, the authors noted that the anastomosis between the flaps could be performed separately on an operating table and hence, only one arterial anastomosis was required in the patient. In 2007, Schoeller *et al* (522) harvested a flap

based on end-to-end anastomosis between DIEA and contralateral paraumbilical perforator (PUP). The authors reasoned that stacked hemi-DIEP and hemi-PUP flaps were quicker than stacked two hemi-DIEP flaps, which is essentially two operations.

In 2011, DellaCroce *et al* (34) published the largest case series of stacked DIEP flaps to date. They reported their experience with 55 patients and 110 flaps over three years. The flaps were usually separated and anastomosed before connecting to a single common feeding recipient vessel. In average, they were able to produce a larger combined flap weight compared to the mastectomy weight (596g versus 456g). They noted superior volume and aesthetic achievement leading to higher patient satisfaction. The downfalls were that extra anastomoses were technically more demanding and the operative time increased by 1.5 hours.

As stacked DIEP flaps become more popular, Hamdi *et al* (33) has introduced a method of classifying them (Table 12.3.1.1.1).

Class	
I	SIEA/SIEA flap
II	SIEA/DIEP flap
III	DIEP/DIEP flap
IV	DIEP/perforator flap

Table 12.3.1.1.1. Classification of stacked DIEP flaps. Adapted from Hamdi *et al* (33). Abbreviations: SIEA: superficial inferior epigastric artery; DIEP: deep inferior epigastric artery perforator.

Class I is a flap composed of two SIEA flaps; class II is a SIEA and a DIEP flap; class III is two DIEP flaps; and class IV is between a DIEP flap and a perforator-based flap like a PUP flap. Class III is further divided into two groups depending on whether the DIEP pedicle is anastomosed to a side branch (class IIIa) or to the superior continuity (class IIIb) of the second DIEP pedicle. The authors commented that the class I were least flexible when insetting the flap - and class III the most flexible - due to the length of their respective vascular pedicle.

Extended DIEP by Volume: Shelving Flap

Traditionally, DIEP flaps are raised in a transverse elliptical shape centered at the umbilicus. In recent times, some researchers have endeavored to increase the volume of tissue harvested by extending the flap harvest at their peripheries. Shafighi *et al* (523) reported a prospective case series of ten patients where large volume was required for unilateral breasts reconstruction, a hemi-DIEP flap was raised using “shelving” technique (Figures 12.3.1.1.7 and 12.3.1.1.8).

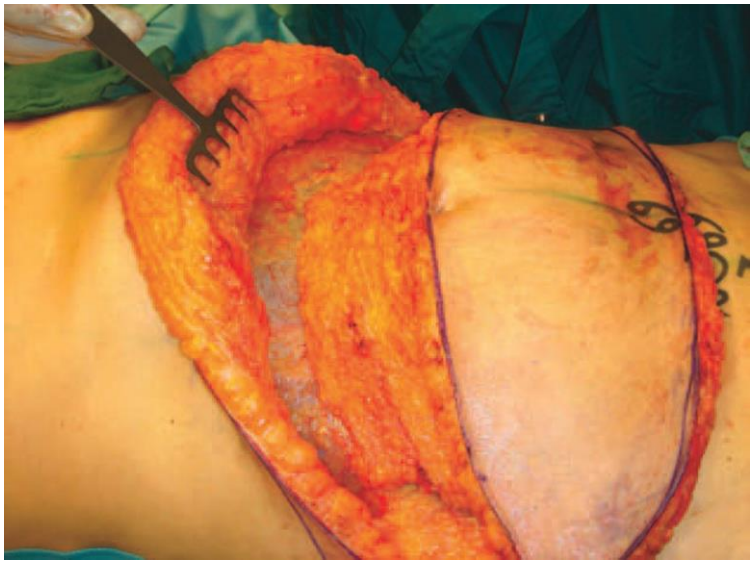

Figure 12.3.1.1.7. Harvest of the cranial extension of the DIEP flap with subscarpal fat extension. (34) (Reproduced with permission)

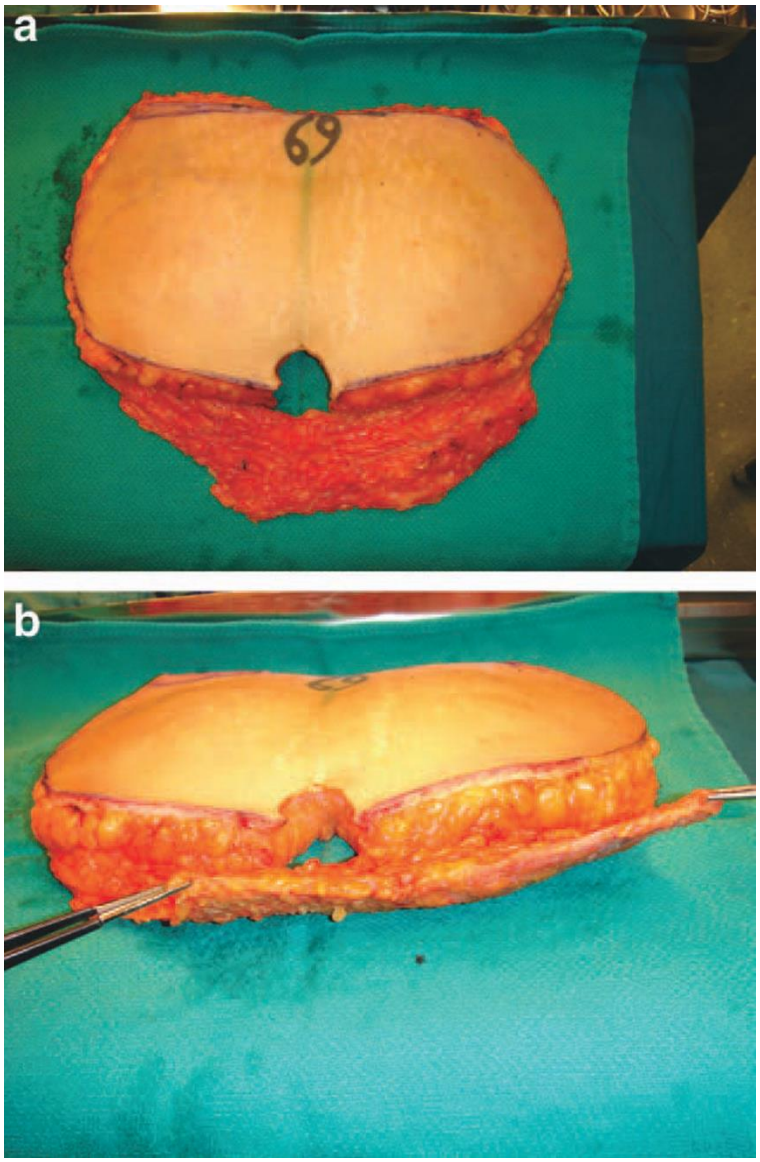

Figure 12.3.1.1.8. Demonstration of the thickness of the cranial extension of the DIEP flap with subscarpal fat extension (A) and subscarpal fat extension lifted with forceps (B). (Reproduced with permission)

At the cranial edge of the flap, the surgeon would incise down until they reach the Scarpa's fascia. Immediately below the fascia, the incision was made in cranial direction resulting in addition of triangular tissue at an average gain of 6-8cm and 98.6g in length and weight respectively. The authors noted that the technique was easy to perform and safe. Minor episodes of fat necrosis occurred but none in the extended volume. Interestingly, the finding was in apparent contradiction to an earlier study that demonstrated that adipose tissue deep to the Scarpa's fascia is relatively poorly vascularized and hence, DIEP flap thinning can only be safely performed deep to the Scarpa's fascia (139). In order to prevent flap failure from the shelving technique Rozen *et al* (524) suggest that the distance

of cranial extension be limited as much as possible, a more cranial DIEP flap perforator must be chosen, and recommended harvesting as much of Scarpa's fascia as possible for superior vascularity at the counter-risk to the upper abdominal flap.

Conclusion:

In recent decades, encouraged by improved imaging and microsurgical techniques, postmastectomy autologous breast reconstruction has become popular. The reconstructive options have evolved significantly over time and currently, the DIEP flap is considered the gold standard. In thin patients where there is an insufficient abdominal integument and the presence of abdominal scars have complicated DIEP flap operations. We present here options to extend the standard DIEP flap by its vasculature or tissue volume in order to achieve a greater flap volume for a superior aesthetic outcome.

12.3.1.2 Imaging-Based Volumetric Analysis

PUBLISHED (Publication): ***Chae MP***, Rozen WM, Spychal RT, Hunter-Smith DJ. (2016) Breast volumetric analysis for aesthetic planning in breast reconstruction: a literature review of techniques. Gland Surg. 5(2):212-26. PMID: 27047788

Chapter Summary

Introduction: Accurate volumetric analysis is an essential component of preoperative planning in both reconstructive and aesthetic breast procedures towards achieving symmetrization and patient-satisfactory outcome. Numerous comparative studies and reviews of individual techniques have been reported. However, a unifying review of all techniques comparing their accuracy, reliability, and practicality has been lacking.

Methods: A review of the published English literature dating from 1950 to 2015 using databases, such as PubMed, Medline, Web of Science, and EMBASE, was undertaken.

Results: Since Bouman's first description of water displacement method, a range of volumetric assessment techniques have been described: thermoplastic casting, direct anthropomorphic measurement, two-dimensional (2D) imaging, and computed tomography (CT)/magnetic resonance imaging (MRI) scans. However, most have been unreliable, difficult to execute and demonstrate limited practicability. Introduction of 3D surface imaging has revolutionized the field due to its ease of use, fast speed, accuracy, and reliability. However, its widespread use has been limited by its high cost and lack of high level of evidence. Recent developments have unveiled the first web-based 3D surface imaging program, 4D imaging, and 3D printing.

Conclusion: Despite its importance, an accurate, reliable, and simple breast volumetric analysis tool has been elusive until the introduction of 3D surface imaging technology. However, its high cost has limited its wide usage. Novel adjunct technologies, such as web-based 3D surface imaging program, 4D imaging, and 3D printing, appear promising.

Introduction

Accurate assessment of breast volume is an essential component of preoperative planning in both reconstructive and aesthetic breast operations for achieving breast symmetrization and satisfactory outcome (525-529). Breast shape is dynamic and highly dependent on patient position, and is also highly variable between patients, therefore any objective method of volumetric analysis requires a high degree of versatility. However, an accurate and reliable method of objective breast volumetric analysis, that is also clinically useful, has been elusive (530). Currently, most surgeons rely on visual estimation and two-dimensional (2D) photographs to evaluate breast volume that is irreproducible and is subject to individual clinical experiences. An ideal breast volume assessment technique should be accurate, reliable, simple, and practical.

Since the earliest report of breast volume measurement by Bouman (531), various techniques have been described of varying accuracy and reliability: water displacement technique using Archimedean principle, negative molding using thermoplastic casts, direct anthropomorphic measurements, indirect anthropomorphic measurements using two-dimensional (2D) imaging and standard (or 3D) imaging, and 3D surface scanning technology (526, 532-547). Countless number of comparative studies (380, 455, 530, 537, 542, 548-559) and reviews of individual techniques (560, 561) have been described. However, a unifying, updated review of all techniques comparing their accuracy, reliability and practicality has been lacking (380, 530, 562).

In this review, we summarize all the currently available techniques calculating breast volume and compare their accuracy, reproducibility, and practicality.

Methods

We reviewed the published English literature from 1950 to 2015 from well-established databases, such as PubMed, Medline, Web of Science, and EMBASE, using various combination of search terms, such as “breast volumetric analysis”, “breast reconstruction”, “breast asymmetry”, “aesthetic breast surgery”, “anthropomorphic”, “mammography”, “Archimedean”, “thermoplastic”, “computed tomographic angiograph”, “magnetic resonance imaging”, “3D surface scanning”, and “3D printing”.

Results / Discussion

Various techniques for breast volumetric analysis have been reported in the literature, such as Archimedean principle, thermoplastic casting, anthropomorphic measurement, 2D imaging, 3D imaging, and 3D surface imaging (Tables 12.3.1.2.1 and 12.3.1.2.2).

Techniques		Accuracy & Reliability	Practicality			Reference
			Time	Portability	Cost (USD)	
Archimedian Principle						
	Schultz Method	MD 5.6% (550)	N/A	Yes	0	(532)
	Tezel Device	N/A	10 min (563)	Yes	1 (563)	(533)
Thermoplastic Casting						
	Conventional	MD 7.97% (556)	25 min (563)	Yes	20-150 (534, 558)	(534)
Anthropomorphic Measurement						
	Grossman-Roudner Device	MD 3.61% (535)	3-10 min (558, 563)	Yes	1 (558)	(535)
	Qiao Formula	MD 3.89% (564)	N/A	Yes	0	(564)
	Brown Formula	MD 5.54% (556)	N/A	Yes	0	(565)
	Sigurdson Formula	R^2 = 0.89 (566)	N/A	Yes	0	(566)
	BREAST-V Formula	R^2 = 0.73 (536)	N/A	Yes	0	(536)
2D Imaging						
	Mammogram	1.09-3.15% (567)	20 min (563)	No	N/A	(537)
3D Imaging						
	CT	CC 0.782-0.873 (540)	90 min (13)	No	390 (7)	(539)
	MRI	MD 1.1% (555)	13-30 min (558, 568)	No	280-1,400 (558, 569)	(540)

Table 12.3.1.2.1. Summary of all reported breast volumetric analysis techniques, except 3D surface imaging. Abbreviations: N/A: not available; CT: computed tomography; MRI: magnetic resonance imaging; MD: mean deviation; CC: correlation coefficient.

Devices	Accuracy	Reliability	Practicality					Reference
			Time			Portability	Cost (USD)	
			Calibr	Captur	Proces			

			ation	e	sing			
Konica Minolta Vivid	0.1-0.22 mm (570)	MD 1.24% (541)	None	0.3-2.5 s	1-1.5 s	Yes	20,000-100,000	(571)
Axis Three	<0.05 mm (560)	CC >0.8 (542)	<5 min	<2 s	<30 s	No	30,000	(542)
JRCB-D	≤0.1 mm (543)	ICC 0.9999 (572)	N/A	<5 s	N/A	Yes	N/A	(543)
VECTRA XT	< 1 mm (544)	EE <1.2% (573)	None	3.5 ms	80 s	No	40,000	(544)
Di3D	≤ 0.2 mm (574)	ICC 0.999 (545)	5 min	1 ms	60 s	Yes	30,000	(545)
3dMD Torso System	<0.2 mm (575)	CR <0.92 (455)	45 s	1.5 ms	<12 s	Yes	130,000	(546)
Crisalix	2-4 mm (547)	None	None	N/A	10-15 min	Yes	4,790 per yr	(547)
Di4D	0.17 mm (576)	ME 0.4 mm (577)	5 min	60 fps	N/A	Yes	105,000	(576)
3dMD Dynamic	≤0.5 mm (578)	ME ≤1.32 mm (579)	100 s	60 fps	N/A	Yes	N/A	(580)

Table 12.3.1.2.2. Summary of all 3D surface imaging techniques. Abbreviations: N/A: not available; MD: mean deviation; CC: correlation coefficient; ICC: interclass coefficient; EE: estimate of error; CR: coefficient of reproducibility; ME: mean error; yr: year; fps: frames per second; s: second; ms: millisecond.

Archimedean Principle

First reported by Bouman in 1970 (531), water displacement technique works on the Archimedean principle where the volume of water displaced equals the volume of breast submerged in water (Table 12.3.1.2.1) (532, 581). Discouragingly, the earlier method described by Schultz *et al* (532) are wet and messy, require complete patient cooperation, and cannot be performed intraoperatively. To this effect, investigators have devised various forms of calibrated measurement cylinders containing liquid with a flexible

diaphragm at the base (533, 566, 582-585). In contrast to commercial devices (583, 585), Tezel and Numanoglu describe a free, easy-to-assemble device that can be assembled from equipments that can be readily found on a sterile operating table (533). In comparison to the gold standard mastectomy specimens, water displacement technique shows only -2% difference (586). However, against mammography-derived volume estimation, it correlates less favorably (regression coefficient = 0.608) (530). Major disadvantages of the Archimedean techniques are that the breast tissue lateral to pectoral fold is often missed leading to underestimation in hypertrophic breasts.

Thermoplastic Casting

Thermoplastic cast method uses a fast-setting plaster or a thermoplastic sheet that is applied on to the thoracic wall and creates a negative mold of the breasts, from which volume can be measured with either sand or water (Table 12.3.1.2.1) (530, 534, 559). Despite its advantages, such as it can be performed with patient sitting upright and the breast shape can be visualized additionally, it has numerous failings that prevent it from being used routinely. It is a subjective technique and during the process of manually pressing the thermoplastic material to the thorax, the breast becomes compressed and its boundaries become arbitrary, making it difficult to determine the breast footprint reliably. Moreover, if the material is relatively inflexible, it cannot mold perfectly around the breast form. It incurs high material cost ($150 per breast) and has a relatively poor accuracy (coefficient variable = 6%) (534).

Anthropomorphic Measurement

Anthropomorphic measurement is one of the earliest methods of calculating breast volume that is still used by physicians (Table 12.3.1.2.1). A volume is derived from a mathematical formula using predefined end-to-end measurements that are obtained either directly from the patient or indirectly via imaging modalities. In order to define a set of “ideal” measurement values for comparison, Penn has derived parameters from “aesthetically perfect” breasts, which, however, did not correlate well clinically (587). Smith *et al* have studied 55 consecutive women to determine a set of “average” measurements, but they utilized soft tissue parameters that are difficult to reproduce (588). Later, Westreich *et al* has described a standardized protocol for assessing female breasts using a measuring tape and a Grossman-Roudner device, achieving a mean measurement deviation of only

3.61% (535). Grossman-Roudner device is an adjustable cone made out of flat envelope that changes to the size of the breast and volume can be read off a scale (589). Similarly, Palin *et al* have used a set of graduated discs to calculate volume (562). However, the Palin discs only work for volumes up to 450 ml and overestimates in firm breasts. More lately, Sigurdson and Kirkland have introduced an equation to predict volume based on two anthropomorphic variables that significantly correlated with the volumes measured by the water displacement method, demonstrating high accuracy (R^2 = 0.89) in 101 normal female volunteers (566).

In contrast to the conventional formulae that have been standardized against water displacement techniques, Qiao *et al* report a modified method where a breast is equated to a half-ellipse and the parameters of the mathematical formula of half-ellipse are applied to estimate volume (564). The authors have applied the formula to 125 Chinese women and reported a mean measurement deviation of 3.89% (564). This is reproduced by Bulstrode *et al*, demonstrating its high correlation with mammogram-derived volume measurements (R^2 = 0.830) (530). However, the Qiao formula is more appropriate for smaller conical-shaped breasts and its accuracy is significantly reduced in hypertrophic cylindrical breasts (566). In 2013, Longo *et al* have introduced the BREAST-V formula that has been derived by correlating anthropomorphic measurements against mastectomy specimen weight in 88 women undergoing modified radical mastectomy (536). It is a relatively simple and objective method only requiring 3 parameters. The authors demonstrate that the formula is significantly superior to the Sigurdson formula from their own experience (R^2 = 0.73 vs 0.55). However, it remains to be validated in a larger trial.

Major advantages of direct anthropomorphic measurements are that they are relatively easy to perform, cheap, require minimal apparatus, and can be measured with patient standing up. However, since most mathematical formulae used rely on imposing certain geometrical shapes on to breasts, they ignore the wide variability and individuality in breast shapes. Furthermore, most anatomical landmarks chosen as parameters can be subjective and arbitrary. Where anatomical landmarks and submammary regions are not well-defined, accuracy can be significantly compromised (571).

Imaging

2D Imaging

Various 2D imaging modalities have been utilized, from which anthropomorphic variables can be derived and estimate breast volume, mainly mammography (537), 2D photography (590, 591), and 2D ultrasound (538) (Table 12.3.1.2.1). A major advantage of utilizing imaging is that measurements and calculations can be conducted away from the patient, which can lead to objective assessment and standardization. Furthermore, imagings like mammograms are already being performed routinely for breast cancer screening (592). Applying parameters of the mathematical formula of cone on mammograms, volumes can be estimated to the accuracy of 1.09-3.15% (567). Unsurprisingly, due to radiation exposure, it is the least acceptable volumetric analysis tool by the patients (530) and is not indicated for utility in benign breast conditions, such as Poland syndrome. Brown *et al* have utilized 2D photographs, to which they have applied the Qiao formula and calculated volume (565). However, 2D photographs fail to adequately demonstrate depth and shape, which significantly limits its accuracy (593). Similarly, an ultrasound probe has been used to scan a breast on either sagittal or transverse slices, from which an “area” of the breast is calculated and summed to yield a volume (538). However, it has a mean measurement deviation of 8% (538).

3D Imaging

In contrast to other breast volumetric analysis techniques, the conventional 3D imaging modalities, such as computed tomography (CT) and magnetic resonance imaging (MRI), enable visualization of internal structures leading to potentially more accurate estimation of the breast parenchymal volume (Table 12.3.1.2.1) (35, 530, 534, 539, 540, 555, 556, 558, 562, 569, 594-596). Furthermore, CT and MRI data are usually readily available since they are routinely performed as preoperative planning tool in autologous breast reconstructions and for diagnosis of breast cancers, respectively. Using a computer software either manually by an operator or automatically by an underlying mathematical algorithm, a region of interest encompassing the breast tissue can be segmented on individual axial slices. Given that all slices have equal thickness, the sum of all segmented volumes indicate the total parenchymal volume. Kim *et al* have compared the modalities and demonstrated that MRI is more accurate than CT in determining the volume of the resected breast tissue (0.928 vs 0.782, $P = 0.001$) and the final autologous flap (0.959 vs 0.873, $P = 0.001$) (540). Moreover, MRI has a reported mean measurement deviation of only 4.3% (596). This is most likely related to the superior soft tissue resolution in MRI.

Furthermore, CT scans involve radiation exposure, making them an unattractive option. In contrast, MRI does not involve radiation or require the use of intravenous contrast, and it can be performed in prone position facilitating accurate definition of the breast boundaries and its shape. Major disadvantages of MRI are its cost ($1,400 per scan) (558), it is time-consuming, and is contraindicated in patients with claustrophobia. Moreover, segmentation on imaging softwares are still mostly conducted manually, which is labor-intensive, and evidences supporting commercially available automatic segmentation tools are scarce (35, 273).

3D Surface Imaging

3D surface imaging is the latest and the most extensively studied technique of breast volumetric analysis (Table 12.3.1.2.2). It describes a technology where the light reflected off a surface is captured to build a virtual 3D model, from which both quantitative and qualitative analysis of volume and shape can be deduced. 3D surface scanning has been utilized in the automotive and aerospace industry for decades where accuracy is paramount. One of the first uses of this technology in medical application has been evaluation of facial asymmetry in orthognathic conditions (597-602). In breast evaluation, Galdino *et al* have first used 3D surface scanners to quantitate parameters, such as volume and shape, to assess symmetry (526). Interestingly, a follow-up study by the same authors fail to show any clinical improvement in achieving volumetric symmetry after autologous breast reconstructions despite using 3D scanners during preoperative planning (603). However, the authors note that the approach was not standardized and the anatomical landmarks were inconsistent (603).

Early 3D surface imaging techniques utilized by clinicians have been cumbersome and unreliable, such as image-subtraction technique (604), liquid-crystal scanning (605), light-luminance scanning (606), basic laser scanning (607-609), stereolithography (610), video system (611-614), and moiré topography (615-617). Recent advances in optical imaging systems and software developments facilitated by growing databases of anatomical profiles, 3D surface scanning has become more accurate and reliable, and the patient protocols have become simplified (560, 618, 619). For clinical application, laser imaging, structured light and stereophotogrammetry 3D scanning techniques have been most commonly studied (Table 2).

Laser Imaging Technique

The latest laser imaging technology projects a certain pattern of laser (i.e. spot and stripe) to a surface, which is captured by a calibrated camera placed at a known triangulation distance from the laser source (570). Triangulation is a mathematical calculation used to derive at 3D coordinate (i.e. *x*, *y*, and *z*) of a point on the object surface where the laser has hit (619). In contrast to the optical techniques, laser scanning technology can produce a more regular grid of points (570). However, it is less sensitive to edge effect, occlusion, and sharp transition in depth (570). One of the limitations of laser scanners is their inability to differentiate the posterior surface of the breasts from the chest wall and image 360 degrees. To this effect, proprietary softwares have been standardized to recognize breast boundaries according to the "mammometric" parameters defined by Tepper *et al* (620), and subsequently accurately estimate the posterior surface (541). In addition, rotating subjects on a turntable to image 360 degrees, as seen with inanimate objects in industrial practice, is not feasible in clinical application without creating significant motion artifacts. To this effect, Tepper *et al* have demonstrated that standing patients with arms by their side in anatomical position and introducing fluorescent illumination that reduces shadowing effect improve visualization (621).

Currently, numerous commercial 3D laser scanners are available, such as Cyberware Whole Body Color 3D Scanner (Cyberware, Monterey, CA) (550, 551). However, Konica Minolta 3D scanners (Konica Minolta Inc, Tokyo, Japan) are the most extensively investigated one in the literature (525, 541, 555, 556, 571, 620-627).

Konica Minolta 3D Scanner

Konica Minolta Vivid 910 3D Scanners contain a linear laser scanner with a reported accuracy of 0.1-0.22 mm (570) and high reproducibility (541, 628) (Table 12.3.1.2.2). Kovacs *et al* report that the technique most reliably measures breast volumes between 300 and 1,600 ml (571) and it has a high correlation with MRI (556). In addition, its reliability can be improved by connecting two or more scanners together reducing motion artifacts, however, multiplying costs (541). For ptotic and hypertrophic breasts, obtaining multiple views and manually merging them together on the accompanying free computer software facilitates accurate volumetric analysis (541). Major advantages of the Konica Minolta scanners are that they are simple to operate, require no calibration, have a fast

capture and processing speed, and are portable (11kg). However, its price (USD 20,000-100,000) is a significant drawback, especially where more than one devices are necessary. To date, Konica Minolta scanners have been used to facilitate preoperative planning and postoperative monitoring in implant breast reconstruction (626), reduction mammoplasty (626), and breast augmentation (627).

Structured Light Technique

When an organized pattern of light (i.e. stripe, grid, and dots) is projected on to an object, it becomes distorted in a predictable manner. Structured light technology utilizes a camera system calibrated to the predicted distortion of the light patterns to capture and generate a 3D surface data (618, 629). Placing cameras at two separate viewpoints further eliminates pattern interference (618). Numerous non-commercial devices, such as MTV camera (Mintron, New Taipei City, Taiwan) (630), Daly Shape Measurement System (631), Malata Bodymap System (632), and Precision Light Imaging System (633, 634), and commercial units, such as CAM3D (3D-Shape, Erlangen, Germany) (552), C3D (C3D, Beirut, Lebanon), Voxelan (Hamano Engineering, Kanagawa, Japan) (557), and Rainbow 3D Camera (Genex Technologies Inc, Kensington, MD) (526), have been described. However, the most frequently studied structured light device is Axis Three scanner (Axis Three, Miami, FL).

Axis Three Scanner

Axis Three Torso System extrapolates 3D data using color-coded triangulation (CCT^{TM}) technique conceived from collaboration between Axis Three and Siemens (Siemens Technology Accelerator, Munich, Germany) (Table 12.3.1.2.2). CCT^{TM} consists of sequential firing of images from three separate cameras and has a reported accuracy of 0.05 mm. The system requires calibration (less than 5 min) every time it is physically relocated and has a relatively slow capture (2 sec) and processing speed (30 sec). Interestingly, Axis Three has developed a physics-driven tissue behavior simulation (TBS) software program using its database of real patients. Furthermore, a physician can individualize the tissue elasticity to the patient in real-time while navigating the program in a consulting room. An initial report suggests that the software quality may be compromised due to the relatively slow image acquisition speed of the hardware (619). Studying 22 patients undergoing breast augmentation, Mailey *et al* demonstrate that mean difference

between the simulation and the actual outcome is 12% (0.4-30%), but the system still has high reproducibility (correlation coefficient of >0.8). To date, more studies are required to validate this technology.

Stereophotogrammetry

Stereophotogrammetry is an imaging method similar to the human eye physiology where a stereo pair of cameras shoots a single object from multiple angles and their points of intersections are recorded (619, 635, 636). 3D surface data is rendered using triangulation technique where 3D coordinates are calculated for each 2D surface points. Depending on the presence of an additional light source being projected on to the object, stereophotogrammetry technology can be classified into active, passive, and hybrid (560).

Active Stereophotogrammetry

In active stereophotogrammetry, the surface information is gathered from two sources: random, unstructured light being projected on to the object and natural reflections from the innate patterns on the object's surface. The inclusion of projected light makes it easier for the software to compute triangulation and resists interference from ambient lighting. The most frequently studied commercial device using active stereophotogrammetry is JRCB-D 3D scanner (Jirui, Beijing, China) (197, 543, 572, 637).

JRCB-D Scanner:
JRCB-D system consists of two paired cameras that capture light illuminated by a grating projector (Table 12.3.1.2.2) (543). The standard protocol requires patients to stand leaning against a flat wall and their hands on the anterior superior iliac spine, also known as akimbo. The wall is also captured and analyzed to help generate the *x-y* Cartesian plane. Using ideal models from virtual breast augmentation, Liu *et al* demonstrate that a JRCB-D scanner calculate volume to 1 ml accuracy and its analysis is reliable (interclass coefficient of 0.9999) (572). Interestingly, the same group reports that maintaining patients in the same respiratory state during image capture is also critical (197). To date, the technology has been used for preoperative assessment (543) and postoperative monitoring in breast augmentation (637).

Passive Stereophotogrammetry

A 3D imaging system using passive stereophotogrammetry lacks the projected light source and relies alone on the natural reflections from the innate patterns on an object's surface. As a result, a requirement for high-quality cameras is crucial to achieving adequate detail. Similarly, choosing an object to visualize that has sufficient surface textures (e.g. pores, freckles, scars, and rhytids) is essential. Furthermore, ambient lighting must be carefully controlled and identifying 3D coordinates for triangulation by the software is comparably more difficult. The most commonly used commercial passive stereophotogrammetry devices are VECTRA scanners (Canfield Scientific, Fairfield, NJ) (544, 573, 638) and Di3D scanners (Dimensional Imaging, Glasgow, Scotland) (545, 553, 574, 639, 640).

VECTRA Scanner:

VECTRA XT scanners are modular 3D imaging systems equipped with three stereo pods containing two color single-lens reflex (SLR) cameras each. These are capable of capturing high-resolution photos at a fast speed (3.5 milliseconds) (Table 12.3.1.2.2). VECTRA systems are accompanied by two types of softwares. Mirror® medical imaging (Canfield Scientific, Fairfield, NJ) is a well-respected patented program that simulates surgical procedures on 2D photographs. Canfield Sculptor® is the latest suite of programs that enables tissue simulation on 3D reconstructed surface images. Namely, the Breast Sculptor® software is capable of performing automatic measurements and simulate outcomes of virtual breast augmentation procedures. Using faces of normal adult subjects, de Menezes *et al* report that VECTRA scanners are accurate with low mean measurement error (<1 mm) and are reliable, as demonstrated by negligible intra- and inter-observer variability ($P > 0.05$) (544). Similarly, Rosati *et al* show that using VECTRA scanners to compare measurements on virtual dental models to in vivo, the estimate of error is less than 1.2% and there are also no significant differences between repeated measurements (573). In a single-blinded study, Roostaeian *et al* have compared the software simulation to the actual patient measurements after primary breast augmentation procedure and demonstrate a mean accuracy of 90.8% (549). Moreover, VECTRA scanners have been used to illustrate the "bottoming out" phenomenon after breast reduction (638). Major limitations of VECTRA systems are its high cost, relatively slow image processing speed, and lack of portability (Table 2).

Di3D Scanner:

Di3D scanners utilize four high-quality digital SLR (DSLR) cameras, Canon EOS 550D (Canon Inc, Tokyo, Japan), to generate ultra high quality 3D images (Table 12.3.1.2.2). The system has been used extensively in the entertainment industry by video game producers. Unique features of Di3D include the optional capability in the proprietary software that combines CT scan data with the 3D surface images, and the revolutionary 4D imaging technology by Di4D (Dimensional Imaging, Glasgow, Scotland) that captures dynamically changing anatomical structures. Earlier studies using Di3D scanners on facial models have shown that its accuracy is clinical acceptable and reliable (repeatability error of 0.0016 mm) (574, 639). In a comparative study using cadaver heads, Fourie *et al* demonstrate that Di3D system is as accurate and reliable as Konica Minolta laser 3D scanners and CT scans (640). Catherwood *et al* are the first to report its use on breasts demonstrating that it is reliable (interclass coefficient of 0.999) and the linear measurements derived from the 3D surface data are accurate (<0.5 mm) (545). To date, no clinical application of this technology in breast surgery has been reported.

Hybrid Stereophotogrammetry

Hybrid stereophotogrammetry combines active and passive stereophotogrammetry to achieve higher accuracy and image quality. Currently, the most well-studied hybrid scanner is 3dMD scanner (3dMD, Atlanta, GA) (455, 546, 553, 575, 586, 641-645).

3dMD Scanner:

3dMDtorso system consists of four modular units of twelve synchronized machine vision quality cameras that are of engineering and industrial standards and are superior to the regular SLR cameras (Table 12.3.1.2.2). The accompanying software has novel functions, such as the ability to track patient history and simulate soft tissue behaviors using biomechanical mass-spring method (641). Furthermore, there are optional additional softwares, such as 3dMDvultus that allows 3D image fusion with CT data and 3dMDdynamic that facilitates 4D imaging. 3dMDtorso system has a reported accuracy of 0.2 mm (0.1-0.5 mm) (575, 643) and high reliability as depicted by low intra- and inter-observer errors (1.2 and 1.0 mm, respectively) (642). Moreover, its high capture speed (1.5 millisecond) makes it resistant to motion artifacts. In breast volumetric analysis, Losken *et al* have applied 3dMD system in the preoperative work-up for skin-sparing mastectomy and demonstrate that the mean difference between the calculated and the actual volume is only -2% and the coefficient of reproducibility is less than 0.92 (455). In

addition, Henseler *et al* report that the 3D imaging system is superior to the traditional water displacement technique in accuracy ($P \leq 0.017$) and reproducibility (36 vs 62.6 units/cc) (553). To date, clinicians have utilized 3dMD scanners to demonstrate baseline breast asymmetry in 87 normal women (586) and study the compressive effect of implants on breast volume after augmentation (546). Significantly, in the latter study, the authors report no difference between the imaging-derived expected breast volume and the actual augmented volume ($P = 0.3483$) (546). Despite its fast processing speed and mobility, a major limitation of the imaging system is related to its high cost.

Novel 3D Imaging Technologies

Crisalix

Crisalix (Crisalix, Lausanne, Switzerland) is the first, web-based 3D imaging technology that generates 3D surface data from three 2D photographs (front, left, and right) taken by patients on their own consumer cameras (Table 12.3.1.2.2). In addition, a user needs to upload the physical distance from which the photo was taken and a set of anatomical landmarks. Calculation and simulation is performed via a cloud computing storage database based in Switzerland. The program contains two simulation engines, 3D FACE Simulator (646) and 3D MAMMO Simulator (547). The latter enables a patient to examine and choose their preferred choice of breast implant size and brands prior to attending an aesthetic plastic surgeon's consultation. In eleven cases of women planning for breast augmentation, de Heras Ciechomski *et al* compared Crisalix program and a consumer handheld 3D laser scanner, EScan 3D (3D Digital Corp, New Town, CT) (547). The program performs comparably to the laser scanner and reports a mean error of 2-4 mm (547). Despite its ease of access and a reasonable price, more robust evidence is required to validate this novel technology.

4D Imaging

In contrast to static 3D imaging techniques, 4D imaging adds temporal resolution facilitating dynamic analysis of 3D structures, such as breasts (Table 12.3.1.2.2). In the literature, numerous 4D imaging systems have been used to study mainly facial animation and asymmetry (560, 578, 647). The most commonly investigated commercial 4D system has been Di4D (Dimensional Imaging, Glasgow, Scotland) (576, 577, 648) and

3dMDdynamic (3dMD, Atlanta, GA) (579, 580). Di4D Scanners consist of 2 pods with two greyscale and a color digital video camera each. Main advantages of the system are that it requires only the standard video lighting and has an inbuilt optical flow tracking capability with automatized digitization of facial landmarks to track every pixel in every image being shot. However, it remains expensive and is yet to be validated in breast surgery. The latest 3dMDdynamic body system consists of 9-22 modular units of 27-66 machine vision quality cameras and an LED-based lighting system that minimizes interference and yields smooth sequential playback. In addition, the accompanying 3dMDtempus surface tracking software helps analyze skin dynamics reliably from different positions. To date, 3dMDdynamic system has been studied in facial anatomy showing high accuracy and reliability (579). However, it has yet to be applied in breast volumetric assessment.

3D Printing

3D printing, also known as additive manufacturing or rapid prototyping, is the latest novel technology to aid clinicians, in combination with 3D imaging, for assessing breast volume (17, 18, 273, 561, 649, 650). 3D printing describes a process where a computer-aided design (CAD) is fabricated into an end product in a layer-by-layer fashion (17, 35, 182, 275, 279, 318, 397). The resultant haptic biomodel provides a 360-degree visualization and tactile feedback, enabling a superior visuospatial appreciation of the anatomy (15). In medical application, CAD files can be derived from any conventional imaging source, such as CT and MRI, or 3D surface imaging. Chae *et al* have reported a case where routine preoperative CT scan is used to calculate the breast volume differential (Figure 12.3.1.2.1) and a model of the anterior chest wall is 3D printed to enhance visualization of the asymmetry (Figure 12.3.1.2.2) (18).

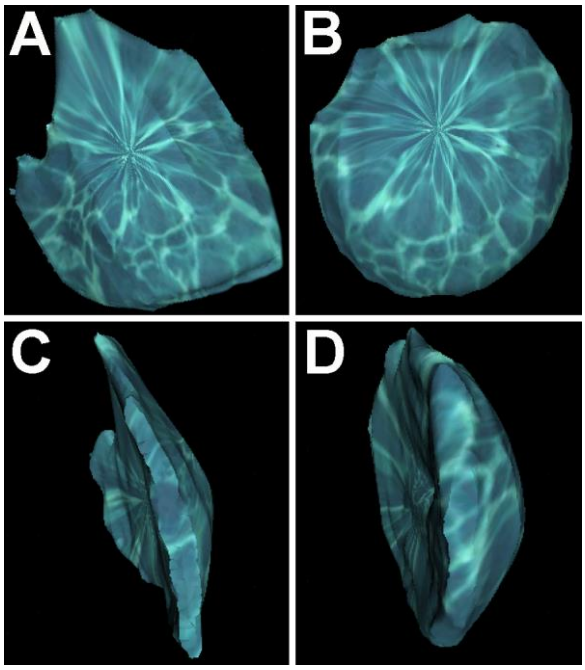

Figure 12.3.1.2.1. Volume-rendered 3D reconstructed images of breasts segmented from a computer tomographic (CT) scan using Osirix software (Pixmeo, Geneva, Switzerland), from which volume differential can be calculated. A: anterior view of the right breast; B: anterior view of the left breast; C: lateral view of the right breast; D: lateral view of the left breast. Reproduced with permission from Chae *et al* (35).

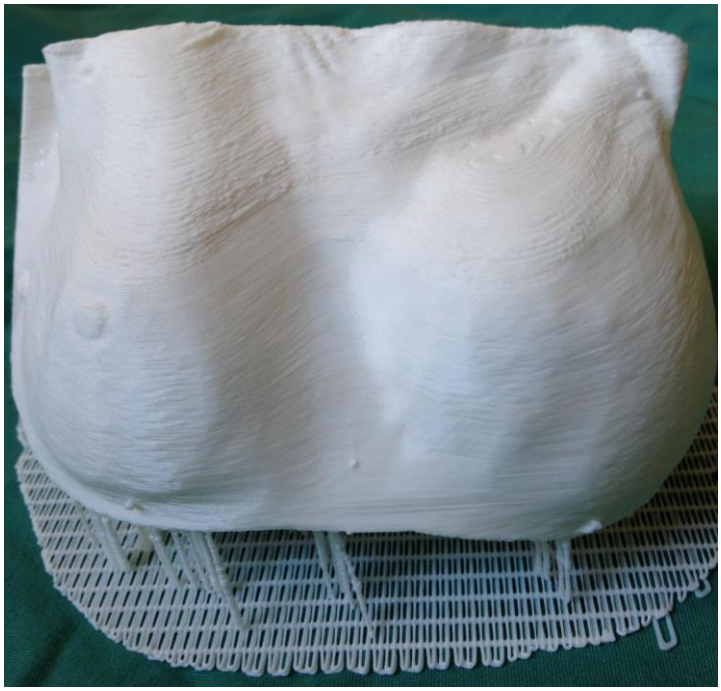

Figure 12.3.1.2.2. 3D printed haptic model of the breasts in Figure 12.3.1.2.1 using Cube 2 printer (3D Systems, Rock Hill, SC) and polylactic acid (PLA) filaments. Reproduced with permission from Chae *et al* (35).

As 3D printing becomes more affordable and intuitive to use by physicians, combining 3D printing and 3D imaging may revolutionize preoperative planning in breast reconstruction and the manufacturing of customized breast implants (273, 561, 649, 651).

Recently, the concept of 4D printing has been described, in which the fourth dimension, time, is incorporated into the conventional 3D printing by utilizing 4D CT scan data (276). The technique of 4D CT has been initially developed to minimize motion artifacts and enhance the image quality of lungs for accurate assess of lung tumor volume and planning precise delivery of radiotherapy (652). Moreover, using the previously described “single volume acquisition” scanning method, overexposure to radiation is prevented and the overall dose is reduced to 1.78 mSv, equivalent of three plain abdominal x-rays (141). In addition to respiratory medicine, 4D CT has been used in breast cancers, renal tumors, and pancreatic cancers (653-655). In plastic surgery, clinicians have used 4D CT mainly to study perforator vascular dynamics (169, 425, 656). In 2015, Chae *et al* have used 4D CT for 4D printing the bones of the thumb ray to depict the translation of metacarpal bones during various thumb movements and validated their technique (276). To date, 4D printing has not been applied in breast volumetric analysis. However, studies are currently underway to investigate dynamic changes in breast volume by 3D printing breasts during movement of the arm and torso.

Conclusion

Accurate volume measurement is an integral part of preoperative planning in both reconstructive and aesthetic breast procedures. Before the introduction of 3D scanning, most previous methods have been unreliable, difficult to execute, and had limited practicability. 3D surface imaging has revolutionized the field with its ease of use, reliability, fast speed, and improving portability. However, it is not yet being used widely due to its high cost and lack of published high level of evidence. Recently, interesting advancements and adjuncts to 3D scanning have been introduced, mainly the first web-based 3D surface imaging program, 4D imaging, and 3D printing.

12.3.1.3 Imaging-Based Perforasome Visualisation

Chapter Summary

Introduction: Perforator flaps are widely used in reconstructive plastic surgery and technological advances in preoperative imaging have facilitated improvements in flap perfusion and clinical outcomes. The 'perforasome' concept describes the vascular territory supplied by a single arterial perforator and the imaging of these zones of perfusion has become increasingly advanced.

Methods: This paper presents a qualitative analysis of the current literature on perforasome imaging. A review of the literature was performed using PubMed and Medline. Historical and background studies were also included for completeness.

Results: The review identified an initial 858 records for assessment, with 52 studies formally reviewed. To date, there is largely level III and IV evidence for the available imaging techniques, although level II studies are emerging. There is currently no level I evidence for any imaging technique.

Conclusion: There have been significant developments in imaging techniques since the introduction of the perforasome concept nearly a decade ago. In this review we have described the evolution of these methods over time, from simple perforator location to advanced three- and four-dimensional imaging and real-time dynamic perfusion imaging. With this progression and ongoing innovation, we believe perforasome imaging has the potential to improve outcomes in perforator flap surgery.

Introduction

Perforator flaps are widely used throughout reconstructive surgery. From pedicled 'free-style' perforator flaps in lower limb reconstruction, to free perforator flaps in breast reconstruction, the micro-dissection of perforators as the basis for flap vascularisation is routinely performed. An understanding of flap perfusion is essential and imaging techniques continue to evolve in order to better demonstrate this anatomy. Early imaging techniques in perforator flap surgery only focused on identifying the location and calibre of perforators, however, greater sophistication in both imaging and flap design has led to a clinical need to map the perfusion zones of individual perforators thus, facilitating favourable surgical outcomes in flap reconstruction.

The perforasome concept describes the vascular territory supplied by a single arterial perforator and is an evolution of the angiosome concept described and imaged in 1987 by Taylor and Palmer (478). Since those initial descriptions of the perforasomes by Saint-Cyr et *al* (657) and Rozen *et al* (425) nearly a decade ago, several studies have employed various methods to explore and describe these territories, with varying efficacy.

The current paper comprises a review of the evolving techniques for mapping perforator territories, used in varying capacities as a means to successful perforator flap design, reduction of fat necrosis and peripheral flap ischaemia. As yet, no imaging technique has been identified as the 'ideal' perforasome imaging method, making this an exciting time to be at the forefront of this emerging field of discovery.

Methods

This article presents a qualitative analysis of the current literature on perforasome imaging. A literature review of PubMed and Medline was performed using a combination of the key words ‘perforasome’, ‘perforator angiosome’, ‘perforator flap’, ‘perfusion’ and ‘imaging’ and limited to English language studies of humans published in the period 1980–2017. Additional references were identified through bibliographic linkage were also considered. A total of 858 articles were identified.

Articles were excluded if they did not specifically describe or focus on a perforator or perforasome imaging technique. Studies that did not meet inclusion criteria but were relevant for historical reasons were included in the discussion but not in the formal review.

Results

After exclusions, 51 studies met criteria for inclusion in this review (Figure 12.3.1.3.1).

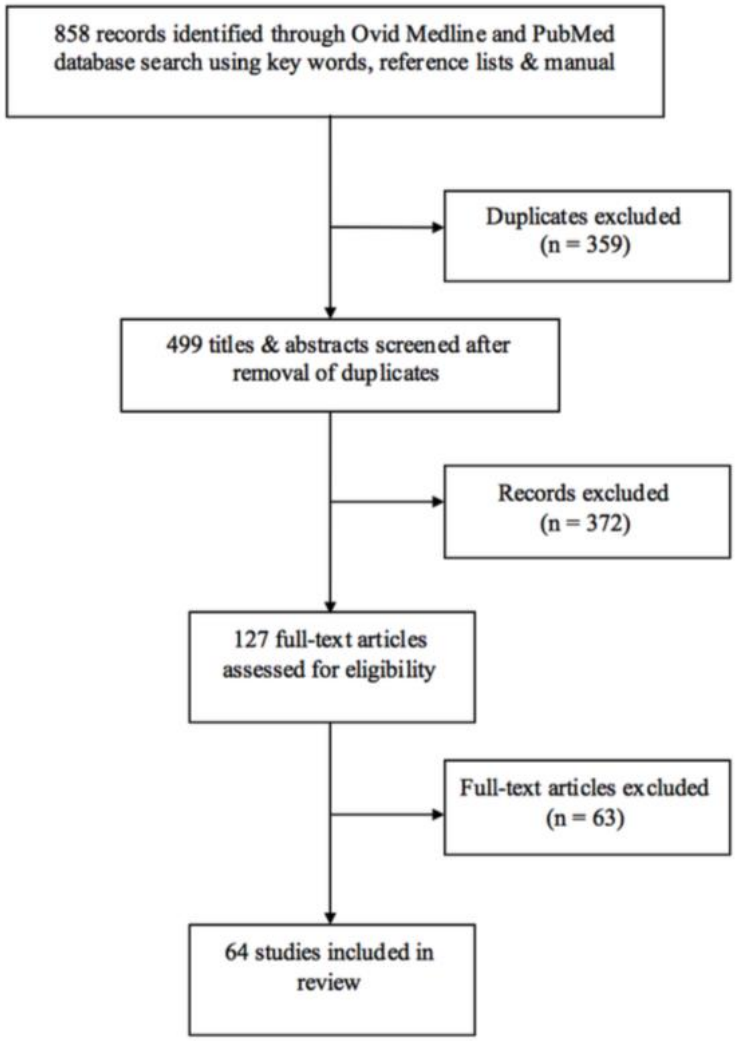

Figure 12.3.1.3.1. PRISMA attrition flow diagram (36)

Six imaging techniques were discussed within these studies (Table 12.3.1.3.1).

Imaging Technique	**Number of Included Studies**	**Highest Level of Evidence* & Study Type**				
		Diagnostic	Therapeutic	Cadaveric, Experimental	Pre-operative Clinical	Intra-operative Clinical
Handheld Doppler	6	IV	II			
CDU	9	IV	III			

CTA	19	II	III			
MRA	12	III	III			
DIRT	7	II	II			
ICG Angiography	11	III	III			

Table 12.3.1.3.1. Demographics of included studies. *: based on the American Society of Plastic Surgeons Rating Levels of Evidence and Grading Recommendations. Abbreviations: CDU: colour Doppler ultrasound; CTA: computed tomographic angiography; MRA: magnetic resonance angiography; DIRT: dynamic infrared thermography; ICG: indocyanine-green.

To date, there is mostly level III and IV evidence for these techniques, although level II studies are emerging. There is currently no level I evidence for any imaging technique. Table 12.3.1.3.1 also categorises the study types, which explore these techniques. This paper addresses established perforator imaging techniques and subsequently, their potential for application to perforasome imaging.

Perforator Imaging Techniques

Doppler Sonography

While not strictly an imaging technique, hand- held Doppler ultrasound has long been used to locate perforators in flap planning (166). This use of sonography has significant limitations, such as both high false-positive (658, 659) and false-negative rates (659, 660), lack of information regarding calibre, flow volume (659) and perforator course (661), and operator dependence (662). However, the method is cheap, simple to use, non-invasive and risk-free for the patient and can be used in conjunction with preoperative imaging.

Colour Duplex Ultrasonography

Colour duplex ultrasonography holds many of the benefits of hand-held Doppler while providing more information on the flow volume, calibre and course (659) of perforator vessels. Its accuracy is superior to hand-held Doppler (658, 659, 663), given its added ability to visualise vessels. Other studies show CDU to be inferior to CTA for identifying

perforators in the abdomen (8, 80), though Feng *et al* describe CDU as having higher accuracy than CTA in mapping of perforators in the lower extremities (664). Notably, contrast-enhanced ultrasonography plus three-dimensional reconstruction has been reported to increase accuracy and precision (665) when compared with regular CDU and hand-held Doppler.

While CDU involves no radiation exposure and is negligibly invasive, it only gives two-dimensional detail, cannot display perforator branching networks and other relevant vessels (80) and it is operator-dependent (662). However, preoperative sonography is routinely used (666).

Computed Tomographic Angiography

Computed tomographic angiography is generally accepted as state-of-the-art for perforator visualization (72, 667). Its high accuracy (8, 12, 96, 97, 117, 118) and excellent image quality mapping of location, calibre, course and branching of a perforator (8, 13) have led to reduced operation times and fewer postoperative complications (13, 668).

As the first technique to produce highly detailed perforator images (667), CTA is well-studied as a preoperative perforator visualisation technique in multiple types of perforator flaps. While CTA requires radiation exposure and an iodinated contrast injection, there are many benefits. It is affordable, accessible and operator-independent, gives significant detail on perforator anatomy and can visualise small vessels to 0.3 mm in diameter (669). Additionally, CTA has better fat-to-vessel contrast than MRA, allowing easier mapping of a perforator's subcutaneous course, though intramuscular course is clearer on MRA (316, 670).

Another feature of CTA is its potential for three- dimensional image processing (671), such as volume rendering reconstruction (72), which can facilitate interpretation of scans and provide visual representations of perforator location and course.

Given CTA's main and significant disadvantage is its use of contrast and radiation (13, 316, 668), there has been investigation into using lower doses of both (672). Several studies have found that low-dose techniques achieve high-quality vascular imaging similar to conventional CTA (672, 673).

Overall, CTA is an excellent resource for preoperative perforator imaging with continuing developments to mitigate the risks of iodinated- contrast and radiation exposure.

Magnetic Resonance Angiography

Magnetic resonance angiography provides a three- dimensional image of perforator vessels but often using safer, non-iodinated contrast-enhancement. There are several contrast agents that provide varying levels of resolution. With the development of blood-pool contrast agents such as Gadofosveset (also known as Ablavar™ or Vasovist™), MRA can clearly depict perforator intramuscular course due to its superior muscle-to-vessel contrast ratio (316, 670). Kagen *et al* (674) reported that MRA produces a high-resolution image with similar spatial resolution to that of CTA.

Newman et al found high sensitivity and specificity of MRA in identifying perforators (124), and a review by Saint-Cyr *et al* showed that MRA and CTA were essentially equal in preoperative location of perforators (136). Another paper by the same group also illustrated that MRA has high concordance with intraoperative findings and decreases partial flap failure rates (675).

Equilibrium-phase MRA is reported to be superior to first-pass MRA at visualising perforators (127, 145).

A significant advantage of MRA over CTA is its use of magnetism rather than radiation, though this precludes the use of MRA in patients with metal implants. As with CTA, however, there is no operator dependence.

The disadvantages of MRA compared with CTA include cost, poorer accessibility, longer scanning time (and the potential for artefacts), decreased image quality in overweight patients and a slightly lower accuracy for deep inferior epigastric artery (DIEA) branching detection (97). Despite Kagen *et al*'s findings (674), other studies have shown that MRA lacks the ability to show smaller vessels (676) and that currently, CTA image quality is superior to MRA (96, 316).

Yang *et al* (677) investigated the novel concept of magnetic resonance-based perforator phase contrast angiography, reporting that it was superior to CTA in image quality, vessel contrast and accuracy of perforator anatomy.

Magnetic resonance angiography is a worthwhile alternative to CTA, especially when iodinated- contrast and radiation are contraindicated. It is increasingly used for its lower risk profile and is being constantly improved as contrast options and technologies evolve.

Dynamic Infra-Red Thermography

Dynamic infra-red thermography technology in preoperative perforator location has limited evidence (676). Involving cooling of the skin followed by infra-red imaging as the skin re-warms (678), the resulting thermogram displays 'hotspots' which signify perforator location (679). It is therefore non-invasive, with no radiation or contrast exposure. There are varying levels of camera resolution available (680).

Several papers have shown that DIRT accurately identified perforators with some postulating that DIRT's true accuracy is higher than that of hand-held Doppler (678, 679, 681). Chubb *et al* reported that DIRT matched the accuracy of CTA in perforator identification (682).

As with Doppler techniques, DIRT lacks the three-dimensional information on perforator calibre and course (678, 679). Additionally, thermograms only show hotspots for perforators that transport blood to the dermis, meaning that a suitable perforator that ends in the subcutaneous tissue may be missed with DIRT (678). This perhaps limits its use alone as the sole preoperative imaging technique.

At this stage DIRT is a useful adjunct in perforator imaging.

With the introduction of the 'perforasome' concept by Saint-Cyr *et al* (657) and Rozen *et al* (425), the features and capabilities of these perforator imaging techniques have become even more important. Both studies utilised CTA in cadavers to assess the perforasome. Saint-Cyr *et al* investigated perforasomes in anterior and posterior trunk flaps and in upper and lower extremity flaps. Rozen *et al* focused on the perforasomes of the DIEA perforator flap and also conducted a clinical, in-vivo, CTA study into the course, calibre and

branching of the DIEA perforators. Although comprehensive, these studies focused on broadly defining the general characteristics of perforasomes and, while Rozen *et al* included a clinical component to their study there was limited exploration of the techniques of perforasome mapping in vivo. Currently, several perforator imaging methods suitable for in-vivo mapping of the perforasome exist. These methods can be categorised as preoperative or intraoperative.

Perforasome Imaging Techniques

Computed Tomographic Angiography

Computed tomographic angiography perforasomes mapping in cadavers has been well-studied but significantly less so in-vivo. Predominantly, in vivo preoperative CTA is used to locate a perforator vessel with limited consideration of vascular branching patterns. However, a well-developed vascular network is often preferred when selecting a source perforator vessel using CTA (678, 683). Rozen *et al*'s (425) clinical study assessed branching patterns of medial and lateral row perforators but there has been little investigation into the in-vivo mapping of perforasomes based on perforator branching networks using CTA. It stands to reason that this would follow similar principles as cadaveric.

Compared with perfusion-based perforasome imaging techniques, a disadvantage of preoperative CTA is its static nature and possible underestimation of actual perfused territory.

CTA currently has the capability to preoperatively visualise perforator branching networks and inter-perforator zones in vivo (Figures 12.3.1.3.2 and 12.3.1.3.3) but requires further investigation.

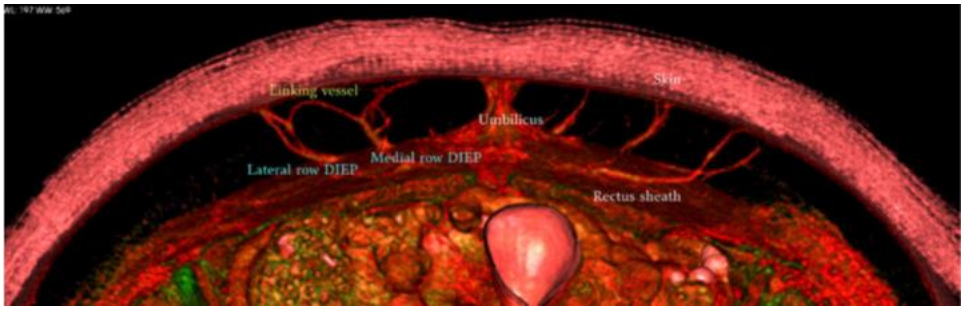

Figure 12.3.1.3.2. A 3D volume-rendered reconstruction from an axial slice CTA of the abdomen, showing DIEA perforators and a true anastomosis linking a medial and lateral row perforator.

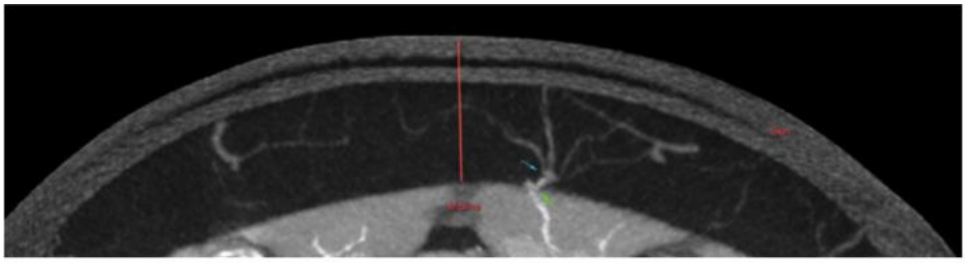

Figure 12.3.1.3.3. Axial slice CTA image of the abdomen with maximum intensity projection, illustrating a left hemi-abdomen medial row perforator vessel and its branches. The green arrow shows the perforator's exit point from rectus sheath; the blue arrow shows the primary branching point.

Indocyanine Green Angiography

Indocyanine green angiography (ICG) is an intraoperative imaging technique involving the intravenous injection of fluorescent indocyanine green dye and laser or infra-red photography, resulting in an image showing the perfusion of the perforator and its branches.

ICG was originally used in cardiothoracic surgery before its application to microvasculature in the free flap transfer (128, 684, 685). The advantage of this real- time perfusion imaging is the ability to dynamically assess flap perfusion and identify viable flap tissue (88), allowing resection and modification of the flap intraoperatively (686, 687), which may reduce post-operative flap necrosis (128, 686, 688). ICG angiography can also confirm the integrity and flow through of inter-perforator zones (316, 676).

ICG's short half-life allows for multiple evaluations (689) and minimal impact on surgical time, though the technique is costly (316, 690).

As a preoperative *perforator* imaging technique, ICG angiography has limited application (88, 686, 690) and is unable to show deeper anatomy (88, 676, 690), rendering it inadequate for flap-planning in fatty tissue (689).

More research is required to ascertain parameters of hypo-perfusion, but ICG angiography shows promise in dynamically assessing perforasomes intra-operatively.

DIRT

As a perforasome mapping technique, DIRT can be used preoperatively in flap planning and intraoperatively to assess flap viability.

On a thermogram, the perfusion territory of a perforator is indicated by the 're-warming' areas surrounding the hotspot (680) and the rate and pattern of re-warming may provide information on the haemodynamic properties of a perforasome.

Chubb *et al* (681) and Taylor *et al* (691) use DIRT to map both the perforasome and the inter-perforator zone, quantitatively showing that the re-warming of a perforasome fits a logarithmic curve. They hypothesise that inter-perforator zones with rapid re-warming that also resemble this logarithmic curve are more robust linking vessels than those that display slow re-warming and do not fit this curve (681).

A disadvantage is DIRT inability to measure perfusion of subcutaneous tissue (678), which may impact rates of postoperative fat necrosis.

Discussion

The angiosomes of the body were detailed and mapped by Taylor and Palmer in 1987 (478), providing the anatomical basis of our understanding of vascular territories today. Their studies were undertaken in cadavers, using dye, lead oxide and X-ray imaging. They defined an angiosome as a composite block of tissue supplied by a named source artery and showed true and choke anastomoses (or direct and indirect linking vessels (657)) between adjacent angiosomes (478). More recently, Taylor further explored these anastomoses with angiosome mapping in animals, using lead oxide and radiographic images in cadavers and fluorescein and ink in vivo (692). He described choke anastomoses (indirect linking vessels) as reduced calibre vessels, and the most common inter- connection. Less frequently, a true anastomosis (or direct linking vessel) exists between angiosomes, and this linking vessel is of the same calibre as the vessels it joins (Figure 12.3.1.3.2). These anastomoses control flow between angiosomes and hence flap design should be dictated by the type of linking vessels present (692). Interestingly, choke anastomoses can be converted to true, via hyperplasia, after hyper-perfusion in the setting of flap reconstruction (692). These findings may be applied to perforasomes and have significant implications in perforator flap reconstruction, especially if the discussed imaging techniques can be applied to inter-perforator zones and the assessment of anastomotic calibre.

With a growing number of ways to visualise perforasomes, the condition under which imaging is performed becomes increasingly important. First, in vivo imaging is subject to various factors that affect vessel behaviour and hence impact the picture of perfused territory produced. Thermal, hormonal and neuronal (693) elements can all influence perfusion zones by altering the dilatation and calibre of vessels. Cadaveric imaging, in contrast, is not influenced by these dynamic factors, leading to a different perforasome image than when carried out in-vivo. Similarly, pre-, intra- and post-operative imaging can each lead to slightly different perfusion pictures due to neuronal, hormonal, thermal and pressure differences.

Finally, a note on nomenclature of the perforasome and its imaging. The generally accepted definition of a perforasome, as mentioned in this review, is the territory supplied by a single perforator and its branches, the border being at the inter-perforator zone. Taylor et al summarise that this is the *anatomical* territory of a perforator, defined by a line

drawn through the anastomotic zone, while the *clinical* territory of a perforator comprises the *anatomical* territory as well as the adjacently- perfused perforasomes (694).

Conclusion

Significant developments in imaging techniques have occurred since the introduction of the perforasome concept nearly a decade ago. These imaging techniques each offer different information on perforasomes and have been investigated in many environments — cadaveric, invivo, pre- and intraoperatively. In this review, we have illustrated the evolution of these methods from simple perforator location to advanced three-dimensional imaging and real-time dynamic perfusion imaging.

In plastic and reconstructive surgery, the purpose of imaging the perforasome ultimately lies in the reduction and postoperative complications in perforator flap reconstruction and consequently an improvement in outcome measures such as flap loss and fat necrosis. While further research into newer techniques and their translation into clinical outcomes are required, it is clear that with advances and ongoing innovation, perforasome imaging has the potential to improve patient outcomes in perforator flap surgery.

12.3.2 Prospective Clinical Studies

12.3.2.1 Preoperative Volumetric Analysis Using 3D-Printed Breast Model

PUBLISHED (Publication): ***Chae MP***, Hunter-Smith DJ, Spychal RT, Rozen WM. (2014) 3D volumetric analysis for planning breast reconstructive surgery. Breast Cancer Res Treat. 146(2), 457-460. PMID: 24939062

Chapter Summary

Introduction: Breast reconstruction plays an integral role in the holistic management of breast cancer, with assessment of breast volume, shape, and projection vital in planning breast reconstruction surgery. Current practice includes two-dimensional (2D) photography and visual estimation in selecting ideal volume and shape of breast implants or soft-tissue flaps. Other objective quantitative means of calculating breast volume have been reported, such as direct anthropomorphic measurements or three-dimensional (3D) photography, but none have proven reliably accurate. We describe a novel approach to volumetric analysis of the breast, through the creation of a haptic, tactile model, or 3D print of scan data.

Methods: This approach comprises use of a single computed tomography (CT) or magnetic resonance imaging (MRI) scan for volumetric analysis, which we use to compare to simpler estimation techniques, create software-generated 3D reconstructions, calculate, and visualize volume differences, and produce biomodels of the breasts using a 3D printer for tactile appreciation of volume differential.

Results: Using the technique described, parenchymal volume was assessed and calculated using CT data. A case report was utilized in a pictorial account of the technique, in which a volume difference of 116 cm3 was calculated, aiding reconstructive planning.

Conclusion: Preoperative planning, including volumetric analysis can be used as a tool to aid esthetic outcomes and attempt to reduce operative times in post-mastectomy breast reconstruction surgery. The combination of accurate volume calculations and the production of 3D-printed haptic models for tactile feedback and operative guidance are

evolving techniques in volumetric analysis and preoperative planning in breast reconstruction.

Introduction

Breast reconstruction plays an integral role in the holistic management of breast cancer, with assessment of breast volume, shape, and projection is vital in planning breast reconstruction surgery. This analysis is for the ipsilateral breast in immediate reconstruction cases, or the contralateral breast for symmetry in delayed reconstruction. Current practice includes two-dimensional (2D) photography and visual estimation in selecting ideal volume and shape of breast implants or soft-tissue flaps. This subjective method is limited by individual surgeons' experience and ability. Historically, numerous objective quantitative means of calculating breast volume have been reported, such as direct anthropomorphic measurements or three-dimensional (3D) photography, but none have proven reliably accurate (526). Other surface imaging modalities are limited by their inability to map the posterior breast surface, where individual variation in anterior chest wall contour exists. Both magnetic resonance imaging (MRI) and computed tomography (CT) have been used as imaging modalities to accurately map breast volume (388, 695), with a single CT angiogram (CTA) for flap planning able to combine breast volumetric and both donor and recipient vasculature analyses (72). These scans for volumetric analysis are performed lying supine, where breasts assume an unnatural shape. Creating a model or 3D print of scan data is a novel approach to bypassing such limitations.

Bio-modeling may provide improved accuracy in pre- operative planning and operative flap harvest. This has been shown successfully in craniofacial surgery, where stereolithographic models of both mandibular defects and planned donor sites have been performed (179), with advances in these biomodels able to incorporate vasculature (178). A limitation of these techniques is the need for out-sourcing, with lengthy production times, expensive materials, and dependence on external teams for explaining specific requirements and transportation. Both software and hardware have improved markedly, with 3D printers offering cheap and freely available hardware, readily used by reconstructive surgeons themselves. The use of 3D printing has been described in this journal recently, as a modality for printing cadaveric vascular anatomy (275), but has not been described for breast reconstruction. Further- more, software advances can now subtract skin, model chest wall contour and offer comparative analyses between sides.

Methods

The following pictorial account describes a novel method for calculating asymmetric breast volumes. This approach comprises use of a single CT or MRI scan for volumetric analysis, which we use to compare to simpler estimation techniques, create software-generated 3D reconstructions, calculate and visualize volume differences, and produce biomodels of the breasts using a 3D printer for tactile appreciation of volume differential. The following example maps a patient with breast asymmetry following right breast free flap reconstruction (Figure 12.3.2.1.1).

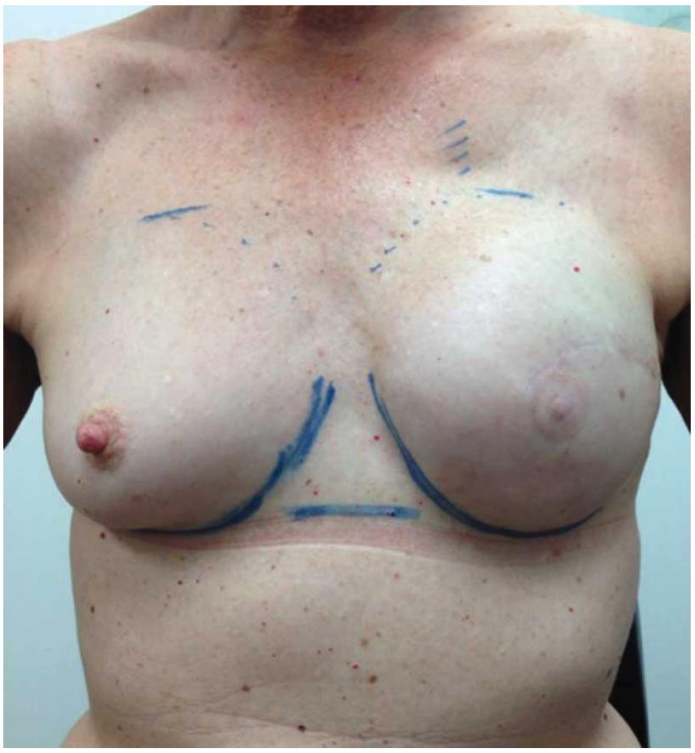

Figure 12.3.2.1.1. Preoperative clinical photograph, demonstrating breast asymmetry in the setting of previous left post-mastectomy breast reconstruction.

Results

A preoperative CT scan is performed, with surface-rendered 3D reconstruction used to map breast contour and assess chest wall anatomy. Scanning is performed with the patient lying inclined at 45 degrees, ensuring the breasts are positioned subject to gravity. Surface-rendering, using software modifications in Osirix (Pixmeo, Geneva, Switzerland), a free third-party software modality, facilitates analysis of breast skin contour, including nipple-areolar projection, depressed or prominent regions, and the breast mound borders (Figure 12.3.2.1.2).

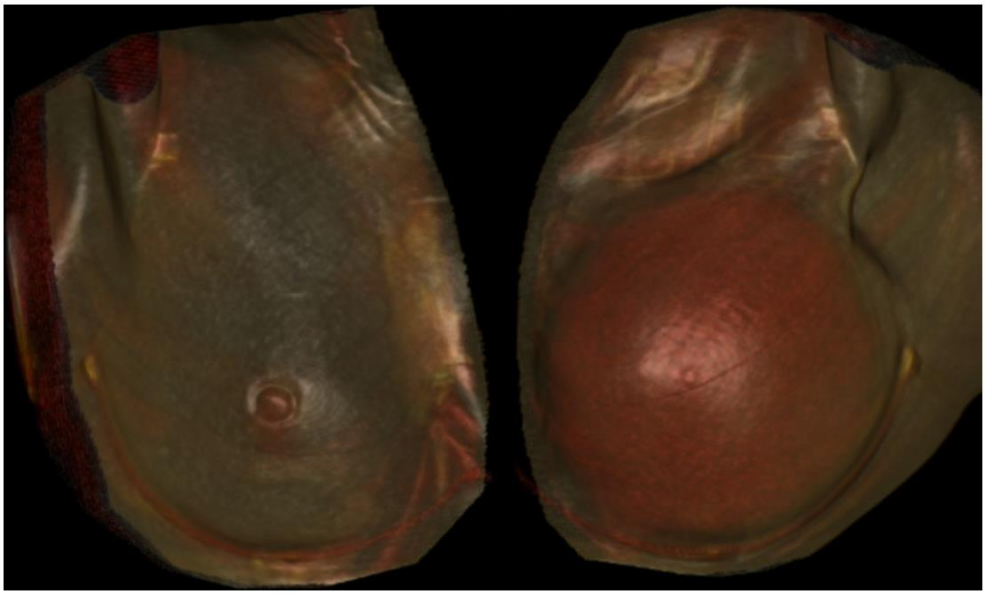

Figure 12.3.2.1.2. Surface-rendered three-dimensional (3D) reconstruction of a computed tomographic (CT) scan of the breasts, performed with Osirix (Pixmeo, Geneva, Switzerland) software.

Parenchymal volume is assessed and calculated using CT data from Osirix using the volume-rendering function (Figure 12.3.2.1.3), with skin and chest wall able to be selectively cropped. Using transverse slices of CT data, breast tissue is highlighted using the ‘‘closed polygon mouse’’ function and volume calculated using the ‘‘compute volume’’ function. Calculated left breast volume was 403 cm^3 and right breast volume was 287 cm^3, with the volume difference thus 116 cm^3. When compared to an approach of filling a bra for volume calculation, a very similar volume difference was calculated. This technique comprised offering the patient varying bag volumes of uncooked rice. This patient

estimated a difference of 85 g. With the density of uncooked rice being 0.82 g/cm^3 (696), this difference was thus 104 cm^3.

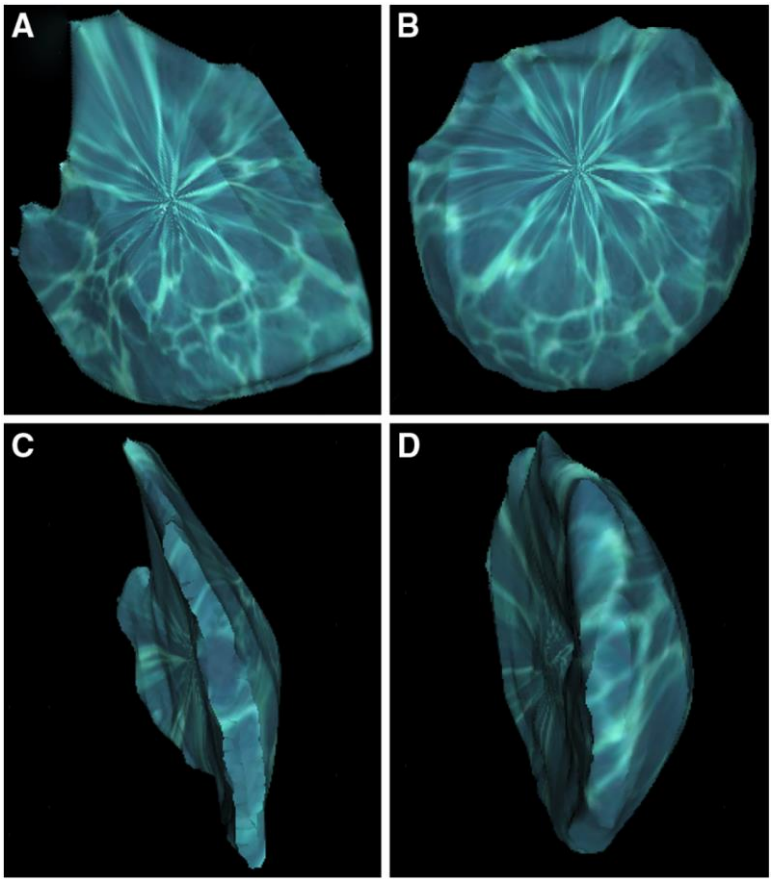

Figure 12.3.2.1.3. Three-dimensional analysis of breast parenchymal volume, after selective cropping of the skin and chest wall from scan data, using volume-rendered three-dimensional (3D) reconstruction of a computed tomographic (CT) scan of the breasts with Osirix (Pixmeo) software: (A) right breast anterior view; (B) left breast anterior view; (C) right breast lateral view; (D) left breast lateral view.

Recent software advances enable 3D demonstration of the volume difference between breasts. This modeling can evaluate shape and contour of the volume difference, rather than just static measurement of this volume. To achieve this, 2D CT data are 3D-reconstructed using the volume- rendering function in Osirix. Exported files of each breast saved in standard tessellation language (STL) format are loaded simultaneously on Magics Software (Materialize, Leuven, Belgium). The 3D images are aligned (Figure 12.3.2.1.4A), a mirror image of one breast is created to align both breasts unidirectionally (Figure 12.3.2.1.4B), and the two volumes superimposed (Figure 12.3.2.1.4C). The

volumes are ‘‘subtracted’’ from one another, and the volume difference in 3D is presented (Figure 12.3.2.1.4D).

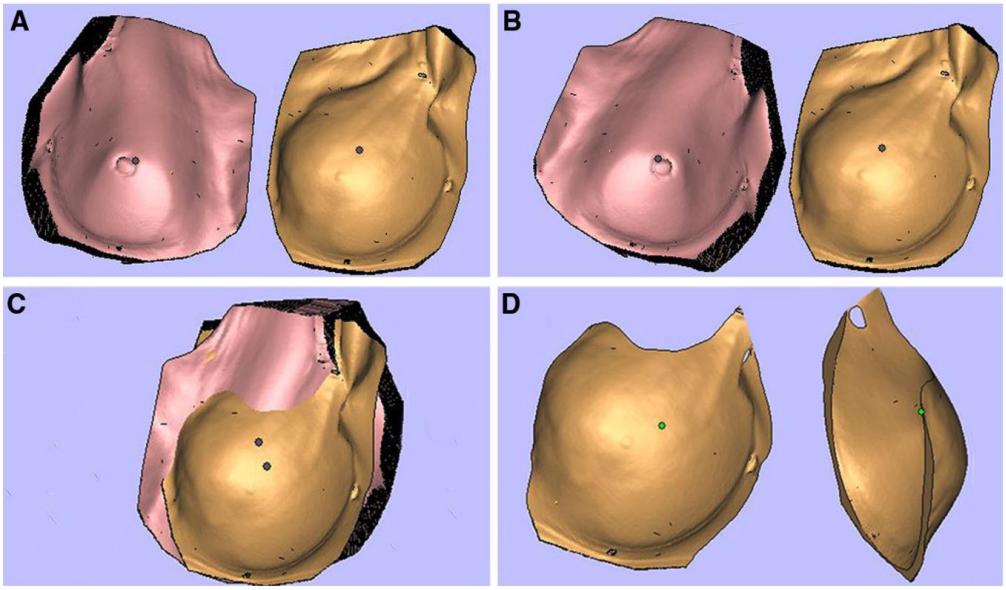

Figure 12.3.2.1.4. Production of a three-dimensional “subtracted” volume difference between breasts, using volume-rendered CT data in Magics software (Materialize, Leuven, Belgium). Volume-rendered computed tomography (CT) images are aligned. (A) a mirror image of one breast is created to align both breasts unidirectionally; (B) the two volumes superimposed; (C) and the volumes are “subtracted” from one another to produce the volume difference (D).

A further advance in volumetric analysis of the breast is the creation of haptic, tactile biomodels, produced in stereolithographic or 3D-printed form from CT. The breasts are 3D-reconstructed from 2D data with volume-rendering and surface-rendering in Osirix, and then saved in STL format for printing (Cube 2 printer, 3D Systems, Rock Hill, SC, USA) using Cubify software (3D Systems). Printing is performed using white polylactic acid (PLA) filament (Figure 12.3.2.1.5).

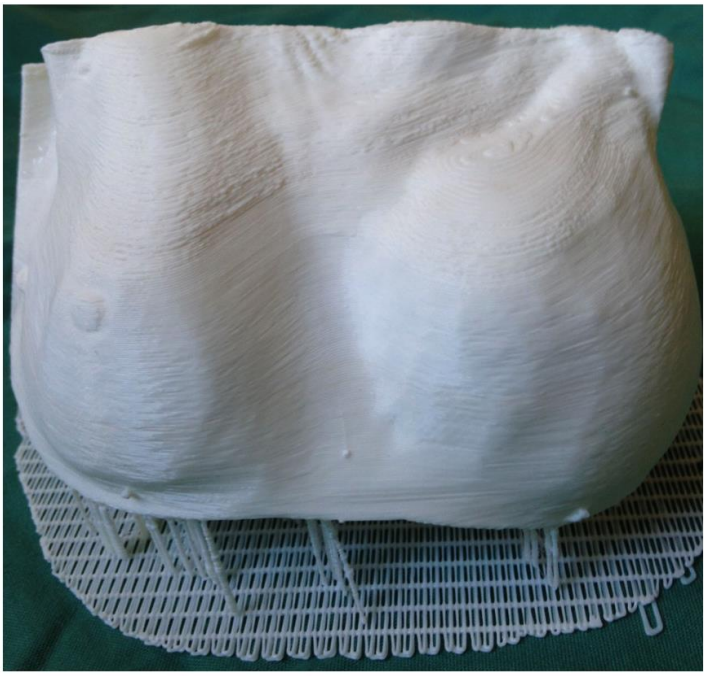

Figure 12.3.2.1.5. A three-dimensional (3D)-printed haptic, tactile biomodel of the breasts, produced from computed tomography (CT) data. Printing performed with the Cube 2 printer (3D Systems, Rock Hill, SC, USA) using Cubify software (3D Systems), and using white polylactic acid (PLA) filament ink.

Discussion

Preoperative planning, including volumetric analysis, can be broadly associated with improved esthetic outcomes and reduced operative times in breast reconstruction surgery (8). Historically, various techniques of objective volumetric analysis have been reported, with limited reported success (526). While 3D imaging based on stereophotogrammetry or laser scanning (where reflected light or laser derives a 3D surface image) can readily examine breast volume and shape in the natural upright position, it cannot provide accurate volumetric analysis, as it does not image the anterior chest wall. Evidence supports the benefits of preoperative imaging in breast reconstruction (8), with Dionyssiou *et al* (388) demonstrating recently that preoperative CTA can significantly decrease the duration of flap shaping and inset, and reduce the number of secondary operations for asymmetry correction.

Conclusion

The last decade has seen an increasing use of anatomic biomodels for medical use (17). In contrast to the most advanced 2D or 3D imaging prints available, graspable 3D objects enable surgeons to manipulate volume in their hands, with visualization in multiple planes. The 3D printer is one example of biomodeling, producing 3D models from photopolymer materials. Recent descriptions in this journal have highlighted the increasing role for 3D printing in reconstructive surgery (17, 275). In this study, we report multiple techniques for volumetric analysis in the setting of breast asymmetry, with breast volumes able to be visualized through 3D images, calculated accurately and produced as 3D haptic models for tactile feedback and operative guidance. While the current study has not evaluated patient or operative outcomes, the approach presented has proven a reproducible, practical, and valuable addition to reported approaches for preoperative planning, and should form the basis for future outcome studies.

12.3.2.2 Preoperative Perforator Localisation Using 3D-Printed DIEP Template

Submitted (Publication): ***Chae MP***, Hunter-Smith DJ, Chung RD, Smith JA, Rozen WM. (2018) 3D-printed, patient-specific DIEP flap templates for preoperative planning in breast reconstruction: A prospective case series. Microsurg

Chapter Summary

Introduction: Modern imaging technologies, such as computed tomographic angiography (CTA), can be useful for preoperative assessment in deep inferior epigastric artery perforator (DIEP) flap surgery. Planning perforator flap design can lead to improved surgical efficiency. However, current imaging modalities are limited by being displayed on a two-dimensional (2D) surface. In contrast, a 3D-printed model provides tactile feedback that facilitates superior understanding. Hence, we have 3D-printed patient-specific deep inferior epigastric artery perforator (DIEP) templates, in an affordable and convenient manner, for preoperative planning.

Method: 20 consecutive patients undergoing 25 immediate or delayed post-mastectomy autologous breast reconstruction with DIEP or muscle-sparing transverse rectus abdominis (MS-TRAM) flaps are recruited prospectively. Using free, open-source softwares (3D Slicer, Autodesk MeshMixer, and Cura) and desktop 3D printers (Ultimaker 3E and Moment), we have created a template based on the patient's abdominal wall from the CTA with holes and lines indicating the position of the perforators, their intramuscular course and the DIEA pedicle.

Result: Mean age of the patients was 52 (38-67). There were 15 immediate and 10 delayed reconstructions. 3D printing time took mean 18 hours and 123.7 g of plastic filament, which calculates to a mean material cost of AUD 8.25. DIEP templates accurately identified the perforators and reduced intraoperative perforator identification by 7.29 minutes (p = 0.02). However, the intramuscular dissection time was not affected (p = 0.34). Surgeons found the template useful for preoperative marking (8.6/10) and planning (7.9/10), but not for intramuscular dissection (5.9/10). There were no immediate flap-related complications.

Conclusion: Our 3D-printed, patient-specific DIEP template is accurate, significantly reduces intraoperative perforator identification time and, hence, may be a useful tool for preoperative planning in autologous breast reconstruction.

Introduction

The incidence of breast cancer diagnosis has been rising steadily (41) and an increasing number of women are opting for post-mastectomy reconstruction (697). In comparison to implant-based techniques, autologous breast reconstruction based on deep inferior epigastric artery perforator (DIEP) flap yields long-lasting, natural-appearing outcome and is, hence, considered the gold standard reconstruction (48-50, 460, 698-700).

Due to high individual variation in the vascular anatomy of the DIEA perforators (701), computed tomographic angiography (CTA) is performed to help select ideal perforator and flap design preoperatively (5, 6, 10-13). Advances in the hardware of CTA, such as an increasing number of detector rows (3), and software, such as OsiriX (Pixmeo, Geneva, Switzerland) (671), have ensured its precision, fast speed and reliability.

As a result, the use of CTA in DIEP flap planning has led to reduced postoperative flap complications, such as fat necrosis, flap loss and donor site morbidity (5, 80, 119, 120, 131). Interestingly, Smit *et al* have reported a significant reduction in operating time using CTA in DIEP reconstructions (264 vs 354 mins, $p < 0.001$) (13). However, Rozen *et al* have reported no statistically significant reduction in the total operating time of both unilateral and bilateral cases ($p = 0.57$ and 0.079, respectively) (5). This may be attributed to the fact that current imaging modalities are limited by being displayed on a two-dimensional (2D) surface like a computer screen. Novel ways of utilising the CTA data, such as 3D printing, may enable intuitive spatio-temporal understanding of the involved anatomical structures.

In the last decade, 3D printing has become affordable and readily accessible (176, 189). In plastic and reconstructive surgery, 3D printing appears most useful in preoperative planning, designing intraoperative guidance devices, patient education, and building customized implants (16, 17, 318). Recently, we have developed an affordable and convenient method of 3D printing for clinicians using free, open-source softwares and desktop 3D printers (35, 272, 273, 276). Using this technique, we have 3D-printed patient-specific DIEP templates and utilized them in 20 consecutive patients receiving autologous breast reconstruction with abdominal-wall based free flaps.

This prospective study aims to assess the feasibility and usefulness of 3D designed DIEP perforator templates as a practical tool for DIEP breast reconstruction.

Methods

In this prospective case series of 25 abdominal wall-based flaps in 20 patients over 12-month period (June 2016- June 2017), we use routine CTA scan data to create patient-specific DIEP templates for preoperative planning. This study has been approved by our institutional ethics committee.

CTA

CTA was performed using standardized “single-volume” acquisition technique that ensures maximal image quality and minimal radiation exposure, as previously described by Rozen *et al* (141). Siemens SOMATOM Sensation 64 multi-detector row computed tomography scanner (Siemens Medical Solutions, Erlangen, Germany) is used and the scan parameters are summarized in Table 12.3.2.2.1.

Parameters	
Scanner	Siemens SOMATOM Sensation 64
Scan type	Helical multi-detector row CT angiography
Slice thickness	64 detector row x 0.6 mm collimator width
Helical detector pitch	0.9
Gantry rotation speed	0.37 sec
Tube potential	120 kV
Tube current	180 mA
Contrast	Omnipaque 350 100 ml IV injection 4 ml per second
Scanning range	Pubic symphysis to 4 cm above umbilicus
Scanning direction	Caudo-cranial
Bolus tracking	+100 HU from common femoral artery with minimal delay
Automatic dose modulation (Siemens Care Dose 4D)	Disabled
Imaging reconstruction	1 mm/0.75 mm overlapping axial images

Table 12.3.2.2.1. Computed tomographic angiography scan parameters.

Design of the DIEP Template

CTA data is exported from the scanner in DICOM (Digital Imaging and COmmunications in Medicine) format and is processed using free, open-source software (Figure 12.3.2.2.1): 3D Slicer (Surgical Planning Laboratory, Boston, MA, USA), Autodesk MeshMixer (Autodesk, Inc., San Rafael, CA, USA), and Cura (Ultimaker, Geldermalsen, Netherlands).

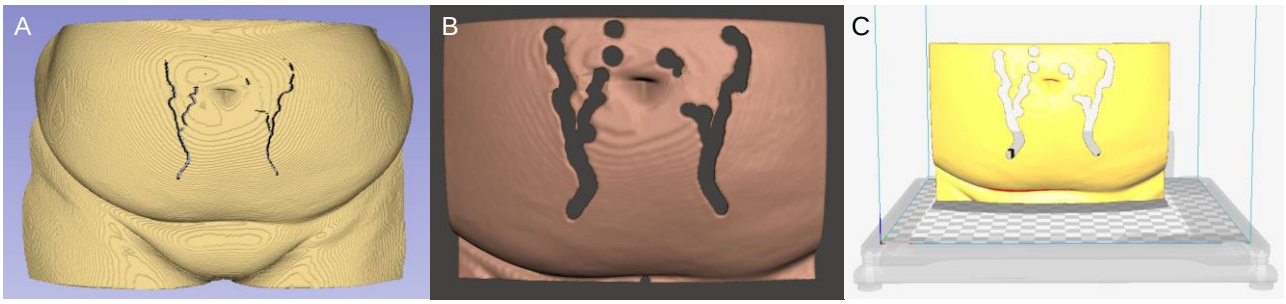

Figure 12.3.2.2.1. 3D printing software. (A) Using 3D Slicer software (Surgical Planning Laboratory, Boston, MA USA), CTA scan data is converted into a 3D image of the abdominal wall and holes and lines are placed appropriately to indicate the location of DIEA perforators, their intramuscular course and the DIEA pedicle. (B) Using Autodesk MeshMixer software (Autodesk, Inc., San Rafael, CA USA), the 3D image is cropped into appropriate size and the holes/lines are enlarged to fit marking pens. (C) Using Cura software (Ultimaker, Geldermalsen, Netherlands), the final file is converted to a 3D printer-friendly file. Abbreviations: CTA: computed tomographic angiography; DIEA: deep inferior epigastric artery.

Firstly, a 3D image of the patient's abdominal wall with perforations indicating the location of perforators is created from the DICOM files in 3D Slicer. Using the "threshold" function, a range of Hounsfield unit-derived arbitrary values can be selected to automatically generate a 3D image of the abdominal wall. Scrolling through the axial slices, using "RectangleEffect" tool and erase function, holes and lines are created in the 3D image at the location of DIEA perforators, their intramuscular course and the DIEA pedicle. Similarly, a notch in the 3D image is created at pubic symphysis. The final 3D image is exported in STL (standard tessellation language) format.

In Autodesk MeshMixer, the STL file is made suitable for clinical application. Using "SphereDisc" brush tool, the perforators, their intramuscular course and the DIEA are

enlarged to enable a marking pen to fit. Then, the 3D image is cropped around four edges to fit inside a 3D printer. Using “separate” function, anterior surface of the 3D image is isolated and then, using “extrude” function, it is thickened 5 mm into a physical template. Finally, using “smooth” function, the file is smoothed out and then exported in STL format.

In Cura, this final STL file is transformed into a 3D printer-friendly file. 3D slicing softwares, like Cura, automatically generates support structures and creates an instruction for a 3D printer to follow. This file is exported in G-code format via an external storage device.

3D Printing

The templates are 3D-printed in thermoplastic polylactic acid (PLA) filament using one of our two desktop fused filament fabrication (FFF) 3D printers (Figure 12.3.2.2.2): Ultimaker 3 Extended 3D printer (Ultimaker, Geldermalsen, Netherlands) and Moment 3D printer (Moment, Seoul, South Korea). They cost approximately AUD 6,000 and 3,000, respectively. The latter is used to print smaller-sized templates.

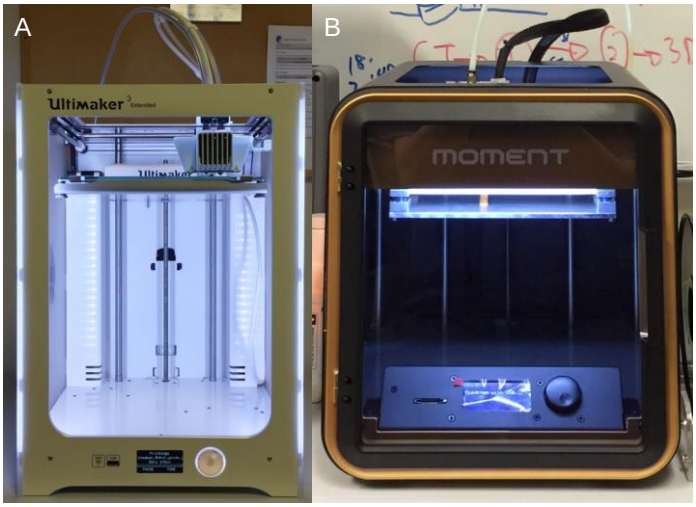

Figure 12.3.2.2.2. 3D printers. (A) Ultimaker 3E printer (Ultimaker, Geldermalsen, Netherlands). (B) Moment 3D printer (Moment, Seoul, South Korea).

Patient Recruitment

All patients undergoing postmastectomy autologous breast reconstruction with abdominal wall-based free flaps, regardless of whether immediate or delayed, unilateral or bilateral,

and DIEP or MS-TRAM flaps, a recruited from three Monash University-affiliated hospital networks: Peninsula Health, Eastern Health and Ramsay Health. Exclusion criteria include contraindication to intravenous contrast preventing preoperative investigation with CTA, patient decline and pregnancy. Historical control is derived from reconstructions performed at Peninsula Health and Ramsay over the preceding 12 months (June 2015 – June 2016). Data from Eastern Health was not collected during this earlier period and, hence, was not available for analysis.

Accuracy of the DIEP Template

In order to assess the templates accuracy and reliability, perforator distance from the base of umbilicus (horizontal & vertical) was measured using a calibrated calliper (Figure 12.3.2.2.3).

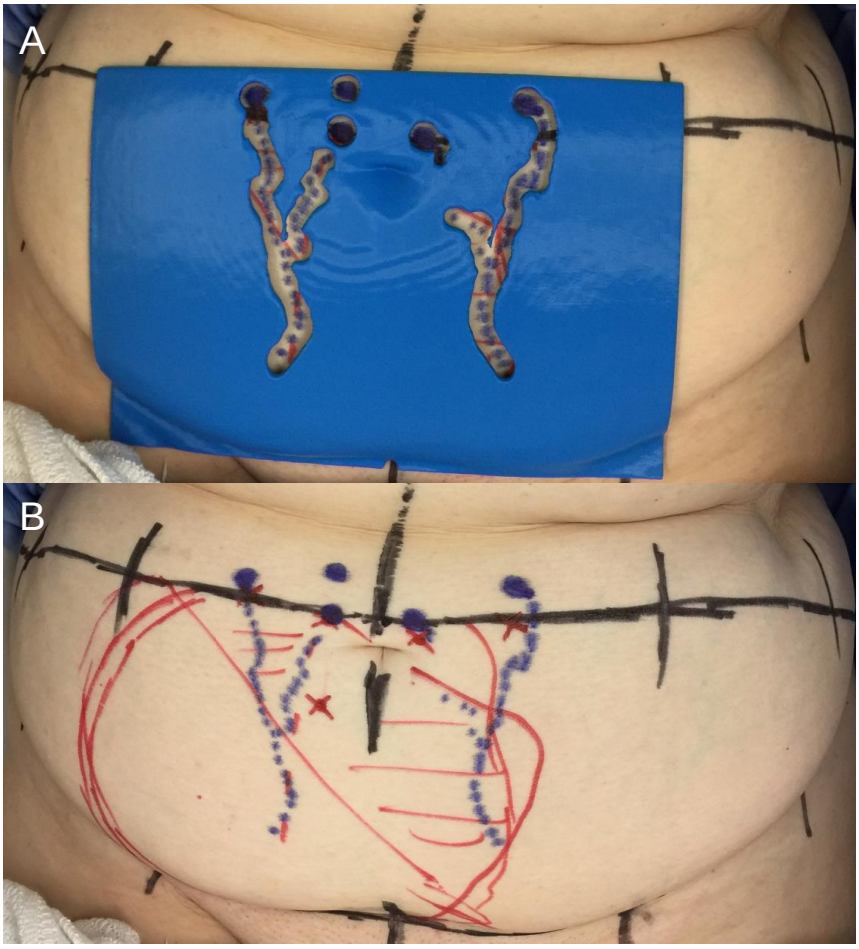

Figure 12.3.2.2.3. Clinical application of the 3D-printed DIEP template in use. The template was orientated on the abdomen by the umbilicus, notch at the pubic symphysis

and the abdominal skin crease (A). Markings from the template were used for flap design and the skin island (B). Abbreviation: DIEP: deep inferior epigastric artery perforator.

We selected the biggest perforator from each hemi-abdomen. This step was repeated using perforators detected using handheld Doppler probes (166) and reported measurements from the patients CTA (142). Intraoperative measurement of the perforator distances was made using a sterile metal ruler and performed just prior to the flap being disconnected at the DIEA origin.

Utility of the DIEP Template: Operating Time

In order to assess the potential role of the template in improving intraoperative perforator identification, we have measured the time taken during suprafascial flap dissection. Recently, Marsh *et al* from Chelmsford, UK, have divided DIEP flap reconstruction into 101 individual steps (702). As a result, we have measured the time taken during the steps 24 ("lateral raise of flap off rectus fascia with handheld diathermy to just lateral to lateral row perforator") and 25 ("dissection down to and identification of perforator [match to CT] using bipolar diathermy and/or McIndoe's dissection scissors").

Similarly, in order to assess its potential role in improving intramuscular dissection, we have measured the time taken during steps 29 ("subfascial/intramuscular dissection [muscle relaxant or lignocaine] using McIndoe dissecting forceps and bipolar") and 30 ("submuscular dissection of perforator") (702).

Since June 2015, at our institution, we have been routinely recording the operating time of Chelmsford 101 individual steps in free DIEP flap breast reconstructions. As a result, our outcomes from the current study could be accurately correlated to the historical control.

Utility of the DIEP Template: Surgeon Perception Surveys

After each operation, both primary and second surgeons and surgical trainees have completed a 5-part survey that assesses their perceived utility of the template on a 10-score visual analogue scale. It consisted of the following questions: "how useful was the device in preoperative marking?", "how useful was the device in preoperative planning?",

"how useful was the device in intramuscular dissection?", "did it change your management?" and "would you use it again?".

Statistical Analysis

Perforator distances from the template, handheld Doppler probes, CTA report, and intraoperative findings are recorded using calibrated callipers and sterile rulers. They are rounded to the nearest 1 mm. Intraoperative perforator identification time and intramuscular dissection time are recorded using a stopwatch and rounded to the nearest 1 second. The comparative analysis was performed using Stata statistical software package (StataCorp, College Station, TX, USA). The perforator distances are analysed using Kruskal-Wallis equality-of-populations rank test while the surgical times and the survey responses are analysed using the Student's *t*-test. P value of less than 0.05 is accepted as statistically significant.

Results

Total of 20 patient-specific DIEP templates were 3D-printed for 25 consecutive autologous breast reconstructions in 20 patients between July 2016 – June 2017 (12 months). Mean age of the patients was 52 (range: 38-67) and the mean BMI was 27.8 (21-36.4). Immediate reconstruction made up 15 out of 25 flaps (60%), unilateral reconstruction 15 out of 20 cases (75%), and DIEP flaps 18 out of 25 flaps (72%). Historical control consisted of 9 consecutive autologous reconstructions in 7 patients. Both study groups were similar and summarized in Table 12.3.2.2.2.

		DIEP Template	**Historical Control**
Number of patients		20	7
Number of abdominal wall-based free flaps		25	9
Patient age		52 (38-67)	54 (46-64)
BMI		27.8 (21-36.4)	28.7 (23-32)
Timing of reconstruction	Immediate	15 (60%)	6 (67%)
	Delayed	10 (40%)	3 (33%)
Side of reconstruction	Unilateral	15 (60%)	5 (71%)
	Bilateral	5 (40%)	2 (29%)
Type of reconstruction	DIEP	18 (72%)	7 (78%)
	MS-TRAM	7 (28%)	2 (22%)

Table 12.3.2.2.2. Comparison of patient demographics between the group using the 3D-printed DIEP template and the historical control. Abbreviations: BMI: body mass index; DIEP: deep inferior epigastric artery perforator flap; MS-TRAM: muscle-sparing transverse rectus abdominis muscle flap.

3D Printing

Each template took mean 18.03 hours to 3D print and used 123.7 g of filament. Given that 750 g of PLA filament costs approximately AUD 50, mean material cost was less than AUD 8.25 per template.

Accuracy of the DIEP Template

The template accurately identified DIEA perforators and is as accurate as current gold standard imaging modalities: handheld Doppler and CTA (Table 12.3.2.2.3).

	Horizontal Distance	**Vertical Distance**
DIEP template vs intraoperative measurement	0.09	0.87
DIEP template vs handheld Doppler probe vs CTA	0.42	0.74

Table 12.3.2.2.3. Comparison of perforator distance measurements between 3D-printed DIEP template, intraoperative measurement, handheld Doppler probe, and CTA. Abbreviation: DIEP: deep inferior epigastric artery perforator; CTA: computed tomographic angiography.

There was no statistical difference between the template and intraoperative measurements (horizontal and vertical distances; p = 0.09 and 0.87, respectively). Similarly, there was no statistical difference between the template, handheld Doppler and CTA (horizontal and vertical distances; p = 0.42 and 0.74, respectively).

Utility of the DIEP Template: Operating Time

The template had a dissimilar impact on different stages of the operation (Table 12.3.2.2.4).

Mean	**DIEP template (mins)**	**Historical control (mins)**	**Difference (mins)**	**P value**
Intraoperative perforator identification	15.07	22.36	7.29	0.02
Intramuscular dissection	93.95	79.62	-14.33	0.34

Table 12.3.2.2.4. Impact on operating time using the DIEP template. Abbreviation: DIEP: deep inferior epigastric artery perforator.

Mean intraoperative perforator identification time was significantly reduced by 7.29 minutes (15.07 vs 22.36 mins; p = 0.02). However, there was no statistically significant difference in mean intramuscular dissection time (93.95 vs 79.62 mins; p = 0.34).

Utility of the DIEP Template: Surgeon Perception Survey

The template was useful for preoperative marking (mean score: 8.6/10) and planning (7.9/10) (Table 12.3.2.2.5).

	"How useful was the device in preoperative marking"	**"How useful was the device in preoperative planning"**	**"How useful was the device in intramuscular dissection"**	**"Did it change your management"**	**"Would you use the template again"**
Average response	8.6/10	7.9	5.9	5.3	8.8
Flap-raising surgeon vs second surgeon	p = 0.94	0.28	0.29	0.73	0.67
Surgeon vs Surgical trainees	p = 0.78	0.98	0.07	0.73	0.95

Table 12.3.2.2.5. Summary of responses from the surgeon perception survey and comparison of responses between flap-raising surgeons against the second surgeons and surgeons against surgical trainees.

However, it was not useful for intramuscular dissection (5.9/10) and, as a result, did not influence the clinical management significantly (5.3/10). Encouragingly, the surgeons appeared enthused about its potential and were keen to use the template again (8.8/10). When the responses were compared between flap-raising surgeons and the second

surgeons, there was no difference. Similarly, there was no statistical differences between surgeons and surgical trainees. Interestingly, there was a trend in the difference between surgeons and surgical trainees in their perceived utility of the template in intramuscular dissection (4.7 vs 6.3, p = 0.07). However, since the response from trainees was equally low (6.3/10), it is most likely that trainees had similar doubts about its usefulness in intramuscular dissection.

Clinical Outcome

There were no immediate flap-related postoperative complications. Mean length of stay was 6.4 days (range: 5-8). At 3-month follow-up, there was no reported donor-site morbidity clinically, such as abdominal wall bulge and ventral hernia.

Discussion

In the current prospective case series, we demonstrate our technique of creating a 3D-printed, patient-specific DIEP template, assess its accuracy and utility and illustrate outcomes to our historical control.

Usually, a radiologist would report from CTA the diameter of suitable perforators and their location in horizontal and vertical distances from the umbilicus. This is marked out on the patient by the surgeon preoperatively and confirmed using a handheld Doppler probe. Unsurprisingly, during observation, transcription and interpretation of the report, errors can be introduced and compromise efficiency (703). Thus, Miranda *et al* have proposed, in their proof-of-concept study, a method of creating patient-specific 2D DIEP templates using transparent acetate sheets, punch biopsy holes, and coronal images from the CTA (703). However, this technique is rather cumbersome and is significantly susceptible to observation and transcription errors. Moreover, the flat acetate sheet ignores the curved contour of the abdominal wall. To this effect, 3D printing can be useful.

Aided by expiration of key patents, 3D printing, also known as additive manufacturing or rapid prototyping, has become affordable and readily accessible for clinicians in the last decade (16, 17, 189, 318, 704). In comparison to the traditional manufacturing process, 3D printing enables easy customization in a cost-efficient and convenience manner. In plastic and reconstructive surgery, 3D printing appears most useful in preoperative planning, designing intraoperative guidance devices, patient education, and building customized implants (16, 17, 318). Using free, open-source softwares (i.e. 3D Slicer, Autodesk MeshMixer, and Cura) and desktop 3D printers (i.e. Ultimaker 3E and Moment), we have produced each template at a material cost of less than AUD 10.

The template accurately identifies the position of DIEA perforators, their intramuscular course and the DIEA pedicle. Furthermore, it improves preoperative marking and planning, leading to statistically quicker intraoperative identification of the perforators. This may be because the template removes the guesswork and interpretation errors from traditional written CTA reports and is more intuitive to apply since they lie accurately on the abdomen. Furthermore, the tactile feedback from templates likely enhances visuospatial understanding of the involved perforator anatomy, leading to more confident dissection (15). However, despite being statistically significant, the reduction of 7.29 minutes may be

too small to be clinical significant. Notably, the template appears not useful for intramuscular dissection, which is arguably one of the most technically challenging aspects of DIEP flaps. This is most likely because despite being 3D-printed, clinical information is essentially embossed in 2D on to the template.

3D printing the entire course of a DIEA perforator and its surrounding soft tissues, similar to what Mehta *et al* have reported in a proof-of-concept study, may be more useful for intramuscular dissection (705). However, their technique would have been difficult to reproduce for routine clinical application due to software- and hardware-related issues. Using any latest imaging software, it remains difficult to differentiate DIEA perforators from the rectus abdominis in CTA both visually and digitally, especially in patients with physiologically smaller vessels, without significantly increasing the contrast dose and radiation. Using MRA, the image resolution is even poorer (5.0 vs 0.5 mm slice thickness) since scans have to be performed quickly to prevent motion artefacts. Recent advances in MRA technology can account for motion artefacts without compromising image quality, but they are not yet available widely (447). In contrast to the multi-colour, multi-material, industrial-grade 3D printer used by Mehta *et al* that costs in excess of AUD 100,000, our desktop 3D printers (Ultimaker 3E, Moment) can only print in single material, making it difficult to print intramuscular course of DIEA perforators. As a result, most clinicians currently outsource 3D printing at a cost of more than AUD 1,000 per model.

Conclusion

We demonstrate that our 3D-printed, patient-specific DIEP template accurately identifies DIEA perforators, and significantly reduces intraoperative perforator identification time by, albeit 7.29 minutes, and, as a result, it may become a useful tool in preoperative marking and planning.

12.3.2.3 Preoperative Flap Designing Using 3D-Printed DIEP Perforasome Template

PUBLISHED (Publication): ***Chae MP***, Hunter-Smith DJ, Rostek M, Smith JA, Rozen WM. (2018) Enhanced preoperative deep inferior epigastric artery perforator flap planning with a 3D-printed perforasome template: Technique and case report. Plast Reconstr Surg Glob Open. 6(1):e1644. PMID: 29464169

Chapter Summary

Introduction: Optimising preoperative planning is widely sought in deep inferior epigastric artery perforator (DIEP) flap surgery. One reason for this is that rates of fat necrosis remain relatively high (up to 35%), and that adjusting flap design by an improved understanding of individual perforasomes and perfusion characteristics may be useful in reducing the risk of fat necrosis. Imaging techniques have substantially improved over the past decade, and with recent advances in 3D printing, an improved demonstration of imaged anatomy has become available. We describe a 3D-printed a template that can be used preoperatively to mark out a patient's indivisualised perforasome for flap planning in DIEP flap surgery.

Method: We describe this "perforasome template" technique in a case of a 46-year-old woman undergoing immediate unilateral breast reconstruction with a DIEP flap. Routine preoperative CTA was performed, with open-source software (3D Slicer, Autodesk MeshMixer and Cura) and a desktop 3D printer (Ultimaker 3E) used to create a template used to mark intra-flap, subcutaneous branches of DIEA perforators on the abdomen.

Result: An individualised 3D printed template was used to estimate the size and boundaries of a perforasome and perfusion map. The information was used to aid flap design.

Conclusion: We describe a new technique of 3D printing a patient-specific perforasome template that can be used preoperatively to infer perforasomes and aid flap design.

Introduction

Autologous breast reconstruction using the deep inferior epigastric artery perforator (DIEP) flap has become an integral component of the holistic treatment of breast cancer patients (43). However, to this day, perfusion of DIEP flaps remains a key difficulty with this flap, and the rate of fat necrosis remains relatively high (8.7-35%) (706). Fat necrosis is a frequent cause of secondary surgical refinements (707). Using the classification of fat necrosis by Lie *et al* (707), grade III-IV necrosis, involving greater than 15% of the flap, can significantly compromise aesthetic outcome and inevitably requires revision with lipofilling, skin grafts or an entirely new flap. Fat necrosis can be prevented, and is well described, by improving the flap design to improve perfusion that adequately captures perforasomes and flow of DIEA perforators (425, 657, 707).

Modern imaging technologies, such as computed tomographic angiography (CTA), has assisted in preoperative flap and perforator selection, leading to improved clinical outcomes. However, they are limited by being displayed on a two-dimensional (2D) surface. In contrast, a 3D-printed model provides additional tactile feedback that facilitates superior spatial understanding (318). Recently, we have developed an affordable, convenient method of 3D printing a patient-specific DIEP template that can be used to draw preoperatively the location of DIEA perforators, their intramuscular course and the DIEA pedicle (37). Using this new technique, we have fashioned a template that maps intra-flap course of DIEA perforators, thus defining their perforasomes.

Methods

In this study, we describe our technique of 3D printing a DIEP perforasome template. Henceforth, we will call it the “perforasome template” in order to differentiate it from our previously-reported DIEP template, which identifies the location of perforators and their intramuscular course (37).

Scan Acquisition

CTA was performed using standardized “single-volume” acquisition technique that ensures maximal image quality and minimal radiation exposure.

Case Report

A 46-year-old woman underwent immediate unilateral breast reconstruction with a DIEP flap. She was otherwise well, with no comorbidities and had a BMI of 20.

Technique

Design of the Perforasome Template

Digital Imaging and COmmunications in Medicine (DICOM) files from CTA are processed using free, open-source software (Figure 12.3.2.3.1): 3D Slicer (Surgical Planning Laboratory, Boston, MA, USA), Autodesk MeshMixer (Autodesk, Inc., San Rafael, CA, USA), and Cura (Ultimaker, Geldermalsen, Netherlands).

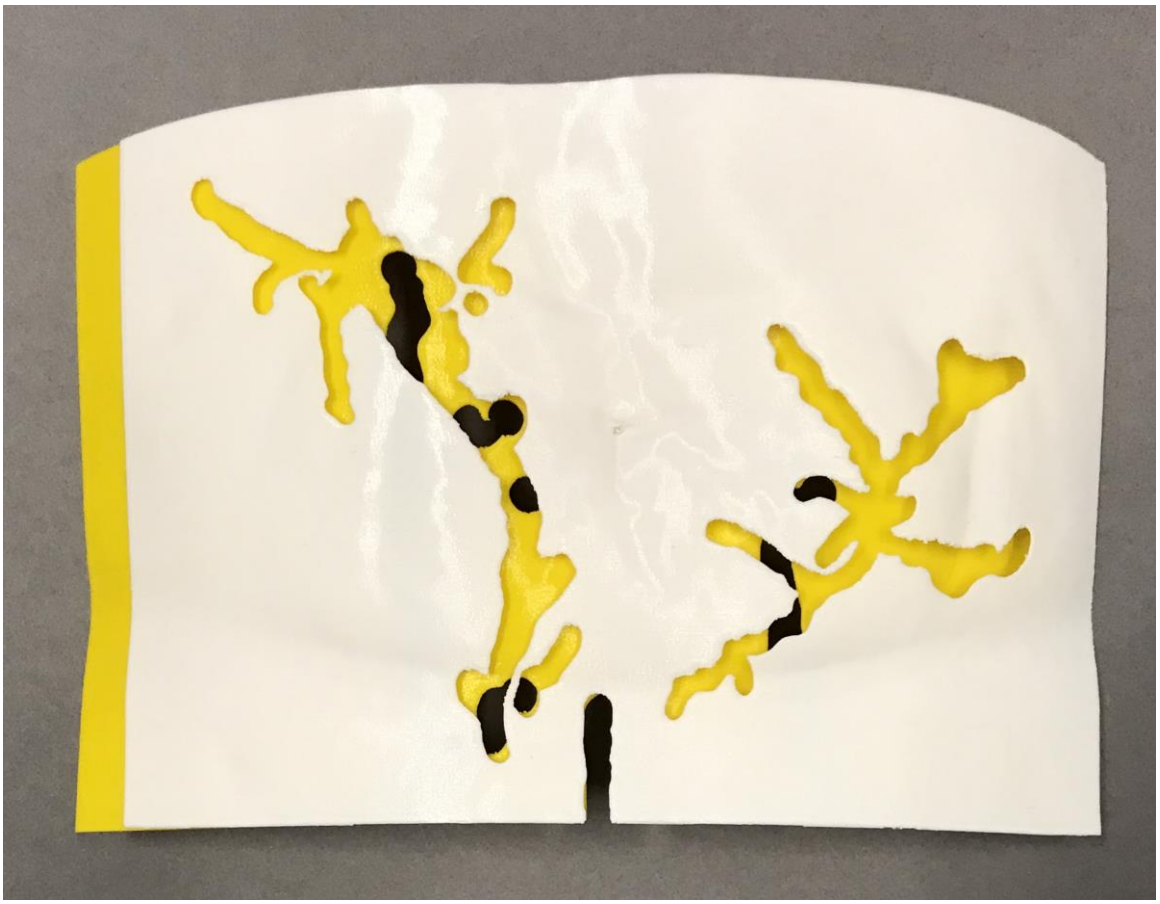

Figure 12.3.2.3.1. 3D-printed perforasome template placed on top of 3D-printed DIEP template of the same patient demonstrating their accurate alignment.

In 3D Slicer, holes/lines are created into the 3D image of the patient's abdominal wall, where subcutaneous branches of each DIEA perforator are found. Similarly, a notch is created at the level of pubic symphysis, which will be used to orientate the template on the abdomen. The final 3D image is exported in Standard Tessellation Language (STL) format.

In Autodesk MeshMixer, the holes/lines within the STL file are enlarged to fit surgical marking pens and the entire template is made thicker to enable manual handling. The final 3D image is again exported in STL format.

In Cura, the STL file is converted into a 3D printer-compatible file and exported in G-code format.

3D Printing

Both the perforasome and the DIEP templates are 3D-printed for the case using polylactic acid (PLA) filaments in Ultimaker 3E printer (Ultimaker, Geldermalsen, Netherlands) (Figure 12.3.2.3.2).

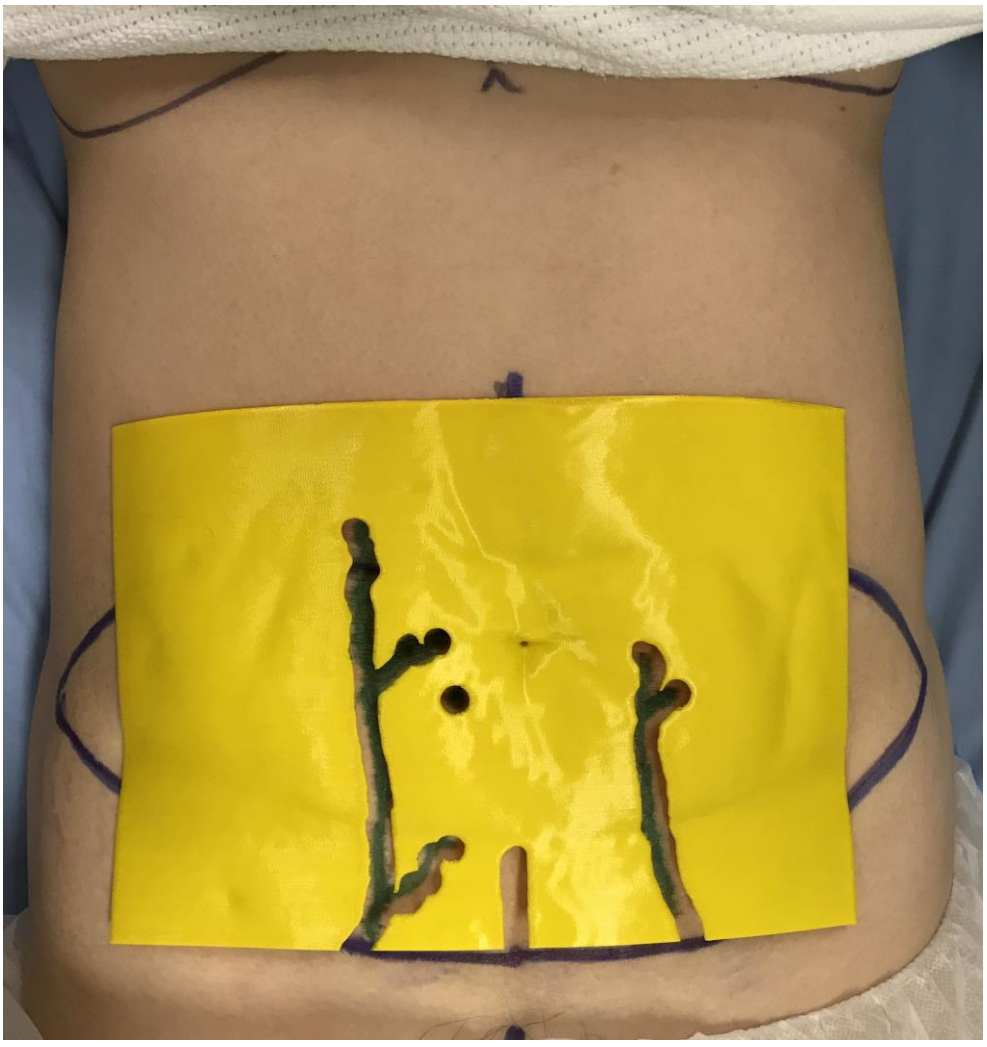

Figure 12.3.2.3.2. 3D-printed DIEP template used to mark the location of DIEA perforators, their intramuscular course, and the DIEA pedicle.

The DIEP template took 15.1 hours and 94 g of filament while the perforasome template took 15.4 hours and 80 g, respectively (Figure 12.3.2.3.3).

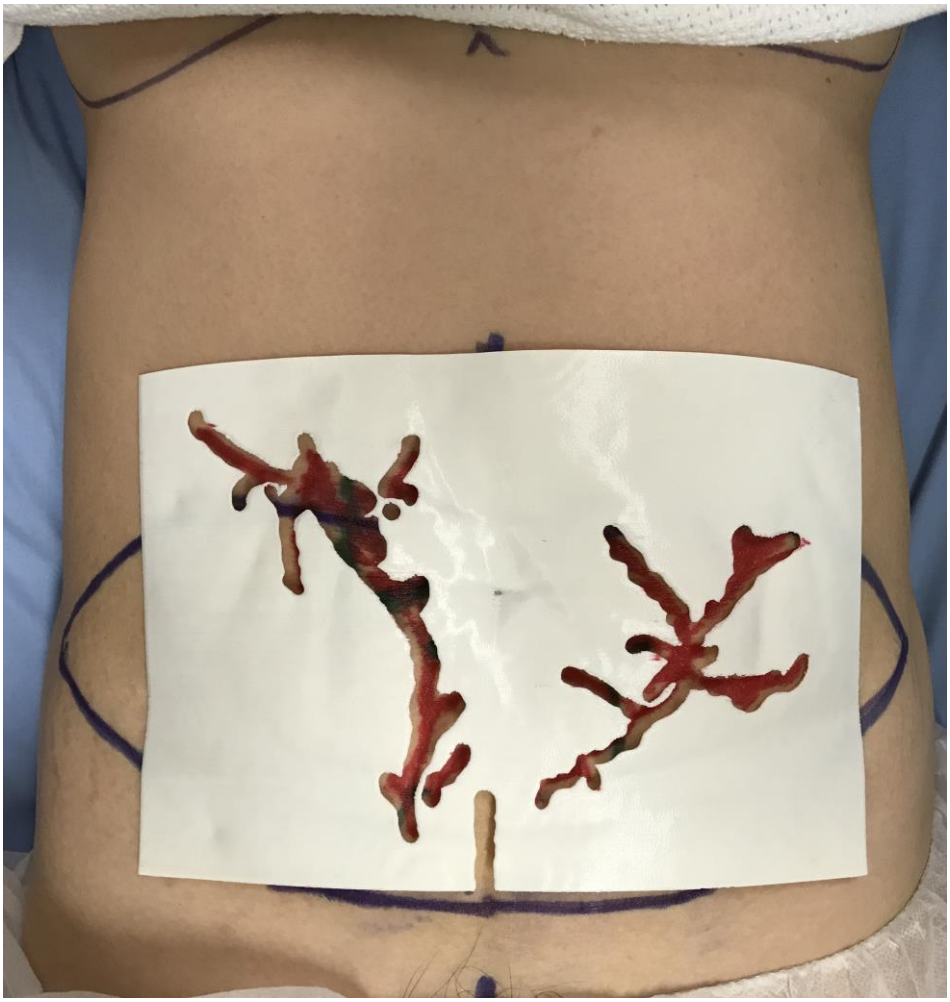

Figure 12.3.2.3.3. 3D-printed perforasome template used to mark the subcutaneous branches of DIEA perforators and their linking vessels.

Clinical Outcome

Perforasomes were drawn using the template, providing the precise location of the relevant perforator exit point and intra-muscular course, which was useful for designing the final flap (Figure 12.3.2.3.4). There were no immediate flap-related complications.

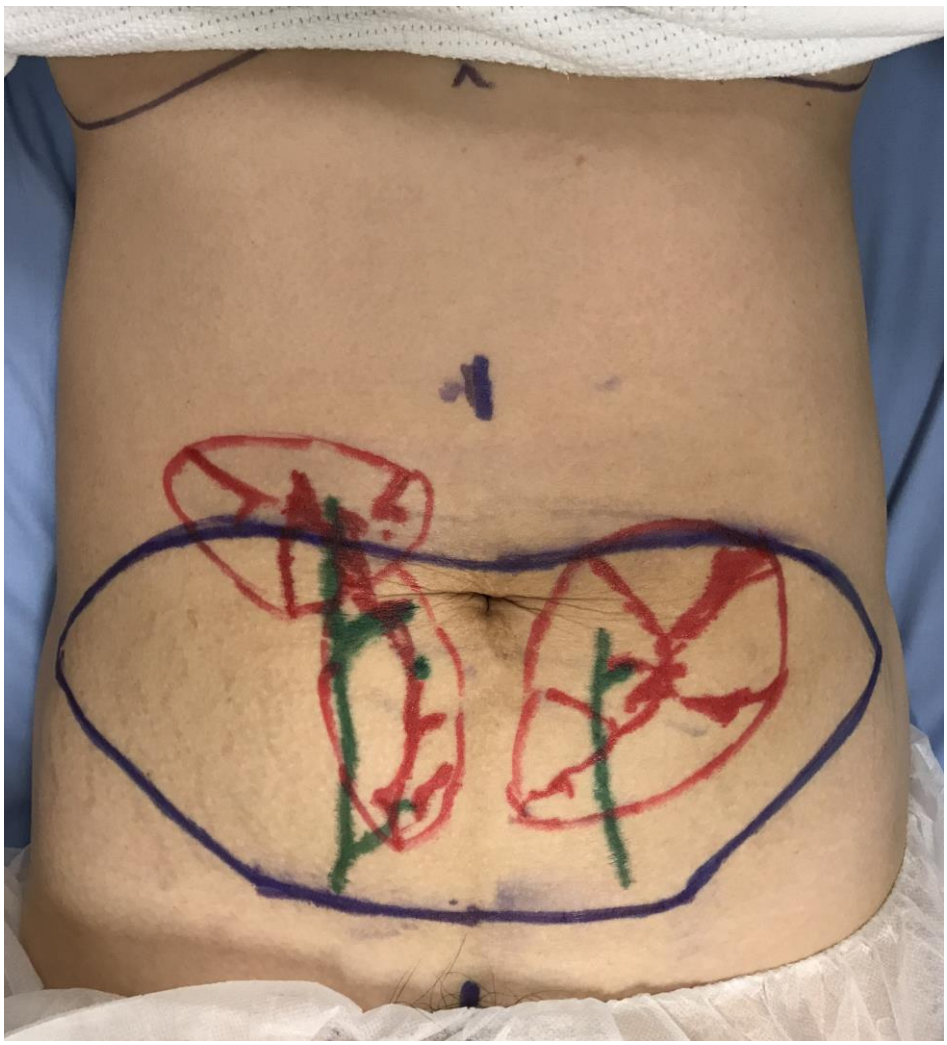

Figure 12.3.2.3.4. The markings are used to estimate the size and shape of each perforasome to aide with flap design.

Discussion

Fat necrosis transforms into disfiguring palpable lumps and is associated with significantly lower patient-reported aesthetic satisfaction (708). In 2013, Lie *et al* have recommended a classification system in order to encourage consistent reporting of fat necrosis, ranging from grade I where <5% of flap is involved resulting in minimal impact on the overall outcome to grade V or complete flap loss (707). In grade II fat necrosis involving 5-15% of the flap, lumpiness and discomfort may be subtle. However, in grade III involving 15-50%, aesthetic outcome is significantly compromised and may require substantial refinements with lipofilling or skin grafts. In grade IV involving >50%, necrosectomy inevitably needs to be followed by reconstruction with an additional or an entirely new flap. Less frequently, fat necrosis (2.8%) and partial flap necrosis (1.2%) may necessitate revision operation during the same admission of original reconstruction. One of the main reasons for grade I-IV fat necrosis is due to insufficient flap perfusion and its microvascular architecture stemming from a suboptimal flap design.

Understanding its vascular territory and perforator flow characteristics is critical for flap design and, to date, capturing dynamic vascularity of perforator flaps using imaging modalities has been challenging since routine CTA only provides static images. An ideal method remains to directly inject the perforator with contrast and use dynamic imaging modalities, such as 4D CTA, in order to demonstrate its axiality of flow, connection with subdermal plexus and outline its physiologic perforasome (657). However, this is difficult to perform routinely for clinical application. CTA has largely been utilised in its arterial phase, as we have similarly done in the current study, although imaging (and 3D prints of such imaging) could equally be done for venous anatomy, should it be sought.

Encouragingly, when its parameters are optimized (14), CTA can maximally opacify intra-flap, subcutaneous branches at minimal radiation exposure (141). Phillips *et al* report the importance of supine positioning without compressive clothing, limiting the scan range to the flap area, triggering contrast bolus at the common femoral artery, scanning caudo-cranially in the direction of DIEA flow and setting acquisition time to 4 seconds (14).

Conclusion

We describe a new technique of 3D printing patient-specific perforasome template that illustrates intra-flap, subcutaneous branches of DIEA perforators. This can be used to derive perforasome anatomy and may help flap design preoperatively. A larger longitudinal study to assess the utility of these templates in improving clinical outcomes, such as rates of fat necrosis is underway.

12.3.2.4 Intraoperative Flap Shaping Using 3D-Printed Mirrored Breast Model

PUBLISHED (Publication): ***Chae MP***, Rozen WM, Patel NG, Hunter-Smith DJ, Ramakrishnan VV. (2017) Enhancing breast projection in autologous reconstruction using the St Andrew's Coning Technique and 3D volumetric analysis. Gland Surg. 10:1-7. PMID: 27489617

Chapter Summary

Introduction: An increasing number of women undergo mastectomy for breast cancer and post-mastectomy autologous breast reconstruction has been shown to significantly improve the psychosexual wellbeing of the patients. A goal of treatment is to achieve symmetry and projection to match the native breast, and/or the contralateral breast in the case of a unilateral reconstruction. Autologous reconstruction, particularly with the deep inferior epigastric artery perforator (DIEP) flap, is particularly advantageous as it can be manipulated to mimic the shape and turgor of the native breast. However, very few techniques of shaping the breast conus when insetting the DIEP flap to enhance aesthetic outcome have been reported to date. With the aide of 3D photography and 3D-printed mirrored image of the contralateral breast as a guide intraoperatively, we describe our St Andrew's coning technique to create a personalized flap projection.

Methods: We report a prospective case series of 3 delayed unilateral breast reconstructions where symmetrization procedure to the contralateral breast was not indicated. Using a commercial 3D scanner (VECTRA XR, Canfield Scientific), the breast region was imaged. The mirrored image was 3D-printed in-house using a desktop 3D printer.

Results: In all cases, projection of the breast mound was able to be safely achieved, with a demonstrated central volume (or 'cone') able to be highlighted on imaging and a 3D printed breast. A 3D print of the contralateral breast was able to be used intraoperatively to guide the operative approach.

Conclusion: The St Andrew's coning technique is a useful aesthetic manoeuvre for achieving breast projection during DIEP flap breast reconstruction, with 3D imaging techniques able to assist in perioperative assessment of breast volume.

Introduction

The number of patients undergoing both prophylactic and therapeutic mastectomy has grown exponentially in the last decade due to the increased availability of genetic testing and breast cancer surveillance (709-712). For post-mastectomy patients, autologous breast reconstruction has shown to significantly improve their psychosexual well-being and has subsequently become an integral part of the breast cancer treatment (43, 459, 713). Using advanced imaging modalities, such as computed tomographic angiography (CTA), as a routine preoperative planning tool, deep inferior epigastric artery perforator (DIEP) free flap reconstruction has become a safe, reliable surgical technique, associated with enhanced clinical outcomes and patient satisfaction (5, 119, 129, 475, 714),(715). In contrast to the vast number of studies investigating the vascular anatomy and imaging of the abdominal wall, the number of studies exploring various surgical techniques to enhance the aesthetic outcome of DIEP flaps is substantially fewer.

The influence of several preoperative factors on the aesthetic outcome of DIEP flaps has been documented, such as adjuvant radiotherapy, the timing of reconstruction, the choice of donor site, and the role of appropriate symmetrization procedure to the contralateral breast**.** However, an individual surgeon's ability to design a flap and manipulate it in three-dimension (3D) to fashion a patient-specific breast mound with appropriate shape and projection is ultimately one of the most important factors. To this effect, Blondeel *et al* have outlined a "three-step" approach that can be applied systematically when shaping and insetting a DIEP flap in any clinical case: prepare the breast footprint, shape the conus, and cover the flap with appropriate skin envelope (716). Since then, a number of studies have published methods to improve the preparation of breast footprint and safe, reliable skin envelope by incorporating the breast aesthetic subunit principle and the "dual-plane" insetting techniques (717-722). In contrast, it is challenging to report in writing how a surgeon transforms a 2D flap into a 3D structure and only a small number of authors have described their technique of shaping the breast conus (716, 723-725).

Blondeel *et al* have outlined their "three-suture" technique for shaping DIEP flap, where the Scarpa's fascia is first sutured to the pectoralis fascia acing the flap under the pectoralis tendon, the second suture holds the lateral edge of the flap to the lateral inframammary fold in tension, and the last suture is placed medially to form a smooth medial cleavage (716). In bilateral reconstruction, Nahabedian describes a similar technique of ensuring

appropriate flap projection with sutures at the medial and lateral edges, and additional superomedial, inferomedial or lateral sutures as required (723). However, in unilateral reconstruction, the author either “rolls” the flap into a cone or creates a lateral fold so that the zone 2 is placed under the zone 1 to provide projection (723). Using the conical folding technique in 126 unilateral reconstructions, Wang *et al* demonstrated satisfactory projection and volume at 6-month follow-up (724).

Recently, Tomita *et al* have exploited the growing accessibility and availability of imaging technologies, such as 3D photography, and 3D printing to assist preoperative planning and guide intraoperatively flap shaping and insetting in unilateral reconstructions (725). Using a commercial 3D scanner, the authors have scanned the breast region and created a mirrored image of the unaffected contralateral breast. This was 3D-printed as a mould and intraoperatively, the flap was placed inside it to trim and shape to fit. They report subjective assessment of satisfactory symmetrization and project at 2-month follow-up.

In recent times, reports using 3D photography, also known as 3D scanning or surface imaging, for volumetric analysis in breast reconstruction has been growing (377, 525, 526, 542, 544, 549, 560, 573, 618, 619, 629, 635, 636, 726). Compared to the conventional imaging modalities, such as CT scans, 3D photography forgoes radiation exposure and a growing number of investigators have demonstrated its accuracy and reliability in breast application (542, 544, 549, 560, 573, 618, 619). Three types of 3D photography are most commonly utilized in medical application: laser imaging, structured light technique, and stereophotogrammetry. Based on passive stereophotogrammetry, VECTRA XR scanners (Canfield Scientific, Fairfield, NJ, USA) are arguably one of the most frequently investigated 3D scanners (544, 549, 573).

3D printing, also known as additive manufacturing or rapid prototyping, is a novel technology that can fabricate haptic biomodels of patient-specific anatomical structures using various imaging sources, such as 3D photography, CT scan, and magnetic resonance imaging (MRI) (16, 17, 318). In the last decade, 3D printers have become more affordable and convenient to use. In breast reconstruction, clinicians have used 3D printing to demonstrate breast volume differential both qualitatively and quantitatively for preoperative planning (35).

In the current study, we describe our St Andrew's coning technique for the first time, where circular rounds of suture are placed within the cutaneous layer of DIEP flaps to create projection. We have used a 3D-printed model of the mirror image of the contralateral breast on the operating table to help determine desired flap projection prior to insetting the flap. We detail our suturing technique in a prospective case series of three delayed unilateral breast reconstructions where symmetrization to the contralateral breast was not indicated.

Methods

Patients

We describe the coning technique used on 1000 consecutive patients, with the volumetric analyses detailed having been performed in a prospective case series of 3 female patients who underwent delayed unilateral autologous breast reconstruction with DIEP flaps at St Andrew's Centre for Plastic Surgery and Burns, Chelmsford, UK. The mean age of the patients was 54 (range: 43 to 63 years). The inclusion criteria comprised unilateral reconstructions, in patients for who no contralateral symmetrisation procedure was planned, such as a reduction or augmentation mammoplasty. All procedures were performed by a single surgeon (VV).

3D Photography

3D photography of the breast region was taken in all patients during the routine preoperative work-up using a commercial 3D scanner, VECTRA XR scanner (Canfield Scientific, Fairfield, NJ, USA). Patients were asked to stand with their arms in varying positions and each scanning took approximately 1-2 seconds. Photographs were created in both standard format and pixelated format to highlight surface contour (Figures 12.3.2.4.1 and 12.3.2.4.2).

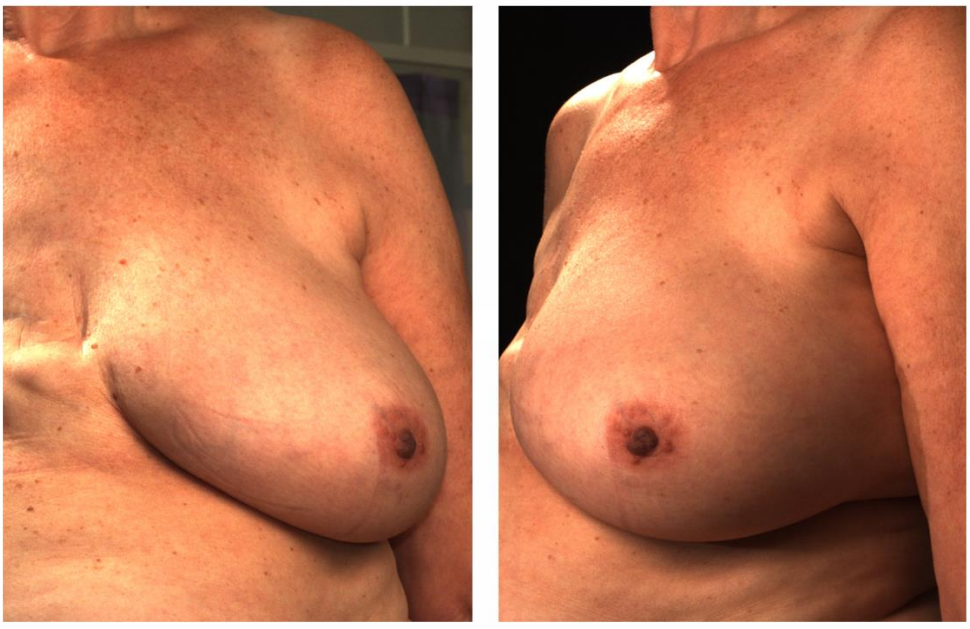

Figure 12.3.2.4.1. Standard preoperative photograph of a patient planned for breast reconstruction, with 2D images achieved using a commercial 3D scanner, VECTRA XR scanner (Canfield Scientific, Fairfield, NJ, USA).

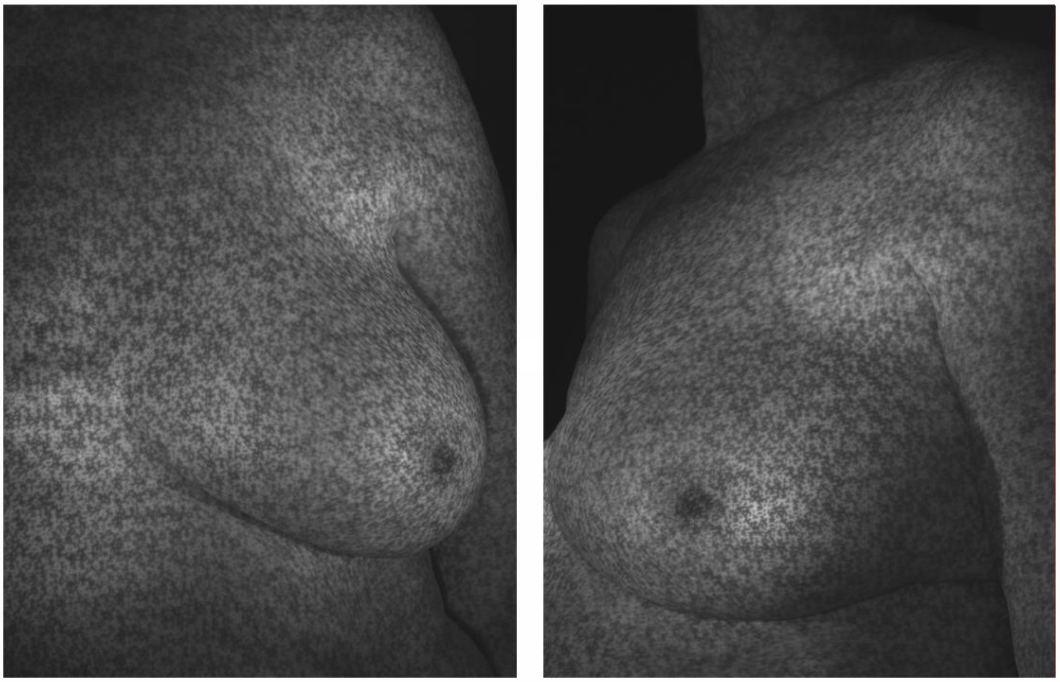

Figure 12.3.2.4.2. Pixelated photograph of the same patient as Figure 1, with contoured images achieved using a commercial 3D scanner, VECTRA XR scanner (Canfield Scientific, Fairfield, NJ, USA).

After waiting less than 5 minutes for image processing, a 3D image of the bilateral breasts was created (Figure 12.3.2.4.3), able to manipulated in a multi-planar fashion as required, and exported from the proprietary software in a Standard Tessellation Language (STL) file format to be prepared for 3D printing.

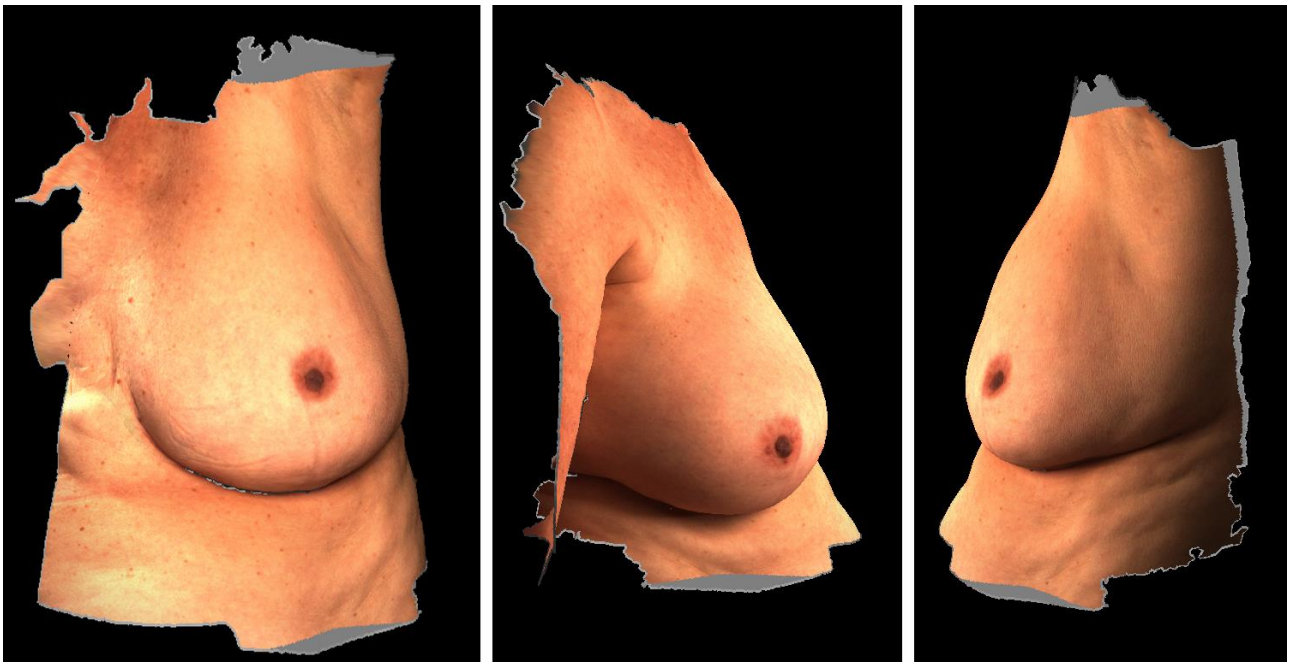

Figure 12.3.2.4.3. 3D photograph of the same patient as Figure 1, with contoured images achieved using a commercial 3D scanner, VECTRA XR scanner (Canfield Scientific, Fairfield, NJ, USA).

3D Printing

Firstly, the 3D image was cropped to isolate the contralateral breast and then, mirrored using the Magics software (Materialise NV, Leuven, Belgium). The file was exported and converted into a printer-friendly file using the MakerBot Desktop software (MakerBot Industries, New York, New York, USA). Subsequently, the mirrored images were 3D-printed using the MakerBot Z18 3D printer (MakerBot Industries), which took mean 10.5 hours per patient (range: 8.5-12 hours). The final products were immediately useful after removing from the printer's build plate (Figure 12.3.2.4.4).

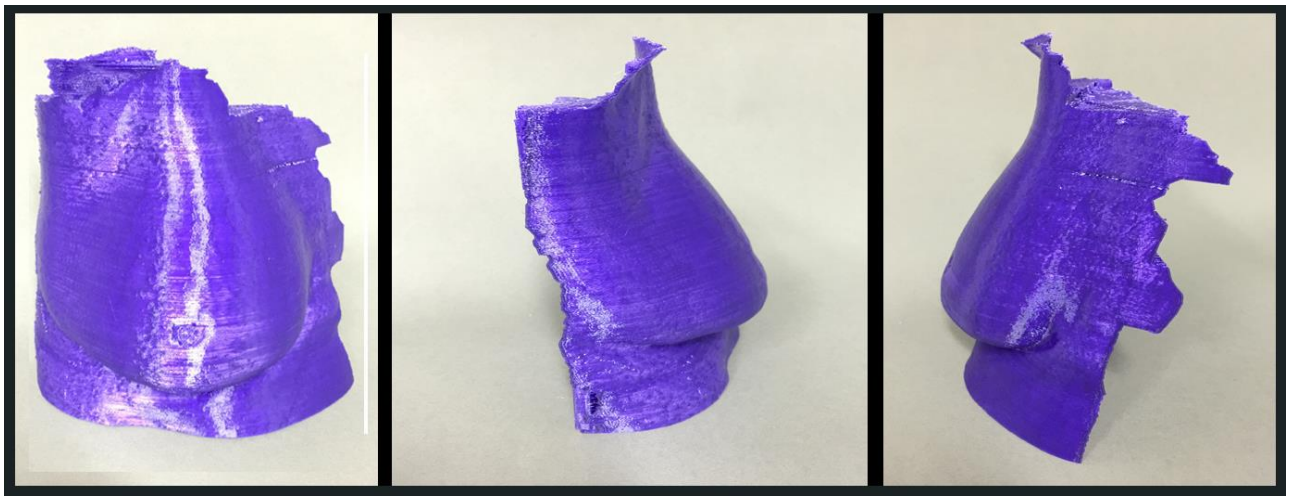

Figure 12.3.2.4.4. 3D-print using the MakerBot Z18 3D printer (MakerBot Industries), of the same patient as Figure 12.3.2.4.1.

Coning Technique

The surgical coning technique began after completion of flap harvest, after disconnection of the vascular pedicle. The breast base is transcribed onto the skin surface of the flap (Figure 12.3.2.4.5A), in order to plan the central focus of coning for maximum projection. The non-projected flap can be highlighted at this point (Figure 12.3.2.4.5B).

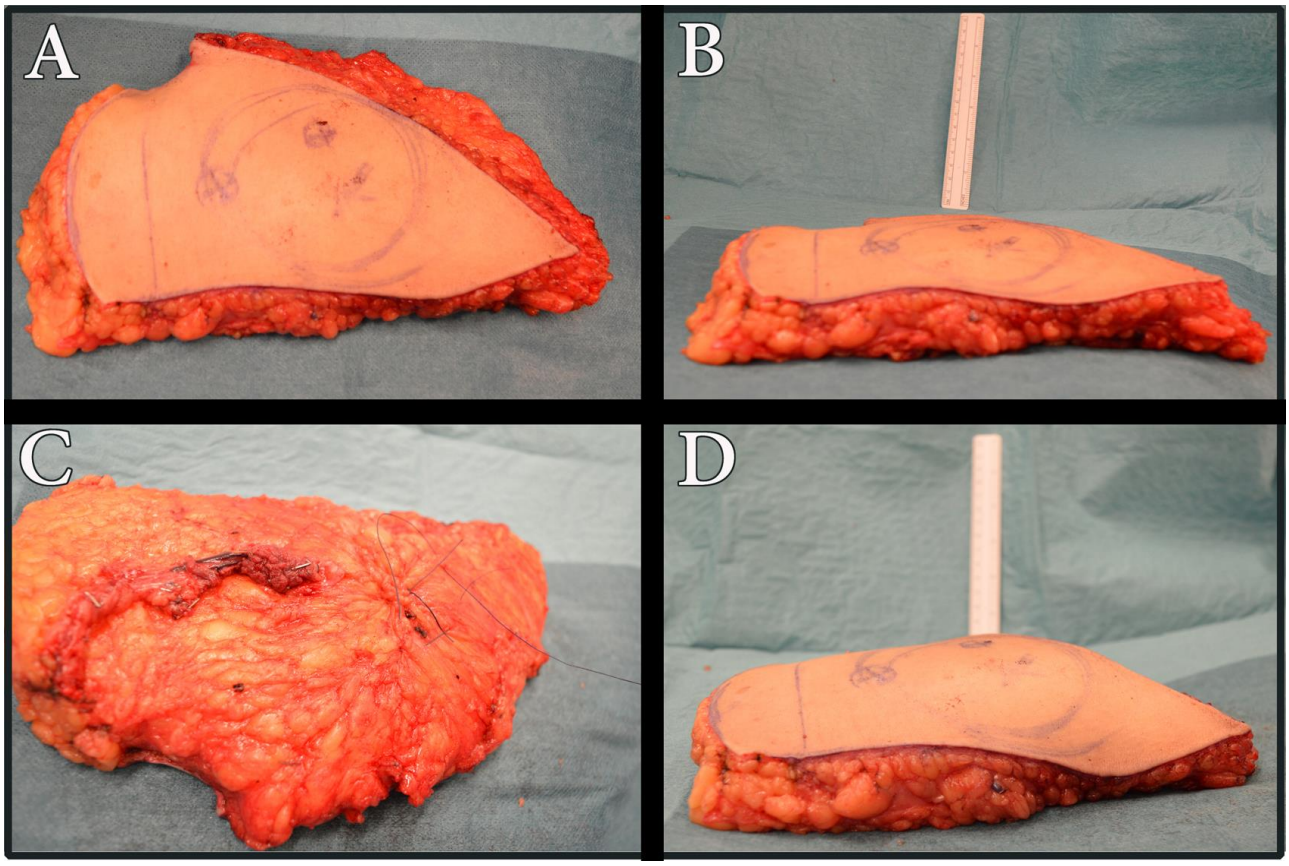

Figure 12.3.2.4.5. The surgical coning technique (same patient as other Figures): The breast base is transcribed onto the skin surface of the flap (A), in order to plan the central focus of coning for maximum projection. The non-projected flap is highlighted (B). The flap undersurface is used for placement of the coning sutures, placed through the sub-scarpa's fat, and a continuous loose purse-string technique is used in this fashion to encircle the planned breast base, before tying the suture loosely (C). The sutures are placed superficially in order to avoid deep penetration which may occlude intra-flap vasculature. Two to three further such purse-string rings are created as needed, in increasing diameters from the initial purse-string, in order to create the desired amount of projection (D).

The flap undersurface is used for placement of the coning sutures. A multi-filament, absorbable suture is placed through the sub-scarpa's fat, and a continuous loose purse-string technique is used in this fashion to encircle the planned breast base, before tying the suture loosely (Figure 12.3.2.4.5C). The sutures are placed superficially in order to avoid deep penetration which may occlude intra-flap vasculature. Two to three further such purse-string rings are created as needed, in increasing diameters from the initial purse-string, in order to create the desired amount of projection (Figure 12.3.2.4.5D).

Results

In all cases, a demonstrable increase in central flap projection was achieved. The mean increase in central flap projection was 2.5cm (range 2 – 3.5cm), achieving over 100% increases in central flap projection (Figure 12.3.2.4.2).

There were no partial or complete flap failures, and no complications recorded attributed to the St Andrew's coning technique, or otherwise. In fact, no complications in the author's preceding 1000 cases of using this technique were attributable to the coning technique described.

Discussion

We describe the St Andrew's coning technique, where we supinate the DIEP flap after the flap harvest and place rounds of dissolvable sutures in the adipose tissue prior to the flap inset, in order to create an appropriate conus. We have individualized each flap to achieve optimal symmetrization by utilizing the 3D-printed haptic models of the mirrored image of the contralateral breast to adjust the suturing.

With increasing population, the rate of prevalence and incidence of breast cancer continues to rise and, in the United States alone, one in eight women will be affected by the disease in their lifetime (41). Furthermore, an increasing number of women are receiving both therapeutic and prophylactic mastectomy for breast cancer, boosted by the increased availability of genetic testing (709-712). Encouragingly, post-mastectomy breast reconstruction has demonstrated to significantly improve the psychosexual wellbeing of patients and, as a result, it has become an integral part of the comprehensive treatment of breast cancer (43, 459, 713). Unlike synthetic implants, autologous reconstruction with abdominal wall as donor site yields a more natural-appearing and a longer-lasting outcome, without encountering the conventional prosthesis-related complications (48, 727-729). Compared to the earlier TRAM flaps, DIEP flaps can provide adequate volume replacement, without significantly compromising the donor site to ventral bulge or hernia (49, 68). Advancement of modern imaging technologies, especially the establishment of CTA as a routine preoperative planning tool in DIEP flap reconstruction, has enabled surgeons to select appropriate perforators and flap designs, leading to improved clinical outcomes (5, 119, 129, 475, 714), (715).

In contrast to the studies investigating the vascular anatomy and imaging of the abdominal wall (28), (119, 377, 559, 561, 586),(32, 455, 540), there is a relative paucity of studies exploring surgical techniques to enhance aesthetic outcome in DIEP flap reconstructions. Several preoperative considerations are considered critical in order to ensure aesthetically satisfactory result, such as adjuvant radiotherapy, the timing of reconstruction, choice of donor site, and symmetrization of the contralateral breast via augmentation or reduction mammoplasty depending on the patient preference (723). However, the aesthetic outcome of DIEP flaps ultimately relies on an individual surgeon's technique and experience in flap shaping and insetting.

To this effect, Blondeel *et al* have presented a systematic approach that reproducibly produces aesthetically-pleasing breast mound with DIEP flaps in any clinical situation: firstly, prepare the breast footprint; secondly, shape the conus; and lastly, cover the flap with suitable skin envelope (716). Creating the breast footprint and the skin envelope requires defining the inframammary fold and replacing the mastectomy scar with aesthetic lines applying the breast aesthetic subunit principle (717). Initially, devised for planning nasal and facial reconstructive surgeries (730-733), aesthetic subunit principle has also demonstrated to improve the cosmetic outcome and patient satisfaction when applied in autologous breast reconstructions (718-720). Recently, in a direct comparison study, Gravvanis *et al* have reported that insetting DIEP flaps as a single aesthetic subunit, where the inferior mastectomy skin flap is deepithelialized and overlaid by the free flap so that a new inframammary fold (IMF) is defined using the edge of the free flap, yields a more natural shape and a satisfactory scar pattern than flap insetting as a double subunit, where the IMF is preserved (721). Similarly, when the mastectomy skin envelope is compromised due to radiation or is lacking in volume due to the reconstruction being delayed, this can be overcome by insetting the DIEP flap in “dual-plane”, below and above the pectoral muscle in the upper and lower pole respectively (722).

In contrast, only a few techniques of shaping the breast conus have been reported to date and the evidence is limited to sporadic case series and descriptive accounts (716, 723-725). As Blondeel *et al* points out this is likely attributable to the fact that describing how to manipulate a 2D structure (i.e. DIEP flap) into a 3D form (i.e. conus) is difficult to achieve in writing (716). Furthermore, the ability to think and handle tissue in 3D is considered a key skill of a well-trained plastic surgeon and the significance of its discussion may be overlooked (716). Nonetheless, the shape and the projection of an ideal conus is patient-specific and is critical towards achieving an aesthetically pleasing outcome and ensuring a high quality of life. Blondeel *et al* describe a “three-suture” technique where the first key suture connects the Scarpa’s fascia to the pectoralis fascia and positions the DIEP flap underneath the pectoralis tendon. The second suture is used to affix the lateral edge of the flap to the most lateral edge of the inframammary fold in tension. The last one is placed in the medial edge of the inframammary fold to create a smooth medial cleavage (716). Similarly, Nahabedian reports his technique of securing medial and lateral edges of the free flap to the sternal border and the lateral chest wall respectively, in bilateral breast reconstructions, with superomedial, inferomedial and lateral sutures (723). In unilateral reconstructions, Nahabedian uses the contralateral breast as a template and folds the free

flap either in a conical fashion or creates a lateral fold where the zone 2 is placed under the zone 1 and secured with a lateral suture (723). In 2015, Wang *et al* reports a retrospective case series of 126 unilateral DIEP reconstructions where the flap is folded into a cone before insetting (724). Regardless of the shape in which the flaps were harvested – fusiform, semi-circle, or crescent – the authors have noted satisfactory breast projection and volume at 6-month follow-up. Interestingly, they have not reported patient satisfaction or quality of life data.

Recently, Tomita *et al* have presented an algorithm incorporating the use of novel 3D scanning technology to guide surgeons shape patient-specific DIEP flaps in a prospective cohort of 11 delayed unilateral reconstructions (725). Preoperatively, the breast region is scanned with the patient sitting up, using a commercial 3D scanner, David Structured Light Scanner SLS-1 (David Vision Systems GmbH, Koblenz, Germany), from which the required flap volume is calculated. In addition, the scanned image of the contralateral breast is mirrored and 3D-printed as a mould. On the operating table, after the microvascular anastomosis, the flap is carefully placed inside the sterilized mould, from where it was trimmed to fit and the shape was secured with randomly-placed dissolvable sutures. The authors report good symmetrization and cosmetic effect at 2-month follow-up. One of the major limitations of this technique is that it is only applicable in unilateral reconstructions where the contralateral breast does not require a symmetrization procedure. Furthermore, the hard plastic mould does not account for postoperative swelling and facilitate “over-correction” of the volume of the reconstructed breast. Interestingly, the authors do not report the thickness of the breast mould, which may have led to further “under-correction” of the reconstruction. In comparison, the St Andrew’s coning sutures are readily reproducible and are flexible enough for the surgeon to tailor the technique to accommodate individual differences. In our series, none of our patients required a symmetrization procedure to the contralateral breast and we utilized the 3D-printed mirror image from 3D photography of the contralateral side to help surgeons guide placement of the St Andrew’s coning sutures.

3D photography captures the light reflected off a surface to construct a virtual 3D model (377). Originally used in automotive and aerospace industries, Galdino *et al* first used the technology in plastic surgery to quantitatively assess breast symmetry (526). Similar to other medical imaging modalities, 3D surface imaging has advanced significantly in the last decade and is accurate, reliable, and simple to use (560, 618, 619). In clinical

application for breast volumetric analysis and imaging, three 3D scanning techniques have been studied: laser imaging, structured light technique, and stereophotogrammetry. 3D laser imaging projects a particular pattern of laser (i.e. spot or stripe) and utilizes the triangulation calculation method to determine a 3D coordinate (570, 619). Konica Minolta 3D scanner (Konica Minolta Inc., Tokyo, Japan), one of the most extensively studied clinical laser scanner, has been utilized in planning implant breast reconstructions (525). However, its accuracy and validity has not yet been reported. Likewise, structured light technique projects an organised pattern of light (i.e. stripe, grid, or dots) and captures the distortion in the light pattern using multiple calibrated cameras to derive at 3D surface data (618, 629). Axis Three Torso System (Axis Three, Miami, FL, USA) is the most frequently reported structured light 3D scanner and has demonstrated its accuracy and reliability in simulating breast augmentation outcomes (542). However, it has not been studied in autologous breast reconstructions. Based on the human eye physiology, stereophotogrammetry utilizes a stereo pair of cameras to derive 3D data from the points of light intersection (619, 635, 636). Depending on the presence of additional light being directly projected on to the object, stereophotogrammetry can be classified into: active, passive, and hybrid. Lacking the additional lighting to resist interference from the ambient light, passive stereophotogrammetry requires high-quality cameras in a carefully controlled environment. However, as a result, passive stereophotogrammetry scanners such as, our VECTRA XR scanners (Canfield Scientific), can capture high-resolution 3D photographs at fast speed and is one of the most extensively investigated commercial scanner in breast application (377). Several studies have demonstrated high accuracy and reliability of the VECTRA devices (544, 549, 573). However, its widespread use is limited by its high cost, relatively slow image-processing speed, and lack of portability.

3D printing describes a technology where haptic biomodels are fabricated in a layer-by-layer fashion using CAD files derived from routine medical imaging sources, such as 3D photography, CT and MRI scans (16, 17, 318). In contrast to the current medical imaging techniques, clinicians are able to interact hands-on with the 3D-printed biomodels, which enables a superior understanding of visuospatial relationship between the patient-specific anatomical structures. In clinical application, 3D printing is useful for preoperative planning, building intraoperative guidance devices, education of patients and junior doctors, and designing customized prosthesis. To date, investigators have utilized routine preoperative CTA scans in breast reconstructions to 3D-print accurate models that enables both qualitative and quantitative appreciation of the breast volume differential (35).

In the current case series, 3D-printed biomodels of mirrored image of the contralateral breast are brought into the operating theatre to help guide surgeons when performing the described St Andrew's coning sutures.

One of the major limitations of our study was that none of the patients required secondary corrective surgery, such as reduction mammoplasty, augmentation or mastopexy, to the contralateral side. It may be useful in the future utilize the Canfield Scientific's Breast Sculptor ® software that reliably simulates breast procedure outcomes (549) in order to create the 3D image of an ideal reconstructed breast in each case that could be 3D-printed for use intraoperatively. Furthermore, assessment of outcome at long-term follow-up may have been useful to demonstrate clinical utility of the St Andrew's coning suture technique. In order to demonstrate the accuracy and reliability of our 3D scanning technique, the current study needs to be replicated in a larger, comparative study.

Conclusion

The St Andrew's coning technique is a useful aesthetic maneouver for achieving breast projection during DIEP flap breast reconstruction, with 3D imaging techniques able to assist in perioperative assessment of breast volume.

12.3.3 The Future: 3D Bioprinting

12.3.3.1 3D Bioprinting Breast Adipose Tissue

PUBLISHED (Peer-Reviewed Book Chapter): ***Chae MP***, Hunter-Smith DJ, Murphy SV, Findlay M. (2017) 3D bioprinting adipose tissue for breast reconstruction. In D. J. Thomas, Z. M. Jessop, I. S. Whitaker eds., *3D bioprinting for connective regenerative tissue engineering: Techniques and applications.* Cambridge, UK: Woodhead Publishing; 2017

Chapter Summary

Introduction: Three dimensional (3D) bioprinting has garnered immense interest over the past decade based on its potential to provide a means to rapidly manufacture replacement body parts that replace like with like and are immediately biocompatible. In comparison to traditional tissue engineering techniques, it provides novel means of combining cells, scaffolds and growth factors into a carefully designed 3-dimensional structure, such as a breast.

Methods: A review of the published English literature dating from 1950 to 2015 using databases, such as PubMed, Medline, Web of Science, and EMBASE was undertaken.

Results: A 3D bioprinted construct is typically composed of a scaffold and cells or precursor cells of the desired tissue. The scaffold provides necessary 3D structural integrity, mimicking local microenvironment, contains appropriate cell-specific signalling cues. Stem cells, such as mesenchymal stem cells (MSC), are most commonly used cells. 3D bioprinting techniques can be broadly classified by their mechanism of cell deposition: inkjet, microextrusion, or laser. Recently, a novel 3D bioprinting technique has been described, integrated tissue organ printer (ITOP), which simultaneously deposits cell-laden hydrogel with synthetic polymer by a pneumatic microextrusion controller.

Conclusion: Researchers in the past have faced difficulty in producing adipose tissue in clinically-relevant large volumes using standard tissue engineering practices. With the advent of 3D printing and subsequent 3D bioprinting technology, investigators are now able to fabricate custom-shape, complex internal porous design scaffolds with multiple cell

types. Building on promising *in vitro* and animal studies, 3D bioprinting of adipose tissue is poised for clinical translation.

Introduction

Three dimensional (3D) bioprinting has garnered immense interest over the past decade based on its potential to provide a means to rapidly manufacture replacement body parts that replace like with like and are immediately biocompatible. Despite promising advances in bioprinting, it is still immensely difficult to reproduce the delicate structure-function relationships of complex tissues and organs using this approach. In this way, the bioprinting of functional autologous solid organs (e.g. kidney or heart) remains an aspirational goal. However, the formation of more simple tissues such as adipose tissue for breast reconstruction, represents lower-hanging fruit in translational bioprinting research. The ability to bioprint autologous fat tissue would be transformational in the management of breast cancer patients. This centers around the combination of great need for breast reconstruction in today's society and a lack of an ideal form of breast reconstruction characterised by simplicity along with a low complication profile.

Post-mastectomy breast reconstruction has become an important component of breast cancer treatment due to its high prevalence and incidence in our aging populations and the significant improvements in patient survival over the past few decades (43). One in eight women in the United States will develop breast cancer in their lifetime (41) and it accounts for 14.6% of all new cancers affecting women (734). In addition to breast reconstruction following mastectomy for established breast cancer, an increasing number of women (25%) are opting for earlier as a prophylactic measure for gene mutations (BRCA mutations) or as definitive management of earlier breast cancers where there is a strong family history. (459) The five-year survival rate for patients following therapy has improved significantly in the last decade (89.7%) (734). To this effect, numerous studies have demonstrated that post-mastectomy breast reconstruction improves the psychosexual well-being of these women and the above factors have significantly increased demand for breast reconstruction. (43-47).

Breast reconstruction can be largely classified into two groups: implant-based or autologous. Implant-based reconstruction can be performed in a single stage (i.e. direct-to-implant) if there is adequate mastectomy skin flap or in two stages using tissue expanders (735, 736). Despite their shorter operative time and faster recovery, breast implants are not considered the gold-standard in breast reconstruction due to their significant risk of

long-term complications, such as infection, foreign body reaction, capsular contracture and anaplastic large-cell lymphoma (460, 737-740).

In contrast, autologous breast reconstruction, most commonly using the abdominal wall-based free deep inferior epigastric artery perforator (DIEP) flaps or muscle-sparing transverse rectus abdominus myocutaneous (TRAM) flaps, can produce more aesthetically-pleasing, natural-looking breasts with fewer long-term complications (48). Microsurgical breast reconstruction has evolved into a safe, reliable procedure due to recent advancements in microsurgical techniques (33, 50, 51, 129, 137). In order to improve aesthetic outcome of free flaps, numerous surgical techniques have been described, such as Blondeel's "three-suture" technique (716), Nahabedian's technique of flap inset (723), Wang's conical folding technique (724), St Andrew's coning sutures (741), and breast aesthetic unit-based flap inset (721). One of the major disadvantages of free flaps is related to donor site morbidity. Overall rate of abdominal wall hernia repair after a DIEP or transverse rectus abdominis muscle (TRAM) flap reconstruction is low (2.45% out of 7,929 cases) (742). However, this is still greater than the age-matched population risk (0.28% out of 15,679 women) (742). Furthermore, in some women, abdominal pannus may not a suitable donor site due to lack of adequate volume (743-745).

First described by van der Meulen in 1889 and Neuber in 1893 (746), fat grafting for breast reconstruction in the last decade has returned to popularity following the improvement of liposuction techniques (747). Fat grafting offers numerous advantages for use in breast reconstruction as it provides (usually) abundant autologous donor tissue, low donor site morbidity, and relative ease of harvest (748, 749). However, the need for engraftment and variable survival of fat following fat grafting, make this more suited as an adjunct to conventional breast reconstruction techniques with injections of smaller volumes, spread over multiple stages (750-755). Investigators have attempted to improve the adipogenic potential of fat grafts by enriching them with additional adipose-derived stem cells (ADSC), platelet-rich plasms (PRP) or growth factors, however, results remain mixed (749, 756-766). Despite these advances, the current consensus recommends that fat grafting is most appropriately reserved to supplement the conventional breast reconstructive techniques during secondary contouring procedures (767, 768).

3D bioprinting provides a novel means to combine cells, scaffolds and growth factors into a carefully designed 3-dimensional structure that includes an intrinsic circulation (either de

novo or ex-vivo) (769) and builds on decades of experience and expertise in autologous fat grafting, adipose-derived stem cell biology and tissue engineering. Today's highly flexible 3D printing technology provides a potential solution unmet clinical needs in breast reconstruction. Here we discuss the advances in 3D bioprinting technology with regard to tissue engineering and its use and potential in breast reconstruction.

Methods

A review of the published English literature dating from 1950 to 2015 using databases, such as PubMed, Medline, Web of Science, and EMBASE was undertaken. Search terms used are: “3D bioprinting”, “3D printing”, “tissue engineering”, “scaffold”, “growth factors”, “adipose derived stem cells”, “breast reconstruction”, “post-mastectomy”.

Results

3D Bioprinting

Background

3D bioprinting describes a method of creating individualized 3D tissue constructs by incorporating novel 3D printing technology in more traditional tissue engineering (770).

Tissue Engineering

Tissue engineering utilizes cells, biomaterials, and biologically active growth factors to produce tissues that mature into functional, vascularized structures (771). Cells are usually derived from a sample of the desired tissue and are enriched through selection strategies and/or expanded *ex vivo*. (772-777). Biomaterials and growth factors must provide a controlled gradient in mechanical properties and cellular signalling for optimal cell growth *in vitro* (778). As tissues and organs grow, it is essential that they develop an intrinsic vascular network. Given that the maximum nutrient diffusion distance for cells for survival is only 100-200 microns (779), manufacturing complex, well-vascularized tissues of clinically-relevant size has proved challenging using conventional laboratory techniques (771, 780). To this effect, investigators have studied 3D culture systems, such as cell suspension culture (781) and ceiling culture (782), that can regulate cell tension (783) and enhance adipogenic differentiation (784). However, they fail to accurately reproduce the *in vivo* microenvironment (785, 786). Furthermore, adipocytes in cell suspension cultures are not exposed to nutrition equally leading to progressive cell lysis within 72 hours of incubation (787). In ceiling cultures, preadipocytes proliferate and differentiate, however, they display spindle, fibroblast-like morphology, rather than the round unilocular phenotype typical of mature adipocytes (782, 788, 789). Addition of angiogenic growth factors and endothelial precursor cells may address these issues, however, conditions for their culture and expansion are not readily compatibility with adipocytes, which poses practical issues that will be discussed later in this review (778, 790, 791).

Additional approaches have included the use of existing tissues to try to generate new tissues and organs through decellularization. In this technique, cells are carefully removed from a donor tissue while its extracellular matrix (ECM) and mechanical properties are

preserved (792). These constructs elicit minimal host immune response (793) (794) and the donor ECM is gradually replaced by ECM excreted by repopulated cells (795). Unfortunately, allogeneic donor tissues are rare and autologous options pose donor site morbidity. Various synthetic scaffolds have been described that seek to encourage neovascularisation, tissue ingrowth and development, such as 3D fiber deposition (796), particulate leaching technique (797), and electrospinning (798). The microarchitecture of these can be very difficult to control across the entire construct. In comparison, 3D-printed scaffolds can be generated with customizable form and interconnected pores (799-801) to facilitate neovascularization and nutrient flow and the control offered by this technology is preferable to existing techniques (802) (770, 803-809).

3D Printing

3D printing, also known as rapid prototyping or additive manufacturing, describes a process by which a 3D construct derived from computer-aided design (CAD) is built in layer-by-layer fashion (16-18, 318). One of the major advantages of 3D printing is the ability to produce custom designs with complex internal details (171-173). 3D printing has been utilized in industrial design for decades, however, it has only been adopted for medical application in the last decade (20). Imaging data from routine computed tomography (CT) or magnetic resonance imaging (MRI) scans is converted into a CAD file using 3D printing softwares, such as 3D Slicer (Surgical Planning Laboratory; Boston, MA, USA). The file is used by a 3D printer to fabricate the final model. Aided by expiration of key patents in the last decade, 3D printers have become affordable to lay consumers and has been adopted for 3D bioprinting.

3D Bioprinting Composition

A 3D bioprinted construct is typically composed of a scaffold and cells or precursor cells of the desired tissue.

Scaffold

The scaffold provides necessary 3D structural integrity, mimicking local microenvironment, contains appropriate cell-specific signalling cues, and must possess negligible cytotoxicity (810, 811). The external shape of a scaffold can be designed using CT/MRI scans of the

desired organ and the internal porous architecture must be optimized for vascular growth and nutrient diffusion (812). There is a distinct absence of an ideal scaffold material for 3D bioprinting. A variety of biological and synthetic materials have been used to build scaffolds, such as alginate (801, 813-816), fibrin (801, 813-815, 817), gelatin (817), hyaluronic acid (817), glycerol (817), and Pluronic® F-127 Derby, 2012 #2409}(813-815). Despite their superior biocompatibility and cytocompatibility, biological scaffolds often lack mechanical strength. Likewise, synthetic polymers can often lack biocompatibility but this can be reversed by incorporating biologically active domains (775, 818-820), such as cell-adhesion peptides (821), silk functionalized with titanium-binding peptides (822), and collagen (823).

One of the most commonly used polymers in 3D bioprinted scaffolds is polycaprolactone (PCL) (824, 825). PCL has a low melting temperature (60 ^{o}C) and cools rapidly upon deposition, making it cytocompatible (824). It is durable with a long degradation period (1.5-2 years), and is completely excreted by the body (825). However, it is elastic and therefore one of its main disadvantages is its inability to provide mechanical strength. In contrast, polymers, such as Pluronic® F-127 (BASF SE; Ludwigshafen, Germany) composed of hydrophobic polypropylene glycol and hydrophilic polyethylene glycol, can provide strength, is easy to use (826), but lacks good cytocompatibility (827).

Cells

Stem cells, such as mesenchymal stem cells (MSC), are the most commonly used cells in 3D bioprinting. The microenvironment of these pluripotent or multipotent cells must be tightly regulated during tissue growth so that the necessary tissue is produced, rather than any of the other tissues that the stem cell is capable of producing (or some mixture of these). As a result, the final construct is most commonly matured *ex vivo* or inside an *in vivo* bioreactor before implantation (828-832). Autologous or allogeneic cells are required. Despite their obvious advantages, autologous stem cells can be difficult to culture and expand to a sufficient number for clinical application without a significant loss of proliferative function, phenotype and additional regulatory hurdles (833, 834). Encouragingly, this can be partly addressed by co-culture with precursor, progenitor and supportive cells as well as seen with the co-culture of preadipocytes and endothelial cells for adipose tissue engineering (835). In contrast, allogeneic stem cells can be stored and accessed when needed. However, they pose a risk of immune rejection.

3D Bioprinting Techniques

3D bioprinting techniques can be broadly classified by their mechanism of cell deposition: inkjet (808, 836-838), microextrusion (839-841), or laser (842-844). Integrated tissue organ printer (ITOP) is a novel 3D bioprinting technique that simultaneously deposits cell-laden hydrogel with synthetic polymer by a pneumatic microextrusion controller (817) (Table 12.3.3.1).

Bioprinting Techniques	Mechanism	Advantages	Disadvantages	Clinical Application
Inkjet	Thermal	High resolution Low cost High speed Biocompatibility	Exposure to high heat (300 ^{o}C) Absolute requirement for biological material to be liquid	Skin (845) Cartilage (846) Bone (847)
	Acoustic	High resolution Low cost High speed Biocompatibility	Cell lysis at 15-25 kHz Absolute requirement for biological material to be liquid	
Microextrusion	Pneumatic	Affordable Simpler components Viscous biologic material	Lower spatial control Low cell viability Low resolution Slow speed	Aortic valve (848) Blood vessels (849) Ovarian cancer model (850)
	Mechanical	Affordable Superior spatial control Viscous biologic material	Sophisticated components Low cell viability Low resolution Slow speed	
Laser-	LIFT	Compatibility with	Slow print speed	Skin (851)

Assisted		range of viscosity, resolution and speed		Skull defect (852)
ITOP	Pneumatic	Microchannel formation Microscale nozzle Produce well-vascularized, human-scale tissue construct	Limited accessibility	Mandibular bony defect (817) Ear cartilage (817) Skeletal muscle (817)

Table 12.3.3.1.1. Summary of 3D bioprinting techniques. Abbreviations: LIFT: laser-induced forward transfer; ITOP: integrated tissue organ printer.

Inkjet Bioprinting

Inkjet bioprinting is the earliest described technique where either thermal (838) or acoustic (853-855) forces are used to eject drops of liquid on to a scaffold. Electrically-heated thermal print-heads can produce a localized temperature increase to 200-300 ^{o}C for a short duration (2 microseconds) but produce only 4-10 ^{o}C rise in the overall temperature (856). Despite some studies demonstrating minimal impact on the stability of biological molecules, such as DNA (853, 854), there still remains a potential risk using thermal inkjet bioprinters by exposing cells and the tissue construct to heat and mechanical stress. Acoustically-based printing uses acoustic waves created by a piezoelectric crystal to break liquid into regular droplets (857). Pulse, duration and amplitude of the sound wave can be adjusted to alter the size of droplets and rate of ejection. The major disadvantage of using acoustic forces lies with the potential risk of cell damage and lysis from 15-25 kHz frequencies emitted by the piezoelectric crystals (858). In summary, despite their low cost, high resolution, high speed and biocompatibility, both thermal and acoustic inkjet bioprinting is limited by its requirement of the biological material to be in liquid form. This limitation can be potentially addressed by immediately curing the material with chemical, pH or ultraviolet (859, 860). However, this increases the printing time significantly and introduces chemical modifications leading to cell damage. To date, inkjet 3D bioprinters have been utilized to fabricate functional skin (845), cartilage (846), and bone (847) in preclinical models but not adipose tissue.

Microextrusion Bioprinting

Microextrusion bioprinters are the most common and affordable bioprinters used in research (812). In comparison to an inkjet bioprinter that extrudes liquid droplets, a microextrusion bioprinter ejects microbeads of a material, such as hydrogel, biocompatible copolymers, and cell spheroids, using pneumatic (826, 860-862) or mechanical (863, 864) dispensing systems. Pneumatic printers are built with simpler components but mechanical dispensers provide a greater spatial control. Major advantages of microextrusion printers include their compatibility with materials with a wide range of fluid properties, such as viscosity (806), and the ability to deposit very high cell densities, such as tissue spheroids that can self-assemble directly into complex structures (865, 866). One of the major disadvantages of microextrusion as a technique is its relatively low cell viability rate (40-86%) due to shear stress (862, 867), low print resolution and speed (847). To date, microextrusion technology has been used to fabricate aortic valves (848), blood vessels (849), and *in vitro* ovarian cancer model (850) in preclinical studies.

Laser-Assisted Bioprinting

Laser-assisted bioprinting (LAB) is the least commonly used technique and relies on the principle of laser-induced forward transfer (LIFT) (868, 869). In a LIFT system, a pulsed laser beam is directed on to the laser-energy-absorbing layer (e.g. gold or titanium) over a "ribbon" containing the donor transport system. The laser induces formation of a high-pressure bubble that propels biological material containing cells forward towards a scaffold. Microscale resolution of LAB means that, in addition to cells (870), it can be used to deposit peptides (871) and DNA (872). One of the main advantages of LAB technology is its flexibility, as it is compatible with a wide range of viscosity, resolution (i.e. single cell per drop to 10^8 cell per milliliter), and speed (i.e. 5 kHz to 1,600 mm/s) (844). Moreover, this technique has a negligible effect on cell viability and function (873-875). A major drawback is its slow print speed due to the requirement of rapid gelation of the deposited material due to its high resolution (876). In preclinical studies, LAB has been used to create a small cellularized skin construct (851) and a skull defect (852).

Integrated Tissue Organ Printer (ITOP)

Integrated tissue organ printer (ITOP) is an innovative bioprinting technique, developed by Kang *et al*, that consists of a multimaterial-dispensing printer system controlled by a custom-designed microscale nozzle motion program enabling simultaneous deposition of both cell-laden hydrogel and synthetic biodegradable polymer to deliver a human-scale tissue construct (817). Despite its relatively high resolution, inkjet bioprinting is limited by its requirement of liquid hydrogel that results in low structural integrity and mechanical strength. Microextrusion method utilizes viscous fluid and can produce more stable 3D constructs, but the generated shear stress reduces cell viability, printing resolution, speed and size. LAB technique requires rapid gelation of hydrogels to achieve its very high resolution, leading to low flow rates.

ITOP deposits PCL-based scaffolds in various designs that provide mechanical strength to the construct and forms networks of microchannels that facilitate cell nutrient and oxygen diffusion. However, the bulk of mechanical stability is provided by Pluronic® F-127 hydrogel extruded from a separate nozzle that acts as an outer sacrificial support layer. The composite hydrogel system in ITOP consists of fibrinogen, gelatin, hyaluronic acid, and glycerol in disparate concentrations optimized for each target tissue. The nozzle motion program is customized based on the printing pattern and the fabrication condition (i.e. scan speed, temperature, material information, and air pressure). Once the printing is completed, thrombin is added to cross-link fibrinogen into stable fibrin while the other hydrogels, including Pluronic® F-127, are washed out. Using 3T3 fibroblast cell model, authors demonstrate ≥95% cell viability at 6 days and persistent tissue growth at 15 days.

As a result, ITOP can manufacture well-vascularized, human-scale, complex shape, structurally stable tissue constructs. ITOP has demonstrated proof of principle in the use of human amniotic fluid-derived stem cells to forma construct for a human mandibular bony defect *in vitro* and ITOP-printed constructs have been successfully implanted skull defects in rodents. Rabbit chondrocytes have been used with ITOP to form a human ear-shaped cartilage with demonstrated viability at 1 month after implantation in preclinical models. Furthermore, functional 15 x 5 x 1 mm rodent skeletal muscle tissue has been formed.

3D Bioprinting Adipose Tissue for Breast Reconstruction

Challenges Facing Adipose Tissue Engineering

For decades, researchers have investigated adipose tissue engineering for post-mastectomy breast reconstruction (877). In contrast to other organs and tissues, such as bladder (772) and mandible (878, 879) that have already been tissue-engineered and successfully implanted in patients, building stable, large-volume adipose tissue by conventional tissue engineering presents numerous challenges. Standard subcutaneous adipose tissue consists of fully-differentiated adipocytes that constitutes 90% of total volume and 15% of total cells (880). All adipocytes are found in close proximity to a capillary network (within 200 μm) (881) and are mechanically supported by a thin layer of basement membrane and the stromal ECM (882). As a result, they are highly sensitive to hypoxia and physically fragile. Moreover, adipogenesis is closely accompanied by angiogenesis in physiological circumstances (881). Therefore, adipose tissue engineering cannot be achieved without concomitant neovascularization, posing further challenges (883-887). To this effect, the ability of 3D bioprinters that can deposit multiple types of cells, materials, and build composite structures appears promising (e.g. ITOP).

Composition of 3D-Bioprinted Adipose Tissue

The two major components in the formation of a 3D-bioprinted adipose tissue construct for breast reconstruction are a scaffold and cells.

Scaffolds for 3-D Bioprinted Adipose Tissue

Role of a Scaffold

In addition to providing form and encasing biological materials, the mechanical properties of a scaffold are important in determining the differentiation fate of stem cell differentiation lineages (888). Cytoskeletal tension transmitted from actomyosin contractility and reaction forces generated from surrounding ECM can influence gene expression, cell shape and differentiation (889). Extracellularly, mechanical forces on ECM, such as tissue stretch, compression or shear stress, is transmitted to cells via integrin-regulated adhesions (890) into cytoskeleton and cell nucleus (891), leading to the activation of various signalling pathways (892-896) and mechanosensitive ion channels (897). As a result, a scaffold that mimics adipose tissue stiffness (i.e. Young's elastic modulus of 2-4 kPa) promotes adipogenic differentiation even in the absence of exogenous adipogenic growth factors

(888, 898-903). On the contrary, if the stiffness is increased, ADSCs lose their typical rounded morphology and fail to upregulate adipogenic markers (888). Likewise, the pattern of microstructure (i.e. square vs rectangle) (904) and the surface nanotopography (i.e. round nanogroove vs straight grooves and grids) (894) of a scaffold can all influence adipogenic differentiation.

Scaffold Design

In order to support concomitant angiogenesis, the design of a scaffold must incorporate microchannels that enable vascular infiltration and growth, facilitating subsequent oxygen and nutrient perfusion (905, 906). Furthermore, the porosity of interconnect cell structure is crucial for stem cell migration, proliferation and differentiation (907). The pore size must be able to accommodate co-existence of ADSC, differentiated adipocytes, and mature adipose tissue lobules (i.e. 10 vs 100 vs 300-500 μm, respectively) (899, 908, 909). In addition, surface coating scaffolds with silica nanoparticles can increase ADSC proliferation by activating downstream ERK 1/2 pathways and improves mechanical strength (910).

Scaffold Building Techniques

Numerous techniques for constructing 3D scaffolds have been described in the past, such as cell patterning (911), particulate leaching (797), electrospinning (798, 912), lithography (913), and microfabrication (913). In comparison, 3D bioprinting provides unique advantages of being able to rapidly create 3D spheroid constructs with complex internal structures like microchannels, and perform controlled material extrusion to achieve the desired biomechanical properties (826, 867, 871, 914-916). Moreover, 3D bioprinters can safely handle delicate stem cells like ADSC (858, 917).

Scaffold Materials

Materials used to construct 3D scaffolds for tissue engineering and 3D bioprinting of adipose tissue can be broadly classified into biological materials, biodegradable polymers, and composite scaffolds (Table 12.3.3.1.2).

	Description	Advantages	Limitations	Adipose Tissue Regeneration *in vivo*
Biological Materials				
Collagen	Natural protein found abundantly in ECM	• Biocompatibility • Non-toxic • Excellent for ADSC adhesion, differentiation, and proliferation • FDA approved for clinical use	• Rapid degradation • Cross-linking, required for durability, compromises downstream cell signaling	(918) (919) (920) (921) (922)
Gelatin	Hydrolysed, water-soluble derivative of collagen	• Mimic natural ECM	• Relatively unstable at room temperature	(923)
HA	Natural polymer that is a component of ECM, of which the insoluble (derivatized or cross-linked) form is used in tissue engineering	• Biocompatibility • Non-immunogenicity • Intrinsic porosity • High hygroscopicity • Degrade into safe byproducts	• Too fragile	(924) (925)
Silk	Proteinaceous substance (fibroin and sericin) extracted from *Bombyx mori*	• Good cytocompatibility • Low immunogenicity • Intrinsic porosity • No requirement	• Available in aqueous form for use as an injectable	(903)

	silkworm cocoons	for further chemical or photo-crosslinking for stability • Slow degradation *in vivo* • Modifiable to express various growth factors		
Fibrin	Natural polymer of fibrous protein found in blood clots	• Clinically used as a surgical sealant for haemostasis • More angiogenic than collagen	• Relatively weak mechanical properties • Rapid degradation *in vivo*	(926)
Alginate	Seaweed-derived anionic polysaccharide	• Biocompatibility • Semi-permeability • High malleability • Available in gel, foam, nanoparticles, beads	• Negative overall change, which prevents mammalian cell attachment	(927)
DAT	Technique where cells are removed from a tissue but its native ultrastructure and ECM are preserved	• Retention of mechanical properties of native tissue • Preservation of essential ECM components for adipogenesis • Low	• Laborious tissue preparation and manual handling • Availability of allogeneic tissue	(928) (929) (901) (930) (902) (931)

		immunogenicity due to allogeneicity		
Matrigel™	Natural polymers secreted by EHS mouse sarcoma cells	• Commonly used cell culture matrix • Sensitive to cell culture conditions • Contain growth factors and cytokines for cells	• Derived from mouse sarcoma cell lines	(932) (933) (885)
Biodegradable Polymers				
PCL	Most commonly used filament in 3D bioprinting	• Readily available • Used in FDA-approved suture (Monocryl®) • Completely excreted by body	• Long degradation (1.5-2 years) • Stiff mechanical properties favouring osteogenic differentiation of ADSC	N/A
PLA	Most commonly used filament in desktop 3D printers	• Readily available • Used in FDA-approved suture (Vicryl®) • Completely excreted by body	• Long degradation (up to 2 years) • Stiff mechanical properties favouring osteogenic differentiation of ADSC	N/A
PLGA	Copolymer synthesized by	• Adjustable mechanical	• Poor cell adhesion	(934) (935)

	combining monomers, glycolic acid and lactic acid	properties • Safe by-products	and differentiation • Relatively rapid degradation	
PEG	Polymer of ethylene oxide	• Water-soluble • Elastic • Adequate degradation time • Minimal inflammatory reaction • Chemical versatility	• Toxic degradation products	(936) (905)
OPAA	Created by free radical polymerisation of agamantine-containing, cross-linked PAA oligomers and RGD tripeptide	• Macroporous foam of OPAA has the same mechanical properties as adipose tissue • Macroporous structure supports nutrient supply and complex tissue growth	• Expensive to prepare	(937)
Composite Scaffolds				
Collagen-HA	Cross-linked 3D porous scaffold	• Enhanced efficiency of collagen cross-linkage • More robust collagen scaffold	• Requires manually-intensive preparation	N/A

Collagen-gelatin	3D porous scaffold	• Cytocompatibility • Improved scaffold stability at room temperature • Improved scaffold strength	• Relatively weak scaffold still	N/A
Alginate-gelatin	Microspheres	• Flexible mechanical properties • Improved cell adhesion	• Large-volume tissue production may be limited	N/A
PGS-PLLA	Porous scaffold	• Alter mechanical properties to closely mimic adipose tissue • Hydrophilic • Large-volume tissue production	• Requires manually-intensive preparation	N/A
PDM-XLHA	3D scaffold	• Improved angiogenesis and adipogenesis	• Relative lack of availability of PDM • Potential ethical issues	(938)

Table 12.3.3.1.2. Summary of 3D scaffold materials used in adipose tissue regeneration. Abbreviations: ECM: extracellular matrix; ADSC: adipose-derived stem cells; N/A: not applicable; HA: hyaluronic acid; DAT: decellularized adipose tissue; EHS: Engelbreth-Holm-Swarm; polycaprolactone: PCL; polylactic acid: PLA; poly(lactic-*co*-glycolic acid): PLGA; polyethylene glycol: PEG; poly(amidoamine) oligomer: OPAA; PAA: poly(amidoamine); PGS: poly(glycerol sebacate); PLLA: poly(L-lactic acid); PDM: placental decellular matrix; XLHA: cross-linked hyaluronic acid.

Biological Materials

Biological materials used to build 3D scaffolds consist of naturally-derived substances that resemble human ECM (930, 939). Their major advantages are biocompatibility, biodegradability and inherent biological functions that make them suitable for tissue engineering (940-943). Their potential limitations, such as immunogenicity stemming from allogeneic or xenogenic origin or contamination from endotoxins, can be controlled by careful preparation and routine quality control measures (944). To date, the following biological scaffold materials have been used for adipose tissue regeneration: collagen, hyaluronic acid, silk, gelatin sponge, fibrin, alginate, agarose, chitosan, calcium phosphate, Matrigel^{TM}, and decellularized adipose tissue (DAT).

Collagen

Collagen is a natural protein that provides structural support and is found abundantly in extracellular space across the human body (945). It is non-toxic, biocompatible and, via other clinical indications, already approved by the Food and Drug Administration (FDA) for use in humans. Moreover, it provides an ideal microenvironment for ADSC adhesion, differentiation, and proliferation both *in vitro* and *in vivo* (901, 918, 929, 946-949), which is superior to other biological substances, such as silk, and synthetic polymers, such as polylactic acid (PLA) (950). In animal models, ADSC cultured on 3D collagen scaffolds have increased ECM production and subsequently yield a well-vascularized adipose tissue construct (919-921). In an interesting study, Xu *et al* report that adding ginsenoside Rg1, an active component of ginseng, and platelet-rich fibrin (PRF) promotes adipogenesis of ADSC in collagen sponges (922). Nonetheless, one of the major limitations of collagen scaffolds is its rapid degradation upon implantation (950). Cross-linking of collagen is required to improve its durability, but can be cytotoxic and compromise cell signalling (951).

Gelatin

Gelatin is a hydrolysed, water-soluble derivative of collagen. It closely mimics the natural ECM and when a gelatin sponge is populated with bone marrow-derived mesenchymal stem cells (BM-MSC) in adipogenic medium, lipid droplets accumulate *in vitro* (952). Without any cells, Vashi *et al* report that simply implanting a dome tissue engineering chamber filled with gelatin microspheres impregnated with slow-release basic fibroblast

growth factor-2 (bFGF-2) suspended in collagen gel leads to successful adipogenesis in mice, similar to the popular cell culture matrix, Matrigel^{TM} (923). One of the major limitations of gelatin sponges as scaffolds is their relative instability at room temperature. This can be improved by using more stable, photo-crosslinked methacrylated gelatin (GM), instead.

Hyaluronic Acid

Hyaluronic acid is a natural component of ECM, of which its insoluble form, via derivatization or cross-linkage, is utilized in tissue engineering. Its advantages include excellent cytocompatibility, biocompatibility, non-immunogenicity, high hygroscopicity, intrinsic porosity for ideal cell proliferation, and its ability to degrade into safe by-products (953-957). In 2001, von Heimburg *et al* have reported that preadipocytes embedded in esterified hyaluronic acid (or HYAFF 11) sponges lead to more vascularized, higher cell-density adipose tissue in nude mice (924). In a later study, the same group show that coating HYAFF 11 sponges with ECM glycosaminoglycan hyaluronic acid results in superior cell penetration and tissue vascularisation (925). However, the authors concede that the volume of fully-differentiated adipose tissue from this method is still inadequate for clinical application (925). One of the major limitations of hyaluronic acid scaffolds is related to its high hygroscopicity, which results in fragile structure (954). As a result, hyaluronic acid is increasingly being used as a cytocompatible cell carrier, rather than as a solid scaffold.

Silk

Silk is a naturally-occurring substance extracted from *Bombyx mori* silkworm cocoons, consisting of core filament protein, fibroin, coated by glue-like sericin protein (958, 959). It is a well-known, clinically-accepted, biocompatible material that is already being used to manufacture FDA-approved surgical sutures. The major advantages of silk are its good cytocompatibility, low immunogenicity, intrinsic porosity, no requirement for toxic chemical or photo-crosslinking for stability and function (960), slow-degradation rate (950), and modifiability to express various growth factors (958). Numerous *in vitro* experiments demonstrate that silk scaffolds can support cell adhesion and viability for long-term co-culture (i.e. up to 6 months) (961) between undifferentiated (962-964) and differentiated (961, 964, 965) adipocytes with endothelial cells. One of the significant limitations of silk is its existence in mainly aqueous form, which deems it more suitable as injectable form.

Recently, Bellas *et al* have injected silk foams embedded with ADSC subcutaneously in rats showing that the neo-adipose tissue integrates well with the host tissue (903).

Fibrin

Fibrin is a natural polymer of fibrous proteins found in blood clots during haemostasis (966). It is already being used routinely as a surgical sealant to protect wounds from infection and allow cellular repair (966-968). Ironically, it is more angiogenic than collagen (969). Experiments using fibrin gel demonstrate that it can provide a suitable microenvironment for adipogenesis in adipocyte/endothelial cell co-culture *in vitro* (970, 971). Wittmann *et al* report that implanting cultivated adipocytes in stable fibrin gel into mice leads to formation of well-vascularized adipose tissue *in vivo* (926). However, fibrin has weak mechanical properties and degrades rapidly *in vivo*. To this effect, Chung *et al* report the use of PEGylated fibrin (P-fibrin), where fibrin is covalently modified with amine-reactive polyethylene glycol (PEG), which improves its strength and durability, but also maintains its adipogenic and angiogenic effect on ADSC (969).

Alginate

Alginate is a seaweed-derived anionic polysaccharide that is available in several forms for tissue engineering: soft gel, foam, nanoparticles, and spherical beads (972). Its biocompatibility, semi-permeability, and high malleability make it an attractive scaffold material for tissue engineering and in drug delivery. One of the major limitations of alginate is its negative overall charge preventing mammalian cell binding (973, 974). This can be overcome by structural modification with laminin, which enables cell adhesion (975), facilitates physiological adipogenesis by binding to integrin (976, 977), and supports angiogenesis (978). A number of studies support the use of alginate-based scaffolds to facilitate adequate proliferation and differentiation of ADSC to yield mature adipose tissue both *in vitro* (979, 980) and *in vivo* (927).

Scaffolds from Decellularized Tissues

Flynn *et al* first described decellularized adipose tissue (DAT) in 2010, where cells are removed but its native ultrastructure and ECM are preserved (981), and Wang *et al* have first utilized DAT for adipose tissue engineering (930). The main advantages of DAT are retention of mechanical properties, preservation of essential ECM components for adipogenesis, such as collagen, glycosaminoglycan, and growth factors (792, 982-984),

and low immunogenicity (793, 794). Interestingly, ECM of DAT undergoes host integration and is replaced by the ECM produced by the seeded cells (795, 931). Encouragingly, DAT produced using adipose tissue from abdomen, flank, and omentum, all have similar mechanical properties to *ex vivo* breast adipose tissue (985, 986). Numerous animal studies have demonstrated that ADSC-laden DAT can facilitate adipogenesis and concomitant angiogenesis *in vivo* up to 8 weeks (901, 902, 928-930). Current limitations that prevent widespread application of DAT are laborious manual handling required for safe tissue preparation and relative unavailability of allogeneic tissues.

Decellularized Muscle Tissue

Muscle was first used over a decade ago in unprocessed form within tissue engineering chambers to promote de novo adipogenesis around an arteriovenous loop based on the propensity for denervated muscle to undergo fatty change (987). The same group then derived an adipogenic matrix from muscle with successful adipogenesis demonstrated from the matrix derived from various species, but significant batch to batch variation. (Myogel, a novel, basement membrane-rich extracellular matrix derived from skeletal muscle, is highly adipogenic in vivo and in vitro (988). The composite nature of the matrix make it suitable for injection but direct application, co-delivered with cells in 3D bioprinting would be challenging.

Matrigel™

Matrigel™ is a commonly used cell culture matrix, consisting of natural polymers secreted by Engelbreth-Holm-Swarm (EHS) mouse sarcoma cells. It contains critical growth factors and cytokines for cell growth (989, 990). Kawaguchi *et al* report that autografting preadipocytes reconstituted in Matrigel™ and bFGF in mice leads to successful growth of the fat pad for three weeks and is maintained over ten weeks (932). Interestingly, implanting a silicone dome filled with Matrigel™ and bFGF without cells also leads to adipose tissue growth due to infiltrative host preadipocytes in rats (933). Subsequently, Findlay *et al* have shown that implanting a silicone chamber encasing an epigastric vascular pedicle, filled with Matrigel™, facilitates early angiogenesis and adipogenesis in mice with long-term stability of the adipose tissue through to 18 months (991). Despite its excellent biocompatibility and cytocompatibility, its derivation from murine sarcoma cell lines makes Matrigel™ unsuitable for clinical application.

Other Biological Materials

Other biocompatible and cytocompatible materials, such as agarose, seaweed-derived polysaccharide (992), and chitosan, crustacean shell-derived polysaccharide (993), have shown to promote adipogenesis *in vitro*. However, more studies are required to support their adipogenic utility *in vivo*.

Biodegradable Polymers

A number of synthetic biodegradable polymers have been utilized in adipose tissue engineering: polycaprolactone (PCL), polylactic acid (PLA), poly(lactic-*co*-glycolic acid) (PLGA), polyethylene glycol (PEG), and poly(amidoamine) oligomer (OPAA). Major advantages of synthetic polymers are their versatility; researchers can achieve optimal porosity, surface characteristics, and degradation rate by altering their chemical and physical characteristics (994-997). Moreover, there is low batch-to-batch variability leading to consistent outcomes (998). However, their main limitation is poor cytocompatibility, which requires expensive surface design or time-consuming chemical modification to promote cell adhesion (999-1004).

PCL

PCL is the most commonly used plastic filament in 3D bioprinting. It is readily available, biodegradable, and is already used as a FDA-approved suture material found in Monocryl® (Ethicon Inc, Somerville, NJ USA). However, PCL prior to any chemical modification may be unsuitable for adipose tissue engineering since ADSC cultured on PCL-based scaffolds preferentially undergoes osteogenic differentiation due to its mechanical properties (974).

PLA

Similar to PCL, PLA is the most commonly used plastic filament in desktop 3D printers (318); hence, it is readily available and is already being used in FDA-approved sutures like Vicryl® (Ethicon Inc). *In vitro* experiments demonstrate that ADSC attaches well to PLA-based scaffolds and undergoes adipogenic differentiation under appropriate culture medium (1005). However, its long degradation rate *in vivo* may be undesirable for adipose tissue engineering.

PLGA

PLGA is a copolymer synthesized by combining monomers, glycolic acid and lactic acid. It is a versatile material with adjustable mechanical properties by altering the ratio of monomers. Furthermore, its by-products, glycolic and lactic acid, are also physiological metabolites and, thus, are safe. Under favourable culture conditions, preadipocytes and BM-MSC undergo adipogenic differentiation and produce functional secretory adipose tissue *in vitro* and in animal models (934, 935). However, its utility in adipose tissue engineering has been limited due to its rapid degradation *in vivo* and its hydrophobic surface, which prevents strong cell adhesion and differentiation (1006). This can be overcome by combining PLGA with cytocompatible silk fibroin and hydroxyapatite nanoparticles creating a hybrid scaffold (1006).

PEG

PEG is a polymer of ethylene oxide that is used widely in several medical applications already, such as laxatives and bowel preparation before colonoscopy (1007). It is water-soluble, elastic, has degradation time of 16 weeks, and exerts minimal inflammatory response *in vivo* (1008). Furthermore, its chemical versatility enables various modifications to enhance cytocompatibility (1009-1012). Patel *et al* demonstrate that PEG hydrogel containing collagen-like peptide (LGPA), which is degraded by ADSC-secreted collagenase, and laminin-binding peptide (YIGSR), which promotes cell adhesion, can promote adipogenic differentiation of preadipocytes *in vitro* (1013). More recently, Clevenger *et al* report that adding RGD tripeptide (Arg-Gly-Asp) enhances its biostability by increasing the degradation time by a month (1014). Interestingly, when the authors added another peptide (MMPc), which contains matrix metalloproteinase (MMP) cleavage sites for MMP secreted by differentiating ADSC (1015), this provides more space for ADSC to deposit ECM in its microenvironment and promote angiogenesis (1014). In animal models, Alhadlaq *et al* present that BM-MSC in PEG hydrogel must be differentiated *in vitro* prior to *in vivo* implantation for adipogenesis (936). Similarly, Stosich *et al* demonstrate that microchanneled PEG cylinders seeded with BM-MSC and bFGF successfully lead to adipose tissue formation (905). One of the major limitations of PEG-based scaffold is its potentially toxic degradation products including ethylene oxide.

OPAA

OPAA is created by free radical polymerisation of agamantine-containing, cross-linked poly(amidoamine) (PAA) oligomers and RGD tripeptide (995, 996). Cell adhesion and cytocompatibility of PAA is improved by the addition of agamantine (1016) and RGD

tripeptide (1001). Recently, Rossi *et al* have created a microporous foam of OPAA (OPAAF), using a gas foaming technique (937). OPAAF has a complex, porous 3D architecture that resembles the mechanical properties of a native adipose tissue (Young's modulus of elasticity of 3.2-4.4 kPa). It enhances cell infiltration and nutrient delivery for successful adipogenesis both *in vitro* and *in vivo* (937). Building on from this finding, the authors need to upscale the tissue volume generated for clinical translation.

Composite Scaffold

To overcome deficiencies of individual scaffold materials, researchers have developed composite scaffolds that complement the benefits of each material. Davidenko *et al* describe a cross-linked 3D porous collagen-hyaluronic acid composite scaffold for culturing mouse preadipocytes *in vitro* (1017). Despite its excellent biocompatibility and cytocompatibility, collagen undergoes rapid degradation *in vivo*, which can be improved by cross-linking with 1-ethyl-3-(3-dimethylaminopropyl)-carbodiimide hydrochloride. The presence of hyaluronic acid enhances the efficiency of the cross-linkage and robustness of the overall scaffold, and facilitates the adipogenic differentiation of preadipocytes. Similarly, Lin *et al* report their 3D porous collagen-gelatin composite scaffold supports growth of viable adipocytes for 28 days from lipoaspirate-derived stromal volume fraction (SVF) cells *in vitro* (1018). Weak mechanical properties of gelatin and its instability at room temperature are ameliorated by the addition of collagen matrix. Yao *et al* describe alginate-gelatin composite microspheres, which enables flexible control of the scaffold's mechanical properties *in vitro* (980). Alginate is malleable, which allows researchers to alter its porosity and swelling behaviour to suit cultured cells, but it has poor cell adhesion. This is amended by the addition of cytocompatible gelatin. However, it is not yet clear if a large-volume adipose tissue with pre-defined shape can be manufactured using microsphere-based scaffolds. Frydrych *et al* report that adding poly(glycerol sebacate) (PGS) to stiff poly(L-lactic acid) (PLLA) enables manipulation of scaffold strength to closely mimic adipose tissue while still providing robustness (tensile Young's modulus of 30 kPa and tensile strength of 7 kPa) for large-volume adipose tissue generation *in vitro* (1019). In an interesting study, Flynn *et al* demonstrate that placental decellularized matrix (PDM) combined with cross-linked hyaluronic acid (XLHA) can improve angiogenesis and adipogenesis *in vivo*, compared to PDM alone (938). Lack of availability and potential ethical issues surrounding the usage of placental tissues may curtail the future application of this scaffold.

Cells

Without exogenous cells, an empty 3D-bioprinted scaffold will elicit host inflammatory response after implantation resulting in fibrotic scarring and dysregulated tissue regeneration (1020). Various stem cells have been utilized for adipose tissue engineering. However, current evidence suggests that using ADSC seeded with appropriate growth factors and endothelial precursor cells in co-culture appears to be most successful.

Cell Types

In animal models, mouse-derived preadipocyte cell lines, such as 3T3L1 (1021-1025) and 3T3-F442 A (1026, 1027), have been well-characterised to generate adipose tissue both *in vitro* and *in vivo*. However, their fully differentiated state cannot reproduce the full endocrine function of a mature human adipose tissue (1021, 1028). Furthermore, their xenogeneic origin precludes direct translation into clinical application. To this effect, a variety of human stem cells can be harvested and induced for adipogenesis: embryonic (1029, 1030), foetal (1031), adult stem cells, and induced pluripotent stem cells (iPSC) (1032). Despite their excellent pluripotency and non-immunogenicity, embryonic and foetal stem cells pose significant ethical issues and lack of large sources for practical application. First discovered in 2007 (1032), iPSCs are derived from fully-differentiated adult somatic cells, such as skin fibroblasts, and are advantageous since they avoid ethical issues and are potentially available in abundance. With current technology, iPSCs are relatively difficult to induce, limiting its widespread application. In comparison, adult stem cells, such as BM-MSC and ADSC, are more readily accessible and available. BM-MSC is harvested most commonly from the iliac crest and is used extensively in the treatment of hemato-oncological disorders (1033). However, BM-MSC is relatively difficult and painful to extract, poses significant donor site morbidity, and has a low cell yield rate for tissue engineering (1034). In contrast, ADSC is abundantly available (1035), easy to harvest (1014, 1036-1039), generates a high cell yield (1040), is multipotent (1041) and is safe (1042).

ADSC

First described by Zuk *et al* in 2001, ADSC represents a host of mesenchymal stem cells isolated from the SVF of adipose tissue (1043). They are found perivascularly along

capillaries between adipocytes (880, 1044) and are the main cell population in adipocyte regeneration (1041). ADSC has excellent self-renewal properties and demonstrates multipotent differentiation into osteoblasts (1045), (1046-1050), chondrocytes (1051), myocytes (1052), neurocytes (1053), vascular endothelial cells (1054), and adipocytes (1045). Currently, the immune-modulatory and regenerative capacity of ADSC are already being exploited for therapeutic application in multiple disorders: graft-versus-host disease (1055), autoimmune diseases (1056, 1057), multiple sclerosis (1058), type 1 diabetes mellitus (1059), tracheomediastinal fistula (1060), and wound healing (1061-1063).

ADSC Harvest

ADSC is most commonly harvested from the abdomen, thighs, flanks, and axilla (1064, 1065) using liposuction (1066) or direct excision technique (1036). Compared to the flank and axilla, more SVF cells can be obtained from the abdomen (1065). Moreover, the latest Coleman liposuction technique (747) yields more ADSC than the conventional liposuction technique (1065). In contrast, the difference in ADSC yield rate between Coleman method and direction excision appears unclear (1066, 1067). Nevertheless, if a large number of cells are required, ADSCs can be expanded *in vitro* or pooled from multiple donor sites. Interestingly, the number of mature adipocytes per volume remains constant throughout adulthood (1068). However, proliferative activity and differentiation potential of ADSC are reduced in older adults (age of 50-70), compared to young adults (greater than 20) (1069).

ADSC Isolation

Once they are harvested, ADSCs are isolated by enzymatic digestion, cell culture, and surface marker antibodies. Collagenase is the most commonly used digestive enzyme before the tissue is centrifuged to separate the SVF (1039, 1070-1073). Alternatively, researchers have used trypsin and red blood cell lysis buffer solution to lyse adipose tissue blocks with varying results (1074). Subsequently, the SVF is set in a cell culture, from which multipotent cells can be segregated, since they will float while other cells will adhere strongly to the plastic surface (1043, 1075-1079). Amongst the multipotent cells, ADSC can be separated using fluorochrome-conjugated or magnetic bead-attached antibodies that attaches to specific cell surface markers, known as fluorescence-activated cell sorting (FACS) (1080, 1081) and magnetic-activated cell sorting (MACS) (1077, 1082-1084), respectively. FACS is used widely in basic science experiments and diagnostic tests, but is not suitable for tissue engineering due to its cytotoxicity and poor efficacy. In comparison, MACS is safe, affordable, and readily accessible. Using surface antibodies,

ADSC is defined as $CD73^{+}CD90^{+}CD34^{+}CD45^{-}CD31^{-}CD13/CD105^{+}$ according to International Federation for Adipose Therapeutics (IFATS) and International Society for Cellular Therapy (ISCT) (1085). In a recent study, Lauvrud *et al* report that a subgroup of ADSC expressing CD146 ($CD146^{+}$ ADSC) has superior adipogenic and angiogenic potential through increased gene expression of *VEGF-A*, *FGF-1*, and *angiopoietin-1*, differentiates more efficiently, and proliferates faster (1086).

ADSC Adjuncts

ADSC alone may not consistently produce mature adipose tissue and require addition of growth factors, endothelial precursor cell co-culture, and interaction with immune cells.

Growth Factors

Growth factors are important for activating adipogenesis and promoting angiogenesis from ADSC (1087) (Table 12.3.3.1.3). Researchers have reported the use of numerous adipogenic growth factors, such as FGF-2 (1088), transforming growth factor-beta 1 (TGF-β1) (1089), and PDGF-BB (1090), and angiogenic growth factors, such as VEGF (1091), PDGF-BB (1092), bFGF (923, 1093), and epidermal growth factor (EGF) (1094, 1095). Notably, TGF-β1 may be associated with tumorigenesis due to their action via MAPK cell signaling pathway and, hence, must be used with extreme caution (1096-1098).

Growth Factors	References
Adipogenic	
FGF-2	(1088)
TGF-β1	(1089)
PDGF-BB	(1090)
Angiogenic	
VEGF	(1091)
PDGF-BB	(1092)
bFGF	(1096) (1093)
EGF	(1094) (1095)
IGF-1	(1099)

	(1100)
Ascorbic acid	(1101)
Heparin	(1102)

Table 12.3.3.1.3. List of adipogenic and angiogenic growth factors used to support 3D bioprinting adipose tissue. Abbreviations: FGF-2: fibroblast growth factor-2; TGF-β1: transforming growth factor-beta 1; PDGF-BB: platelet-derived growth factor receptor B; vascular endothelial growth factor; bFGF: basic fibroblast growth factor: EGF: epidermal growth factor; IGF-1: insulin-like growth factor.

Co-Culture with Endothelial Precursor Cells

Unsurprisingly, adding endothelial progenitor cells appears to facilitate simultaneous neovascularization and complement adipogenesis both *in vitro* and *in vivo* (961-964, 970, 971, 1103-1106). However, practically this is difficult to achieve due to differing culture conditions preferred by either cell type. Endothelial cell culture typically contains: VEGF and FGF that are known mitogenic reagents (1107-1109); EGF has controversial effect on adipocytes as some reports suggest it inhibits preadipocyte differentiation (1110-1112) while others suggest it improves lipogenesis (1113-1115); and hydrocortisone, at high level exclusively, induces dedifferentiation of mature adipocytes leading to lipolysis (1116-1118). As a result, other angiogenic growth factors with no lipolytic effect, albeit weaker angiogenic effect, may have to be preferred, such as insulin-like growth factor-1 (IGF-1) (1099, 1100), ascorbic acid (1101), and heparin (1102).

Role of Immune System

In recent times, investigators have highlighted potential importance of the immune cells in adipose tissue engineering. For example, Chazaud *et al* acknowledges that different macrophage phenotypes affect adipose tissue expansion, metabolism, and remodelling (1119). Similar to the physiological tissue repair process, called M1-to-M2 macrophage shift, where pro-inflammatory M1 macrophages that initially infiltrate an wound are eventually replaced by anti-inflammatory M2 macrophages (1120-1123), Li *et al* note similar changes in infiltrating macrophage profiles at day 3 after implanting a synthetic tissue engineering chamber (TEC) with a vascular pedicle in rats (1124). Furthermore, Rophael *et al* and Debels *et al* demonstrate that depleting macrophages in host mouse significantly impairs adipogenesis and angiogenesis (885, 1125).

ADSC Limitations

The main limitations of ADSC are their potential role in tumorigenesis and their preparation using xenogenic substances. Current literature presents contrasting views of ADSC in carcinogenesis. Chandler *et al* (1126) and Koellensperger *et al* (1127) report that co-culturing ADSC with glioma or squamous cell carcinoma cells increases tumour cell viability, invasiveness, and induces apoptosis of the surrounding normal cells. In contrast, Cousin *et al* (1128) and Zhao *et al* (1129) report that ADSC can inhibit proliferation and induce apoptosis of pancreatic tumour and hepatic cell carcinoma cells. Importantly for adipose tissue engineering in breast reconstruction, when ADSC are co-cultured with breast cancer cells, they undergo myofibroblastic differentiation behaving like breast cancer cells (1126, 1130). This has not been found in-vivo to date and there is currently no compelling evidence to suggest that autologous fat transfer, the most common form of ADSC use in clinical practice, has any association with increased recurrence of breast cancer in humans. However, several key reagents used for ADSC preparation are animal-derived: cell culture media from foetal bovine serum, collagen scaffold from rat tail, and gelatin from porcine skin (1131, 1132). Xenogenic substances can potentially elicit acute graft rejection or chronic inflammation and may lead to host antibody production resulting in severe autoimmune reactions. Currently, serum-free or xeno-free culture media, such as human serum-based media and platelet-rich plasma (PRP), are not readily available and have not been proved for safety and efficacy *in vivo* (1132-1135).

3D-Bioprinted Adipose Tissue *In Vitro*

A number of *in vitro* studies have demonstrated that 3D bioprinting is not cytotoxic, preserves proliferative and adipogenic differentiation capabilities of ADSC, and produces lasting mature lipid droplets, while enabling flexible design of the final adipose tissue (979, 1136-1138).

3D Bioprinting ADSC

Concerned about potential cytotoxicity of laser, Ovsianikov *et al* seed ADSC on to the photopolymerized, methacrylamide-modified gelatin scaffold after it has been laser 3D-printed (1136). Modified gelatin maintains its biodegradability while supporting ADSC adhesion, proliferation, and adipogenic differentiation. In 2010, Koch *et al* have described

a laser bioprinting technique using two coplanar glass slides in close proximity to each other (500 μm) so that direct exposure of laser to cells could be avoided (875). When laser is directed on to the gold-coated upper slide, it generates a jet dynamic that pushes the cell-laden hydrogel forward and drops on to the lower slide while the laser energy is absorbed by gold. Using this method, Gruene *et al* have successfully 3D-bioprinted an alginate-blood plasma product-based composite scaffold, laden with ADSC that has been cultured for seven days prior in adipogenic medium (979). Importantly, the authors demonstrate that laser bioprinting does not compromise ADSC proliferation or differentiation. Similarly, Williams *et al* show that a pressure-based microextrusion 3D bioprinting technique (826, 867, 914) is safe for depositing human adipose-derived SVF spheroids in alginate-based scaffolds (1137).

3D Bioprinting Mature Adipocytes

In an interesting proof-of-concept study, Huber *et al* demonstrate that laser 3D bioprinting of photocurable GM scaffold laden with mature adipocytes can produce a larger (7 mm in height), functional adipose tissue that can last up to 14 days *in vitro* (1138). The authors cite benefits of using mature adipocytes including improved efficiency since only 42% of ADSC undergo adipogenic differentiation physiologically (1043, 1139), potentially less immunogenicity of mature cells, ability to forego extensive laboratory processes to isolate ADSC, time spent inducing adipogenic differentiation *ex vivo* prior to implantation, and producing immediately functional, long-lasting mature adipose tissue (1068). One of the main limitations of using mature adipocytes are their fragile univacuolar morphology and reduced renewal capacity due to their terminal differentiation and low adipocyte yearly turnover rate (938, 1140).

3D-Bioprinted Adipose Tissue *In Vivo*

3D bioprinting adipose tissue for breast reconstruction is such a novel technology that only a small number of studies have explored its *in vivo* application to date.

Tissue Engineering Chamber

Tissue engineering chamber (TEC) has revolutionized adipose tissue engineering in the last decade, enabling researchers to produce a large amount of tissue (up to 78.5 ml)

without exogenous scaffold implantation, growth factors, and *ex vivo* cell preparation (1141). Using this method, investigators surgically prepare a vascular pedicle, usually from superficial inferior epigastric vessels (1142). This arterio-venous (AV) loop is placed inside a larger, perforated, dome-shaped TEC, which can be manufactured using a range of biocompatible synthetic polymers: polycarbonate (991, 1141, 1143-1146), PLGA (1142, 1147-1149), and silicone (923, 933, 1093, 1150, 1151). Most studies have relied on standard manufactured TEC, however, as 3D printing has become more affordable and convenient to use in the past few years (16, 17, 318), future investigators have the potential to 3D print patient-specific TECs. Encouragingly, Morrison *et al* have recently reported their use of customized acrylic-based TEC that was produced by a well-known medical 3D printing company, called Anatomics® (Melbourne, VIC, Australia), however, using conventional manufacturing technology (1152).

TEC Mechanism of Action

The exact mechanism of tissue growth within TEC is still unclear, be it mechanotransduction (1153, 1154), intra-chamber oedema-induced adipogenesis (1155), or immune-mediated response (1144). It is most likely that once a TEC is implanted subcutaneously, it induces ischaemia and apoptosis of the separated adipocytes (1150) stimulating aseptic inflammatory response (1145), generating mitogenic stimuli that promote angiogenesis and adipogenesis (1156), leading to infiltration by a host of endogenous cells, such as immune cells like macrophages (1124), preadipocytes (1145), fibroblasts that differentiate into myofibroblasts upon entry and deposit collagen (1157, 1158), and endothelial precursor cells that develop into a complicated vascular network (1093, 1142, 1159, 1160). In addition, TEC protects the developing adipose tissue from deforming external mechanical forces (1143). Despite lacking exogenous scaffolds for cell adhesion, proliferation, and differentiation, pro-inflammatory environment created by the TEC induces self-synthesis of ECM, on to which adipogenesis and neovascularization occur (1150).

TEC in Human Patients

In contrast to other animal studies where TEC could only produce small volume of adipose tissue (0.44-30.7 ml) (991, 1142, 1146, 1147, 1149-1151, 1161), Findlay *et al*, in a landmark paper, have successfully regenerated up to 78.5 ml of well-vascularized adipose

tissue in eight pigs using polycarbonate-based TEC encasing a small pedicled superficial circumflex iliac artery flap (<5 ml) (1141). Encouraged by this finding, the research group, in a proof-of-concept study, have implanted acrylic-based perforated TEC that was size-matched to the contralateral breast, encasing thoracodorsal artery perforator flap, into five patients undergoing unilateral post-mastectomy reconstruction (1152). Although well-tolerated, there was no tissue growth beyond the original flap in three out of five patients. In one case, TEC had to be explanted earlier than planned due to pain. Ironically, in the fifth patient with diabetes, adipose tissue growth of 210 ml was demonstrated at TEC removal in 12 months. However, this tissue did not aesthetically match the contralateral breast and, hence, required further surgical intervention.

Patient-Specific Scaffold Prevascularization and Delayed Lipoinjection Technique

Recently, Chhaya *et al* have reported an innovative proof-of-concept study using prevascularized patient-specific scaffold and delayed lipoaspirate injection in minipigs (649). The authors subcutaneously implanted 3D-printed PCL-based porous scaffold (volume of 75 mm^3) with immediate or delayed (two weeks) fat graft injection (4 cm^3). In the delayed group, it was hypothesized that the scaffold would undergo host integration and neovascularisation, preparing a rich vascular bed for adipocyte adhesion and proliferation. After six months of incubation, angiogenesis and adipogenesis were noted in all groups. However, the relative adipose tissue content in the scaffold is greatest in the delayed lipoinjection group, compared to the immediate group (47.32 vs 39.67%). Encouragingly, this result is similar to the ratio of adiposity in native porcine adipose tissue (44.97%). This technique has not yet been translated in humans.

Current Limitations

Currently, researchers are faced with difficulty vascularizing large-volume adipose tissue using the latest 3D bioprinters. Furthermore, a wide-scale production of clnically-suitable 3D-bioprinted adipose tissue is hindered by the exorbitant cost associated with scaling up to complex Good Manufacturing Practice (GMP)-certified laboratory practices (1162-1166). Recent introduction of novel ITOP 3D bioprinters that can deposit multiple polymeric and cellular materials to produce large vascularized tissue appears promising (817).

Conclusion

Researchers have faced difficulty in producing adipose tissue in clinically-relevant large volumes using standard tissue engineering practices. Most studies have used ADSC with varying success. However, it requires laborious *ex vivo* preparation, long term tissue integration and volume maintenance is uncertain and its potential to support tumorigenesis needs to be thoroughly addressed prior to therapeutic application. Using mature adipocytes may bypass such risks. Nevertheless, adipogenesis may need to be supported by inclusion of growth factors, endothelial precursor cells, and immune cells. Unfortunately, adipocytes and endothelial cells have disparate preferred culture conditions, requiring compromised solutions. With the advent of 3D printing and subsequent 3D bioprinting technology, investigators are now able to fabricate custom-shape, complex internal porous design scaffolds with multiple cell types. Building on promising *in vitro* and animal studies, 3D bioprinting of adipose tissue is poised for clinical translation.

12.3.3.2 3D Bioprinting Nipple-Areola Complex

PUBLISHED (Peer-Reviewed Book Chapter): ***Chae MP***, Hunter-Smith DJ, Murphy SV, Atala A, Rozen WM. (2017) 3D bioprinting nipple-areolar complex reconstruction. In M. A. Shiffman eds., *Nipple-areolar complex reconstruction: Principles and clinical techniques.* Berlin, Germany: Springer; 2017

Chapter Summary

Introduction: Nipple-areola complex (NAC) constitutes an important landmark on a breast and its loss due to breast cancer treatment can be devastating. In order to achieve cure, an increasing number of women are opting for aggressive mastectomy early and evidences demonstrate that post-mastectomy breast reconstruction significantly improves the patient well-being. Similarly, evidences demonstrate that significant improvement in psychosexual well-being and patient satisfaction can achieved following a successful NAC reconstruction.

Methods: A review of the published English literature dating from 1950 to 2015 using databases, such as PubMed, Medline, Web of Science, and EMBASE was undertaken.

Results: Historically various reconstructive options have been reported, such as local flaps, pigmented skin grafts, tattooing, local flaps with autologous, allograft, or alloplastic graft augmentation. However, current reconstructive techniques have inconsistent long-term outcomes regarding maintenance of the neo-nipple projection, color, size, shape and texture, leading to polarizing patient satisfaction rates. To this effect, novel regenerative medicine technology, three-dimensional (3D) bioprinting, which combines the conventional tissue engineering with 3D printing platform, has been touted as a potential solution. In comparison to other tissue types, reconstructing a 3D solid organ, such as a NAC, undoubtedly commands a higher degree of complexity.

Conclusion: Various tissue-engineered NAC reconstructions using synthetic or decellularized allograft scaffolds have been reported. Recently, TeVido BioDevices company has begun developing an entirely 3D-printed NAC graft but the results are currently limited to preclinical studies.

Introduction

Nipple-areola complex (NAC) constitutes an important landmark on a breast and, as a result, it is not difficult to appreciate the devastation induced by the loss of NAC from breast cancer treatment and the significance of NAC reconstruction to these patients. Due to increasing population, the prevalence and incidence of breast cancer continues to rise and one in eight women in the Unites States are expected to be diagnosed with breast cancer in their lifetime (41). In order to achieve cure, an increasing number of women are opting for mastectomy early (459) and evidences demonstrate that post-mastectomy breast reconstruction significantly improves the psychosexual well-being (43, 1167, 1168).

Recently, the rate of nipple-sparing mastectomy (NSM) has increased dramatically, spurred on by a perceived notion that it preserves the integrity of the body, improves cosmesis and reduces psychological distress surrounding the loss of breasts (1169-1171). Interestingly, numerous publications report minimally increased oncological risk from NSM compared to the traditional radical mastectomy or skin-sparing mastectomy (SSM) (1172-1176). However, currently there is lack of a large-scale prospective data and a reliable national guideline to enable clinicians to offer appropriate type of mastectomy (1171). Encouragingly, recent studies demonstrate that SSM provide a similar rate of overall satisfaction as NSM (1177, 1178). Furthermore, NSM is associated with an increased rate of nipple necrosis and loss (1179, 1180). Therefore, combining SSM with subsequent NAC reconstruction would most reliably achieve complete oncological control and an aesthetically-pleasing outcome (1177, 1181).

NAC reconstruction is generally performed 4-6 months post-mastectomy, depending on the type of breast reconstruction, surgeon's experience, presence of complications, and postoperative chemotherapy or radiotherapy (1182). A number of studies have reported statistically significant improvement in psychological well-being and patient satisfaction following a NAC reconstruction (1183-1186). Reconstructive options range from local flaps with tattooing, pigmented skin grafts, to local flaps with autologous, allograft or alloplastic graft augmentation (1181, 1187). However, current reconstructive techniques have inconsistent long-term outcomes regarding maintenance of the neo-nipple projection, color, size, shape and texture, leading to polarizing patient satisfaction (1188). To this effect, the novel regenerative medicine technology, three-dimensional (3D) bioprinting, which combines tissue engineering with 3D printing platform, has been touted as a

potential solution. In this review, we discuss the current medical application of 3D bioprinting and its use in NAC reconstruction so far.

Methods

A review of the published English literature dating from 1950 to 2015 using databases, such as PubMed, Medline, Web of Science, and EMBASE was undertaken. Search terms used are: “nipple-areola complex reconstruction”, “nipple reconstruction”, “flap”, “graft”, “post-mastectomy”, “3D bioprinting”, “3D printing”, “tissue engineering” and “imaging”.

Results

3D Bioprinting

Background

3D bioprinting describes a method of creating individualized 3D tissue constructs from traditional tissue engineering by incorporating the novel 3D printing technology, which has become more affordable and easy to use in recent times (770).

Tissue Engineering

Tissue engineering utilizes cells, biomaterials, and biologically active factors to produce a biological tissue that matures into functional, vascularized tissue upon implantation *in vivo* (771). The cells are obtained by culturing and expanding the primary cells from a small biopsy of the desired tissue. (772-777). The biomaterial and the growth factors must provide a controlled gradient in mechanical properties and cellular signalling, respectively, for optimal cell growth *in vitro* (778). Given that the maximum nutrient diffusion distance for cells to survive without vascularity is only 100-200 microns (779), manufacturing a well-vascularized, complex tissue in a clinically-suitable size using conventional laboratory techniques has been challenging (771, 780). The addition of angiogenic growth factors may be helpful (778, 790, 791), but ultimately a 3D scaffold with interconnected pores to enable vascularity is required.

Early researchers used decellularization technique, where the cellular component of a donor tissue is removed either mechanically or chemically while retaining its mechanical properties and is re-popularized with desired culture cells (792). These constructs elicit minimal host immune response (793) (794) and the donor extracellular matrix (ECM) is gradually replaced by ECM excreted by the implanted cells (795). However, allogeneic donor tissues are rare and autologous options may lead to potential donor site morbidity. As a result, various methods of fabricating synthetic material-based scaffolds have been described, such as 3D fiber deposition (796), particulate leaching technique (797), and electrospinning (798). In comparison, 3D printing can additionally produce fine-scale internal porous structures with desired complexity (799-801) that facilitate nutrient and

oxygen diffusion (802-804) and the creation of patient-specific composite tissue constructs (770, 805-809).

3D Printing

3D printing, also known as rapid prototyping or additive manufacturing, describes a process by which a 3D construct derived from a computer-aided design (CAD) is built in a layer-by-layer fashion (17-19, 318). One of the major advantages of 3D printing is its convenience in building custom designs with complex geometries in a cost-efficient manner in comparison to the traditional manufacturing process (171-173). 3D printing has been utilized in industrial designs for decades; however, it has only been adapted for medical application in the last decade (20). Imaging data from routine computed tomography (CT) or magnetic resonance imaging (MRI) scans can be converted into a CAD file using a variety of 3D software programs, such as 3D Slicer (Surgical Planning Laboratory; Boston, MA, USA). The file is subsequently manufactured into 3D object using a 3D printer, such as a fused filament fabrication (FFF) printer, where a melted filament of thermoplastic material is deposited on to a build-plate in a layer-by-layer fashion (Figures 12.3.3.2.1 and 12.3.3.2.2) (192). Aided by expiration of key patents in early 2000s, FFF 3D printers have become readily available and this technology has been adopted in 3D bioprinters.

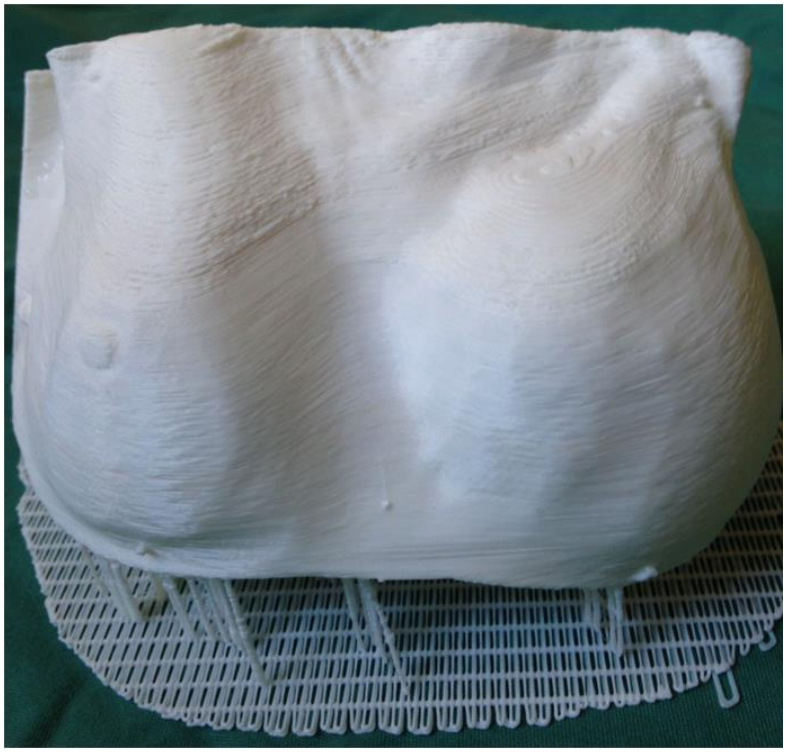

Figure 12.3.3.2.1. A 3D-printed biomodel of breasts, produced from routine CT data. Printing performed using Cube 2 printer (3D Systems, Rock Hill, SC, USA), 3D Slicer software (Surgical Planning Laboratory, Boston, MA, USA), and white polylactic acid (PLA) filaments.

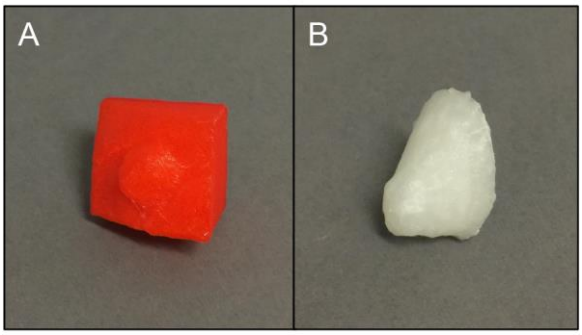

Figure 12.3.3.2.2. A 3D-printed biomodel of nipple using (A) CT and (B) MRI scans. Printing performed using Moment 3D printer (Moment, Seoul, South Korea) and 3D Slicer.

3D Bioprinting Composition

A 3D bioprinter typically consists of a structural scaffold, cell carrier, and cells.

Scaffold

The scaffold provides a 3D structure to support tissue growth, mimic ECM and local microenvironment, and induce tissue formation. The external shape of the scaffold is based on the CT/MRI-derived CAD file of the desired organ or tissue while the internal porous architecture must be based on vascularization and support oxygen diffusion gradient (812). In addition, synthetic polymers used by 3D bioprinters can be incorporated with biologically active domains to enhance tissue regeneration *in vivo* (775, 818-820), such as cell-adhesion peptides (821), silk functionalized with titanium-binding peptides (822), collagen (823), and growth factors (1189). One of the most commonly used polymers for 3D-bioprinted scaffold is polycaprolactone (PCL) (824, 825). PCL has a low melting temperature (60^{o}C) and cools rapidly upon deposition, making it cell compatible (824). It also has a relatively long degradation period (1.5-2 years), deeming it durable and becomes completely excreted from the body, hence, its biocompatibility (825). One of its

main disadvantage is its flexibility and inability to provide mechanical strength. To this effect, Pluronic® F-127 (BASF SE; Ludwigshafen, Germany) polymer, composed of hydrophobic polypropylene glycol and hydrophilic polyethylene glycol, can provide mechanical strength and also extrudes easily from a nozzle (826). Furthermore, it is rapidly degradable and can be washed out immediately once printing is complete. Its main disadvantage is poor cell compatibility (827).

Cell Carrier

A cell carrier, also known as hydrogel, should protect the cells from physical stress during printing, contain appropriate cell-specific signalling cues, possess negligible cytotoxicity, and provide adequate mechanical support (810, 811). A variety of both natural and synthetic cell carriers have been reported, such as alginate (801, 813-816), fibrin (801, 813-815, 817), gelatin (817), hyaluronic acid (817), glycerol (817), and Pluronic® F-127 Derby, 2012 #2409}(813-815). Fibrin can provide stability to the hydrogel and enhances cell adhesion and proliferation. Hyaluronic acid and glycerol can improve uniform cell dispension and prevent nozzle clogging.

Cells

Typically, stem cells, such as mesenchymal stem cells (MSC), are deposited by a 3D bioprinter so that the final construct can differentiate and mature inside an *ex vivo* or an *in vivo* bioreactor (828-832). Cells can be classified into autologous or allogeneic. Despite its indisputable advantage, autologous stem cells can be difficult to culture and expand *in vitro* to a sufficient number for clinical application (833, 834). This can be partly addressed by including the use of precursor and progenitor cells (835). Furthermore, MSCs are difficult to maintain in culture and attach to 3D-printed scaffolds (1190). In contrast, allogeneic stem cells can be stored and accessed readily when needed. However, there is a risk of graft-versus-host disease and subsequent graft failure.

3D Bioprinting Techniques

3D bioprinting techniques can be broadly classified by their mechanism of cell deposition into inkjet (808, 836-838), microextrusion (839-841), or laser-assisted bioprinting (842-844). Integrated tissue organ printer (ITOP) is a novel 3D bioprinting technique that

simultaneously deposits cell-laden hydrogel and synthetic biodegradable polymer in microextrusion fashion using a pneumatic pressure controller (817) (Table 12.3.3.2.1).

Bioprinting Techniques	Mechanism	Advantages	Disadvantages	Clinical Application
Inkjet	Thermal	High resolution Low cost High speed Biocompatibility	Exposure to high heat (300 ^{o}C) Absolute requirement for biological material to be liquid	Skin (845) Cartilage (846) Bone (847)
	Acoustic	High resolution Low cost High speed Biocompatibility	Cell lysis at 15-25 kHz Absolute requirement for biological material to be liquid	
Microextrusion	Pneumatic	Affordable Simpler components Viscous biologic material	Lower spatial control Low cell viability Low resolution Slow speed	Aortic valve (848) Blood vessels (849) Ovarian cancer model (850)
	Mechanical	Affordable Superior spatial control Viscous biologic material	Sophisticated components Low cell viability Low resolution Slow speed	
Laser-Assisted	LIFT	Compatibility with range of viscosity, resolution and speed	Slow print speed	Skin (851) Skull defect (852)
ITOP	Pneumatic	Microchannel formation Microscale nozzle	Limited accessibility	Mandibular bony defect (817)

		Produce well-vascularized, human-scale tissue construct		Ear cartilage (817) Skeletal muscle (817)

Table 12.3.3.2.1. Summary of 3D bioprinting techniques. Abbreviations: LIFT: laser-induced forward transfer; ITOP: integrated tissue organ printer.

Inkjet Bioprinting

Inkjet bioprinting is the earliest described technique where either thermal (838) or acoustic (853-855) forces are used to eject drops of liquid on to a scaffold. Electrically-heated thermal print-heads can produce localized temperature increase to 200-300 ^{o}C for a short duration (2 microseconds) but produce only 4-10 ^{o}C rise in the overall temperature (856). Despite some studies demonstrating minimal impact on the stability of biological molecules, such as DNA (853, 854), there still remains a potential risk using thermal inkjet bioprinters to exposing cell and the tissue construct to heat and mechanical stress. Acoustic waves created by piezoelectric crystal break liquid into regular droplets (857). Pulse, duration and amplitude of the sound wave can be adjusted to alter the size of droplets and rate of ejection. The major disadvantage of using acoustic forces lies with the potential risk of cell damage and lysis from 15-25 kHz frequencies emitted by the piezoelectric crystals (858). In summary, despite their low cost, high resolution, high speed and biocompatibility, both thermal and acoustic inkjet bioprinting is limited by its requirement of the biological material to be in liquid form. This limitation can be potentially addressed by immediately curing the material with chemical, pH or ultraviolet (859, 860). However, this increases the printing time significantly and introduces chemical modifications leading to cell damage. To date, inkjet 3D bioprinters have been utilized to fabricate functional skin (845), cartilage (846), and bone (847) only in preclinical models.

Microextrusion Bioprinting

Microextrusion bioprinters are the most common and affordable bioprinters used in research (812). In comparison to an inkjet bioprinter that extrudes liquid droplets, a microextrusion bioprinter ejects microbeads of a material, such as hydrogel, biocompatible copolymers, and cell spheroids, using pneumatic (826, 860-862) or mechanical (863, 864)

dispensing systems. Pneumatic printers are built with simpler components but mechanical dispensers provide a greater spatial control. Major advantages of microextrusion printers include their compatibility with materials with a wide range of fluid properties, such as viscosity (806), and the ability to deposit very high cell densities, such as tissue spheroids that can self-assemble directly into complex structures (865, 866). One of the major disadvantages of microextrusion technique is its relatively low cell viability rate (40-86%) (862, 867), low print resolution and speed (847). To date, microextrusion technology has been used to fabricate aortic valves (848), blood vessels (849), and *in vitro* ovarian cancer model (850) in preclinical studies.

Laser-Assisted Bioprinting

Laser-assisted bioprinting (LAB) is the least commonly used technique and relies on the principle of laser-induced forward transfer (LIFT) (868, 869). In a LIFT system, a pulsed laser beam is directed on to the laser-energy-absorbing layer (e.g. gold or titanium) over a "ribbon" containing the donor transport system. The laser induces formation of a high-pressure bubble that propels biological material containing cells forward towards a scaffold. Microscale resolution of LAB means that, in addition to cells (870), it can be used to deposit peptides (871) and DNAs (872). One of the main advantages of LAB technology is its flexibility, as it is compatible with a wide range of viscosity, resolution (i.e. single cell per drop to 10^8 cell per milliliter), and speed (i.e. 5 kHz to 1,600 mm/s) (844). Moreover, this technique has a negligible effect on cell viability and function (873-875). A major drawback is its slow print speed due to the requirement of rapid gelation of the deposited material due to its high resolution (876). In preclinical studies, LAB has been used to create a small cellularized skin construct (851) and a skull defect (852).

Integrated Tissue Organ Printer (ITOP)

Integrated tissue organ printer (ITOP) is an innovative bioprinting technique, developed by Kang *et al*, that consists of a multimaterial-dispensing printer system controlled by a custom-designed microscale nozzle motion program enabling simultaneous deposition of both cell-laden hydrogel and synthetic biodegradable polymer to deliver a human-scale tissue construct (817). Despite its relatively high resolution, inkjet bioprinting is limited by its requirement of liquid hydrogel that results in low structural integrity and mechanical strength. Microextrusion method utilizes viscous fluid and can produce more stable 3D

constructs, but the generated shear stress reduces cell viability, printing resolution, speed and size. LAB technique requires rapid gelation of hydrogels to achieve its very high resolution, leading to low flow rates.

ITOP deposits PCL-based scaffolds in various designs that provide mechanical strength to the construct and also forms networks of microchannels that facilitate cell nutrient and oxygen diffusion. However, the bulk of mechanical stability is provided by Pluronic® F-127 hydrogel extruded from a separate nozzle that acts as an outer sacrificial support layer. The composite hydrogel system in ITOP consists of fibrinogen, gelatin, hyaluronic acid, and glycerol in disparate concentrations optimized for each target tissue. The nozzle motion program is customized based on the printing pattern and the fabrication condition (i.e. scan speed, temperature, material information, and air pressure). Once the printing is completed, thrombin is added to cross-link fibrinogen into stable fibrin while the other hydrogels, including Pluronic® F-127, are washed out. Using 3T3 fibroblast cell model, authors demonstrate ≥95% cell viability at 6 days and persistent tissue growth at 15 days.

As a result, ITOP can manufacture well-vascularized, human-scale, complex shape, structurally stable tissue constructs. Using human amniotic fluid-derived stem cells, authors have demonstrated its application in constructing a human mandibular bony defect *in vitro* and successfully implanted a ITOP-printed skull defect in rodents. Using rabbit chondrocytes, authors have built a human ear-shaped cartilage and demonstrated viability at 1 month after implantation in preclinical models. Furthermore, the authors have fabricated functional 15 x 5 x 1 mm rodent skeletal muscle tissue.

3D Bioprinted Medical Applications

Encouraged by its increasing accessibility and rapid improvements in the last decade, clinicians have expanded the application of 3D bioprinting to various human tissues in increasing engineering complexity: flat tissues, tubular structures, hollow viscus, and complex solid organs.

Flat Tissues

Earliest attempts in tissue engineering have been spent to regenerate flat tissue types that are predominantly populated by a single cell type, such as the integument and cornea.

Integument

Tissue engineered skin have received numerous attention due to its potential utility in the management of severe burns injury and chronic wound healing (1191). Researchers have developed method of harvesting autologous skin cells that harvested in the operating room and either immediately “sprayed-on” the area of need (1192, 1193) or expanded *ex vivo* and then implanted in the future (1194, 1195). Despite their early commercial success, wide-scale adoption of tissue engineered skin has been limited by their cost and accessibility (1196, 1197). Furthermore, future consideration for improvements may include reconstituting the skin adnexa, such as hair follicle, pigment and secretory glands.

Cornea

Cornea plays an important role in light refraction for vision via its maintenance of shape, organisation of highly aligned collagen matrix and active secretion of aqueous humor. As such, corneal damage from injury can lead to vision loss. Currently, gold standard treatment of corneal blindness is transplantation; however, there is a worldwide significant shortage of donor tissue. Fagerholm *et al* have developed a tissue-engineered biosynthetic corneal implant that mimic corneal ECM and showed improved vision at 24 months (1198, 1199)

Tubular Structures

Tubular anatomical structures generally consist of two different cell types arranged in a circular, bilayered manner, where the inner layer lined by endothelial or epithelial cells provide a function barrier and the outer layer lined by smooth muscle or connective tissue provide structural support. Their main function is acting as a conduit for air or fluid, such as urethra and blood vessels.

Urethra

Current surgical management of urethral defects and permanent strictures caused by traumatic injury or oncological clearance likely require complex autologous reconstructive surgery that results in significant donor site morbidity (1200-1202). Raya-Rivera *et al* developed a tissue-engineered urethra by seeding biodegradable polyglycolic acid (PGA)/polylactic-co-glycolic acid (PLGA) scaffolds with autologous urethral muscle and

epithelial cells and showed successful functional outcome in 5 patients at 6 year follow-up (773).

Blood Vessels

Shin'oka *et al* have constructed a pulmonary artery by seeding biodegradable collagen and synthetic scaffold with autologous cells from peripheral vein biopsy and successfully transplanted in a 4-year-old girl with total right pulmonary artery occlusion at 7 month follow-up (1203). L'Heureux *et al* have used a sheet of autologous fibroblasts and endothelial cells wrapped around a stainless steel cylinder to fabricate a vascular graft for 10 patients requiring hemodialysis for the management of end-stage renal disease (1204). More recently, Dahl *et al* have developed a vessel allograft by seeding smooth cells on a tubular PGA scaffold and then inducing it acellular by washing away cells with detergents (1205). This method allowed the authors to store the allografts long-term and showed successful implantation in preclinical animal models.

Hollow Viscus

Similar to tubular structures, hollow viscus structures, such as bladder and vagina, consist of inner and outer layers of cells for functional and structure capacity, respectively. However, hollow viscus comprises at least two cell different cell types and require more complex scaffold design for regenerative therapy due to its wider functional parameters, higher metabolic requirements and more intricate intracellular and inter-organ interactions (833, 1206, 1207).

Bladder

Researchers at Wake Forest (Winston-Salem, NC, USA) have harvested and *ex vivo* expanded autologous urothelial and smooth cells from bladder biopsy that they have seeded on to image-derived patient-specific bladder-shaped biodegradable polymer scaffold. Their initial study in animal models (1208) was successfully translated in 7 patients with myelomeningocoele (772).

Vagina

De Filippo *et al* have seeded PGA/PLGA scaffolds with rabbit epithelial cells and maintained its perfusion in a bioreactor before successfully transplanting as total vaginal

replacement in animal models (1209). Clinical trials involving human participants are currently ongoing (COFEPRIS HIM87120BSO).

Complex Solid Organs

In comparison to the previous tissue types, a solid organ undoubtedly commands the highest level of complexity. Tissue engineering or 3D bioprinting a solid organ requires precise organization of multiple, disparate cell types, integration with surrounding tissues, incorporation of vascular networks, and gradients of biologically-active factors (1210). As a result, despite a wide range of organs being studied in regenerative medicine, only a small number of studies have been translated to human studies. Furthermore, cells harvested from solid organs of diseased patients for *ex vivo* expansion and autologous implantation may also be affected by the disease, the density of stem and progenitor cells may be compromised (1211). Hence, in recent times, researchers have focused on developing targeted 3D-bioprinted solid organ regenerative solutions for specific clinical indications.

Soft Tissues

Numerous regenerative efforts have been made to build breasts, kidneys, penis, heart, liver, and functional pancreatic islets. However, currently these studies are limited to preclinical animal models, most commonly using decellularization techniques, and have not been translated in humans yet.

Breast

Earlier studies where breast-shaped polymer scaffolds were implanted in animal models without cells, were filled with non-specific fibrovascular tissue due to lack of adipogenic stimulus (1141, 1212). Lin *et al* seeded human adipose tissue-derived mesenchymal stem cells on to synthetic polymer scaffold and successfully grew vascularized adipose tissue in animal models (1213). Similarly, Chhaya *et al* seeded human umbilical cord perivascular stem cells to patient-specific 3D-printed polymer scaffolds derived from 3D laser scanning, and implanted them successfully in animal models after *ex vivo* maturation (649). Current limitations in wide-scale production of 3D-bioprinted breast tissue are due to the cost related to scaling up tissue culture to complex Good Manufacturing Practice (GMP)-certified laboratory (1162-1166) and difficulty vascularizing a clinical relevant volume of breast tissue (>75 ml) using current techniques. Introduction of ITOP this year that

facilitates construction of well-vascularized large-volume tissue in breast reconstruction appears promising (817).

Kidney

Lanza *et al* built miniature kidney structures by seeding bovine renal cells on to collagen-coated biodegradable scaffolds in animal studies (1214). Orlando *et al* used decellularized porcine kidney to yield a ECM-based scaffold that was implanted in pigs showing successfully integration with native tissue (1215).

Penis

Chen *et al* implanted a decellularized rabbit penis, repopulated with corpora cavernosa penile muscle and endothelial cells in animals and demonstrated successful function outcome (1216).

Heart

Ott *et al* perfused a decellularized rodent heart with endothelial cells and neonatal cardiac cells and showed successful function outcome in animal models (1217).

Liver

Baptista *et al* repopulated decellularized animal livers with human fetal hepatocytes and human umbilical vein endothelial cells and implanted successfully in animal models (1218).

Pancreatic Islet Replacement

De Carlo *et al* were able to regenerate insulin-producing pancreatic islets in animal models by implanting decellularized rodent pancreatic scaffolds (1219).

Bones and Cartilages

Most studies aimed at regenerating bones have focused on treating mandibular defects created from traumatic injury or oncological resection (817, 1220-1222). Warnke *et al* reported an interesting technique where a patient-specific design, ceramic scaffold seeded with bone marrow-derived mesenchymal stem cells is implanted in patient's latissimus dorsi, so that the patient is acting as their own bioreactor (878, 879). More evidence in large-scale randomized clinical trials remain to be seen. Similarly, efforts to construct

tissue- engineered (1220-1223) or 3D-bioprinted (817) have not yet been translated in prospective human trials.

Nipple-Areola Complex Reconstruction

Background

An ideal NAC reconstruction must achieve symmetry in nipple position, size, shape, texture, and pigmentation, and additionally offer lasting projection (1187). To date, an exhaustive list of surgical techniques has been described, local flap, skin graft, nipple tattooing, local flap with autologous, allograft, or alloplastic graft augmentation.

Local Flap

First described by Berson in 1946 (1224), local flaps are the most commonly used surgical technique in immediate and delayed nipple reconstruction and unsurprisingly, an astonishing number of techniques and their modifications have been reported in the literature. The details and clinical outcomes following each approaches are covered in more details in the current book and are beyond the scope of current book chapter. Currently, two modifications of Little's skate flap (1225), Anton's star flap (1226) and Jones' C-V flap (1227), are the most commonly used local techniques used due to their reliability, easy to perform and well described (1228-1234).

Skin Graft

First skin graft using pigmented skin from labia minora was described by Adams in 1949 (1235). Since then, skin graft from other hyperpigmented cutaneous locations (1236)and contralateral nipple graft (1237) have been reported. Similarly, detailed descriptions of these grafts are discussed elsewhere in this book. In summary, skin grafts alone have been unreliable due to fading of pigmentation with time (1238) and loss of projection at 3-6 months (1239).

Tattooing

In order to address loss of pigmentation with time, adjuvant tattooing by nursing practitioners or professional tattoo artists have accompanied other traditional surgical approaches (1226, 1228, 1240-1244). Tattooing is associated with minimal complication rate (1.6%) and high patient satisfaction rate (>90%) (1243, 1245-1249). Recently, 3D tattooing techniques have also been described where depth is created on a 2D chest wall (1250). This work is also described in more detail elsewhere in the current book.

Local Flap with Graft Augmentation

In order to enhance and maintain adequate nipple projection, augmentation with various autologous, allograft and alloplastic grafts to existing local flap approaches have been described.

Autologous Grafts

Historically, augmentation with autologous cartilage graft has been well-described due to their longevity without pedicled blood supply.

Costal Cartilage

Early studies utilized costal cartilage harvested when preparing the internal mammary artery recipient site during free flap breast reconstruction for immediate NAC reconstruction and demonstrated excellent long-term projection (1242). However, this approach was associated a relatively high rate of complication (4%), such as graft exposure and skin flap ischaemia. In later studies, clinicians “banked” the cartilage graft in the abdominal wall that was used in delayed NAC reconstruction (1251-1255). As a result, the authors generally reported a reduced rate of complications and reasonable long-term projection (up to 8.5 mm at 45 months).

Auricular Cartilage

Using auricular cartilage graft was first described by Brent in 1977 (1256). Tanabe *et al* rolled the graft and wrapped inside a bilobed flap surrounded by skin graft, showing moderate success (1257). More recently, Collis *et al* utilized the cartilage harvested from the posterior extension of the sharp fold in the upper conchal fossa palpable in the postauricular sulcus, which reduced scarring of the donor site and maintained nipple projection at 2 years (1240). Later, Norton *et al* described a “hamburger” technique where

a punch biopsy is used to harvest conchal cartilage discs and stacking them (1258). Jones *et al* reported in a long-term study using the stacked conchal cartilage discs only modest nipple projection at 2 years (mean of 3.3 mm), despite low complication rate (1259). Furthermore, in general, auricular cartilage has been relatively unpopular due to potential risk of donor site morbidity.

Allograft Materials

In search of a more permanent augmentative material, clinicians have investigated allograft materials, such as acellular dermal matrix (ADM) and biologic collagen cylinders.

Acellular Dermal Matrix (ADM)

AlloDerm (LifeCell Corp, Branchburg, NJ, USA) is a cadaveric split-thickness dermal graft with low antigenicity (1260, 1261) and fast host integration (7 days) (1262). Garramone *et al* implanted 1.5 x 4.5 cm piece of AlloDerm in 30 NAC reconstructions and demonstrated 47-56% rate of projection at 12 months (1245). Interestingly, Rao *et al* used ADM as an onlay graft for areola reconstruction and demonstrated high graft take rate but did not use it to provide nipple projection (1263).

Biologic Collagen Cylinder

Tierney *et al* reported the use of Biodesign Nipple Reconstruction Cylinder (NRC; Cook Inc, Bloomington, IN, USA) in 115 nipple reconstructions (1264). NRC is created by rolling ECM collagen derived from porcine small intestine submucosa and adhesive glycoprotein as scaffold. The study reports low complication rate (3.5%) and modest sustained nipple projection of 3-5 mm at 6 month follow-up. It remains to be validated and demonstrated effective in a multi-center randomized clinical trial.

Alloplastic Materials

Similarly, numerous inert, biocompatible alloplastic materials have been used, such as silicone rod, Artecoll injection, and artificial bones.

Silicone Rod

Jankau *et al* report good projection from using silicone rod for augmentation in 30 NAC reconstructions (1265, 1266). Interestingly, however, the study found that all 10 silicone

rods used in combined tissue expander and latissimus dorsi free flap reconstructions lead to overlying skin necrosis leading to material removal.

Artecoll Injection

Polymethymethacrylate is an inert, non-biodegradable poly(methyl methacrylate) microspheres suspended in a partially denatured bovine collagen, marketed as Artecoll by Artes Medical (San Diego, CA, USA) and Canderm Pharma Inc (Saint-Laurent, Canada) (1267). Artecoll is injected subcutaneously as a delayed secondary procedure after the primary nipple reconstruction. While the bovine collagen will be degraded in 3 months and replaced by autologous collagen, the synthetic microspheres are too large for degradation by macrophages and provide nipple projection. At 9 months, the authors report a modest nipple projection (2.93 mm) but statistically significant ($P < 0.001$) improvement.

Artificial Bone

Ceratite (Chugai Medical Device, Tokyo, Japan) is a composite material of 20% tricalcium phosphate and 80% hydroxyapatite (1268). The material was initially developed for use in craniomaxillofacial reconstruction (1269). In 100 NAC reconstructions over 8 years, the authors report good projection in all patients from the clinician's subjective assessment and a low complication rate (5%) (1268). Radiesse^{TM} (Bioform Inc, Franksville, WI, USA) is composed of calcium hydroxylapatite that was used in 6 patients with relatively modest improvements (1270). It has an added disadvantage of remaining radiopaque in mammograms and interfering with breast cancer screening (1271).

3D-Bioprinted Nipple-Areola Complex

Background

Despite improvement in local flap techniques and availability of advanced materials, an ideal NAC reconstructive option has eluded clinicians historically. Current reconstructive techniques lead to loss of nipple projection in 40-75% overall in long-term (1181), ultimately result in loss of pigmentation (1238), and do not have significant impact on patient satisfaction. Furthermore, there are no significant difference between various local flap designs and large-scale studies report an overall complication rate of all current reconstructive approaches up to 10% (1242, 1272-1274).

To this effect, 3D bioprinting can be useful, since novel 3D bioprinters like ITOP printers produce well-vascularized, sustainable, human-scale tissue constructs that integrates well with surrounding structures (Table 12.3.3.2.2).

Type	Company	Technique	Reference
Synthetic scaffold	N/A	Pluronic® F-127 seeded with porcine chondrocytes, secured with purse-string suture	(1275)
Decellularized allograft scaffold	NovoThelium LLC	Decellularized donor NAC scaffold seeded with autologous nipple cells	(1276)
3D-bioprinted NAC graft	TeVido BioDevices LLC	Cellatier™ 3D-bioprinted pigmented autologous skin graft overlying volume-stable adipose tissue	(1277)

Table 12.3.3.2.2. Summary of 3D-bioprinted or tissue-engineered NAC reconstructions. Abbreviations: N/A: not applicable.

Tissue Engineered NAC

Synthetic Scaffold

In a preclinical animal study, Cao *et al* demonstrated the utility of seeding biocompatible Pluronic F-127 with porcine chondrocytes and implanting them into desired shape using purse-string suture technique (1275). The authors report satisfactory nipple projection, size and shape at 10 weeks. Interestingly, this technique has not been re-investigated since 1998.

Decellularized Allograft Scaffold

Recently, a biotechnology company, called NovoThelium LLC, has been launched based on patent-pending technology where decellularized NAC scaffold from donor tissues are seeded with patient's nipple cells obtained at mastectomy (1276). The allograft scaffold is matured in an *ex vivo* bioreactor before being implanted on to a thick, deepithelialized

dermal base as a delayed procedure. The major advantage of utilizing decellularized allograft is the preservation of intrinsic NAC cell signalling cues that submicron level tissue architecture. However, the company does not explain the potential risk of harvesting nipple cells from patients undergoing breast cancer treatment and how oncogenic cells will be removed and controlled. Preclinical studies are underway.

3D Bioprinted NAC Graft

In 2011, TeVido BioDevices LLC biotechnology company was set up to market and produce 3D-bioprinted NAC graft based on their patent-pending technique, called Cellatier^{TM} (1277). The company aims to manufacture autologous NAC graft with pigmented skin layer, supported by volume-stable, patient-specific design adipose tissue base. Since commencement, TeVido has generated immense media attention and has secured large funds from National Science Foundation (Arlington, VA, USA) and raised crowdfunding from Indiegogo (San Francisco, CA, USA). Currently, preclinical *in vitro* and animal studies are underway.

Conclusion

Nipple-areola complex (NAC) constitutes an important landmark on a breast and its loss due to breast cancer treatment can be devastating. Evidences demonstrate significant improvement in psychosexual well-being and patient satisfaction can be achieved following a successful NAC reconstruction. Various reconstructive options have been reported historically. However, they are all associated with inconsistent long-term outcomes regarding maintenance of the neo-nipple projection, color, size, shape and texture, leading to polarizing patient satisfaction rates. To this effect, novel regenerative medicine technology, three-dimensional (3D) bioprinting, which combines the conventional tissue engineering with 3D printing platform, has been touted as a potential solution. Recently, TeVido BioDevices company has begun developing an entirely 3D-printed NAC graft but the results are currently limited to preclinical studies.

13 Discussion and Conclusion

13.1 3D Imaging and Printing Techniques in Plastic and Reconstructive Surgery: Established Techniques

Submitted (Publication): ***Chae MP***, Hunter-Smith DJ, Rozen WM. (2018) 3D imaging and printing techniques in plastic and reconstructive surgery: Established techniques. Aust J of Plast Surg.

Chapter Summary

Introduction: An increasing number of reconstructive surgeons use modern imaging technologies for preoperative planning and intraoperative surgical guidance. Conventional imaging modalities such as computed tomography (CT) and magnetic resonance imaging (MRI) are relatively affordable, widely accessible and offer powerful functionalities. In this first review of two-part series, we evaluate the established techniques of 3D imaging and printing techniques based on CT and MRI in plastic and reconstructive surgery.

Method: A review of the published English literature dating from 1950 to 2017 using databases, such as PubMed, Medline, Web of Science and Embase was taken.

Result: In plastic and reconstructive surgery, the most commonly used free software platforms are 3D Slicer (Surgical Planning Laboratory, Boston, MA, USA) and OsiriX (Pixmeo, Geneva, Switzerland). 3D perforator mapping using 3D-reconstructed images from CTA and MRA is commonly used for preoperative planning. 3D volumetric analysis using current software techniques remain labour-intensive and reliant on operator experience. 3D printing has been investigated extensively since its introduction. As more free open-source software suites and affordable 3D printers become available, 3D printing is becoming accessible for clinicians.

Conclusion: Numerous studies have explored the application of 3D-rendered conventional imaging modalities for 3D perforator mapping, 3D volumetric analysis and 3D printing. However, there is a lack of comprehensive review of all established 3D imaging and printing techniques in a language suitable for clinicians.

Introduction

Performing perforator-based flap reconstruction requires careful selection of the perforator, flap design and donor site. A suitable perforator is ideally harvested from a donor site with minimal morbidity, and is large enough to facilitate microsurgical anastomosis and adequately supply all portions of the flap.(1278) In recent times, an increasing number of plastic and reconstructive surgeons have begun using modern 3D imaging and printing technologies to aid preoperative planning, intraoperative guidance and medical education.(3, 318) However, there is a lack of comprehensive review of these 3D techniques that provides a global understanding of this novel field in a language suitable for clinicians.

Currently, a plethora of imaging modalities is being used in plastic and reconstructive surgery, mainly computed tomography angiography (CTA) and magnetic resonance angiography (MRA).(5, 13, 96, 117, 126, 129) First reported for perforator-based flap planning in 2006,(117, 129) CTA is widely used in preoperative investigations by institutions around the world and is considered the gold standard due to its high accuracy and reliability.(5, 6, 10-13) However, CTA poses potential risk of additional radiation exposure, involves intravenous administration of iodinated contrast media and does not provide haemodynamic features such as flow velocity and direction.

MRA bypasses radiation exposure but is limited by only being able to detect vessels greater than 1 mm in diameter.(1279) It also has lower spatial resolution(97) and poorer contrast differentiation from the surrounding soft tissue.(99) As a result, MRA has a lower sensitivity (50%) for detecting abdominal wall perforators than CTA.(96) Enhanced by recent advances in imaging techniques,(4) contrast agents(159) and increasing availability of higher field-strength scanners,(160) more recent studies have reported improved sensitivity in identifying perforators (91.3-100%).(98, 122-126) As a result, MRA remains an investigation of choice for younger patients, and for those with iodine allergy and impaired renal function.(316)

In this review, we evaluate the established techniques of 3D imaging and printing based on CT and MRI in plastic and reconstructive surgery.

Methods

We reviewed the published English literature from 1950 to 2017 from well-established databases such as PubMed, Medline, Web of Science and Embase. We included all studies that analyse 3D imaging and printing techniques used in surgery, especially plastic and reconstructive surgery. We used search terms such as “3D imaging”, “CTA”, “MRA”, “3D image software”, “volumetric analysis”, “3D printing”, “preoperative planning”, “intraoperative guidance”, “education”, “training”, and “customised implant”. We also retrieved secondary references found through bibliographical linkage.

3D Imaging Rendering Software

Through our literature review, we identified the most commonly used 3D image rendering software suites in medical application. We identified their specifications, such as software language on which it is based, cost, open-source capability and its function, by accessing their manufacturer’s website or from publications.

3D Perforator Mapping

We identified that CTA and MRA are the most commonly used imaging modalities for 3D perforator mapping. Hence, we evaluated the software suites based on these modalities.

3D Volumetric Analysis

We focused our analysis of 3D volumetric analysis based on conventional 3D imaging techniques, CT and MRI. Similar to the previous sections, we systemically identified a list of software suites used to analyse 3D volumetric data from CT or MRI and examined their application in plastic and reconstructive surgery.

3D Printing

Studies using 3D printing for preoperative planning in plastic and reconstructive surgery are assessed using Oxford Centre for Evidence-Based Medicine levels of evidence.(1280) Given that the most common 3D printing application in plastic and reconstructive surgery

is mandibular reconstruction with free fibular flap, we performed a focused further qualitative analysis of this application.

Results / Discussion

Numerous studies have explored the application of 3D-rendering conventional imaging modalities for 3D perforator mapping, 3D volumetric analysis and 3D printing.

3D Image Rendering

Proprietary software provided by manufacturers of CT and MRI scanners generally offers only two-dimensional (2D) image-viewing capabilities. As a result, numerous free, open-source software platforms have been developed that are capable of 3D image rendering. They are built on robust, but limited, open-source software libraries that provide the basic architecture. In plastic and reconstructive surgery, the most commonly used free software platforms are 3D Slicer (Surgical Planning Laboratory, Boston, MA, USA) and OsiriX (Pixmeo, Geneva, Switzerland) (Table 13.1.1).

Product	Manufacturer	Software Language	Free	Open-Source	Function
3D Slicer	Surgical Planning Laboratory (Boston, MA, USA)	C++ Python	Yes	Yes	Built on ITK and VTK Easy-to-use graphical user interface Creates 3D images of regions of interest suitable for 3D printing
OsiriX	Pixmeo (Geneva, Switzerland)	Objective-C	Yes	No	Built on ITK and VTK Enables both viewing and 3D rendering of anatomical structures Easy-to-use graphical user interface Has both 3D rendering techniques: volume-rendered technique and maximum intensity projection

Table 13.1.1. Summary of 3D image rendering software.

- 3D Slicer(263)
    - Well-supported, open-source platform built on ITK and VTK using C++ and Python.(318)
    - Developed to segment brain tumours from MRI scans(264) and used in a variety of medical applications ranging from lung cancer diagnosis (1281) to cancer imaging.(1282)
    - Adept at generating volumetric images for 3D printing through thresholding and segmentation techniques (see below).
- OsiriX(262)
    - Image-viewing software platform built on ITK and VTK, for Macintosh computers only.
    - Intuitive graphical user interface and fast processing speed make it popular with clinicians worldwide.(262)
    - Enables viewing of multidimensional data such as positron emission tomography (PET)-CT(1283) and cardiac-CT as well as standard tomographic scans (CT and MRI).(1284)
    - Suitable for viewing 3D and 4D datasets but limited to 3D anatomical models of large organs such as long bones and the heart.

3D Perforator Mapping

In perforator-based free flap reconstruction, plastic surgeons commonly rely on CTA or MRA-based 3D reconstructed images of the relevant perforators for preoperative planning (Figure 13.1.1).

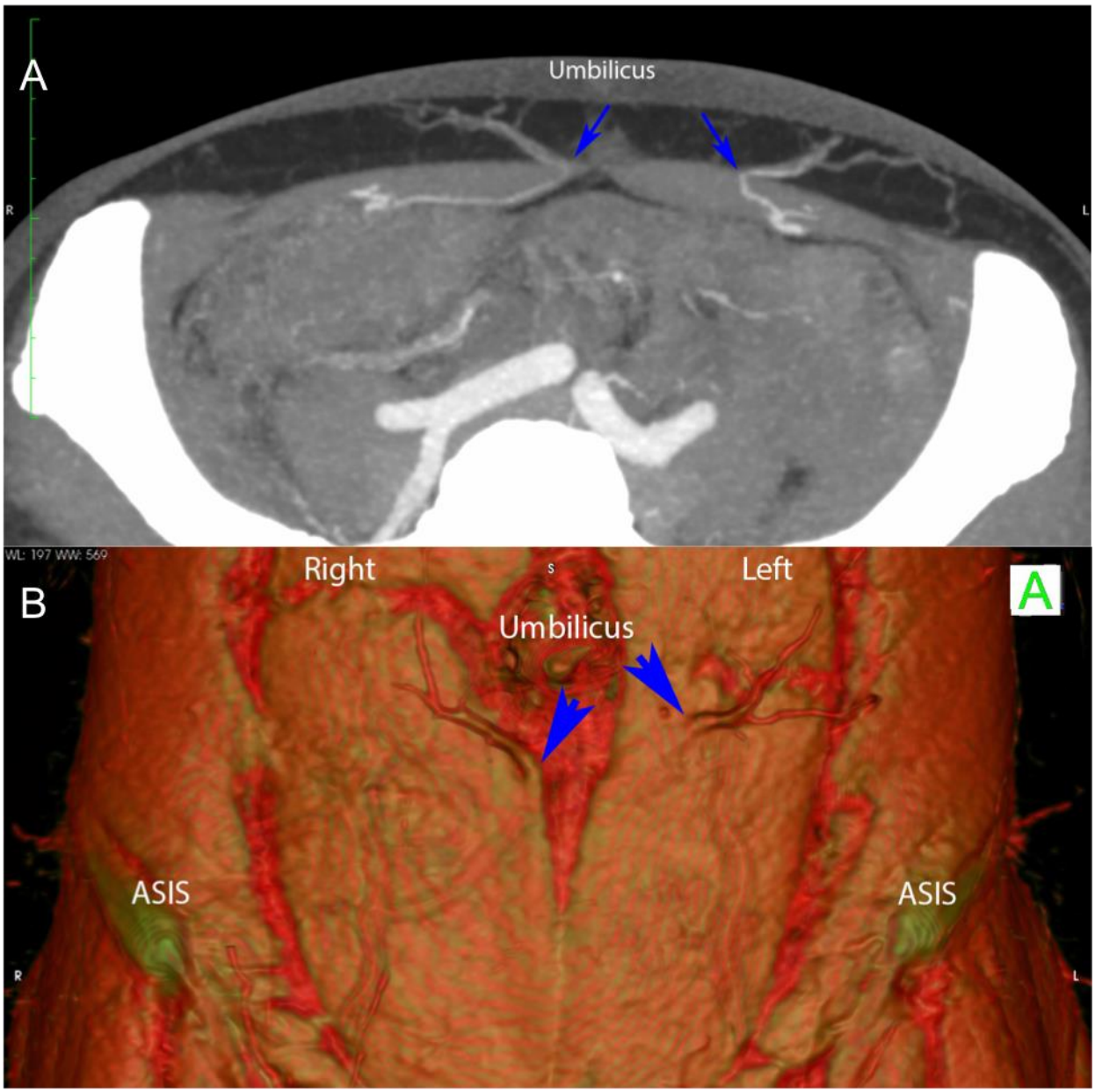

Figure 13.1.1. CTA-based 3D perforator mapping in DIEP flap planning performed using OsiriX software. (A) MIP reconstruction demonstrating the intramuscular and subcutaneous course of each perforator, (B) VRT reconstruction demonstrating the location of the perforators (blue arrows) as they emerge from the rectus sheath in reference to the umbilicus (marked). CTA: computed tomographic angiography; 3D: three-dimensional; DIEP: deep inferior epigastric artery perforator; MIP: maximum intensity projection; VRT: volume-rendered technique; DIEA: deep inferior epigastric artery.

- CTA
    - The most commonly used imaging modality for 3D perforator mapping
    - This is achieved using MIP and VRT 3D software reconstruction techniques.

  - Compared to Siemens Syngo InSpace 4D and VoNaviX, which are expensive, and virSSPA, which is not available outside the original institution, OsiriX software platform is free and has been demonstrated to be as accurate.
- MRA
  - Modern magnetic resonance technology can provide superior 3D reconstructed images. However, they are expensive, time-consuming and relatively difficult to perform.
  - Similar to CTA, free OsiriX software can be used for 3D perforator mapping from MRA.
  - Recently, investigators have developed a semi-automated plugin tool for analysing MRA images using OsiriX. However, it remains to be validated in a large cohort.

3D Volumetric Analysis

Accurate assessment of tissue volume is an important aspect of preoperative planning in plastic surgery.(525-529) Particularly in breast reconstructive surgery, volumetric analysis is paramount for achieving symmetrisation and a satisfactory outcome.(385, 569, 695, 1285-1287) However, an accurate, reliable and convenient method of objective breast volumetric analysis has remained elusive (Figure 13.1.2 and Table 13.1.2).(530)

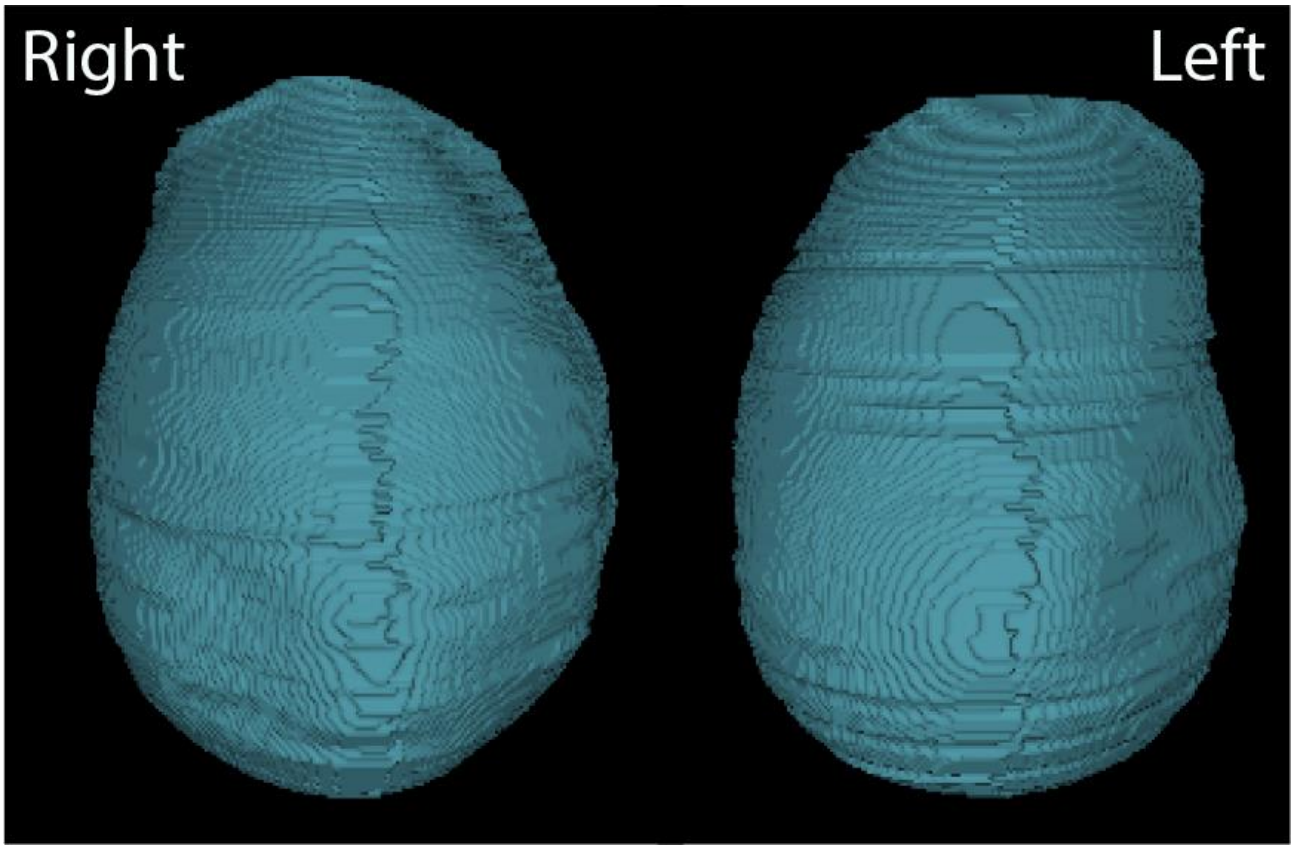

Figure 13.1.2. MRI-based 3D volumetric analysis in planning breast reconstructive surgery demonstrating 611 mL on the right breast and 635 mL on the left breast, performed using OsiriX software (Pixmeo).

Product	Manufacturer	Free	Open-Source	Clinical Application
CT				
OsiriX	Pixmeo, Geneva, Switzerland	Yes	No	Breast
Aquarius Workstation	TeraRecon Inc., San Mateo, CA, USA	No	No	Breast DIEP flap
Mimics	Materialise NV, Leuven, Belgium	No	No	DIEP flap
Leonardo Workstation	Siemens AG, Munich, Germany	No	No	DIEP flap
ImageJ	NIH, Rockville, MD, USA	Yes	No	Orbital volume

Vevo LAB	Fujifilm ViewSonics, Toronto, Canada	No	No	Autologous fat graft in mice
SkyScan CTan	Bruker, Kontich, Belgium	No	No	Limb lymphedema in mice
MRI				
OsiriX	Pixmeo, Geneva, Switzerland	Yes	No	Breast Breast implant
				Limb lymphedema in mice
Volume Viewer Plus	GE Healthcare, Waukesha, WI, USA	No	No	Breast
BrainLAB	BrainLAB AG, Feldkirchen, Germany	No	No	Breast Breast implant
Medis Suite MR	Medis Medical Imaging Systems BV, Leiden, The Netherlands	No	No	Breast Breast implant
AW Server	GE Healthcare, Waukesha, WI, USA	No	No	Breast glandular tissue
				Muscle (pectoralis major)
Dextroscope	Volume Interactions, Singapore	No	No	Malar fat pad
ImageJ	National Institutes of Health, Rockville, MD, USA	Yes	No	Breast

Table 13.1.2. Summary of software platforms capable of performing 3D volumetric analysis from CT and MRI. Abbreviations: CT: computed tomography; MRI: magnetic resonance imaging; DIEP: deep inferior epigastric artery perforator.

- CTA

- Calculating the flap volume from CTA and comparing it to the intraoperative flap weight, Eder et al reported high correlation between the two measurements (r = 0.998, p < 0.001) demonstrating high prediction accuracy of CTA (0.29%; -8.77 to 5.67%).(1285)
- In order to further improve its accuracy, Rosson et al placed fiducial markers on the surgical incision line before the CTA and achieved accuracy of up to 99.7% (91-109%).(385)
- Lee et al calculated a ratio using volume of the breast and the potential DIEP flap from CTA and created a treatment algorithm.(1288) If >50% of the harvested flap is required for reconstruction, surgeons have made modifications to the flap design by increasing its height, capturing more adipose tissue by bevelling superiorly from the flap's upper margin, like Ramakrishnan's extended DIEP technique,(1289) and incorporating multiple perforators if available. If >75% of the flap is required, venous augmentation is performed with contralateral superficial inferior epigastric vein.
- Using this algorithm in 109 consecutive patients, the authors noted a significant reduction in perfusion-related complications (5.6 vs 22.9%, p = 0.006) and fat necrosis (5.6 vs 19.1%, p = 0.03).

- MRI
  - In comparison to CT, MRI has superior soft-tissue resolution and is thus more accurate at measuring breast volumes (r = 0.928 vs 0.782, p = 0.001),(540) and has a mean measurement deviation of only 4.3%.(596)
  - Furthermore, Rha et al show that MRI-derived breast volume is more accurate than the traditional volumetric method using plaster cast (r^2 = 0.945 vs 0.625).(695)
  - Using manufacturer specifications as gold standard, Herold et al measured volume of breast implants using MRI in patients with bilateral augmentation mammaplasty.(569) Furthermore, they compared accuracy of three commonly available 3D image processing software platforms: OsiriX, BrainLAB (BrainLAB AG, Feldkirchen, Germany) and Medis Suite MR (Medis Medical Imaging Systems BV, Leiden, The Netherlands). BrainLAB had the lowest mean deviation of 2.2 +/– 1.7%, followed by OsiriX at 2.8 +/– 3.0% and Medis Suite MR at 3.1 +/– 3.0%. However, all software platforms correlated highly accurately with the reference overall (r = 0.99).

Interestingly, software analysis is fastest using OsiriX at 30 seconds per implant, followed by BrainLAB and Medis Suite MR at 5 minutes.

To date, most software techniques remain manual, that is labour-intensive and reliant on operator experience, while validated evidence of commercially available automatic segmentation tool is scarce.(35, 1290) Interestingly, Rha et al have used ImageJ, a free NIH-developed image processing program, to successfully perform volumetric analysis of the orbit and breast from CT and MRI, respectively.(1291) However, ImageJ has yet to be investigated in clinical application.

3D Printing

In contrast to medical imaging modalities that are limited by being displayed on a 2D surface, such as a computer screen, a 3D-printed biomodel can additionally provide haptic feedback.(16, 17, 318, 379, 1292) 3D printing, also known as rapid prototyping or additive manufacturing, describes a process by which a product derived from a computer-aided design (CAD) is built in a layer-by-layer manner.(176, 189, 704) Main advantages of 3D printing lie with the ability to customise, cost-efficiency and convenience.(171, 173) Since its introduction, its use in surgery has been extensively investigated.

3D printing software

In clinical application, two types of software platforms are required: 3D modelling software that can convert standard Digital Imaging and COmmunications in Medicine (DICOM) files from CTA/MRA into a CAD file; and 3D slicing software that divides the CAD file into thin data slices suitable for 3D printing.(261) A range of 3D modelling software is available but only the following are user-friendly and commonly reported: 3D Slicer,(35, 273) OsiriX(378) and Mimics (Materialise NV, Leuven, Belgium).(430) In contrast, 3D slicing software usually accompany 3D printers at no additional cost and possess simple user interface such as Cube software (3D Systems, Rock Hill, SC, USA), MakerBot Desktop (MakerBot Industries, New York, NY, USA) and Cura (Ultimaker BV, Geldermalsen, The Netherlands).

3D printing hardware

In clinical application, a host of 3D printer types have been used: fused filament fabrication (FFF), selective laser sintering (SLS), stereolithography (SLA), binder jetting and multijet modelling (MJM).(318) FFF is the most common and most affordable desktop 3D printing technology available.(182, 190, 191) In a FFF 3D printer, a melted filament of thermoplastic material is extruded from a nozzle moving in the x–y plane and solidifies upon deposition on a build plate.(192) More recently, 3D metal printing using SLS has gained popularity in creating sterilisable surgical guides(1293, 1294) and customised dental implants.(1295)

3D printing in plastic and reconstructive surgery

Encouraged by its potential, surgeons from a wide range of specialities have applied 3D printing such as neurosurgery,(294, 322, 1296-1301) cranio-maxillofacial surgery,(1302-1309) cardiothoracic surgery,(1310, 1311) orthopaedic surgery,(229, 1312) transplantation,(219-221) ear, nose and throat surgery(1313, 1314) and breast cancer surgery.(1315) Similarly, in reconstructive plastic surgery, 3D printing appears most useful for preoperative planning, intraoperative guidance, medical education and creating custom implants. 3D printing bespoke implants overlaps significantly with 3D bioprinting(770, 1316, 1317) and is beyond the scope of this article.

<u>Preoperative planning</u>

3D printing has been most commonly used in plastic and reconstructive surgery for preoperative planning (Table 13.1.3).

Clinical Application	3D-Printed Model	Imaging	3D Modelling Software	3D Printer
DIEP Case report	Asymmetrical breast	CTA	Osirix (Pixmeo, Geneva, Switzerland)	Cube 2 (3D Systems, Rock Hill, SC, USA)
DIEP Case series of 35	Breast	CTA	AYRA (Virgen del Rocio University Hospital, Sevilla,	FFF 3D printer

			Spain)	
DIEP Cadaver	IMA perforator	CT	Mimics (Materialise NV, Leuven, Belgium)	ProJet x60 (3D Systems, Rock Hill, SC, USA)
DIEP Case report	DIEP flap	CTA	Mimics (Materialise NV, Leuven, Belgium)	Objet500 Connex1 (Stratasys, Eden Prairie, MN, USA)
Lower limb soft-tissue defect Case report	“reverse” model of the defect	CTA	Osirix (Pixmeo, Geneva, Switzerland)	Cube 2 (3D Systems, Rock Hill, SC, USA)
Sacral soft-tissue defect Case series of 5	Sacral defect	CT/MRI	Osirix (Pixmeo, Geneva, Switzerland)	Cube 2 (3D Systems, Rock Hill, SC, USA)
Hemi-mandibulectomy Case report	Mandible and giant invasive SCC	CTA	3D Slicer (Surgical Planning Laboratory, Boston, MA, USA)	MakerBot Z18 (MakerBot Industries, New York, NY, USA)
Bony defect of the wrist Case series of 3	Bony defect	CT	MeshMixer (Autodesk, San Rafael, CA, USA)	Micro 3D printer (M3D, Fulton, MD, USA)
4D printing of thumb movements Case report	Hand	4D CT	Osirix (Pixmeo, Geneva, Switzerland)	Cube 2 (3D Systems, Rock Hill, SC, USA)
Nasal cartilaginous defect Cadaver Human	Nasal alar cartilage	MRI	GOM Inspect (GOM GmbH, Braunschweigh, Germany)	ZPrinter 250 (3D Systems, Rock Hill, SC, USA)

volunteer				
Augmentative rhinoplasty Case series of 7	Individualised nasal implant	CT	Rhinoceros (McNeel, Seattle, WA, USA)	Cubicon Single (Hyvision System, Seongnam, South Korea

Table 13.1.3. Use of CT/MRI-based 3D-printed haptic models for preoperative planning in plastic and reconstructive surgery. Abbreviations: CT: computed tomography; CTA: computed tomographic angiography; MRI: magnetic resonance imaging; DIEP: deep inferior epigastric artery perforator; SCC: squamous cell carcinoma; FFF: fused filament fabrication; IMA: internal mammary artery.

Autologous breast reconstruction

In 2014, Gillis and Morris reported the first case of 3D-printed internal mammary artery (IMA) and its perforators, a common recipient site in free flap breast reconstruction.(275) Similarly, Mehta et al 3D-printed a multi-colour, multi-material model of deep inferior epigastric artery (DIEA) and its perforators.(705) Despite its benefits, both studies revealed high cost of 3D printing (USD 400–1200 per model), mainly due to outsourcing the manufacturing. In addition, outsourcing introduces delay of up to six to eight weeks that may not be appropriate in some clinical settings. As a result, Suarez-Mejias et al developed their own 3D modelling software, called AYRA (Virgen del Rocio University Hospital, Sevilla, Spain).(1318) More recently, Chae et al described an affordable and convenient technique of 3D printing using free software platforms and desktop 3D printers (Figure 13.1.3).(35)

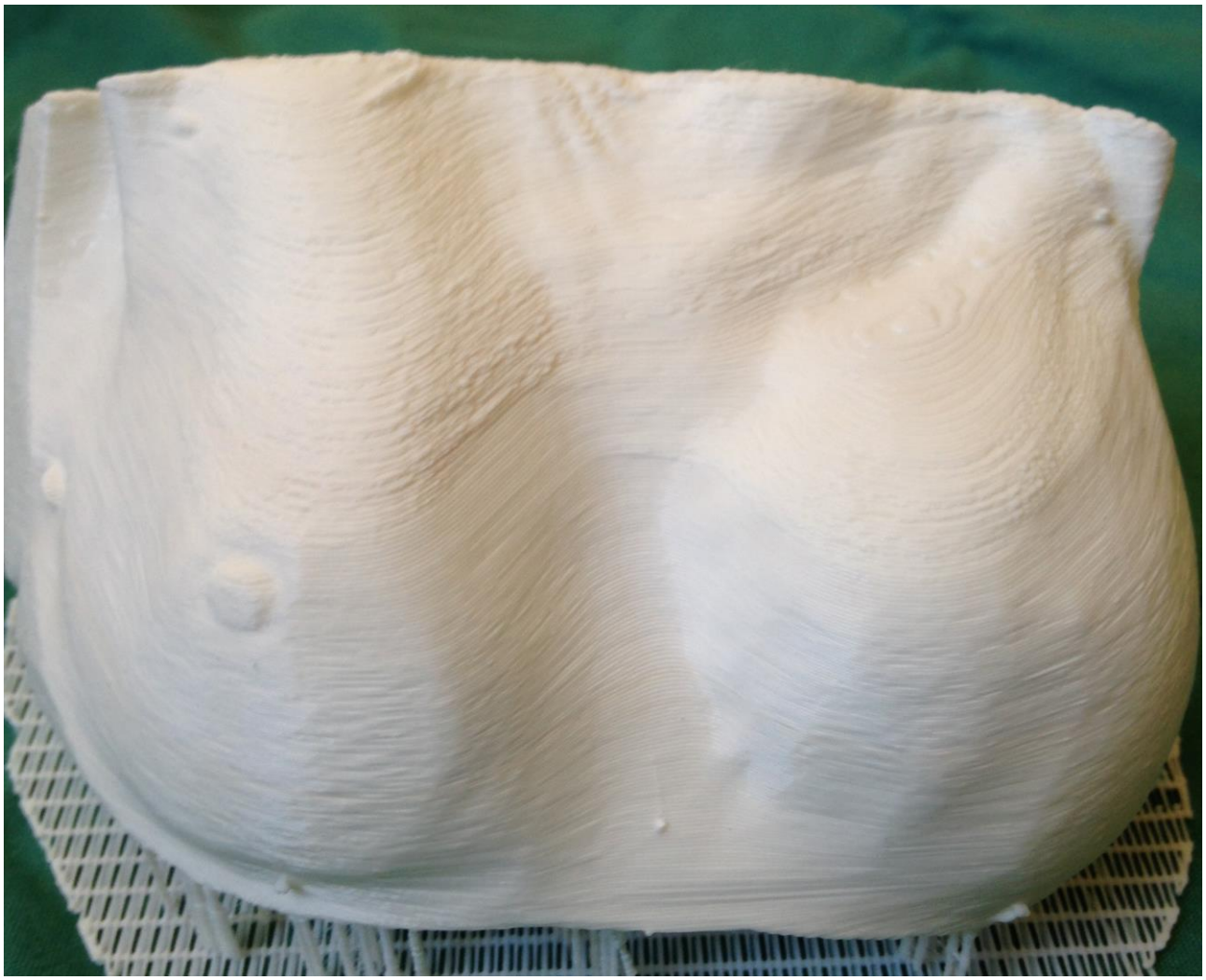

Figure 13.1.3. 3D-printed biomodel of breasts in planning reconstruction using Cube 2 printer (3D Systems, Rock Hill, SC, USA). Reproduced with permission from (35).

Soft-tissue modelling

In a case of lower limb reconstruction, Chae et al 3D-printed a model of the soft tissue defect that aided in flap designing.(273) Similarly, Garcia-Tutor et al used 3D-printed models of large sacral defects to perform qualitative and quantitative volumetric assessment (378). Cabalag et al fabricated a model of giant squamous cell carcinoma that was useful for planning hemi-mandibulectomy and determining the length of free fibular flap required.(272)

Bony modelling

Taylor and Iorio 3D-printed in-house a negative mould of scaphoid/lunate defect from avascular necrosis, from which a silicone model was created, sterilised and used intraoperatively for flap planning.(1319) In an interesting application, Chae et al described their technique of 4D printing where multiple models of the thumb and wrist bones were 3D-printed from 4D CT scans to demonstrate their dynamic relationship.

Cartilage modelling

3D assessment of nasal cartilaginous defect can be useful for planning reconstruction. Visscher et al demonstrated that 3D-printing alar cartilages using MRI showed mean error of 2.5 mm.(1320) Interestingly, most of the difference was found in 3D-printing medial crus but lateral crus remained highly accurate likely attributable to its more linear shape. Recently, Choi et al 3D-printed patient-specific negative mould from CT to create silicone nasal implants for augmentative rhinoplasty using an in-house software.(1321) The authors demonstrated mean accuracy of 0.07 mm (0.17%) and no complications.

Intraoperative guidance

Use of 3D-printed fibular osteotomy guides for mandibular reconstruction has been studied extensively (Table 13.1.4).(1322-1325) (382, 1326-1334) (182, 1335)

Year	Patients	Source of 3D Printing	Imaging	3D Rendering Software	3D Printers
2017	18	In-house	CT	AYRA (Virgen del Rocio University Hospital, Sevilla, Spain) Osirix (Pixmeo, Geneva, Switzerland) 3D Slicer (Surgical Planning Laboratory, Boston, MA, USA) MeshMixer (Autodesk, San Rafael, CA, USA)	Objet30 Pro (Stratasys, Eden Prairie, MN, USA) Zortrax M200 (Zortrax, Olsztyn, Poland)

				Blender (Blender Foundation, Amsterdam, The Netherlands)	
2017	3	Outsourced	CT	Osirix (Pixmeo, Geneva, Switzerland) MeshLab (ISTI, Pisa, Italy) Netfabb (Autodesk, San Rafael, CA, USA) Blender (Blender Foundation, Amsterdam, The Netherlands)	Formiga P 100 (EOS, Munich, Germany)
2017	7	Outsourced	CT	E3D Online (E3D Online, Oxfordshire, UK)	ProJet 3510 HD (3D Systems, Rock Hill, SC, USA)
2016	1	In-house	CT	Amira (FEI Company, Hillsboro, OR, USA) Blender (Blender Foundation, Amsterdam, The Netherlands)	PolyJet (Stratasys, Eden Prairie, MN, USA)
2015	1	Outsourced	CT	SurgiCase CMF (Materialise NV, Leuven, Belgium)	SLM
2013	68	Outsourced	CT	ProPlan CMF (Dupuy Synthes CMF, West Chester, PA, USA)	SLA
2013	48	Outsourced	CT	VoXim (IVS Technology, Chemnitz, Germany)	SLA
2013	10	Outsourced	CT	ProPlan CMF (Dupuy Synthes CMF, West	SLA

				Chester, PA, USA)	
2013	38	Outsourced	CT	SurgiCase CMF (Materialise NV, Leuven, Belgium)	SLA
2012	1	Outsourced	CT	SurgiCase CMF (Materialise NV, Leuven, Belgium) Rhinoceros (McNeel, Seattle, WA, USA)	M 270 (EOS, Munich, Germany)
2012	1	In-house	CTA	AYRA (Virgen del Rocio University Hospital, Sevilla, Spain)	FFF 3D printer
2012	9	In-house	CT	Mimics (Materialise NV, Leuven, Belgium)	SLA 3500 (3D Systems, Rock Hill, SC, USA)
2012	15	Outsourced	CT	Magics (Materialise NV, Leuven, Belgium)	SLA
2011	5	Outsourced	CT	N/A	SLS
2009	3	Outsourced	CT	Extended Brilliance Workspace (Philips Healthcare)	Objet Eden 500V (Stratasys, Eden Prairie, MN, USA)
2009	1	Outsourced	CT	SurgiCase CMF (Materialise NV, Leuven, Belgium)	SLS nylon

Table 13.1.4. Summary of all studies investigating the use of image-guided 3D-printed surgical guide in mandibular reconstruction with free fibular flap. Abbreviations: CT: computed tomography; CTA: computed tomographic angiography; SLM: selective laser melting; SLA: stereolithography; SLS: selective laser sintering; FFF: fused filament fabrication.

Investigators have demonstrated their accuracy of up to 0.1–0.4 mm(182, 1323-1325, 1330) Moreover, they can significantly reduce flap ischaemia time (120 minutes vs 170

minutes, p = 0.004) (1327) and the total operating time (8.8 hours vs 10.5 hours, p = 0.0006).(1330)

Medical education

Educating junior surgical trainees and medical students 3D pathological defects such as cleft lip and palate without hands-on interaction and demonstration is notoriously difficult. As the supply of cadavers for medical education continues to dwindle due to rising maintenance costs(1336) and concerns regarding occupational health and safety,(1337) the use of 3D-printed biomodels has become popular.(1338, 1339) Moreover, Zheng et al have used 3D-printed negative moulds to fabricate soft silicone models of cleft lip and palate for students to directly perform cheiloplasty.(1340) Subsequently, in a randomised clinical trial of 67 medical students, Al Ali et al have demonstrated that the knowledge gained was significantly higher using 3D-printed models of cleft lip and palate than standard slide presentations (44.65% vs 32.16%, p = 0.038).(1341) Similarly, clinicians have 3D-printed negative moulds of paediatric microtia for practical demonstration.(1342)

Conclusion

Numerous studies have explored the application of 3D-rendered conventional imaging modalities for 3D perforator mapping, 3D volumetric analysis and 3D printing. Numerous free, open-source software platforms have been developed that are capable of 3D image rendering, such as 3D Slicer and OsiriX. For perforator mapping, most plastic surgeons rely on CTA or MRA-based 3D reconstructed images. Current 3D volumetric analysis technologies remain labour-intensive and are yet to be automatized. 3D printing has been most commonly used in plastic and reconstructive surgery for preoperative planning mandibular reconstruction with free fibular flap. Majority of these studies have lower level of evidence, consisting of case series and reports. The current review is a lack of comprehensive review of all established 3D imaging and printing techniques in a language suitable for clinicians.

13.2 3D Imaging and Printing Techniques in Plastic and Reconstructive Surgery: Emerging Techniques

Submitted (Publication): ***Chae MP***, Hunter-Smith DJ, Rozen WM. (2018) 3D imaging and printing techniques in plastic and reconstructive surgery: Emerging techniques. Aust J of Plast Surg.

Chapter Summary:

Introduction: In this second review of a two-part series, we evaluate the emerging techniques of 3D imaging and printing techniques based on CT (computed tomography) and MRI (magnetic resonance imaging) in plastic and reconstructive surgery.

Method: A review of the published English literature dating from 1950 to 2017 using databases, such as PubMed, Medline, Web of Science and Embase was taken.

Results: Image-guided navigation system using fiducial markers has demonstrated utility numerous surgical disciplines, including perforator-based flap surgery. However, it has largely been superseded by augmented reality technology with superior convenience and speed. With added benefit of tactile feedback, holograms appear promising. However, it has yet to be developed beyond prototypic stage. Aided by growing volume of digitalised clinical data, machine learning poses significant benefit in future image-based decision-making process.

Conclusion: To date, most studies have been presented in small case series and they remain to be analysed using outcomes-based validation studies. However, together they illustrate an exciting future where clinicians will be armed with intuitive technologies for surgical planning and guidance.

Introduction

To date, a plethora of imaging modalities has been used in plastic and reconstructive surgery to aid preoperative planning, intraoperative guidance and medical education.(3, 318) However, conventional tomographic imaging modalities such as computed tomography angiography (CTA) and magnetic resonance angiography (MRA) remain relatively affordable and commonly accessible.(5, 13, 96, 117, 126, 129) As a result, clinicians have investigated novel technologies to expand their utility such as image-guided navigation system, augmented reality/virtual reality, holograms and machine learning.

In this second review of a two-part series, we evaluate the emerging techniques of 3D imaging and printing techniques based on CT and MRI in plastic and reconstructive surgery.

Methods

A review of the published English literature from 1950 to 2017 from well-established databases such as PubMed, Medline, Web of Science and Embase, was undertaken. We included all studies that analyse 3D imaging and printing techniques used in surgery, especially plastic and reconstructive surgery. We used search terms such as “3D imaging”, “CTA”, “MRA”, “3D image software”, “simulation surgery”, “stereotactic navigation-assisted surgery”, “augmented reality”, “virtual reality”, “hologram”, “automation”, “machine learning”, “artificial intelligence”, “preoperative planning”, “intraoperative guidance”, “education”, “training”, and “customised implant”. We also retrieved secondary references found through bibliographical linkage.

Through literature review, hardware and software programs used for image-guided navigation-assisted surgery, augmented/virtual reality and holograms and machine learning are qualitatively analysed, evaluating their cost, affordability arbitrarily being defined as less than Australian 500 dollars and up-to-date clinical applications. Papers were assessed using Oxford Centre for Evidence-Based Medicine levels of evidence (1280).

Results / Discussion

Advances in recent technology have introduced the use of image-guided navigation systems, augmented/virtual reality and holograms, and machine learning to surgical planning.

Image-guided navigation-assisted surgery

Technology

An image-guided navigation system tracks surgical instruments in real-time and matches their location to the preoperative CTA and MRI for viewing them intraoperatively.(1343, 1344) The earliest system used external stereotactic frames fixed to the skull or other bony landmarks.(1345) Modern frameless navigation systems using fiducial markers(1346), surface landmarks(1347) and surface-matching laser registration(1348) are faster, safer and more convenient.(1349) As a result, stereotactic navigation is used routinely in neurosurgery,(1350) spinal surgery,(1351) orthopaedic surgery,(1352) craniofacial surgery,(1353) ear, nose and throat surgery(1354) and endovascular surgery.(1355)

Application in plastic and reconstructive surgery

In plastic surgery, Rozen et al demonstrated that registration systems using fiducial markers – six to seven in DIEP and nine to ten in anterolateral thigh (ALT) flaps – are reliable for viewing CTA-derived perforator anatomy.(9, 669, 1356, 1357) Durden et al developed a novel electrocautery pen attached to a stereotactic frame and reported a global error of 2.1–2.4 mm during DIEP flap harvest.(1358) However, the longer, heavier diathermy handle may compromise surgical dexterity and requires its large reference frame to be fixed to the operating table. In an interesting application, Chao et al developed a robot (KUKA Lightweight Robot; KUKA, Augsburg, Germany) that can perform osteotomy on a 3D-printed acrylic fibula with the aid of stereotactic navigation.(1359) Out of 18 robotic osteotomies executed, it reported average linear variation of 1.3 +/– 0.4 mm and angular variation of 4.2 +/– 1.7 degrees. It remains to be seen how this can be translated in vivo but its potential is intriguing. Overall, navigation systems are seldom used in soft-tissue surgery due to lack of reliable bony landmarks and are superseded by augmented reality platforms (Table 13.2.1).

Product	Manufacturer	Free	Open-Source	Clinical Application
BrainLAB	BrainLAB AG, Feldkirchen, Germany	No	No	DIEP
				ALT
				DCIA
StealthStation	Medtronic Inc., Minneapolis, MN, USA	No	No	DIEP
KUKA Lightweight Robot	KUKA, Augsberg, Germany	No	No	Free fibular flap

Table 13.2.1. Summary of image-guided navigation systems used in reconstructive plastic surgery. Abbreviations: DIEP: deep inferior epigastric artery perforator; ALT: anterolateral thigh; DCIA: deep circumflex iliac artery.

Augmented/virtual reality and holograms

In comparison to 2D imaging modalities, augmented reality (AR), virtual reality (VR) and holograms can provide natural 3D visual perception and haptic feedback, respectively. First described by Boeing engineers, Caudell and Mizell in 1992,(448) the view of one's real environment is superimposed by real-time virtual images in AR.(1360) They can be displayed directly on the object in real-life, also known as projection method, or indirectly on a portable device, such as a head-mount display or smartphone.(449) In contrast, one's entire visual perception is completely shrouded by a computer-simulated graphics environment in VR.(1360)

VR

VR is an attractive platform to generate anatomically accurate surgical simulations to perform preoperative planning, medical training and enable visual communication with multidisciplinary team members and patients.(1361) Arora et al have shown that mental practice using virtual simulator can significantly improve surgical skill of novice surgeons in laparoscopic cholecystectomy ($p < 0.05$).(1362) However, currently most VR surgical simulators are pre-programmed, offer only limited interactions and exhibit such low image quality that it impedes the immersive experience.(1363-1365)

AR

AR produces an extended “layer” or field of view that leads to intuitive real-time 3D visualisation of anatomical structures. Currently, most AR devices are expensive, slow and complicated. Nonetheless, their potential application has been explored in numerous surgical specialities: calibrating stereotactic instruments in neurosurgery,(450) fashioning craniofacial implants in maxillofacial surgery,(451) enhancing visualisation in laparoscopic surgery(452) and sentinel lymph node biopsy in head and neck cancer(1366) and breast cancer surgery.(453) In plastic and reconstructive surgery, AR appears to be most useful for preoperative planning, intraoperative image navigation and surgical training (Table 13.2.2 and Figure 13.2.1).(454)

Product	Manufacturer	Type/Function	Affordability	Clinical Application
Hardware				
PicoPix PPX2480	Koninklijke Philips NV, Amsterdam, The Netherlands	Projector	Yes	DIEP Inguinal lymph nodes
PRJ-5	Sanwa Electronic, Osaka, Japan	Projector	Yes	DIEP
nVisor ST60	NVIS Inc., Reston, VA, USA	Head-mounted display	No	Thoracodorsal artery perforator flap
Projective Imaging System	University Science and Technology of China, Anhui, People’s Republic of China	Projector	N/A	Skin flap perfusion
Google Glass	Alphabet, Mountain View, CA, USA	Head-mounted display	No	Rhinoplasty
Software				
VitreaAdvanced fX Workstation	Vital Images, Minnetonka, MN,	3D rendering	No	DIEP Inguinal lymph nodes

	USA			
OsiriX	Pixmeo, Geneva, Switzerland	3D rendering	Yes	DIEP
ARToolKit	ARToolworks, Seattle, WA, USA	AR virtual modelling	Yes	Thoracodorsal artery perforator flap
Bespoke software written in OpenCV	University Science and Technology of China, Anhui, People's Republic of China	AR virtual modelling	N/A	Skin flap perfusion

Table 13.2.2. Summary of augmented reality devices used in reconstructive plastic surgery. Affordability of each device and software is determined by whether it costs less than AUD $500 outright or per year in subscription or is free. DIEP: deep inferior epigastric artery perforator; N/A: not available.

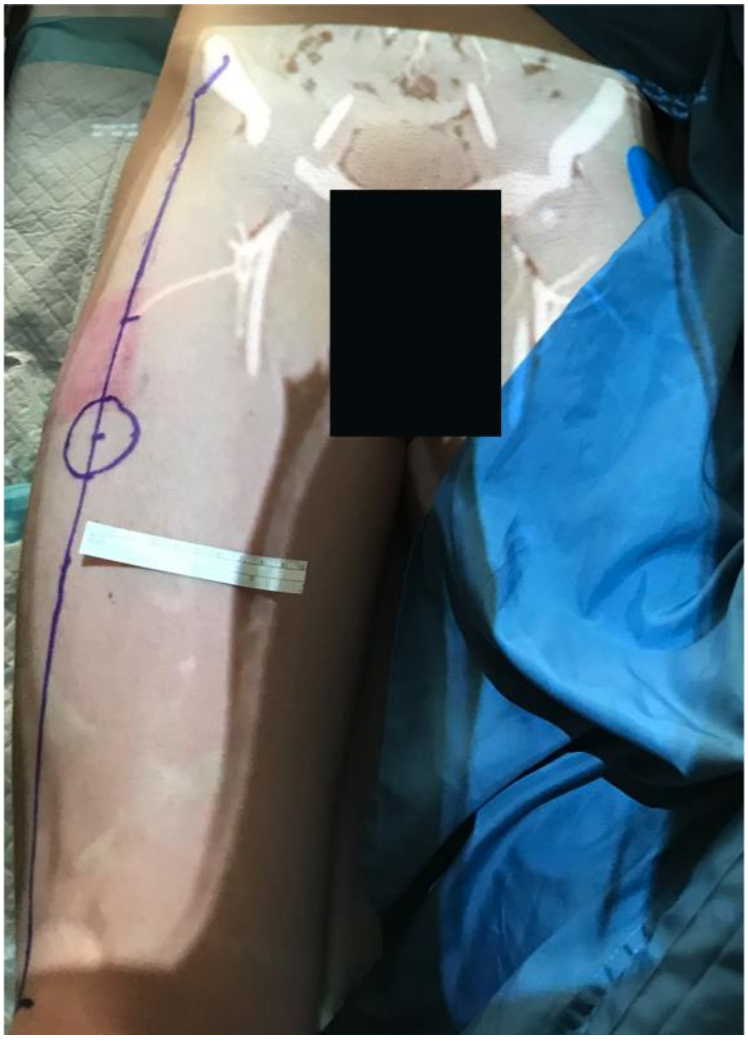

Figure 13.2.1. Projection of ALT perforators preoperatively using CTA-based direct augmented reality technique performed using OsiriX software (Pixmeo) and Philips PicoPix pocket projector (Koninklijke Philips NV, Amsterdam, The Netherlands). Purple line indicates marking of a line between traditional anatomical landmarks. The mark on the line correlated exactly with the location of the ALT perforator. Abbreviations: ALT: anterolateral thigh perforator; CTA: computed tomographic angiography.

Application in Plastic and Reconstructive Surgery

Hummelink et al describe a projection-based direct AR technique using an affordable handheld projector and proprietary software suites in three case series.(440, 443, 444) In the first series, they projected 3D-reconstructed CTA image of DIEA perforators onto the abdominal wall and demonstrated its high accuracy (84.3 vs 56.9%, p = 0.03).(443) In the following series, they extended its application by including the location of inguinal lymph nodes.(444) In the latest series, they calculated required flap volume and dimension using 3D surface scanning and projected the combined 3D-reconstructed image to aid flap designing and planning.(440) One of the major limitations of this technique is operator dependence since the projector must be held steadily above the patient at the correct height without significant tremor. Sotsuka et al attempted to resolve this by mounting the projector onto a fixed handstand.(456) However, its reliability remains to be seen.

In animal studies, Jiang et al developed a highly accurate (3.5 mm) direct AR technique for raising thoracodorsal artery perforator flaps that, however, requires invasive positioning of image registration system via percutaneous screws.(439) Gan et al developed a compact, direct AR technique consisting of a mini-projector and a near-infrared camera to detect skin perfusion after tail vein injection of ICG dye.(441) However, their system is too small for clinical application.

Recent Advances in AR

Conventional AR devices require large stereoscopic towers for image registration and viewing that are inconvenient and occupy space in the operating theatre. Wearable devices can now carry sufficient computing power for AR and several investigators have developed bespoke wearable devices for surgical application.(442, 1367) Mela et al

reports a device capable of project fluorescent angiography, 2D ultrasound and 3D CTA with depth perception in a compact, user-friendly interface.(1367) Similarly, Liu et al have developed a compact, wireless, battery-operated device for hands-free viewing of fluorescent angiography for sentinel lymph node biopsy and tumour cell localisation.(442) The latest and most promising wearable AR device has been Google Glass (Alphabet, Mountain View, CA, USA). In plastic and reconstructive surgery, clinicians have reported its benefits for viewing images and recording videos.(1368-1371) Unfortunately, in 2015, Google Glass has been taken off the market due to persistent software bugs and privacy concerns.(1372)

Recently, researchers in Australia have developed a high-resolution, immersive, 3D virtual/augmented reality environments using integrated supercomputers and multiple projectors with a cylindrical matrix of stereoscopic panels.(1373) This bespoke CAVE2, developed at Monash University, consists of 80 high-resolution, stereo-capable displays producing 8-metre diameter, 320-degree panoramic view (Figure 13.2.2).

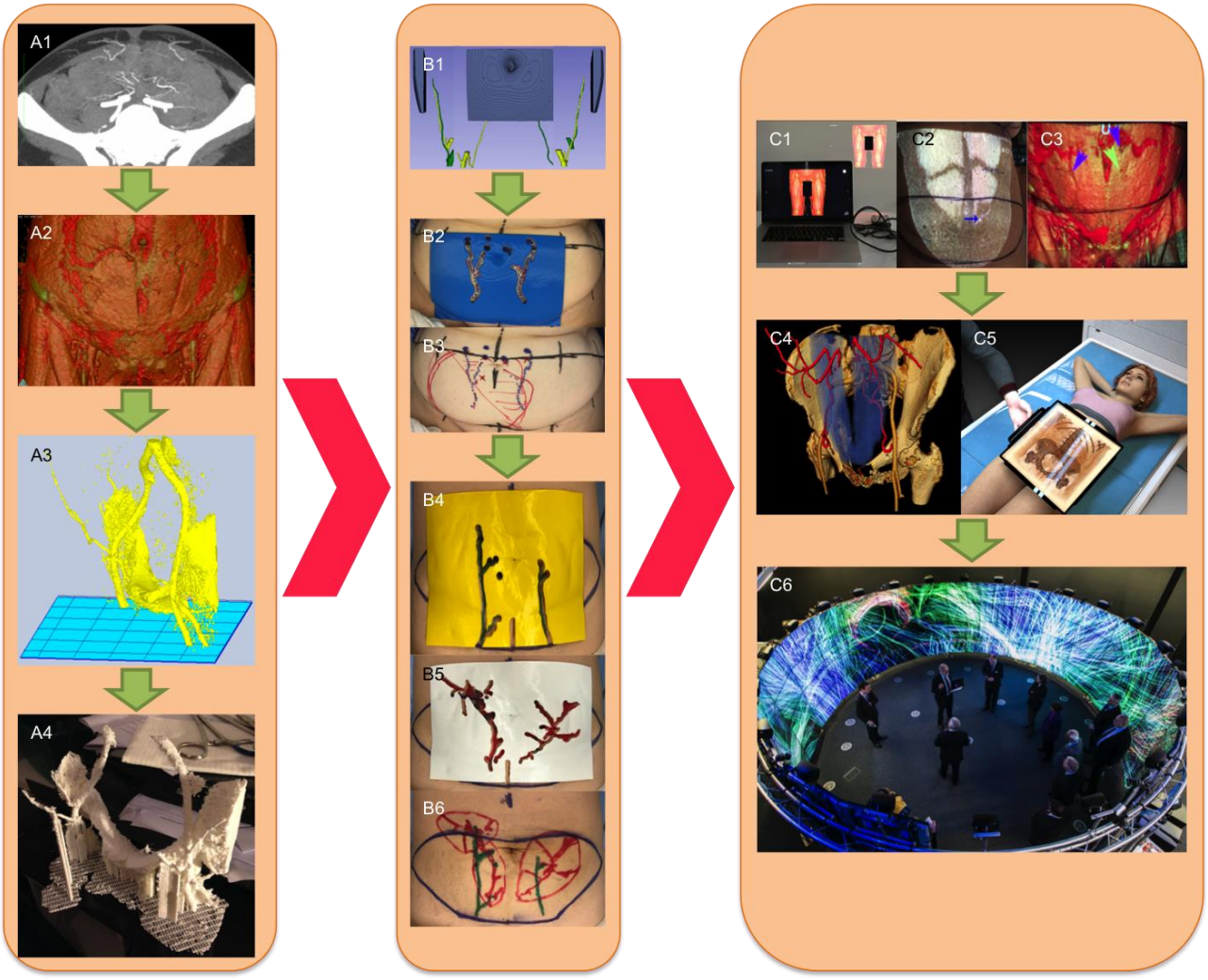

Figure 13.2.2. Evolution of 3D imaging and printing technique from 3D-reconstructed images and a basic 3D-printed model (A1-4) to clinically useful 3D printing application in perforator-based breast reconstructive surgery (B1-6) to advanced image analysis technology, such as augmented reality and CAVE2 facility (C1-6). (A1) 2D-reconstructed CTA image of the abdominal wall vasculature. (A2) 3D-reconstructed CTA image of the same patient in A1. (A3) Segmented image of the DIEA of the same patient in A1. (A4) 3D-printed model of the DIEA in A3. (B1) Segmented image of the abdominal wall and DIEA that spurned the idea of creating a template for preoperative planning. (B2) Patient-specific, bespoke "DIEP template" is 3D-printed and placed on the patient's abdominal wall to help locate DIEA perforators and its pedicle. (B3) This information is used for flap designing. As 3D printing technique advanced, we are able to create both a standard DIEP template (B4) and a "perforasome template" (B5), which can additionally identify each perforasome (B6). (C1-6) Augmented reality can significantly reduce the time and labour cost involved in 3D printing by enabling direct viewing and real-time interaction with the image data. (C1) Our published direct ARC (augmented reality CTA) technique set-up using a handheld projector demonstrating 2D-reconstructed (C2) and 3D-reconstructed (C3) images on the patient's abdomen. As technology advances, we envision that greater software processing power will enable display of greater anatomical information, such as intramuscular course of a DIEP (C4), and translation into a user-friendly, interactive platform for clinicians (C5). (C6) The latest CAVE2 facility at Monash University (Melbourne, Victoria, Australia) housing 84 million pixel stereoscopic display with powerful real-time motion tracking capability will enable interactive, seamless visualisation of relevant anatomy for preoperative planning and collaborative discussion. Reprinted with permission from Chae *et al* (37), Chae *et al* (38) and Chae *et al* (39). Abbreviations: CTA: computed tomographic angiography; DIEA: deep inferior epigastric artery; DIEP: deep inferior epigastric artery perforator.

Medical images can be processed relatively easily by a dedicated laboratory technician and a clinician can view them realistically in a three-dimensional manner as if they are "walking through" the anatomy. Currently, the set-up is too large to be portable and expensive, but as lithium-ion battery technology improves and technology becomes more mobile, the potential of such technology being transferred on to a portable head-mounted display appears enticing.

Holograms

A hologram exhibits reflective auto-stereoscopic (i.e. no wearable device) 3D visuals that contain hogels (i.e. holographic elements instead of pixels or voxels), where each hogel contains up to one million different perspective views. Hackett et al evaluated the role of holograms in teaching cardiac anatomy in 19 volunteers (10 intervention versus 9 control) and found a superior overall test performance after using it (89% vs 68%, p <0.05).(457) Furthermore, volunteers demonstrated a trend in lower mental effort required in learning (4.9 vs 6.0, p = 0.16). Recently Makino et al added tactile feedback to holograms by using concentrated ultrasonic energy.(458) However, this technology has yet to advance beyond prototypic stage.

Machine learning

Machine learning (ML) is a branch of artificial intelligence that uses computer algorithm to aid clinical decision-making and predict clinical outcomes based on knowledge acquisition from data mining of historical examples without explicit programming.(1374-1376) The algorithm statistically analyses each hypothesis, compares multiple combinations and yields data models that are descriptive or predictive in nature. ML has already transformed popular search engines, such as Google,(1377) and speech recognition software on smartphones, such as Siri.(1378) Owing to an ever-growing volume of digitalised clinical data, ML presents a superior form of data interpretation to the traditional statistical methods.(1379)

ML techniques can be classified according to their mathematical structure: predictive, where learning is supervised by using pre-labelled datasets;(1380) descriptive, where learning is unsupervised and similar data points are clustered;(1381) or reinforcement, where ideal behaviour is determined by computer based on a simple reward feedback system on their actions.(1382) Evidently, it is difficult for non-statistically-inclined clinical investigators to analyse how an algorithm has reached its conclusion.(1383, 1384) As a result, when using ML, clinicians need to collaborate with data scientists who can accurately evaluate the validity of output obtained.(1385)

In the last decade, investigators have applied ML to improve clinical challenges in various fields within plastic surgery.

ML as a diagnostic tool

In melanoma detection, Safran et al conducted a systematic review of 50 different ML screening techniques and found mean sensitivity of 87.60% (95% confidence interval: 72.72–100) and mean specificity of 83.54% (60.92–100).(1386) Encouragingly, there was no statistically significant difference between MR and dermoscopy examination by experienced professionals.(1387) In craniofacial surgery, Mendoza *et al* used a statistical shape model to help diagnosis non-syndromic craniosynostosis from CT.(1388) The algorithm yielded sensitivity of 92.3% and specificity of 98.9%, similar to the trained radiologists.

ML as a predictive tool

In burns surgery, Yeong et al developed a ML algorithm to analyse reflectance spectrometry images and assess burns area and depth.(1389) The authors demonstrated average predictive accuracy of 86%. In free flap reconstructions, Kiranantawat et al developed a ML-based smartphone application (SilpaRamanitor) that can predict vascular compromise from 2D photographs with overall sensitivity of 94%, specificity of 98% and accuracy of 95%.(1390) In hand surgery, Conforth et al developed an algorithm capable of estimating the likelihood of tissue-engineered peripheral nerve graft take at 92.59% accuracy.(1391) In aesthetic surgery, Gunes et al developed an automated classifier of facial beauty by analysing 165 images of attractive female faces as graded by human referees.(1392)

Conclusion

To date, most studies have been presented in small case series and they remain to be analysed using outcomes-based validation studies. Image-guided navigation systems are used less frequently in software tissue surgery, in comparison to orthopaedic and neurosurgery, due to unreliable landmarks being available for image registration. Augmented reality platforms, such as CAVE2, that leads to intuitive real-time 3D visualisation of anatomical structures appears promising. Machine learning is a rapidly emerging, disruptive technology that may become highly useful as a diagnostic and predictive tool. Together, they illustrate an exciting future where clinicians will be armed with numerous intuitive technologies for surgical planning and guidance.

14 Conclusion

The current study has established an affordable, in-house 3D printing technique, or Peninsula 3D printing workflow using free, open-source software suites, such as OsiriX (Pixmeo; Geneva, Switzerland), 3D Slicer (Surgical Planning Laboratory; Boston, MA USA) and MeshMixer (Autodesk Inc; San Rafael, CA, USA), and affordable fused filament fabrication (FFF) desktop 3D printers, such as Ultimaker 3E (Ultimaker; Geldermalsen, Netherlands) and Moment (Moment; Seoul, South Korea), and investigated its utility in plastic and reconstructive surgery.

Firstly, the study has demonstrated that the Peninsula 3D printing technique can reliably produce accurate anatomical models. Chapter 12.1.2 (Chae *et al* Gland Surg) has demonstrated the accuracy of 3D software suite with 99.6% concordance and Chapters 12.1.3.1 (Chae *et al* Gland Surg) and 12.1.3.2 have demonstrated the accuracy of 3D printing hardware within 1.16 mm (2.84%) using linear and volumetric assessments, respectively.

Secondly, the study has demonstrated that this technique can utilised in plastic and reconstructive surgery to produce anatomically accurate 3D biomodels for improved preoperative planning, intraoperative surgical guidance and patient education. Peninsula 3D printing technique has been used for bony mapping, such as mandible in Chapter 12.2.1.1 (Cabalag *et al* ANZ J Surg) and spine in Chapter 12.2.1.2 (Chae *et al* Celebrating Research at Peninsula Health), and soft tissue mapping, such as “reverse image” of soft tissue ankle defect in Chapter 12.2.2.1 (Chae *et al* Microsurg), sacral defect in Chapter 12.2.2.2 (Garcia-Tutor *et al* Front Surg). Furthermore, the study has explored novel methods of utilising 3D printing, such as 3D/4D printing technique illustrated in Chapter 12.2.4.1 (Chae *et al* J Reconstr Microsurg), and introducing augmented reality to surgical planning in Chapter 12.2.4.2 (Chae *et al* Eur J Plast Surg).

Finally, the study has demonstrated direct clinical applicability of 3D printing in post-mastectomy autologous breast reconstruction. In Chapter 12.3.2.1 (Chae *et al* Breast Cancer Res Treat), the utility of 3D-printed biomodels in volumetric analysis for preoperative planning is illustrated in a case report. Subsequently, the technique is developed to produce patient-specific “DIEP templates” that can help localise DIEP perforators on the abdominal wall for preoperative flap designing. This is illustrated in a

prospective case series in Chapter 12.3.2.2 (Chae *et al* Microsurg), demonstrating its accuracy (0.09-0.87 mm) and ability to significantly reduce perforator identification by 7.29 minutes (p = 0.02). As software has become more powerful, more complex "perforasome templates" have been devised in Chapter 12.3.2.3 (Chae *et al* Plast Reconstr Surg Glob Open). Furthermore, Chapter 12.3.2.4 (Chae *et al* Gland Surg) demonstrates how a 3D-printed mirrored breast model from 3D photography can be used for intraoperative flap shaping.

This study captures the evolution of 3D imaging and printing technique in plastic and reconstructive surgery (Figure 14.1). The future may combine the use of 3D printing with augmented reality platforms, such as handheld devices and immersive visualization CAVE2 facility at Monash University, to review patient anatomy in real-time interactive manner.

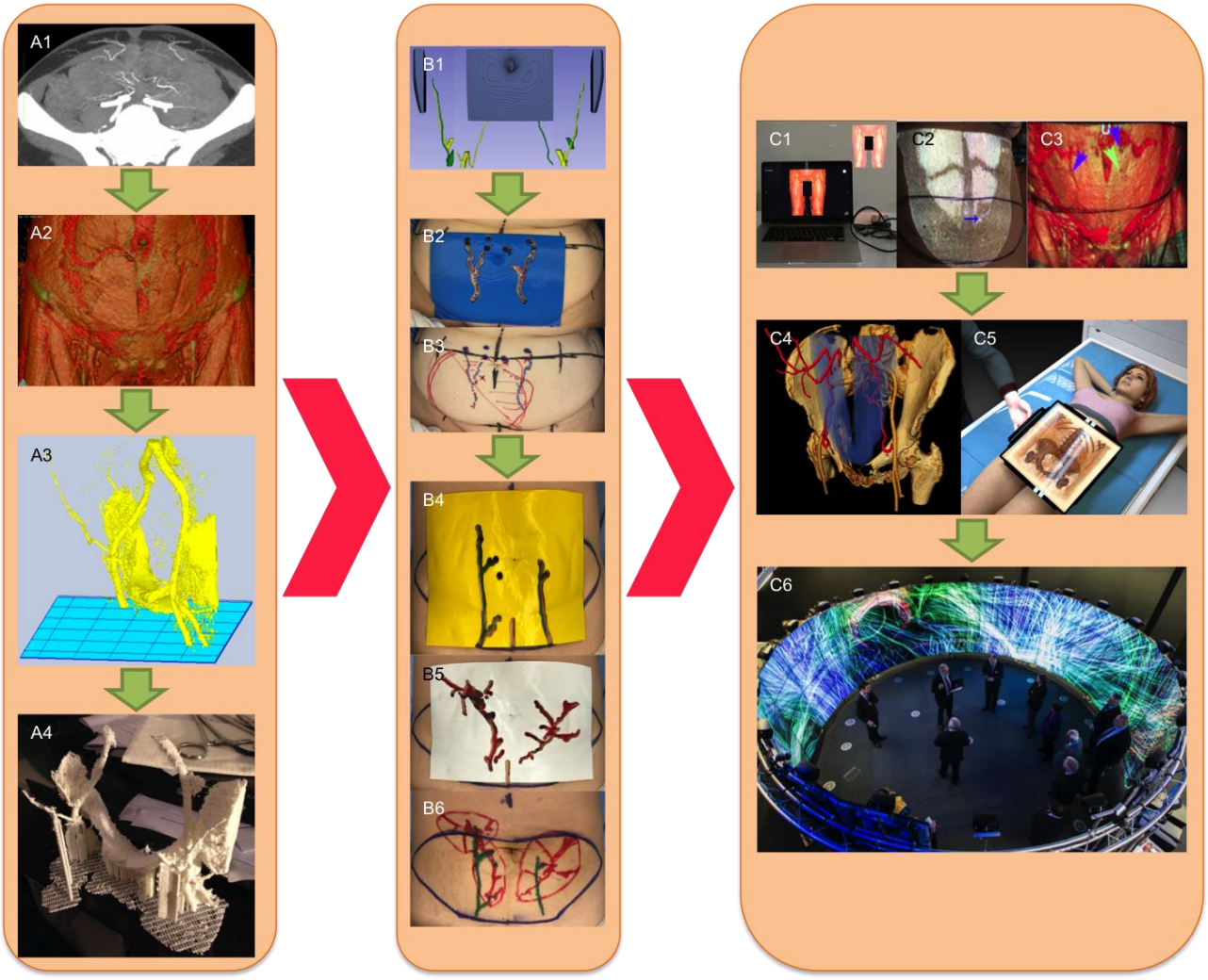

Figure 14.1. Evolution of 3D imaging and printing technique from 3D-reconstructed images and a basic 3D-printed model (A1-4) to clinically useful 3D printing application in perforator-based breast reconstructive surgery (B1-6) to advanced image analysis technology, such as augmented reality and CAVE2 facility (C1-6). (A1) 2D-reconstructed CTA image of the abdominal wall vasculature. (A2) 3D-reconstructed CTA image of the same patient in A1. (A3) Segmented image of the DIEA of the same patient in A1. (A4) 3D-printed model of the DIEA in A3. (B1) Segmented image of the abdominal wall and DIEA that spurned the idea of creating a template for preoperative planning. (B2) Patient-specific, bespoke "DIEP template" is 3D-printed and placed on the patient's abdominal wall to help locate DIEA perforators and its pedicle. (B3) This information is used for flap designing. As 3D printing technique advanced, we are able to create both a standard DIEP template (B4) and a "perforasome template" (B5), which can additionally identify each perforasome (B6). (C1-6) Augmented reality can significantly reduce the time and labour cost involved in 3D printing by enabling direct viewing and real-time interaction with the image data. (C1) Our published direct ARC (augmented reality CTA) technique set-up using a handheld projector demonstrating 2D-reconstructed (C2) and 3D-reconstructed (C3) images on the patient's abdomen. As technology advances, we envision that greater software processing power will enable display of greater anatomical information, such as intramuscular course of a DIEP (C4), and translation into a user-friendly, interactive platform for clinicians (C5). (C6) The latest CAVE2 facility at Monash University (Melbourne, Victoria, Australia) housing 84 million pixel stereoscopic display with powerful real-time motion tracking capability will enable interactive, seamless visualisation of relevant anatomy for preoperative planning and collaborative discussion.

Abbreviations: CTA: computed tomographic angiography; DIEA: deep inferior epigastric artery; DIEP: deep inferior epigastric artery perforator

15 References

1. Smit, J. M., Negenborn, V. L., Jansen, S. M., et al. Intraoperative evaluation of perfusion in free flap surgery: A systematic review and meta-analysis. *Microsurgery* 2018.
2. Thimmappa, N. D., Vasile, J. V., Ahn, C. Y., Levine, J. L., Prince, M. R. MRA of the skin: mapping for advanced breast reconstructive surgery. *Clin Radiol* 2018.
3. Pratt, G. F., Rozen, W. M., Chubb, D., Ashton, M. W., Alonso-Burgos, A., Whitaker, I. S. Preoperative imaging for perforator flaps in reconstructive surgery: a systematic review of the evidence for current techniques. *Ann Plast Surg* 2012;69:3-9.
4. Mathes, D. W., Neligan, P. C. Current techniques in preoperative imaging for abdomen-based perforator flap microsurgical breast reconstruction. *J Reconstr Microsurg* 2010;26:3-10.
5. Rozen, W. M., Anavekar, N. S., Ashton, M. W., et al. Does the preoperative imaging of perforators with CT angiography improve operative outcomes in breast reconstruction? *Microsurgery* 2008;28:516-523.
6. Rozen, W. M., Ashton, M. W., Grinsell, D., Stella, D. L., Phillips, T. J., Taylor, G. I. Establishing the case for CT angiography in the preoperative imaging of abdominal wall perforators. *Microsurgery* 2008;28:306-313.
7. Rozen, W. M., Ashton, M. W. Improving outcomes in autologous breast reconstruction. *Aesthetic Plast Surg* 2009;33:327-335.
8. Rozen, W. M., Phillips, T. J., Ashton, M. W., Stella, D. L., Gibson, R. N., Taylor, G. I. Preoperative imaging for DIEA perforator flaps: a comparative study of computed tomographic angiography and Doppler ultrasound. *Plast Reconstr Surg* 2008;121:9-16.
9. Rozen, W. M., Ashton, M. W., Stella, D. L., et al. Developments in perforator imaging for the anterolateral thigh flap: CT angiography and CT-guided stereotaxy. *Microsurgery* 2008;28:227-232.
10. Clavero, J. A., Masia, J., Larranaga, J., et al. MDCT in the preoperative planning of abdominal perforator surgery for postmastectomy breast reconstruction. *AJR Am J Roentgenol* 2008;191:670-676.
11. Masia, J., Larranaga, J., Clavero, J. A., Vives, L., Pons, G., Pons, J. M. The value of the multidetector row computed tomography for the preoperative planning of deep inferior epigastric artery perforator flap: our experience in 162 cases. *Ann Plast Surg* 2008;60:29-36.
12. Rosson, G. D., Williams, C. G., Fishman, E. K., Singh, N. K. 3D CT angiography of abdominal wall vascular perforators to plan DIEAP flaps. *Microsurgery* 2007;27:641-646.
13. Smit, J. M., Dimopoulou, A., Liss, A. G., et al. Preoperative CT angiography reduces surgery time in perforator flap reconstruction. *J Plast Reconstr Aesthet Surg* 2009;62:1112-1117.
14. Phillips, T. J., Stella, D. L., Rozen, W. M., Ashton, M., Taylor, G. I. Abdominal wall CT angiography: a detailed account of a newly established preoperative imaging technique. *Radiology* 2008;249:32-44.
15. Way, T. P., Barner, K. E. Automatic visual to tactile translation--Part II: Evaluation of the TACTile Image Creation System. *IEEE Trans Rehabil Eng* 1997;5:95-105.
16. Kamali, P., Dean, D., Skoracki, R., et al. The Current Role of Three-Dimensional (3D) Printing in Plastic Surgery. *Plast Reconstr Surg* 2016.
17. Gerstle, T. L., Ibrahim, A. M., Kim, P. S., Lee, B. T., Lin, S. J. A plastic surgery application in evolution: three-dimensional printing. *Plast Reconstr Surg* 2014;133:446-451.
18. Chae, M. P., Hunter-Smith, D. J., Rozen, W. M. Image-guided 3D-printing and haptic modeling in plastic surgery. In L. Saba, W. M. Rozen, A. Alonso-Burgos, D. Ribuffo eds., *Imaging in plastic surgery*. London, UK: CRC Taylor and Francis Press; 2014.

19. Goiato, M. C., Santos, M. R., Pesqueira, A. A., Moreno, A., dos Santos, D. M., Haddad, M. F. Prototyping for surgical and prosthetic treatment. *J Craniofac Surg* 2011;22:914-917.
20. Klein, G. T., Lu, Y., Wang, M. Y. 3D printing and neurosurgery--ready for prime time? *World Neurosurg* 2013;80:233-235.
21. van Baar, G. J. C., Forouzanfar, T., Liberton, N., Winters, H. A. H., Leusink, F. K. J. Accuracy of computer-assisted surgery in mandibular reconstruction: A systematic review. *Oral Oncol* 2018;84:52-60.
22. Bekisz, J. M., Liss, H. A., Maliha, S. G., Witek, L., Coelho, P. G., Flores, R. L. The In-House Manufacture of Sterilizable, Scaled, Patient-Specific 3D-Printed Models for Rhinoplasty. *Aesthet Surg J* 2018.
23. Suszynski, T. M., Serra, J. M., Weissler, J. M., Amirlak, B. Three-Dimensional Printing in Rhinoplasty. *Plast Reconstr Surg* 2018;141:1383-1385.
24. Kang, S., Kwon, J., Ahn, C. J., et al. Generation of customized orbital implant templates using 3-dimensional printing for orbital wall reconstruction. *Eye (Lond)* 2018.
25. Lee Ventola, C. Medical Applications for 3D Printing: Current and Projected Uses. *P T* 2014;39:704-711.
26. Fullerton, J. N., Frodsham, G. C., Day, R. M. 3D printing for the many, not the few. *Nat Biotechnol* 2014;32:1086-1087.
27. Rozen, W. M., Ashton, M. W., Taylor, G. I. Reviewing the vascular supply of the anterior abdominal wall: redefining anatomy for increasingly refined surgery. *Clin Anat* 2008;21:89-98.
28. Moon, H. K., Taylor, G. I. The vascular anatomy of rectus abdominis musculocutaneous flaps based on the deep superior epigastric system. *Plast Reconstr Surg* 1988;82:815-832.
29. Boyd, J. B., Taylor, G. I., Corlett, R. The vascular territories of the superior epigastric and the deep inferior epigastric systems. *Plast Reconstr Surg* 1984;73:1-16.
30. Rozen, W. M., Ashton, M. W., Pan, W. R., Taylor, G. I. Raising perforator flaps for breast reconstruction: the intramuscular anatomy of the deep inferior epigastric artery. *Plast Reconstr Surg* 2007;120:1443-1449.
31. Hartrampf, C. R., Scheflan, M., Black, P. W. Breast reconstruction with a transverse abdominal island flap. *Plast Reconstr Surg* 1982;69:216-225.
32. Holm, C., Mayr, M., Hofter, E., Ninkovic, M. Perfusion zones of the DIEP flap revisited: a clinical study. *Plast Reconstr Surg* 2006;117:37-43.
33. Hamdi, M., Khuthaila, D. K., Van Landuyt, K., Roche, N., Monstrey, S. Double-pedicle abdominal perforator free flaps for unilateral breast reconstruction: new horizons in microsurgical tissue transfer to the breast. *J Plast Reconstr Aesthet Surg* 2007;60:904-912; discussion 913-904.
34. DellaCroce, F. J., Sullivan, S. K., Trahan, C. Stacked deep inferior epigastric perforator flap breast reconstruction: a review of 110 flaps in 55 cases over 3 years. *Plast Reconstr Surg* 2011;127:1093-1099.
35. Chae, M. P., Hunter-Smith, D. J., Spychal, R. T., Rozen, W. M. 3D volumetric analysis for planning breast reconstructive surgery. *Breast Cancer Res Treat* 2014;146:457-460.
36. Moher, D., Liberati, A., Tetzlaff, J., Altman, D. G., Group, P. Preferred reporting items for systematic reviews and meta-analyses: the PRISMA statement. *Int J Surg* 2010;8:336-341.
37. Chae, M. P., Hunter-Smith, D. J., Chung, R. D., Smith, J. A., Rozen, W. M. 3D-printed, patient-specific, DIEP template for preoperative planning autologous breast reconstruction: prospective case series in 20 patients. *Microsurgery* 2018;[Manuscript Under Review].

38. Chae, M. P., Hunter-Smith, D. J., Rostek, M., Smith, J. A., Rozen, W. M. Enhanced Preoperative Deep Inferior Epigastric Artery Perforator Flap Planning with a 3D-Printed Perforasome Template: Technique and Case Report. *Plast Reconstr Surg Glob Open* 2018;6:e1644.
39. Chae, M. P., Ganhewa, D., Hunter-Smith, D. J., Rozen, W. M. Direct augmented reality computed tomographic angiography technique (ARC): an innovation in preoperative imaging. *Eur J Plast Surg* 2018;41:415-420.
40. Rozen, W. M., Ashton, M. W. The venous anatomy of the abdominal wall for Deep Inferior Epigastric Artery (DIEP) flaps in breast reconstruction. *Gland Surg* 2012;1:92-110.
41. DeSantis, C., Ma, J., Bryan, L., Jemal, A. Breast cancer statistics, 2013. *CA Cancer J Clin* 2014;64:52-62.
42. Lucas, D. J., Sabino, J., Shriver, C. D., Pawlik, T. M., Singh, D. P., Vertrees, A. E. Doing more: trends in breast cancer surgery, 2005 to 2011. *Am Surg* 2015;81:74-80.
43. Ng, S. K., Hare, R. M., Kuang, R. J., Smith, K. M., Brown, B. J., Hunter-Smith, D. J. Breast Reconstruction Post Mastectomy: Patient Satisfaction and Decision Making. *Ann Plast Surg* 2014.
44. Wilkins, E. G., Cederna, P. S., Lowery, J. C., et al. Prospective analysis of psychosocial outcomes in breast reconstruction: one-year postoperative results from the Michigan Breast Reconstruction Outcome Study. *Plast Reconstr Surg* 2000;106:1014-1025; discussion 1026-1017.
45. Nano, M. T., Gill, P. G., Kollias, J., Bochner, M. A., Malycha, P., Winefield, H. R. Psychological impact and cosmetic outcome of surgical breast cancer strategies. *ANZ J Surg* 2005;75:940-947.
46. Al-Ghazal, S. K., Fallowfield, L., Blamey, R. W. Comparison of psychological aspects and patient satisfaction following breast conserving surgery, simple mastectomy and breast reconstruction. *Eur J Cancer* 2000;36:1938-1943.
47. Neto, M. S., de Aguiar Menezes, M. V., Moreira, J. R., Garcia, E. B., Abla, L. E., Ferreira, L. M. Sexuality after breast reconstruction post mastectomy. *Aesthetic Plast Surg* 2013;37:643-647.
48. Kroll, S. S. Why autologous tissue? *Clin Plast Surg* 1998;25:135-143.
49. Allen, R. J., Treece, P. Deep inferior epigastric perforator flap for breast reconstruction. *Ann Plast Surg* 1994;32:32-38.
50. Blondeel, P. N. One hundred free DIEP flap breast reconstructions: a personal experience. *Br J Plast Surg* 1999;52:104-111.
51. Healy, C., Allen, R. J., Sr. The evolution of perforator flap breast reconstruction: twenty years after the first DIEP flap. *J Reconstr Microsurg* 2014;30:121-125.
52. Kiricuta, I. [The use of the great omentum in the surgery of breast cancer]. *Presse Med* 1963;71:15-17.
53. Schneider, W. J., Hill, H. L., Jr., Brown, R. G. Latissimus dorsi myocutaneous flap for breast reconstruction. *Br J Plast Surg* 1977;30:277-281.
54. Muhlbauer, W., Olbrisch, R. The latissimus dorsi myocutaneous flap for breast reconstruction. *Chir Plast (Berl)* 1977;4:27 (Abstract).
55. Olivari, N. The latissimus flap. *Br J Plast Surg* 1976;29:126-128.
56. Saijo, M. The vascular territories of the dorsal trunk: a reappraisal for potential flap donor sites. *Br J Plast Surg* 1978;31:200-204.
57. Hartrampf, C. R., Jr., Noel, R. T., Drazan, L., Elliott, F. L., Bennett, G. K., Beegle, P. H. Ruben's fat pad for breast reconstruction: a peri-iliac soft-tissue free flap. *Plast Reconstr Surg* 1994;93:402-407.
58. Serafin, D., Georgiade, N. G. Transfer of free flaps to provide well-vascularized, thick cover for breast reconstructions after radical mastectomy. *Plast Reconstr Surg* 1978;62:527-536.

59. Elliott, L. F., Beegle, P. H., Hartrampf, C. R., Jr. The lateral transverse thigh free flap: an alternative for autogenous-tissue breast reconstruction. *Plast Reconstr Surg* 1990;85:169-178; discussion 179-181.
60. Fujino, T., Harasina, T., Aoyagi, F. Reconstruction for aplasia of the breast and pectoral region by microvascular transfer of a free flap from the buttock. *Plast Reconstr Surg* 1975;56:178-181.
61. Fujino, T., Abe, O., Enomoto, K. Primary reconstruction of the breast by free myocutaneous gluteal flap. *Int Adv Surg Oncol* 1981;4:127-143.
62. Shaw, W. W. Breast reconstruction by superior gluteal microvascular free flaps without silicone implants. *Plast Reconstr Surg* 1983;72:490-501.
63. Paletta, C. E., Bostwick, J., 3rd, Nahai, F. The inferior gluteal free flap in breast reconstruction. *Plast Reconstr Surg* 1989;84:875-883; discussion 884-875.
64. Peek, A., Muller, M., Exner, K. [The free gracilis perforator flap for autologous breast reconstruction]. *Handchir Mikrochir Plast Chir* 2002;34:245-250.
65. Hartrampf, C. R., Jr., Elliott, L. F., Feldman, S. A triceps musculocutaneous flap for chest-wall defects. *Plast Reconstr Surg* 1990;86:502-509.
66. Holmstrom, H. The free abdominoplasty flap and its use in breast reconstruction. An experimental study and clinical case report. *Scand J Plast Reconstr Surg* 1979;13:423-427.
67. Blondeel, P. N., Boeckx, W. D. Refinements in free flap breast reconstruction: the free bilateral deep inferior epigastric perforator flap anastomosed to the internal mammary artery. *Br J Plast Surg* 1994;47:495-501.
68. Koshima, I., Soeda, S. Inferior epigastric artery skin flaps without rectus abdominis muscle. *Br J Plast Surg* 1989;42:645-648.
69. Onishi, K., Maruyama, Y., Iwahira, Y. Cutaneous and fascial vasculature of the leg: anatomic study of fasciocutaneous vessels. *J Reconstr Microsurg* 1986;2:181-189.
70. Bottero, L., Lefaucheur, J. P., Fadhul, S., Raulo, Y., Collins, E. D., Lantieri, L. Electromyographic assessment of rectus abdominis muscle function after deep inferior epigastric perforator flap surgery. *Plast Reconstr Surg* 2004;113:156-161.
71. Man, L. X., Selber, J. C., Serletti, J. M. Abdominal wall following free TRAM or DIEP flap reconstruction: a meta-analysis and critical review. *Plast Reconstr Surg* 2009;124:752-764.
72. Rozen, W. M., Garcia-Tutor, E., Alonso-Burgos, A., et al. Planning and optimising DIEP flaps with virtual surgery: the Navarra experience. *J Plast Reconstr Aesthet Surg* 2010;63:289-297.
73. Rozen, W. M., Chubb, D., Grinsell, D., Ashton, M. W. Computed tomographic angiography: clinical applications. *Clin Plast Surg* 2011;38:229-239.
74. Giunta, R. E., Geisweid, A., Feller, A. M. The value of preoperative Doppler sonography for planning free perforator flaps. *Plast Reconstr Surg* 2000;105:2381-2386.
75. Tsukino, A., Kurachi, K., Inamiya, T., Tanigaki, T. Preoperative color Doppler assessment in planning of anterolateral thigh flaps. *Plast Reconstr Surg* 2004;113:241-246.
76. Rand, R. P., Cramer, M. M., Strandness, D. E., Jr. Color-flow duplex scanning in the preoperative assessment of TRAM flap perforators: a report of 32 consecutive patients. *Plast Reconstr Surg* 1994;93:453-459.
77. Cina, A., Salgarello, M., Barone-Adesi, L., Rinaldi, P., Bonomo, L. Planning breast reconstruction with deep inferior epigastric artery perforating vessels: multidetector CT angiography versus color Doppler US. *Radiology* 2010;255:979-987.
78. Hallock, G. G. Doppler sonography and color duplex imaging for planning a perforator flap. *Clin Plast Surg* 2003;30:347-357, v-vi.
79. Taylor, G. I., Caddy, C. M., Watterson, P. A., Crock, J. G. The venous territories (venosomes) of the human body: experimental study and clinical implications. *Plast Reconstr Surg* 1990;86:185-213.

80. Scott, J. R., Liu, D., Said, H., Neligan, P. C., Mathes, D. W. Computed tomographic angiography in planning abdomen-based microsurgical breast reconstruction: a comparison with color duplex ultrasound. *Plast Reconstr Surg* 2010;125:446-453.
81. Blondeel, P. N., Beyens, G., Verhaeghe, R., et al. Doppler flowmetry in the planning of perforator flaps. *Br J Plast Surg* 1998;51:202-209.
82. Benson, R. C., Kues, H. A. Fluorescence properties of indocyanine green as related to angiography. *Phys Med Biol* 1978;23:159-163.
83. Eren, S., Rubben, A., Krein, R., Larkin, G., Hettich, R. Assessment of microcirculation of an axial skin flap using indocyanine green fluorescence angiography. *Plast Reconstr Surg* 1995;96:1636-1649.
84. O'Goshi, K., Serup, J. Safety of sodium fluorescein for in vivo study of skin. *Skin Res Technol* 2006;12:155-161.
85. Pang, C. Y., Neligan, P., Nakatsuka, T., Sasaki, G. H. Assessment of the fluorescein dye test for prediction of skin flap viability in pigs. *J Surg Res* 1986;41:173-181.
86. Yamaguchi, S., De Lorenzi, F., Petit, J. Y., et al. The "perfusion map" of the unipedicled TRAM flap to reduce postoperative partial necrosis. *Ann Plast Surg* 2004;53:205-209.
87. Pestana, I. A., Coan, B., Erdmann, D., Marcus, J., Levin, L. S., Zenn, M. R. Early experience with fluorescent angiography in free-tissue transfer reconstruction. *Plast Reconstr Surg* 2009;123:1239-1244.
88. Pestana, I. A., Zenn, M. R. Correlation between abdominal perforator vessels identified with preoperative CT angiography and intraoperative fluorescent angiography in the microsurgical breast reconstruction patient. *Ann Plast Surg* 2014;72:S144-149.
89. Lee, B. T., Hutteman, M., Gioux, S., et al. The FLARE intraoperative near-infrared fluorescence imaging system: a first-in-human clinical trial in perforator flap breast reconstruction. *Plast Reconstr Surg* 2010;126:1472-1481.
90. Meijer, D. K., Weert, B., Vermeer, G. A. Pharmacokinetics of biliary excretion in man. VI. Indocyanine green. *Eur J Clin Pharmacol* 1988;35:295-303.
91. Kuebler, W. M., Sckell, A., Habler, O., et al. Noninvasive measurement of regional cerebral blood flow by near-infrared spectroscopy and indocyanine green. *J Cereb Blood Flow Metab* 1998;18:445-456.
92. Speich, R., Saesseli, B., Hoffmann, U., Neftel, K. A., Reichen, J. Anaphylactoid reactions after indocyanine-green administration. *Ann Intern Med* 1988;109:345-346.
93. Hope-Ross, M., Yannuzzi, L. A., Gragoudas, E. S., et al. Adverse reactions due to indocyanine green. *Ophthalmology* 1994;101:529-533.
94. Duggal, C. S., Madni, T., Losken, A. An outcome analysis of intraoperative angiography for postmastectomy breast reconstruction. *Aesthet Surg J* 2014;34:61-65.
95. Rozen, W. M., Ashton, M. W., Whitaker, I. S., Wagstaff, M. J., Acosta, R. The financial implications of computed tomographic angiography in DIEP flap surgery: a cost analysis. *Microsurgery* 2009;29:168-169.
96. Rozen, W. M., Stella, D. L., Bowden, J., Taylor, G. I., Ashton, M. W. Advances in the pre-operative planning of deep inferior epigastric artery perforator flaps: magnetic resonance angiography. *Microsurgery* 2009;29:119-123.
97. Cina, A., Barone-Adesi, L., Rinaldi, P., et al. Planning deep inferior epigastric perforator flaps for breast reconstruction: a comparison between multidetector computed tomography and magnetic resonance angiography. *Eur Radiol* 2013;23:2333-2343.
98. Pauchot, J., Aubry, S., Kastler, A., Laurent, O., Kastler, B., Tropet, Y. Preoperative imaging for deep inferior epigastric perforator flaps: a comparative study of computed tomographic angiography and magnetic resonance angiography. *Eur J Plast Surg* 2012;35:795-801.

99. Aubry, S., Pauchot, J., Kastler, A., Laurent, O., Tropet, Y., Runge, M. Preoperative imaging in the planning of deep inferior epigastric artery perforator flap surgery. *Skeletal Radiol* 2013;42:319-327.
100. Balacumaraswami, L., Abu-Omar, Y., Choudhary, B., Pigott, D., Taggart, D. P. A comparison of transit-time flowmetry and intraoperative fluorescence imaging for assessing coronary artery bypass graft patency. *J Thorac Cardiovasc Surg* 2005;130:315-320.
101. Desai, N. D., Miwa, S., Kodama, D., et al. Improving the quality of coronary bypass surgery with intraoperative angiography: validation of a new technique. *J Am Coll Cardiol* 2005;46:1521-1525.
102. Taggart, D. P., Choudhary, B., Anastasiadis, K., Abu-Omar, Y., Balacumaraswami, L., Pigott, D. W. Preliminary experience with a novel intraoperative fluorescence imaging technique to evaluate the patency of bypass grafts in total arterial revascularization. *Ann Thorac Surg* 2003;75:870-873.
103. Sekijima, M., Tojimbara, T., Sato, S., et al. An intraoperative fluorescent imaging system in organ transplantation. *Transplant Proc* 2004;36:2188-2190.
104. Wang, H. D., Singh, D. P. The use of indocyanine green angiography to prevent wound complications in ventral hernia repair with open components separation technique. *Hernia* 2013;17:397-402.
105. Oda, J., Kato, Y., Chen, S. F., et al. Intraoperative near-infrared indocyanine green-videoangiography (ICG-VA) and graphic analysis of fluorescence intensity in cerebral aneurysm surgery. *J Clin Neurosci* 2011;18:1097-1100.
106. Murawa, D., Hunerbein, M., Spychala, A., Nowaczyk, P., Polom, K., Murawa, P. Indocyanine green angiography for evaluation of gastric conduit perfusion during esophagectomy--first experience. *Acta Chir Belg* 2012;112:275-280.
107. Flower, R. W. Injection technique for indocyanine green and sodium fluorescein dye angiography of the eye. *Invest Ophthalmol* 1973;12:881-895.
108. Flower, R. W., Hochheimer, B. F. Indocyanine green dye fluorescence and infrared absorption choroidal angiography performed simultaneously with fluorescein angiography. *Johns Hopkins Med J* 1976;138:33-42.
109. Holm, C., Mayr, M., Hofter, E., Becker, A., Pfeiffer, U. J., Muhlbauer, W. Intraoperative evaluation of skin-flap viability using laser-induced fluorescence of indocyanine green. *Br J Plast Surg* 2002;55:635-644.
110. Holm, C., Mayr, M., Hofter, E., Dornseifer, U., Ninkovic, M. Assessment of the patency of microvascular anastomoses using microscope-integrated near-infrared angiography: a preliminary study. *Microsurgery* 2009;29:509-514.
111. Holm, C., Dornseifer, U., Sturtz, G., Ninkovic, M. Sensitivity and specificity of ICG angiography in free flap reexploration. *J Reconstr Microsurg* 2010;26:311-316.
112. Mothes, H., Donicke, T., Friedel, R., Simon, M., Markgraf, E., Bach, O. Indocyanine-green fluorescence video angiography used clinically to evaluate tissue perfusion in microsurgery. *J Trauma* 2004;57:1018-1024.
113. Liu, D. Z., Mathes, D. W., Zenn, M. R., Neligan, P. C. The application of indocyanine green fluorescence angiography in plastic surgery. *J Reconstr Microsurg* 2011;27:355-364.
114. Losken, A., Styblo, T. M., Schaefer, T. G., Carlson, G. W. The use of fluorescein dye as a predictor of mastectomy skin flap viability following autologous tissue reconstruction. *Ann Plast Surg* 2008;61:24-29.
115. Newman, M. I., Samson, M. C., Tamburrino, J. F., Swartz, K. A. Intraoperative laser-assisted indocyanine green angiography for the evaluation of mastectomy flaps in immediate breast reconstruction. *J Reconstr Microsurg* 2010;26:487-492.

116. Phillips, B. T., Lanier, S. T., Conkling, N., et al. Intraoperative perfusion techniques can accurately predict mastectomy skin flap necrosis in breast reconstruction: results of a prospective trial. *Plast Reconstr Surg* 2012;129:778e-788e.
117. Alonso-Burgos, A., Garcia-Tutor, E., Bastarrika, G., Cano, D., Martinez-Cuesta, A., Pina, L. J. Preoperative planning of deep inferior epigastric artery perforator flap reconstruction with multislice-CT angiography: imaging findings and initial experience. *J Plast Reconstr Aesthet Surg* 2006;59:585-593.
118. Gacto-Sanchez, P., Sicilia-Castro, D., Gomez-Cia, T., et al. Computed tomographic angiography with VirSSPA three-dimensional software for perforator navigation improves perioperative outcomes in DIEP flap breast reconstruction. *Plast Reconstr Surg* 2010;125:24-31.
119. Masia, J., Kosutic, D., Clavero, J. A., Larranaga, J., Vives, L., Pons, G. Preoperative computed tomographic angiogram for deep inferior epigastric artery perforator flap breast reconstruction. *J Reconstr Microsurg* 2010;26:21-28.
120. Tong, W. M., Dixon, R., Ekis, H., Halvorson, E. G. The impact of preoperative CT angiography on breast reconstruction with abdominal perforator flaps. *Ann Plast Surg* 2012;68:525-530.
121. Pellegrin, A., Stocca, T., Belgrano, M., et al. Preoperative vascular mapping with multislice CT of deep inferior epigastric artery perforators in planning breast reconstruction after mastectomy. *Radiol Med* 2013;118:732-743.
122. Chernyak, V., Rozenblit, A. M., Greenspun, D. T., et al. Breast reconstruction with deep inferior epigastric artery perforator flap: 3.0-T gadolinium-enhanced MR imaging for preoperative localization of abdominal wall perforators. *Radiology* 2009;250:417-424.
123. Greenspun, D., Vasile, J., Levine, J. L., et al. Anatomic imaging of abdominal perforator flaps without ionizing radiation: seeing is believing with magnetic resonance imaging angiography. *J Reconstr Microsurg* 2010;26:37-44.
124. Newman, T. M., Vasile, J., Levine, J. L., et al. Perforator flap magnetic resonance angiography for reconstructive breast surgery: a review of 25 deep inferior epigastric and gluteal perforator artery flap patients. *J Magn Reson Imaging* 2010;31:1176-1184.
125. Alonso-Burgos, A., Garcia-Tutor, E., Bastarrika, G., Benito, A., Dominguez, P. D., Zubieta, J. L. Preoperative planning of DIEP and SGAP flaps: preliminary experience with magnetic resonance angiography using 3-tesla equipment and blood-pool contrast medium. *J Plast Reconstr Aesthet Surg* 2010;63:298-304.
126. Masia, J., Kosutic, D., Cervelli, D., Clavero, J. A., Monill, J. M., Pons, G. In search of the ideal method in perforator mapping: noncontrast magnetic resonance imaging. *J Reconstr Microsurg* 2010;26:29-35.
127. Versluis, B., Tuinder, S., Boetes, C., et al. Equilibrium-phase high spatial resolution contrast-enhanced MR angiography at 1.5T in preoperative imaging for perforator flap breast reconstruction. *PLoS One* 2013;8:e71286.
128. Komorowska-Timek, E., Gurtner, G. C. Intraoperative perfusion mapping with laser-assisted indocyanine green imaging can predict and prevent complications in immediate breast reconstruction. *Plast Reconstr Surg* 2010;125:1065-1073.
129. Masia, J., Clavero, J. A., Larranaga, J. R., Alomar, X., Pons, G., Serret, P. Multidetector-row computed tomography in the planning of abdominal perforator flaps. *J Plast Reconstr Aesthet Surg* 2006;59:594-599.
130. Uppal, R. S., Casaer, B., Van Landuyt, K., Blondeel, P. The efficacy of preoperative mapping of perforators in reducing operative times and complications in perforator flap breast reconstruction. *J Plast Reconstr Aesthet Surg* 2009;62:859-864.
131. Casey, W. J., 3rd, Chew, R. T., Rebecca, A. M., Smith, A. A., Collins, J. M., Pockaj, B. A. Advantages of preoperative computed tomography in deep inferior epigastric artery perforator flap breast reconstruction. *Plast Reconstr Surg* 2009;123:1148-1155.

132. Ghattaura, A., Henton, J., Jallali, N., et al. One hundred cases of abdominal-based free flaps in breast reconstruction. The impact of preoperative computed tomographic angiography. *J Plast Reconstr Aesthet Surg* 2010;63:1597-1601.
133. Minqiang, X., Lanhua, M., Jie, L., Dali, M., Jinguo, L. The value of multidetector-row CT angiography for pre-operative planning of breast reconstruction with deep inferior epigastric arterial perforator flaps. *Br J Radiol* 2010;83:40-43.
134. Fansa, H., Schirmer, S., Frerichs, O., Gehl, H. B. [Significance of abdominal wall CT-angiography in planning DIEA perforator flaps, TRAM flaps and SIEA flaps]. *Handchir Mikrochir Plast Chir* 2011;43:81-87.
135. Malhotra, A., Chhaya, N., Nsiah-Sarbeng, P., Mosahebi, A. CT-guided deep inferior epigastric perforator (DIEP) flap localization -- better for the patient, the surgeon, and the hospital. *Clin Radiol* 2013;68:131-138.
136. Schaverien, M. V., Ludman, C. N., Neil-Dwyer, J., McCulley, S. J. Contrast-enhanced magnetic resonance angiography for preoperative imaging of deep inferior epigastric artery perforator flaps: advantages and disadvantages compared with computed tomography angiography: a United Kingdom perspective. *Ann Plast Surg* 2011;67:671-674.
137. Rozen, W. M., Phillips, T. J., Stella, D. L., Ashton, M. W. Preoperative CT angiography for DIEP flaps: 'must-have' lessons for the radiologist. *J Plast Reconstr Aesthet Surg* 2009;62:e650-651.
138. Pacifico, M. D., See, M. S., Cavale, N., et al. Preoperative planning for DIEP breast reconstruction: early experience of the use of computerised tomography angiography with VoNavix 3D software for perforator navigation. *J Plast Reconstr Aesthet Surg* 2009;62:1464-1469.
139. Rozen, W. M., Ashton, M. W. Modifying techniques in deep inferior epigastric artery perforator flap harvest with the use of preoperative imaging. *ANZ J Surg* 2009;79:598-603.
140. Niumsawatt, V., Rozen, W. M., Ashton, M. W., Whitaker, I. S., Garcia-Tutor, E., Alonso-Burgos, A. Angio-CT imaging of deep inferior epigastric artery and deep superior epigastric artery perforators. In L. Saba, W. M. Rozen, A. Alonso-Burgos, D. Ribuffo eds., *Imaging for Plastic Surgery*. London, UK: CRC Taylor and Francis Press; 2014.
141. Rozen, W. M., Whitaker, I. S., Stella, D. L., et al. The radiation exposure of Computed Tomographic Angiography (CTA) in DIEP flap planning: low dose but high impact. *J Plast Reconstr Aesthet Surg* 2009;62:e654-655.
142. Rozen, W. M., Ashton, M. W., Stella, D. L., Phillips, T. J., Taylor, G. I. The accuracy of computed tomographic angiography for mapping the perforators of the DIEA: a cadaveric study. *Plast Reconstr Surg* 2008;122:363-369.
143. Midgley, S. M., Einsiedel, P. F., Phillips, T. J., Stella, D. L. Justifying the use of abdominal wall computed tomographic angiography in deep inferior epigastric artery perforator flap planning. *Ann Plast Surg* 2011;67:457-459.
144. Swanson, E. W., Hsu, Y. C., Cheng, H. T. CTA and contrast-enhanced MRA are equally accurate for localizing deep inferior epigastric perforator flap arteries: A systematic review. *J Plast Reconstr Aesthet Surg* 2014.
145. Zou, Z., Kate Lee, H., Levine, J. L., et al. Gadofosveset trisodium-enhanced abdominal perforator MRA. *J Magn Reson Imaging* 2012;35:711-716.
146. Vasile, J. V., Newman, T. M., Prince, M. R., et al. Contrast-enhanced magnetic resonance angiography. *Clin Plast Surg* 2011;38:263-275.
147. Niendorf, H. P., Felix, R., Laniado, M., Schorner, W., Claussen, C., Weinmann, H. J. Gadolinium-DTPA: a new contrast agent for magnetic resonance imaging. *Radiat Med* 1985;3:7-12.
148. Lauffer, R. B., Parmelee, D. J., Dunham, S. U., et al. MS-325: albumin-targeted contrast agent for MR angiography. *Radiology* 1998;207:529-538.

149. Rohrer, M., Bauer, H., Mintorovitch, J., Requardt, M., Weinmann, H. J. Comparison of magnetic properties of MRI contrast media solutions at different magnetic field strengths. *Invest Radiol* 2005;40:715-724.
150. Ersoy, H., Jacobs, P., Kent, C. K., Prince, M. R. Blood pool MR angiography of aortic stent-graft endoleak. *AJR Am J Roentgenol* 2004;182:1181-1186.
151. Klessen, C., Hein, P. A., Huppertz, A., et al. First-pass whole-body magnetic resonance angiography (MRA) using the blood-pool contrast medium gadofosveset trisodium: comparison to gadopentetate dimeglumine. *Invest Radiol* 2007;42:659-664.
152. Hadizadeh, D. R., Gieseke, J., Lohmaier, S. H., et al. Peripheral MR angiography with blood pool contrast agent: prospective intraindividual comparative study of high-spatial-resolution steady-state MR angiography versus standard-resolution first-pass MR angiography and DSA. *Radiology* 2008;249:701-711.
153. Barth, M. M., Smith, M. P., Pedrosa, I., Lenkinski, R. E., Rofsky, N. M. Body MR imaging at 3.0 T: understanding the opportunities and challenges. *Radiographics* 2007;27:1445-1462; discussion 1462-1444.
154. Huang, B. Y., Castillo, M. Neurovascular imaging at 1.5 tesla versus 3.0 tesla. *Magn Reson Imaging Clin N Am* 2009;17:29-46.
155. Tomasian, A., Salamon, N., Lohan, D. G., Jalili, M., Villablanca, J. P., Finn, J. P. Supraaortic arteries: contrast material dose reduction at 3.0-T high-spatial-resolution MR angiography--feasibility study. *Radiology* 2008;249:980-990.
156. Krautmacher, C., Willinek, W. A., Tschampa, H. J., et al. Brain tumors: full- and half-dose contrast-enhanced MR imaging at 3.0 T compared with 1.5 T--Initial Experience. *Radiology* 2005;237:1014-1019.
157. Katayama, H., Yamaguchi, K., Kozuka, T., Takashima, T., Seez, P., Matsuura, K. Adverse reactions to ionic and nonionic contrast media. A report from the Japanese Committee on the Safety of Contrast Media. *Radiology* 1990;175:621-628.
158. Dillman, J. R., Ellis, J. H., Cohan, R. H., Strouse, P. J., Jan, S. C. Frequency and severity of acute allergic-like reactions to gadolinium-containing i.v. contrast media in children and adults. *AJR Am J Roentgenol* 2007;189:1533-1538.
159. Neil-Dwyer, J. G., Ludman, C. N., Schaverien, M., McCulley, S. J., Perks, A. G. Magnetic resonance angiography in preoperative planning of deep inferior epigastric artery perforator flaps. *J Plast Reconstr Aesthet Surg* 2009;62:1661-1665.
160. Hartung, M. P., Grist, T. M., Francois, C. J. Magnetic resonance angiography: current status and future directions. *J Cardiovasc Magn Reson* 2011;13:19.
161. Gathings, R. M., Reddy, R., Santa Cruz, D., Brodell, R. T. Gadolinium-Associated Plaques: A New, Distinctive Clinical Entity. *JAMA Dermatol* 2014.
162. Edwards, B. J., Laumann, A. E., Nardone, B., et al. Advancing pharmacovigilance through academic-legal collaboration: the case of gadolinium-based contrast agents and nephrogenic systemic fibrosis-a Research on Adverse Drug Events and Reports (RADAR) report. *Br J Radiol* 2014;87:20140307.
163. Perazella, M. A., Rodby, R. A. Gadolinium-induced nephrogenic systemic fibrosis in patients with kidney disease. *Am J Med* 2007;120:561-562.
164. Hedley, A. J., Molan, M. P., Hare, D. L., Anavekar, N. S., Ierino, F. L. Nephrogenic systemic fibrosis associated with gadolinium-containing contrast media administration in patients with reduced glomerular filtration rate. *Australas Radio* 2007;51:300-308.
165. Internal Agency for Research on Cancer. GLOBOCAN 2008: cancer incidence and mortality worldwide. Available at: http://www.iarc.fr/en/media-centre/iarcnews/2010/globocan2008.php. Accessed February 1, 2015. 2010.
166. Taylor, G. I., Doyle, M., McCarten, G. The Doppler probe for planning flaps: anatomical study and clinical applications. *Br J Plast Surg* 1990;43:1-16.

167. Azuma, R., Morimoto, Y., Masumoto, K., et al. Detection of skin perforators by indocyanine green fluorescence nearly infrared angiography. *Plast Reconstr Surg* 2008;122:1062-1067.
168. Rozen, W. M., Ting, J. W., Grinsell, D., Ashton, M. W. Superior and inferior gluteal artery perforators: In-vivo anatomical study and planning for breast reconstruction. *J Plast Reconstr Aesthet Surg* 2011;64:217-225.
169. Colohan, S., Wong, C., Lakhiani, C., et al. The free descending branch muscle-sparing latissimus dorsi flap: vascular anatomy and clinical applications. *Plast Reconstr Surg* 2012;130:776e-787e.
170. Nie, J. Y., Lu, L. J., Gong, X., Li, Q., Nie, J. J. Delineating the vascular territory (perforasome) of a perforator in the lower extremity of the rabbit with four-dimensional computed tomographic angiography. *Plast Reconstr Surg* 2013;131:565-571.
171. Levy, G. N., Schindel, R., Kruth, J. P. Rapid manufacturing and rapid tooling with layer manufacturing (LM) technologies, state of the art and future perspectives. *CIRP Ann-Manuf Techn* 2003;52:589-609.
172. Sealy, W. Additive manufacturing as a disruptive technology: how to avoid the pitfall. *Am J Eng Technol Res* 2011;11:86-93.
173. Hoy, M. B. 3D printing: making things at the library. *Med Ref Serv Q* 2013;32:93-99.
174. Srinivasan, V., Bassan, J. 3D printing and the future of manufacturing. In CSC ed., *CSC leading edge forum*. USA: CSC, 2012.
175. Schubert, C., van Langeveld, M. C., Donoso, L. A. Innovations in 3D printing: a 3D overview from optics to organs. *Br J Ophthalmol* 2014;98:159-161.
176. Hull, C. W. Apparatus for production of three-dimensional objects by stereolithography.US Patent No. 4,575,330:March 11, 1986.
177. Hannen, E. J. Recreating the original contour in tumor deformed mandibles for plate adapting. *Int J Oral Maxillofac Surg* 2006;35:183-185.
178. Rozen, W. M., Ting, J. W., Baillieu, C., Leong, J. Stereolithographic modeling of the deep circumflex iliac artery and its vascular branching: a further advance in computed tomography-guided flap planning. *Plast Reconstr Surg* 2012;130:380e-382e.
179. Rozen, W. M., Ting, J. W., Leung, M., Wu, T., Ying, D., Leong, J. Advancing image-guided surgery in microvascular mandibular reconstruction: combining bony and vascular imaging with computed tomography-guided stereolithographic bone modeling. *Plast Reconstr Surg* 2012;130:227e-229e.
180. Ono, I., Gunji, H., Suda, K., Kaneko, F. Method for preparing an exact-size model using helical volume scan computed tomography. *Plast Reconstr Surg* 1994;93:1363-1371.
181. Herlin, C., Koppe, M., Beziat, J. L., Gleizal, A. Rapid prototyping in craniofacial surgery: using a positioning guide after zygomatic osteotomy - A case report. *J Craniomaxillofac Surg* 2011;39:376-379.
182. Cohen, A., Laviv, A., Berman, P., Nashef, R., Abu-Tair, J. Mandibular reconstruction using stereolithographic 3-dimensional printing modeling technology. *Oral Surg Oral Med Oral Pathol Oral Radiol Endod* 2009;108:661-666.
183. Tumbleston, J. R., Shirvanyants, D., Ermoshkin, N., et al. Additive manufacturing. Continuous liquid interface production of 3D objects. *Science* 2015;347:1349-1352.
184. Almquist, T. A., Smalley, D. R. Thermal stereolithography.US Patent No. 5,141,680:August 25, 1992.
185. Deckard, C. Method and apparatus for producing parts by selective sintering.US Patent No. 4,863,538:September 5, 1989.
186. Rengier, F., Mehndiratta, A., von Tengg-Kobligk, H., et al. 3D printing based on imaging data: review of medical applications. *Int J Comput Assist Radiol Surg* 2010;5:335-341.
187. Mottl-Link, S., Hubler, M., Kuhne, T., et al. Physical models aiding in complex congenital heart surgery. *Ann Thorac Surg* 2008;86:273-277.

188. McGurk, M., Amis, A. A., Potamianos, P., Goodger, N. M. Rapid prototyping techniques for anatomical modelling in medicine. *Ann R Coll Surg Engl* 1997;79:169-174.
189. Sachs, E. M., Haggerty, J. S., Cima, M. J., Williams, P. A. Three-dimensional printing techniques.US Patent No. 5,204,055:April 20, 1993.
190. Watson, R. A. A low-cost surgical application of additive fabrication. *J Surg Educ* 2014;71:14-17.
191. Olszewski, R., Szymor, P., Kozakiewicz, M. Accuracy of three-dimensional, paper-based models generated using a low-cost, three-dimensional printer. *J Craniomaxillofac Surg* 2014.
192. Crump, S. S. Apparatus and method for creating three-dimensional objects. 1992;US Patent No. 5,121,329:June 9.
193. Dikovsky, D., Napadensky, E. Three-dimensional printing process for producing a self-destructible temporary structure.US Patent No. 8,470,231:June 25, 2013.
194. Chen, Y., Niu, F., Yu, B., Liu, J., Wang, M., Gui, L. Three-dimensional preoperative design of distraction osteogenesis for hemifacial microsomia. *J Craniofac Surg* 2014;25:184-188.
195. D'Urso, P. S., Barker, T. M., Earwaker, W. J., et al. Stereolithographic biomodelling in cranio-maxillofacial surgery: a prospective trial. *J Craniomaxillofac Surg* 1999;27:30-37.
196. Guarino, J., Tennyson, S., McCain, G., Bond, L., Shea, K., King, H. Rapid prototyping technology for surgeries of the pediatric spine and pelvis: benefits analysis. *J Pediatr Orthop* 2007;27:955-960.
197. Liu, Y. F., Xu, L. W., Zhu, H. Y., Liu, S. S. Technical procedures for template-guided surgery for mandibular reconstruction based on digital design and manufacturing. *Biomed Eng Online* 2014;13:63.
198. Tsai, M. J., Wu, C. T. Study of mandible reconstruction using a fibula flap with application of additive manufacturing technology. *Biomed Eng Online* 2014;13:57.
199. Lim, C. G., Campbell, D. I., Clucas, D. M. Rapid prototyping technology in orbital floor reconstruction: application in three patients. *Craniomaxillofac Trauma Reconstr* 2014;7:143-146.
200. Engel, M., Hoffmann, J., Castrillon-Oberndorfer, G., Freudlsperger, C. The value of three-dimensional printing modelling for surgical correction of orbital hypertelorism. *Oral Maxillofac Surg* 2014.
201. Azuma, M., Yanagawa, T., Ishibashi-Kanno, N., et al. Mandibular reconstruction using plates prebent to fit rapid prototyping 3-dimensional printing models ameliorates contour deformity. *Head Face Med* 2014;10:45.
202. Jeong, H. S., Park, K. J., Kil, K. M., et al. Minimally invasive plate osteosynthesis using 3D printing for shaft fractures of clavicles: technical note. *Arch Orthop Trauma Surg* 2014;134:1551-1555.
203. Tam, M. D., Laycock, S. D., Bell, D., Chojnowski, A. 3-D printout of a DICOM file to aid surgical planning in a 6 year old patient with a large scapular osteochondroma complicating congenital diaphyseal aclasia. *J Radiol Case Rep* 2012;6:31-37.
204. Schmauss, D., Haeberle, S., Hagl, C., Sodian, R. Three-dimensional printing in cardiac surgery and interventional cardiology: a single-centre experience. *Eur J Cardiothorac Surg* 2014.
205. Witschey, W. R., Pouch, A. M., McGarvey, J. R., et al. Three-dimensional ultrasound-derived physical mitral valve modeling. *Ann Thorac Surg* 2014;98:691-694.
206. Schmauss, D., Gerber, N., Sodian, R. Three-dimensional printing of models for surgical planning in patients with primary cardiac tumors. *J Thorac Cardiovasc Surg* 2013;145:1407-1408.
207. Schmauss, D., Schmitz, C., Bigdeli, A. K., et al. Three-dimensional printing of models for preoperative planning and simulation of transcatheter valve replacement. *Ann Thorac Surg* 2012;93:e31-33.

208. Sodian, R., Weber, S., Markert, M., et al. Pediatric cardiac transplantation: three-dimensional printing of anatomic models for surgical planning of heart transplantation in patients with univentricular heart. *J Thorac Cardiovasc Surg* 2008;136:1098-1099.
209. Sodian, R., Schmauss, D., Markert, M., et al. Three-dimensional printing creates models for surgical planning of aortic valve replacement after previous coronary bypass grafting. *Ann Thorac Surg* 2008;85:2105-2108.
210. Markert, M., Weber, S., Lueth, T. C. A beating heart model 3D printed from specific patient data. *Conf Proc IEEE Eng Med Biol Soc* 2007;2007:4472-4475.
211. Nakada, T., Akiba, T., Inagaki, T., Morikawa, T. Thoracoscopic anatomical subsegmentectomy of the right S2b + S3 using a 3D printing model with rapid prototyping. *Interact Cardiovasc Thorac Surg* 2014.
212. Akiba, T., Inagaki, T., Nakada, T. Three-dimensional printing model of anomalous bronchi before surgery. *Ann Thorac Cardiovasc Surg* 2014;20 Suppl:659-662.
213. Tam, M. D., Laycock, S. D., Brown, J. R., Jakeways, M. 3D printing of an aortic aneurysm to facilitate decision making and device selection for endovascular aneurysm repair in complex neck anatomy. *J Endovasc Ther* 2013;20:863-867.
214. Hakansson, A., Rantatalo, M., Hansen, T., Wanhainen, A. Patient specific biomodel of the whole aorta - the importance of calcified plaque removal. *Vasa* 2011;40:453-459.
215. Sodian, R., Schmauss, D., Schmitz, C., et al. 3-dimensional printing of models to create custom-made devices for coil embolization of an anastomotic leak after aortic arch replacement. *Ann Thorac Surg* 2009;88:974-978.
216. Silberstein, J. L., Maddox, M. M., Dorsey, P., Feibus, A., Thomas, R., Lee, B. R. Physical models of renal malignancies using standard cross-sectional imaging and 3-dimensional printers: a pilot study. *Urology* 2014;84:268-272.
217. Daniel, M., Watson, J., Hoskison, E., Sama, A. Frontal sinus models and onlay templates in osteoplastic flap surgery. *J Laryngol Otol* 2011;125:82-85.
218. Suzuki, M., Ogawa, Y., Kawano, A., Hagiwara, A., Yamaguchi, H., Ono, H. Rapid prototyping of temporal bone for surgical training and medical education. *Acta Otolaryngol* 2004;124:400-402.
219. Igami, T., Nakamura, Y., Hirose, T., et al. Application of a Three-dimensional Print of a Liver in Hepatectomy for Small Tumors Invisible by Intraoperative Ultrasonography: Preliminary Experience. *World J Surg* 2014.
220. Ikegami, T., Maehara, Y. Transplantation: 3D printing of the liver in living donor liver transplantation. *Nat Rev Gastroenterol Hepatol* 2013;10:697-698.
221. Zein, N. N., Hanouneh, I. A., Bishop, P. D., et al. Three-dimensional print of a liver for preoperative planning in living donor liver transplantation. *Liver Transpl* 2013;19:1304-1310.
222. Kang, S. H., Kim, M. K., Kim, B. C., Lee, S. H. Orthognathic Y-splint: a CAD/CAM-engineered maxillary repositioning wafer assembly. *Br J Oral Maxillofac Surg* 2014;52:667-669.
223. Adolphs, N., Liu, W., Keeve, E., Hoffmeister, B. RapidSplint: virtual splint generation for orthognathic surgery - results of a pilot series. *Comput Aided Surg* 2014;19:20-28.
224. Cousley, R. R., Turner, M. J. Digital model planning and computerized fabrication of orthognathic surgery wafers. *J Orthod* 2014;41:38-45.
225. Kim, B. C., Lee, C. E., Park, W., et al. Clinical experiences of digital model surgery and the rapid-prototyped wafer for maxillary orthognathic surgery. *Oral Surg Oral Med Oral Pathol Oral Radiol Endod* 2011;111:278-285 e271.
226. Li, B., Zhang, L., Sun, H., Yuan, J., Shen, S. G., Wang, X. A novel method of computer aided orthognathic surgery using individual CAD/CAM templates: a combination of osteotomy and repositioning guides. *Br J Oral Maxillofac Surg* 2013;51:e239-244.

227. Metzger, M. C., Hohlweg-Majert, B., Schwarz, U., Teschner, M., Hammer, B., Schmelzeisen, R. Manufacturing splints for orthognathic surgery using a three-dimensional printer. *Oral Surg Oral Med Oral Pathol Oral Radiol Endod* 2008;105:e1-7.
228. D'Urso, P. S., Williamson, O. D., Thompson, R. G. Biomodeling as an aid to spinal instrumentation. *Spine (Phila Pa 1976)* 2005;30:2841-2845.
229. Spottiswoode, B. S., van den Heever, D. J., Chang, Y., et al. Preoperative three-dimensional model creation of magnetic resonance brain images as a tool to assist neurosurgical planning. *Stereotact Funct Neurosurg* 2013;91:162-169.
230. Fuller, S. M., Butz, D. R., Vevang, C. B., Makhlouf, M. V. Application of 3-dimensional printing in hand surgery for production of a novel bone reduction clamp. *J Hand Surg Am* 2014;39:1840-1845.
231. Rankin, T. M., Giovinco, N. A., Cucher, D. J., Watts, G., Hurwitz, B., Armstrong, D. G. Three-dimensional printing surgical instruments: are we there yet? *J Surg Res* 2014;189:193-197.
232. Waran, V., Narayanan, V., Karuppiah, R., Owen, S. L., Aziz, T. Utility of multimaterial 3D printers in creating models with pathological entities to enhance the training experience of neurosurgeons. *J Neurosurg* 2014;120:489-492.
233. Abla, A. A., Lawton, M. T. Three-Dimensional Hollow Intracranial Aneurysm Models and Their Potential Role for Teaching, Simulation, and Training. *World Neurosurg* 2014.
234. Mashiko, T., Otani, K., Kawano, R., et al. Development of Three-Dimensional Hollow Elastic Model for Cerebral Aneurysm Clipping Simulation Enabling Rapid and Low Cost Prototyping. *World Neurosurg* 2013.
235. Wurm, G., Tomancok, B., Pogady, P., Holl, K., Trenkler, J. Cerebrovascular stereolithographic biomodeling for aneurysm surgery. Technical note. *J Neurosurg* 2004;100:139-145.
236. Wurm, G., Lehner, M., Tomancok, B., Kleiser, R., Nussbaumer, K. Cerebrovascular biomodeling for aneurysm surgery: simulation-based training by means of rapid prototyping technologies. *Surg Innov* 2011;18:294-306.
237. Waran, V., Narayanan, V., Karuppiah, R., et al. Neurosurgical Endoscopic Training via a Realistic 3-Dimensional Model With Pathology. *Simul Healthc* 2014.
238. Costello, J. P., Olivieri, L. J., Su, L., et al. Incorporating Three-dimensional Printing into a Simulation-based Congenital Heart Disease and Critical Care Training Curriculum for Resident Physicians. *Congenit Heart Dis* 2014.
239. Biglino, G., Verschueren, P., Zegels, R., Taylor, A. M., Schievano, S. Rapid prototyping compliant arterial phantoms for in-vitro studies and device testing. *J Cardiovasc Magn Reson* 2013;15:2.
240. Bustamante, S., Bose, S., Bishop, P., Klatte, R., Norris, F. Novel application of rapid prototyping for simulation of bronchoscopic anatomy. *J Cardiothorac Vasc Anesth* 2014;28:1134-1137.
241. Cheung, C. L., Looi, T., Lendvay, T. S., Drake, J. M., Farhat, W. A. Use of 3-dimensional printing technology and silicone modeling in surgical simulation: development and face validation in pediatric laparoscopic pyeloplasty. *J Surg Educ* 2014;71:762-767.
242. Li, J., Hsu, Y., Luo, E., Khadka, A., Hu, J. Computer-aided design and manufacturing and rapid prototyped nanoscale hydroxyapatite/polyamide (n-HA/PA) construction for condylar defect caused by mandibular angle ostectomy. *Aesthetic Plast Surg* 2011;35:636-640.
243. Klammert, U., Gbureck, U., Vorndran, E., Rodiger, J., Meyer-Marcotty, P., Kubler, A. C. 3D powder printed calcium phosphate implants for reconstruction of cranial and maxillofacial defects. *J Craniomaxillofac Surg* 2010;38:565-570.
244. Saijo, H., Igawa, K., Kanno, Y., et al. Maxillofacial reconstruction using custom-made artificial bones fabricated by inkjet printing technology. *J Artif Organs* 2009;12:200-205.

245. Wurm, G., Tomancok, B., Holl, K., Trenkler, J. Prospective study on cranioplasty with individual carbon fiber reinforced polymer (CFRP) implants produced by means of stereolithography. *Surg Neurol* 2004;62:510-521.
246. D'Urso, P. S., Earwaker, W. J., Barker, T. M., et al. Custom cranioplasty using stereolithography and acrylic. *Br J Plast Surg* 2000;53:200-204.
247. Bicanic, G., Barbaric, K., Bohacek, I., Aljinovic, A., Delimar, D. Current concept in dysplastic hip arthroplasty: Techniques for acetabular and femoral reconstruction. *World J Orthop* 2014;5:412-424.
248. Koulouvaris, P., Stafylas, K., Sculco, T., Xenakis, T. Distal femoral shortening in total hip arthroplasty for complex primary hip reconstruction. A new surgical technique. *J Arthroplasty* 2008;23:992-998.
249. Zopf, D. A., Hollister, S. J., Nelson, M. E., Ohye, R. G., Green, G. E. Bioresorbable airway splint created with a three-dimensional printer. *N Engl J Med* 2013;368:2043-2045.
250. Reeves, P. Additive manufacturing & 3D printing medical & healthcare: a new industrial perspective. *The 3D printing & additive manufacturing people*. Derbyshire, UK, 2014.
251. Wozniak, K., Rzepecka-Wozniak, E., Moskala, A., Pohl, J., Latacz, K., Dybala, B. Weapon identification using antemortem computed tomography with virtual 3D and rapid prototype modeling--a report in a case of blunt force head injury. *Forensic Sci Int* 2012;222:e29-32.
252. McMenamin, P. G., Quayle, M. R., McHenry, C. R., Adams, J. W. The production of anatomical teaching resources using three-dimensional (3D) printing technology. *Anat Sci Educ* 2014;7:479-486.
253. Giovinco, N. A., Dunn, S. P., Dowling, L., et al. A novel combination of printed 3-dimensional anatomic templates and computer-assisted surgical simulation for virtual preoperative planning in Charcot foot reconstruction. *J Foot Ankle Surg* 2012;51:387-393.
254. Groth, C., Kravitz, N. D., Jones, P. E., Graham, J. W., Redmond, W. R. Three-dimensional printing technology. *J Clin Orthod* 2014;48:475-485.
255. Chen, J., Zhang, Z., Chen, X., Zhang, C., Zhang, G., Xu, Z. Design and manufacture of customized dental implants by using reverse engineering and selective laser melting technology. *J Prosthet Dent* 2014;112:1088-1095 e1081.
256. Flugge, T. V., Nelson, K., Schmelzeisen, R., Metzger, M. C. Three-dimensional plotting and printing of an implant drilling guide: simplifying guided implant surgery. *J Oral Maxillofac Surg* 2013;71:1340-1346.
257. Goyanes, A., Buanz, A. B., Hatton, G. B., Gaisford, S., Basit, A. W. 3D printing of modified-release aminosalicylate (4-ASA and 5-ASA) tablets. *Eur J Pharm Biopharm* 2014.
258. Skowyra, J., Pietrzak, K., Alhnan, M. A. Fabrication of extended-release patient-tailored prednisolone tablets via fused deposition modelling (FDM) 3D printing. *Eur J Pharm Sci* 2014;68C:11-17.
259. Lueders, C., Jastram, B., Hetzer, R., Schwandt, H. Rapid manufacturing techniques for the tissue engineering of human heart valves. *Eur J Cardiothorac Surg* 2014;46:593-601.
260. Chang, J. W., Park, S. A., Park, J. K., et al. Tissue-engineered tracheal reconstruction using three-dimensionally printed artificial tracheal graft: preliminary report. *Artif Organs* 2014;38:E95-E105.
261. Hieu, L. C., Zlatov, N., Vander Sloten, J., et al. Medical rapid prototyping applications and methods. *Assembly Autom* 2005;25:284-292.
262. Rosset, A., Spadola, L., Ratib, O. OsiriX: an open-source software for navigating in multidimensional DICOM images. *J Digit Imaging* 2004;17:205-216.
263. Fedorov, A., Beichel, R., Kalpathy-Cramer, J., et al. 3D Slicer as an image computing platform for the Quantitative Imaging Network. *Magn Reson Imaging* 2012;30:1323-1341.

264. Gering, D. T., Nabavi, A., Kikinis, R., et al. An integrated visualization system for surgical planning and guidance using image fusion and an open MR. *J Magn Reson Imaging* 2001;13:967-975.
265. Golby, A. J., Kindlmann, G., Norton, I., Yarmarkovich, A., Pieper, S., Kikinis, R. Interactive diffusion tensor tractography visualization for neurosurgical planning. *Neurosurgery* 2011;68:496-505.
266. Ibrahim, D., Broilo, T. L., Heitz, C., et al. Dimensional error of selective laser sintering, three-dimensional printing and PolyJet models in the reproduction of mandibular anatomy. *J Craniomaxillofac Surg* 2009;37:167-173.
267. Silva, D. N., Gerhardt de Oliveira, M., Meurer, E., Meurer, M. I., Lopes da Silva, J. V., Santa-Barbara, A. Dimensional error in selective laser sintering and 3D-printing of models for craniomaxillary anatomy reconstruction. *J Craniomaxillofac Surg* 2008;36:443-449.
268. Fitzwater, K. L., Marcellin-Little, D. J., Harrysson, O. L., Osborne, J. A., Poindexter, E. C. Evaluation of the effect of computed tomography scan protocols and freeform fabrication methods on bone biomodel accuracy. *Am J Vet Res* 2011;72:1178-1185.
269. Bos, E. J., Scholten, T., Song, Y., et al. Developing a parametric ear model for auricular reconstruction: a new step towards patient-specific implants. *J Craniomaxillofac Surg* 2015;43:390-395.
270. Nishimoto, S., Sotsuka, Y., Kawai, K., Fujita, K., Kakibuchi, M. Three-dimensional mock-up model for chondral framework in auricular reconstruction, built with a personal three-dimensional printer. *Plast Reconstr Surg* 2014;134:180e-181e.
271. Xu, Y., Fan, F., Kang, N., et al. Tissue engineering of human nasal alar cartilage precisely by using three-dimensional printing. *Plast Reconstr Surg* 2015;135:451-458.
272. Cabalag, M. S., Chae, M. P., Miller, G. S., Rozen, W. M., Hunter-Smith, D. J. Use of three-dimensional printed 'haptic' models for preoperative planning in an Australian plastic surgery unit. *ANZ J Surg* 2015.
273. Chae, M. P., Lin, F., Spychal, R. T., Hunter-Smith, D. J., Rozen, W. M. 3D-printed haptic "reverse" models for preoperative planning in soft tissue reconstruction: a case report. *Microsurgery* 2015;35:148-153.
274. Garcia-Tutor, E., Romeo, M., Chae, M. P., Hunter-Smith, D. J., Rozen, W. M. 3D volumetric modeling and microvascular reconstruction of irradiated lumbosacral defects after oncologic resection. *J Reconstr Microsurg* 2015:Manuscript in Press.
275. Gillis, J. A., Morris, S. F. Three-dimensional printing of perforator vascular anatomy. *Plast Reconstr Surg* 2014;133:80e-82e.
276. Chae, M. P., Hunter-Smith, D. J., De-Silva, I., Tham, S., Spychal, R. T., Rozen, W. M. Four-Dimensional (4D) Printing: A New Evolution in Computed Tomography-Guided Stereolithographic Modeling. Principles and Application. *J Reconstr Microsurg* 2015.
277. Sutradhar, A., Park, J., Carrau, D., Miller, M. J. Experimental validation of 3D printed patient-specific implants using digital image correlation and finite element analysis. *Comput Biol Med* 2014;52:8-17.
278. Ciocca, L., De Crescenzio, F., Fantini, M., Scotti, R. Rehabilitation of the nose using CAD/CAM and rapid prototyping technology after ablative surgery of squamous cell carcinoma: a pilot clinical report. *Int J Oral Maxillofac Implants* 2010;25:808-812.
279. Ciocca, L., De Crescenzio, F., Fantini, M., Scotti, R. CAD/CAM bilateral ear prostheses construction for Treacher Collins syndrome patients using laser scanning and rapid prototyping. *Comput Methods Biomech Biomed Engin* 2010;13:379-386.
280. Donfrancesco, A., Montemurro, P., Heden, P. Three-dimensional simulated images in breast augmentation surgery: an investigation of patients' satisfaction and the correlation between prediction and actual outcome. *Plast Reconstr Surg* 2013;132:810-822.

281. Lee, J. W., Fang, J. J., Chang, L. R., Yu, C. K. Mandibular defect reconstruction with the help of mirror imaging coupled with laser stereolithographic modeling technique. *J Formos Med Assoc* 2007;106:244-250.
282. Cao, D., Yu, Z., Chai, G., Liu, J., Mu, X. Application of EH compound artificial bone material combined with computerized three-dimensional reconstruction in craniomaxillofacial surgery. *J Craniofac Surg* 2010;21:440-443.
283. Katsuragi, Y., Kayano, S., Akazawa, S., et al. Mandible reconstruction using the calcium-sulphate three-dimensional model and rubber stick: a new method, 'mould technique', for more accurate, efficient and simplified fabrication. *J Plast Reconstr Aesthet Surg* 2011;64:614-622.
284. Hsieh, M. K., Chen, A. C., Cheng, C. Y., Chou, Y. C., Chan, Y. S., Hsu, K. Y. Repositioning osteotomy for intra-articular malunion of distal radius with radiocarpal and/or distal radioulnar joint subluxation. *J Trauma* 2010;69:418-422.
285. Gan, Y., Xu, D., Lu, S., Ding, J. Novel patient-specific navigational template for total knee arthroplasty. *Comput Aided Surg* 2011;16:288-297.
286. Kunz, M., Ma, B., Rudan, J. F., Ellis, R. E., Pichora, D. R. Image-guided distal radius osteotomy using patient-specific instrument guides. *J Hand Surg Am* 2013;38:1618-1624.
287. Kataoka, T., Oka, K., Miyake, J., Omori, S., Tanaka, H., Murase, T. 3-Dimensional prebent plate fixation in corrective osteotomy of malunited upper extremity fractures using a real-sized plastic bone model prepared by preoperative computer simulation. *J Hand Surg Am* 2013;38:909-919.
288. Minns, R. J., Bibb, R., Banks, R., Sutton, R. A. The use of a reconstructed three-dimensional solid model from CT to aid the surgical management of a total knee arthroplasty: a case study. *Med Eng Phys* 2003;25:523-526.
289. Reinhardt, J. M., Ding, K., Cao, K., Christensen, G. E., Hoffman, E. A., Bodas, S. V. Registration-based estimates of local lung tissue expansion compared to xenon CT measures of specific ventilation. *Med Image Anal* 2008;12:752-763.
290. Chang, J. Y., Li, Q. Q., Xu, Q. Y., et al. Stereotactic ablative radiation therapy for centrally located early stage or isolated parenchymal recurrences of non-small cell lung cancer: how to fly in a "no fly zone". *Int J Radiat Oncol Biol Phys* 2014;88:1120-1128.
291. Kontio, R., Bjorkstrand, R., Salmi, M., et al. Designing and additive manufacturing a prototype for a novel instrument for mandible fracture reduction. *Surgery* 2012;S1:002.
292. Sugawara, T., Higashiyama, N., Kaneyama, S., et al. Multistep pedicle screw insertion procedure with patient-specific lamina fit-and-lock templates for the thoracic spine: clinical article. *J Neurosurg Spine* 2013;19:185-190.
293. Lambrecht, J. T., Berndt, D. C., Schumacher, R., Zehnder, M. Generation of three-dimensional prototype models based on cone beam computed tomography. *Int J Comput Assist Radiol Surg* 2009;4:175-180.
294. Kimura, T., Morita, A., Nishimura, K., et al. Simulation of and training for cerebral aneurysm clipping with 3-dimensional models. *Neurosurgery* 2009;65:719-725; discussion 725-716.
295. Chueh, J. Y., Wakhloo, A. K., Gounis, M. J. Neurovascular modeling: small-batch manufacturing of silicone vascular replicas. *AJNR Am J Neuroradiol* 2009;30:1159-1164.
296. Sulaiman, A., Boussel, L., Taconnet, F., et al. In vitro non-rigid life-size model of aortic arch aneurysm for endovascular prosthesis assessment. *Eur J Cardiothorac Surg* 2008;33:53-57.
297. Kalejs, M., von Segesser, L. K. Rapid prototyping of compliant human aortic roots for assessment of valved stents. *Interact Cardiovasc Thorac Surg* 2009;8:182-186.
298. Armillotta, A., Bonhoeffer, P., Dubini, G., et al. Use of rapid prototyping models in the planning of percutaneous pulmonary valved stent implantation. *Proc Inst Mech Eng H* 2007;221:407-416.

299. Bruyere, F., Leroux, C., Brunereau, L., Lermusiaux, P. Rapid prototyping model for percutaneous nephrolithotomy training. *J Endourol* 2008;22:91-96.
300. Kim, M. S., Sbalchiero, J. C., Reece, G. P., Miller, M. J., Beahm, E. K., Markey, M. K. Assessment of breast aesthetics. *Plast Reconstr Surg* 2008;121:186e-194e.
301. Chan, Y. C., Qing, K. X., Cheng, S. W. Custom-made fenestrated stent grafts to preserve accessory renal arteries in patients with abdominal aortic aneurysms. *Acta Chir Belg* 2014;114:183-188.
302. Hourfar, J., Kanavakis, G., Goellner, P., Ludwig, B. Fully customized placement of orthodontic miniplates: a novel clinical technique. *Head Face Med* 2014;10:14.
303. Lee, S. J., Lee, H. P., Tse, K. M., Cheong, E. C., Lim, S. P. Computer-aided design and rapid prototyping-assisted contouring of costal cartilage graft for facial reconstructive surgery. *Craniomaxillofac Trauma Reconstr* 2012;5:75-82.
304. Wu, G., Zhou, B., Bi, Y., Zhao, Y. Selective laser sintering technology for customized fabrication of facial prostheses. *J Prosthet Dent* 2008;100:56-60.
305. Sykes, L. M., Parrott, A. M., Owen, C. P., Snaddon, D. R. Applications of rapid prototyping technology in maxillofacial prosthetics. *Int J Prosthodont* 2004;17:454-459.
306. Subburaj, K., Nair, C., Rajesh, S., Meshram, S. M., Ravi, B. Rapid development of auricular prosthesis using CAD and rapid prototyping technologies. *Int J Oral Maxillofac Surg* 2007;36:938-943.
307. Karayazgan-Saracoglu, B., Gunay, Y., Atay, A. Fabrication of an auricular prosthesis using computed tomography and rapid prototyping technique. *J Craniofac Surg* 2009;20:1169-1172.
308. De Crescenzio, F., Fantini, M., Ciocca, L., Persiani, F., Scotti, R. Design and manufacturing of ear prosthesis by means of rapid prototyping technology. *Proc Inst Mech Eng H* 2011;225:296-302.
309. Ciocca, L., Scotti, R. Oculo-facial rehabilitation after facial cancer removal: Updated CAD/CAM procedures. A pilot study. *Prosthet Orthot Int* 2013:[Epub ahead of print].
310. Xie, P., Hu, Z., Zhang, X., et al. Application of 3-dimensional printing technology to construct an eye model for fundus viewing study. *PLoS One* 2014;9:e109373.
311. Tsuji, M., Noguchi, N., Ihara, K., Yamashita, Y., Shikimori, M., Goto, M. Fabrication of a maxillofacial prosthesis using a computer-aided design and manufacturing system. *J Prosthodont* 2004;13:179-183.
312. Fantini, M., De Crescenzio, F., Ciocca, L. Design and rapid manufacturing of anatomical prosthesis for facial rehabilitation. *Int J Interact Des Manuf* 2013;7:51-62.
313. De Laurentis, K. J., Mavroidis, C. Mechanical design of a shape memory alloy actuated prosthetic hand. *Technol Health Care* 2002;10:91-106.
314. Eppley, B. L. Craniofacial reconstruction with computer-generated HTR patient-matched implants: use in primary bony tumor excision. *J Craniofac Surg* 2002;13:650-657.
315. Sammartino, G., Della Valle, A., Marenzi, G., et al. Stereolithography in oral implantology: a comparison of surgical guides. *Implant Dent* 2004;13:133-139.
316. Chae, M. P., Hunter-Smith, D. J., Rozen, W. M. Comparative analysis of fluorescent angiography, computed tomographic angiography and magnetic resonance angiography for planning autologous breast reconstruction. *Gland Surg* 2015;4:164-178.
317. Gacto-Sanchez, P., Sicilia-Castro, D., Gomez-Cia, T., et al. Use of a three-dimensional virtual reality model for preoperative imaging in DIEP flap breast reconstruction. *J Surg Res* 2010;162:140-147.
318. Chae, M. P., Rozen, W. M., McMenamin, P. G., Findlay, M. W., Spychal, R. T., Hunter-Smith, D. J. Emerging Applications of Bedside 3D Printing in Plastic Surgery. *Front Surg* 2015;2:25.
319. Sallent, A., Vicente, M., Reverte, M. M., et al. How 3D patient-specific instruments improve accuracy of pelvic bone tumour resection in a cadaveric study. *Bone Joint Res* 2017;6:577-583.

320. Erickson, D. M., Chance, D., Schmitt, S., Mathis, J. An opinion survey of reported benefits from the use of stereolithographic models. *J Oral Maxillofac Surg* 1999;57:1040-1043.
321. Martelli, N., Serrano, C., van den Brink, H., et al. Advantages and disadvantages of 3-dimensional printing in surgery: A systematic review. *Surgery* 2016;159:1485-1500.
322. Anderson, J. R., Thompson, W. L., Alkattan, A. K., et al. Three-dimensional printing of anatomically accurate, patient specific intracranial aneurysm models. *J Neurointerv Surg* 2016;8:517-520.
323. Naftulin, J. S., Kimchi, E. Y., Cash, S. S. Streamlined, Inexpensive 3D Printing of the Brain and Skull. *PLoS One* 2015;10:e0136198.
324. George, E., Liacouras, P., Rybicki, F. J., Mitsouras, D. Measuring and Establishing the Accuracy and Reproducibility of 3D Printed Medical Models. *Radiographics* 2017;37:1424-1450.
325. Mitsouras, D., Liacouras, P., Imanzadeh, A., et al. Medical 3D Printing for the Radiologist. *Radiographics* 2015;35:1965-1988.
326. Huotilainen, E., Jaanimets, R., Valasek, J., et al. Inaccuracies in additive manufactured medical skull models caused by the DICOM to STL conversion process. *J Craniomaxillofac Surg* 2014;42:e259-265.
327. Smith, E. J., Anstey, J. A., Venne, G., Ellis, R. E. Using additive manufacturing in accuracy evaluation of reconstructions from computed tomography. *Proc Inst Mech Eng H* 2013;227:551-559.
328. Primo, B. T., Presotto, A. C., de Oliveira, H. W., et al. Accuracy assessment of prototypes produced using multi-slice and cone-beam computed tomography. *Int J Oral Maxillofac Surg* 2012;41:1291-1295.
329. Taft, R. M., Kondor, S., Grant, G. T. Accuracy of rapid prototype models for head and neck reconstruction. *J Prosthet Dent* 2011;106:399-408.
330. Nizam, A., Gopal, R. N., Naing, L., Hakim, A. B., Samsudin, A. R. Dimensional accuracy of the skull models produced by rapid prototyping technology using stereolithography apparatus. *Arch Orofac Sci* 2006;1:60-66.
331. Choi, J. Y., Choi, J. H., Kim, N. K., et al. Analysis of errors in medical rapid prototyping models. *Int J Oral Maxillofac Surg* 2002;31:23-32.
332. Asaumi, J., Kawai, N., Honda, Y., Shigehara, H., Wakasa, T., Kishi, K. Comparison of three-dimensional computed tomography with rapid prototype models in the management of coronoid hyperplasia. *Dentomaxillofac Radiol* 2001;30:330-335.
333. Bouyssie, J. F., Bouyssie, S., Sharrock, P., Duran, D. Stereolithographic models derived from x-ray computed tomography. Reproduction accuracy. *Surg Radiol Anat* 1997;19:193-199.
334. Barker, T. M., Earwaker, W. J., Lisle, D. A. Accuracy of stereolithographic models of human anatomy. *Australas Radiol* 1994;38:106-111.
335. Santana, R. R., Lozada, J., Kleinman, A., Al-Ardah, A., Herford, A., Chen, J. W. Accuracy of cone beam computerized tomography and a three-dimensional stereolithographic model in identifying the anterior loop of the mental nerve: a study on cadavers. *J Oral Implantol* 2012;38:668-676.
336. Salmi, M., Paloheimo, K. S., Tuomi, J., Wolff, J., Makitie, A. Accuracy of medical models made by additive manufacturing (rapid manufacturing). *J Craniomaxillofac Surg* 2013;41:603-609.
337. Murugesan, K., Anandapandian, P. A., Sharma, S. K., Vasantha Kumar, M. Comparative evaluation of dimension and surface detail accuracy of models produced by three different rapid prototype techniques. *J Indian Prosthodont Soc* 2012;12:16-20.
338. Chang, P. S., Parker, T. H., Patrick, C. W., Jr., Miller, M. J. The accuracy of stereolithography in planning craniofacial bone replacement. *J Craniofac Surg* 2003;14:164-170.

339. Petropolis, C., Kozan, D., Sigurdson, L. Accuracy of medical models made by consumer-grade fused deposition modelling printers. *Plast Surg (Oakv)* 2015;23:91-94.
340. Ogden, K. M., Aslan, C., Ordway, N., Diallo, D., Tillapaugh-Fay, G., Soman, P. Factors Affecting Dimensional Accuracy of 3-D Printed Anatomical Structures Derived from CT Data. *J Digit Imaging* 2015;28:654-663.
341. Maschio, F., Pandya, M., Olszewski, R. Experimental Validation of Plastic Mandible Models Produced by a "Low-Cost" 3-Dimensional Fused Deposition Modeling Printer. *Med Sci Monit* 2016;22:943-957.
342. Schweizer, A., Mauler, F., Vlachopoulos, L., Nagy, L., Furnstahl, P. Computer-Assisted 3-Dimensional Reconstructions of Scaphoid Fractures and Nonunions With and Without the Use of Patient-Specific Guides: Early Clinical Outcomes and Postoperative Assessments of Reconstruction Accuracy. *J Hand Surg Am* 2016;41:59-69.
343. Hu, Y., Yuan, Z. S., Spiker, W. R., et al. A comparative study on the accuracy of pedicle screw placement assisted by personalized rapid prototyping template between pre- and post-operation in patients with relatively normal mid-upper thoracic spine. *Eur Spine J* 2016;25:1706-1715.
344. Gan, Y., Ding, J., Xu, Y., Hou, C. Accuracy and efficacy of osteotomy in total knee arthroplasty with patient-specific navigational template. *Int J Clin Exp Med* 2015;8:12192-12201.
345. Stumpel, L. J. Deformation of stereolithographically produced surgical guides: an observational case series report. *Clin Implant Dent Relat Res* 2012;14:442-453.
346. Ozan, O., Turkyilmaz, I., Ersoy, A. E., McGlumphy, E. A., Rosenstiel, S. F. Clinical accuracy of 3 different types of computed tomography-derived stereolithographic surgical guides in implant placement. *J Oral Maxillofac Surg* 2009;67:394-401.
347. Ersoy, A. E., Turkyilmaz, I., Ozan, O., McGlumphy, E. A. Reliability of implant placement with stereolithographic surgical guides generated from computed tomography: clinical data from 94 implants. *J Periodontol* 2008;79:1339-1345.
348. Van Assche, N., van Steenberghe, D., Guerrero, M. E., et al. Accuracy of implant placement based on pre-surgical planning of three-dimensional cone-beam images: a pilot study. *J Clin Periodontol* 2007;34:816-821.
349. Fasel, J. H., Beinemann, J., Schaller, K., Gailloud, P. A critical inventory of preoperative skull replicas. *Ann R Coll Surg Engl* 2013;95:401-404.
350. Khalil, W., EzEldeen, M., Van De Casteele, E., et al. Validation of cone beam computed tomography-based tooth printing using different three-dimensional printing technologies. *Oral Surg Oral Med Oral Pathol Oral Radiol* 2016;121:307-315.
351. El-Katatny, I., Masood, S. H., Morsi, Y. S. Error analysis of FDM fabricated medical replicas. *Rapid Prototyping J* 2010;16:36-43.
352. Berry, E., Brown, J. M., Connell, M., et al. Preliminary experience with medical applications of rapid prototyping by selective laser sintering. *Med Eng Phys* 1997;19:90-96.
353. Kragskov, J., Sindet-Pedersen, S., Gyldensted, C., Jensen, K. L. A comparison of three-dimensional computed tomography scans and stereolithographic models for evaluation of craniofacial anomalies. *J Oral Maxillofac Surg* 1996;54:402-411; discussion 411-402.
354. Garrido Varas, C. E., Thompson, T. J. Metric dimensions of the proximal phalanges of the human hand and their relationship to side, position, and asymmetry. *Homo* 2011;62:126-143.
355. Chae, M. P., Hunter-Smith, D. J., Rostek, M., Smith, J. A., Rozen, W. M. Enhanced preoperative DIEP flap planning with a 3D-printed perforasome template: technique and case report. *Plast Reconstr Surg Glob Open* 2017:Accepted for Publication.
356. Posadzy, M., Desimpel, J., Vanhoenacker, F. Cone beam CT of the musculoskeletal system: clinical applications. *Insights Imaging* 2018.

357. Huotilainen, E., Paloheimo, M., Salmi, M., et al. Imaging requirements for medical applications of additive manufacturing. *Acta Radiol* 2014;55:78-85.
358. Wang, D., Doddrell, D. M., Cowin, G. A novel phantom and method for comprehensive 3-dimensional measurement and correction of geometric distortion in magnetic resonance imaging. *Magn Reson Imaging* 2004;22:529-542.
359. Liang, X., Lambrichts, I., Sun, Y., et al. A comparative evaluation of Cone Beam Computed Tomography (CBCT) and Multi-Slice CT (MSCT). Part II: On 3D model accuracy. *Eur J Radiol* 2010;75:270-274.
360. Fleischmann, D., Rubin, G. D., Paik, D. S., et al. Stair-step artifacts with single versus multiple detector-row helical CT. *Radiology* 2000;216:185-196.
361. Winder, J., Bibb, R. Medical rapid prototyping technologies: state of the art and current limitations for application in oral and maxillofacial surgery. *J Oral Maxillofac Surg* 2005;63:1006-1015.
362. Favero, C. S., English, J. D., Cozad, B. E., Wirthlin, J. O., Short, M. M., Kasper, F. K. Effect of print layer height and printer type on the accuracy of 3-dimensional printed orthodontic models. *Am J Orthod Dentofacial Orthop* 2017;152:557-565.
363. Stoor, P., Suomalainen, A., Lindqvist, C., et al. Rapid prototyped patient specific implants for reconstruction of orbital wall defects. *J Craniomaxillofac Surg* 2014;42:1644-1649.
364. Fasel, J. H. D., Beinemann, J., SChaller, K., Peitgen, H. O. Computer science tools for manual editing of computed tomographic images: impact on the quality of 3D printed models. *Surg Sci* 2014;5:439-443.
365. Otsu, N. A threshold selection method from gray-level histograms. *Automatica* 1975;20:62-66.
366. Canny, J. A computational approach to edge detection. *IEEE Trans Pattern Anal Mach Intell* 1986;8:679-698.
367. Adams, R., Bischof, L. Seeded region growing. *IEEE Trans Pattern Anal Mach Intell* 1994;16:641-647.
368. van Eijnatten, M., Koivisto, J., Karhu, K., Forouzanfar, T., Wolff, J. The impact of manual threshold selection in medical additive manufacturing. *Int J Comput Assist Radiol Surg* 2017;12:607-615.
369. Rathnayaka, K., Momot, K. I., Noser, H., et al. Quantification of the accuracy of MRI generated 3D models of long bones compared to CT generated 3D models. *Med Eng Phys* 2012;34:357-363.
370. Gelaude, F., Vander Sloten, J., Lauwers, B. Accuracy assessment of CT-based outer surface femur meshes. *Comput Aided Surg* 2008;13:188-199.
371. Gassman, E. E., Powell, S. M., Kallemeyn, N. A., et al. Automated bony region identification using artificial neural networks: reliability and validation measurements. *Skeletal Radiol* 2008;37:313-319.
372. Karron, D. B. SpiderWeb algorithm for surface construction in noisy volume data. *Proc of SPIE* 1992;1808:462-476.
373. van Eijnatten, M., van Dijk, R., Dobbe, J., Streekstra, G., Koivisto, J., Wolff, J. CT image segmentation methods for bone used in medical additive manufacturing. *Med Eng Phys* 2017.
374. Di Prima, M., Coburn, J., Hwang, D., Kelly, J., Khairuzzaman, A., Ricles, L. Additively manufactured medical products - the FDA perspective. *3D Print Med* 2016;2:1-6.
375. Diment, L. E., Thompson, M. S., Bergmann, J. H. M. Clinical efficacy and effectiveness of 3D printing: a systematic review. *BMJ Open* 2017;7:e016891.
376. Soon, D. S., Chae, M. P., Pilgrim, C. H., Rozen, W. M., Spychal, R. T., Hunter-Smith, D. J. 3D haptic modelling for preoperative planning of hepatic resection: A systematic review. *Ann Med Surg (Lond)* 2016;10:1-7.

377. Chae, M. P., Rozen, W. M., Spychal, R. T., Hunter-Smith, D. J. Breast volumetric analysis for aesthetic planning in breast reconstruction: a literature review of techniques. *Gland Surg* 2016;5:212-226.
378. Garcia-Tutor, E., Romeo, M., Chae, M. P., Hunter-Smith, D. J., Rozen, W. M. 3D Volumetric Modeling and Microvascular Reconstruction of Irradiated Lumbosacral Defects after Oncologic Resection. *Front Surg* 2016;3:66.
379. Bauermeister, A. J., Zuriarrain, A., Newman, M. I. Three-Dimensional Printing in Plastic and Reconstructive Surgery: A Systematic Review. *Ann Plast Surg* 2016;77:569-576.
380. Xi, W., Perdanasari, A. T., Ong, Y., et al. Objective breast volume, shape and surface area assessment: a systematic review of breast measurement methods. *Aesthetic Plast Surg* 2014;38:1116-1130.
381. Cone, J. A., Martin, T. M., Marcellin-Little, D. J., Harrysson, O. L. A., Griffith, E. H. Accuracy and repeatability of long-bone replicas of small animals fabricated by use of low-end and high-end commercial three-dimensional printers. *Am J Vet Res* 2017;78:900-905.
382. Ciocca, L., Mazzoni, S., Fantini, M., et al. A CAD/CAM-prototyped anatomical condylar prosthesis connected to a custom-made bone plate to support a fibula free flap. *Med Biol Eng Comput* 2012;50:743-749.
383. Schwartz, A., Money, K., Spangehl, M., Hattrup, S., Claridge, R. J., Beauchamp, C. Office-based rapid prototyping in orthopedic surgery: a novel planning technique and review of the literature. *Am J Orthop (Belle Mead NJ)* 2015;44:19-25.
384. Teunis, T., van Voss, M. R., Kon, M., van Maurik, J. F. CT-angiography prior to DIEP flap breast reconstruction: a systematic review and meta-analysis. *Microsurgery* 2013;33:496-502.
385. Rosson, G. D., Shridharani, S. M., Magarakis, M., et al. Three-dimensional computed tomographic angiography to predict weight and volume of deep inferior epigastric artery perforator flap for breast reconstruction. *Microsurgery* 2011;31:510-516.
386. Onoda, S., Azumi, S., Hasegawa, K., Kimata, Y. Preoperative identification of perforator vessels by combining MDCT, doppler flowmetry, and ICG fluorescent angiography. *Microsurgery* 2013;33:265-269.
387. Gravvanis, A., Tsoutsos, D., Papanikolaou, G., Diab, A., Lambropoulou, P., Karakitsos, D. Refining perforator selection for deep inferior epigastric perforator flap: the impact of the dominant venous perforator. *Microsurgery* 2014;34:169-176.
388. Dionyssiou, D., Demiri, E., Tsimponis, A., Boorman, J. Predesigned breast shaping assisted by multidetector-row computed tomographic angiography in autologous breast reconstruction. *Plast Reconstr Surg* 2014;133:100-108e.
389. Mankovich, N. J., Samson, D., Pratt, W., Lew, D., Beumer, J., 3rd. Surgical planning using three-dimensional imaging and computer modeling. *Otolaryngol Clin North Am* 1994;27:875-889.
390. Wallmichrath, J., Baumeister, R. G., Giunta, R. E., Holzbach, T., Frick, A. Correction of asymmetric pectus excavatum using a virtually designed silicone implant. *Aesthetic Plast Surg* 2014;38:146-150.
391. Xu, H., Han, D., Dong, J. S., et al. Rapid prototyped PGA/PLA scaffolds in the reconstruction of mandibular condyle bone defects. *Int J Med Robot* 2010;6:66-72.
392. Wang, J., Liu, J. F., Liu, W., Wang, J. C., Wang, S. Y., Gui, L. Application of computer techniques in repair of oblique facial clefts with outer-table calvarial bone grafts. *J Craniofac Surg* 2013;24:957-960.
393. Ono, I., Abe, K., Shiotani, S., Hirayama, Y. Producing a full-scale model from computed tomographic data with the rapid prototyping technique using the binder jet method: a comparison with the laser lithography method using a dry skull. *J Craniofac Surg* 2000;11:527-537.

394. Phan, T. Q., Spilker, G., Theodorou, P., Gossmann, A., Heiss, M., Weinand, C. Combined latissimus dorsi and serratus anterior flaps for pelvic reconstruction. *Microsurgery* 2011;31:529-534.
395. Stone, H. B., Coleman, C. N., Anscher, M. S., McBride, W. H. Effects of radiation on normal tissue: consequences and mechanisms. *Lancet Oncol* 2003;4:529-536.
396. Marx, R. E. A new concept in the treatment of osteoradionecrosis. *J Oral Maxillofac Surg* 1983;41:351-357.
397. Chen, Y. X., Zhang, K., Hao, Y. N., Hu, Y. C. Research status and application prospects of digital technology in orthopaedics. *Orthop Surg* 2012;4:131-138.
398. Janis, J. E., Kwon, R. K., Attinger, C. E. The new reconstructive ladder: modifications to the traditional model. *Plast Reconstr Surg* 2011;127 Suppl 1:205S-212S.
399. Gottlieb, L. J., Krieger, L. M. From the reconstructive ladder to the reconstructive elevator. *Plast Reconstr Surg* 1994;93:1503-1504.
400. Gaster, R. S., Bhatt, K. A., Shelton, A. A., Lee, G. K. Free transverse rectus abdominis myocutaneous flap reconstruction of a massive lumbosacral defect using superior gluteal artery perforator vessels. *Microsurgery* 2012;32:388-392.
401. Lin, C. T., Chang, S. C., Chen, S. G., Tzeng, Y. S. Modification of the superior gluteal artery perforator flap for reconstruction of sacral sores. *J Plast Reconstr Aesthet Surg* 2014;67:526-532.
402. Chen, Y. C., Huang, E. Y., Lin, P. Y. Comparison of gluteal perforator flaps and gluteal fasciocutaneous rotation flaps for reconstruction of sacral pressure sores. *J Plast Reconstr Aesthet Surg* 2014;67:377-382.
403. Weitao, Y., Qiqing, C., Songtao, G., Jiaqiang, W. Use of gluteus maximus adipomuscular sliding flaps in the reconstruction of sacral defects after tumor resection. *World J Surg Oncol* 2013;11:110.
404. Gupta, S., Chattopadhyay, D., Agarwal, A. K., et al. Paraspinal transposition flap for reconstruction of sacral soft tissue defects: a series of 53 cases from a single institute. *Asian Spine J* 2014;8:309-314.
405. Kesan, K., Kothari, P., Gupta, R., et al. Closure of Large Meningomyelocele Wound Defects with Subcutaneous Based Pedicle Flap with Bilateral V-Y Advancement: Our Experience and Review of Literature. *Eur J Pediatr Surg* 2014.
406. Olenczak, J. B., Stanwix, M. G., Rosson, G. D. CASE REPORT Complex Wound Closure of Partial Sacrectomy Defect With Human Acellular Dermal Matrix and Bilateral V to Y Gluteal Advancement Flaps in a Pediatric Patient. *Eplasty* 2013;13:e20.
407. Santanelli Di Pompeo, F., Longo, B., Pagnoni, M., Laporta, R. Sensate anterolateral thigh perforator flap for ischiatic sores reconstruction in meningomyelocele patients. *Microsurgery* 2015;35:279-283.
408. Unal, C., Eren, G. G., Isil, E., Alponat, A., Sarlak, A. Utility of the omentum in sacral reconstruction following total sacrectomy due to recurrent and irradiated giant cell tumour of the spine. *Indian J Plast Surg* 2012;45:140-143.
409. Loessin, S. J., Meland, N. B., Devine, R. M., Wolff, B. G., Nelson, H., Zincke, H. Management of sacral and perineal defects following abdominoperineal resection and radiation with transpelvic muscle flaps. *Dis Colon Rectum* 1995;38:940-945.
410. Garvey, P. B., Clemens, M. W., Rhines, L. D., Sacks, J. M. Vertical rectus abdominis musculocutaneous flow-through flap to a free fibula flap for total sacrectomy reconstruction. *Microsurgery* 2013;33:32-38.
411. Cheong, Y. W., Sulaiman, W. A., Halim, A. S. Reconstruction of large sacral defects following tumour resection: a report of two cases. *J Orthop Surg (Hong Kong)* 2008;16:351-354.
412. Hung, S. J., Chen, H. C., Wei, F. C. Free flaps for reconstruction of the lower back and sacral area. *Microsurgery* 2000;20:72-76.

413. Feliciano, B., Paige, K. T., Beshlian, K. M. Latissimus dorsi free flaps for complex ischiosacral defects. *Am J Surg* 2007;193:648-650.
414. Feinendegen, D. L., Niederhauser, T., Herrmann, G., et al. The subcostal artery perforator flap; an anatomical study. *J Plast Reconstr Aesthet Surg* 2008;61:1496-1502.
415. Badran, H. A., El-Helaly, M. S., Safe, I. The lateral intercostal neurovascular free flap. *Plast Reconstr Surg* 1984;73:17-26.
416. Hamdi, M., Van Landuyt, K., de Frene, B., Roche, N., Blondeel, P., Monstrey, S. The versatility of the inter-costal artery perforator (ICAP) flaps. *J Plast Reconstr Aesthet Surg* 2006;59:644-652.
417. Ting, J. W., Rozen, W. M., Chubb, D., Ferris, S., Ashton, M. W., Grinsell, D. Improving the utility and reliability of the deep circumflex iliac artery perforator flap: the use of preoperative planning with CT angiography. *Microsurgery* 2011;31:603-609.
418. Ting, J. W., Rozen, W. M., Grinsell, D., Stella, D. L., Ashton, M. W. The in vivo anatomy of the deep circumflex iliac artery perforators: defining the role for the DCIA perforator flap. *Microsurgery* 2009;29:326-329.
419. Ting, J. W., Rozen, W. M., Leong, J., Crock, J. Free deep circumflex iliac artery vascularised bone flap for reconstruction of the distal radius: planning with CT angiography. *Microsurgery* 2010;30:163-167.
420. Rietzel, E., Pan, T., Chen, G. T. Four-dimensional computed tomography: image formation and clinical protocol. *Med Phys* 2005;32:874-889.
421. Ding, Y., Li, J., Wang, W., et al. A comparative study on the volume and localization of the internal gross target volume defined using the seroma and surgical clips based on 4DCT scan for external-beam partial breast irradiation after breast conserving surgery. *Radiat Oncol* 2014;9:76.
422. Pham, D., Kron, T., Foroudi, F., Siva, S. Effect of different breathing patterns in the same patient on stereotactic ablative body radiotherapy dosimetry for primary renal cell carcinoma: a case study. *Med Dosim* 2013;38:304-308.
423. Hunter, G. J., Ginat, D. T., Kelly, H. R., Halpern, E. F., Hamberg, L. M. Discriminating parathyroid adenoma from local mimics by using inherent tissue attenuation and vascular information obtained with four-dimensional CT: formulation of a multinomial logistic regression model. *Radiology* 2014;270:168-175.
424. Numata, S., Tsutsumi, Y., Monta, O., et al. Mechanical valve evaluation with four-dimensional computed tomography. *J Heart Valve Dis* 2013;22:837-842.
425. Rozen, W. M., Ashton, M. W., Le Roux, C. M., Pan, W. R., Corlett, R. J. The perforator angiosome: a new concept in the design of deep inferior epigastric artery perforator flaps for breast reconstruction. *Microsurgery* 2010;30:1-7.
426. Kapandji, A. I. Clinical evaluation of the thumb's opposition. *J Hand Ther* 1992;5:102-106.
427. Kapandji, A., Moatti, E., Raab, C. [Specific radiography of the trapezo-metacarpal joint and its technique (author's transl)]. *Ann Chir* 1980;34:719-726.
428. Taleisnik, J. The ligaments of the wrist. *J Hand Surg Am* 1976;1:110-118.
429. Sandow, M. J., Fisher, T. J., Howard, C. Q., Papas, S. Unifying model of carpal mechanics based on computationally derived isometric constraints and rules-based motion - the stable central column theory. *J Hand Surg Eur Vol* 2014;39:353-363.
430. Mavili, M. E., Canter, H. I., Saglam-Aydinatay, B., Kamaci, S., Kocadereli, I. Use of three-dimensional medical modeling methods for precise planning of orthognathic surgery. *J Craniofac Surg* 2007;18:740-747.
431. Stoker, N. G., Mankovich, N. J., Valentino, D. Stereolithographic models for surgical planning: preliminary report. *J Oral Maxillofac Surg* 1992;50:466-471.
432. Knox, K., Kerber, C. W., Singel, S. A., Bailey, M. J., Imbesi, S. G. Rapid prototyping to create vascular replicas from CT scan data: making tools to teach, rehearse, and choose treatment strategies. *Catheter Cardiovasc Interv* 2005;65:47-53.

433. Saint-Cyr, M., Schaverien, M., Arbique, G., Hatef, D., Brown, S. A., Rohrich, R. J. Three- and four-dimensional computed tomographic angiography and venography for the investigation of the vascular anatomy and perfusion of perforator flaps. *Plast Reconstr Surg* 2008;121:772-780.
434. Mahajan, A., Starker, L. F., Ghita, M., Udelsman, R., Brink, J. A., Carling, T. Parathyroid four-dimensional computed tomography: evaluation of radiation dose exposure during preoperative localization of parathyroid tumors in primary hyperparathyroidism. *World J Surg* 2012;36:1335-1339.
435. Tibbits, S. SJET @ MIT. Available at: http://www.sjet.us/MIT_4D PRINTING.html.
436. Tibbits, S. 4D printing: multi-material shape change. *Archit design* 2012;82:68-73.
437. Seidenberg, B., Rosenak, S. S., Hurwitt, E. S., Som, M. L. Immediate reconstruction of the cervical esophagus by a revascularized isolated jejunal segment. *Ann Surg* 1959;149:162-171.
438. Rozen, W. M., Ashton, M. W., Pan, W. R., et al. Anatomical variations in the harvest of anterolateral thigh flap perforators: a cadaveric and clinical study. *Microsurgery* 2009;29:16-23.
439. Jiang, T., Zhu, M., Zan, T., Gu, B., Li, Q. A Novel Augmented Reality-Based Navigation System in Perforator Flap Transplantation - A Feasibility Study. *Ann Plast Surg* 2017;79:192-196.
440. Hummelink, S., Verhulst, A. C., Maal, T. J. J., Hoogeveen, Y. L., Schultze Kool, L. J., Ulrich, D. J. O. An innovative method of planning and displaying flap volume in DIEP flap breast reconstructions. *J Plast Reconstr Aesthet Surg* 2017;70:871-875.
441. Gan, Q., Wang, D., Ye, J., et al. Benchtop and Animal Validation of a Projective Imaging System for Potential Use in Intraoperative Surgical Guidance. *PLoS One* 2016;11:e0157794.
442. Liu, Y., Bauer, A. Q., Akers, W. J., et al. Hands-free, wireless goggles for near-infrared fluorescence and real-time image-guided surgery. *Surgery* 2011;149:689-698.
443. Hummelink, S., Hameeteman, M., Hoogeveen, Y., Slump, C. H., Ulrich, D. J., Schultze Kool, L. J. Preliminary results using a newly developed projection method to visualize vascular anatomy prior to DIEP flap breast reconstruction. *J Plast Reconstr Aesthet Surg* 2014.
444. Hummelink, S., Schultze Kool, L. J., Ulrich, D. J. Displaying inguinal lymph nodes before transplantation in a deep inferior epigastric perforator flap breast reconstruction using an innovative projection method. *J Plast Reconstr Aesthet Surg* 2016;69:376-380.
445. Smit, J. M., Klein, S., Werker, P. M. An overview of methods for vascular mapping in the planning of free flaps. *J Plast Reconstr Aesthet Surg* 2010;63:e674-682.
446. Tregaskiss, A. P., Goodwin, A. N., Acland, R. D. The cutaneous arteries of the anterior abdominal wall: a three-dimensional study. *Plast Reconstr Surg* 2007;120:442-450.
447. Ma, C., Clifford, B., Liu, Y., et al. High-resolution dynamic 31 P-MRSI using a low-rank tensor model. *Magn Reson Med* 2017.
448. Caudell, T. P., Mizell, D. W. Augmented reality: an application of heads-up display technology to manual manufacturing processes. In *Twenty-Fifth International Conference on System Sciences,* Kauai, HI, USA1992.
449. Mann, S. Wearable computing: A first step toward personal imaging. *IEEE Comput* 1997;30:25-32.
450. Zeng, B., Meng, F., Ding, H., Wang, G. A surgical robot with augmented reality visualization for stereoelectroencephalography electrode implantation. *Int J Comput Assist Radiol Surg* 2017.
451. Murphy, R. J., Liacouras, P. C., Grant, G. T., Wolfe, K. C., Armand, M., Gordon, C. R. A Craniomaxillofacial Surgical Assistance Workstation for Enhanced Single-Stage Reconstruction Using Patient-Specific Implants. *J Craniofac Surg* 2016;27:2025-2030.

452. Marzano, E., Piardi, T., Soler, L., et al. Augmented reality-guided artery-first pancreatico-duodenectomy. *J Gastrointest Surg* 2013;17:1980-1983.
453. Tagaya, N., Aoyagi, H., Nakagawa, A., et al. A novel approach for sentinel lymph node identification using fluorescence imaging and image overlay navigation surgery in patients with breast cancer. *World J Surg* 2011;35:154-158.
454. Kim, Y., Kim, H., Kim, Y. O. Virtual Reality and Augmented Reality in Plastic Surgery: A Review. *Arch Plast Surg* 2017;44:179-187.
455. Losken, A., Seify, H., Denson, D. D., Paredes, A. A., Jr., Carlson, G. W. Validating three-dimensional imaging of the breast. *Ann Plast Surg* 2005;54:471-476; discussion 477-478.
456. Sotsuka, Y., Matsuda, K., Fujita, K., Fujiwara, T., Kakibuchi, M. Image overlay of deep inferior epigastric artery in breast reconstruction. *Plast Reconstr Surg Glob Open* 2014;2:e235.
457. Hackett, M. Medical holography for basic anatomy training. In *Interservice/Industry Training, Simulation, and Education Conference,* Orlando, FL, USA2013.
458. Makino, Y., Furuyama, Y., Inoue, S., Shinoda, H. HaptoClone (Haptic-Optical Clone) for mutual tele-environment by real-time 3D image transfer with midair force feedback. In *CHI Conference on Human Factors in Computing Systems,* Santa Clara, CA, USA2016.
459. Shons, A. R., Mosiello, G. Postmastectomy breast reconstruction: current techniques. *Cancer Control* 2001;8:419-426.
460. Spear, S. L., Onyewu, C. Staged breast reconstruction with saline-filled implants in the irradiated breast: recent trends and therapeutic implications. *Plast Reconstr Surg* 2000;105:930-942.
461. Czerny, V. Plastischer ersatz der brustdrusse durch ein lipom. *Drei Plastiche Operationen Verhand Deutsch Gesellsch Chir* 1895;24:216-217.
462. Hokin, J. A. Mastectomy reconstruction without a prosthetic implant. *Plast Reconstr Surg* 1983;72:810-818.
463. Marshall, D. R., Anstee, E. J., Stapleton, M. J. Soft tissue reconstruction of the breast using an extended composite latissimus dorsi myocutaneous flap. *Br J Plast Surg* 1984;37:361-368.
464. Germann, G., Steinau, H. U. Breast reconstruction with the extended latissimus dorsi flap. *Plast Reconstr Surg* 1996;97:519-526.
465. McCraw, J. B., Papp, C. T. Latissimus dorsi myocutaneous flap: "Fleur de lis" reconstruction. In C. R. Hartrampf ed., *Breast reconstruction with living tissue*. Norfolk, VA: Hampton Press; 1991:211.
466. Denewer, A., Setit, A., Hussein, O., Farouk, O. Skin-sparing mastectomy with immediate breast reconstruction by a new modification of extended latissimus dorsi myocutaneous flap. *World J Surg* 2008;32:2586-2592.
467. Taylor, G. I., Daniel, R. K. The anatomy of several free flap donor sites. *Plast Reconstr Surg* 1975;56:243-253.
468. Robbins, T. H. Rectus abdominis myocutaneous flap for breast reconstruction. *Aust N Z J Surg* 1979;49:527-530.
469. Cohen, B. E., Cronin, E. D. Breast reconstruction with the latissimus dorsi musculocutaneous flap. *Clin Plast Surg* 1984;11:287-302.
470. Nahabedian, M. Y., Momen, B., Galdino, G., Manson, P. N. Breast Reconstruction with the free TRAM or DIEP flap: patient selection, choice of flap, and outcome. *Plast Reconstr Surg* 2002;110:466-475; discussion 476-467.
471. Nahabedian, M. Y., Momen, B. Lower abdominal bulge after deep inferior epigastric perforator flap (DIEP) breast reconstruction. *Ann Plast Surg* 2005;54:124-129.
472. Taylor, G. I., Corlett, R. J., Boyd, J. B. The versatile deep inferior epigastric (inferior rectus abdominis) flap. *Br J Plast Surg* 1984;37:330-350.

473. Koshima, I., Moriguchi, T., Soeda, S., Tanaka, H., Umeda, N. Free thin paraumbilical perforator-based flaps. *Ann Plast Surg* 1992;29:12-17.
474. Kroll, S. S., Sharma, S., Koutz, C., et al. Postoperative morphine requirements of free TRAM and DIEP flaps. *Plast Reconstr Surg* 2001;107:338-341.
475. Gill, P. S., Hunt, J. P., Guerra, A. B., et al. A 10-year retrospective review of 758 DIEP flaps for breast reconstruction. *Plast Reconstr Surg* 2004;113:1153-1160.
476. Rozen, W. M., Rajkomar, A. K., Anavekar, N. S., Ashton, M. W. Post-mastectomy breast reconstruction: a history in evolution. *Clin Breast Cancer* 2009;9:145-154.
477. Taylor, G. I. The angiosomes of the body and their supply to perforator flaps. *Clin Plast Surg* 2003;30:331-342, v.
478. Taylor, G. I., Palmer, J. H. The vascular territories (angiosomes) of the body: experimental study and clinical applications. *Br J Plast Surg* 1987;40:113-141.
479. Manchot, C. Die Hautarterien des Menschlichen Korpers. *Leipzig: Vogel* 1889:1-120.
480. Manchot, C. *The cutaneous arteries of the human body (Ristic J, Morain WD, transls.)*. New York: Springer-Verlag; 1983.
481. Salmon, M., Taylor, G. I., Tempest, M. N. *Arteries of the skin*. London: Churchill Livingstone; 1987.
482. Milloy, F. J., Anson, B. J., McAfee, D. K. The rectus abdominis muscle and the epigastric arteries. *Surg Gynecol Obstet* 1960;110:293-302.
483. Tansatit, T., Chokrungvaranont, P., Sanguansit, P., Wanidchaphloi, S. Neurovascular anatomy of the deep inferior epigastric perforator flap for breast reconstruction. *J Med Assoc Thai* 2006;89:1630-1640.
484. Ohjimi, H., Era, K., Fujita, T., Tanaka, T., Yabuuchi, R. Analyzing the vascular architecture of the free TRAM flap using intraoperative ex vivo angiography. *Plast Reconstr Surg* 2005;116:106-113.
485. Ohjimi, H., Era, K., Tanahashi, S., Kawano, K., Manabe, T., Naitoh, M. Ex vivo intraoperative angiography for rectus abdominis musculocutaneous free flaps. *Plast Reconstr Surg* 2002;109:2247-2256.
486. Itoh, Y., Arai, K. The deep inferior epigastric artery free skin flap: anatomic study and clinical application. *Plast Reconstr Surg* 1993;91:853-863; discussion 864.
487. El-Mrakby, H. H., Milner, R. H. The vascular anatomy of the lower anterior abdominal wall: a microdissection study on the deep inferior epigastric vessels and the perforator branches. *Plast Reconstr Surg* 2002;109:539-543; discussion 544-537.
488. Heitmann, C., Felmerer, G., Durmus, C., Matejic, B., Ingianni, G. Anatomical features of perforator blood vessels in the deep inferior epigastric perforator flap. *Br J Plast Surg* 2000;53:205-208.
489. Kikuchi, N., Murakami, G., Kashiwa, H., Homma, K., Sato, T. J., Ogino, T. Morphometrical study of the arterial perforators of the deep inferior epigastric perforator flap. *Surg Radiol Anat* 2001;23:375-381.
490. Rozen, W. M., Palmer, K. P., Suami, H., et al. The DIEA branching pattern and its relationship to perforators: the importance of preoperative computed tomographic angiography for DIEA perforator flaps. *Plast Reconstr Surg* 2008;121:367-373.
491. Hyakusoku, H., Gao, J. H. The "super-thin" flap. *Br J Plast Surg* 1994;47:457-464.
492. Rozen, W. M., Grinsell, D., Koshima, I., Ashton, M. W. Dominance between angiosome and perforator territories: a new anatomical model for the design of perforator flaps. *J Reconstr Microsurg* 2010;26:539-545.
493. Shayan, R., Rozen, W. M., Bernard, S., Corlett, R. J., Ashton, M. W., Taylor, G. I. Perforator dilatation induced by body weight gain is not reversed by subsequent weight loss: implications for perforator flaps. *Plast Reconstr Surg* 2008;122:1765-1772.

494. Munhoz, A. M., Ishida, L. H., Sturtz, G. P., et al. Importance of lateral row perforator vessels in deep inferior epigastric perforator flap harvesting. *Plast Reconstr Surg* 2004;113:517-524.
495. Shoaib, T., Marucci, D. Adjacent angiosomes instead of zones II and III: reply to "Perfusion zones of the DIEP flap revisited--a clinical study". *Plast Reconstr Surg* 2006;118:817-818; author reply 818.
496. English, J. M., Tittle, B. J., Barton, F. E. Breast cancer, cancer prophylaxis, and breast reconstruction. *Select Readings Plast Surg* 1994;29:1-36.
497. Dinner, M. I., Dowden, R. V., Scheflan, M. Refinements in the use of the transverse abdominal island flap for postmastectomy reconstruction. *Ann Plast Surg* 1983;11:362-372.
498. Hallock, G. G. Physiological studies using laser Doppler flowmetry to compare blood flow to the zones of the free TRAM flap. *Ann Plast Surg* 2001;47:229-233.
499. Keller, A. Perfusion zones of the DIEP flap revisited: a clinical study. *Plast Reconstr Surg* 2006;118:1076-1077; author reply 1077.
500. Tregaskiss, A. Perfusion zones of the DIEP flap revisited: a clinical study. *Plast Reconstr Surg* 2006;118:816; author reply 816-817.
501. Carramenha e Costa, M. A., Carriquiry, C., Vasconez, L. O., Grotting, J. C., Herrera, R. H., Windle, B. H. An anatomic study of the venous drainage of the transverse rectus abdominis musculocutaneous flap. *Plast Reconstr Surg* 1987;79:208-217.
502. Blondeel, P. N., Arnstein, M., Verstraete, K., et al. Venous congestion and blood flow in free transverse rectus abdominis myocutaneous and deep inferior epigastric perforator flaps. *Plast Reconstr Surg* 2000;106:1295-1299.
503. Wechselberger, G., Schoeller, T., Bauer, T., Ninkovic, M., Otto, A., Ninkovic, M. Venous superdrainage in deep inferior epigastric perforator flap breast reconstruction. *Plast Reconstr Surg* 2001;108:162-166.
504. Hadad, I., Ibrahim, A. M., Lin, S. J., Lee, B. T. Augmented SIEA flap for microvascular breast reconstruction after prior ligation of bilateral deep inferior epigastric arteries. *J Plast Reconstr Aesthet Surg* 2013;66:845-847.
505. Spiegel, A. J., Khan, F. N. An Intraoperative algorithm for use of the SIEA flap for breast reconstruction. *Plast Reconstr Surg* 2007;120:1450-1459.
506. Gregoric, M., Flis, V., Milotic, F., Mrda, B., Stirn, B., Arnez, Z. M. Delaying the superficial inferior epigastric artery flap: a solution to the problem of the small calibre of the donor artery. *J Plast Reconstr Aesthet Surg* 2011;64:1181-1186.
507. Shaw, W. W. Superior gluteal free flap breast reconstruction. *Clin Plast Surg* 1998;25:267-274.
508. Codner, M. A., Nahai, F. The gluteal free flap breast reconstruction. Making it work. *Clin Plast Surg* 1994;21:289-296.
509. Allen, R. J., Tucker, C., Jr. Superior gluteal artery perforator free flap for breast reconstruction. *Plast Reconstr Surg* 1995;95:1207-1212.
510. Weiler-Mithoff, E., Hodgson, E. L., Malata, C. M. Perforator flap breast reconstruction. *Breast Dis* 2002;16:93-106.
511. Allen, R. J., Haddock, N. T., Ahn, C. Y., Sadeghi, A. Breast reconstruction with the profunda artery perforator flap. *Plast Reconstr Surg* 2012;129:16e-23e.
512. Serletti, J. M., Moran, S. L. The combined use of the TRAM and expanders/implants in breast reconstruction. *Ann Plast Surg* 1998;40:510-514.
513. Spear, S. L., Wolfe, A. J. The coincidence of TRAM flaps and prostheses in the setting of breast reconstruction. *Plast Reconstr Surg* 2002;110:478-486.
514. Moran, S. L., Herceg, S., Kurtelawicz, K., Serletti, J. M. TRAM flap breast reconstruction with expanders and implants. *AORN J* 2000;71:354-362; quiz 363-358.
515. Figus, A., Canu, V., Iwuagwu, F. C., Ramakrishnan, V. DIEP flap with implant: a further option in optimising breast reconstruction. *J Plast Reconstr Aesthet Surg* 2009;62:1118-1126.

516. Roehl, K. R., Baumann, D. P., Chevray, P. M., Chang, D. W. Evaluation of outcomes in breast reconstructions combining lower abdominal free flaps and permanent implants. *Plast Reconstr Surg* 2010;126:349-357.
517. Moore, T. S., Farrell, L. D. Latissimus dorsi myocutaneous flap for breast reconstruction: long-term results. *Plast Reconstr Surg* 1992;89:666-672; discussion 673-664.
518. Kronowitz, S. J., Robb, G. L., Youssef, A., et al. Optimizing autologous breast reconstruction in thin patients. *Plast Reconstr Surg* 2003;112:1768-1778.
519. Figus, A., Fioramonti, P., Ramakrishnan, V. Stacked free SIEA/DIEP flap for unilateral breast reconstruction in a thin patient with an abdominal vertical midline scar. *J Reconstr Microsurg* 2007;23:523-525.
520. Pennington, D. G., Nettle, W. J., Lam, P. Microvascular augmentation of the blood supply of the contralateral side of the free transverse rectus abdominis musculocutaneous flap. *Ann Plast Surg* 1993;31:123-126; discussion 126-127.
521. Ali, R. S., Garrido, A., Ramakrishnan, V. Stacked free hemi-DIEP flaps: a method of autologous breast reconstruction in a patient with midline abdominal scarring. *Br J Plast Surg* 2002;55:351-353.
522. Schoeller, T., Wechselberger, G., Roger, J., Hussl, H., Huemer, G. M. Management of infraumbilical vertical scars in DIEP-flaps by crossover anastomosis. *J Plast Reconstr Aesthet Surg* 2007;60:524-528.
523. Shafighi, M., Constantinescu, M. A., Huemer, G. M., et al. The extended diep flap: extending the possibilities for breast reconstruction with tissue from the lower abdomen. *Microsurgery* 2013;33:24-31.
524. Rozen, W. M., Ashton, M. W., Taylor, G. I. Re: The extended diep flap: extending the possibilities for breast reconstruction with tissue from the lower abdomen. *Microsurgery* 2013;33:166-167.
525. Tepper, O. M., Karp, N. S., Small, K., et al. Three-dimensional imaging provides valuable clinical data to aid in unilateral tissue expander-implant breast reconstruction. *Breast J* 2008;14:543-550.
526. Galdino, G. M., Nahabedian, M., Chiaramonte, M., Geng, J. Z., Klatsky, S., Manson, P. Clinical applications of three-dimensional photography in breast surgery. *Plast Reconstr Surg* 2002;110:58-70.
527. Hudson, D. A. Factors determining shape and symmetry in immediate breast reconstruction. *Ann Plast Surg* 2004;52:15-21.
528. Kovacs, L., Zimmermann, A., Papadopulos, N. A., Biemer, E. Re: factors determining shape and symmetry in immediate breast reconstruction. *Ann Plast Surg* 2004;53:192-194.
529. Lee, H. Y., Hong, K., Kim, E. A. Measurement protocol of women's nude breasts using a 3D scanning technique. *Appl Ergon* 2004;35:353-359.
530. Bulstrode, N., Bellamy, E., Shrotria, S. Breast volume assessment: comparing five different techniques. *Breast* 2001;10:117-123.
531. Bouman, F. G. Volumetric measurement of the human breast and breast tissue before and during mammaplasty. *Br J Plast Surg* 1970;23:263-264.
532. Schultz, R. C., Dolezal, R. F., Nolan, J. Further applications of Archimedes' principle in the correction of asymmetrical breasts. *Ann Plast Surg* 1986;16:98-101.
533. Tezel, E., Numanoglu, A. Practical do-it-yourself device for accurate volume measurement of breast. *Plast Reconstr Surg* 2000;105:1019-1023.
534. Edsander-Nord, A., Wickman, M., Jurell, G. Measurement of breast volume with thermoplastic casts. *Scand J Plast Reconstr Surg Hand Surg* 1996;30:129-132.
535. Westreich, M. Anthropomorphic breast measurement: protocol and results in 50 women with aesthetically perfect breasts and clinical application. *Plast Reconstr Surg* 1997;100:468-479.

536. Longo, B., Farcomeni, A., Ferri, G., Campanale, A., Sorotos, M., Santanelli, F. The BREAST-V: a unifying predictive formula for volume assessment in small, medium, and large breasts. *Plast Reconstr Surg* 2013;132:1e-7e.
537. Katariya, R. N., Forrest, A. P., Gravelle, I. H. Breast volumes in cancer of the breast. *Br J Cancer* 1974;29:270-273.
538. Malini, S., Smith, E. O., Goldzieher, J. W. Measurement of breast volume by ultrasound during normal menstrual cycles and with oral contraceptive use. *Obstet Gynecol* 1985;66:538-541.
539. Sotsuka, Y., Fujikawa, M., Izumi, K. Volume of deep inferior epigastric perforator flap quantified preoperatively by using 64-multidetector-row computed tomography. *J Plast Reconstr Aesthet Surg* 2012;65:1601-1603.
540. Kim, H., Mun, G. H., Wiraatmadja, E. S., et al. Preoperative magnetic resonance imaging-based breast volumetry for immediate breast reconstruction. *Aesthetic Plast Surg* 2015;39:369-376.
541. Kovacs, L., Eder, M., Hollweck, R., et al. New aspects of breast volume measurement using 3-dimensional surface imaging. *Ann Plast Surg* 2006;57:602-610.
542. Mailey, B., Freel, A., Wong, R., Pointer, D. T., Khoobehi, K. Clinical accuracy and reproducibility of Portrait 3D Surgical Simulation Platform in breast augmentation. *Aesthet Surg J* 2013;33:84-92.
543. Liu, C., Luan, J., Mu, L., Ji, K. The role of three-dimensional scanning technique in evaluation of breast asymmetry in breast augmentation: a 100-case study. *Plast Reconstr Surg* 2010;126:2125-2132.
544. de Menezes, M., Rosati, R., Ferrario, V. F., Sforza, C. Accuracy and reproducibility of a 3-dimensional stereophotogrammetric imaging system. *J Oral Maxillofac Surg* 2010;68:2129-2135.
545. Catherwood, T., McCaughan, E., Greer, E., Spence, R. A., McIntosh, S. A., Winder, R. J. Validation of a passive stereophotogrammetry system for imaging of the breast: a geometric analysis. *Med Eng Phys* 2011;33:900-905.
546. Hill, S. M., Huettner, F., Murray, J., Elwood, E., Barrick, R., Jones, G. Contribution of breast density to the volume of the augmented breast: A preliminary study. *Can J Plast Surg* 2011;19:93-96.
547. de Heras Ciechomski, P., Constantinescu, M., Garcia, J., et al. Development and implementation of a web-enabled 3D consultation tool for breast augmentation surgery based on 3D-image reconstruction of 2D pictures. *J Med Internet Res* 2012;14:e21.
548. Yoo, A., Minn, K. W., Jin, U. S. Magnetic resonance imaging-based volumetric analysis and its relationship to actual breast weight. *Arch Plast Surg* 2013;40:203-208.
549. Roostaeian, J., Adams, W. P., Jr. Three-Dimensional Imaging for Breast Augmentation: Is This Technology Providing Accurate Simulations? *Aesthet Surg J* 2014;34:857-875.
550. Yip, J. M., Mouratova, N., Jeffery, R. M., Veitch, D. E., Woodman, R. J., Dean, N. R. Accurate assessment of breast volume: a study comparing the volumetric gold standard (direct water displacement measurement of mastectomy specimen) with a 3D laser scanning technique. *Ann Plast Surg* 2012;68:135-141.
551. Veitch, D., Burford, K., Dench, P., Dean, N., Griffin, P. Measurement of breast volume using body scan technology(computer-aided anthropometry). *Work* 2012;41 Suppl 1:4038-4045.
552. Koch, M. C., Adamietz, B., Jud, S. M., et al. Breast volumetry using a three-dimensional surface assessment technique. *Aesthetic Plast Surg* 2011;35:847-855.
553. Henseler, H., Khambay, B. S., Bowman, A., et al. Investigation into accuracy and reproducibility of a 3D breast imaging system using multiple stereo cameras. *J Plast Reconstr Aesthet Surg* 2011;64:577-582.

554. Thomson, J. G., Kerrigan, C. L. Dermofluorometry: thresholds for predicting flap survival. *Plast Reconstr Surg* 1989;83:859-864; discussion 865.
555. Eder, M., Schneider, A., Feussner, H., et al. [Breast volume assessment based on 3D surface geometry: verification of the method using MR imaging]. *Biomed Tech (Berl)* 2008;53:112-121.
556. Kovacs, L., Eder, M., Hollweck, R., et al. Comparison between breast volume measurement using 3D surface imaging and classical techniques. *Breast* 2007;16:137-145.
557. Isogai, N., Sai, K., Kamiishi, H., Watatani, M., Inui, H., Shiozaki, H. Quantitative analysis of the reconstructed breast using a 3-dimensional laser light scanner. *Ann Plast Surg* 2006;56:237-242.
558. Caruso, M. K., Guillot, T. S., Nguyen, T., Greenway, F. L. The cost effectiveness of three different measures of breast volume. *Aesthetic Plast Surg* 2006;30:16-20.
559. Campaigne, B. N., Katch, V. L., Freedson, P., Sady, S., Katch, F. I. Measurement of breast volume in females: description of a reliable method. *Ann Hum Biol* 1979;6:363-367.
560. Tzou, C. H., Artner, N. M., Pona, I., et al. Comparison of three-dimensional surface-imaging systems. *J Plast Reconstr Aesthet Surg* 2014;67:489-497.
561. Chang, J. B., Small, K. H., Choi, M., Karp, N. S. Three-dimensional surface imaging in plastic surgery: foundation, practical applications, and beyond. *Plast Reconstr Surg* 2015;135:1295-1304.
562. Palin, W. E., Jr., von Fraunhofer, J. A., Smith, D. J., Jr. Measurement of breast volume: comparison of techniques. *Plast Reconstr Surg* 1986;77:253-255.
563. Kayar, R., Civelek, S., Cobanoglu, M., Gungor, O., Catal, H., Emiroglu, M. Five methods of breast volume measurement: a comparative study of measurements of specimen volume in 30 mastectomy cases. *Breast Cancer (Auckl)* 2011;5:43-52.
564. Qiao, Q., Zhou, G., Ling, Y. Breast volume measurement in young Chinese women and clinical applications. *Aesthetic Plast Surg* 1997;21:362-368.
565. Brown, R. W., Cheng, Y. C., Kurtay, M. A formula for surgical modifications of the breast. *Plast Reconstr Surg* 2000;106:1342-1345.
566. Sigurdson, L. J., Kirkland, S. A. Breast volume determination in breast hypertrophy: an accurate method using two anthropomorphic measurements. *Plast Reconstr Surg* 2006;118:313-320.
567. Kalbhen, C. L., McGill, J. J., Fendley, P. M., Corrigan, K. W., Angelats, J. Mammographic determination of breast volume: comparing different methods. *AJR Am J Roentgenol* 1999;173:1643-1649.
568. Pozzobon, A. V., Sabino Neto, M., Veiga, D. F., et al. Magnetic resonance images and linear measurements in the surgical treatment of breast asymmetry. *Aesthetic Plast Surg* 2009;33:196-203.
569. Herold, C., Reichelt, A., Stieglitz, L. H., et al. MRI-based breast volumetry-evaluation of three different software solutions. *J Digit Imaging* 2010;23:603-610.
570. Hill, D. L., Berg, D. C., Raso, V. J., et al. Evaluation of a laser scanner for surface topography. *Stud Health Technol Inform* 2002;88:90-94.
571. Kovacs, L., Yassouridis, A., Zimmermann, A., et al. Optimization of 3-dimensional imaging of the breast region with 3-dimensional laser scanners. *Ann Plast Surg* 2006;56:229-236.
572. Liu, C., Luan, J., Ji, K., Sun, J. Measuring volumetric change after augmentation mammaplasty using a three-dimensional scanning technique: an innovative method. *Aesthetic Plast Surg* 2012;36:1134-1139.
573. Rosati, R., De Menezes, M., Rossetti, A., Sforza, C., Ferrario, V. F. Digital dental cast placement in 3-dimensional, full-face reconstruction: a technical evaluation. *Am J Orthod Dentofacial Orthop* 2010;138:84-88.

574. Khambay, B., Nairn, N., Bell, A., Miller, J., Bowman, A., Ayoub, A. F. Validation and reproducibility of a high-resolution three-dimensional facial imaging system. *Br J Oral Maxillofac Surg* 2008;46:27-32.
575. Lubbers, H. T., Medinger, L., Kruse, A., Gratz, K. W., Matthews, F. Precision and accuracy of the 3dMD photogrammetric system in craniomaxillofacial application. *J Craniofac Surg* 2010;21:763-767.
576. Al-Anezi, T., Khambay, B., Peng, M. J., O'Leary, E., Ju, X., Ayoub, A. A new method for automatic tracking of facial landmarks in 3D motion captured images (4D). *Int J Oral Maxillofac Surg* 2013;42:9-18.
577. Shujaat, S., Khambay, B. S., Ju, X., et al. The clinical application of three-dimensional motion capture (4D): a novel approach to quantify the dynamics of facial animations. *Int J Oral Maxillofac Surg* 2014;43:907-916.
578. Popat, H., Richmond, S., Benedikt, L., Marshall, D., Rosin, P. L. Quantitative analysis of facial movement--a review of three-dimensional imaging techniques. *Comput Med Imaging Graph* 2009;33:377-383.
579. Popat, H., Richmond, S., Marshall, D., Rosin, P. L. Facial movement in 3 dimensions: average templates of lip movement in adults. *Otolaryngol Head Neck Surg* 2011;145:24-29.
580. Popat, H., Richmond, S., Playle, R., Marshall, D., Rosin, P., Cosker, D. Three-dimensional motion analysis - an exploratory study. Part 1: assessment of facial movement. *Orthod Craniofac Res* 2008;11:216-223.
581. Wilmore, J. H., Atwater, A. E., Maxwell, B. D., Wilmore, D. L., Constable, S. H., Buono, M. J. Alterations in breast morphology consequent to a 21-day bust developer program. *Med Sci Sports Exerc* 1985;17:106-112.
582. Kirianoff, T. G. Volume measurements of unequal breasts. *Plast Reconstr Surg* 1974;54:616.
583. Tegtmeier, R. E. A quick, accurate mammometer. *Ann Plast Surg* 1978;1:625-626.
584. Ward, C., Harrison, B. The search for volumetric symmetry in reconstruction of the breast after mastectomy. *Br J Plast Surg* 1986;39:379-385.
585. Wilkie, T., Ship, A. G. Volumetric breast measurement during surgery. *Aesthetic Plast Surg* 1976;1:301-305.
586. Losken, A., Fishman, I., Denson, D. D., Moyer, H. R., Carlson, G. W. An objective evaluation of breast symmetry and shape differences using 3-dimensional images. *Ann Plast Surg* 2005;55:571-575.
587. Penn, J. Breast reduction. *Br J Plast Surg* 1955;7:357-371.
588. Smith, D. J., Jr., Palin, W. E., Jr., Katch, V. L., Bennett, J. E. Breast volume and anthropomorphic measurements: normal values. *Plast Reconstr Surg* 1986;78:331-335.
589. Grossman, A. J., Roudner, L. A. A simple means for accurate breast volume determination. *Plast Reconstr Surg* 1980;66:851-852.
590. Rohrich, R. J., Hartley, W., Brown, S. Incidence of breast and chest wall asymmetry in breast augmentation: a retrospective analysis of 100 patients. *Plast Reconstr Surg* 2006;118:7S-13S; discussion 14S, 15S-17S.
591. Jacobs, R. A., Plastic Surgery Educational Foundation, D. C. Three-dimensional photography. *Plast Reconstr Surg* 2001;107:276-277.
592. Harding, C., Pompei, F., Burmistrov, D., Welch, H. G., Abebe, R., Wilson, R. Breast Cancer Screening, Incidence, and Mortality Across US Counties. *JAMA Intern Med* 2015.
593. Da Silveira, A. C., Daw, J. L., Jr., Kusnoto, B., Evans, C., Cohen, M. Craniofacial applications of three-dimensional laser surface scanning. *J Craniofac Surg* 2003;14:449-456.
594. Neal, A. J., Torr, M., Helyer, S., Yarnold, J. R. Correlation of breast dose heterogeneity with breast size using 3D CT planning and dose-volume histograms. *Radiother Oncol* 1995;34:210-218.

595. Fujii, T., Yamaguchi, S., Yajima, R., Tsutsumi, S., Asao, T., Kuwano, H. Accurate assessment of breast volume by computed tomography using three-dimensional imaging device. *Am Surg* 2012;78:933-935.
596. Fowler, P. A., Casey, C. E., Cameron, G. G., Foster, M. A., Knight, C. H. Cyclic changes in composition and volume of the breast during the menstrual cycle, measured by magnetic resonance imaging. *Br J Obstet Gynaecol* 1990;97:595-602.
597. Thalmaan-Degen, P. *Die stereogrammetrie: ein diagnostisches hilfsmittel in der kieferorthopaedie (Stereophotogrammetry: a diagnostic device in orthodontology)*. Zurich, Switzerland: University of Zurich; 1944.
598. Tanner, J. M., Weiner, J. S. The reliability of the photogrammetric method of anthropometry, with a description of a miniature camera technique. *Am J Phys Anthropol* 1949;7:145-186.
599. Beard, L. F., Burke, P. H. Evolution of a system of stereophotogrammetry for the study of facial morphology. *Med Biol Illus* 1967;17:20-25.
600. Burke, P. Serial stereophotogrammetric measurements of the soft tissues of the face. A case of a girl with mild facial asymmetry from 3 weeks to 10 years of age. *Br Dent J* 1983;155:373-379.
601. Burke, P. Four-dimensional facial change. *Br J Orthod* 1984;11:170-184.
602. Ferrario, V. F., Sforza, C., Dellavia, C., Vizzotto, L., Caru, A. Three-dimensional nasal morphology in cleft lip and palate operated adult patients. *Ann Plast Surg* 2003;51:390-397.
603. Nahabedian, M. Y., Galdino, G. Symmetrical breast reconstruction: is there a role for three-dimensional digital photography? *Plast Reconstr Surg* 2003;112:1582-1590.
604. Neely, J. G., Cheung, J. Y., Wood, M., Byers, J., Rogerson, A. Computerized quantitative dynamic analysis of facial motion in the paralyzed and synkinetic face. *Am J Otol* 1992;13:97-107.
605. Inokuchi, I., Sato, K., Ozaki, Y. Range-imaging system for 3-D range imaging. In *7th ICPR Proceeding,* Montreal, Canada1984.
606. Meier-Gallati, V., Scriba, H., Fisch, U. Objective scaling of facial nerve function based on area analysis (OSCAR). *Otolaryngol Head Neck Surg* 1998;118:545-550.
607. Moss, J. P., Coombes, A. M., Linney, A. D., Campos, J. Methods of three dimensional analysis of patients with asymmetry of the face. *Proc Finn Dent Soc* 1991;87:139-149.
608. Esme, D. L., Bucksch, A., Beekman, W. H. Three-dimensional laser imaging as a valuable tool for specifying changes in breast shape after augmentation mammaplasty. *Aesthetic Plast Surg* 2009;33:191-195.
609. Bush, K., Antonyshyn, O. Three-dimensional facial anthropometry using a laser surface scanner: validation of the technique. *Plast Reconstr Surg* 1996;98:226-235.
610. Moss, J. P., Grindrod, S. R., Linney, A. D., Arridge, S. R., James, D. A computer system for the interactive planning and prediction of maxillofacial surgery. *Am J Orthod Dentofacial Orthop* 1988;94:469-475.
611. Bajaj-Luthra, A., Mueller, T., Johnson, P. C. Quantitative analysis of facial motion components: anatomic and nonanatomic motion in normal persons and in patients with complete facial paralysis. *Plast Reconstr Surg* 1997;99:1894-1902; discussion 1903-1894.
612. Ferrario, V. F., Sforza, C., Poggio, C. E., Tartaglia, G. Distance from symmetry: a three-dimensional evaluation of facial asymmetry. *J Oral Maxillofac Surg* 1994;52:1126-1132.
613. Trotman, C. A., Gross, M. M., Moffatt, K. Reliability of a three-dimensional method for measuring facial animation: a case report. *Angle Orthod* 1996;66:195-198.
614. Frey, M., Giovanoli, P., Gerber, H., Slameczka, M., Stussi, E. Three-dimensional video analysis of facial movements: a new method to assess the quantity and quality of the smile. *Plast Reconstr Surg* 1999;104:2032-2039.

615. Takasaki, H. Moire topography. *Appl Opt* 1970;9:1467-1472.
616. Hajeer, M. Y., Ayoub, A. F., Millett, D. T., Bock, M., Siebert, J. P. Three-dimensional imaging in orthognathic surgery: the clinical application of a new method. *Int J Adult Orthodon Orthognath Surg* 2002;17:318-330.
617. Thomson, J. G., Liu, Y. J., Restifo, R. J., Rinker, B. D., Reis, A. Surface area measurement of the female breast: phase I. Validation of a novel optical technique. *Plast Reconstr Surg* 2009;123:1588-1596.
618. Olesen, O. V., Paulsen, R. R., Hojgaar, L., Roed, B., Larsen, R. Motion tracking in narrow spaces: a structured light approach. *Med Image Comput Comput Assist Interv* 2010;13:253-260.
619. Lane, C., Harrell, W., Jr. Completing the 3-dimensional picture. *Am J Orthod Dentofacial Orthop* 2008;133:612-620.
620. Tepper, O. M., Unger, J. G., Small, K. H., et al. Mammometrics: the standardization of aesthetic and reconstructive breast surgery. *Plast Reconstr Surg* 2010;125:393-400.
621. Tepper, O. M., Small, K., Rudolph, L., Choi, M., Karp, N. Virtual 3-dimensional modeling as a valuable adjunct to aesthetic and reconstructive breast surgery. *Am J Surg* 2006;192:548-551.
622. Eder, M., Kloppel, M., Muller, D., Papadopulos, N. A., Machens, H. G., Kovacs, L. 3-D analysis of breast morphology changes after inverted T-scar and vertical-scar reduction mammaplasty over 12 months. *J Plast Reconstr Aesthet Surg* 2013;66:776-786.
623. Eder, M., v Waldenfels, F., Sichtermann, M., et al. Three-dimensional evaluation of breast contour and volume changes following subpectoral augmentation mammaplasty over 6 months. *J Plast Reconstr Aesthet Surg* 2011;64:1152-1160.
624. Kovacs, L., Eder, M., Papadopulos, N. A., Biemer, E. Validating 3-dimensional imaging of the breast. *Ann Plast Surg* 2005;55:695-696.
625. Kovacs, L., Eder, M., Zimmermann, A., et al. Three-dimensional evaluation of breast augmentation and the influence of anatomic and round implants on operative breast shape changes. *Aesthetic Plast Surg* 2012;36:879-887.
626. Tepper, O. M., Choi, M., Small, K., et al. An innovative three-dimensional approach to defining the anatomical changes occurring after short scar-medial pedicle reduction mammaplasty. *Plast Reconstr Surg* 2008;121:1875-1885.
627. Tepper, O. M., Small, K. H., Unger, J. G., et al. 3D analysis of breast augmentation defines operative changes and their relationship to implant dimensions. *Ann Plast Surg* 2009;62:570-575.
628. Kau, C. H., Zhurov, A., Scheer, R., Bouwman, S., Richmond, S. The feasibility of measuring three-dimensional facial morphology in children. *Orthod Craniofac Res* 2004;7:198-204.
629. Geng, J. Structured-light 3D surface imaging: a tutorial. *Adv Opt Phot* 2011;3:128-160.
630. Zha, X. P., Du, F., Gao, J. H., et al. [Three-dimensional breast non-contact measurement]. *Di Yi Jun Yi Da Xue Xue Bao* 2005;25:262-266.
631. Daly, S. E., Kent, J. C., Huynh, D. Q., et al. The determination of short-term breast volume changes and the rate of synthesis of human milk using computerized breast measurement. *Exp Physiol* 1992;77:79-87.
632. Malata, C. M., Boot, J. C., Bradbury, E. T., Ramli, A. R., Sharpe, D. T. Congenital breast asymmetry: subjective and objective assessment. *Br J Plast Surg* 1994;47:95-102.
633. Creasman, C. N., Mordaunt, D., Liolios, T., Chiu, C., Gabriel, A., Maxwell, G. P. Four-dimensional breast imaging, part I: introduction of a technology-driven, evidence-based approach to breast augmentation planning. *Aesthet Surg J* 2011;31:914-924.
634. Gabriel, A., Fritzsche, S., Creasman, C., Baqai, W., Mordaunt, D., Maxwell, G. P. Incidence of breast and chest wall asymmetries: 4D photography. *Aesthet Surg J* 2011;31:506-510.

635. Halazonetis, D. J. Acquisition of 3-dimensional shapes from images. *Am J Orthod Dentofacial Orthop* 2001;119:556-560.
636. Moyer, H. R., Carlson, G. W., Styblo, T. M., Losken, A. Three-dimensional digital evaluation of breast symmetry after breast conservation therapy. *J Am Coll Surg* 2008;207:227-232.
637. Ji, K., Luan, J., Liu, C., et al. A prospective study of breast dynamic morphological changes after dual-plane augmentation mammaplasty with 3D scanning technique. *PLoS One* 2014;9:e93010.
638. Quan, M., Fadl, A., Small, K., et al. Defining pseudoptosis (bottoming out) 3 years after short-scar medial pedicle breast reduction. *Aesthetic Plast Surg* 2011;35:357-364.
639. Winder, R. J., Darvann, T. A., McKnight, W., Magee, J. D., Ramsay-Baggs, P. Technical validation of the Di3D stereophotogrammetry surface imaging system. *Br J Oral Maxillofac Surg* 2008;46:33-37.
640. Fourie, Z., Damstra, J., Gerrits, P. O., Ren, Y. Evaluation of anthropometric accuracy and reliability using different three-dimensional scanning systems. *Forensic Sci Int* 2011;207:127-134.
641. Schendel, S. A., Montgomery, K. A Web-based, integrated simulation system for craniofacial surgical planning. *Plast Reconstr Surg* 2009;123:1099-1106.
642. Maal, T. J., van Loon, B., Plooij, J. M., et al. Registration of 3-dimensional facial photographs for clinical use. *J Oral Maxillofac Surg* 2010;68:2391-2401.
643. Aldridge, K., Boyadjiev, S. A., Capone, G. T., DeLeon, V. B., Richtsmeier, J. T. Precision and error of three-dimensional phenotypic measures acquired from 3dMD photogrammetric images. *Am J Med Genet A* 2005;138A:247-253.
644. Chen, Z. C., Albdour, M. N., Lizardo, J. A., Chen, Y. A., Chen, P. K. Precision of three-dimensional stereo-photogrammetry (3dMD) in anthropometry of the auricle and its application in microtia reconstruction. *J Plast Reconstr Aesthet Surg* 2015;68:622-631.
645. Reece, G. P., Merchant, F., Andon, J., et al. 3D surface imaging of the human female torso in upright to supine positions. *Med Eng Phys* 2015;37:375-383.
646. Oliveira-Santos, T., Baumberger, C., Constantinescu, M., et al. 3D face reconstruction from 2D pictures: first results of a web-based computer aided system for aesthetic procedures. *Ann Biomed Eng* 2013;41:952-966.
647. Tzou, C. H., Frey, M. Evolution of 3D surface imaging systems in facial plastic surgery. *Facial Plast Surg Clin North Am* 2011;19:591-602, vii.
648. Al-Hiyali, A., Ayoub, A., Ju, X., Almuzian, M., Al-Anezi, T. The Impact of Orthognathic Surgery on Facial Expressions. *J Oral Maxillofac Surg* 2015.
649. Chhaya, M. P., Melchels, F. P., Holzapfel, B. M., Baldwin, J. G., Hutmacher, D. W. Sustained regeneration of high-volume adipose tissue for breast reconstruction using computer aided design and biomanufacturing. *Biomaterials* 2015;52:551-560.
650. Kiarashi, N., Nolte, A. C., Sturgeon, G. M., et al. Development of realistic physical breast phantoms matched to virtual breast phantoms based on human subject data. *Med Phys* 2015;42:4116.
651. Melchels, F., Wiggenhauser, P. S., Warne, D., et al. CAD/CAM-assisted breast reconstruction. *Biofabrication* 2011;3:034114.
652. Siva, S., Chesson, B., Callahan, J. W., et al. Dosimetric Consequences of 3D Versus 4D PET/CT for Target Delineation of Lung Stereotactic Radiotherapy. *J Thorac Oncol* 2015;10:1112-1115.
653. Meattini, I., Marrazzo, L., Zani, M., et al. Four-dimensional computed tomography in accelerated partial breast irradiation planning: single series from a phase III trial. *Radiol Med* 2015.
654. Siva, S., Pham, D., Gill, S., et al. An analysis of respiratory induced kidney motion on four-dimensional computed tomography and its implications for stereotactic kidney radiotherapy. *Radiat Oncol* 2013;8:248.

655. Huguet, F., Yorke, E. D., Davidson, M., et al. Modeling pancreatic tumor motion using 4-dimensional computed tomography and surrogate markers. *Int J Radiat Oncol Biol Phys* 2015;91:579-587.
656. Wettstein, R., Tremp, M., Baumberger, M., Schaefer, D. J., Kalbermatten, D. F. Local flap therapy for the treatment of pressure sore wounds. *Int Wound J* 2013.
657. Saint-Cyr, M., Wong, C., Schaverien, M., Mojallal, A., Rohrich, R. J. The perforasome theory: vascular anatomy and clinical implications. *Plast Reconstr Surg* 2009;124:1529-1544.
658. Stekelenburg, C. M., Sonneveld, P. M., Bouman, M. B., et al. The hand held Doppler device for the detection of perforators in reconstructive surgery: what you hear is not always what you get. *Burns* 2014;40:1702-1706.
659. Khan, U. D., Miller, J. G. Reliability of handheld Doppler in planning local perforator-based flaps for extremities. *Aesthetic Plast Surg* 2007;31:521-525.
660. Imai, R., Matsumura, H., Tanaka, K., Uchida, R., Watanabe, K. Comparison of Doppler sonography and multidetector-row computed tomography in the imaging findings of the deep inferior epigastric perforator artery. *Ann Plast Surg* 2008;61:94-98.
661. Klasson, S., Svensson, H., Malm, K., Wasselius, J., Velander, P. Preoperative CT angiography versus Doppler ultrasound mapping of abdominal perforator in DIEP breast reconstructions: A randomized prospective study. *J Plast Reconstr Aesthet Surg* 2015;68:782-786.
662. Ono, S., Hayashi, H., Ohi, H., Ogawa, R. Imaging Studies for Preoperative Planning of Perforator Flaps: An Overview. *Clin Plast Surg* 2017;44:21-30.
663. Dorfman, D., Pu, L. L. The value of color duplex imaging for planning and performing a free anterolateral thigh perforator flap. *Ann Plast Surg* 2014;72 Suppl 1:S6-8.
664. Feng, S., Min, P., Grassetti, L., et al. A Prospective Head-to-Head Comparison of Color Doppler Ultrasound and Computed Tomographic Angiography in the Preoperative Planning of Lower Extremity Perforator Flaps. *Plast Reconstr Surg* 2016;137:335-347.
665. Su, W., Lu, L., Lazzeri, D., et al. Contrast-enhanced ultrasound combined with three-dimensional reconstruction in preoperative perforator flap planning. *Plast Reconstr Surg* 2013;131:80-93.
666. Gunnarsson, G. L., Tei, T., Thomsen, J. B. Color Doppler Ultrasonography-Targeted Perforator Mapping and Angiosome-Based Flap Reconstruction. *Ann Plast Surg* 2016;77:464-468.
667. Nahabedian, M. Y. Overview of perforator imaging and flap perfusion technologies. *Clin Plast Surg* 2011;38:165-174.
668. Fitzgerald O'Connor, E., Rozen, W. M., Chowdhry, M., Band, B., Ramakrishnan, V. V., Griffiths, M. Preoperative computed tomography angiography for planning DIEP flap breast reconstruction reduces operative time and overall complications. *Gland Surg* 2016;5:93-98.
669. Rozen, W. M., Ashton, M. W., Stella, D. L., Phillips, T. J., Taylor, G. I. Stereotactic image-guided navigation in the preoperative imaging of perforators for DIEP flap breast reconstruction. *Microsurgery* 2008;28:417-423.
670. Vasile, J. V., Levine, J. L. Magnetic resonance angiography in perforator flap breast reconstruction. *Gland Surg* 2016;5:197-211.
671. Chae, M. P., Hunter-Smith, D. J., Rozen, W. M. Comparative study of software techniques for 3D mapping of perforators in deep inferior epigastric artery perforator flap planning. *Gland Surg* 2016;5:99-106.
672. Gao, Z., Meng, D., Lu, H., Yao, B., Huang, N., Ye, Z. Utility of dual-energy spectral CT and low-iodine contrast medium in DIEP angiography. *Int J Clin Pract* 2016;70 Suppl 9B:B64-71.

673. Niumsawatt, V., Debrotwir, A. N., Rozen, W. M. Reducing radiation dose without compromising image quality in preoperative perforator flap imaging with CTA using ASIR technology. *Int Surg* 2014;99:485-491.
674. Kagen, A. C., Hossain, R., Dayan, E., et al. Modern Perforator Flap Imaging with High-Resolution Blood Pool MR Angiography. *Radiographics* 2015;35:901-915.
675. Schaverien, M. V., Ludman, C. N., Neil-Dwyer, J., et al. Contrast-enhanced magnetic resonance angiography for preoperative imaging in DIEP flap breast reconstruction. *Plast Reconstr Surg* 2011;128:56-62.
676. Mohan, A. T., Saint-Cyr, M. Advances in imaging technologies for planning breast reconstruction. *Gland Surg* 2016;5:242-254.
677. Yang, X., Miller, M. J., Friel, H. T., Slijepcevic, A., Knopp, M. V. Perforator Phase Contrast Angiography of Deep Inferior Epigastric Perforators: A Better Preoperative Imaging Tool for Flap Surgery than Computed Tomographic Angiography? *Invest Radiol* 2017;52:334-342.
678. Weum, S., Mercer, J. B., de Weerd, L. Evaluation of dynamic infrared thermography as an alternative to CT angiography for perforator mapping in breast reconstruction: a clinical study. *BMC Med Imaging* 2016;16:43.
679. Sheena, Y., Jennison, T., Hardwicke, J. T., Titley, O. G. Detection of perforators using thermal imaging. *Plast Reconstr Surg* 2013;132:1603-1610.
680. Hardwicke, J. T., Osmani, O., Skillman, J. M. Detection of Perforators Using Smartphone Thermal Imaging. *Plast Reconstr Surg* 2016;137:39-41.
681. Chubb, D. P., Taylor, G. I., Ashton, M. W. True and 'choke' anastomoses between perforator angiosomes: part II. dynamic thermographic identification. *Plast Reconstr Surg* 2013;132:1457-1464.
682. Chubb, D., Rozen, W. M., Whitaker, I. S., Ashton, M. W. Images in plastic surgery: digital thermographic photography ("thermal imaging") for preoperative perforator mapping. *Ann Plast Surg* 2011;66:324-325.
683. Hijjawi, J. B., Blondeel, P. N. Advancing deep inferior epigastric artery perforator flap breast reconstruction through multidetector row computed tomography: an evolution in preoperative imaging. *J Reconstr Microsurg* 2010;26:11-20.
684. Newman, M. I., Samson, M. C. The application of laser-assisted indocyanine green fluorescent dye angiography in microsurgical breast reconstruction. *J Reconstr Microsurg* 2009;25:21-26.
685. Holm, C., Tegeler, J., Mayr, M., Becker, A., Pfeiffer, U. J., Muhlbauer, W. Monitoring free flaps using laser-induced fluorescence of indocyanine green: a preliminary experience. *Microsurgery* 2002;22:278-287.
686. Burnier, P., Niddam, J., Bosc, R., Hersant, B., Meningaud, J. P. Indocyanine green applications in plastic surgery: A review of the literature. *J Plast Reconstr Aesthet Surg* 2017;70:814-827.
687. Bigdeli, A. K., Gazyakan, E., Schmidt, V. J., et al. Indocyanine Green Fluorescence for Free-Flap Perfusion Imaging Revisited: Advanced Decision Making by Virtual Perfusion Reality in Visionsense Fusion Imaging Angiography. *Surg Innov* 2015.
688. Casey, W. J., 3rd, Connolly, K. A., Nanda, A., Rebecca, A. M., Perdikis, G., Smith, A. A. Indocyanine green laser angiography improves deep inferior epigastric perforator flap outcomes following abdominal suction lipectomy. *Plast Reconstr Surg* 2015;135:491e-497e.
689. Muntean, M. V., Muntean, V., Ardelean, F., Georgescu, A. Dynamic perfusion assessment during perforator flap surgery: an up-to-date. *Clujul Med* 2015;88:293-297.
690. Wu, C., Kim, S., Halvorson, E. G. Laser-assisted indocyanine green angiography: a critical appraisal. *Ann Plast Surg* 2013;70:613-619.

691. Taylor, G. I., Chubb, D. P., Ashton, M. W. True and 'choke' anastomoses between perforator angiosomes: part i. anatomical location. *Plast Reconstr Surg* 2013;132:1447-1456.
692. Taylor, G. I., Corlett, R. J., Ashton, M. W. The Functional Angiosome: Clinical Implications of the Anatomical Concept. *Plast Reconstr Surg* 2017;140:721-733.
693. Lee, K. T., Mun, G. H. Perfusion of the diep flaps: A systematic review with meta-analysis. *Microsurgery* 2018;38:98-108.
694. Taylor, G. I., Corlett, R. J., Dhar, S. C., Ashton, M. W. The anatomical (angiosome) and clinical territories of cutaneous perforating arteries: development of the concept and designing safe flaps. *Plast Reconstr Surg* 2011;127:1447-1459.
695. Rha, E. Y., Choi, I. K., Yoo, G. Accuracy of the method for estimating breast volume on three-dimensional simulated magnetic resonance imaging scans in breast reconstruction. *Plast Reconstr Surg* 2014;133:14-20.
696. Charrondiere, U. R., Haytowitz, D., Stadlmayr, B. FAO/INFOODS Density Database Version 2.0. Food and Agriculture Organization of the United Nations, 2012.
697. Wong, S. M., Freedman, R. A., Sagara, Y., Aydogan, F., Barry, W. T., Golshan, M. Growing Use of Contralateral Prophylactic Mastectomy Despite no Improvement in Long-term Survival for Invasive Breast Cancer. *Ann Surg* 2017.
698. Jeevan, R., Browne, J. P., Gulliver-Clarke, C., et al. Surgical Determinants of Patient-Reported Outcomes following Postmastectomy Reconstruction in Women with Breast Cancer. *Plast Reconstr Surg* 2017;139:1036e-1045e.
699. Patel, N. G., Ramakrishnan, V. Microsurgical Tissue Transfer in Breast Reconstruction. *Clin Plast Surg* 2017;44:345-359.
700. Matthews, H., Carroll, N., Renshaw, D., et al. Predictors of satisfaction and quality of life following post-mastectomy breast reconstruction. *Psychooncology* 2017.
701. Ireton, J. E., Lakhiani, C., Saint-Cyr, M. Vascular anatomy of the deep inferior epigastric artery perforator flap: a systematic review. *Plast Reconstr Surg* 2014;134:810e-821e.
702. Marsh, D., Patel, N. G., Rozen, W. M., Chowdhry, M., Sharma, H., Ramakrishnan, V. V. Three routine free flaps per day in a single operating theatre: principles of a process mapping approach to improving surgical efficiency. *Gland Surg* 2016;5:107-114.
703. Miranda, B. H., Pywell, M., Floyd, D. A preoperative marking template for deep inferior epigastric artery perforator flap perforators in breast reconstruction. *Arch Plast Surg* 2014;41:171-173.
704. Hull, C. W. Method for production of three-dimensional objects by stereolithography.US Patent No. 4,929,402:May 29, 1990.
705. Mehta, S., Byrne, N., Karunanithy, N., Farhadi, J. 3D printing provides unrivalled bespoke teaching tools for autologous free flap breast reconstruction. *J Plast Reconstr Aesthet Surg* 2016;69:578-580.
706. Peeters, W. J., Nanhekhan, L., Van Ongeval, C., Fabre, G., Vandevoort, M. Fat necrosis in deep inferior epigastric perforator flaps: an ultrasound-based review of 202 cases. *Plast Reconstr Surg* 2009;124:1754-1758.
707. Lie, K. H., Barker, A. S., Ashton, M. W. A classification system for partial and complete DIEP flap necrosis based on a review of 17,096 DIEP flaps in 693 articles including analysis of 152 total flap failures. *Plast Reconstr Surg* 2013;132:1401-1408.
708. Colakoglu, S., Khansa, I., Curtis, M. S., et al. Impact of complications on patient satisfaction in breast reconstruction. *Plast Reconstr Surg* 2011;127:1428-1436.
709. Kurian, A. W., Lichtensztajn, D. Y., Keegan, T. H., Nelson, D. O., Clarke, C. A., Gomez, S. L. Use of and mortality after bilateral mastectomy compared with other surgical treatments for breast cancer in California, 1998-2011. *JAMA* 2014;312:902-914.
710. Kummerow, K. L., Du, L., Penson, D. F., Shyr, Y., Hooks, M. A. Nationwide trends in mastectomy for early-stage breast cancer. *JAMA Surg* 2015;150:9-16.

711. Tuttle, T. M., Habermann, E. B., Grund, E. H., Morris, T. J., Virnig, B. A. Increasing use of contralateral prophylactic mastectomy for breast cancer patients: a trend toward more aggressive surgical treatment. *J Clin Oncol* 2007;25:5203-5209.
712. Wong, S. M., Freedman, R. A., Sagara, Y., Aydogan, F., Barry, W. T., Golshan, M. Growing Use of Contralateral Prophylactic Mastectomy Despite no Improvement in Long-term Survival for Invasive Breast Cancer. *Ann Surg* 2016.
713. Elder, E. E., Brandberg, Y., Bjorklund, T., et al. Quality of life and patient satisfaction in breast cancer patients after immediate breast reconstruction: a prospective study. *Breast* 2005;14:201-208.
714. Bui, D. T., Cordeiro, P. G., Hu, Q. Y., Disa, J. J., Pusic, A., Mehrara, B. J. Free flap reexploration: indications, treatment, and outcomes in 1193 free flaps. *Plast Reconstr Surg* 2007;119:2092-2100.
715. Macadam, S. A., Zhong, T., Weichman, K., et al. Quality of Life and Patient-Reported Outcomes in Breast Cancer Survivors: A Multicenter Comparison of Four Abdominally Based Autologous Reconstruction Methods. *Plast Reconstr Surg* 2016;137:758-771.
716. Blondeel, P. N., Hijjawi, J., Depypere, H., Roche, N., Van Landuyt, K. Shaping the breast in aesthetic and reconstructive breast surgery: an easy three-step principle. *Plast Reconstr Surg* 2009;123:455-462.
717. Restifo, R. J. The "aesthetic subunit" principle in late TRAM flap breast reconstruction. *Ann Plast Surg* 1999;42:235-239.
718. Spear, S. L., Davison, S. P. Aesthetic subunits of the breast. *Plast Reconstr Surg* 2003;112:440-447.
719. Song, A. Y., Fernstrom, M. H., Scott, J. A., Ren, D. X., Rubin, J. P., Shestak, K. C. Assessment of TRAM aesthetics: the importance of subunit integration. *Plast Reconstr Surg* 2006;117:15-24.
720. Pulzl, P., Schoeller, T., Wechselberger, G. Respecting the aesthetic unit in autologous breast reconstruction improves the outcome. *Plast Reconstr Surg* 2006;117:1685-1691; discussion 1692-1683.
721. Gravvanis, A., Smith, R. W. Shaping the breast in secondary microsurgical breast reconstruction: single- vs. two-esthetic unit reconstruction. *Microsurgery* 2010;30:509-516.
722. Gravvanis, A., Samouris, G., Galani, E., Tsoutsos, D. Dual plane diep flap inset: Optimizing esthetic outcome in delayed autologous breast reconstruction. *Microsurgery* 2015;35:432-440.
723. Nahabedian, M. Y. Achieving ideal breast aesthetics with autologous reconstruction. *Gland Surg* 2015;4:134-144.
724. Wang, T., He, J., Xu, H., Ma, S., Dong, J. Achieving Symmetry in Unilateral DIEP Flap Breast Reconstruction: An Analysis of 126 Cases over 3 Years. *Aesthetic Plast Surg* 2015;39:63-68.
725. Tomita, K., Yano, K., Hata, Y., Nishibayashi, A., Hosokawa, K. DIEP Flap Breast Reconstruction Using 3-dimensional Surface Imaging and a Printed Mold. *Plast Reconstr Surg Glob Open* 2015;3:e316.
726. Thoma, A., Veltri, K., Khuthaila, D., Rockwell, G., Duku, E. Comparison of the deep inferior epigastric perforator flap and free transverse rectus abdominis myocutaneous flap in postmastectomy reconstruction: a cost-effectiveness analysis. *Plast Reconstr Surg* 2004;113:1650-1661.
727. Pomahac, B., Recht, A., May, J. W., Hergrueter, C. A., Slavin, S. A. New trends in breast cancer management: is the era of immediate breast reconstruction changing? *Ann Surg* 2006;244:282-288.
728. Saulis, A. S., Mustoe, T. A., Fine, N. A. A retrospective analysis of patient satisfaction with immediate postmastectomy breast reconstruction: comparison of three common procedures. *Plast Reconstr Surg* 2007;119:1669-1676; discussion 1677-1668.

729. Brinkman, J. N., Timman, R., Gopie, J. P., Kleijne, A., Tibben, A., Mureau, M. A. Aesthetic outcome after implant and DIEP flap breast reconstruction: An exploratory, prospective comparison of 25 cases. *J Plast Reconstr Aesthet Surg* 2015;68:1018-1019.
730. Menick, F. J. Artistry in aesthetic surgery. Aesthetic perception and the subunit principle. *Clin Plast Surg* 1987;14:723-735.
731. Burget, G. C., Menick, F. J. The subunit principle in nasal reconstruction. *Plast Reconstr Surg* 1985;76:239-247.
732. Gonzalez-Ulloa, M. Restoration of the face covering by means of selected skin in regional aesthetic units. *Br J Plast Surg* 1956;9:212-221.
733. Warpeha, R. L. Resurfacing the burned face. *Clin Plast Surg* 1981;8:255-267.
734. Howlader, N., Noone, A. M., Krapcho, M., et al. SEER Cancer Statistics Review, 1975-2013. Bethesda, MD: National Cancer Institute, 2015.
735. Kalus, R., Dixon Swartz, J., Metzger, S. C. Optimizing Safety, Predictability, and Aesthetics in Direct to Implant Immediate Breast Reconstruction: Evolution of Surgical Technique. *Ann Plast Surg* 2016;76 Suppl 4:S320-327.
736. Ascherman, J. A., Zeidler, K., Morrison, K. A., et al. Carbon Dioxide-Based versus Saline Tissue Expansion for Breast Reconstruction: Results of the XPAND Prospective, Randomized Clinical Trial. *Plast Reconstr Surg* 2016;138:1161-1170.
737. Henriksen, T. F., Holmich, L. R., Fryzek, J. P., et al. Incidence and severity of short-term complications after breast augmentation: results from a nationwide breast implant registry. *Ann Plast Surg* 2003;51:531-539.
738. Siggelkow, W., Klosterhalfen, B., Klinge, U., Rath, W., Faridi, A. Analysis of local complications following explantation of silicone breast implants. *Breast* 2004;13:122-128.
739. Handel, N., Garcia, M. E., Wixtrom, R. Breast implant rupture: causes, incidence, clinical impact, and management. *Plast Reconstr Surg* 2013;132:1128-1137.
740. Doren, E. L., Miranda, R. N., Selber, J. C., et al. United States Epidemiology of Breast Implant-Associated Anaplastic Large Cell Lymphoma. *Plast Reconstr Surg* 2017.
741. Chae, M. P., Rozen, W. M., Hunter-Smith, D. J., Ramakrishnan, V. Enhancing breast projection in autologous reconstruction using St Andrew's coning technique and 3D photography: case series. *Gland Surg* 2017.
742. Mennie, J. C., Mohanna, P. N., O'Donoghue, J. M., Rainsbury, R., Cromwell, D. A. Donor-Site Hernia Repair in Abdominal Flap Breast Reconstruction: A Population-Based Cohort Study of 7929 Patients. *Plast Reconstr Surg* 2015;136:1-9.
743. Serletti, J. M., Moran, S. L. Microvascular reconstruction of the breast. *Semin Surg Oncol* 2000;19:264-271.
744. Wu, L. C., Bajaj, A., Chang, D. W., Chevray, P. M. Comparison of donor-site morbidity of SIEA, DIEP, and muscle-sparing TRAM flaps for breast reconstruction. *Plast Reconstr Surg* 2008;122:702-709.
745. Arnez, Z. M., Khan, U., Pogorelec, D., Planinsek, F. Rational selection of flaps from the abdomen in breast reconstruction to reduce donor site morbidity. *Br J Plast Surg* 1999;52:351-354.
746. Neuber, F. Fettransplantation. *Chir Kongr Verhandl Dtsch Ges Chir* 1893;22:66.
747. Coleman, S. R. Structural fat grafting: more than a permanent filler. *Plast Reconstr Surg* 2006;118:108S-120S.
748. Lafontan, M. Fat cells: afferent and efferent messages define new approaches to treat obesity. *Annu Rev Pharmacol Toxicol* 2005;45:119-146.
749. Kolle, S. F., Fischer-Nielsen, A., Mathiasen, A. B., et al. Enrichment of autologous fat grafts with ex-vivo expanded adipose tissue-derived stem cells for graft survival: a randomised placebo-controlled trial. *Lancet* 2013;382:1113-1120.
750. Ersek, R. A. Transplantation of purified autologous fat: a 3-year follow-up is disappointing. *Plast Reconstr Surg* 1991;87:219-227; discussion 228.

751. Largo, R. D., Tchang, L. A., Mele, V., et al. Efficacy, safety and complications of autologous fat grafting to healthy breast tissue: a systematic review. *J Plast Reconstr Aesthet Surg* 2014;67:437-448.
752. Trojahn Kolle, S., Oliveri, R., Glovinski, P., Elberg, J., Fischer-Nielsen, A., Drzewiecki, K. Importance of mesenchymal stem cells in autologous fat grafting: a systematic review of existing studies. *J Plast Surg Hand Surg* 2012;42:59-68.
753. Choi, M., Small, K., Levovitz, C., Lee, C., Fadl, A., Karp, N. S. The volumetric analysis of fat graft survival in breast reconstruction. *Plast Reconstr Surg* 2013;131:185-191.
754. Chung, M. T., Hyun, J. S., Lo, D. D., et al. Micro-computed tomography evaluation of human fat grafts in nude mice. *Tissue Eng Part C Methods* 2013;19:227-232.
755. Saint-Cyr, M., Rojas, K., Colohan, S., Brown, S. The role of fat grafting in reconstructive and cosmetic breast surgery: a review of the literature. *J Reconstr Microsurg* 2012;28:99-110.
756. Matsumoto, D., Sato, K., Gonda, K., et al. Cell-assisted lipotransfer: supportive use of human adipose-derived cells for soft tissue augmentation with lipoinjection. *Tissue Eng* 2006;12:3375-3382.
757. Moseley, T. A., Zhu, M., Hedrick, M. H. Adipose-derived stem and progenitor cells as fillers in plastic and reconstructive surgery. *Plast Reconstr Surg* 2006;118:121S-128S.
758. Toyserkani, N. M., Quaade, M. L., Sorensen, J. A. Cell-Assisted Lipotransfer: A Systematic Review of Its Efficacy. *Aesthetic Plast Surg* 2016;40:309-318.
759. Zhou, Y., Wang, J., Li, H., et al. Efficacy and Safety of Cell-Assisted Lipotransfer: A Systematic Review and Meta-Analysis. *Plast Reconstr Surg* 2016;137:44e-57e.
760. Conde-Green, A., Wu, I., Graham, I., et al. Comparison of 3 techniques of fat grafting and cell-supplemented lipotransfer in athymic rats: a pilot study. *Aesthet Surg J* 2013;33:713-721.
761. Gentile, P., Orlandi, A., Scioli, M. G., et al. A comparative translational study: the combined use of enhanced stromal vascular fraction and platelet-rich plasma improves fat grafting maintenance in breast reconstruction. *Stem Cells Transl Med* 2012;1:341-351.
762. Perez-Cano, R., Vranckx, J. J., Lasso, J. M., et al. Prospective trial of adipose-derived regenerative cell (ADRC)-enriched fat grafting for partial mastectomy defects: the RESTORE-2 trial. *Eur J Surg Oncol* 2012;38:382-389.
763. Yoshimura, K., Asano, Y., Aoi, N., et al. Progenitor-enriched adipose tissue transplantation as rescue for breast implant complications. *Breast J* 2010;16:169-175.
764. Peltoniemi, H. H., Salmi, A., Miettinen, S., et al. Stem cell enrichment does not warrant a higher graft survival in lipofilling of the breast: a prospective comparative study. *J Plast Reconstr Aesthet Surg* 2013;66:1494-1503.
765. Missana, M. C., Laurent, I., Barreau, L., Balleyguier, C. Autologous fat transfer in reconstructive breast surgery: indications, technique and results. *Eur J Surg Oncol* 2007;33:685-690.
766. Weichman, K. E., Broer, P. N., Tanna, N., et al. The role of autologous fat grafting in secondary microsurgical breast reconstruction. *Ann Plast Surg* 2013;71:24-30.
767. Nelissen, X., Lhoest, F., Preud'Homme, L. Refined Method of Lipofilling following DIEP Breast Reconstruction: 3D Analysis of Graft Survival. *Plast Reconstr Surg Glob Open* 2015;3:e526.
768. Kim, H. Y., Jung, B. K., Lew, D. H., Lee, D. W. Autologous Fat Graft in the Reconstructed Breast: Fat Absorption Rate and Safety based on Sonographic Identification. *Arch Plast Surg* 2014;41:740-747.
769. Chang, E. I., Bonillas, R. G., El-ftesi, S., et al. Tissue engineering using autologous microcirculatory beds as vascularized bioscaffolds. *FASEB J* 2009;23:906-915.
770. Murphy, S. V., Atala, A. 3D bioprinting of tissues and organs. *Nat Biotechnol* 2014;32:773-785.

771. Atala, A., Kasper, F. K., Mikos, A. G. Engineering complex tissues. *Sci Transl Med* 2012;4:160rv112.
772. Atala, A., Bauer, S. B., Soker, S., Yoo, J. J., Retik, A. B. Tissue-engineered autologous bladders for patients needing cystoplasty. *Lancet* 2006;367:1241-1246.
773. Raya-Rivera, A., Esquiliano, D. R., Yoo, J. J., Lopez-Bayghen, E., Soker, S., Atala, A. Tissue-engineered autologous urethras for patients who need reconstruction: an observational study. *Lancet* 2011;377:1175-1182.
774. Raya-Rivera, A. M., Esquiliano, D., Fierro-Pastrana, R., et al. Tissue-engineered autologous vaginal organs in patients: a pilot cohort study. *Lancet* 2014;384:329-336.
775. Amini, A. R., Laurencin, C. T., Nukavarapu, S. P. Bone tissue engineering: recent advances and challenges. *Crit Rev Biomed Eng* 2012;40:363-408.
776. Bichara, D. A., O'Sullivan, N. A., Pomerantseva, I., et al. The tissue-engineered auricle: past, present, and future. *Tissue Eng Part B Rev* 2012;18:51-61.
777. Ostrovidov, S., Hosseini, V., Ahadian, S., et al. Skeletal muscle tissue engineering: methods to form skeletal myotubes and their applications. *Tissue Eng Part B Rev* 2014;20:403-436.
778. Lee, Y. B., Polio, S., Lee, W., et al. Bio-printing of collagen and VEGF-releasing fibrin gel scaffolds for neural stem cell culture. *Exp Neurol* 2010;223:645-652.
779. Jain, R. K., Au, P., Tam, J., Duda, D. G., Fukumura, D. Engineering vascularized tissue. *Nat Biotechnol* 2005;23:821-823.
780. Mikos, A. G., Herring, S. W., Ochareon, P., et al. Engineering complex tissues. *Tissue Eng* 2006;12:3307-3339.
781. Wang, Y. H., Wu, J. Y., Chou, P. J., et al. Characterization and evaluation of the differentiation ability of human adipose-derived stem cells growing in scaffold-free suspension culture. *Cytotherapy* 2014;16:485-495.
782. Sugihara, H., Yonemitsu, N., Miyabara, S., Yun, K. Primary cultures of unilocular fat cells: characteristics of growth in vitro and changes in differentiation properties. *Differentiation* 1986;31:42-49.
783. Kural, M. H., Billiar, K. L. Regulating tension in three-dimensional culture environments. *Exp Cell Res* 2013;319:2447-2459.
784. Wang, W., Itaka, K., Ohba, S., et al. 3D spheroid culture system on micropatterned substrates for improved differentiation efficiency of multipotent mesenchymal stem cells. *Biomaterials* 2009;30:2705-2715.
785. Cukierman, E., Pankov, R., Yamada, K. M. Cell interactions with three-dimensional matrices. *Curr Opin Cell Biol* 2002;14:633-639.
786. Edelman, D. B., Keefer, E. W. A cultural renaissance: in vitro cell biology embraces three-dimensional context. *Exp Neurol* 2005;192:1-6.
787. Zhang, H. H., Kumar, S., Barnett, A. H., Eggo, M. C. Ceiling culture of mature human adipocytes: use in studies of adipocyte functions. *J Endocrinol* 2000;164:119-128.
788. Sugihara, H., Yonemitsu, N., Miyabara, S., Toda, S. Proliferation of unilocular fat cells in the primary culture. *J Lipid Res* 1987;28:1038-1045.
789. Shen, J. F., Sugawara, A., Yamashita, J., Ogura, H., Sato, S. Dedifferentiated fat cells: an alternative source of adult multipotent cells from the adipose tissues. *Int J Oral Sci* 2011;3:117-124.
790. Lee, W., Debasitis, J. C., Lee, V. K., et al. Multi-layered culture of human skin fibroblasts and keratinocytes through three-dimensional freeform fabrication. *Biomaterials* 2009;30:1587-1595.
791. Boland, T., Xu, T., Damon, B., Cui, X. Application of inkjet printing to tissue engineering. *Biotechnol J* 2006;1:910-917.
792. Dahms, S. E., Piechota, H. J., Dahiya, R., Lue, T. F., Tanagho, E. A. Composition and biomechanical properties of the bladder acellular matrix graft: comparative analysis in rat, pig and human. *Br J Urol* 1998;82:411-419.

793. Chen, F., Yoo, J. J., Atala, A. Acellular collagen matrix as a possible "off the shelf" biomaterial for urethral repair. *Urology* 1999;54:407-410.
794. Probst, M., Dahiya, R., Carrier, S., Tanagho, E. A. Reproduction of functional smooth muscle tissue and partial bladder replacement. *Br J Urol* 1997;79:505-515.
795. Brown, B. N., Valentin, J. E., Stewart-Akers, A. M., McCabe, G. P., Badylak, S. F. Macrophage phenotype and remodeling outcomes in response to biologic scaffolds with and without a cellular component. *Biomaterials* 2009;30:1482-1491.
796. Moroni, L., de Wijn, J. R., van Blitterswijk, C. A. 3D fiber-deposited scaffolds for tissue engineering: influence of pores geometry and architecture on dynamic mechanical properties. *Biomaterials* 2006;27:974-985.
797. Kretlow, J. D., Mikos, A. G. Founder's award to Antonios G. Mikos, Ph.D., 2011 Society for Biomaterials annual meeting and exposition, Orlando, Florida, April 13-16, 2011: Bones to biomaterials and back again--20 years of taking cues from nature to engineer synthetic polymer scaffolds. *J Biomed Mater Res A* 2011;98:323-331.
798. Tan, J. Y., Chua, C. K., Leong, K. F. Fabrication of channeled scaffolds with ordered array of micro-pores through microsphere leaching and indirect Rapid Prototyping technique. *Biomed Microdevices* 2013;15:83-96.
799. Hutmacher, D. W. Scaffolds in tissue engineering bone and cartilage. *Biomaterials* 2000;21:2529-2543.
800. Hollister, S. J. Porous scaffold design for tissue engineering. *Nat Mater* 2005;4:518-524.
801. Derby, B. Printing and prototyping of tissues and scaffolds. *Science* 2012;338:921-926.
802. Stachowiak, A. N., Bershteyn, A., Tzatzalos, E., Irvine, D. J. Bioactive hydrogels with an ordered cellular structure combine interconnected macroporosity and robust mechanical properties. *Adv Mater* 2005;17:399-403.
803. Cabodi, M., Choi, N. W., Gleghorn, J. P., Lee, C. S., Bonassar, L. J., Stroock, A. D. A microfluidic biomaterial. *J Am Chem Soc* 2005;127:13788-13789.
804. Ling, Y., Rubin, J., Deng, Y., et al. A cell-laden microfluidic hydrogel. *Lab Chip* 2007;7:756-762.
805. Mironov, V., Visconti, R. P., Kasyanov, V., Forgacs, G., Drake, C. J., Markwald, R. R. Organ printing: tissue spheroids as building blocks. *Biomaterials* 2009;30:2164-2174.
806. Jones, N. Science in three dimensions: the print revolution. *Nature* 2012;487:22-23.
807. Ferris, C. J., Gilmore, K. G., Wallace, G. G., In het Panhuis, M. Biofabrication: an overview of the approaches used for printing of living cells. *Appl Microbiol Biotechnol* 2013;97:4243-4258.
808. Xu, T., Zhao, W., Zhu, J. M., Albanna, M. Z., Yoo, J. J., Atala, A. Complex heterogeneous tissue constructs containing multiple cell types prepared by inkjet printing technology. *Biomaterials* 2013;34:130-139.
809. Durmus, N. G., Tasoglu, S., Demirci, U. Bioprinting: Functional droplet networks. *Nat Mater* 2013;12:478-479.
810. Schuurman, W., Khristov, V., Pot, M. W., van Weeren, P. R., Dhert, W. J., Malda, J. Bioprinting of hybrid tissue constructs with tailorable mechanical properties. *Biofabrication* 2011;3:021001.
811. Shim, J. H., Lee, J. S., Kim, J. Y., Cho, D. W. Bioprinting of a mechanically enhanced three-dimensional dual cell-laden construct for osteochondral tissue engineering using a multi-head tissue/organ building system. *J Micromech Microeng* 2012;22:085014.
812. Peltola, S. M., Melchels, F. P., Grijpma, D. W., Kellomaki, M. A review of rapid prototyping techniques for tissue engineering purposes. *Ann Med* 2008;40:268-280.
813. Fedorovich, N. E., De Wijn, J. R., Verbout, A. J., Alblas, J., Dhert, W. J. Three-dimensional fiber deposition of cell-laden, viable, patterned constructs for bone tissue printing. *Tissue Eng Part A* 2008;14:127-133.

814. Jakab, K., Neagu, A., Mironov, V., Markwald, R. R., Forgacs, G. Engineering biological structures of prescribed shape using self-assembling multicellular systems. *Proc Natl Acad Sci U S A* 2004;101:2864-2869.
815. Landers, R., Hubner, U., Schmelzeisen, R., Mulhaupt, R. Rapid prototyping of scaffolds derived from thermoreversible hydrogels and tailored for applications in tissue engineering. *Biomaterials* 2002;23:4437-4447.
816. Joddar, B., Garcia, E., Casas, A., Stewart, C. M. Development of functionalized multi-walled carbon-nanotube-based alginate hydrogels for enabling biomimetic technologies. *Sci Rep* 2016;6:32456.
817. Kang, H. W., Lee, S. J., Ko, I. K., Kengla, C., Yoo, J. J., Atala, A. A 3D bioprinting system to produce human-scale tissue constructs with structural integrity. *Nat Biotechnol* 2016;34:312-319.
818. Fong, E. L., Watson, B. M., Kasper, F. K., Mikos, A. G. Building bridges: leveraging interdisciplinary collaborations in the development of biomaterials to meet clinical needs. *Adv Mater* 2012;24:4995-5013.
819. Lu, L., Zhu, X., Valenzuela, R. G., Currier, B. L., Yaszemski, M. J. Biodegradable polymer scaffolds for cartilage tissue engineering. *Clin Orthop Relat Res* 2001:S251-270.
820. Butler, D. L., Goldstein, S. A., Guldberg, R. E., et al. The impact of biomechanics in tissue engineering and regenerative medicine. *Tissue Eng Part B Rev* 2009;15:477-484.
821. Silva, N. A., Cooke, M. J., Tam, R. Y., et al. The effects of peptide modified gellan gum and olfactory ensheathing glia cells on neural stem/progenitor cell fate. *Biomaterials* 2012;33:6345-6354.
822. Vidal, G., Blanchi, T., Mieszawska, A. J., et al. Enhanced cellular adhesion on titanium by silk functionalized with titanium binding and RGD peptides. *Acta Biomater* 2013;9:4935-4943.
823. Engelhardt, E. M., Micol, L. A., Houis, S., et al. A collagen-poly(lactic acid-co-varepsilon-caprolactone) hybrid scaffold for bladder tissue regeneration. *Biomaterials* 2011;32:3969-3976.
824. Serrano, M. C., Pagani, R., Vallet-Regi, M., et al. In vitro biocompatibility assessment of poly(epsilon-caprolactone) films using L929 mouse fibroblasts. *Biomaterials* 2004;25:5603-5611.
825. Sun, H., Mei, L., Song, C., Cui, X., Wang, P. The in vivo degradation, absorption and excretion of PCL-based implant. *Biomaterials* 2006;27:1735-1740.
826. Chang, C. C., Boland, E. D., Williams, S. K., Hoying, J. B. Direct-write bioprinting three-dimensional biohybrid systems for future regenerative therapies. *J Biomed Mater Res B Appl Biomater* 2011;98:160-170.
827. Lippens, E., Swennen, I., Girones, J., et al. Cell survival and proliferation after encapsulation in a chemically modified Pluronic(R) F127 hydrogel. *J Biomater Appl* 2013;27:828-839.
828. Brivanlou, A. H., Gage, F. H., Jaenisch, R., Jessell, T., Melton, D., Rossant, J. Stem cells. Setting standards for human embryonic stem cells. *Science* 2003;300:913-916.
829. Condic, M. L., Rao, M. Regulatory issues for personalized pluripotent cells. *Stem Cells* 2008;26:2753-2758.
830. Hochedlinger, K., Jaenisch, R. Nuclear transplantation, embryonic stem cells, and the potential for cell therapy. *N Engl J Med* 2003;349:275-286.
831. Bae, H., Puranik, A. S., Gauvin, R., et al. Building vascular networks. *Sci Transl Med* 2012;4:160ps123.
832. Lovett, M., Lee, K., Edwards, A., Kaplan, D. L. Vascularization strategies for tissue engineering. *Tissue Eng Part B Rev* 2009;15:353-370.
833. Cilento, B. G., Freeman, M. R., Schneck, F. X., Retik, A. B., Atala, A. Phenotypic and cytogenetic characterization of human bladder urothelia expanded in vitro. *J Urol* 1994;152:665-670.

834. Zhang, Y. Y., Ludwikowski, B., Hurst, R., Frey, P. Expansion and long-term culture of differentiated normal rat urothelial cells in vitro. *In Vitro Cell Dev Biol Anim* 2001;37:419-429.
835. Caplan, A. I., Correa, D. The MSC: an injury drugstore. *Cell Stem Cell* 2011;9:11-15.
836. Klebe, R. J. Cytoscribing: a method for micropositioning cells and the construction of two- and three-dimensional synthetic tissues. *Exp Cell Res* 1988;179:362-373.
837. Xu, T., Jin, J., Gregory, C., Hickman, J. J., Boland, T. Inkjet printing of viable mammalian cells. *Biomaterials* 2005;26:93-99.
838. Cui, X., Boland, T., D'Lima, D. D., Lotz, M. K. Thermal inkjet printing in tissue engineering and regenerative medicine. *Recent Pat Drug Deliv Formul* 2012;6:149-155.
839. Cohen, D. L., Malone, E., Lipson, H., Bonassar, L. J. Direct freeform fabrication of seeded hydrogels in arbitrary geometries. *Tissue Eng* 2006;12:1325-1335.
840. Iwami, K., Noda, T., Ishida, K., Morishima, K., Nakamura, M., Umeda, N. Bio rapid prototyping by extruding/aspirating/refilling thermoreversible hydrogel. *Biofabrication* 2010;2:014108.
841. Shor, L., Guceri, S., Chang, R., et al. Precision extruding deposition (PED) fabrication of polycaprolactone (PCL) scaffolds for bone tissue engineering. *Biofabrication* 2009;1:015003.
842. Barron, J. A., Wu, P., Ladouceur, H. D., Ringeisen, B. R. Biological laser printing: a novel technique for creating heterogeneous 3-dimensional cell patterns. *Biomed Microdevices* 2004;6:139-147.
843. Guillemot, F., Souquet, A., Catros, S., et al. High-throughput laser printing of cells and biomaterials for tissue engineering. *Acta Biomater* 2010;6:2494-2500.
844. Guillotin, B., Souquet, A., Catros, S., et al. Laser assisted bioprinting of engineered tissue with high cell density and microscale organization. *Biomaterials* 2010;31:7250-7256.
845. Skardal, A., Mack, D., Kapetanovic, E., et al. Bioprinted amniotic fluid-derived stem cells accelerate healing of large skin wounds. *Stem Cells Transl Med* 2012;1:792-802.
846. Cui, X., Breitenkamp, K., Finn, M. G., Lotz, M., D'Lima, D. D. Direct human cartilage repair using three-dimensional bioprinting technology. *Tissue Eng Part A* 2012;18:1304-1312.
847. De Coppi, P., Bartsch, G., Jr., Siddiqui, M. M., et al. Isolation of amniotic stem cell lines with potential for therapy. *Nat Biotechnol* 2007;25:100-106.
848. Duan, B., Hockaday, L. A., Kang, K. H., Butcher, J. T. 3D bioprinting of heterogeneous aortic valve conduits with alginate/gelatin hydrogels. *J Biomed Mater Res A* 2013;101:1255-1264.
849. Norotte, C., Marga, F. S., Niklason, L. E., Forgacs, G. Scaffold-free vascular tissue engineering using bioprinting. *Biomaterials* 2009;30:5910-5917.
850. Xu, F., Celli, J., Rizvi, I., Moon, S., Hasan, T., Demirci, U. A three-dimensional in vitro ovarian cancer coculture model using a high-throughput cell patterning platform. *Biotechnol J* 2011;6:204-212.
851. Michael, S., Sorg, H., Peck, C. T., et al. Tissue engineered skin substitutes created by laser-assisted bioprinting form skin-like structures in the dorsal skin fold chamber in mice. *PLoS One* 2013;8:e57741.
852. Keriquel, V., Guillemot, F., Arnault, I., et al. In vivo bioprinting for computer- and robotic-assisted medical intervention: preliminary study in mice. *Biofabrication* 2010;2:014101.
853. Okamoto, T., Suzuki, T., Yamamoto, N. Microarray fabrication with covalent attachment of DNA using bubble jet technology. *Nat Biotechnol* 2000;18:438-441.
854. Goldmann, T., Gonzalez, J. S. DNA-printing: utilization of a standard inkjet printer for the transfer of nucleic acids to solid supports. *J Biochem Biophys Methods* 2000;42:105-110.

855. Xu, T., Kincaid, H., Atala, A., Yoo, J. J. High-throughput production of single-cell microparticles using an inkjet printing technology. *J Manuf Sci Eng* 2008;130:021017.
856. Cui, X., Dean, D., Ruggeri, Z. M., Boland, T. Cell damage evaluation of thermal inkjet printed Chinese hamster ovary cells. *Biotechnol Bioeng* 2010;106:963-969.
857. Tekin, E., Smith, P. J., Schubert, U. S. Inkjet printing as a deposition and patterning tool for polymers and inorganic particles. *Soft Matter* 2008;4:703-713.
858. Tasoglu, S., Demirci, U. Bioprinting for stem cell research. *Trends Biotechnol* 2013;31:10-19.
859. Murphy, S. V., Skardal, A., Atala, A. Evaluation of hydrogels for bio-printing applications. *J Biomed Mater Res A* 2013;101:272-284.
860. Khalil, S., Sun, W. Biopolymer deposition for freeform fabrication of hydrogel tissue constructs. *Mater Sci Eng C* 2007;27:469-478.
861. Fedorovich, N. E., Swennen, I., Girones, J., et al. Evaluation of photocrosslinked Lutrol hydrogel for tissue printing applications. *Biomacromolecules* 2009;10:1689-1696.
862. Chang, R., Nam, J., Sun, W. Effects of dispensing pressure and nozzle diameter on cell survival from solid freeform fabrication-based direct cell writing. *Tissue Eng Part A* 2008;14:41-48.
863. Jakab, K., Damon, B., Neagu, A., Kachurin, A., Forgacs, G. Three-dimensional tissue constructs built by bioprinting. *Biorheology* 2006;43:509-513.
864. Visser, J., Peters, B., Burger, T. J., et al. Biofabrication of multi-material anatomically shaped tissue constructs. *Biofabrication* 2013;5:035007.
865. Marga, F., Jakab, K., Khatiwala, C., et al. Toward engineering functional organ modules by additive manufacturing. *Biofabrication* 2012;4:022001.
866. Mironov, V., Kasyanov, V., Markwald, R. R. Organ printing: from bioprinter to organ biofabrication line. *Curr Opin Biotechnol* 2011;22:667-673.
867. Smith, C. M., Stone, A. L., Parkhill, R. L., et al. Three-dimensional bioassembly tool for generating viable tissue-engineered constructs. *Tissue Eng* 2004;10:1566-1576.
868. Bohandy, J., Kim, B., Adrian, F. Metal deposition from a supported metal film using an excimer laser. *J Appl Phys* 1986;60:1538-1539.
869. Barron, J. A., Ringeisen, B. R., Kim, H., Spargo, B. J., Chrisey, D. B. Application of laser printing to mammalian cells. *Thin Solid Films* 2004;453:383-387.
870. Ringeisen, B. R., Kim, H., Barron, J. A., et al. Laser printing of pluripotent embryonal carcinoma cells. *Tissue Eng* 2004;10:483-491.
871. Chrisey, D. B. MATERIALS PROCESSING: The Power of Direct Writing. *Science* 2000;289:879-881.
872. Colina, M., Serra, P., Fernandez-Pradas, J. M., Sevilla, L., Morenza, J. L. DNA deposition through laser induced forward transfer. *Biosens Bioelectron* 2005;20:1638-1642.
873. Hopp, B., Smausz, T., Kresz, N., et al. Survival and proliferative ability of various living cell types after laser-induced forward transfer. *Tissue Eng* 2005;11:1817-1823.
874. Gruene, M., Deiwick, A., Koch, L., et al. Laser printing of stem cells for biofabrication of scaffold-free autologous grafts. *Tissue Eng Part C Methods* 2011;17:79-87.
875. Koch, L., Kuhn, S., Sorg, H., et al. Laser printing of skin cells and human stem cells. *Tissue Eng Part C Methods* 2010;16:847-854.
876. Guillotin, B., Guillemot, F. Cell patterning technologies for organotypic tissue fabrication. *Trends Biotechnol* 2011;29:183-190.
877. Bielli, A., Scioli, M. G., Gentile, P., et al. Adult adipose-derived stem cells and breast cancer: a controversial relationship. *Springerplus* 2014;3:345.
878. Warnke, P. H., Springer, I. N., Wiltfang, J., et al. Growth and transplantation of a custom vascularised bone graft in a man. *Lancet* 2004;364:766-770.

879. Warnke, P. H., Wiltfang, J., Springer, I., et al. Man as living bioreactor: fate of an exogenously prepared customized tissue-engineered mandible. *Biomaterials* 2006;27:3163-3167.
880. Eto, H., Suga, H., Matsumoto, D., et al. Characterization of structure and cellular components of aspirated and excised adipose tissue. *Plast Reconstr Surg* 2009;124:1087-1097.
881. Christiaens, V., Lijnen, H. R. Angiogenesis and development of adipose tissue. *Mol Cell Endocrinol* 2010;318:2-9.
882. Chiu, Y. C., Cheng, M. H., Uriel, S., Brey, E. M. Materials for engineering vascularized adipose tissue. *J Tissue Viability* 2011;20:37-48.
883. Hutley, L. J., Herington, A. C., Shurety, W., et al. Human adipose tissue endothelial cells promote preadipocyte proliferation. *Am J Physiol Endocrinol Metab* 2001;281:E1037-1044.
884. Cao, Y. Angiogenesis modulates adipogenesis and obesity. *J Clin Invest* 2007;117:2362-2368.
885. Rophael, J. A., Craft, R. O., Palmer, J. A., et al. Angiogenic growth factor synergism in a murine tissue engineering model of angiogenesis and adipogenesis. *Am J Pathol* 2007;171:2048-2057.
886. Tsuji, T., Yamaguchi, K., Kikuchi, R., et al. Promotion of adipogenesis by an EP2 receptor agonist via stimulation of angiogenesis in pulmonary emphysema. *Prostaglandins Other Lipid Mediat* 2014;112:9-15.
887. Li, J., Qiao, X., Yu, M., et al. Secretory factors from rat adipose tissue explants promote adipogenesis and angiogenesis. *Artif Organs* 2014;38:E33-45.
888. Young, D. A., Choi, Y. S., Engler, A. J., Christman, K. L. Stimulation of adipogenesis of adult adipose-derived stem cells using substrates that mimic the stiffness of adipose tissue. *Biomaterials* 2013;34:8581-8588.
889. Ingber, D. E. Cellular mechanotransduction: putting all the pieces together again. *FASEB J* 2006;20:811-827.
890. Juliano, R. L., Haskill, S. Signal transduction from the extracellular matrix. *J Cell Biol* 1993;120:577-585.
891. Maniotis, A. J., Chen, C. S., Ingber, D. E. Demonstration of mechanical connections between integrins, cytoskeletal filaments, and nucleoplasm that stabilize nuclear structure. *Proc Natl Acad Sci U S A* 1997;94:849-854.
892. Prusty, D., Park, B. H., Davis, K. E., Farmer, S. R. Activation of MEK/ERK signaling promotes adipogenesis by enhancing peroxisome proliferator-activated receptor gamma (PPARgamma) and C/EBPalpha gene expression during the differentiation of 3T3-L1 preadipocytes. *J Biol Chem* 2002;277:46226-46232.
893. Tanabe, Y., Koga, M., Saito, M., Matsunaga, Y., Nakayama, K. Inhibition of adipocyte differentiation by mechanical stretching through ERK-mediated downregulation of PPARgamma2. *J Cell Sci* 2004;117:3605-3614.
894. McBeath, R., Pirone, D. M., Nelson, C. M., Bhadriraju, K., Chen, C. S. Cell shape, cytoskeletal tension, and RhoA regulate stem cell lineage commitment. *Dev Cell* 2004;6:483-495.
895. Shoham, N., Gottlieb, R., Sharabani-Yosef, O., Zaretsky, U., Benayahu, D., Gefen, A. Static mechanical stretching accelerates lipid production in 3T3-L1 adipocytes by activating the MEK signaling pathway. *Am J Physiol Cell Physiol* 2012;302:C429-441.
896. Tanabe, Y., Saito, M. T., Nakayama, K. Mechanical stretching and signaling pathways in adipogenesis. *Stud Mechanobiol Tissue Eng Biomater* 2013;16:35-62.
897. Ruknudin, A., Sachs, F., Bustamante, J. O. Stretch-activated ion channels in tissue-cultured chick heart. *Am J Physiol* 1993;264:H960-972.
898. Samani, A., Bishop, J., Luginbuhl, C., Plewes, D. B. Measuring the elastic modulus of ex vivo small tissue samples. *Phys Med Biol* 2003;48:2183-2198.

899. Comley, K., Fleck, N. A. A micromechanical model for the Young's modulus of adipose tissue. *Int J Solids Struct* 2010;47:2982-2990.
900. Wiggenhauser, P. S., Muller, D. F., Melchels, F. P., et al. Engineering of vascularized adipose constructs. *Cell Tissue Res* 2012;347:747-757.
901. Yu, C., Bianco, J., Brown, C., et al. Porous decellularized adipose tissue foams for soft tissue regeneration. *Biomaterials* 2013;34:3290-3302.
902. Cheung, H. K., Han, T. T., Marecak, D. M., Watkins, J. F., Amsden, B. G., Flynn, L. E. Composite hydrogel scaffolds incorporating decellularized adipose tissue for soft tissue engineering with adipose-derived stem cells. *Biomaterials* 2014;35:1914-1923.
903. Bellas, E., Lo, T. J., Fournier, E. P., et al. Injectable silk foams for soft tissue regeneration. *Adv Healthc Mater* 2015;4:452-459.
904. Kilian, K. A., Bugarija, B., Lahn, B. T., Mrksich, M. Geometric cues for directing the differentiation of mesenchymal stem cells. *Proc Natl Acad Sci U S A* 2010;107:4872-4877.
905. Stosich, M. S., Bastian, B., Marion, N. W., Clark, P. A., Reilly, G., Mao, J. J. Vascularized adipose tissue grafts from human mesenchymal stem cells with bioactive cues and microchannel conduits. *Tissue Eng* 2007;13:2881-2890.
906. Kaully, T., Kaufman-Francis, K., Lesman, A., Levenberg, S. Vascularization--the conduit to viable engineered tissues. *Tissue Eng Part B Rev* 2009;15:159-169.
907. Loh, Q. L., Choong, C. Three-dimensional scaffolds for tissue engineering applications: role of porosity and pore size. *Tissue Eng Part B Rev* 2013;19:485-502.
908. Abrahamson, D. R. Recent studies on the structure and pathology of basement membranes. *J Pathol* 1986;149:257-278.
909. Patrick, C. W., Jr. Tissue engineering strategies for adipose tissue repair. *Anat Rec* 2001;263:361-366.
910. Kim, K. J., Joe, Y. A., Kim, M. K., et al. Silica nanoparticles increase human adipose tissue-derived stem cell proliferation through ERK1/2 activation. *Int J Nanomedicine* 2015;10:2261-2272.
911. Choi, Y. S., Vincent, L. G., Lee, A. R., et al. The alignment and fusion assembly of adipose-derived stem cells on mechanically patterned matrices. *Biomaterials* 2012;33:6943-6951.
912. Francis, M. P., Sachs, P. C., Madurantakam, P. A., et al. Electrospinning adipose tissue-derived extracellular matrix for adipose stem cell culture. *J Biomed Mater Res A* 2012;100:1716-1724.
913. Shadjou, N., Hasanzadeh, M. Bone tissue engineering using silica-based mesoporous nanobiomaterials:Recent progress. *Mater Sci Eng C Mater Biol Appl* 2015;55:401-409.
914. Smith, C. M., Christian, J. J., Warren, W. L., Williams, S. K. Characterizing environmental factors that impact the viability of tissue-engineered constructs fabricated by a direct-write bioassembly tool. *Tissue Eng* 2007;13:373-383.
915. Lee, W., Pinckney, J., Lee, V., et al. Three-dimensional bioprinting of rat embryonic neural cells. *Neuroreport* 2009;20:798-803.
916. Jakab, K., Norotte, C., Marga, F., Murphy, K., Vunjak-Novakovic, G., Forgacs, G. Tissue engineering by self-assembly and bio-printing of living cells. *Biofabrication* 2010;2:022001.
917. Chang, C. C., Krishnan, L., Nunes, S. S., et al. Determinants of microvascular network topologies in implanted neovasculatures. *Arterioscler Thromb Vasc Biol* 2012;32:5-14.
918. Zhang, Y. S., Gao, J. H., Lu, F., Zhu, M., Liao, Y. J. [Cellular compatibility of type collagen I scaffold and human adipose-derived stem cells]. *Nan Fang Yi Ke Da Xue Xue Bao* 2007;27:223-225.

919. Lequeux, C., Oni, G., Wong, C., et al. Subcutaneous fat tissue engineering using autologous adipose-derived stem cells seeded onto a collagen scaffold. *Plast Reconstr Surg* 2012;130:1208-1217.
920. Ferraro, G. A., De Francesco, F., Nicoletti, G., et al. Human adipose CD34+ CD90+ stem cells and collagen scaffold constructs grafted in vivo fabricate loose connective and adipose tissues. *J Cell Biochem* 2013;114:1039-1049.
921. Chan, E. C., Kuo, S. M., Kong, A. M., et al. Three Dimensional Collagen Scaffold Promotes Intrinsic Vascularisation for Tissue Engineering Applications. *PLoS One* 2016;11:e0149799.
922. Xu, F. T., Liang, Z. J., Li, H. M., et al. Ginsenoside Rg1 and platelet-rich fibrin enhance human breast adipose-derived stem cell function for soft tissue regeneration. *Oncotarget* 2016;7:35390-35403.
923. Vashi, A. V., Abberton, K. M., Thomas, G. P., et al. Adipose tissue engineering based on the controlled release of fibroblast growth factor-2 in a collagen matrix. *Tissue Eng* 2006;12:3035-3043.
924. von Heimburg, D., Zachariah, S., Low, A., Pallua, N. Influence of different biodegradable carriers on the in vivo behavior of human adipose precursor cells. *Plast Reconstr Surg* 2001;108:411-420; discussion 421-412.
925. Hemmrich, K., von Heimburg, D., Rendchen, R., Di Bartolo, C., Milella, E., Pallua, N. Implantation of preadipocyte-loaded hyaluronic acid-based scaffolds into nude mice to evaluate potential for soft tissue engineering. *Biomaterials* 2005;26:7025-7037.
926. Wittmann, K., Dietl, S., Ludwig, N., et al. Engineering vascularized adipose tissue using the stromal-vascular fraction and fibrin hydrogels. *Tissue Eng Part A* 2015;21:1343-1353.
927. Hsueh, Y. S., Chen, Y. S., Tai, H. C., et al. Laminin-alginate Beads as Preadipocyte Carriers to Enhance Adipogenesis in vitro and in vivo. *Tissue Eng Part A* 2016.
928. Choi, J. S., Yang, H. J., Kim, B. S., et al. Human extracellular matrix (ECM) powders for injectable cell delivery and adipose tissue engineering. *J Control Release* 2009;139:2-7.
929. Wu, I., Nahas, Z., Kimmerling, K. A., Rosson, G. D., Elisseeff, J. H. An injectable adipose matrix for soft-tissue reconstruction. *Plast Reconstr Surg* 2012;129:1247-1257.
930. Wang, L., Johnson, J. A., Zhang, Q., Beahm, E. K. Combining decellularized human adipose tissue extracellular matrix and adipose-derived stem cells for adipose tissue engineering. *Acta Biomater* 2013;9:8921-8931.
931. Debels, H., Gerrand, Y. W., Poon, C. J., Abberton, K. M., Morrison, W. A., Mitchell, G. M. An adipogenic gel for surgical reconstruction of the subcutaneous fat layer in a rat model. *J Tissue Eng Regen Med* 2015.
932. Kawaguchi, N., Toriyama, K., Nicodemou-Lena, E., Inou, K., Torii, S., Kitagawa, Y. De novo adipogenesis in mice at the site of injection of basement membrane and basic fibroblast growth factor. *Proc Natl Acad Sci U S A* 1998;95:1062-1066.
933. Walton, R. L., Beahm, E. K., Wu, L. De novo adipose formation in a vascularized engineered construct. *Microsurgery* 2004;24:378-384.
934. Fischbach, C., Spruss, T., Weiser, B., et al. Generation of mature fat pads in vitro and in vivo utilizing 3-D long-term culture of 3T3-L1 preadipocytes. *Exp Cell Res* 2004;300:54-64.
935. Neubauer, M., Hacker, M., Bauer-Kreisel, P., et al. Adipose tissue engineering based on mesenchymal stem cells and basic fibroblast growth factor in vitro. *Tissue Eng* 2005;11:1840-1851.
936. Alhadlaq, A., Tang, M., Mao, J. J. Engineered adipose tissue from human mesenchymal stem cells maintains predefined shape and dimension: implications in soft tissue augmentation and reconstruction. *Tissue Eng* 2005;11:556-566.

937. Rossi, E., Gerges, I., Tocchio, A., et al. Biologically and mechanically driven design of an RGD-mimetic macroporous foam for adipose tissue engineering applications. *Biomaterials* 2016;104:65-77.
938. Flynn, L., Prestwich, G. D., Semple, J. L., Woodhouse, K. A. Adipose tissue engineering in vivo with adipose-derived stem cells on naturally derived scaffolds. *J Biomed Mater Res A* 2009;89:929-941.
939. Wang, M., Yu, L. Transplantation of adipose-derived stem cells combined with decellularized cartilage ECM: a novel approach to nasal septum perforation repair. *Med Hypotheses* 2014;82:781-783.
940. Liu, X., Holzwarth, J. M., Ma, P. X. Functionalized synthetic biodegradable polymer scaffolds for tissue engineering. *Macromol Biosci* 2012;12:911-919.
941. Hosseinzadeh, E., Davarpanah, M., Hassanzadeh Nemati, N., Tavakoli, S. A. Fabrication of a hard tissue replacement using natural hydroxyapatite derived from bovine bones by thermal decomposition method. *Int J Organ Transplant Med* 2014;5:23-31.
942. Li, Y., Meng, H., Liu, Y., Lee, B. P. Fibrin gel as an injectable biodegradable scaffold and cell carrier for tissue engineering. *ScientificWorldJournal* 2015;2015:685690.
943. Taghiabadi, E., Nasri, S., Shafieyan, S., Jalili Firoozinezhad, S., Aghdami, N. Fabrication and characterization of spongy denuded amniotic membrane based scaffold for tissue engineering. *Cell J* 2015;16:476-487.
944. Mano, J. F., Silva, G. A., Azevedo, H. S., et al. Natural origin biodegradable systems in tissue engineering and regenerative medicine: present status and some moving trends. *J R Soc Interface* 2007;4:999-1030.
945. Gentleman, E., Nauman, E. A., Livesay, G. A., Dee, K. C. Collagen composite biomaterials resist contraction while allowing development of adipocytic soft tissue in vitro. *Tissue Eng* 2006;12:1639-1649.
946. Rubin, J. P., Bennett, J. M., Doctor, J. S., Tebbets, B. M., Marra, K. G. Collagenous microbeads as a scaffold for tissue engineering with adipose-derived stem cells. *Plast Reconstr Surg* 2007;120:414-424.
947. Toda, S., Uchihashi, K., Aoki, S., et al. Adipose tissue-organotypic culture system as a promising model for studying adipose tissue biology and regeneration. *Organogenesis* 2009;5:50-56.
948. Kim, B. S., Kim, J. S., Lee, J. Improvements of osteoblast adhesion, proliferation, and differentiation in vitro via fibrin network formation in collagen sponge scaffold. *J Biomed Mater Res A* 2013;101:2661-2666.
949. Klar, A. S., Guven, S., Biedermann, T., et al. Tissue-engineered dermo-epidermal skin grafts prevascularized with adipose-derived cells. *Biomaterials* 2014;35:5065-5078.
950. Mauney, J. R., Nguyen, T., Gillen, K., Kirker-Head, C., Gimble, J. M., Kaplan, D. L. Engineering adipose-like tissue in vitro and in vivo utilizing human bone marrow and adipose-derived mesenchymal stem cells with silk fibroin 3D scaffolds. *Biomaterials* 2007;28:5280-5290.
951. Lucero, H. A., Kagan, H. M. Lysyl oxidase: an oxidative enzyme and effector of cell function. *Cell Mol Life Sci* 2006;63:2304-2316.
952. Hong, L., Peptan, I., Clark, P., Mao, J. J. Ex vivo adipose tissue engineering by human marrow stromal cell seeded gelatin sponge. *Ann Biomed Eng* 2005;33:511-517.
953. Tonello, C., Vindigni, V., Zavan, B., et al. In vitro reconstruction of an endothelialized skin substitute provided with a microcapillary network using biopolymer scaffolds. *FASEB J* 2005;19:1546-1548.
954. La Gatta, A., De Rosa, M., Marzaioli, I., Busico, T., Schiraldi, C. A complete hyaluronan hydrodynamic characterization using a size exclusion chromatography-triple detector array system during in vitro enzymatic degradation. *Anal Biochem* 2010;404:21-29.

955. Yoon, I. S., Chung, C. W., Sung, J. H., et al. Proliferation and chondrogenic differentiation of human adipose-derived mesenchymal stem cells in porous hyaluronic acid scaffold. *J Biosci Bioeng* 2011;112:402-408.
956. Desiderio, V., De Francesco, F., Schiraldi, C., et al. Human Ng2+ adipose stem cells loaded in vivo on a new crosslinked hyaluronic acid-Lys scaffold fabricate a skeletal muscle tissue. *J Cell Physiol* 2013;228:1762-1773.
957. Mathews, S., Mathew, S. A., Gupta, P. K., Bhonde, R., Totey, S. Glycosaminoglycans enhance osteoblast differentiation of bone marrow derived human mesenchymal stem cells. *J Tissue Eng Regen Med* 2014;8:143-152.
958. Wang, Y., Kim, H. J., Vunjak-Novakovic, G., Kaplan, D. L. Stem cell-based tissue engineering with silk biomaterials. *Biomaterials* 2006;27:6064-6082.
959. Rockwood, D. N., Preda, R. C., Yucel, T., Wang, X., Lovett, M. L., Kaplan, D. L. Materials fabrication from Bombyx mori silk fibroin. *Nat Protoc* 2011;6:1612-1631.
960. Altman, G. H., Diaz, F., Jakuba, C., et al. Silk-based biomaterials. *Biomaterials* 2003;24:401-416.
961. Bellas, E., Marra, K. G., Kaplan, D. L. Sustainable three-dimensional tissue model of human adipose tissue. *Tissue Eng Part C Methods* 2013;19:745-754.
962. Kang, J. H., Gimble, J. M., Kaplan, D. L. In vitro 3D model for human vascularized adipose tissue. *Tissue Eng Part A* 2009;15:2227-2236.
963. Hanken, H., Gohler, F., Smeets, R., et al. Attachment, Viability and Adipodifferentiation of Pre-adipose Cells on Silk Scaffolds with and Without Co-expressed FGF-2 and VEGF. *In Vivo* 2016;30:567-572.
964. Abbott, R. D., Wang, R. Y., Reagan, M. R., et al. The Use of Silk as a Scaffold for Mature, Sustainable Unilocular Adipose 3D Tissue Engineered Systems. *Adv Healthc Mater* 2016;5:1667-1677.
965. Choi, J. H., Bellas, E., Gimble, J. M., Vunjak-Novakovic, G., Kaplan, D. L. Lipolytic function of adipocyte/endothelial cocultures. *Tissue Eng Part A* 2011;17:1437-1444.
966. Currie, L. J., Sharpe, J. R., Martin, R. The use of fibrin glue in skin grafts and tissue-engineered skin replacements: a review. *Plast Reconstr Surg* 2001;108:1713-1726.
967. Feng, X., Clark, R. A., Galanakis, D., Tonnesen, M. G. Fibrin and collagen differentially regulate human dermal microvascular endothelial cell integrins: stabilization of alphav/beta3 mRNA by fibrin1. *J Invest Dermatol* 1999;113:913-919.
968. Janmey, P. A., Winer, J. P., Weisel, J. W. Fibrin gels and their clinical and bioengineering applications. *J R Soc Interface* 2009;6:1-10.
969. Chung, E., Rytlewski, J. A., Merchant, A. G., Dhada, K. S., Lewis, E. W., Suggs, L. J. Fibrin-based 3D matrices induce angiogenic behavior of adipose-derived stem cells. *Acta Biomater* 2015;17:78-88.
970. Zimmerlin, L., Rubin, J. P., Pfeifer, M. E., Moore, L. R., Donnenberg, V. S., Donnenberg, A. D. Human adipose stromal vascular cell delivery in a fibrin spray. *Cytotherapy* 2013;15:102-108.
971. Rohringer, S., Hofbauer, P., Schneider, K. H., et al. Mechanisms of vasculogenesis in 3D fibrin matrices mediated by the interaction of adipose-derived stem cells and endothelial cells. *Angiogenesis* 2014;17:921-933.
972. Hunt, N. C., Grover, L. M. Cell encapsulation using biopolymer gels for regenerative medicine. *Biotechnol Lett* 2010;32:733-742.
973. Smetana, K., Jr. Cell biology of hydrogels. *Biomaterials* 1993;14:1046-1050.
974. Burdick, J. A., Vunjak-Novakovic, G. Engineered microenvironments for controlled stem cell differentiation. *Tissue Eng Part A* 2009;15:205-219.
975. Sasaki, T., Fassler, R., Hohenester, E. Laminin: the crux of basement membrane assembly. *J Cell Biol* 2004;164:959-963.
976. Patrick, C. W., Jr., Wu, X. Integrin-mediated preadipocyte adhesion and migration on laminin-1. *Ann Biomed Eng* 2003;31:505-514.

977. Noro, A., Sillat, T., Virtanen, I., et al. Laminin production and basement membrane deposition by mesenchymal stem cells upon adipogenic differentiation. *J Histochem Cytochem* 2013;61:719-730.
978. Davis, G. E., Senger, D. R. Endothelial extracellular matrix: biosynthesis, remodeling, and functions during vascular morphogenesis and neovessel stabilization. *Circ Res* 2005;97:1093-1107.
979. Gruene, M., Pflaum, M., Deiwick, A., et al. Adipogenic differentiation of laser-printed 3D tissue grafts consisting of human adipose-derived stem cells. *Biofabrication* 2011;3:015005.
980. Yao, R., Zhang, R., Luan, J., Lin, F. Alginate and alginate/gelatin microspheres for human adipose-derived stem cell encapsulation and differentiation. *Biofabrication* 2012;4:025007.
981. Flynn, L. E. The use of decellularized adipose tissue to provide an inductive microenvironment for the adipogenic differentiation of human adipose-derived stem cells. *Biomaterials* 2010;31:4715-4724.
982. Fu, R. H., Wang, Y. C., Liu, S. P., et al. Decellularization and recellularization technologies in tissue engineering. *Cell Transplant* 2014;23:621-630.
983. Sano, H., Orbay, H., Terashi, H., Hyakusoku, H., Ogawa, R. Acellular adipose matrix as a natural scaffold for tissue engineering. *J Plast Reconstr Aesthet Surg* 2014;67:99-106.
984. Hruschka, V., Saeed, A., Slezak, P., et al. Evaluation of a thermoresponsive polycaprolactone scaffold for in vitro three-dimensional stem cell differentiation. *Tissue Eng Part A* 2015;21:310-319.
985. Omidi, E., Fuetterer, L., Reza Mousavi, S., Armstrong, R. C., Flynn, L. E., Samani, A. Characterization and assessment of hyperelastic and elastic properties of decellularized human adipose tissues. *J Biomech* 2014;47:3657-3663.
986. Haddad, S. M., Omidi, E., Flynn, L. E., Samani, A. Comparative biomechanical study of using decellularized human adipose tissues for post-mastectomy and post-lumpectomy breast reconstruction. *J Mech Behav Biomed Mater* 2016;57:235-245.
987. Messina, A., Bortolotto, S. K., Cassell, O. C., Kelly, J., Abberton, K. M., Morrison, W. A. Generation of a vascularized organoid using skeletal muscle as the inductive source. *FASEB J* 2005;19:1570-1572.
988. Abberton, K. M., Bortolotto, S. K., Woods, A. A., et al. Myogel, a novel, basement membrane-rich, extracellular matrix derived from skeletal muscle, is highly adipogenic in vivo and in vitro. *Cells Tissues Organs* 2008;188:347-358.
989. Kleinman, H. K., McGarvey, M. L., Liotta, L. A., Robey, P. G., Tryggvason, K., Martin, G. R. Isolation and characterization of type IV procollagen, laminin, and heparan sulfate proteoglycan from the EHS sarcoma. *Biochemistry* 1982;21:6188-6193.
990. Kleinman, H. K., Martin, G. R. Matrigel: basement membrane matrix with biological activity. *Semin Cancer Biol* 2005;15:378-386.
991. Findlay, M. W., Messina, A., Thompson, E. W., Morrison, W. A. Long-term persistence of tissue-engineered adipose flaps in a murine model to 1 year: an update. *Plast Reconstr Surg* 2009;124:1077-1084.
992. Baptista, L. S., Silva, K. R., Santos, M. F. S., et al. Scalable and reproducible biofabrication of spheroids from human adipose-derived tissue stem cells isolated by mechanical dissociation. In *Tissue Engineering and Regenerative Medicine International Society - EU Meeting,* Genova, Italy2014.
993. Cheng, N. C., Wang, S., Young, T. H. The influence of spheroid formation of human adipose-derived stem cells on chitosan films on stemness and differentiation capabilities. *Biomaterials* 2012;33:1748-1758.
994. FitzGerald, J. F., Kumar, A. S. Biologic versus Synthetic Mesh Reinforcement: What are the Pros and Cons? *Clin Colon Rectal Surg* 2014;27:140-148.

995. Martello, F., Tocchio, A., Tamplenizza, M., et al. Poly(amido-amine)-based hydrogels with tailored mechanical properties and degradation rates for tissue engineering. *Acta Biomater* 2014;10:1206-1215.
996. Tocchio, A., Martello, F., Tamplenizza, M., et al. RGD-mimetic poly(amidoamine) hydrogel for the fabrication of complex cell-laden micro constructs. *Acta Biomater* 2015;18:144-154.
997. Znaleziona, J., Ginterova, P., Petr, J., et al. Determination and identification of synthetic cannabinoids and their metabolites in different matrices by modern analytical techniques - a review. *Anal Chim Acta* 2015;874:11-25.
998. Moroni, L., de Wijn, J. R., van Blitterswijk, C. A. Integrating novel technologies to fabricate smart scaffolds. *J Biomater Sci Polym Ed* 2008;19:543-572.
999. Angelova, N., Hunkeler, D. Rationalizing the design of polymeric biomaterials. *Trends Biotechnol* 1999;17:409-421.
1000. Hu, Y., Winn, S. R., Krajbich, I., Hollinger, J. O. Porous polymer scaffolds surface-modified with arginine-glycine-aspartic acid enhance bone cell attachment and differentiation in vitro. *J Biomed Mater Res A* 2003;64:583-590.
1001. Tanahashi, K., Mikos, A. G. Protein adsorption and smooth muscle cell adhesion on biodegradable agmatine-modified poly(propylene fumarate-co-ethylene glycol) hydrogels. *J Biomed Mater Res A* 2003;67:448-457.
1002. Kim, T. G., Park, T. G. Biomimicking extracellular matrix: cell adhesive RGD peptide modified electrospun poly(D,L-lactic-co-glycolic acid) nanofiber mesh. *Tissue Eng* 2006;12:221-233.
1003. Blit, P. H., Shen, Y. H., Ernsting, M. J., Woodhouse, K. A., Santerre, J. P. Bioactivation of porous polyurethane scaffolds using fluorinated RGD surface modifiers. *J Biomed Mater Res A* 2010;94:1226-1235.
1004. Guarnieri, D., De Capua, A., Ventre, M., et al. Covalently immobilized RGD gradient on PEG hydrogel scaffold influences cell migration parameters. *Acta Biomater* 2010;6:2532-2539.
1005. Tuin, S. A., Pourdeyhimi, B., Loboa, E. G. Creating tissues from textiles: scalable nonwoven manufacturing techniques for fabrication of tissue engineering scaffolds. *Biomed Mater* 2016;11:015017.
1006. Sheikh, F. A., Ju, H. W., Moon, B. M., et al. Hybrid scaffolds based on PLGA and silk for bone tissue engineering. *J Tissue Eng Regen Med* 2016;10:209-221.
1007. Zangaglia, R., Martignoni, E., Glorioso, M., et al. Macrogol for the treatment of constipation in Parkinson's disease. A randomized placebo-controlled study. *Mov Disord* 2007;22:1239-1244.
1008. Ozcelik, B., Blencowe, A., Palmer, J., et al. Highly porous and mechanically robust polyester poly(ethylene glycol) sponges as implantable scaffolds. *Acta Biomater* 2014;10:2769-2780.
1009. Ruoslahti, E., Pierschbacher, M. D. Arg-Gly-Asp: a versatile cell recognition signal. *Cell* 1986;44:517-518.
1010. Lin, C. C., Anseth, K. S. PEG hydrogels for the controlled release of biomolecules in regenerative medicine. *Pharm Res* 2009;26:631-643.
1011. Garcia, A. J. PEG-maleimide hydrogels for protein and cell delivery in regenerative medicine. *Ann Biomed Eng* 2014;42:312-322.
1012. Briquez, P. S., Hubbell, J. A., Martino, M. M. Extracellular Matrix-Inspired Growth Factor Delivery Systems for Skin Wound Healing. *Adv Wound Care (New Rochelle)* 2015;4:479-489.
1013. Patel, P. N., Gobin, A. S., West, J. L., Patrick, C. W., Jr. Poly(ethylene glycol) hydrogel system supports preadipocyte viability, adhesion, and proliferation. *Tissue Eng* 2005;11:1498-1505.

1014. Clevenger, T. N., Hinman, C. R., Ashley Rubin, R. K., et al. Vitronectin-Based, Biomimetic Encapsulating Hydrogel Scaffolds Support Adipogenesis of Adipose Stem Cells. *Tissue Eng Part A* 2016;22:597-609.
1015. Niedzwiecki, L., Teahan, J., Harrison, R. K., Stein, R. L. Substrate specificity of the human matrix metalloproteinase stromelysin and the development of continuous fluorometric assays. *Biochemistry* 1992;31:12618-12623.
1016. Ferruti, P., Bianchi, S., Ranucci, E., Chiellini, F., Piras, A. M. Novel agmatine-containing poly(amidoamine) hydrogels as scaffolds for tissue engineering. *Biomacromolecules* 2005;6:2229-2235.
1017. Davidenko, N., Campbell, J. J., Thian, E. S., Watson, C. J., Cameron, R. E. Collagen-hyaluronic acid scaffolds for adipose tissue engineering. *Acta Biomater* 2010;6:3957-3968.
1018. Lin, S. D., Huang, S. H., Lin, Y. N., et al. Engineering adipose tissue from uncultured human adipose stromal vascular fraction on collagen matrix and gelatin sponge scaffolds. *Tissue Eng Part A* 2011;17:1489-1498.
1019. Frydrych, M., Roman, S., MacNeil, S., Chen, B. Biomimetic poly(glycerol sebacate)/poly(l-lactic acid) blend scaffolds for adipose tissue engineering. *Acta Biomater* 2015;18:40-49.
1020. Julier, Z., Park, A. J., Briquez, P. S., Martino, M. M. Promoting tissue regeneration by modulating the immune system. *Acta Biomater* 2017.
1021. MacDougald, O. A., Hwang, C. S., Fan, H., Lane, M. D. Regulated expression of the obese gene product (leptin) in white adipose tissue and 3T3-L1 adipocytes. *Proc Natl Acad Sci U S A* 1995;92:9034-9037.
1022. Pittenger, M. F., Mackay, A. M., Beck, S. C., et al. Multilineage potential of adult human mesenchymal stem cells. *Science* 1999;284:143-147.
1023. Serlachius, M., Andersson, L. C. Upregulated expression of stanniocalcin-1 during adipogenesis. *Exp Cell Res* 2004;296:256-264.
1024. Saiki, A., Watanabe, F., Murano, T., Miyashita, Y., Shirai, K. Hepatocyte growth factor secreted by cultured adipocytes promotes tube formation of vascular endothelial cells in vitro. *Int J Obes (Lond)* 2006;30:1676-1684.
1025. Zebisch, K., Voigt, V., Wabitsch, M., Brandsch, M. Protocol for effective differentiation of 3T3-L1 cells to adipocytes. *Anal Biochem* 2012;425:88-90.
1026. Farmer, S. R. Transcriptional control of adipocyte formation. *Cell Metab* 2006;4:263-273.
1027. Frye, C. A., Patrick, C. W. Three-dimensional adipose tissue model using low shear bioreactors. *In Vitro Cell Dev Biol Anim* 2006;42:109-114.
1028. Bouillon, R., Carmeliet, G., Lieben, L., et al. Vitamin D and energy homeostasis: of mice and men. *Nat Rev Endocrinol* 2014;10:79-87.
1029. Thomson, J. A., Itskovitz-Eldor, J., Shapiro, S. S., et al. Embryonic stem cell lines derived from human blastocysts. *Science* 1998;282:1145-1147.
1030. Cuaranta-Monroy, I., Simandi, Z., Nagy, L. Differentiation of Adipocytes in Monolayer from Mouse Embryonic Stem Cells. *Methods Mol Biol* 2016;1341:407-415.
1031. Gucciardo, L., Lories, R., Ochsenbein-Kolble, N., Done, E., Zwijsen, A., Deprest, J. Fetal mesenchymal stem cells: isolation, properties and potential use in perinatology and regenerative medicine. *BJOG* 2009;116:166-172.
1032. Takahashi, K., Okita, K., Nakagawa, M., Yamanaka, S. Induction of pluripotent stem cells from fibroblast cultures. *Nat Protoc* 2007;2:3081-3089.
1033. Aversa, F., Tabilio, A., Velardi, A., et al. Treatment of high-risk acute leukemia with T-cell-depleted stem cells from related donors with one fully mismatched HLA haplotype. *N Engl J Med* 1998;339:1186-1193.
1034. Lindroos, B., Suuronen, R., Miettinen, S. The potential of adipose stem cells in regenerative medicine. *Stem Cell Rev* 2011;7:269-291.

1035. Apovian, C. M. The Obesity Epidemic--Understanding the Disease and the Treatment. *N Engl J Med* 2016;374:177-179.
1036. Oedayrajsingh-Varma, M. J., van Ham, S. M., Knippenberg, M., et al. Adipose tissue-derived mesenchymal stem cell yield and growth characteristics are affected by the tissue-harvesting procedure. *Cytotherapy* 2006;8:166-177.
1037. Astori, G., Vignati, F., Bardelli, S., et al. "In vitro" and multicolor phenotypic characterization of cell subpopulations identified in fresh human adipose tissue stromal vascular fraction and in the derived mesenchymal stem cells. *J Transl Med* 2007;5:55.
1038. Zhu, X., Shi, W., Tai, W., Liu, F. The comparition of biological characteristics and multilineage differentiation of bone marrow and adipose derived Mesenchymal stem cells. *Cell Tissue Res* 2012;350:277-287.
1039. Baer, P. C., Geiger, H. Adipose-derived mesenchymal stromal/stem cells: tissue localization, characterization, and heterogeneity. *Stem Cells Int* 2012;2012:812693.
1040. Illouz, Y. G. Body contouring by lipolysis: a 5-year experience with over 3000 cases. *Plast Reconstr Surg* 1983;72:591-597.
1041. Ogura, F., Wakao, S., Kuroda, Y., et al. Human adipose tissue possesses a unique population of pluripotent stem cells with nontumorigenic and low telomerase activities: potential implications in regenerative medicine. *Stem Cells Dev* 2014;23:717-728.
1042. Sterodimas, A., de Faria, J., Nicaretta, B., Pitanguy, I. Tissue engineering with adipose-derived stem cells (ADSCs): current and future applications. *J Plast Reconstr Aesthet Surg* 2010;63:1886-1892.
1043. Zuk, P. A., Zhu, M., Mizuno, H., et al. Multilineage cells from human adipose tissue: implications for cell-based therapies. *Tissue Eng* 2001;7:211-228.
1044. Tavazoie, M., Van der Veken, L., Silva-Vargas, V., et al. A specialized vascular niche for adult neural stem cells. *Cell Stem Cell* 2008;3:279-288.
1045. Halvorsen, Y. D., Bond, A., Sen, A., et al. Thiazolidinediones and glucocorticoids synergistically induce differentiation of human adipose tissue stromal cells: biochemical, cellular, and molecular analysis. *Metabolism* 2001;50:407-413.
1046. Halvorsen, Y. D., Franklin, D., Bond, A. L., et al. Extracellular matrix mineralization and osteoblast gene expression by human adipose tissue-derived stromal cells. *Tissue Eng* 2001;7:729-741.
1047. Tapp, H., Hanley, E. N., Jr., Patt, J. C., Gruber, H. E. Adipose-derived stem cells: characterization and current application in orthopaedic tissue repair. *Exp Biol Med (Maywood)* 2009;234:1-9.
1048. Thesleff, T., Lehtimaki, K., Niskakangas, T., et al. Cranioplasty with adipose-derived stem cells and biomaterial: a novel method for cranial reconstruction. *Neurosurgery* 2011;68:1535-1540.
1049. Pelto, J., Bjorninen, M., Palli, A., et al. Novel polypyrrole-coated polylactide scaffolds enhance adipose stem cell proliferation and early osteogenic differentiation. *Tissue Eng Part A* 2013;19:882-892.
1050. Sandor, G. K., Tuovinen, V. J., Wolff, J., et al. Adipose stem cell tissue-engineered construct used to treat large anterior mandibular defect: a case report and review of the clinical application of good manufacturing practice-level adipose stem cells for bone regeneration. *J Oral Maxillofac Surg* 2013;71:938-950.
1051. Estes, B. T., Wu, A. W., Guilak, F. Potent induction of chondrocytic differentiation of human adipose-derived adult stem cells by bone morphogenetic protein 6. *Arthritis Rheum* 2006;54:1222-1232.
1052. Choi, Y. S., Matsuda, K., Dusting, G. J., Morrison, W. A., Dilley, R. J. Engineering cardiac tissue in vivo from human adipose-derived stem cells. *Biomaterials* 2010;31:2236-2242.

1053. Choi, S. A., Lee, J. Y., Wang, K. C., et al. Human adipose tissue-derived mesenchymal stem cells: characteristics and therapeutic potential as cellular vehicles for prodrug gene therapy against brainstem gliomas. *Eur J Cancer* 2012;48:129-137.
1054. Planat-Benard, V., Silvestre, J. S., Cousin, B., et al. Plasticity of human adipose lineage cells toward endothelial cells: physiological and therapeutic perspectives. *Circulation* 2004;109:656-663.
1055. Fang, B., Song, Y., Liao, L., Zhang, Y., Zhao, R. C. Favorable response to human adipose tissue-derived mesenchymal stem cells in steroid-refractory acute graft-versus-host disease. *Transplant Proc* 2007;39:3358-3362.
1056. Gonzalez-Rey, E., Anderson, P., Gonzalez, M. A., Rico, L., Buscher, D., Delgado, M. Human adult stem cells derived from adipose tissue protect against experimental colitis and sepsis. *Gut* 2009;58:929-939.
1057. Gonzalez-Rey, E., Gonzalez, M. A., Varela, N., et al. Human adipose-derived mesenchymal stem cells reduce inflammatory and T cell responses and induce regulatory T cells in vitro in rheumatoid arthritis. *Ann Rheum Dis* 2010;69:241-248.
1058. Riordan, N. H., Ichim, T. E., Min, W. P., et al. Non-expanded adipose stromal vascular fraction cell therapy for multiple sclerosis. *J Transl Med* 2009;7:29.
1059. Trivedi, H. L., Vanikar, A. V., Thakker, U., et al. Human adipose tissue-derived mesenchymal stem cells combined with hematopoietic stem cell transplantation synthesize insulin. *Transplant Proc* 2008;40:1135-1139.
1060. Alvarez, P. D., Garcia-Arranz, M., Georgiev-Hristov, T., Garcia-Olmo, D. A new bronchoscopic treatment of tracheomediastinal fistula using autologous adipose-derived stem cells. *Thorax* 2008;63:374-376.
1061. Nie, C., Yang, D., Morris, S. F. Local delivery of adipose-derived stem cells via acellular dermal matrix as a scaffold: a new promising strategy to accelerate wound healing. *Med Hypotheses* 2009;72:679-682.
1062. Nie, C., Zhang, G., Yang, D., et al. Targeted delivery of adipose-derived stem cells via acellular dermal matrix enhances wound repair in diabetic rats. *J Tissue Eng Regen Med* 2015;9:224-235.
1063. Kosaraju, R., Rennert, R. C., Maan, Z. N., et al. Adipose-Derived Stem Cell-Seeded Hydrogels Increase Endogenous Progenitor Cell Recruitment and Neovascularization in Wounds. *Tissue Eng Part A* 2016;22:295-305.
1064. Jurgens, W. J., Oedayrajsingh-Varma, M. J., Helder, M. N., et al. Effect of tissue-harvesting site on yield of stem cells derived from adipose tissue: implications for cell-based therapies. *Cell Tissue Res* 2008;332:415-426.
1065. Iyyanki, T., Hubenak, J., Liu, J., Chang, E. I., Beahm, E. K., Zhang, Q. Harvesting technique affects adipose-derived stem cell yield. *Aesthet Surg J* 2015;35:467-476.
1066. Schreml, S., Babilas, P., Fruth, S., et al. Harvesting human adipose tissue-derived adult stem cells: resection versus liposuction. *Cytotherapy* 2009;11:947-957.
1067. Duscher, D., Luan, A., Rennert, R. C., et al. Suction assisted liposuction does not impair the regenerative potential of adipose derived stem cells. *J Transl Med* 2016;14:126.
1068. Spalding, K. L., Arner, E., Westermark, P. O., et al. Dynamics of fat cell turnover in humans. *Nature* 2008;453:783-787.
1069. Kornicka, K., Marycz, K., Tomaszewski, K. A., Maredziak, M., Smieszek, A. The Effect of Age on Osteogenic and Adipogenic Differentiation Potential of Human Adipose Derived Stromal Stem Cells (hASCs) and the Impact of Stress Factors in the Course of the Differentiation Process. *Oxid Med Cell Longev* 2015;2015:309169.
1070. Weisberg, S. P., McCann, D., Desai, M., Rosenbaum, M., Leibel, R. L., Ferrante, A. W., Jr. Obesity is associated with macrophage accumulation in adipose tissue. *J Clin Invest* 2003;112:1796-1808.

1071. Xu, H., Barnes, G. T., Yang, Q., et al. Chronic inflammation in fat plays a crucial role in the development of obesity-related insulin resistance. *J Clin Invest* 2003;112:1821-1830.
1072. Yoshimura, K., Shigeura, T., Matsumoto, D., et al. Characterization of freshly isolated and cultured cells derived from the fatty and fluid portions of liposuction aspirates. *J Cell Physiol* 2006;208:64-76.
1073. Li, H., Zimmerlin, L., Marra, K. G., Donnenberg, V. S., Donnenberg, A. D., Rubin, J. P. Adipogenic potential of adipose stem cell subpopulations. *Plast Reconstr Surg* 2011;128:663-672.
1074. Markarian, C. F., Frey, G. Z., Silveira, M. D., et al. Isolation of adipose-derived stem cells: a comparison among different methods. *Biotechnol Lett* 2014;36:693-702.
1075. Tholpady, S. S., Llull, R., Ogle, R. C., Rubin, J. P., Futrell, J. W., Katz, A. J. Adipose tissue: stem cells and beyond. *Clin Plast Surg* 2006;33:55-62, vi.
1076. Quarto, N., Longaker, M. T. FGF-2 inhibits osteogenesis in mouse adipose tissue-derived stromal cells and sustains their proliferative and osteogenic potential state. *Tissue Eng* 2006;12:1405-1418.
1077. Gierloff, M., Petersen, L., Oberg, H. H., Quabius, E. S., Wiltfang, J., Acil, Y. Adipogenic differentiation potential of rat adipose tissue-derived subpopulations of stromal cells. *J Plast Reconstr Aesthet Surg* 2014;67:1427-1435.
1078. Han, T. T., Toutounji, S., Amsden, B. G., Flynn, L. E. Adipose-derived stromal cells mediate in vivo adipogenesis, angiogenesis and inflammation in decellularized adipose tissue bioscaffolds. *Biomaterials* 2015;72:125-137.
1079. Ghorbani, F. M., Kaffashi, B., Shokrollahi, P., Seyedjafari, E., Ardeshirylajimi, A. PCL/chitosan/Zn-doped nHA electrospun nanocomposite scaffold promotes adipose derived stem cells adhesion and proliferation. *Carbohydr Polym* 2015;118:133-142.
1080. Mays, R. W., van't Hof, W., Ting, A. E., Perry, R., Deans, R. Development of adult pluripotent stem cell therapies for ischemic injury and disease. *Expert Opin Biol Ther* 2007;7:173-184.
1081. Mimeault, M., Hauke, R., Batra, S. K. Stem cells: a revolution in therapeutics-recent advances in stem cell biology and their therapeutic applications in regenerative medicine and cancer therapies. *Clin Pharmacol Ther* 2007;82:252-264.
1082. Miltenyi, S., Muller, W., Weichel, W., Radbruch, A. High gradient magnetic cell separation with MACS. *Cytometry* 1990;11:231-238.
1083. Valli, H., Sukhwani, M., Dovey, S. L., et al. Fluorescence- and magnetic-activated cell sorting strategies to isolate and enrich human spermatogonial stem cells. *Fertil Steril* 2014;102:566-580 e567.
1084. Indumathi, S., Mishra, R., Harikrishnan, R., Rajkumar, J. S., Kantawala, N., Dhanasekaran, M. Lineage depletion of stromal vascular fractions isolated from human adipose tissue: a novel approach towards cell enrichment technology. *Cytotechnology* 2014;66:219-228.
1085. Bourin, P., Bunnell, B. A., Casteilla, L., et al. Stromal cells from the adipose tissue-derived stromal vascular fraction and culture expanded adipose tissue-derived stromal/stem cells: a joint statement of the International Federation for Adipose Therapeutics and Science (IFATS) and the International Society for Cellular Therapy (ISCT). *Cytotherapy* 2013;15:641-648.
1086. Lauvrud, A. T., Kelk, P., Wiberg, M., Kingham, P. J. Characterization of human adipose tissue-derived stem cells with enhanced angiogenic and adipogenic properties. *J Tissue Eng Regen Med* 2016.
1087. Chang, Q., Lu, F. A novel strategy for creating a large amount of engineered fat tissue with an axial vascular pedicle and a prefabricated scaffold. *Med Hypotheses* 2012;79:267-270.

1088. Khan, S., Villalobos, M. A., Choron, R. L., et al. Fibroblast growth factor and vascular endothelial growth factor play a critical role in endotheliogenesis from human adipose-derived stem cells. *J Vasc Surg* 2016.
1089. Awad, H. A., Halvorsen, Y. D., Gimble, J. M., Guilak, F. Effects of transforming growth factor beta1 and dexamethasone on the growth and chondrogenic differentiation of adipose-derived stromal cells. *Tissue Eng* 2003;9:1301-1312.
1090. Kim, W. S., Park, H. S., Sung, J. H. The pivotal role of PDGF and its receptor isoforms in adipose-derived stem cells. *Histol Histopathol* 2015;30:793-799.
1091. Behr, B., Tang, C., Germann, G., Longaker, M. T., Quarto, N. Locally applied vascular endothelial growth factor A increases the osteogenic healing capacity of human adipose-derived stem cells by promoting osteogenic and endothelial differentiation. *Stem Cells* 2011;29:286-296.
1092. Gehmert, S., Gehmert, S., Hidayat, M., et al. Angiogenesis: the role of PDGF-BB on adipose-tissue derived stem cells (ASCs). *Clin Hemorheol Microcirc* 2011;48:5-13.
1093. Ting, A. C., Craft, R. O., Palmer, J. A., et al. The adipogenic potential of various extracellular matrices under the influence of an angiogenic growth factor combination in a mouse tissue engineering chamber. *Acta Biomater* 2014;10:1907-1918.
1094. Morimoto, A., Okamura, K., Hamanaka, R., et al. Hepatocyte growth factor modulates migration and proliferation of human microvascular endothelial cells in culture. *Biochem Biophys Res Commun* 1991;179:1042-1049.
1095. Davis, G. E., Stratman, A. N., Sacharidou, A., Koh, W. Molecular basis for endothelial lumen formation and tubulogenesis during vasculogenesis and angiogenic sprouting. *Int Rev Cell Mol Biol* 2011;288:101-165.
1096. Esteva, F. J., Sahin, A. A., Smith, T. L., et al. Prognostic significance of phosphorylated P38 mitogen-activated protein kinase and HER-2 expression in lymph node-positive breast carcinoma. *Cancer* 2004;100:499-506.
1097. Wagner, E. F., Nebreda, A. R. Signal integration by JNK and p38 MAPK pathways in cancer development. *Nat Rev Cancer* 2009;9:537-549.
1098. Kim, B. S., Kang, K. S., Kang, S. K. Soluble factors from ASCs effectively direct control of chondrogenic fate. *Cell Prolif* 2010;43:249-261.
1099. Shigematsu, S., Yamauchi, K., Nakajima, K., Iijima, S., Aizawa, T., Hashizume, K. IGF-1 regulates migration and angiogenesis of human endothelial cells. *Endocr J* 1999;46 Suppl:S59-62.
1100. Aghdam, S. Y., Eming, S. A., Willenborg, S., et al. Vascular endothelial insulin/IGF-1 signaling controls skin wound vascularization. *Biochem Biophys Res Commun* 2012;421:197-202.
1101. Shima, N., Kimoto, M., Yamaguchi, M., Yamagami, S. Increased proliferation and replicative lifespan of isolated human corneal endothelial cells with L-ascorbic acid 2-phosphate. *Invest Ophthalmol Vis Sci* 2011;52:8711-8717.
1102. Pike, D. B., Cai, S., Pomraning, K. R., et al. Heparin-regulated release of growth factors in vitro and angiogenic response in vivo to implanted hyaluronan hydrogels containing VEGF and bFGF. *Biomaterials* 2006;27:5242-5251.
1103. Hamed, S., Ben-Nun, O., Egozi, D., et al. Treating fat grafts with human endothelial progenitor cells promotes their vascularization and improves their survival in diabetes mellitus. *Plast Reconstr Surg* 2012;130:801-811.
1104. Yao, R., Du, Y., Zhang, R., Lin, F., Luan, J. A biomimetic physiological model for human adipose tissue by adipocytes and endothelial cell cocultures with spatially controlled distribution. *Biomed Mater* 2013;8:045005.
1105. Alfieri, A., Ong, A. C., Kammerer, R. A., et al. Angiopoietin-1 regulates microvascular reactivity and protects the microcirculation during acute endothelial dysfunction: role of eNOS and VE-cadherin. *Pharmacol Res* 2014;80:43-51.

1106. Haug, V., Torio-Padron, N., Stark, G. B., Finkenzeller, G., Strassburg, S. Comparison between endothelial progenitor cells and human umbilical vein endothelial cells on neovascularization in an adipogenesis mouse model. *Microvasc Res* 2015;97:159-166.
1107. Koolwijk, P., van Erck, M. G., de Vree, W. J., et al. Cooperative effect of TNFalpha, bFGF, and VEGF on the formation of tubular structures of human microvascular endothelial cells in a fibrin matrix. Role of urokinase activity. *J Cell Biol* 1996;132:1177-1188.
1108. Cross, M. J., Claesson-Welsh, L. FGF and VEGF function in angiogenesis: signalling pathways, biological responses and therapeutic inhibition. *Trends Pharmacol Sci* 2001;22:201-207.
1109. Silva, E. A., Mooney, D. J. Effects of VEGF temporal and spatial presentation on angiogenesis. *Biomaterials* 2010;31:1235-1241.
1110. Serrero, G., Mills, D. Physiological role of epidermal growth factor on adipose tissue development in vivo. *Proc Natl Acad Sci U S A* 1991;88:3912-3916.
1111. Vassaux, G., Negrel, R., Ailhaud, G., Gaillard, D. Proliferation and differentiation of rat adipose precursor cells in chemically defined medium: differential action of anti-adipogenic agents. *J Cell Physiol* 1994;161:249-256.
1112. Hauner, H., Rohrig, K., Petruschke, T. Effects of epidermal growth factor (EGF), platelet-derived growth factor (PDGF) and fibroblast growth factor (FGF) on human adipocyte development and function. *Eur J Clin Invest* 1995;25:90-96.
1113. Haystead, T. A., Hardie, D. G. Both insulin and epidermal growth factor stimulate lipogenesis and acetyl-CoA carboxylase activity in isolated adipocytes. Importance of homogenization procedure in avoiding artefacts in acetyl-CoA carboxylase assay. *Biochem J* 1986;234:279-284.
1114. Moule, S. K., Edgell, N. J., Welsh, G. I., et al. Multiple signalling pathways involved in the stimulation of fatty acid and glycogen synthesis by insulin in rat epididymal fat cells. *Biochem J* 1995;311 (Pt 2):595-601.
1115. Baba, A. S., Harper, J. M., Buttery, P. J. Effects of gastric inhibitory polypeptide, somatostatin and epidermal growth factor on lipogenesis in ovine adipose explants. *Comp Biochem Physiol B Biochem Mol Biol* 2000;127:173-182.
1116. Cigolini, M., Smith, U. Human adipose tissue in culture. VIII. Studies on the insulin-antagonistic effect of glucocorticoids. *Metabolism* 1979;28:502-510.
1117. Walton, P. E., Etherton, T. D., Evock, C. M. Antagonism of insulin action in cultured pig adipose tissue by pituitary and recombinant porcine growth hormone: potentiation by hydrocortisone. *Endocrinology* 1986;118:2577-2581.
1118. Huber, B., Czaja, A. M., Kluger, P. J. Influence of epidermal growth factor (EGF) and hydrocortisone on the co-culture of mature adipocytes and endothelial cells for vascularized adipose tissue engineering. *Cell Biol Int* 2016;40:569-578.
1119. Chazaud, B. Macrophages: supportive cells for tissue repair and regeneration. *Immunobiology* 2014;219:172-178.
1120. Daley, J. M., Brancato, S. K., Thomay, A. A., Reichner, J. S., Albina, J. E. The phenotype of murine wound macrophages. *J Leukoc Biol* 2010;87:59-67.
1121. Mokarram, N., Merchant, A., Mukhatyar, V., Patel, G., Bellamkonda, R. V. Effect of modulating macrophage phenotype on peripheral nerve repair. *Biomaterials* 2012;33:8793-8801.
1122. Kharraz, Y., Guerra, J., Mann, C. J., Serrano, A. L., Munoz-Canoves, P. Macrophage plasticity and the role of inflammation in skeletal muscle repair. *Mediators Inflamm* 2013;2013:491497.
1123. Ben-Mordechai, T., Holbova, R., Landa-Rouben, N., et al. Macrophage subpopulations are essential for infarct repair with and without stem cell therapy. *J Am Coll Cardiol* 2013;62:1890-1901.

1124. Li, Z., Xu, F., Wang, Z., et al. Macrophages Undergo M1-to-M2 Transition in Adipose Tissue Regeneration in a Rat Tissue Engineering Model. *Artif Organs* 2016;40:E167-E178.
1125. Debels, H., Galea, L., Han, X. L., et al. Macrophages play a key role in angiogenesis and adipogenesis in a mouse tissue engineering model. *Tissue Eng Part A* 2013;19:2615-2625.
1126. Chandler, E. M., Seo, B. R., Califano, J. P., et al. Implanted adipose progenitor cells as physicochemical regulators of breast cancer. *Proc Natl Acad Sci U S A* 2012;109:9786-9791.
1127. Koellensperger, E., Gramley, F., Preisner, F., Leimer, U., Germann, G., Dexheimer, V. Alterations of gene expression and protein synthesis in co-cultured adipose tissue-derived stem cells and squamous cell-carcinoma cells: consequences for clinical applications. *Stem Cell Res Ther* 2014;5:65.
1128. Cousin, B., Ravet, E., Poglio, S., et al. Adult stromal cells derived from human adipose tissue provoke pancreatic cancer cell death both in vitro and in vivo. *PLoS One* 2009;4:e6278.
1129. Zhao, W., Ren, G., Zhang, L., et al. Efficacy of mesenchymal stem cells derived from human adipose tissue in inhibition of hepatocellular carcinoma cells in vitro. *Cancer Biother Radiopharm* 2012;27:606-613.
1130. Karnoub, A. E., Dash, A. B., Vo, A. P., et al. Mesenchymal stem cells within tumour stroma promote breast cancer metastasis. *Nature* 2007;449:557-563.
1131. Mizuno, H. Adipose-derived stem cells for tissue repair and regeneration: ten years of research and a literature review. *J Nippon Med Sch* 2009;76:56-66.
1132. Dai, R., Wang, Z., Samanipour, R., Koo, K. I., Kim, K. Adipose-Derived Stem Cells for Tissue Engineering and Regenerative Medicine Applications. *Stem Cells Int* 2016;2016:6737345.
1133. Lindroos, B., Boucher, S., Chase, L., et al. Serum-free, xeno-free culture media maintain the proliferation rate and multipotentiality of adipose stem cells in vitro. *Cytotherapy* 2009;11:958-972.
1134. Atashi, F., Jaconi, M. E., Pittet-Cuenod, B., Modarressi, A. Autologous platelet-rich plasma: a biological supplement to enhance adipose-derived mesenchymal stem cell expansion. *Tissue Eng Part C Methods* 2015;21:253-262.
1135. Liao, H. T., James, I. B., Marra, K. G., Rubin, J. P. The Effects of Platelet-Rich Plasma on Cell Proliferation and Adipogenic Potential of Adipose-Derived Stem Cells. *Tissue Eng Part A* 2015;21:2714-2722.
1136. Ovsianikov, A., Deiwick, A., Van Vlierberghe, S., et al. Laser fabrication of 3D gelatin scaffolds for the generation of bioartificial tissues. *Materials* 2011;4:288-299.
1137. Williams, S. K., Touroo, J. S., Church, K. H., Hoying, J. B. Encapsulation of adipose stromal vascular fraction cells in alginate hydrogel spheroids using a direct-write three-dimensional printing system. *Biores Open Access* 2013;2:448-454.
1138. Huber, B., Borchers, K., Tovar, G. E., Kluger, P. J. Methacrylated gelatin and mature adipocytes are promising components for adipose tissue engineering. *J Biomater Appl* 2016;30:699-710.
1139. Zuk, P. A., Zhu, M., Ashjian, P., et al. Human adipose tissue is a source of multipotent stem cells. *Mol Biol Cell* 2002;13:4279-4295.
1140. Gomillion, C. T., Burg, K. J. Stem cells and adipose tissue engineering. *Biomaterials* 2006;27:6052-6063.
1141. Findlay, M. W., Dolderer, J. H., Trost, N., et al. Tissue-engineered breast reconstruction: bridging the gap toward large-volume tissue engineering in humans. *Plast Reconstr Surg* 2011;128:1206-1215.

1142. Dolderer, J. H., Abberton, K. M., Thompson, E. W., et al. Spontaneous large volume adipose tissue generation from a vascularized pedicled fat flap inside a chamber space. *Tissue Eng* 2007;13:673-681.
1143. Lokmic, Z., Stillaert, F., Morrison, W. A., Thompson, E. W., Mitchell, G. M. An arteriovenous loop in a protected space generates a permanent, highly vascular, tissue-engineered construct. *FASEB J* 2007;21:511-522.
1144. Lilja, H. E., Morrison, W. A., Han, X. L., et al. An adipoinductive role of inflammation in adipose tissue engineering: key factors in the early development of engineered soft tissues. *Stem Cells Dev* 2013;22:1602-1613.
1145. Peng, Z., Dong, Z., Chang, Q., et al. Tissue engineering chamber promotes adipose tissue regeneration in adipose tissue engineering models through induced aseptic inflammation. *Tissue Eng Part C Methods* 2014;20:875-885.
1146. Wan, J., Dong, Z., Lei, C., Lu, F. Generating an Engineered Adipose Tissue Flap Using an External Suspension Device. *Plast Reconstr Surg* 2016;138:109-120.
1147. Hofer, S. O., Knight, K. M., Cooper-White, J. J., et al. Increasing the volume of vascularized tissue formation in engineered constructs: an experimental study in rats. *Plast Reconstr Surg* 2003;111:1186-1192; discussion 1193-1184.
1148. Cao, Y., Mitchell, G., Messina, A., et al. The influence of architecture on degradation and tissue ingrowth into three-dimensional poly(lactic-co-glycolic acid) scaffolds in vitro and in vivo. *Biomaterials* 2006;27:2854-2864.
1149. Dolderer, J. H., Thompson, E. W., Slavin, J., et al. Long-term stability of adipose tissue generated from a vascularized pedicled fat flap inside a chamber. *Plast Reconstr Surg* 2011;127:2283-2292.
1150. Zhan, W., Chang, Q., Xiao, X., et al. Self-synthesized extracellular matrix contributes to mature adipose tissue regeneration in a tissue engineering chamber. *Wound Repair Regen* 2015;23:443-452.
1151. Lu, Z., Yuan, Y., Gao, J., Lu, F. Adipose tissue extract promotes adipose tissue regeneration in an adipose tissue engineering chamber model. *Cell Tissue Res* 2016;364:289-298.
1152. Morrison, W. A., Marre, D., Grinsell, D., Batty, A., Trost, N., O'Connor, A. J. Creation of a Large Adipose Tissue Construct in Humans Using a Tissue-engineering Chamber: A Step Forward in the Clinical Application of Soft Tissue Engineering. *EBioMedicine* 2016;6:238-245.
1153. Heit, Y. I., Lancerotto, L., Mesteri, I., et al. External volume expansion increases subcutaneous thickness, cell proliferation, and vascular remodeling in a murine model. *Plast Reconstr Surg* 2012;130:541-547.
1154. Liu, Y. S., Lee, O. K. In search of the pivot point of mechanotransduction: mechanosensing of stem cells. *Cell Transplant* 2014;23:1-11.
1155. Brorson, H. Adipose tissue in lymphedema: the ignorance of adipose tissue in lymphedema. *Lymphology* 2004;37:175-177.
1156. Wang, N., Tytell, J. D., Ingber, D. E. Mechanotransduction at a distance: mechanically coupling the extracellular matrix with the nucleus. *Nat Rev Mol Cell Biol* 2009;10:75-82.
1157. Gretzer, C., Emanuelsson, L., Liljensten, E., Thomsen, P. The inflammatory cell influx and cytokines changes during transition from acute inflammation to fibrous repair around implanted materials. *J Biomater Sci Polym Ed* 2006;17:669-687.
1158. Anderson, J. M., Rodriguez, A., Chang, D. T. Foreign body reaction to biomaterials. *Semin Immunol* 2008;20:86-100.
1159. Cronin, K. J., Messina, A., Knight, K. R., et al. New murine model of spontaneous autologous tissue engineering, combining an arteriovenous pedicle with matrix materials. *Plast Reconstr Surg* 2004;113:260-269.

1160. Lokmic, Z., Mitchell, G. M. Engineering the microcirculation. *Tissue Eng Part B Rev* 2008;14:87-103.
1161. Matsuda, K., Falkenberg, K. J., Woods, A. A., Choi, Y. S., Morrison, W. A., Dilley, R. J. Adipose-derived stem cells promote angiogenesis and tissue formation for in vivo tissue engineering. *Tissue Eng Part A* 2013;19:1327-1335.
1162. Reichert, J. C., Cipitria, A., Epari, D. R., et al. A tissue engineering solution for segmental defect regeneration in load-bearing long bones. *Sci Transl Med* 2012;4:141ra193.
1163. Rohner, D., Hutmacher, D. W., Cheng, T. K., Oberholzer, M., Hammer, B. In vivo efficacy of bone-marrow-coated polycaprolactone scaffolds for the reconstruction of orbital defects in the pig. *J Biomed Mater Res B Appl Biomater* 2003;66:574-580.
1164. Schantz, J. T., Lim, T. C., Ning, C., et al. Cranioplasty after trephination using a novel biodegradable burr hole cover: technical case report. *Neurosurgery* 2006;58:ONS-E176; discussion ONS-E176.
1165. Rai, B., Oest, M. E., Dupont, K. M., Ho, K. H., Teoh, S. H., Guldberg, R. E. Combination of platelet-rich plasma with polycaprolactone-tricalcium phosphate scaffolds for segmental bone defect repair. *J Biomed Mater Res A* 2007;81:888-899.
1166. Stevens, M. M., Marini, R. P., Schaefer, D., Aronson, J., Langer, R., Shastri, V. P. In vivo engineering of organs: the bone bioreactor. *Proc Natl Acad Sci U S A* 2005;102:11450-11455.
1167. Zhong, T., Hu, J., Bagher, S., et al. A Comparison of Psychological Response, Body Image, Sexuality, and Quality of Life between Immediate and Delayed Autologous Tissue Breast Reconstruction: A Prospective Long-Term Outcome Study. *Plast Reconstr Surg* 2016;138:772-780.
1168. Duraes, E. F., Durand, P., Duraes, L. C., et al. Comparison of preoperative quality of life in breast reconstruction, breast aesthetic and non-breast plastic surgery patients: A cross-sectional study. *J Plast Reconstr Aesthet Surg* 2016.
1169. Didier, F., Arnaboldi, P., Gandini, S., et al. Why do women accept to undergo a nipple sparing mastectomy or to reconstruct the nipple areola complex when nipple sparing mastectomy is not possible? *Breast Cancer Res Treat* 2012;132:1177-1184.
1170. Peled, A. W., Wang, F., Foster, R. D., et al. Expanding the Indications for Total Skin-Sparing Mastectomy: Is It Safe for Patients with Locally Advanced Disease? *Ann Surg Oncol* 2016;23:87-91.
1171. Sisco, M., Kyrillos, A. M., Lapin, B. R., Wang, C. E., Yao, K. A. Trends and variation in the use of nipple-sparing mastectomy for breast cancer in the United States. *Breast Cancer Res Treat* 2016;160:111-120.
1172. Amanti, C., Vitale, V., Lombardi, A., et al. Importance of perforating vessels in nipple-sparing mastectomy: an anatomical description. *Breast Cancer (Dove Med Press)* 2015;7:179-181.
1173. Shimo, A., Tsugawa, K., Tsuchiya, S., et al. Oncologic outcomes and technical considerations of nipple-sparing mastectomies in breast cancer: experience of 425 cases from a single institution. *Breast Cancer* 2015.
1174. De La Cruz, L., Moody, A. M., Tappy, E. E., Blankenship, S. A., Hecht, E. M. Overall Survival, Disease-Free Survival, Local Recurrence, and Nipple-Areolar Recurrence in the Setting of Nipple-Sparing Mastectomy: A Meta-Analysis and Systematic Review. *Ann Surg Oncol* 2015;22:3241-3249.
1175. Ou, K. W., Yu, J. C., Ho, M. H., et al. Oncological safety and outcomes of nipple-sparing mastectomy with breast reconstruction: a single-centered experience in Taiwan. *Ann Plast Surg* 2015;74 Suppl 2:S127-131.
1176. Adam, H., Bygdeson, M., de Boniface, J. The oncological safety of nipple-sparing mastectomy - a Swedish matched cohort study. *Eur J Surg Oncol* 2014;40:1209-1215.

1177. van Verschuer, V. M., Mureau, M. A., Gopie, J. P., et al. Patient Satisfaction and Nipple-Areola Sensitivity After Bilateral Prophylactic Mastectomy and Immediate Implant Breast Reconstruction in a High Breast Cancer Risk Population: Nipple-Sparing Mastectomy Versus Skin-Sparing Mastectomy. *Ann Plast Surg* 2016;77:145-152.
1178. Krajewski, A. C., Boughey, J. C., Degnim, A. C., et al. Expanded Indications and Improved Outcomes for Nipple-Sparing Mastectomy Over Time. *Ann Surg Oncol* 2015;22:3317-3323.
1179. Cho, J. W., Yoon, E. S., You, H. J., Kim, H. S., Lee, B. I., Park, S. H. Nipple-Areola Complex Necrosis after Nipple-Sparing Mastectomy with Immediate Autologous Breast Reconstruction. *Arch Plast Surg* 2015;42:601-607.
1180. Bingol, U. A., Cinar, C. Skin Necrosis in a Patient with Factor V Leiden Mutation following Nipple Sparing Mastectomy. *Plast Reconstr Surg Glob Open* 2015;3:e529.
1181. Sisti, A., Grimaldi, L., Tassinari, J., et al. Nipple-areola complex reconstruction techniques: A literature review. *Eur J Surg Oncol* 2016;42:441-465.
1182. Losken, A., Duggal, C. S., Desai, K. A., McCullough, M. C., Gruszynski, M. A., Carlson, G. W. Time to completion of nipple reconstruction: what factors are involved? *Ann Plast Surg* 2013;70:530-532.
1183. Wellisch, D. K., Schain, W. S., Noone, R. B., Little, J. W., 3rd. The psychological contribution of nipple addition in breast reconstruction. *Plast Reconstr Surg* 1987;80:699-704.
1184. Delay, E., Mojallal, A., Vasseur, C., Delaporte, T. Immediate nipple reconstruction during immediate autologous latissimus breast reconstruction. *Plast Reconstr Surg* 2006;118:1303-1312.
1185. Chattopadhyay, D., Gupta, S., Jash, P. K., Murmu, M. B., Gupta, S. Skin sparing mastectomy with preservation of nipple areola complex and immediate breast reconstruction in patients with breast cancer: a single centre prospective study. *Plast Surg Int* 2014;2014:589068.
1186. Momoh, A. O., Colakoglu, S., de Blacam, C., et al. The impact of nipple reconstruction on patient satisfaction in breast reconstruction. *Ann Plast Surg* 2012;69:389-393.
1187. Nimboriboonporn, A., Chuthapisith, S. Nipple-areola complex reconstruction. *Gland Surg* 2014;3:35-42.
1188. Jabor, M. A., Shayani, P., Collins, D. R., Jr., Karas, T., Cohen, B. E. Nipple-areola reconstruction: satisfaction and clinical determinants. *Plast Reconstr Surg* 2002;110:457-463; discussion 464-455.
1189. Phipps, M. C., Xu, Y., Bellis, S. L. Delivery of platelet-derived growth factor as a chemotactic factor for mesenchymal stem cells by bone-mimetic electrospun scaffolds. *PLoS One* 2012;7:e40831.
1190. Lam, M. T., Longaker, M. T. Comparison of several attachment methods for human iPS, embryonic and adipose-derived stem cells for tissue engineering. *J Tissue Eng Regen Med* 2012;6 Suppl 3:s80-86.
1191. O'Connor, N. E., Mulliken, J. B., Banks-Schlegel, S., Kehinde, O., Green, H. Grafting of burns with cultured epithelium prepared from autologous epidermal cells. *Lancet* 1981;1:75-78.
1192. Gerlach, J. C., Johnen, C., Ottomann, C., et al. Method for autologous single skin cell isolation for regenerative cell spray transplantation with non-cultured cells. *Int J Artif Organs* 2011;34:271-279.
1193. Wood, F. M., Giles, N., Stevenson, A., Rea, S., Fear, M. Characterisation of the cell suspension harvested from the dermal epidermal junction using a ReCell(R) kit. *Burns* 2012;38:44-51.

1194. Carsin, H., Ainaud, P., Le Bever, H., et al. Cultured epithelial autografts in extensive burn coverage of severely traumatized patients: a five year single-center experience with 30 patients. *Burns* 2000;26:379-387.
1195. Centanni, J. M., Straseski, J. A., Wicks, A., et al. StrataGraft skin substitute is well-tolerated and is not acutely immunogenic in patients with traumatic wounds: results from a prospective, randomized, controlled dose escalation trial. *Ann Surg* 2011;253:672-683.
1196. Bottcher-Haberzeth, S., Biedermann, T., Reichmann, E. Tissue engineering of skin. *Burns* 2010;36:450-460.
1197. Langer, A., Rogowski, W. Systematic review of economic evaluations of human cell-derived wound care products for the treatment of venous leg and diabetic foot ulcers. *BMC Health Serv Res* 2009;9:115.
1198. Fagerholm, P., Lagali, N. S., Merrett, K., et al. A biosynthetic alternative to human donor tissue for inducing corneal regeneration: 24-month follow-up of a phase 1 clinical study. *Sci Transl Med* 2010;2:46ra61.
1199. Fagerholm, P., Lagali, N. S., Carlsson, D. J., Merrett, K., Griffith, M. Corneal regeneration following implantation of a biomimetic tissue-engineered substitute. *Clin Transl Sci* 2009;2:162-164.
1200. Palmer, D. A., Marcello, P. W., Zinman, L. N., Vanni, A. J. Urethral Reconstruction with Rectal Mucosa Graft Onlay: A Novel, Minimally Invasive Technique. *J Urol* 2016;196:782-786.
1201. Lv, X., Xu, Y. M., Xie, H., Feng, C., Zhang, J. The Selection of Procedures in One-stage Urethroplasty for Treatment of Coexisting Urethral Strictures in Anterior and Posterior Urethra. *Urology* 2016;93:197-202.
1202. Bayramicli, M., Akdeniz, Z. D. Urethra reconstruction with lateral pectoral flap in female-to-male transsexual patients. *J Plast Reconstr Aesthet Surg* 2016.
1203. Shin'oka, T., Imai, Y., Ikada, Y. Transplantation of a tissue-engineered pulmonary artery. *N Engl J Med* 2001;344:532-533.
1204. L'Heureux, N., McAllister, T. N., de la Fuente, L. M. Tissue-engineered blood vessel for adult arterial revascularization. *N Engl J Med* 2007;357:1451-1453.
1205. Dahl, S. L., Kypson, A. P., Lawson, J. H., et al. Readily available tissue-engineered vascular grafts. *Sci Transl Med* 2011;3:68ra69.
1206. Scriven, S. D., Booth, C., Thomas, D. F., Trejdosiewicz, L. K., Southgate, J. Reconstitution of human urothelium from monolayer cultures. *J Urol* 1997;158:1147-1152.
1207. Soler, R., Fullhase, C., Atala, A. Regenerative medicine strategies for treatment of neurogenic bladder. *Therapy* 2009;6:177-184.
1208. Oberpenning, F., Meng, J., Yoo, J. J., Atala, A. De novo reconstitution of a functional mammalian urinary bladder by tissue engineering. *Nat Biotechnol* 1999;17:149-155.
1209. De Filippo, R. E., Bishop, C. E., Filho, L. F., Yoo, J. J., Atala, A. Tissue engineering a complete vaginal replacement from a small biopsy of autologous tissue. *Transplantation* 2008;86:208-214.
1210. Pashuck, E. T., Stevens, M. M. Designing regenerative biomaterial therapies for the clinic. *Sci Transl Med* 2012;4:160sr164.
1211. Cuomo, A. V., Virk, M., Petrigliano, F., Morgan, E. F., Lieberman, J. R. Mesenchymal stem cell concentration and bone repair: potential pitfalls from bench to bedside. *J Bone Joint Surg Am* 2009;91:1073-1083.
1212. Lokmic, Z., Thomas, J. L., Morrison, W. A., Thompson, E. W., Mitchell, G. M. An endogenously deposited fibrin scaffold determines construct size in the surgically created arteriovenous loop chamber model of tissue engineering. *J Vasc Surg* 2008;48:974-985.
1213. Lin, S. D., Wang, K. H., Kao, A. P. Engineered adipose tissue of predefined shape and dimensions from human adipose-derived mesenchymal stem cells. *Tissue Eng Part A* 2008;14:571-581.

1214. Lanza, R. P., Chung, H. Y., Yoo, J. J., et al. Generation of histocompatible tissues using nuclear transplantation. *Nat Biotechnol* 2002;20:689-696.
1215. Orlando, G., Farney, A. C., Iskandar, S. S., et al. Production and implantation of renal extracellular matrix scaffolds from porcine kidneys as a platform for renal bioengineering investigations. *Ann Surg* 2012;256:363-370.
1216. Chen, K. L., Eberli, D., Yoo, J. J., Atala, A. Bioengineered corporal tissue for structural and functional restoration of the penis. *Proc Natl Acad Sci U S A* 2010;107:3346-3350.
1217. Ott, H. C., Matthiesen, T. S., Goh, S. K., et al. Perfusion-decellularized matrix: using nature's platform to engineer a bioartificial heart. *Nat Med* 2008;14:213-221.
1218. Baptista, P. M., Siddiqui, M. M., Lozier, G., Rodriguez, S. R., Atala, A., Soker, S. The use of whole organ decellularization for the generation of a vascularized liver organoid. *Hepatology* 2011;53:604-617.
1219. De Carlo, E., Baiguera, S., Conconi, M. T., et al. Pancreatic acellular matrix supports islet survival and function in a synthetic tubular device: in vitro and in vivo studies. *Int J Mol Med* 2010;25:195-202.
1220. Fedorovich, N. E., Schuurman, W., Wijnberg, H. M., et al. Biofabrication of osteochondral tissue equivalents by printing topologically defined, cell-laden hydrogel scaffolds. *Tissue Eng Part C Methods* 2012;18:33-44.
1221. Xu, T., Olson, J., Zhao, W. X., Atala, A., Zhu, J. M., Yoo, J. J. Characterization of cell constructs generated with inkjet printing technology using in vivo magnetic resonance imaging. *J Manuf Sci Eng Trans ASME* 2008;130:021013.
1222. Zhao, W., Xu, T., Aboushwareb, T., Atala, A., Yoo, J. In vivo generation of functional tissues using the inkjet printing technology for reconstructive surgery. *J Am Coll Surg* 2010;211:S87.
1223. Malafaya, P. B., Silva, G. A., Reis, R. L. Natural-origin polymers as carriers and scaffolds for biomolecules and cell delivery in tissue engineering applications. *Adv Drug Deliv Rev* 2007;59:207-233.
1224. Berson, M. I. Construction of pseudoareola. *Surgery* 1946;20:808.
1225. Little, J. W., 3rd, Spear, S. L. The finishing touches in nipple-areolar reconstruction. *Perspect Plast Surg* 1988;2:1-22.
1226. Anton, L. E., Hartrampf, C. R. Nipple reconstruction with local flaps: star and wrap flaps. *Perspect Plast Surg* 1991;5:67-78.
1227. Jones, G., Bostwick, J. Nipple-areolar reconstruction. *Oper Tech Plast Reconstr Surg* 1994;1:35-38.
1228. Mori, H., Hata, Y. Modified C-V flap in nipple reconstruction. *J Plast Reconstr Aesthet Surg* 2008;61:1109-1110.
1229. Brackley, P. T., Iqbal, A. Enhancing your C-V flap nipple reconstruction. *J Plast Reconstr Aesthet Surg* 2009;62:128-130.
1230. El-Ali, K., Dalal, M., Kat, C. C. Modified C-V flap for nipple reconstruction: our results in 50 patients. *J Plast Reconstr Aesthet Surg* 2009;62:991-996.
1231. Witt, P., Dujon, D. G. The V-V flap--a simple modification of the C-V flap for nipple reconstruction. *J Plast Reconstr Aesthet Surg* 2013;66:1009-1010.
1232. Elizabeth Clark, S., Turton, E. The CC-V Flap: A Novel Technique for Augmenting a C-V Nipple Reconstruction Using a Free Dermal Graft. *World J Plast Surg* 2014;3:8-12.
1233. Salgarello, M., Cavalcanti, P., Barone-Adesi, L. Atypical patterns in C-V flap nipple reconstruction: a customisation of the C-V flap. *J Plast Reconstr Aesthet Surg* 2014;67:1598-1599.
1234. Temiz, G., Yesiloglu, N., Sirinoglu, H., Sarici, M. A New Modification of C-V Flap Technique in Nipple Reconstruction: Rolled Triangular Dermal-Fat Flaps. *Aesthetic Plast Surg* 2015;39:173-175.

1235. Adams, W. M. Labial transplant for correction of loss of the nipple. *Plast Reconstr Surg (1946)* 1949;4:295-298.
1236. Gruber, R. P. Nipple-areola reconstruction: a review of techniques. *Clin Plast Surg* 1979;6:71-83.
1237. Millard, D. R., Jr. Nipple and areola reconstruction by split-skin graft from the normal side. *Plast Reconstr Surg* 1972;50:350-353.
1238. Dean, N. R., Neild, T., Haynes, J., Goddard, C., Cooter, R. D. Fading of nipple-areolar reconstructions: the last hurdle in breast reconstruction? *Br J Plast Surg* 2002;55:574-581.
1239. Haslik, W., Nedomansky, J., Hacker, S., Nickl, S., Schroegendorfer, K. F. Objective and subjective evaluation of donor-site morbidity after nipple sharing for nipple areola reconstruction. *J Plast Reconstr Aesthet Surg* 2015;68:168-174.
1240. Collis, N., Garrido, A. Maintenance of nipple projection using auricular cartilage. *Plast Reconstr Surg* 2000;105:2276-2277.
1241. Bernard, R. W., Beran, S. J. Autologous fat graft in nipple reconstruction. *Plast Reconstr Surg* 2003;112:964-968.
1242. Guerra, A. B., Khoobehi, K., Metzinger, S. E., Allen, R. J. New technique for nipple areola reconstruction: arrow flap and rib cartilage graft for long-lasting nipple projection. *Ann Plast Surg* 2003;50:31-37.
1243. Gamboa-Bobadilla, G. M. Nipple reconstruction: the top hat technique. *Ann Plast Surg* 2005;54:243-246.
1244. Hammond, D. C., Khuthaila, D., Kim, J. The skate flap purse-string technique for nipple-areola complex reconstruction. *Plast Reconstr Surg* 2007;120:399-406.
1245. Garramone, C. E., Lam, B. Use of AlloDerm in primary nipple reconstruction to improve long-term nipple projection. *Plast Reconstr Surg* 2007;119:1663-1668.
1246. Zenn, M. R., Garofalo, J. A. Unilateral nipple reconstruction with nipple sharing: time for a second look. *Plast Reconstr Surg* 2009;123:1648-1653.
1247. Wong, W. W., Hiersche, M. A., Martin, M. C. The angel flap for nipple reconstruction. *Can J Plast Surg* 2013;21:e1-4.
1248. Grosdidier, A., Lebeau, J., Ochala, C., Payan, R., Bettega, G. [<< Double flag >> flap nipple reconstruction. Clinical evaluation on 70 cases]. *Ann Chir Plast Esthet* 2014;59:123-129.
1249. Yang, J. D., Ryu, J. Y., Ryu, D. W., et al. Our Experiences in Nipple Reconstruction Using the Hammond flap. *Arch Plast Surg* 2014;41:550-555.
1250. Halvorson, E. G., Cormican, M., West, M. E., Myers, V. Three-dimensional nipple-areola tattooing: a new technique with superior results. *Plast Reconstr Surg* 2014;133:1073-1075.
1251. Cheng, M. H., Ho-Asjoe, M., Wei, F. C., Chuang, D. C. Nipple reconstruction in Asian females using banked cartilage graft and modified top hat flap. *Br J Plast Surg* 2003;56:692-694.
1252. Heitland, A., Markowicz, M., Koellensperger, E., Allen, R., Pallua, N. Long-term nipple shrinkage following augmentation by an autologous rib cartilage transplant in free DIEP-flaps. *J Plast Reconstr Aesthet Surg* 2006;59:1063-1067.
1253. Cheng, M. H., Rodriguez, E. D., Smartt, J. M., Cardenas-Mejia, A. Nipple reconstruction using the modified top hat flap with banked costal cartilage graft: long-term follow-up in 58 patients. *Ann Plast Surg* 2007;59:621-628.
1254. Lipa, J. E., Addison, P. D., Neligan, P. C. Patient satisfaction following nipple reconstruction incorporating autologous costal cartilage. *Can J Plast Surg* 2008;16:85-88.
1255. Mori, H., Uemura, N., Okazaki, M. Nipple reconstruction with banked costal cartilage after vertical-type skin-sparing mastectomy and deep inferior epigastric artery perforator flap. *Breast Cancer* 2015;22:95-97.

1256. Brent, B., Bostwick, J. Nipple-areola reconstruction with auricular tissues. *Plast Reconstr Surg* 1977;60:353-361.
1257. Tanabe, H. Y., Tai, Y., Kiyokawa, K., Yamauchi, T. Nipple-areola reconstruction with a dermal-fat flap and rolled auricular cartilage. *Plast Reconstr Surg* 1997;100:431-438.
1258. Norton, S., Akhavani, M. A., Kang, N. The 'Hamburger' technique for harvesting cartilage grafts in nipple reconstruction. *J Plast Reconstr Aesthet Surg* 2007;60:957-959.
1259. Jones, A. P., Erdmann, M. Projection and patient satisfaction using the "Hamburger" nipple reconstruction technique. *J Plast Reconstr Aesthet Surg* 2012;65:207-212.
1260. Breuing, K. H., Warren, S. M. Immediate bilateral breast reconstruction with implants and inferolateral AlloDerm slings. *Ann Plast Surg* 2005;55:232-239.
1261. Nahabedian, M. Y. Secondary nipple reconstruction using local flaps and AlloDerm. *Plast Reconstr Surg* 2005;115:2056-2061.
1262. Wong, A. K., Schonmeyr, B., Singh, P., Carlson, D. L., Li, S., Mehrara, B. J. Histologic analysis of angiogenesis and lymphangiogenesis in acellular human dermis. *Plast Reconstr Surg* 2008;121:1144-1152.
1263. Rao, S. S., Seaman, B. J., Davison, S. P. The acellular dermal matrix onlay graft for areolar reconstruction. *Ann Plast Surg* 2014;72:508-512.
1264. Tierney, B. P., Hodde, J. P., Changkuon, D. I. Biologic collagen cylinder with skate flap technique for nipple reconstruction. *Plast Surg Int* 2014;2014:194087.
1265. Jankau, J., Jaskiewicz, J., Ankiewicz, A. A new method for using a silicone rod for permanent nipple projection after breast reconstruction procedures. *Breast* 2011;20:124-128.
1266. Jankau, J. Use of silicone rod for permanent nipple projection after breast reconstruction procedures. In M. A. Shiffman ed., *Breast Reconstruction*. Berlin, Germany: Springer; 2016:987-993.
1267. McCarthy, C. M., VanLaeken, N., Lennox, P., Scott, A. M., Pusic, A. L. The efficacy of Artecoll injections for the augmentation of nipple projection in breast reconstruction. *Eplasty* 2010;10:e7.
1268. Yanaga, H. Nipple-areola reconstruction with a dermal-fat flap: technical improvement from rolled auricular cartilage to artificial bone. *Plast Reconstr Surg* 2003;112:1863-1869.
1269. Nishiyama, T., Nakajima, T., Yoshimura, Y., Nakanishi, Y. Utilizing solid models for preoperative shaping of HAP-TCP ceramic bone substitute: application for craniomaxillofacial surgery. *Eur J Plast Surg* 1994;17.
1270. Evans, K. K., Rasko, Y., Lenert, J., Olding, M. The use of calcium hydroxylapatite for nipple projection after failed nipple-areolar reconstruction: early results. *Ann Plast Surg* 2005;55:25-29; discussion 29.
1271. Holbrook, A., Lee, S., Soo, M. S. Mammographic appearance of calcium hydroxylapatite (RadiesseTM) injected into the breast for nipple reconstruction. *Breast J* 2013;19:104-113.
1272. Germano, D., De Biasio, F., Piedimonte, A., Parodi, P. C. Nipple reconstruction using the fleur-de-lis flap technique. *Aesthetic Plast Surg* 2006;30:399-402.
1273. Cronin, T. D., Upton, J., McDonough, J. M. Reconstruction of the breast after mastectomy. *Plast Reconstr Surg* 1977;59:1-14.
1274. Gruber, R. P. Method to produce better areolae and nipples on reconstructed breasts. *Plast Reconstr Surg* 1977;60:505-513.
1275. Cao, Y. L., Lach, E., Kim, T. H., Rodriguez, A., Arevalo, C. A., Vacanti, C. A. Tissue-engineered nipple reconstruction. *Plast Reconstr Surg* 1998;102:2293-2298.
1276. Cerqueira, B., Cornell, L. NovoThelium LLC. Available at: http://www.novothelium.com. Accessed October 23rd 2016.

1277. Bosworth, L., Collins, S., Boland, T. TeVido BioDevices. Available at: http://tevidobiodevices.com/. Accessed October 23rd 2016.
1278. Saint-Cyr, M., Schaverien, M. V., Rohrich, R. J. Perforator flaps: history, controversies, physiology, anatomy, and use in reconstruction. *Plast Reconstr Surg* 2009;123:132e-145e.
1279. Rozen, W. M., Ashton, M. W., Stella, D. L., Phillips, T. J., Taylor, G. I. Magnetic resonance angiography and computed tomographic angiography for free fibular flap transfer. *J Reconstr Microsurg* 2008;24:457-458.
1280. Oxford Centre for Evidence-Based Medicine. Levels of Evidence. *Available at: wwwcebmnet* 2009:Accessed October 1, 2014.
1281. Yip, S. S. F., Parmar, C., Blezek, D., et al. Application of the 3D slicer chest imaging platform segmentation algorithm for large lung nodule delineation. *PLoS One* 2017;12:e0178944.
1282. Hassanzadeh, E., Alessandrino, F., Olubiyi, O. I., et al. Comparison of quantitative apparent diffusion coefficient parameters with prostate imaging reporting and data system V2 assessment for detection of clinically significant peripheral zone prostate cancer. *Abdom Radiol (NY)* 2017.
1283. Vogel, W. V., Oyen, W. J., Barentsz, J. O., Kaanders, J. H., Corstens, F. H. PET/CT: panacea, redundancy, or something in between? *J Nucl Med* 2004;45 Suppl 1:15S-24S.
1284. Flohr, T., Ohnesorge, B., Bruder, H., et al. Image reconstruction and performance evaluation for ECG-gated spiral scanning with a 16-slice CT system. *Med Phys* 2003;30:2650-2662.
1285. Eder, M., Raith, S., Jalali, J., et al. Three-dimensional prediction of free-flap volume in autologous breast reconstruction by CT angiography imaging. *Int J Comput Assist Radiol Surg* 2014;9:541-549.
1286. Eric, M., Anderla, A., Stefanovic, D., Drapsin, M. Breast volume estimation from systematic series of CT scans using the Cavalieri principle and 3D reconstruction. *Int J Surg* 2014;12:912-917.
1287. Kim, H., Lim, S. Y., Pyon, J. K., Bang, S. I., Oh, K. S., Mun, G. H. Preoperative computed tomographic angiography of both donor and recipient sites for microsurgical breast reconstruction. *Plast Reconstr Surg* 2012;130:11e-20e.
1288. Lee, K. T., Mun, G. H. Volumetric Planning Using Computed Tomographic Angiography Improves Clinical Outcomes in DIEP Flap Breast Reconstruction. *Plast Reconstr Surg* 2016;137:771e-780e.
1289. Chae, M. P., Ramakrishnan, V., Hunter-Smith, D. J., Rozen, W. M. The extended DIEP flap. In M. Shiffman ed., *Breast Reconstruction: Art, Science, and New Clinical Techniques*. Heidelberg, Germany: Springer; 2016.
1290. Chae, M. P., Hunter-Smith, D. J., Spychal, R. T., Rozen, W. M. 3D volumetric analysis and haptic modeling for preoperative planning in breast reconstruction. *Anaplastology* 2015;4:1-4.
1291. Rha, E. Y., Kim, J. M., Yoo, G. Volume Measurement of Various Tissues Using the Image J Software. *J Craniofac Surg* 2015;26:e505-506.
1292. Ibrahim, A. M., Jose, R. R., Rabie, A. N., Gerstle, T. L., Lee, B. T., Lin, S. J. Three-dimensional Printing in Developing Countries. *Plast Reconstr Surg Glob Open* 2015;3:e443.
1293. Wang, Y. T., Yu, J. H., Lo, L. J., Hsu, P. H., Lin, C. L. Developing Customized Dental Miniscrew Surgical Template from Thermoplastic Polymer Material Using Image Superimposition, CAD System, and 3D Printing. *Biomed Res Int* 2017;2017:1906197.
1294. Wang, D., Wang, Y., Wang, J., et al. Design and Fabrication of a Precision Template for Spine Surgery Using Selective Laser Melting (SLM). *Materials (Basel)* 2016;9.

1295. Yang, F., Chen, C., Zhou, Q., et al. Laser beam melting 3D printing of Ti6Al4V based porous structured dental implants: fabrication, biocompatibility analysis and photoelastic study. *Sci Rep* 2017;7:45360.
1296. Coelho, G., Chaves, T. M. F., Goes, A. F., Del Massa, E. C., Moraes, O., Yoshida, M. Multimaterial 3D printing preoperative planning for frontoethmoidal meningoencephalocele surgery. *Childs Nerv Syst* 2017.
1297. Chen, X., Possel, J. K., Wacongne, C., van Ham, A. F., Klink, P. C., Roelfsema, P. R. 3D printing and modelling of customized implants and surgical guides for non-human primates. *J Neurosci Methods* 2017;286:38-55.
1298. Egger, J., Gall, M., Tax, A., et al. Interactive reconstructions of cranial 3D implants under MeVisLab as an alternative to commercial planning software. *PLoS One* 2017;12:e0172694.
1299. Skrzat, J., Spulber, A., Walocha, J. Three-dimensional model of the skull and the cranial bones reconstructed from CT scans designed for rapid prototyping process. *Folia Med Cracov* 2016;56:45-52.
1300. Ploch, C. C., Mansi, C., Jayamohan, J., Kuhl, E. Using 3D Printing to Create Personalized Brain Models for Neurosurgical Training and Preoperative Planning. *World Neurosurg* 2016;90:668-674.
1301. Park, E. K., Lim, J. Y., Yun, I. S., et al. Cranioplasty Enhanced by Three-Dimensional Printing: Custom-Made Three-Dimensional-Printed Titanium Implants for Skull Defects. *J Craniofac Surg* 2016;27:943-949.
1302. Wu, T. Y., Lin, H. H., Lo, L. J., Ho, C. T. Postoperative outcomes of two- and three-dimensional planning in orthognathic surgery: A comparative study. *J Plast Reconstr Aesthet Surg* 2017;70:1101-1111.
1303. Callahan, A. B., Campbell, A. A., Petris, C., Kazim, M. Low-Cost 3D Printing Orbital Implant Templates in Secondary Orbital Reconstructions. *Ophthal Plast Reconstr Surg* 2017;33:376-380.
1304. LoPresti, M., Daniels, B., Buchanan, E. P., Monson, L., Lam, S. Virtual surgical planning and 3D printing in repeat calvarial vault reconstruction for craniosynostosis: technical note. *J Neurosurg Pediatr* 2017;19:490-494.
1305. Kim, Y. C., Jeong, W. S., Park, T. K., Choi, J. W., Koh, K. S., Oh, T. S. The accuracy of patient specific implant prebented with 3D-printed rapid prototype model for orbital wall reconstruction. *J Craniomaxillofac Surg* 2017;45:928-936.
1306. Huang, Y. H., Seelaus, R., Zhao, L., Patel, P. K., Cohen, M. Virtual surgical planning and 3D printing in prosthetic orbital reconstruction with percutaneous implants: a technical case report. *Int Med Case Rep J* 2016;9:341-345.
1307. Sutradhar, A., Park, J., Carrau, D., Nguyen, T. H., Miller, M. J., Paulino, G. H. Designing patient-specific 3D printed craniofacial implants using a novel topology optimization method. *Med Biol Eng Comput* 2016;54:1123-1135.
1308. Park, S. W., Choi, J. W., Koh, K. S., Oh, T. S. Mirror-Imaged Rapid Prototype Skull Model and Pre-Molded Synthetic Scaffold to Achieve Optimal Orbital Cavity Reconstruction. *J Oral Maxillofac Surg* 2015;73:1540-1553.
1309. Mendez, B. M., Chiodo, M. V., Patel, P. A. Customized "In-Office" Three-Dimensional Printing for Virtual Surgical Planning in Craniofacial Surgery. *J Craniofac Surg* 2015;26:1584-1586.
1310. Al Jabbari, O., Abu Saleh, W. K., Patel, A. P., Igo, S. R., Reardon, M. J. Use of three-dimensional models to assist in the resection of malignant cardiac tumors. *J Card Surg* 2016;31:581-583.
1311. Olivieri, L. J., Su, L., Hynes, C. F., et al. "Just-In-Time" Simulation Training Using 3-D Printed Cardiac Models After Congenital Cardiac Surgery. *World J Pediatr Congenit Heart Surg* 2016;7:164-168.

1312. Osagie, L., Shaunak, S., Murtaza, A., Cerovac, S., Umarji, S. Advances in 3D Modeling: Preoperative Templating for Revision Wrist Surgery. *Hand (N Y)* 2017;12:NP68-NP72.
1313. Chan, H. H., Siewerdsen, J. H., Vescan, A., Daly, M. J., Prisman, E., Irish, J. C. 3D Rapid Prototyping for Otolaryngology-Head and Neck Surgery: Applications in Image-Guidance, Surgical Simulation and Patient-Specific Modeling. *PLoS One* 2015;10:e0136370.
1314. Mowry, S. E., Jammal, H., Myer, C. t., Solares, C. A., Weinberger, P. A Novel Temporal Bone Simulation Model Using 3D Printing Techniques. *Otol Neurotol* 2015;36:1562-1565.
1315. Barth, R. J., Jr., Krishnaswamy, V., Paulsen, K. D., et al. A Patient-Specific 3D-Printed Form Accurately Transfers Supine MRI-Derived Tumor Localization Information to Guide Breast-Conserving Surgery. *Ann Surg Oncol* 2017.
1316. Chae, M. P., Hunter-Smith, D. J., Murphy, S. V., Findlay, M. 3D bioprinting adipose tissue for breast reconstruction. In D. J. Thomas, Z. M. Jessop, I. S. Whitaker eds., *3D Bioprinting for Reconstructive Surgery: Techniques and Applications*. Sawston, Cambridge, UK: Woodhead Publishing; 2017.
1317. Chae, M. P., Hunter-Smith, D. J., Murphy, S. V., Atala, A., Rozen, W. M. 3D Bioprinting in Nipple-Areolar Complex Reconstruction. In M. A. Shiffman ed., *Nipple-Areolar Complex Reconstruction: Principles and Clinical Techniques*. Heidelberg, Germany: Springer; 2016.
1318. Suarez-Mejias, C., Gomez-Ciriza, G., Valverde, I., Parra Calderon, C., Gomez-Cia, T. New technologies applied to surgical processes: Virtual Reality and rapid prototyping. *Stud Health Technol Inform* 2015;210:669-671.
1319. Taylor, E. M., Iorio, M. L. Surgeon-Based 3D Printing for Microvascular Bone Flaps. *J Reconstr Microsurg* 2017;33:441-445.
1320. Visscher, D. O., van Eijnatten, M., Liberton, N., et al. MRI and Additive Manufacturing of Nasal Alar Constructs for Patient-specific Reconstruction. *Sci Rep* 2017;7:10021.
1321. Choi, Y. D., Kim, Y., Park, E. Patient-Specific Augmentation Rhinoplasty Using a Three-Dimensional Simulation Program and Three-Dimensional Printing. *Aesthet Surg J* 2017;37:988-998.
1322. Bosc, R., Hersant, B., Carloni, R., et al. Mandibular reconstruction after cancer: an in-house approach to manufacturing cutting guides. *Int J Oral Maxillofac Surg* 2017;46:24-31.
1323. Ganry, L., Quilichini, J., Bandini, C. M., Leyder, P., Hersant, B., Meningaud, J. P. Three-dimensional surgical modelling with an open-source software protocol: study of precision and reproducibility in mandibular reconstruction with the fibula free flap. *Int J Oral Maxillofac Surg* 2017;46:946-957.
1324. Liang, Y., Jiang, C., Wu, L., Wang, W., Liu, Y., Jian, X. Application of Combined Osteotomy and Reconstruction Pre-Bent Plate Position (CORPPP) Technology to Assist in the Precise Reconstruction of Segmental Mandibular Defects. *J Oral Maxillofac Surg* 2017;75:2026 e2021-2026 e2010.
1325. Mottini, M., Seyed Jafari, S. M., Shafighi, M., Schaller, B. New approach for virtual surgical planning and mandibular reconstruction using a fibula free flap. *Oral Oncol* 2016;59:e6-e9.
1326. Schouman, T., Khonsari, R. H., Goudot, P. Shaping the fibula without fumbling: the SynpliciTi customised guide-plate. *Br J Oral Maxillofac Surg* 2015;53:472-473.
1327. Seruya, M., Fisher, M., Rodriguez, E. D. Computer-assisted versus conventional free fibula flap technique for craniofacial reconstruction: an outcomes comparison. *Plast Reconstr Surg* 2013;132:1219-1228.

1328. Rohner, D., Bucher, P., Hammer, B. Prefabricated fibular flaps for reconstruction of defects of the maxillofacial skeleton: planning, technique, and long-term experience. *Int J Oral Maxillofac Implants* 2013;28:e221-229.
1329. Saad, A., Winters, R., Wise, M. W., Dupin, C. L., St Hilaire, H. Virtual surgical planning in complex composite maxillofacial reconstruction. *Plast Reconstr Surg* 2013;132:626-633.
1330. Hanasono, M. M., Skoracki, R. J. Computer-assisted design and rapid prototype modeling in microvascular mandible reconstruction. *Laryngoscope* 2013;123:597-604.
1331. Infante-Cossio, P., Gacto-Sanchez, P., Gomez-Cia, T., Gomez-Ciriza, G. Stereolithographic cutting guide for fibula osteotomy. *Oral Surg Oral Med Oral Pathol Oral Radiol* 2012;113:712-713; author reply 712.
1332. Zheng, G. S., Su, Y. X., Liao, G. Q., et al. Mandible reconstruction assisted by preoperative virtual surgical simulation. *Oral Surg Oral Med Oral Pathol Oral Radiol* 2012;113:604-611.
1333. Hou, J. S., Chen, M., Pan, C. B., et al. Application of CAD/CAM-assisted technique with surgical treatment in reconstruction of the mandible. *J Craniomaxillofac Surg* 2012;40:e432-437.
1334. Antony, A. K., Chen, W. F., Kolokythas, A., Weimer, K. A., Cohen, M. N. Use of virtual surgery and stereolithography-guided osteotomy for mandibular reconstruction with the free fibula. *Plast Reconstr Surg* 2011;128:1080-1084.
1335. Leiggener, C., Messo, E., Thor, A., Zeilhofer, H. F., Hirsch, J. M. A selective laser sintering guide for transferring a virtual plan to real time surgery in composite mandibular reconstruction with free fibula osseous flaps. *Int J Oral Maxillofac Surg* 2009;38:187-192.
1336. Greene, J. R. Design and development of a new facility for teaching and research in clinical anatomy. *Anat Sci Educ* 2009;2:34-40.
1337. Raja, D. S., Sultana, B. Potential health hazards for students exposed to formaldehyde in the gross anatomy laboratory. *J Environ Health* 2012;74:36-40.
1338. Mogali, S. R., Yeong, W. Y., Tan, H. K. J., et al. Evaluation by medical students of the educational value of multi-material and multi-colored three-dimensional printed models of the upper limb for anatomical education. *Anat Sci Educ* 2017.
1339. Lioufas, P. A., Quayle, M. R., Leong, J. C., McMenamin, P. G. 3D Printed Models of Cleft Palate Pathology for Surgical Education. *Plast Reconstr Surg Glob Open* 2016;4:e1029.
1340. Zheng, Y., Lu, B., Zhang, J., Wu, G. CAD/CAM silicone simulator for teaching cheiloplasty: description of the technique. *Br J Oral Maxillofac Surg* 2015;53:194-196.
1341. AlAli, A. B., Griffin, M. F., Calonge, W. M., Butler, P. E. Evaluating the Use of Cleft Lip and Palate 3D-Printed Models as a Teaching Aid. *J Surg Educ* 2017.
1342. Berens, A. M., Newman, S., Bhrany, A. D., Murakami, C., Sie, K. C., Zopf, D. A. Computer-Aided Design and 3D Printing to Produce a Costal Cartilage Model for Simulation of Auricular Reconstruction. *Otolaryngol Head Neck Surg* 2016;155:356-359.
1343. Iseki, H., Kawamura, H., Tanikawa, T., et al. An image-guided stereotactic system for neurosurgical operations. *Stereotact Funct Neurosurg* 1994;63:130-138.
1344. Unsgaard, G., Ommedal, S., Rygh, O. M., Lindseth, F. Operation of arteriovenous malformations assisted by stereoscopic navigation-controlled display of preoperative magnetic resonance angiography and intraoperative ultrasound angiography. *Neurosurgery* 2007;61:407-415; discussion 415-406.
1345. Jensen, R. L., Stone, J. L., Hayne, R. Use of the Horsley-Clarke stereotactic frame in humans. *Stereotact Funct Neurosurg* 1995;65:194-197.
1346. Woerdeman, P. A., Willems, P. W., Noordmans, H. J., Tulleken, C. A., van der Sprenkel, J. W. Application accuracy in frameless image-guided neurosurgery: a comparison study of three patient-to-image registration methods. *J Neurosurg* 2007;106:1012-1016.

1347. West, J. B., Fitzpatrick, J. M., Toms, S. A., Maurer, C. R., Jr., Maciunas, R. J. Fiducial point placement and the accuracy of point-based, rigid body registration. *Neurosurgery* 2001;48:810-816; discussion 816-817.
1348. Raabe, A., Krishnan, R., Wolff, R., Hermann, E., Zimmermann, M., Seifert, V. Laser surface scanning for patient registration in intracranial image-guided surgery. *Neurosurgery* 2002;50:797-801; discussion 802-793.
1349. Quinones-Hinojosa, A., Ware, M. L., Sanai, N., McDermott, M. W. Assessment of image guided accuracy in a skull model: comparison of frameless stereotaxy techniques vs. frame-based localization. *J Neurooncol* 2006;76:65-70.
1350. Spivak, C. J., Pirouzmand, F. Comparison of the reliability of brain lesion localization when using traditional and stereotactic image-guided techniques: a prospective study. *J Neurosurg* 2005;103:424-427.
1351. Papadopoulos, E. C., Girardi, F. P., Sama, A., Sandhu, H. S., Cammisa, F. P., Jr. Accuracy of single-time, multilevel registration in image-guided spinal surgery. *Spine J* 2005;5:263-267; discussion 268.
1352. Kraus, M. D., Dehner, C., Riepl, C., Scholl, H., Gebhard, F. A novel method of image-based navigation in fracture surgery. *Arch Orthop Trauma Surg* 2012;132:741-750.
1353. Weissler, J. M., Sosin, M., Dorafshar, A. H., Garcia, J. R. Combining Virtual Surgical Planning, Intraoperative Navigation, and 3-Dimensional Printing in Prosthetic-Based Bilateral Microtia Reconstruction. *J Oral Maxillofac Surg* 2017;75:1491-1497.
1354. Klapan, I., Vranjes, Z., Risavi, R., Simicic, L., Prgomet, D., Glusac, B. Computer-assisted surgery and computer-assisted telesurgery in otorhinolaryngology. *Ear Nose Throat J* 2006;85:318-321.
1355. de Lambert, A., Esneault, S., Lucas, A., Haigron, P., Cinquin, P., Magne, J. L. Electromagnetic tracking for registration and navigation in endovascular aneurysm repair: a phantom study. *Eur J Vasc Endovasc Surg* 2012;43:684-689.
1356. Rozen, W. M., Buckland, A., Ashton, M. W., Stella, D. L., Phillips, T. J., Taylor, G. I. Image-guided, stereotactic perforator flap surgery: a prospective comparison of current techniques and review of the literature. *Surg Radiol Anat* 2009;31:401-408.
1357. Ting, J. W., Rozen, W. M., Niumsawatt, V., Baillieu, C., Leung, M., Leong, J. C. Developments in image-guided deep circumflex iliac artery flap harvest: a step-by-step guide and literature review. *J Oral Maxillofac Surg* 2014;72:186-197.
1358. Durden, F., Carruthers, K. H., Haran, O., Kocak, E. Intraoperative navigation-assisted identification of deep inferior epigastric artery perforators. *Plast Reconstr Surg* 2012;129:880e-882e.
1359. Chao, A. H., Weimer, K., Raczkowsky, J., et al. Pre-programmed robotic osteotomies for fibula free flap mandible reconstruction: A preclinical investigation. *Microsurgery* 2016;36:246-249.
1360. Milgram, P., Kishino, F. A taxonomy of mixed reality visual displays. *IEICE Transact on Info Syst* 1994;E77-D.
1361. Pensieri, C., Pennacchini, M. Overview: virtual reality in medicine. *J Virtual Worlds Res* 2014;7:1-34.
1362. Arora, S., Aggarwal, R., Sirimanna, P., et al. Mental practice enhances surgical technical skills: a randomized controlled study. *Ann Surg* 2011;253:265-270.
1363. Sutton, C., McCloy, R., Middlebrook, A., Chater, P., Wilson, M., Stone, R. MIST VR. A laparoscopic surgery procedures trainer and evaluator. *Stud Health Technol Inform* 1997;39:598-607.
1364. Hyltander, A., Liljegren, E., Rhodin, P. H., Lonroth, H. The transfer of basic skills learned in a laparoscopic simulator to the operating room. *Surg Endosc* 2002;16:1324-1328.
1365. Fairhurst, K., Strickland, A., Maddern, G. The LapSim virtual reality simulator: promising but not yet proven. *Surg Endosc* 2011;25:343-355.

1366. Profeta, A. C., Schilling, C., McGurk, M. Augmented reality visualization in head and neck surgery: an overview of recent findings in sentinel node biopsy and future perspectives. *Br J Oral Maxillofac Surg* 2016;54:694-696.
1367. Mela, C. A., Papay, F. A., Liu, Y. Intraoperative Fluorescence Imaging and Multimodal Surgical Navigation Using Goggle System. *Methods Mol Biol* 2016;1444:85-95.
1368. Rahman, O. F., Nahabedian, M. Y., Sinkin, J. C. Augmented Reality and Wearable Technology in Image-guided Navigation and Preoperative Planning. *Plast Reconstr Surg Glob Open* 2016;4:e1057.
1369. Peregrin, T. Surgeons see future applications for Google Glass. *Bull Am Coll Surg* 2014;99:9-16.
1370. Berger, A. J., Gaster, R. S., Lee, G. K. Development of an affordable system for personalized video-documented surgical skill analysis for surgical residency training. *Ann Plast Surg* 2013;70:442-446.
1371. Sinkin, J. C., Rahman, O. F., Nahabedian, M. Y. Google Glass in the Operating Room: The Plastic Surgeon's Perspective. *Plast Reconstr Surg* 2016;138:298-302.
1372. Bilton, N. Why Google Glass Broke. *The New York Times*. New York City, NY: The New York Times Company, 2015.
1373. Vohl, D., Barnes, D. G., Fluke, C. J., et al. Large-scale comparative visualisation of sets of multidimensional data. *PeerJ Comp Sci* 2016;2:e88.
1374. Ghahramani, Z. Probabilistic machine learning and artificial intelligence. *Nature* 2015;521:452-459.
1375. Obermeyer, Z., Emanuel, E. J. Predicting the Future - Big Data, Machine Learning, and Clinical Medicine. *N Engl J Med* 2016;375:1216-1219.
1376. Jordan, M. I., Mitchell, T. M. Machine learning: Trends, perspectives, and prospects. *Science* 2015;349:255-260.
1377. Metz, C. AI is transforming Google Search. The reset of the web is next. *Wired*. San Francisco, CA, USA: Conde Nast Publications, 2016.
1378. Siri Team. Deep learning for Siri's voice: on-device deep mixture density networks for hybrid unit selection synthesis. *Apple Machine Learning J* 2017;1.
1379. Murdoch, T. B., Detsky, A. S. The inevitable application of big data to health care. *JAMA* 2013;309:1351-1352.
1380. Meyfroidt, G., Guiza, F., Ramon, J., Bruynooghe, M. Machine learning techniques to examine large patient databases. *Best Pract Res Clin Anaesthesiol* 2009;23:127-143.
1381. Deo, R. C. Machine Learning in Medicine. *Circulation* 2015;132:1920-1930.
1382. Furnkranz, J., Gamberger, D., Lavrac, N. *Foundations of rule learning*. Heidelberg, Germany: Springer; 2012.
1383. Waschkowski, F., Hesse, S., Rieck, A. C., et al. Development of very large electrode arrays for epiretinal stimulation (VLARS). *Biomed Eng Online* 2014;13:11.
1384. Imhoff, M., Kuhls, S. Alarm algorithms in critical care monitoring. *Anesth Analg* 2006;102:1525-1537.
1385. Kanevsky, J., Corban, J., Gaster, R., Kanevsky, A., Lin, S., Gilardino, M. Big Data and Machine Learning in Plastic Surgery: A New Frontier in Surgical Innovation. *Plast Reconstr Surg* 2016;137:890e-897e.
1386. Safran, T., Viezel-Mathieu, A., Corban, J., Kanevsky, A., Thibaudeau, S., Kanevsky, J. Machine Learning and Melanoma: The Future of Screening. *J Am Acad Dermatol* 2017.
1387. Rajpara, S. M., Botello, A. P., Townend, J., Ormerod, A. D. Systematic review of dermoscopy and digital dermoscopy/ artificial intelligence for the diagnosis of melanoma. *Br J Dermatol* 2009;161:591-604.
1388. Mendoza, C. S., Safdar, N., Okada, K., Myers, E., Rogers, G. F., Linguraru, M. G. Personalized assessment of craniosynostosis via statistical shape modeling. *Med Image Anal* 2014;18:635-646.

1389. Yeong, E. K., Hsiao, T. C., Chiang, H. K., Lin, C. W. Prediction of burn healing time using artificial neural networks and reflectance spectrometer. *Burns* 2005;31:415-420.
1390. Kiranantawat, K., Sitpahul, N., Taeprasartsit, P., et al. The first Smartphone application for microsurgery monitoring: SilpaRamanitor. *Plast Reconstr Surg* 2014;134:130-139.
1391. Conforth, M., Meng, Y., Valmikinathan, C., Xiaojun, Y. Nerve graft selection for peripheral nerve regeneration using neural networks trained by a hybrid ACO/PSO method. In *6th Annual IEEE Symposium on Computational Intelligence in Bioinformatics and Computational Biology,* Nashville, TN, USA; March 30-Aprl 2, 2009.
1392. Gunes, H., Piccardi, M. Assessing facial beauty through proportion analysis by image processing and supervised learning. *Int J Hum-Comput St* 2006;64:1184-1199.
1393. Dai, K. R., Yan, M. N., Zhu, Z. A., Sun, Y. H. Computer-aided custom-made hemipelvic prosthesis used in extensive pelvic lesions. *J Arthroplasty* 2007;22:981-986.
1394. Harrysson, O. L., Hosni, Y. A., Nayfeh, J. F. Custom-designed orthopedic implants evaluated using finite element analysis of patient-specific computed tomography data: femoral-component case study. *BMC Musculoskelet Disord* 2007;8:91.
1395. He, J., Li, D., Lu, B., Wang, Z., Tao, Z. Custom fabrication of composite tibial hemi-knee joint combining CAD/CAE/CAM techniques. *Proc Inst Mech Eng H* 2006;220:823-830.
1396. Wang, Z., Teng, Y., Li, D. [Fabrication of custom-made artificial semi-knee joint based on rapid prototyping technique: computer-assisted design and manufacturing]. *Zhongguo Xiu Fu Chong Jian Wai Ke Za Zhi* 2004;18:347-351.
1397. Waran, V., Narayanan, V., Karuppiah, R., et al. Injecting realism in surgical training-initial simulation experience with custom 3D models. *J Surg Educ* 2014;71:193-197.
1398. Muller, A., Krishnan, K. G., Uhl, E., Mast, G. The application of rapid prototyping techniques in cranial reconstruction and preoperative planning in neurosurgery. *J Craniofac Surg* 2003;14:899-914.
1399. Poukens, J., Haex, J., Riediger, D. The use of rapid prototyping in the preoperative planning of distraction osteogenesis of the cranio-maxillofacial skeleton. *Comput Aided Surg* 2003;8:146-154.
1400. Sinnatamby, C. S. *Last's Anatomy*. Edinburgh, UK: Elsevier; 2011.
1401. Jemal, A., Bray, F., Center, M. M., Ferlay, J., Ward, E., Forman, D. Global cancer statistics. *CA Cancer J Clin* 2011;61:69-90.
1402. Faivre, J., Manfredi, S., Bouvier, A. M. [Epidemiology of colorectal cancer liver metastases]. *Bull Acad Natl Med* 2003;187:815-822; discussion 822-813.
1403. Yoo, P. S., Enestvedt, C. K., Kulkarni, S. Anatomic considerations in the surgical resection of hepatocellular carcinoma. *J Clin Gastroenterol* 2013;47 Suppl:S11-15.
1404. Quintini, C., Aucejo, F., Hashimoto, K., Zein, N., Miller, C. State of the art and future developments for surgical planning in LDLT. *Curr Transpl Rep* 2014;1:35.
1405. Xiang, N., Fang, C., Fan, Y., et al. Application of liver three-dimensional printing in hepatectomy for complex massive hepatocarcinoma with rare variations of portal vein: preliminary experience. *Int J Clin Exp Med* 2015;8:18873-18878.
1406. Bernhard, J. C., Isotani, S., Matsugasumi, T., et al. Personalized 3D printed model of kidney and tumor anatomy: a useful tool for patient education. *World J Urol* 2016;34:337-345.

16 Appendix

16.1 List of All 3D-Printed Models at Peninsula Health 3D PRINT Laboratory

16.1.1 Plastic and Reconstructive Surgery

Patient	Hospital/ Institution	Age	Sex	Pathology	3D Print	
					Material	Time
MO	FH	79	M	Subcutaneous defect left distal pretibial	PLA	12 hr 30 min
KW	FH	58	F	Breast asymmetry	PLA	15 hr
JB	FH	58	F	Sacral pressure sore	PLA	12 hr 30 min
SK	RH	54	F	Left basal thumb arthritis	PLA	10 hr 30 min
JW	FH	53	F	Right rib defect	PLA	8 hr 15 min
JH	FH	68	F	Invasive squamous cell carcinoma right mandible	PLA	14 hr 37 min
				Mandible minus the tumour	PLA	6 hr 15 min
BG	FH	85	M	Large right helical rim defect	PLA	3 hr 6 min
				Mirrored image of contralateral ear	PLA	2 hr 41 min
AC	FH	35	M	Bony defect right middle finger P3	PLA	21 min
RS	EH	77	M	Bony defect left calcaneum	PLA	12 hr 33 min
MJG	StV	10	F	Massive ameloblastoma	PLA	15 hr 40 min
					BJT	7 hr 10 min
MC	AH	71	F	Right shoulder reconstruction	PLA	18 hr 20 min
JG	DH	65	M	Mandibular reconstruction	PLA	2 hr 56 min
RE	EH	72	M	Stoma tumour for DIEP flap reconstruction	PLA	16 hr 49 min
PF	DH	54	M	Andy Gump fracture	PLA	3 hr 32 min
VT	LC	27	M	Feminisation rhinoplasty upper lateral cartilage	PLA	15 min
				Feminisation rhinoplasty lower lateral cartilage	PLA	40 min
AT	RH	23	F	Right breast implant reconstruction for Poland syndrome – left breast	PLA	13 hr
				Mirrored left breast	PLA	11 hr
MM	RH	65	M	Left basal thumb arthritis – trapezium	PLA	13.5 min
MW	RH	58	F	Right basal thumb arthritis – trapezium	PLA	19 min
LD	RH	53	F	Left breast DIEP flap reconstruction – DIEP template	PLA	7 hr 51 min

TW	EH	54	F	Right breast DIEP flap reconstruction – DIEP template	PLA	3 hr 35 min
JC	EH	57	F	Right breast DIEP flap reconstruction – DIEP template	PLA	8 hr 53 min
JA	FH	55	F	Left breast DIEP flap reconstruction – DIEP template	PLA	6 hr 15 min
JC	RH	46	F	Right breast DIEP flap reconstruction – DIEP template	PLA	8 hr 45 min
CG	FH	49	F	Left breast DIEP flap reconstruction – DIEP template	PLA	8 hr 7 min
KC	EH	64	F	Left breast DIEP flap reconstruction – DIEP template	PLA	7 hr 3 min
CV	FH	43	F	Right breast DIEP flap reconstruction – DIEP template	PLA	6 hr 57 min
CW	RH	67	F	Right breast DIEP flap reconstruction – DIEP template	PLA	6 hr 43 min
AR	FH	45	F	Bilateral breast DIEP flap reconstruction – DIEP template	PLA	7 hr 27 min
LB	RH	60	F	Left breast DIEP flap reconstruction – DIEP template	PLA	8 hr 41 min
OP	EH	50	F	Left breast DIEP flap reconstruction – DIEP template	PLA	7 hr 45 min
				Left breast DIEP flap reconstruction – DIEP template + intramuscular course	PLA	20 hr 55 min
VW	EH	40	F	Left breast DIEP flap reconstruction – DIEP template	PLA	8 hr 27 min
JS	RH	65	F	Right breast DIEP flap reconstruction – DIEP template + intramuscular course	PLA	34 hr 46 min
SW	FH	49	F	Bilateral breast DIEP flap reconstruction – DIEP template + intramuscular course	PLA	37 hr 28 min
LCT	EH	38	F	Right breast DIEP flap reconstruction – DIEP template + intramuscular course	PLA	31 hr 46 min
RH	EH	52	F	Bilateral breast DIEP flap reconstruction – DIEP template + intramuscular course	PLA	37 hr 43 min
VS	FH	57	F	Bilateral breast DIEP flap reconstruction – DIEP template + intramuscular course	PLA	36 hr 25 min
EH	FH	51	F	Right breast DIEP flap reconstruction – DIEP template + intramuscular course	PLA	42 hr 23 min
DLN	RH	46	F	Bilateral breast DIEP flap reconstruction – DIEP template + intramuscular course	PLA	31 hr 58 min
JF	FH	44	F	Left breast DIEP flap reconstruction – DIEP template + intramuscular course	PLA	26 hr 39 min
DM	EH	46	F	Left breast DIEP flap reconstruction – DIEP template + intramuscular course	PLA	15 hr 3 min

BS	RH	65	F	Right basal thumb arthritis – whole hand	PLA	10 hr 46 min
				Right basal thumb arthritis – trapezium	PLA	50 min
GT	FH	25	F	4D printing – thumb abduction position 1	PLA	2 hr 6 min
				4D printing – thumb abduction position 3	PLA	1 hr 59 min
				4D printing – thumb abduction position 6	PLA	2 hr 7 min
				4D printing – thumb key pinch position 1	PLA	7 hr 24 min
				4D printing – thumb key pinch position 3	PLA	5 hr 29 min
				4D printing – thumb key pinch position 4	PLA	5 hr 43 min
				4D printing – thumb opposition position 2	PLA	2 hr 9 min
				4D printing – thumb opposition position 5	PLA	2 hr 13 min
				4D printing – thumb opposition position 8	PLA	2 hr 9 min
TC	StA	35	F	Breast reconstruction – 3D photography	PLA	14 hr
CAW	StA	43	F	Breast reconstruction – 3D photography	PLA	16 hr 40 min

Abbreviations: FH: Frankston Hospital; RH: Ramsey Health; EH: Eastern Health; StV: St Vincent's Hospital; AH: Austin Hospital; DH: Dandenong Hospital; LC: Linley Clinic; StA: St Andrew's Hospital; PLA: polylactic acid; BJT: binder jet technology

16.1.2 Orthopaedic Surgery

Patient	Hospital/ Institution	Age	Sex	Pathology	3D Print	
					Material	Time
JG	FH	35	F	Left patellar dislocation	PLA	29 min
CJ	FH	28	F	Bilateral radio-ulnar joint mal-union – left	PLA	2 hr 8 min
				Bilateral radio-ulnar joint mal-union – right	PLA	4 hr 32 min
GT	FH	78	F	Right hip fracture	PLA	19 hr 3 min
VB	FH	82	F	Right ankle fracture	PLA	8 hr 28 min
PF	VHSA	24	M	Right scaphoid fracture	PLA	33 min
MC	VHSA	69	M	Right scaphoid fracture	PLA	57 min
JA	VHSA	18	M	Left scaphoid fracture – whole wrist	PLA	4 hr 20 min
SR	FH	34	F	Left radio-ulnar joint mal-union	PLA	1 hr 25 min
MM	FH	79	F	Left acetabular fracture	PLA	47 hr
BR	FH	56	M	Left hip fracture	PLA	3 hr 22 min
TS	FH	76	M	Right pelvic tumour – pelvis	PLA	35 hr 29 min
				Right pelvic tumour – femur	PLA	8 hr 30 min
JS	FH	44	F	Left neck of femur fracture	PLA	1 hr 22 min
JH	FH	44	F	Left femur fracture	PLA	2 hr 29 min
HS	FH	82	M	Recurrent right femur fracture	PLA	3 hr 40 min
SG	RH	32	M	Left shoulder fusion – Ultimaker 3E printer	PLA	44 hr 28 min
				Left shoulder fusion – Moment printer	PLA	30 hr 2 min

Abbreviations: FH: Frankston Hospital; VHSA: Victoria Hand Surgery Associates; PLA: polylactic acid

16.1.3 Urology

Patient	Hospital/ Institution	Age	Sex	Pathology	3D Print	
					Material	Time
ST	FH	67	M	Right partial nephrectomy	PLA	9 hr 56 min
MA	FH	36	M	Right partial nephrectomy	PLA	6 hr 16 min
RA	FH	41	M	Right partial nephrectomy	PLA	9 hr 50 min
GH	FH	63	M	Right partial nephrectomy	PLA	8 hr 46 min
CC	FH	69	F	Left partial nephrectomy	PLA	6 hr 30 min
JA	FH	84	M	Right partial nephrectomy	PLA	11 hr 30 min

Abbreviations: FH: Frankston Hospital; PLA: polylactic acid.

16.1.4 Vascular Surgery

Patient	Hospital/ Institution	Age	Sex	Pathology	3D Print	
					Material	Time
RS	FH	81	M	Abdominal aortic aneurysm	PLA	6 hr 40 min
DC	FH	75	M	Thoracic aortic aneurysm	PLA	13 hr 22 min

Abbreviations: FH: Frankston Hospital; PLA: polylactic acid.

16.1.5 General Surgery

Patient	Hospital/ Institution	Age	Sex	Pathology	3D Print	
					Material	Time
RC	FH	45	M	Hepatic metastasis	PLA	32 hr

Abbreviations: FH: Frankston Hospital; PLA: polylactic acid.

16.1.6 Pain Medicine

Patient	Hospital/ Institution	Age	Sex	Pathology	3D Print	
					Material	Time
ER	RH	29	M	Sphenopalatine ganglion block	PLA	46 hr
DW	RH	75	F	Intra-thecal block – cervical/thoracic/lumbar spine	PLA	72 hr

Abbreviations: FH: Frankston Hospital; PLA: polylactic acid.

16.2 Other 3D Printing Studies Performed

16.2.1 Liver Metastasis

Chapter Summary

Introduction: Three-dimensional (3D) printing has gained popularity in the medical field because of increased research in the field of haptic 3D modeling. We review the role of 3D printing with specific reference to liver directed applications.

Methods: A literature search was performed using the scientific databases Medline and PubMed. We performed this in-line with the PRISMA statement. We only included articles in English, available in full text, published about adults, about liver surgery and published between 2005 and 2015. The 3D model of a patient's liver venous vasculature and metastasis was prepared from a CT scan using Osirix software (Pixmeo, Gineva, Switzerland) and printed using our 3D printer (MakerBot Replicator Z18, US). To validate the model, measurements from the inferior vena cava (IVC) were compared between the CT scan and the 3D printed model.

Results: A total of six studies were retrieved on 3D printing directly related to a liver application. While stereolithography (STL) remains the gold standard in medical additive manufacturing, Fused Filament Fabrication (FFF), is cheaper and may be more applicable. We found our liver 3D model made by FFF had a 0.1 ± 0.06 mm margin of error (mean ± standard deviation) compared with the CT scans.

Conclusion: 3D printing in general surgery is yet to be thoroughly exploited. The most relevant feature of interest with regard to liver surgery is the ability to view the 3D dimensional relationship of the various hepatic and portal veins with respect to tumor deposits when planning hepatic resection.

Introduction

Three dimensional (3D) printing has gained popularity in medicine since the 1980s. As 3D printers have become more affordable, the real strength of this technique has been recognized; its ability to deliver anatomical models based on the unique characteristics of individual patients. Surgeries in fields as diverse as orthopedics (1393-1396), neurosurgery (1397), maxilla-facial (182, 246, 812, 1398, 1399) and especially plastic and reconstructive [13e15] have published reports of examples of 3D printing being used in their fields. However, this technology has only slowly been adopted in general surgery.

3D printing should be of great advantage in liver surgery. Functional hepatic anatomy is separated into 8 segments known as Couinaud segments, labeled I to VIII, and defined in part by the course of the hepatic and portal veins (1400). Currently identification of these structures and delineation of hepatic segments relies on pre-operative imaging and intra-operative ultrasound. Resection of these various segments is mainly carried out for malignancies (metastatic and primary lesions) although various benign diseases may also be treated surgically.

The hepatocellular carcinoma (HCC) is the most common primary liver tumor with a prevalence in adults of 4.9 per 100,000 making it the 5th most commonly diagnosed gastrointestinal malignancy in adults (1401). HCC most commonly presents in patients with cirrhosis who have a reduced physiological reserve to with- stand major liver resection. This makes preoperative planning critical to minimize removal of liver volume and avoiding post- operative liver failure. More commonly, hepatic resection is per- formed for colorectal liver metastases (CRLM), that have a cumulative risk of 16% of distance metastasis spreading from the primary tumor within 5 years (1402). In appropriate patients, repeat hepatectomy following recurrence of CRLM may be feasible, and for this population preoperative planning and preservation of hepatic venous structures is of even greater clinical importance. This is also true for living-donor liver transplantation (LDLT) where the venous inflow and outflow to both the recipient and donor component livers must be maintained and therefore characterized with certainty, both pre- and intraoperatively. Currently, preoperative imaging with contrast-enhanced CT or MRI remains the most important planning tool for surgery (1403). Computer based 3D CT scans have been developed for pre-operative planning, however interpretation on a 2D

computer screen is inherently limited. We believe a 3D printed model will provide tactile (haptic) feedback to the user and facilitate spatial recognition of important structures.

Here, we report a systematic review of the literature and describe the use of a low cost 3D printer to create a liver model for a patient undergoing liver resection.

Methods

Systematic literature review

The PRISMA (36) statement was used to guide the systematic literature review. A checklist is available and attached. Ovid Medline (2006-present) and Pubmed (2006-present) databases were searched using the following terms and keywords alone or in combination: 3D printing, liver, Upper GI, general surgery. Inclusion criteria for studies to be included: published in English, available full text, about adults, about liver surgery and published between 2005 and 2015. Two independent reviewers decided the criterion in a standardized manner. Any disagreements were solved with consensus. Ultimately, six studies were found to be directly related to liver surgery and 3D printing that satisfies the inclusion criteria. The date last searched was on the 14th of June 2016. The data were extracted based on the Cochrane effective practice and organization of care, data collection form. Main information that was extracted involved what type of liver model was made, what type of 3D printer used and how it affected peri-operative outcome. In order to access risk of bias, we looked at variability of outcome in the studies as well as analyzed whether there were any possible external funding.

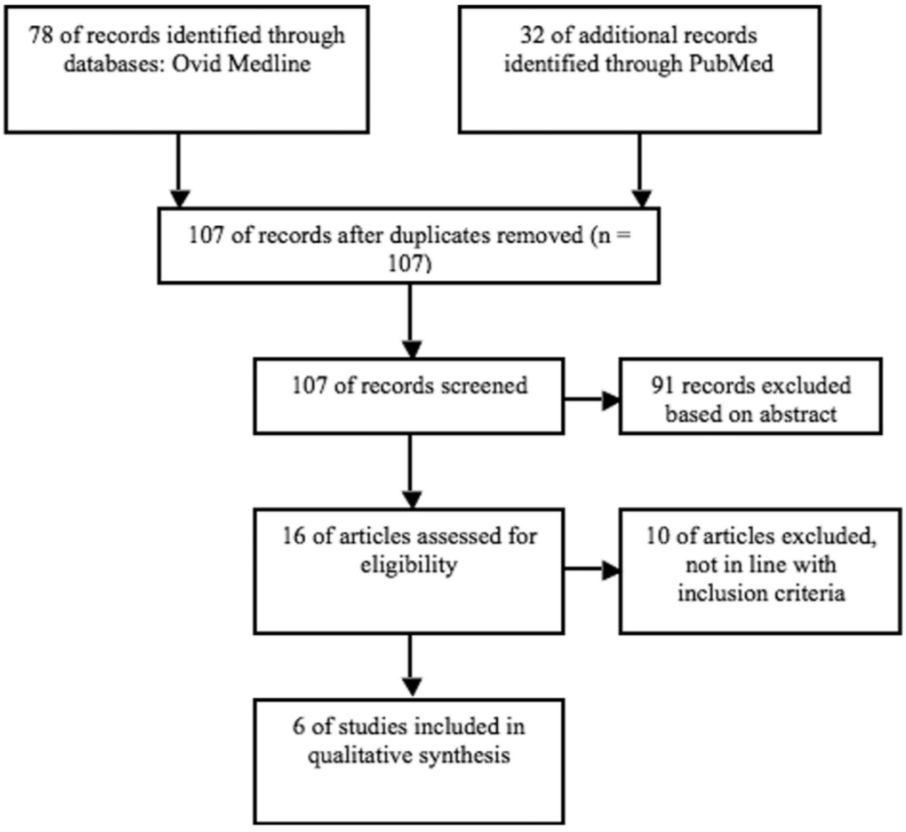

Figure 16.2.1.1: PRISMA flow diagram for study selection.

Printed 3D model

We used a 3D printer to create a model of a liver's venous vasculature and metastases for a patient undergoing liver resection to test the feasibility of using a low cost 3D printer for pre-operative planning. The conversion of 2D scan into 3D printing instructions are described in detail elsewhere (273). Briefly, a 70-year-old man presented with liver metastases from a colorectal primary in Couinaud segments 4a and 4b, segment 6 and outer segment 7. Thin, axial view slices (<1 mm) of his pre-operative CT scan were examined using Osirix software (Version 4.1, Pixmeo, Geneva, Switzerland). The Region of Interest (ROI) function was used to map the hepatic and portal veins and map the metastases. The ROI areas were projected as 3D structures to produce a surface area mesh and instruction for the 3D printer. The resultant model was then printed using a 3D printer (MakerBot Replicator Z18, US) with polylactic acid (PLA) filament. The print time was 32 hours and materials cost AUD 30. The end product was manually cleaned of all possible supporting plastic columns (needed for printing process) with forceps and sand paper.

Validation

The models were then validated by comparing the diameters of the inferior vena cava from the CT scan and comparing with those from the 3D printed model at 3 separate points (Figure 12.2.3.1.2a, b, c, d). As the data were normally distributed, the measurements were compared with a paired t-test.

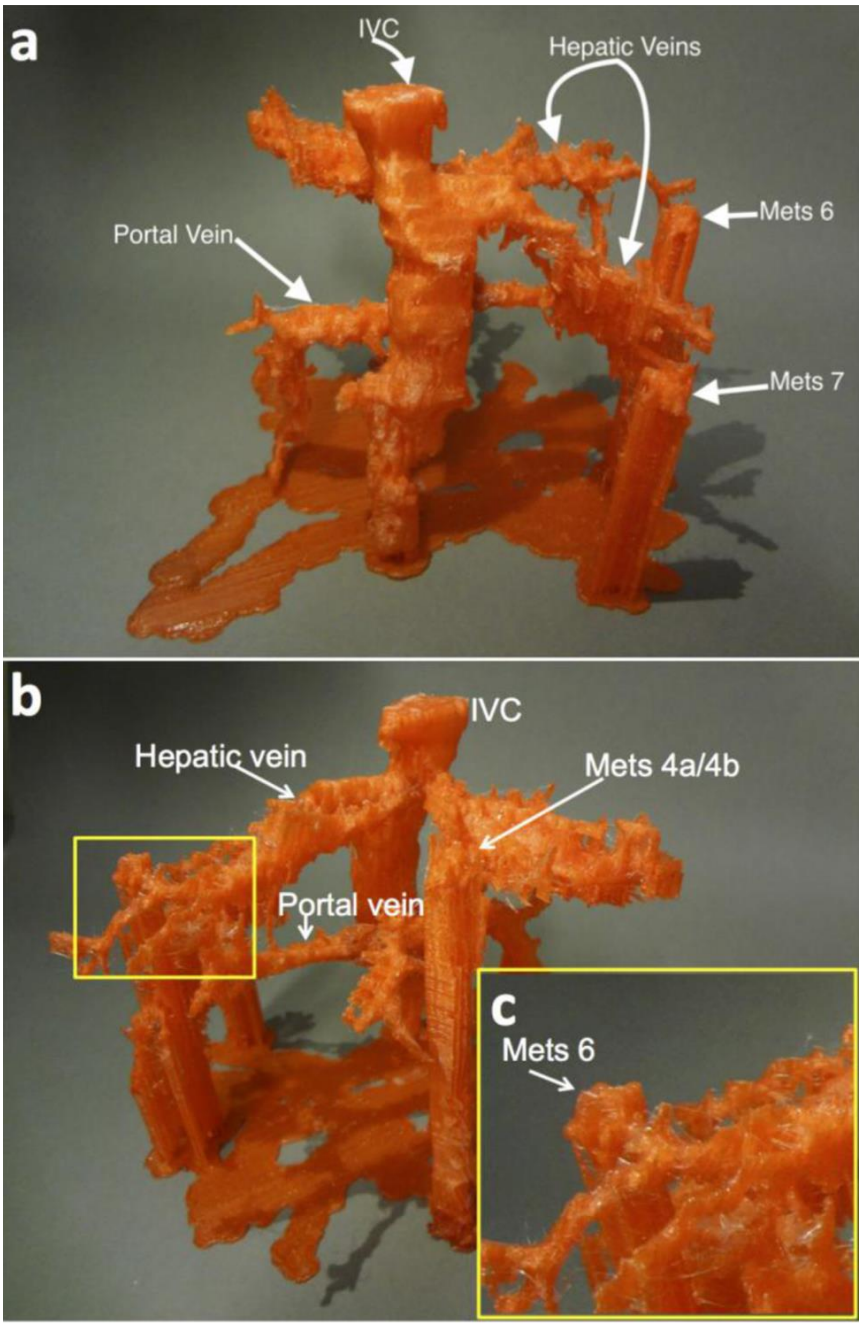

Figure 16.2.1.2. Posterior (a) and anterior (b) view of the printed 3D model. Metastases in different segments are labeled as metastasis (mets) 4a/4b, 6 and 7. Inferior vena cava labeled as IVC. Magnified view of metastasis in segment 6 (c).

Results

Only six articles (190, 219-221, 1404, 1405) reported the use of 3D printing to produce anatomical liver models for liver surgery. Ovid Medline and Pubmed databases provided a total of 110 articles. After removing duplicates only 107 remains. Of these, after reading the abstract we excluded 91 papers as they were not related to the liver and 3D printing. 16 studies were examined further. However ten of the articles did not meet the earlier specified inclusion criteria. Three articles were excluded as they were done in a paediatric population, one article was in mandarin, two articles were not performed for hepatobiliary surgery and four articles did not have full text available. No unpublished relevant data was obtained.

Zein *et al* (221) showed that it was possible to 3D print an ac- curate model of a whole liver. They found their model vascular structure was accurate to ±1.3 mm and the whole liver ±4 mm compared to the patient's actual liver. The second article by Igami *et al* (219) described small liver tumours that were undetectable with conventional intra-operative ultrasound could be located using a 3D printed model. Following chemotherapy and the resultant shrinkage of the liver tumour, there is difficulty in tumour detection using intra-operative ultrasound. Therefore a pre- chemotherapy 3D printed model could guide surgeons towards the margins of these small liver tumours. Quintini *et al* (1404) discussed the potential of using a 3D printer to prevent complications in Living Donor 3D transplantations such as “large-for-size syndrome”. They also discussed the potential for 3D printers to be used in hepatobilliary anatomy as an educational tool, where 3D models would provide visual stimulation and tactile feedback during pre- operative planning. Another paper by Nan Xiang *et al* (1405) discussed the benefits of 3D printing in variable portal vein anatomy. By having a 3D model, they discovered a congenital absence of the segment IV of the portal vein, which was close to the tumour. This resulted in a decision to perform a narrow margin hepatectomy to avoid necrosis of segment IV and led to a good postoperative margin outcome. Watson (190) showed it was possible to reproduce liver vasculature using a low cost approach. The review article of Ikegami *et al* (220) highlighted the application of 3D printing in medicine and the many potential benefits of 3D printing in hepatic resections. The focus of this article was on the benefit of overcoming “large-for-size syndrome” during living donor liver transplantation. As this is still a relatively new area of research, there could be observation bias. Researchers are keen that this particular

technology could be a breakthrough and may tend to over-estimate the benefits it could provide.

Printed model

The model took 32 h to print (Figure 12.2.3.1.2). Note that the metastases (Figure 12.2.3.1.2a, b and c) are held up with remaining vertical supporting structures. The metastases are labeled according to the Couinaud segments as metastasis (mets) 4a/4b, 6 and 7 respectively. Fig. 1c shows a magnified view of the metastasis in segment 6 (Figure 12.2.3.1.3).

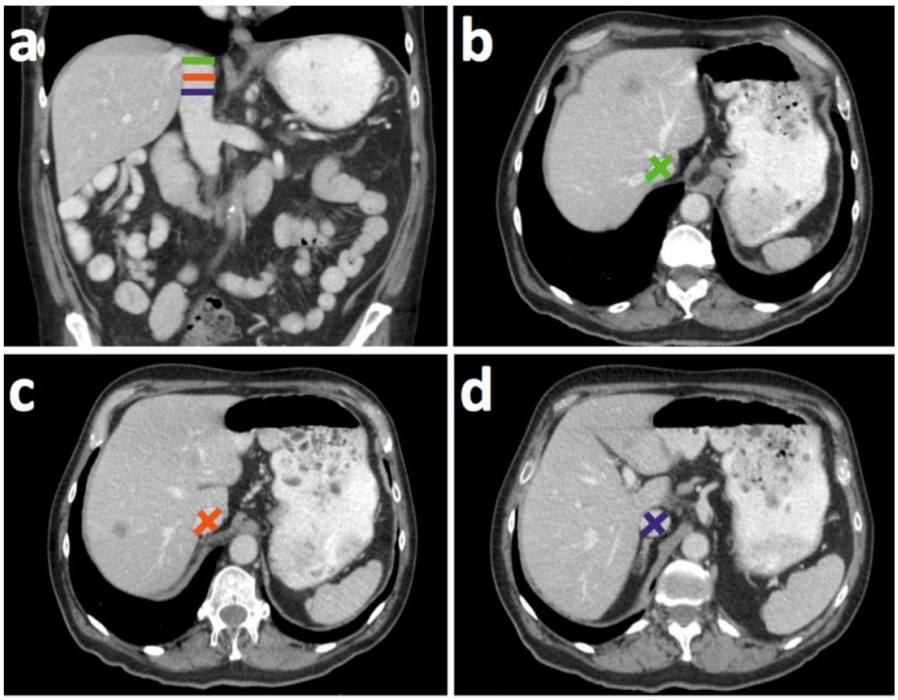

	Measurements from CT (Transver se diameter x Longitudinal diameter)	Measurement from 3D model at corresponding points
b	2.4 x 1.6 cm	2.3 x 1.4 cm
c	2.5 x 1.7 cm	2.4 x 1.6 cm
d	2.5 x 2.0 cm	2.5 x 1.9 cm

Figure 16.2.1.3: CT scan in coronal view (a). Points of measurements in axial view, taken transverse and longitudinal (b, c and d) are colour-coded accordingly. Measurements plotted comparing measurements in CT versus 3D printed model.

Measurements were taken from three points 1 cm apart, beginning from the junction of the hepatic vein and inferior vena cava. This can be appreciated from Figure 2a, where color-coded lines show where the measurements are taken from. Green, orange and blue measurements drawn on Figure 2b, c and 2d show the position of the axial measurements taken from the CT scan respectively. Comparison of diameters measured from the CT and 3D model at the corresponding points had on average an accuracy margin of 0.1 ± 0.06 mm (mean ± standard deviation) which was statistically significantly different from the scan measurements by a paired t- test, $P < 0.05$).

Clinical use

The model was available in the operating theatre on the day of surgery. A left lateral hepatectomy, right-sided localized wedge resection and radio frequency ablation of segment 6 was per- formed. The patient was shown the model pre and post operatively with simple explanation and reported that the model has helped his understanding of the surgery that was performed. Theatre nursing staff reported that the model assisted their understanding of the intended operation, as did the surgical fellow and registrar. The training surgeons felt the model helped in their understanding of the complex operative anatomy of the liver and also in what to expect intraoperatively as the hepatic parenchyma was divided in terms of encountering structures in 3 dimensions and real time. The consultant surgeon reported that the resolution of vessels and their relationship to the metastases was inadequate to plan surgery upon, but agreed that the model had educational and training ad- vantages for junior staff.

Discussion

3D printing in liver surgery is a promising new tool for surgical planning. Our review identified six studies directly related to liver 3D imaging. In these studies, cost and time were the major limiting factors in producing a reliable model. We have shown the technique is feasible and with improvements in accuracy, models may aid preoperative planning for liver resections. This not only aids the operating surgeon, but also aids all theatre staff involved in the operating theatre.

Hepatic resections are challenging operations because of the complex nature of hepatic and venous anatomy within the liver. Preoperatively, CT scans and/or MRI's are obtained from all patients to document tumor distribution, estimate future liver remnant volume and to identify tumor-vessel relationships in order to anticipate intraoperative vascular anatomy (1403). An early step in most hepatic resections is the identification of important vascular structures and tumor deposits using intraoperative ultrasound. With 3D printed haptic models, the surgeon has an additional aid to more accurately visualize individual livers. A 3D model could also potentially facilitate interaction between patients and doctors; operative anatomy could be explained more easily with the model, thus aiding the consent process (1406).

In our hospital, we were able to print a structure of a hepatic and portal vein in relation to metastasis using a commercially available 3D printer costing AUD 10,000 that was already available in the hospital. Ultimately, the cost of printing the structure was AUD 30 for the cost of the plastic used for the model. We have also validated our model by comparing the 3D printed model to the CT scan.

Comparing our study with the studies already available in the literature, our study mainly demonstrated that production of a relatively in-expensive yet accurate 3D model is possible. The model was also well received by various members of healthcare staff and patient. Therefore, it would be a good opportunity to investigate this further in future studies to look at the benefits of patient and workplace education by using 3D printed models. The other present reviews mainly discuss the peri-operative benefits for the surgeon. We were also able to drastically reduce cost compared to the other studies. The 3D printer our institution used in our study is almost 30 times less in cost compared to the 3D printers used by other studies. However, a limitation of our current model includes not

having a liver capsule, which could confuse the anatomical orientation of the model and an aspect that could be improved. Another limitation of our study is that we only managed to produce a 3D model in a single patient. In the future, we plan to expand the scope of this research by increasing the number of patients using this form of technology and also involvement of other surgical specialties.

Conclusion

In summary, 3D printing in liver surgery is a promising new tool for surgical planning. Our review identified six studies directly related to liver 3D imaging. However, in these studies, cost and time were the major limiting factors in producing a reliable model. We have shown the technique is feasible and applicable to liver resection in principle and with improvements in fidelity of modeling may aid preoperative planning for liver resections.

16.2.2 Customised Shoe Filler in Amputees

Chapter Summary

Introduction: Podiatry has seen exponential growth in the use of 3D (three-dimensional) scanning and printing in the clinical domain. We describe a new method of prosthetic construction using 3D printing.

Method: Using CT (computed tomography) and MRI (magnetic resonance imaging) scan data, custom-made shoe fillers are 3D-printed for people undergoing transmetatarsal or toe amputation at Peninsula Health's High Risk Foot Clinic.

Results: Customised 3D-printed shoe fillers improved shoe-fitting at a much lower cost compared to conventional techniques (AUD 30 vs 300).

Conclusion: 3D printing is an exciting frontier in podiatry with numerous potentials that need to be explored in future studies.

Introduction

Advanced and new technologies within the health sector are aimed to increase efficacy and reduce cost. As a profession, podiatry has seen exponential growth in the use of 3D (three-dimensional) scanning in the clinical domain. It has been used within orthotic manufacture to improve timely responses in both production and rapid dispensing. It has also been used within research to better understand foot structure and function.

3D printing is the next technological step, which will impact the podiatric management of common disorders. This presentation explores its potential uses and describes a new method of prosthetic construction based on 3D printing methodology.

Method

The use of 3D printing technology for pre-operative planning is well established at Peninsula Health across multiple surgical disciplines. The 3D-printed models generated from CT (computed tomography) and MRI (magnetic resonance imaging) scans are currently undergoing validation clinical trials. The combination of 2D imaging and 3D haptic models can be useful in podiatry, specifically in the production of custom-made shoe fillers for people who have undergone transmetatarsal amputation or toe amputation. This process is currently being studied within Peninsula Health's High Risk Foot Clinic with the support of Department of Surgery.

Results

The use of a shoe filler to improve shoe fitting is a common practice following amputation, however it is associated with a high cost ($500-$800 per patient). We describe the use of a 3D rendered CT image of the foot within the shoe that enables a 3D printed shoe filler to be constructed at an estimated cost of $30. Our assessment of the practical use of these shoe fillers, durability and patient acceptance will be presented.

Conclusion

3D printing has a role in podiatry however the application, its advantages and disadvantages are yet to be fully explored. This new and innovative technology introduces exciting future opportunities in the clinical setting.